Determination of atmospheric trace gas amounts and corresponding natural isotopic ratios by means of ground-based FTIR spectroscopy in the high Arctic

---

Arndt Meier

Ber. Polarforsch. 236 (1997)
ISSN 0176 - 5027

Arndt Meier[1]

Alfred–Wegener–Institut für Polar– und Meeresfoschung
Forschungsstelle Potsdam
Telegrafenberg A43
D-14473 Potsdam

Die vorliegende Arbeit ist die inhaltlich unveränderte Fassung einer Dissertation, die im Dezember 1996 an der Naturwissenschaftlichen Fakultät der Technischen Universität Carolo-Wilhelmina zu Braunschweig zur Erlangung eines Grades Doktor der Naturwissenschaften eingereicht wurde.

This report, as regards contents, is the unchanged reprint of a dissertation submitted for a doctor of science to the faculty of natural sciences of the technical university *Carolo-Wilhelmina zu Braunschweig* in december 1996.

[1]Since October 1996 at *Institutet för Rymdfysik* (IRF), Box 812, S-98128 Kiruna, Sweden, email: ameier@irf.se

Contents

List of abbreviations used:

a.m.s.l.	Above main sea level, geometric altitude above normal zero
AWI	*Alfred–Wegener–Institut für Polar– und Meeresforschung* Alfred–Wegener–Institute for Polar– and Marine Research
DIN	*Deutsche Industrie–Normen:* German Industrial Standard
DMI	Danish Meteorological Institute, Copenhagen
DOS	Any computer operating system for PCs compatible to MS–DOS $\geq$3.3 from Microsoft Corp. (trademark)
DOSA	Degree of subsidence/ascent, dimensionless parameter defined in section 4.4 (equation 49, page 86)
DU	Dobson Units, 1 $DU = 2.6868 \cdot 10^{16}\, cm^{-2}$
EASOE	European Arctic Stratospheric Ozone Experiment (winter/spring 1991/92)
ECC	Electrochemical concentration cell (ozone sonde sensor)
ECMWF	European Center for Medium–range Weather Forecast
FTIR-	Fourier Transform InfraRed ...
FTS	Fourier Transform Spectrometer
FWHM	half width of a spectral line: Full Width at Half Maximum
IBM	International Business Machines Corp. (trademark)
ILS	Instrumental Line Shape, response of a real spectrometer to an ideal monochromatic spectral line
LIDAR	LIght Detection And Ranging instrument
NASA	US National Aeronautics and Space Administration
NCAR	National Center of Atmospheric Research at Boulder
NDSC	Network for Detection of Stratospheric Change, coordinated by the NASA Langley Research Center at Hampton
NILU	Norwegian institute for air research, *Norsk Institutt for LUftforskning*, Oslo
NPL	National Physics Laboratory, Teddington, UK
OPD	(Maximum) Optical Path Difference
PC	Personal computer
pT–	Pressure–temperature (profile)
PVU	Potential vorticity units, 1 $PVU = 1 \cdot 10^{-6} K m^2 s^{-1} kg^{-1}$

SESAME	Second European Stratospheric Arctic and Mid-latitude Experiment
SFIT	Spectral FITting program, software package by *C. Rinsland* (NASA) for the analysis of ground–based FTIR–spectra
S/N	Signal–to–Noise ratio
SI	*Système International d'Unités*: International system of metric units (m, kg, s, A, K, mol, and cd)
SPA	Stratopause altitude
TPA	Tropopause altitude
UV	Ultraviolet (radiation)
VMR	Volume Mixing Ratio
WMO	The World Meteorological Organisation
ZPD	Zero Path Difference

List of symbols used:

Throughout this manuscript metric SI units are used exclusively, except for the wavelength where its reciprocal, the wavenumber, is used. The valid DIN rules are followed wherever possible for notations, layouts, and typefaces and might occasionally differ from US or British standards. In cases of differences in spelling between US and Oxford English, the British variant is preferred, as given by *Breitsprecher* et al. (1986) and by *Weiner* and *Hawkins* (1989). Fundamental constants are taken from *Cohen* and *Taylor* (1986).

$B(x)$	1	Boxcar-apodisation function
$b(\nu)$	1*	The Fourier transform of $B(x)$
c	m/s	The speed of light ($2.99792458 \cdot 10^8\, m/s$)
$\delta(\xi)$	1*	Dirac's Delta–functional
$\mathcal{F}^{-1}\{..\}$	1†	Inverse Fourier transform of $\{..\}$
h	Js	Planck constant
		$6.6260755(\pm 0.0000040) \cdot 10^{-34}\, Js$
$I(x)$	W/m^2	Intensity of the interferogram
k_B	J/K	Boltzmann constant
		$1.380658(\pm 0.000012) \cdot 10^{-23}\, J/K$
L	m	OPD, maximmum optical path difference
λ	m	Wavelength of light
ν	cm^{-1}	Wavenumber, reciprocal of the wavelength
$p(z)$	Pa	Pressure as function of geometric altitude z
Q	$K\, m^2\, s^{-1}\, kg^{-1}$	Potential vorticity
$S(\nu)$	1	Relative spectral intensity
t	s	Time
T	K	Temperature
Θ	K	Potential temperature
$Tri(x)$	1	Triangular apodisation function
$\Delta trop$	km	Vertical displacement of the tropopause
$\Upsilon(x)$	1	Shah–Function
x	m	Spatial pathlength
z	m	Geometric altitude above normal zero

*The dimension depends on the dimension of the argument and is given by its inverse.
†The dimension depends on the dimension of the independent variable

Abstract

In the given report, scientific results gathered at the *Alfred–Wegener–Institut für Polar– und Meeresforschung* (AWI) within an ScD contract are summarized. The AWI is the German large scale research facility for polar– and marine research. In January 1992 the new research department at Potsdam has been established with the section *Physics and Chemistry of the Atmosphere*. It coordinates the activities at the German polar research station *Carl Koldewey* on Spitsbergen (79°N, 12°E), which is a primary site of the *Network for Detection of Stratospheric Change* (NDSC). Data recorded at this arctic research facility make up an important basic contribution to this report.

There are a lot of different measurement techniques and gauges available to detect atmospheric gases. The main topic in this work is the ground–based Fourier–Transform Infrared (FTIR) spectrometer. With the instrument introduced in chapter 1, more than 25 different chemical species abundant in our atmosphere can be quantified with high quality in terms of their total column amount. Additionally, information on the vertical distribution and on natural isotopic ratios are derivable for selected molecules.

The operational principle of an ideal FTS (Fourier transform spectrometer) and the limitations to real instruments are described in the first chapter. In the following chapter, the principles of the measurement and the analysis procedure are introduced. Basically, information is derived from the comparison of a simulated atmosphere with the recorded interferogram that has been Fourier transformed to a spectrum. In the third chapter, improvements to the standard analysis procedure are discussed to increase the scope and quality of derivable results. This includes the correction of emission that adds to the absorption signal and becomes significant in lunar spectra. Further, the use of information available from other instruments like radio– and ozone–sondes for the model atmosphere is discussed as well as the formulation of strategies for deducing information on the vertical distribution of trace gases, because the volume mixing ratio (VMR) profiles are usually not known *a priori* as has to be assumed in the standard analysis.

Chapter 4 gives a description of the polar atmosphere. After a brief introduction to the basic dynamics, the principles and the efficiency of the computer programs developed to deduce information on the VMR profiles of selected trace gases are illustrated by results from the participation in the intercomparison experiment of the NDSC performed with synthetic spectra. In the two remaining sections of the chapter, these algorithms are applied to real data. First, the conditions in early arctic summer are described that offer the most favorable conditions for recording spectra and the dynamics of the atmosphere are the least complex in this period. The last section deals with data obtained in early spring and include solar and lunar spectra recorded within 12 h. It is the first direct comparison of solar and lunar FTIR spectra reported so far. However, the comparison is not straightforward due to the very high dynamical activity of the atmosphere, the possibility of extensive chemical processing, and the restrictions that apply to the recording geometry due to the very low position of the sun just after the end of the polar night.

In the next chapter, results from the study of natural isotopic ratios are presented. After a brief introduction to natural isotopic fraction processes, results from the study of water vapor isotopomers are presented and isotopic studies in methane and HCl are discussed. An isotopomer is a molecule that contains a rare isotope, e.g. HDO with one deuterium atom replacing a hydrogen atom. The second half of the chapter is devoted to the detailed study of isotopic abundances of ozone. The quality of isotopic ratios is shown to have improved by one order of magnitude compared to previous works and is ascribed to the improvements introduced in chapter 3 and 4. This allows for the first time to quantify a significant symmetry–selective isotopic anomaly in stratospheric ozone by means of a ground–based optical instrument. Moreover, it is so far the first report that includes observations from polar night, which reveals important details about the mechanisms causing the anomaly. The observed isotopic signal gives strong evidence for a new symmetry selective fractionation process in contrast to known fractionation processes that all depend exclusively on mass. Nevertheless, the theoretical understanding of ozone formation is still incomplete and the necessary modifications to theory to account for the observed isotopic signals may become relevant in the global ozone discussion, since each ozone molecule in sunlit air

masses is destroyed and reformed in the middle and upper stratosphere every 15 to 30 minutes on the average.

A summary of the main conclusions is given in the final chapter. Prospects on future tasks conclude the main part of this report. The appendices A and B give additional details on the observation site and on the software that is developed. Appendix C consists of an atlas showing some 60 spectral microwindows used in the analysis. Besides 2 figures per interval showing a typical fit and the individual contributions from interfering species, additional hints on parameter settings used in the retrieval are listed.

Introduction

The atmosphere of our planet contains numerous gases. Near the surface the most abundant constituents of dry air are molecular nitrogen (N_2) and oxygen (O_2), making up roughly 78 % and 21 % vol., respectively, of all gas molecules. Taking into account water vapor and the inert gas argon additionally, these make up more than 99.6 % vol. of all gaseous particles in the troposphere and stratosphere. The remaining atmospheric constituents of some several hundred detectable species make up a total of less than 0.5 % both in volume and in number density. That is why they are summarized by the term *trace gases*. The most abundant species among these trace gases is the carbon dioxide CO_2 with a concentration of about 0.036 % or 360 *ppm* vol. in the lower troposphere. Nevertheless, these minor amounts of trace gases play the key role in the determination of the energetic radiance balance of planet earth and they are important to the chemical removal processes in the atmosphere. The average surface temperatures are approximately 33 K higher, than one might expect in the absence of all trace gases including water vapor (*Schönwiese*, p. 118, 1991). The role of trace gases in the blocking of harmful radiation is of comparable importance. The ultraviolet solar radiation, for instance, is reduced to a biologically tolerable amount at the surface by essentially stratospheric ozone.

The atmosphere underlies inevitably natural variability, because it is part of a complex biogeochemical cycle and it is influenced additionally by variable extraterrestrial parameters, like the 11–year solar–cycle. This variability has a lasting effect on the biosphere and on survival of mankind and can be experienced on largely different time scales, e.g. by the occurrence of glacial and interglacial epoches or in daily weather. This is a sufficient reason by itself to call for a scientific understanding of atmospheric processes, but interest has turned into increasing concern about future living conditions not only among scientists, but also in the public in recent decades. Since numerous scientists have revealed evidence on the fact that the impact of human action on the environment has a significant effect on the atmosphere, the question on the nature and extent of both natural and anthropogenically caused variability has arisen.

Based on laboratory studies, a high number of relevant chemical reactions and the radiative properties of the individual trace gases are generally well understood. Thus, present questions focus on a better understanding of the quantitative spatial distribution of all relevant gases in the atmosphere and their changes with time, to serve as a basis for the prediction of the further evolution of the atmosphere and its implications for life on our planet. That does require improvements in our present knowledge of the dynamics of the atmosphere, the understanding of chemical reaction cycles and determination of the involved rate constants, the role of aerosols, the microphysics of cloud formation, heterogeneous chemical reactions on the surface of clouds and aerosols, cycles of exchange with the oceans, the soil, and the biosphere – to name only a few important items. The complexity of the complete atmospheric system with its uncountable numbers of nonlinear feed–back mechanisms adds further to the difficulty of the task. The total number of scientific publications on the whole item is immense and for a lead–in one may refer to *Houghton* (1984), *Roedel* (1988), *Schönwiese* (1991), *Brasseur* and *Solomon* (1992), *Cubasch* (1992), and *Solomon* (1990).

The global scale of the consequences of atmospheric changes has encouraged a world–wide scientific cooperation that led to the setting–up of global data banks, global long–term monitoring programs, and highly international research campaigns. Besides the participation in European research campaigns like EASOE (*European Arctic Stratospheric Ozone Experiment*) and SESAME I & II (*Second European Stratospheric Arctic and Mid-latitude Experiment*) the integration into the *Network for Detection of Stratospheric Change* (NDSC) has gained major importance for research carried out at AWI Potsdam. The NDSC is designed for the long–term, global documentation of variability in the stratosphere and the investigation of underlying principles. This is achieved by combining a set of different detector systems at each observation site. The primary sites of the net consist of a ground–based IR–spectrometer, a passive microwave radiometer, a LIDAR (*light detection and ranging*) instrument, a UV/VIS spectograph and regular ECC ozone sondes. Besides the primary stations of the NDSC, which make up only 5 sites worldwide, there are numerous secondary sites that operate at least one of these instruments on a regular basis.

1 Instrumentation

1.1 The ideal Fourier–Transform spectrometer

1.1.1 The principles of construction and signal gain

There have been published numerous text and reference books as well as many specific articles in journals on the principles of FTIR–spectroscopy. Commercial instruments for almost any purpose are commonly purchasable. Hence, the following subsections are intended to give a general introduction only, to illustrate the basic ideas. Little attention is drawn to a complete mathematical description. Instead, items of relevance to the experimentalist are given priority. For a comprehensive description of basic FT–spectrometry, *Bell* (1972), *Beer* (1992), *Perkins* (1986), *Gronholz* and *Herres* (1984) and *Brault* (*"Fourier Transform Spectrometry"*, unpublished manuscript of lectures given at Berkeley by *James W. Brault*, National solar observatory, Tucson, Arizona) are recommended.

Contrary to grating– and prism spectrometers, the FTS does not directly split up the incident light into a spectrum. Instead, an interferogram is recorded from which the spectrum is computed. The wanted spectral intensity in coordinates of wavenumbers can be expressed as the Fourier transform of the intensity of the interferogram which is recorded as a function of spatial coordinates (see below). The description of spectral features in terms of wavenumbers in units of cm^{-1} is used in preference to the SI conform wavelength in m in this thesis. This is done for convenience, because the spectrometer software, the data analysis software from NASA and the huge spectroscopic data base is given in wavenumbers only. The wavenumber ν is defined by the reciprocal of the wavelength λ (without a factor of 2π).

In principle, an FTS consists of a Michelson interferometer or technical variants of it, as illustrated in Figure 1.1. The incident light is formed into a parallel beam by the entrance optics and is then splitted by amplitude by the beamsplitter to form two secondary beams. After the reflection from the fixed and the movable mirror, the two beams interfere at the detector with a path difference as given by the displacement of the mov-

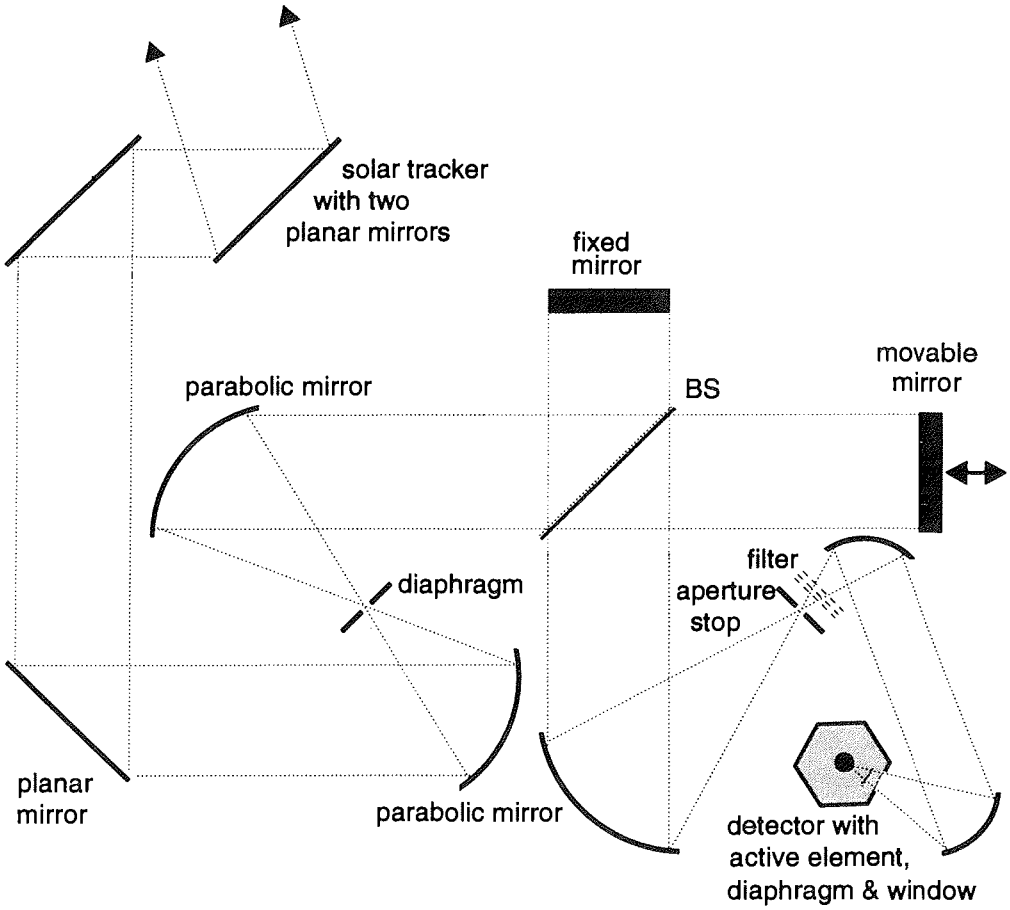

Fig. 1.1: *Sketch of the FTIR–spectrometer used: The solar tracker actively follows the position of the sun (or moon) with its mirror system, allowing for a homogeneous input of solar radiation into the spectrometer. The incident light is formed into a parallel beam by the pair of parabolic mirrors at the entrance of the instrument, which then enters the actual Michelson interferometer consisting of the beamsplitter (BS), the fixed and the movable mirror and the detector optics. The aperture stop and optional optical filters are placed between beamsplitter and detector.*

able mirror relative to the fixed mirror. Hence the detector produces an intensity signal modulated by the optical path difference (OPD) of the two interfering secondary beams. In first approximation, the optical path difference is proportional to two times the displacement x of the movable mirror. Strictly speaking, this relation is exact for monochromatic interferograms only, because dispersion in the beamsplitter or other optical elements like filters introduce wavenumber depen[illegible] phase delays that affect the shape of a typical broadband interferogram (see section 1.2). However, the phase delay caused by the beam splitter is kept very low by adding a compensator made of the same material as the beam splitter substrate and of same thickness under the same angle into the interferometer arm where light crosses the beamsplitter substrate only once.

Let the optical paths be identical between the beamsplitter and both the fixed and the movable mirror in the beginning. Assuming a refraction index of 1 for air and that the movable mirror is displaced by an amount of x parallel to the optical axis, an optical retardation equal to $2 \cdot x$ is caused between the two secondary beams. Due to spatial coherence, an interference pattern is formed at the detector as a function of the path difference $2x$. For any discrete wavenumber ν_i, constructive interference occurres whenever the OPD is an integer multiple of the wavelength λ_i, i.e.:

$$2 \cdot x = n \cdot \lambda_i = n/\nu_i \quad (n = 0, 1, 2, 3, ...). \tag{1}$$

Destructive interference occurs for any OPD that is an odd multiple of half the wavelength.

Let R be the coefficient of reflection and T the coefficient of transmission of the beamsplitter. The amplitude of the electromagnetic wave at the location of the detector can be described by the superposition of the two secondary beams by the relation:

$$A(x_1, x_2, \nu) = R \cdot T \cdot \hat{A}(\nu) \cdot \left\{ e^{i(\omega t - 2\pi\nu x_1)} + e^{i(\omega t - 2\pi\nu x_2)} \right\}. \tag{2}$$

However, it is the intensity not the amplitude that can be measured. The intensity of the interferogram $I(x_1, x_2, \nu)$ is a real and not a complex quantity, which is given by the square of the amplitude. For a monochro-

matic point source this can be written as

$$I(x_1, x_2, \nu) = A(x_1, x_2, \nu) \cdot A^*(x_1, x_2, \nu) \quad (3)$$

$$= 2 \cdot |R \cdot T|^2 \cdot \hat{A}^2(\nu) \cdot \{1 + cos\,(2 \cdot \pi \cdot \nu \cdot (x_1 - x_2))\}\,. \quad (4)$$

The exact position of the movable mirror has to be known with high precision while recording the interferogram. Taking advantage of equation (4), the beam of a frequency stabilized monochromatic laser is added to the interferometer. Knowing the exact frequency of the laser, the relative displacement of the movable mirror can easily be calculated by simply counting the interference fringes of the laser beam. Simultaneously, the signal from the laser can be used for the absolute frequency calibration of the spectrum. This is known as the *Connes* advantage of FT instruments. All path differences are measured relative to the maximum of the interferogram, which gives the zero path difference (ZPD). Only in the case of ZPD, all frequencies interfere constructively.

Let us denote the OPD between the two secondary beams by $x = x_1 - x_2$, the spectral intensity simply by $S(\nu)$, and extend the whole description to non–monochromatic sources. Taking advantage of the superposition principle, the intensity $\tilde{I}(x)$ recorded in the interferogram is then described by the integral of $S(\nu)$ over all wavenumbers:

$$\tilde{I}(x) = 2 \cdot |R \cdot T|^2 \cdot \int_0^{+\infty} S(\nu) \cdot \{1 + cos(2 \cdot \pi \cdot \nu \cdot x)\}\, d\nu \quad (5)$$

$$= 2 \cdot |R \cdot T|^2 \cdot \left\{ \int_0^{+\infty} S(\nu) \cdot cos(0)\, d\nu + \int_0^{+\infty} S(\nu) \cdot cos(2 \cdot \pi \cdot \nu \cdot x)\, d\nu \right\}. \quad (6)$$

The first integral expression in equation (6) is constant in x and equals the intensity of the interferogram for a path difference of zero, where the maximum of the interferogram is located. The second integral on that line describes the modulation of the signal as a function of the OPD. Given an ideal beamsplitter that splits up the incident light among the two secondary beams at any wavenumber equally, i.e. $R = T = 1/\sqrt{2}$, the interferogram can be rewritten as

$$\left[\tilde{I}(x) - \tfrac{1}{2}\tilde{I}(0)\right] = 2 \cdot \frac{1}{4} \cdot \int_0^{+\infty} S(\nu) \cdot cos(2 \cdot \pi \cdot \nu \cdot x)\, d\nu. \quad (7)$$

The intensity $\tilde{I}(x)$ is a directly measurable quantity and thus *real* in the mathematical sense. As a consequence, $S(\nu)$ has to be Hermitian (*Bell*,

1972, chapter 3), i.e. the equation

$$S^*(\nu) = S(-\nu) \tag{8}$$

is valid. With this relation and *Euler's* theorem applied to equation (7), the right hand side of equation (7) can be transformed into a Fourier integral:

$$\begin{aligned}
[\tilde{I}(x) \;-\; \tfrac{1}{2}\tilde{I}(0)] &= \frac{1}{2}\cdot\int_0^{+\infty} \mathrm{Re}\,[S(\nu)\cdot exp(i\cdot 2\pi\nu\cdot x)]\,d\nu && (9)\\
&= \frac{1}{2}\cdot\int_0^{+\infty}\left[\left\{\frac{1}{2}\cdot S(\nu)\cdot exp(i2\pi\nu\cdot x)\right\}^* + \frac{1}{2}\cdot S(\nu)\cdot exp(i2\pi\nu\cdot x)\right] d\nu && (10)\\
&= \frac{1}{4}\cdot\int_{-\infty}^{0} S(\nu)\cdot exp(i2\pi\nu\cdot x)\,d\nu + \frac{1}{4}\cdot\int_0^{+\infty} S(\nu)\cdot exp(i2\pi\nu\cdot x)\,d\nu && (11)\\
&= \frac{1}{4}\cdot\int_{-\infty}^{+\infty} S(\nu)\cdot exp(i2\pi\nu\cdot x)\,d\nu. && (12)
\end{aligned}$$

The limits of the integral are given in the desired form for writing the Fourier integral pair which describes the relation between the recorded interferogram and the desired spectrum:

$$\begin{aligned}
I(x) &= \tilde{I}(x) - \tfrac{1}{2}\tilde{I}(0) = \frac{1}{4}\cdot\int_{-\infty}^{+\infty} S(\nu)\cdot exp\{i\cdot 2\cdot\pi\cdot\nu\cdot x\}\,d\nu && (13)\\
S(\nu) &= 4\cdot\int_{-\infty}^{+\infty}\left[\tilde{I}(x) - \tfrac{1}{2}\tilde{I}(0)\right]\cdot exp\{-i\cdot 2\cdot\pi\cdot\nu\cdot x\}\,dx. && (14)
\end{aligned}$$

1.1.2 Apodization and instrumental line shape

Since in real spectrometers the maximum OPD L is finite (mechanical size) and since the interferogram can be recorded with a finite stepsize Δx only, equation (14) cannot be used directly in the form given. Let us consider the consequences of a finite maximum OPD first, i.e. the consequences of apodization. Mathematically, a finite OPD can be introduced into equation (14) by multiplying the intensity $I(x)$ with a function $B(x)$ which has the characteristics of being unity throughout the interval $[-L, L]$ and being zero outside this interval.

$$\tilde{S}(\nu) = \int_{-\infty}^{+\infty} I(x)\cdot B(x)\cdot exp\{-i\cdot 2\cdot\pi\cdot\nu\cdot x\}\,dx. \tag{15}$$

The function $B(x)$ is known as the boxcar or instrumental line shape (ILS) function, because it effects the answer of the FTS to a recorded

spectral line. Instead of $B(x)$ one can use any other function with the properties of being even, i.e. $f(x) = f(-x)$, being zero outside the interval $[-L, L]$, and being positive and continuous throughout $[0, L]$. Common apodization functions are triangular, trapezoidal, $cos^2(x)$, weak and strong Norton–Beer (*Gronholz* and *Herres*, 1985). However, the boxcar function is the most simple apodization function and preserves the maximum of information from the interferogram for a given maximum OPD.

The convolution theorem of Fourier theory states that *"the Fourier transform of a convolution of two functions is proportional to the product of the individual transforms and conversely the Fourier transform of a product of two functions is proportional to the convolution of their individual transforms"* (*Champeney*, p. 73, 1973). The Fourier transform $b(\nu)$ of the ILS $B(x) = 1/(2L)$ for $x \in [-L, L]$ is known analytically (e.g. *Bell.* 1972):

$$\mathcal{F}^{-1}\{B(x)\} = b(\nu) = \frac{sin(2 \cdot \pi \cdot \nu \cdot L)}{2 \cdot \pi \cdot \nu \cdot L} = sinc(2 \cdot \pi \cdot \nu \cdot L). \qquad (16)$$

Thus, with the convolution theorem and equations 15 and 16 the relation between the desired spectrum $S(\nu)$, the FT $b(\nu)$ of the apodization function $B(x)$, and the convolved spectrum $\tilde{S}(\nu)$ is given by:

$$\tilde{S}(\nu) = S(\nu) \otimes b(\nu). \qquad (17)$$

The effect of apodization on an ideal monochromatic laser beam is illustrated in Figure 1.2 for the boxcar and for the triangular apodization function $Tri(x)$, which is defined by $Tri(x) = 1 - |x|/L$ for $x \in [-L, L]$. In the upper part of the figure, the interferogram is shown after apodization. The lower part illustrates the effects on line shape and resolution. For both apodization functions the half width of the recorded line is significantly increased and is discussed in the next section in detail. Additionally, the occurrence of the so called sidelobes with negative intensities is striking. Their presence is unfavorable in the analysis of crowded spectral regions. Although boxcar apodization gives the highest resolution possible for any given OPD, it is often avoided in practice, because it introduces the strongest sidelobes of all common apodization functions. Other apodization functions like $Tri(x)$, cos^2 or Norton–Beer considerably reduce the strength of sidelobes and avoid negative intensities. However,

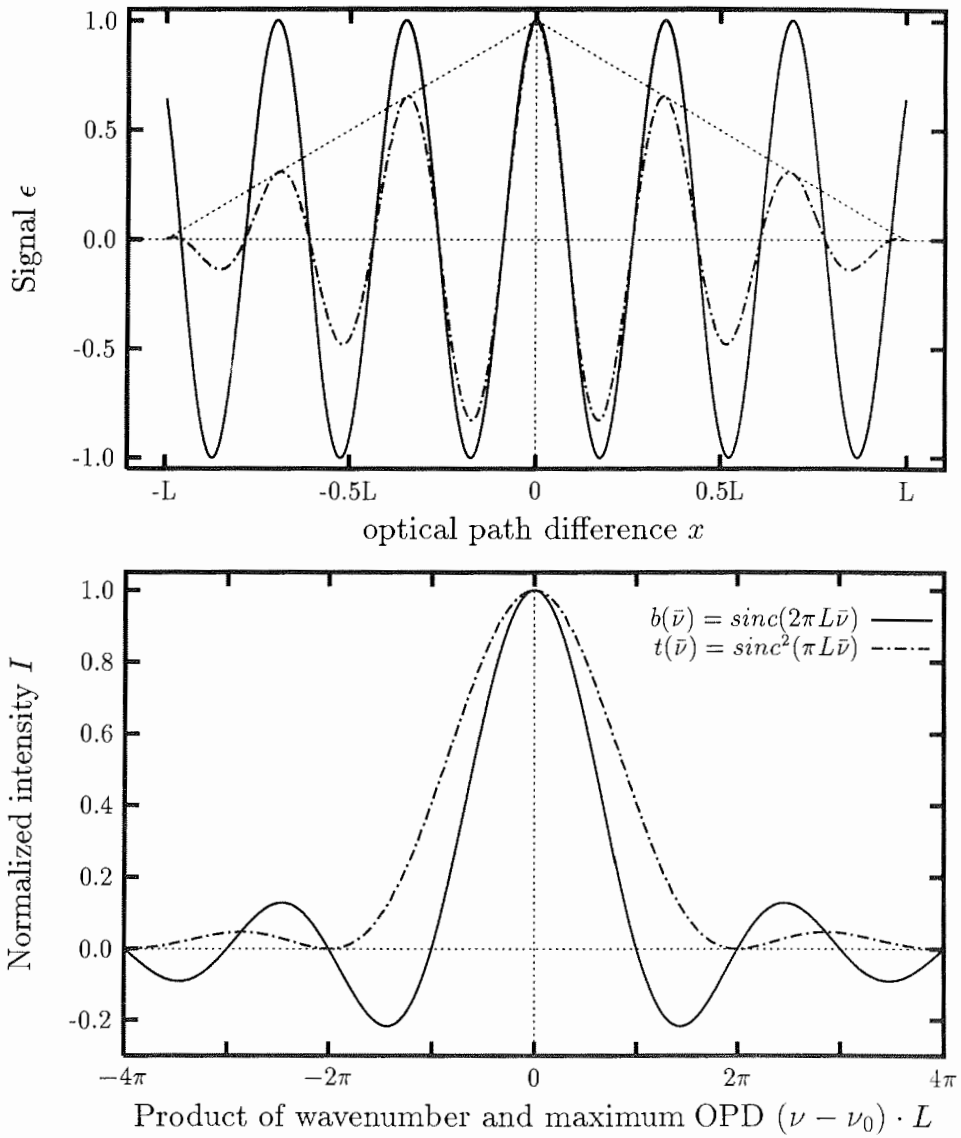

Fig. 1.2: *The effects of apodization on the line shape of an ideal monochromatic spectral line of wavenumber ν_0 are illustrated. a) In the upper part, the recorded interferogram is shown after apodization with boxcar (solid line) and triangular apodization (broken line). The maximum OPD is L. b) In the lower part, the resulting line shape is given.*

the price is a significant loss of information in terms of spectral resolution and the experimentalist has to compromise according to the task.

1.1.3 Spectral resolution

The apodization function used has to be mentioned when stating the spectral resolution of an FTS. Values presented for boxcar apodization are often referred to as the *'unapodized'* resolution, though the term is not correct in its strict sense. Reconsider Figure 1.2b. The function $sinc(x)$, being the FT of the boxcar function, has a value of 0.5 at $x = 0.603354 \cdot \pi$ and the function $sinc^2(x)$, which is the FT of the triangular apodization function, equals 0.5 at $x = 0.885885 \cdot \pi$. That yields a half width (FWHM) of $\Delta\nu \approx 2 \cdot (0.6\pi/2\pi L) = 0.6/L$ for boxcar and $\Delta\nu \approx 0.9/L$ for triangular apodization.

There are different criteria used to decide when 2 closely neighboured spectral lines are said to be resolved. Well known is the *Rayleigh* criterium as quoted from *Born* and *Wolf* (1989):

Two components of equal intensity should be considered to be just resolved when the principal intensity maximum of one coincides with the first intensity minimum of the other.

This is the case for $x = 2\pi$ for triangular apodization, which is equivalent to $\Delta\nu = 1/L$, i.e. the higher the maximum retardation, the closer may any two spectral lines come for being resolvable. Sometimes, the spectral half width of an ideal monochromatic line after triangular apodization ϱ is used instead for specifying the spectral resolution (common practice by commercial FTS manufacturers like BRUKER), which gives almost the same result as the Rayleigh criterium for triangular apodization.

$$\varrho = 0.9/L \tag{18}$$

This convention is followed with our BRUKER instrument for convenience, but the true resolution is higher than stated, if boxcar apodization is used. Comparing the true resolution of two spectra that are calculated from the same interferogram by using either boxcar or triangular apodization, the loss in resolution for triangular apodization is 47 % compared

to the ILS.

1.1.4 The discrete Fourier transformation

The interferogram can only be recorded at a finite number of mirror positions x or, in other words, it can only be recorded with a finite stepsize Δx. In this section it is shown that the integral in equation (14) can be expressed by a summation, if the stepsize is chosen adequately. For this task, it is helpful to introduce the Shah function $\Upsilon(x)$ that relates the continuous interferogram $I_c(x)$ to the sampled spectrum $I_s(x)$ by a series of Dirac Delta–functionals $\delta(\xi)$ (*Bell*, 1972):

$$I_s(x) = \Upsilon(x/\Delta x) \cdot I_c(x) \tag{19}$$

$$\Upsilon(x/\Delta x) = \sum_{n=-\infty}^{+\infty} \delta(\frac{x}{\Delta x} - n), \tag{20}$$

where n is an integer. The Shah function $\Upsilon(x)$ has only two possible values, namely zero and infinity. It equals zero anywhere except for those points where $x/\Delta x$ becomes an integer. Other important characteristics of the Shah function are periodicity and the FT of a Shah function yields a Shah function again (*Bell*, 1972):

$$\Upsilon(x+m) = \Upsilon(x), \quad m \text{ is an integer} \tag{21}$$

$$\mathcal{F}^{-1}\{\Upsilon(ax)\} = \frac{1}{|a|} \cdot \Upsilon(\nu/a) \tag{22}$$

The wanted continuous spectrum $S_c(\nu)$ is the FT of the interferogram $I_c(x)$ (equation (14)). Using equations (19–22) one gets the wanted relation to the sampled interferogram $I_s(x)$ by :

$$\mathcal{F}^{-1}\{I_s(x)\} = S_s(\nu) = \mathcal{F}^{-1}\{\Upsilon(x/\Delta x) \cdot I_c(x)\} \tag{23}$$

$$= \mathcal{F}^{-1}\{\Upsilon(x/\Delta x)\} \otimes \mathcal{F}^{-1}\{I_c(x)\} \tag{24}$$

$$= \Delta x \cdot \Upsilon(\nu \cdot \Delta x) \otimes S_c(\nu). \tag{25}$$

By expressing Δx in the Shah function by $1/\Delta\nu$ and making use of a principle characteristic of the Dirac delta functional that is

$$\delta(ax - n) = \frac{1}{|a|} \cdot \delta(x - \frac{n}{a}), \tag{26}$$

it follows that

$$\frac{1}{\Delta\nu} \cdot \Upsilon(\nu/\Delta\nu) = \frac{1}{\Delta\nu} \cdot \sum_{n=-\infty}^{+\infty} \delta\left(\frac{\nu}{\Delta\nu} - \frac{n\Delta\nu}{\Delta\nu}\right) = \sum_{n=-\infty}^{+\infty} \delta(\nu - n\Delta\nu). \tag{27}$$

Inserting the Shah function in its present form into equation (25) yields the relation between sampled interferogram and the continuous spectrum:

$$\mathcal{F}^{-1}\{I_s(x)\} = S_s(\nu) = \sum_{n=-\infty}^{+\infty} S_c(\nu - n \cdot \Delta\nu). \tag{28}$$

This expression replaces the Fourier integral of equation (14) by an infinite Fourier series. The deduction holds as well for the case of the apodized spectrum from equations (15) and (17). The sampled spectrum $S_s(\nu)$ consists of an infinite series of equidistant Delta functionals. The weights of these equal the values of the continuous spectrum and the whole sampled spectrum repeats itself in intervals of the spectral bandwidth $\Delta\nu$.

The last point made is highly relevant in practice. One has to ensure by restricting the recorded bandwidth that the sampled spectra do not overlap. To avoid band overlap, which is also known as aliasing, the Nyquist condition has to be fulfilled:

$$\Delta\nu \geq 2 \cdot \nu_{max} \Longleftrightarrow 2 \cdot \Delta x \leq \frac{1}{\nu_{max}}, \tag{29}$$

i.e. the stepsize of the movable mirror Δx, which implies a change in the optical path difference of $2\Delta x$, has to be chosen smaller than the reciprocal of the highest wavenumber encountered in the spectrum. If this condition is satisfied, equation (28) is known as the sampling theorem of Fourier theory. The recorded bandwidth is limited in practice by the transmission function of the beamsplitter and by the efficiency function of the detector. However, the bandwidth can be reduced further by adding optical band filters or electronic filters.

1.1.5 Coherence

Any wave train that enters the FTS interferes constructively with itself at the detector, if there is no optical path difference between the fixed

and the movable mirror of the Michelson interferometer. If, on the other hand, the OPD is larger than the length of any wave train of a single photon, interference effects will vanish and incoherent light signals are observed. Let $I(0)$ and $I(\infty)$ be the intensities at the detector for zero and for huge path differences, respectively. Further, let E be the electrical field strength and take the superposition of N secondary light beams into account ($N = 2$ for the FTS). The resulting intensity is proportional to $N^2 \cdot E^2$ in the coherent case $I(0)$ and it is proportional to $N \cdot E^2$ in the incoherent case of $I(\infty)$ (*Bell*, 1972). Thus, for the Michelson interferometer with $N = 2$ one can conclude:

$$I(\infty) \,/\, I(0) = 1/N = 1/2. \tag{30}$$

Hence equation (13) can be interpreted as

$$\left[\tilde{I}(x) - \tfrac{1}{2}\tilde{I}(0)\right] = \left[\tilde{I}(x) - \tilde{I}(\infty)\right]. \tag{31}$$

The recorded interferogram is a variation in intensity about the intensity value of incoherent superposition. The amplitude of this variation relative to $I(\infty)$, i.e. the contrast of the interferogram, and consequently the signal to noise ratio decreases with increasing OPD. Recalling that small values of ϱ (eq. 18) mean high spectral resolution, this is equivalent to the statement that the S/N for otherwise identical settings is lower in high resolution spectra.

One can check whether the temporal coherence length of infrared radiation in solar occultation is basically high enough to record long interferograms that yield high resolution spectra. The interference of two wave trains is possible only if they have a constant phase relation and overlap in time and space. This is generally not given for photons that originate either from two different primary points of emission or that originate from the same source but with some temporal delay before the non–stimulated emission of the second photon. Common IR sources with these properties of emitting incoherent radiation are the sun, the moon, any filament light bulb, the thermal emission of the atmosphere, etc. The primary emitters are atoms or molecules. Electrons that return from an excited state will emit abundant energy in form of a damped electromagnetic wave. The leaving from an excited state is spontaneous and (except for lasers)

independent from the behaviour of other excited electrons. Therefore, coherence can only be expected for wave trains that originate from the same act of emission.

Although absorption spectra are of main concern in this thesis, the discussion of the temporal coherence length is more illustrative in the emission picture. Anyway, the results hold as well for the analogous case of an absorption line (*Bergmann* and *Schaefer*, 1987). The average time τ needed to emit a photon at the frequency f_0 or wavenumber ν_0 is (*Stößel*, 1993)

$$\tau = \frac{10^6}{2\pi f_0} = \frac{10^6}{2\pi c \nu_0}. \tag{32}$$

That yields for an undisturbed emission at 1000 cm^{-1} by multiplication with the speed of light $\tau \approx 5\ ns$ and a coherence length l_c of $\approx 1.5\, m$.

Emission and absorption lines in the atmosphere are not ideally sharp due to the Doppler and pressure broadening (discussed in detail in Chapter 2). that irregularly modify the wave trains. Thus, a more accurate way to describe the coherence length is the putting up of the coherence function $\gamma(\tau)$, as described in *Stößel* (1993). For a Doppler broadened line of a molecule with mass m at temperature T one finds

$$\gamma_D(\tau) = \exp\left\{\frac{-k_B T}{2mc^2} \cdot (2\pi c \nu_0 \tau)^2\right\} \cdot cos(2\pi\nu_0\tau) \tag{33}$$

and for a pressure broadened line

$$\gamma_p(\tau) = \exp\left\{\frac{-|\tau|}{\Delta t_{col}}\right\} \cdot cos(2\pi\nu_0\tau), \tag{34}$$

where Δt_{col} denotes the average time between two collisions of the emitting molecule with another gas particle.

At room temperature and normal pressure, Δt_{col} is some $10^{-11}\ s$ (*Stößel*, 1993) and hence by two orders of magnitude smaller than the emission time τ (equation 32). Thus, a single emission act is frequently disturbed, causing an arbitrary change in phase of the emitted wave train from collision to collision. However, most collisions are elastic in the atmosphere and the wavenumber does not change. According to the Campbell theorem, these partial wave trains still add to the correlation function (*Stößel*,

1993), but the coherence function is *'smeared out'* compared to the coherence function of the natural line shape. At small path differences the contrast is smaller but declines slower towards large path differences.

Hence, in practice, the contrast of the recorded interferogram does not drop sharply with OPD at some well defined coherence length, but declines progressively down to a degree where it is no longer feasible to obtain a sufficient S/N. *Michelson* observed with his white light star interferometer interference patterns up to the maximum OPD of his instrument of more than 6 m (*Stößel*, 1993).

1.1.6 Additional features of an FTIR–spectrometer

Compared to common grating or prism spectrometers, an FTS has a number of important advantages that more than outweigh the mathematical expenses in calculating the FT of the recorded interferogram.

Jaquinot or throughput advantage:
The power through the instrument is typically limited by the the product of the opening angle and the area of the entrance slit for IR grating and prism spectrometers. An FTS has no need for an entrance slit, but may use a circular aperture, allowing for a higher throughput (for opening angles and entrance optics of same size), supposed neither the intensity capabilities of the detector are exceeded nor the size of the source is the limiting factor.

Fellget or multiplex advantage:
The spectral intensity of a broad bandwidth is recorded simultaneously. This improves the S/N in broadband IR spectra for same recording times or allows a more rapid recording with equal S/N, supposed the detector is the dominating source of noise.

High spectral resolution:
The maximum spectral resolution achievable with an FTIR spectrometer is higher than in prism or grating spectrometers. The design of a grating spectrometer achieving a resolution of 0.0035 cm^{-1} in the IR requires a grating with a mechanical width of more than 2 m, which is not possible to built with present technology. However, if an FTS is operated at a

higher resolution, this requires a longer recording time to maintain the same signal to noise ratio. To illustrate this in an example, recording times from our instrument are given: For one scan, i.e. to move once the movable mirror over the maximum path difference in one direction, about 12 seconds are needed at a resolution of 0.1 cm^{-1}, while the same task takes 8 times longer at a resolution of 0.05 cm^{-1} to obtain the same S/N.

Connes advantage:
The built–in frequency stabilized laser, which is needed for the exact positioning of the movable mirror, simultaneously serves for a high quality frequency calibration of the recorded spectrum.

Other properties:
Like for etalon, grating and prism spectrometers, there is an extensive offer of commercial instruments, and the design is about as compact and robust. This allows operation even on stratospheric balloons, like the FTS from the University of Denver (*Goldman*, 1989), on aircrafts, like the MIPAS instrument from the *FzK Forschungszentrum Karlsruhe*[1] on a C–160 Transall (*Blom et al.*, 1994), on space missions, like the ATMOS instrument from NASA (*Norton* and *Rinsland*, 1991), and most recently even ship-borne, like the BRUKER instrument on board the research vessel *Polarstern* from the Alfred–Wegener–Institute (*Notholt* et al., 1995c). Another advantage of an FTS instrument is the broad spectral bandwidth recordable simultaneously. Further advantages and useful properties can be found in *Bell* (1972) and other basic books on FT spectroscopy.

1.2 Limitations to real infrared spectrometers

Real instruments have additional properties. Some of these are disadvantageous for the quality of recorded spectra. Consider first the detector itself. The instrument given, a commercial BRUKER 120M, supports several detectors that can be used alternatively according to the task. There is one MCT (Mercury–Cadmium–Tellurium), one normal InSb

[1]The former *Kernforschungsanstalt Karlsruhe* has been renamed to FzK recently.

(Indium–Antimony) and one specialized lunar InSb detector available. The built–in filter of the lunar InSb detector is cooled with liquid nitrogen. The low temperature of the direct detector optics improve the S/N at low photon rates significantly, because emission from these surfaces is reduced substantially. This is vital for the recording of spectra with the weak lunar IR source, compared to the normal InSb detector, which is operated at high photon rates and where only the active detector element itself is cooled with liquid nitrogen. The MCT detector is used in the spectral interval from 600 to 2000 cm^{-1} and the InSb detectors from 2000 to 10000 cm^{-1}. The special arrangement of the lunar InSb detector operated at wavenumbers above 2000 cm^{-1} is vital, because the lunar spectral flux at about 3000 cm^{-1}, as shown in the next chapter (Figure 2.1), is more than 5 orders of magnitude lower than the solar flux.

The next important aspect is the wavenumber dependent offset of the zerolevel in recorded spectra. This offset is caused by a variety of effects. One aspect is the occurrence of emission that adds to the absorption signal. This thermal emission originates both from the atmosphere (balanced) as well as from optic parts of the instrument itself, like the beamsplitter (unbalanced). (For details see *Schreiber*, 1994.) This emission aspect becomes highly relevant in the discussion of lunar absorption spectra and is treated in detail in sections 3.3 and 3.4. Finally, the nonlinearities in particular in the MCT detector can cause a non negligible zerolevel offset in solar absorption spectra (see also chapter 3).

The third aspect that has to be mentioned for the limitations of real spectra is the phase error. This error occurs, if the interferogram recorded is not symmetric to the determined ZPD. This is caused *a*) by the finite stepsize in sampling: the sample point with the highest intensity and being closest to the exact ZPD does not coincide perfectly with ZPD and *b*) by wavenumber dependent phase delays that are caused by imperfect compensator plates or by wavenumber dependent signal acquisition and processing times due to the imperfect electronics. Mathematically speaking, the resulting spectrum (equation 14) becomes a complex spectrum, with the tangent of the phase angle given by the ratio of the real and the imaginary part of the spectrum (equation 44, section 3.3). The symmetric absorption lines become asymmetric, if the phase error is not

corrected, as is demonstrated in section 3.3 in detail (Figure 3.6). The phase error can be corrected, e.g. by the method of *Mertz* (1967), if a two–sided interferogram is recorded. As the phase delay can be assumed to change slowly with wavenumber, a low resolution spectrum, i.e. short double sided interferogram that can be recorded rapidly, is sufficient for this task (*Gronholz* and *Herres*, 1985). This spectrum is often called the phase spectrum and is generally performed by BRUKER instruments before any spectrum is recorded, with the latter being basically a single sided interferogram to save valuable recording time.

Additional aspects of design and technical details that have an influence on the S/N are the finite quality of the mirror shapes and surfaces, the non ideal amplitude splitting of the beamsplitter, which is also wavenumber dependent, an imperfect alignment, absorption from optical components, the presence of dust particles, multiple reflections between optical boundary layers e.g. of an optical band filter, and the finite precision of the mirror movement. Additionally, significant nonlinearities can be introduced by the preamplifier of the detector and subsequent electronics like the Analog/Digital Converter (ADC) that cause a distortion of the interferogram's intensity signal. Hence when recording a spectrum one has to ensure by selecting an adequate aperture and preamplifier gain that the detector system is not operated close to or beyond saturation to not exceed a tolerable deviation from linearity between input and recorded signal. A very comprehensive description of these aspects is given by *Friedle* (1993) and *Schreiber* (1994).

2 The standard procedure of spectrum analysis

2.1 The principles of the measurement

The sun maintains a rather constant surface temperature for human time scales, that is based on continuous nuclear fusion going on inside the central star of our planetary system. The spectrum of emitted electromagnetic radiation can be described physically in good approximation by the spectrum of a black body having a temperature of 5800 Kelvin (*Zeilik*, 1992). The spectral flux as a function of wavenumber is given by Planck's law and according to Wien's law, the resulting maximum in spectral flux density is located at 500 nm. In wavenumbers, the maximum is located at 12100 cm^{-1}, which is not simply the reciprocal of 500 nm. This is due to the non linear characteristic of Planck's law, which is proportional to λ^{-5} in wavelength, but proportional to ν^3 in wavenumber coordinates. In wavenumbers, Wien's law has the form

$$\nu_{max} = \frac{3k_B T}{hc} = 2.085\, cm^{-1}K^{-1} \cdot T \tag{35}$$

with ν_{max} yielding the wavenumber where the maximum in the spectral flux occurs. In Figure 2.1 the spectral flux density at the surface of our planet's atmosphere is plotted for the sun and additionally for full moon and new moon conditions.

Both astronomic bodies are used for recording absorption spectra of the earth's atmosphere. During polar night conditions, which are lasting for 5 months at the given observation site, the sun is not available and the much weaker IR source of the moon has to be used for recording absorption spectra. The surface temperature of the moon is quite different for its dark and its illuminated side, since its surface temperature is mainly determined by solar illumination. The lowest temperatures measured are 190 K and the highest ones are 390 K (*Zeilik* et al., 1992). An average surface temperature of about 370 K can be assumed for IR observations during full moon phases. The maximum in spectral flux is then found close to 770 cm^{-1}. However, even in this maximum, the intensity is about 2 orders of magnitude smaller than the intensity of the sun at that wavenumber. Towards higher wavenumbers the lunar spectrum

decreases drastically, imposing extensive requirements on the instrument and detectors used (*Notholt*, 1993 and 1994a&b).

The solar spectrum is a continuous spectrum, but shows numerous absorption lines caused by the solar atmosphere. Among the 25000 known absorption features (*Geller*, 1992), the absorption of basically CO and OH in the IR region of the solar spectrum have to be modelled correctly in the analysis of terrestrial spectra. If direct solar spectra are record-

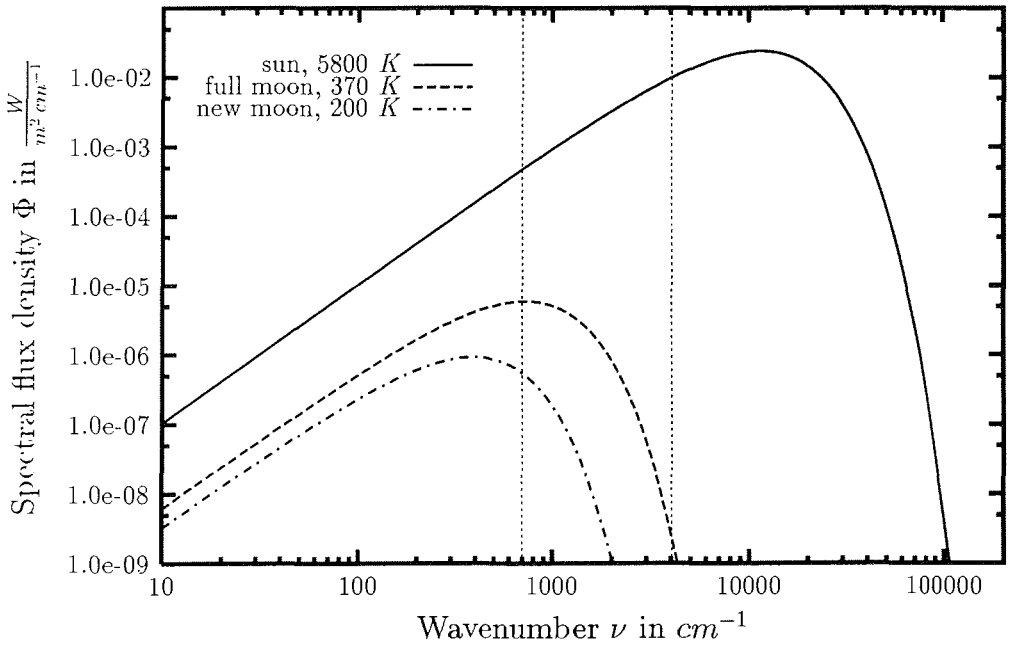

Fig. 2.1: *Comparison of the solar and lunar spectral flux density Φ incident on the surface neglecting atmospheric interaction. In a simple approximation the sun and moon are treated as blackbodies of the temperatures given in the key. The maximum in radiation is found according to* Wien's *law near 12100 cm^{-1} (500 nm) for the solar spectrum and at 770 cm^{-1} (7.8 μm) for the full moon. Integration over wavenumber of the solar flux density yields the solar constant of 1368 W/m^2 (Lide, 1991). The vertical lines bracket the main spectral interval investigated, which ranges from 700 to 4050 cm^{-1}.*

able, as it is the case for satellite based instruments, one can get rid of the solar features by dividing the occultation spectrum by the direct solar spectrum. However, this is difficult to perform with ground based instruments. Instead, the solar spectrum has to be modelled on the basis of a solar spectroscopic database. Only in those spectral intervals where no solar absorption features occur or where at least the solar absorption can be assumed to be constant, the solar simulation can be omitted. The relative strength of a terrestrial absorption line is not effected by the absolute spectral intensity of the continuum solar spectral flux density entering the atmosphere.

The retrieval algorithm used for the data analysis (SFIT 1.09, see below) is capable to treat solar features separately. However, the list of solar CO lines shipped with the diskettes proved to be incomplete in some spectral regions and totally lacks solar OH lines. Therefore, a number of missing lines taken from (*Geller*, 1992) have been added to the data base of solar absorption lines in an empiric approach and some significant lines can be seen in appendix C, e.g. in the microwindows at 782, 829, and 975 cm^{-1} on pages 201, 205, and 217, respectively.

A small fraction of the solar radiation enters the terrestrial atmosphere and is being scattered, absorbed, reflected or gets to the surface without interaction. An individual molecule in the atmosphere can enter an excited state, it can be photolysed or it can be ionized by the absorption of a photon. Photons from infrared radiation possess to little energy to ionize a molecule and can only break up very weak chemical bonds. Rotational and vibrational states of the absorbing molecule are excited instead.

Many of the molecular atmospheric trace gases have absorption lines in the infrared spectral range, i.e. they have discrete excited molecule states that can be occupied by absorption of IR radiation. The largest fraction of the energy absorbed is transformed into heat after collision with another particle or is re–emitted statistically isotrop into any spatial direction, when returning to the ground state directly or by passing through intermediate states. In the spectral interval from 400 to 23 000 cm^{-1} (25 to 0,43 μm) more than 700 000 terrestrial absorption lines are known. These are assigned to about 50 relevant molecules and the spectroscopic features are arranged in extensive data bases. In this work the

revision level 17 of the ATMOS AFGL files (*Brown* et al., 1987) is used, if nothing else is stated. The revised updates have become available from NASA (*C. Rinsland*, priv. comm. 1995) and agree widely with the known HITRAN92 data base from *Rothman* et al. (1992)[2]. However, in section 4.5 and 4.6 the most recent version of the HITRAN data base HITRAN96 is used (*Rothman*, private communication 1996) for the reasons discussed concerning the latest update in the retrieval algorithm SFIT 1.09e. Besides the identification of the line position with the corresponding species, the individual line strength, the lower ground state energy, the line shape parameterized in pressure and temperature, the spectroscopic transition, the overall uncertainties, and other data are listed for each terrestrial absorption line.

The comparison of the solar spectrum before entering the terrestrial atmosphere with the spectrum observable at ground or at any altitude within the atmosphere yields numerous absorption features which contain information on the molecules involved, their total amount along the optical path within the given aperture, and on their vertical distribution. The most exact solution to this inverse problem of retrieving the distribution of molecules in the atmosphere from the analysis of absorption spectra is the mathematical deconvolution[3] of the spectra. To perform this task, one has to determine the response function of the whole instrument precisely, i.e. one has to record well known reference or calibration spectra first. The recorded calibration spectra will deviate from the true spectra due to the ILS (or in spectra from non–FT instruments due to the finite spectral resolution of the detector used), the response function of the detector, the finite aperture, etc. In the next step, the response matrix put up on the basis of the calibration spectra has to be inverted. Multiplication of this inverse response matrix with any spectrum recorded with identical instrumental settings yields all desired quantities.

However, this elegant way is not feasible in FTIR spectroscopy at present. It is not merely the excessive calibration necessary for a typical variety of

[2]Both data sets are based on the Air Force Geophysical Laboratory (AFGL) **hi**gh resolution **tran**smission molecular absorption data base, which yielded the acronym HITRAN92 in the edition by *Rothman* et al. (1992). The set of spectral files from *C. Rinsland* (priv. comm., 1996), originally called AFGL files, use a modified data format and are updated more frequently. After major revisions these files were termed BFGL and most recently CFGL files.

[3]in its strict and thorough sense, not simply the deconvolution of an FT.

instrumental settings, but there are two principal difficulties that cannot be overcome. First, the highly non linear variation of the line shape with altitude is small and leads to a very poor conditioning of the response matrix. This requires an extremely high numerical precision to perform the inversion, in particular in the presence of noise always occurring in recorded spectra. Second, present computing capacities available are insufficient to invert a matrix adequate to typical spectral resolutions and bandwidths. However, the exact deconvolution of spectra is a very successful application in the analysis of α-, β- and γ-spectra (*Keyser* 1985, *Paul* 1995).

2.2 The comparison with a model atmosphere

The common practice to analyse IR spectra is to compare the recorded spectrum to a simulated spectrum. A model atmosphere is calculated on a computer and absorption lines are added according to the spectroscopic data base and to the estimated initial amounts of trace gases. The total number of molecules per species is then adapted in an iterative least squares fit to meet the measured spectrum in a selected spectral interval. Data on the position of the observer and the sun, on the temperature and pressure conditions along this path, *a priori* volume mixing ratio (VMR) profiles, and all properties of the instrument like aperture, maximum OPD, apodization function, etc are needed for the calculation of the synthetic spectra in the model atmosphere. Starting on the initial VMR profiles provided, the absorption of every line is calculated one by one from the spectroscopic data base over the selected spectral interval and takes into account the interference with any closely neighboured spectral line. The line shapes are determined by the vertical distribution of the molecules, the pressure and temperature profiles provided, and the observation geometry as calculated from the positions of the sun and the instrument.

After the first spectrum is calculated from the *a priori* VMR profiles by the forward model, the residuals between recorded and modeled spectrum are analysed and the initial VMR profiles are scaled to minimize the residuals. This procedure is repeated iteratively until the least squares

fit converges or meets a preset quality criterium. Finally, the total column amount is calculated for each species, that is the total number of molecules of a selected species per unit area above the observer for a zenith angle of zero degrees. The calculation is based on the optimally scaled VMR profiles and the observation geometry. A description of the different algorithms and computer programs developed is given in numerous text books and journals like *Clough* (1986 and 1989), *Norton* and *Rinsland* (1991), *v. Clarmann* (1986 and 1990), *Adrian* (1993), *Höpfner* (1994), and *Rao* and *Weber* (1992).

The causes for the increase in line width mentioned in the previous section are Doppler and pressure broadening. While Doppler broadening is dominant above roughly 40 km, it is pressure broadening below 10 km. Doppler broadening results from the relative motion of the molecule towards or from the photon that is absorbed. The mean velocitiy of gaseous molecules increases with temperature and so does the line broadening. Pressure broadening occurs if the absorbing molecule simultaneously undergoes an inelastic collision with another particle. The broadening of the line width increases with the frequency of collisions between molecules, i.e. it increases with pressure and to a lower extend also with temperature. Typically, the line shapes observed in ground based absorption spectra are combinations of the two limiting cases of a pure Doppler broadened and a pure pressure broadened line and are known as *Voigt* lines.

After this description of the line shape in general words, a mathematical formulation is given, since an understanding of the line shape is vital for the discussion in chapter 4, where the line shape is analysed to improve the VMR profiles. However, the following mathematical description is reduced to the aspects essential to this work, since all aspects are well known. A more detailed description can be found e.g. in *Chamberlain* (1979) and *Rao* and *Weber* (1992).

Near ground, where the pressure reaches its maximum, Doppler broadening is negligible compared to pressure broadening. This is the limiting case of the *Lorenz* line shape described by the line shape function $f_L(\nu)$ for a spectral line at the line center position ν_0 and with the halfwidth

(FWHM) of $\mathcal{H}_L(p,T)$:

$$f_L(\nu) = \frac{1}{2\cdot\pi}\cdot\frac{\mathcal{H}_L(p,T)}{(\nu-\nu_0)^2+[0.5\cdot\mathcal{H}_L(p,T)]^2} \tag{36}$$

$$\mathcal{H}_L(p,T) = \mathcal{H}_{L0}\cdot\left(\frac{p}{p_0}\right)\cdot\left(\frac{T}{T_0}\right)^{\kappa}. \tag{37}$$

The quantities T_0, p_0 and $\mathcal{H}_{L0}$ describe the reference temperature (296 K), the reference pressure (1013 hPa) and the halfwidth (FWHM) for the reference conditions, respectively. The values for the exponent κ depend on the species and on the transition considered and are between 0 and 1 with typical values close to 0.5.

In the other limiting case of very low pressure, as encountered in the upper homosphere[4] above $50-60$ km, pressure broadening becomes negligible and the resulting line shape is close to an ideal *Doppler* line shape. The line shape function $f_D(\nu)$ is a Gaussian curve with the halfwidth $\mathcal{H}_D(T,m)$:

$$f_D(\nu) = \frac{2}{\mathcal{H}_D(T,m)}\cdot\sqrt{\frac{\ln 2}{\pi}}\cdot\exp\left\{-4\cdot(\ln 2)\cdot\left(\frac{\nu-\nu_0}{\mathcal{H}_D(T,m)}\right)^2\right\} \tag{38}$$

$$\mathcal{H}_D(T,m) = 2\cdot\nu_0\cdot\sqrt{\frac{2\cdot\ln 2\cdot k_B\cdot T}{m\cdot c^2}} \approx 2.35\cdot\nu_0\cdot\sqrt{\frac{k_B\cdot T}{m\cdot c^2}}. \tag{39}$$

The symbol m denotes the mass of the molecule and k_B is the *Boltzmann* constant. Figure 2.2 illustrates the two line shapes discussed.

Those line shapes are never observed in their pure forms in ground based spectra, but the combination of the *Doppler* and *Lorenz* line shapes yields a very good approximation to the observed line shapes and is known as the *Voigt* line shape. The line shape function of the *Voigt* line $f_V(\nu)$ with the spectral halfwidth $\mathcal{H}_V$ is given by:

$$f_V(\nu) = \frac{\mathcal{H}_V}{\pi}\cdot\int_{-\infty}^{+\infty}\frac{\exp(-v^2)}{(\mathcal{H}_V)^2+[\beta-v]^2}\,dv \tag{40}$$

$$= \mathrm{Re}\left\{(1-erf\,[-i(\beta+i\mathcal{H}_V)])\cdot e^{-(\beta+i\mathcal{H}_V)^2}\right\}, \tag{41}$$

$$\text{with}\quad \mathcal{H}_V = \sqrt{\ln 2}\cdot\frac{\mathcal{H}_L(p,T)}{\mathcal{H}_D(T,m)}\ ,\quad \beta = \sqrt{\ln 2}\cdot\frac{2(\nu-\nu_0)}{\mathcal{H}_D},$$

[4]This is the atmosphere in the well mixed altitude range from ground to about 80 km (see chapter 4).

and $erf()$ is the Gaussian error function, an integral function which is a special case of the incomplete gamma function. Equation (41) is not solvable analytically, but for its numerical solution different algorithms have been developed by *Clough* et al. (1981), *Humlicek* (1982), and *Pierluissi* (1977). The parameters $\mathcal{H}_D$, $\mathcal{H}_L$, and κ needed for the calculation are determined in extensive laboratory studies experimentally and are stored in the spectroscopic data bases.

Figures 2.3 and 2.4 show examples of the *Voigt* line shape. In Figure

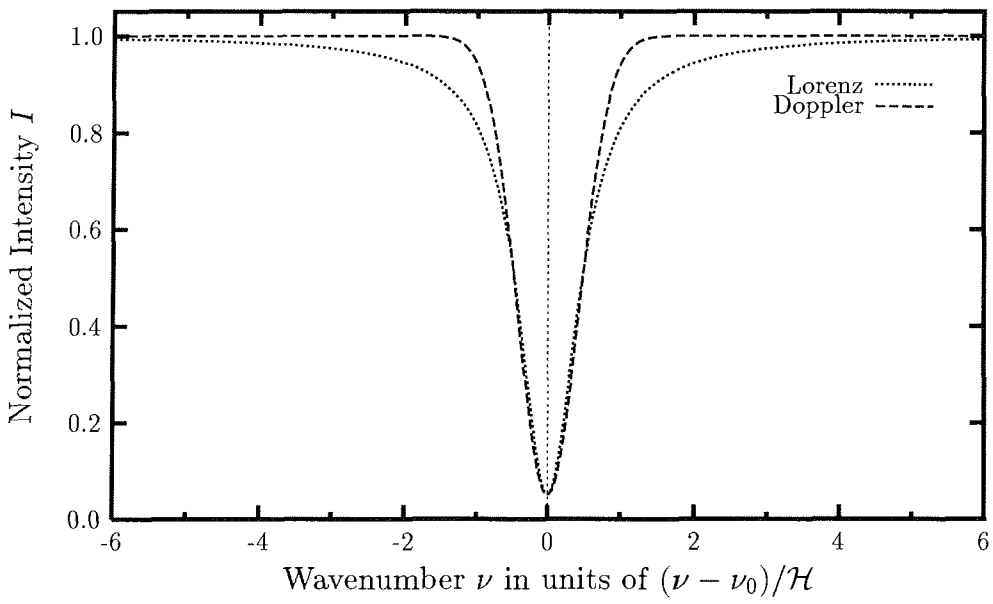

Fig. 2.2: *The spectral line shapes for the limiting cases of a pure* Doppler *and a pure* Lorenz *line shape are shown. In the middle and upper stratosphere, line shapes are close to the* Doppler *limit, while in the lower troposphere pressure broadening dominates, which yields approximately* Lorenz *shaped lines. Observed spectral line shapes are typically a combination of both types known as* Voigt *line, plus the instrumental response function. Both curves shown are normalized to identical maximum absorption values. Note that the ordinate represents different absolute scales for the Doppler and Lorenz lines, because* $\mathcal{H}_\mathcal{L} \neq \mathcal{H}_\mathcal{D}$.

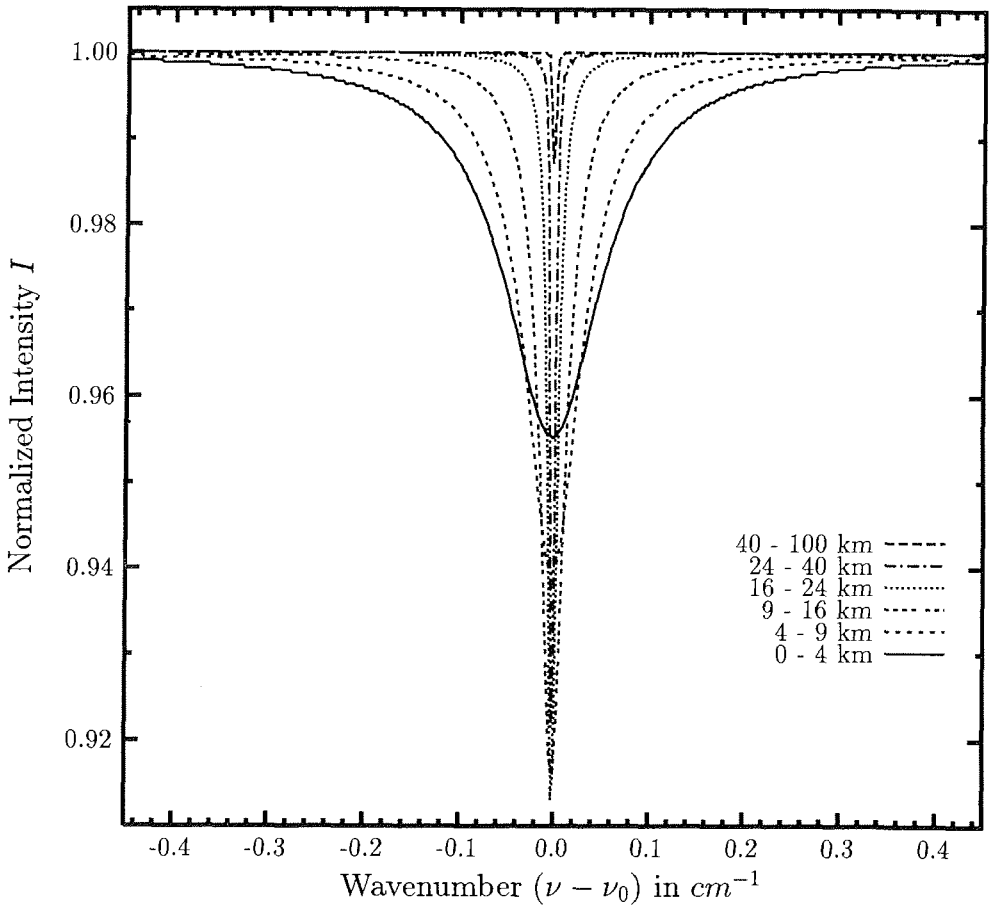

Fig. 2.3: *The composition of a CO_2 absorption signal is illustrated. The contributions from individual height layers, as indicated in the key, are calculated separately. Summed up they give the line shape shown in the lower curve of Figure 2.4. Note the change in line shape with altitude. The absorption is calculated for a constant VMR profile of 360 ppm, ν_0 = 2626.63 cm^{-1}, a zenith angle of 60°, 180 cm OPD, boxcar apodization, 1.3 mrad FOV and the outcome is stretched on the Y–axis by a factor of 3 to meet scales in Figure 2.4.*

2.3 the contributions from individual altitude ranges to the total absorption line are shown for the species CO_2 with the VMR profile assumed constant. Summed up, these contributions form the lineshape observable at ground as shown in the lower curve of Figure 2.4. The total number density decreases exponentially with height and so does the area enclosed by the absorption line.

In Figure 2.4, the line shapes of characteristic atmospheric molecules are compared, which have highly different VMR profiles. HF is a char-

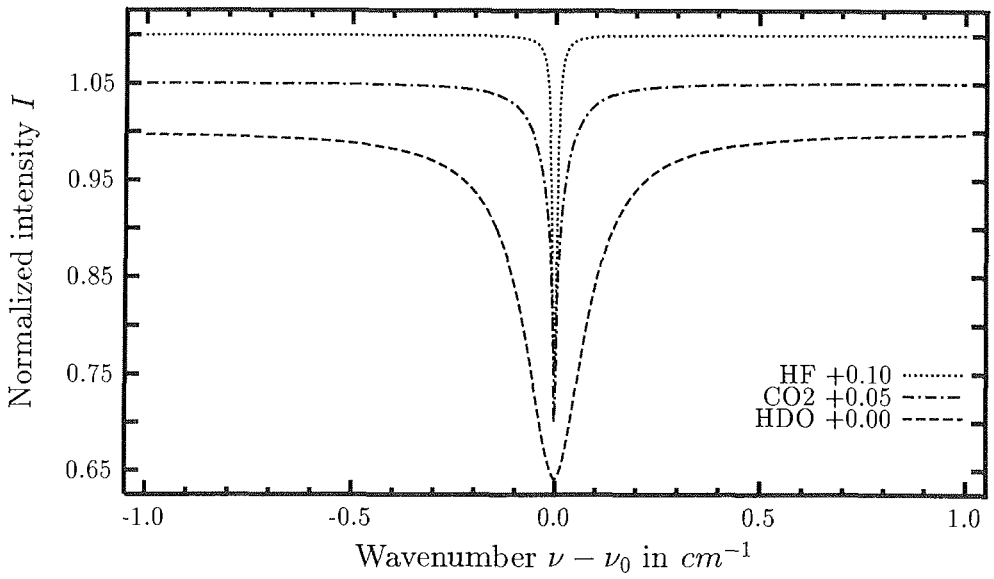

Fig. 2.4: *In this figure the line shapes from 3 different trace gases are compared. HF is a characteristic species for gases mainly distributed in the stratosphere, CO_2 for an almost perfectly mixed species, and finally a heavy isotopomer of water vapor occurring almost entirely in the lower troposphere. The selected lines are 4038.96 cm^{-1} for HF, 2626.63 cm^{-1} for CO_2 and 2660.51 cm^{-1} for HDO and are simulated for the same conditions as in the previous figure. The spectra are shifted for clarity as indicated in the key and are normalized in their line centers to equal absorption strengths as given by the center of the HDO line, which correspond to a total column amount of $9.7 \cdot 10^{21}$ cm^{-2}.*

acteristic species for gases mainly distributed in the stratosphere, CO_2 for an almost perfectly mixed species, and finally a heavy isotopomer of water vapor occurring almost entirely in the lower troposphere. Only about 10 % of all HF molecules are distributed in the troposphere while for water vapor more than 90 % are found below 6 km in the Arctic. The stratospheric HF gives the narrowest line, while the tropospheric water vapor has the broadest shape for the reasons discu...].

In particular, the presence of water vapor is unfavorable in the analysis of ground based FTIR spectra. The very broad and typically strong absorptions by the high number of H_2O and HDO lines are causing interferences in the retrieval of other species in almost any spectral interval. That is the reason why IR spectrometers are often installed at high altitude, preferably on mountain tops of more than 3 km altitude. By this means the absorption lines due to water vapor get significantly weaker and narrower and become a lower disturbance to the retrieval of other species. The observation site of the given instrument is 20 m a.m.s.l. and rather suboptimal from this point of view. The highest mountain on Spitsbergen, the *Newton Toppen*, is about 1300 m high, but the logistical expenses would be high for this rather small improvement of recording conditions. However, the disadvantages of the low altitude of the observation site are compensated to a significant extend by the low humidity of polar air compared to lower latitudes, in particular in winter, due to the low temperatures that reduce the saturation vapor pressure of water.

2.3 Particular features of the algorithms used

The central element in the retrieval software is the forward model that creates the model atmosphere and performs the least squares fitting between the recorded and the synthetic spectrum. The program used is SFIT (Spectral least–squares FITting program) created by *C. Rinsland*, which is based on the ATMOS algorithm (*Norton* and *Rinsland*, 1991). All results presented in this thesis are calculated with the version 1.09d if nothing else is specified. In the sections 4.4 and 4.6 all data is reanalysed for the reasons discussed below with the pre-release of the latest version 1.09e that became available on the 31/May/1996. For more details on

the software see appendix B. The homogeneity and quality of results is assured by regular intercomparison experiments within the NDSC, an example of which is given in chapter 4.2.

The SFIT–TOOLS package (appendix B) is created by the author as an extension to the basic SFIT algorithm and is freely available for non commercial use. Besides a variety of data format conversion programs, which allow the use of radio- and ozone sonde data and the conversion of different data types into formats required for plotting and spread sheet programs, the SFIT–TOOLS include software for the manipulation of VMR profiles, the retrieval of dynamical parameters (chapter 4), for search tasks within the ATMOS and HITRAN database, for the creation of spectral plots as given in appendix C, for the study of isotopic ratios, for the display of essential retrieval results with optional data logging functions etc. For details and sources of supply see appendix B.

The SFIT algorithm has undergone a series of improvements in recent years. One of the difficulties encountered before the latest version 1.09e became available was the treatment of the pressure dependent shift of the line center. This effect is negligible for most species except for methane, in particular at low altitudes. The change in the position of the line center with pressure results in a distortion of the line shape symmetry for the total absorption line, since contributions from different altitudes have different line center positions. If an isolated CH_4 line is studied and the pressure shift is not taken into account, the algorithm gets mislead and ascribes the non symmetry of the line shape to a phase error in the spectrum. The retrieved phase error is unrealistically high and the algorithm gets trapped if other absorption lines are present, which have a negligible pressure shift and show a significantly smaller phase error. This situation proofed to be difficult in the past with SFIT versions prior to 1.09e.

The improvement in the quality of the fits achieved with the latest version of SFIT is demonstrated in Figures 2.5 and 2.6, where the results from SFIT version 1.09d are compared to those from 1.09e. The total column amounts of the major species have been set to the best known values in the *a priori* VMR profiles before the retrieval, as determined in other spectral microwindows. The settings of all parameters are identical

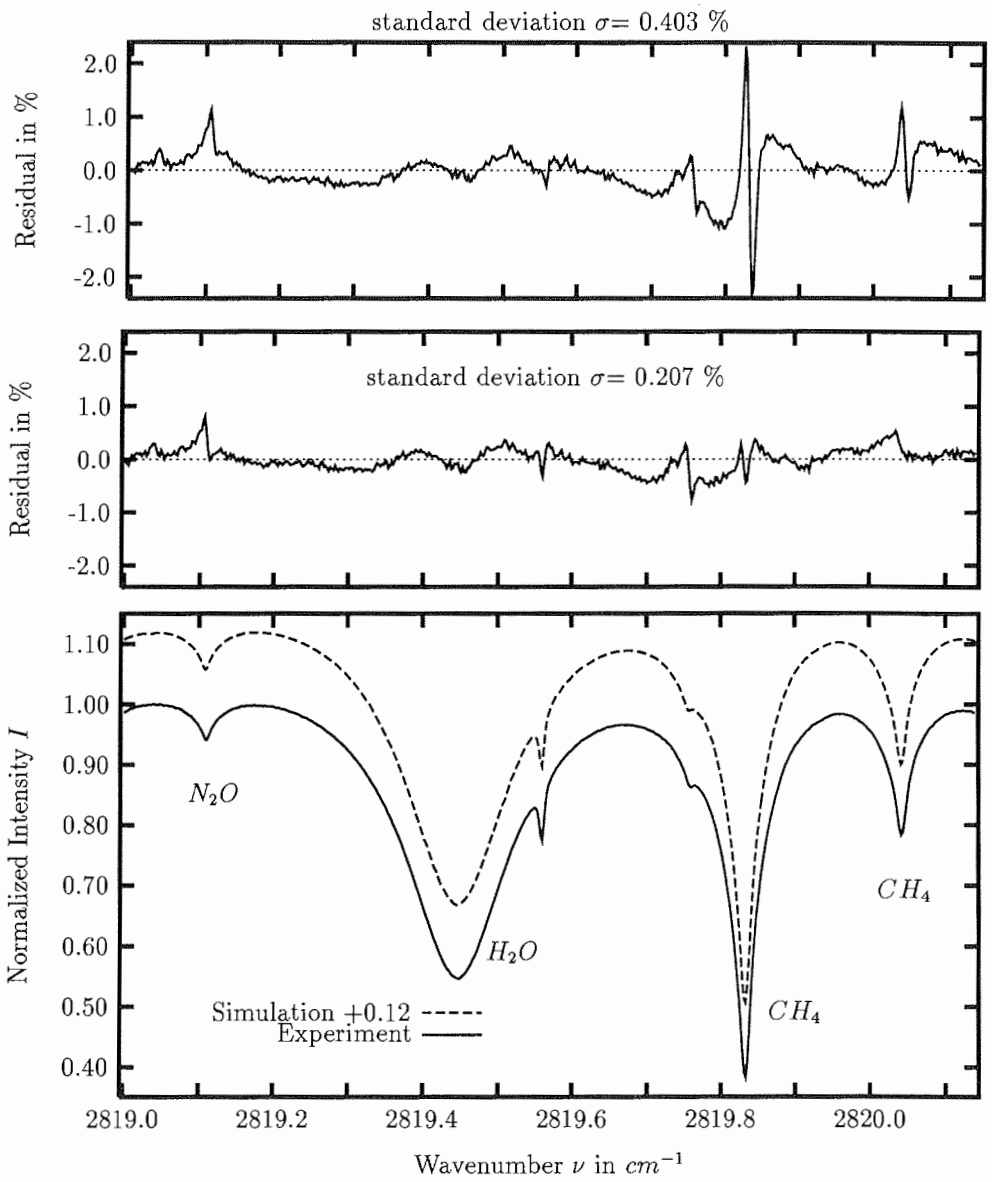

Fig. 2.5: *The upper residuals illustrate the difficulties that arise, if the pressure shift is not taken into account as in the older version 1.09d of SFIT. The residuals in the center plot demonstrate that the more recent version 1.09e yields a significantly improved fit. The phase error in both cases is set to zero in the retrieval and all major species are fitted.*

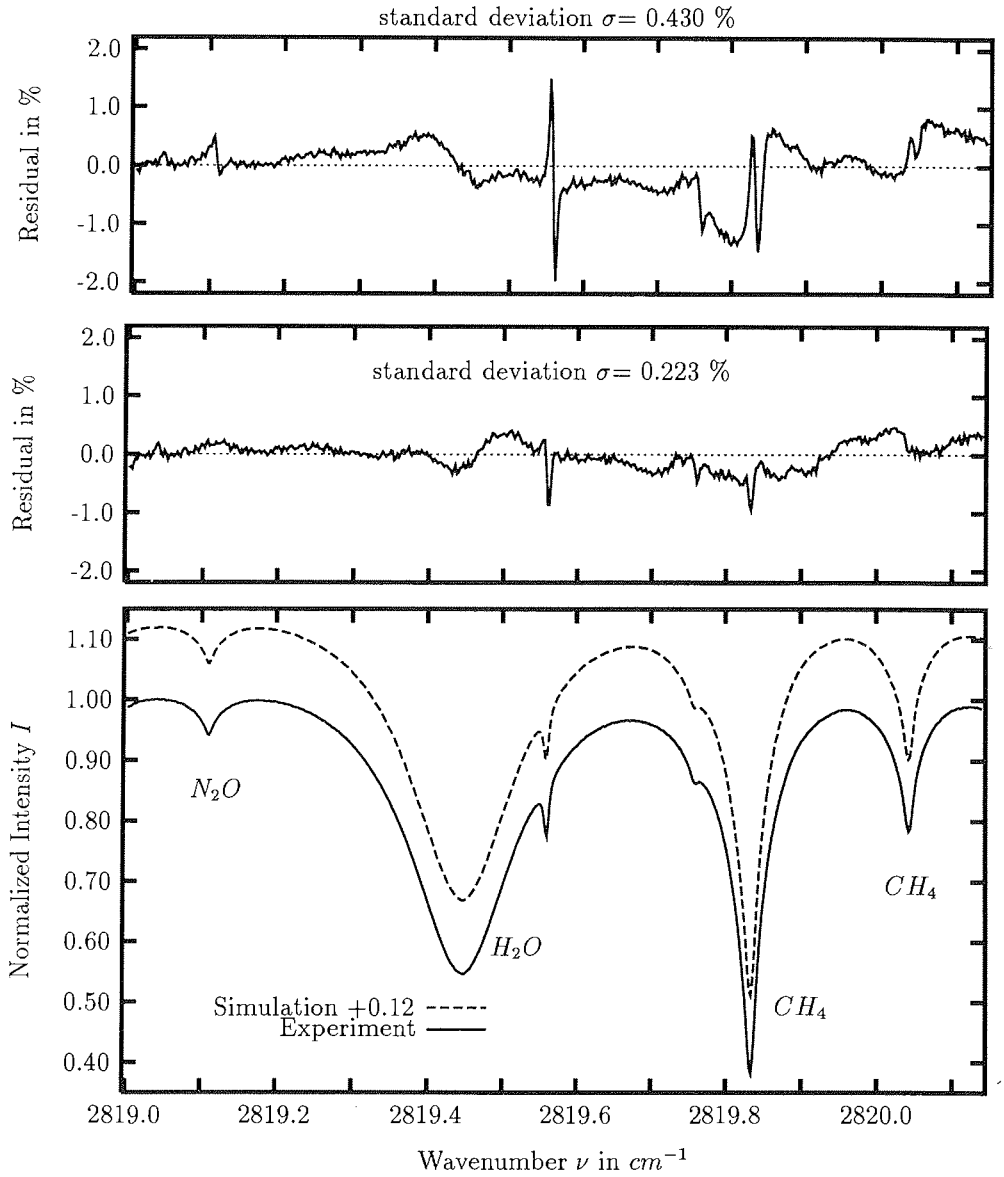

Fig. 2.6: *This is the same plot as in the previous Figure 2.5, but this time the phase error is fitted, too, while all species except H_2O are kept constant. The older SFIT version (upper figure) assigns an unrealistically high phase error to the spectrum to reduce the line shape errors in methane.*

Table 2.1: *Results from the case study on the effects of the pressure shift on the spectral fitting procedure that are illustrated in Figures 2.5 and 2.6. The pressure shift cannot be simulated by SFIT versions prior to 1.09e. The effects are small in total columns Σ for the strong absorbers themselves, but can become large for weak absorbers interfering with methane. Significant effects can also be seen in the total standard deviation of the residuals σ and in the phase error φ retrieved.*

figure	retrieved quantity	SFIT version 1.09d	SFIT version 1.09e
2.5	σ in %	0.403	0.207
	ΣCH_4 in $\cdot 10^{19}\, cm^{-2}$	1.473	1.470
	ΣH_2O in $\cdot 10^{22}\, cm^{-2}$	3.704	3.715
	ΣN_2O in $\cdot 10^{18}\, cm^{-2}$	7.132	6.689
2.6	σ in %	0.430	0.223
	φ in rad	0.0229	0.0017
	ΣH_2O in $\cdot 10^{22}\, cm^{-2}$	1.463	1.463

for both SFIT versions, but the change in residuals is striking. The standard deviation improves by almost a factor of two for the new version.

In Figure 2.5, the phase error is set to zero and the total columns of the species H_2O, CH_4, and N_2O are fitted by multiplicative scaling of the whole VMR profiles. The line shape errors without taking the pressure shift into account are obvious, as is seen in the upper residuals compared to the results with the most recent SFIT version shown below.

In the other fit, illustrated in Figure 2.6, only the amount of water vapor and the phase error are fitted. The older version (upper residuals) tries to assign some unrealistic phase error to the whole spectrum to reduce the line shape errors in the CH_4 lines, as is seen from the systematic features in the residuals at the H_2O line and from the phase error retrieved. The differences in the retrieved total columns and phase errors are listed in Table 2.1 and are small for the strong absorbers, but become large for weaker absorbers that interfere with CH_4 lines, like N_2O in the example. For the identification of individual absorbers see appendix C, page 281.

3 Improvements to the conventional analysis

3.1 General discussion of uncertainties in modelled spectra

The precision achievable in the retrieval of atmospheric trace gases depends decisively on the quality of the recorded spectra and on the quality of the model atmosphere used in the analysis. This section focusses on the discussion of systematic errors in the analysis, which are divided into two groups. On the one hand, there are systematic errors that are likely to be reduced in the future and on the other hand, there are errors that are not. The latter group is characterized by the dependence on the meteorological conditions at the time of spectral recording, which are never known completely.

Considering the first group of systematic error, the retrieval software used may have some unknown biases, due to approximations used in the algorithms or due to a mistyping in the source code. These uncertainties are expected to be reduced in future as well as uncertainties in the spectroscopic data base and recorded spectra can be reanalysed with any improved software without a loss in information.

To perform a good simulation of the atmosphere, a good knowledge of the experimental geometry, the meteorologic conditions along the sampled path, and a realistic vertical distribution of all relevant atmospheric gases is essential. The refraction index of air decreases with altitude, according to the drop in pressure. Assuming that the refraction indices in first approximation are constant within layers of same altitude, a light ray from the sun or the moon[5] entering the earth's atmosphere passes layers of increasing refraction indices. Thus, the light ray is refracted continuously by small amounts for solar zenith angles greater than zero. The resulting path of the light is no longer a straight line but becomes bended. To an observer at ground, this path is concave. Consequently, the sun appears higher above the horizon than it really is, in other words, the observed zenith angle is smaller than the astronomical zenith angle.

[5]In the following section the explicit mentioning of both IR sources is abbreviated to the solar point of view for convenience, but the considerations are valid for the moon analogously.

In the retrieval of total column amounts one has to know the exact optical path. Since the curvature of the light path is given by the atmospheric refraction indices, which depend on pressure, one has to know the pressure profile of the atmosphere along the optical path. In practice, this pressure profile is known only approximately. Hence the calculated total air mass of the atmosphere along the calculated path is subject to a systematic uncertainty. The total air mass is the height in meter that a column of air along the light path would theoretically have, if it were all compressed to normal pressure (1013 hPa) and normal temperature (296 K). The total air mass is proportional to the total number of gas particles within that column and a function of the zenith angle.

The strength of an observed absorption line depends on the total air mass given by the observation geometry. The absorption strength of a line with fixed transition probability is proportional to the total air mass, if the species studied is ideally mixed, otherwise it is a function of the total air mass and the VMR profile. Typically the area enclosed by an absorption line in ground–based spectra increases nonlinearly with increasing zenith angle[6]. The quantity expressing this relation is the air mass factor, which is the ratio of the total air mass at a given observed zenith angle to the total air mass for zenith geometry. The air mass factor for an ideally mixed species as a function of the observed zenith angle is illustrated in Figure 3.1. However, it has to be mentioned that the transition probability of a molecule is also a function of temperature. Thus, the absorption strength observed in a spectrum is a rather complicated function of the temperature profile, the zenith angle and the number density profile, where the number density is calculated from the pressure and the VMR profile. A detailed description including mathematical formulation is found in a number of text books, like e.g. in *Rao* and *Weber* (1992).

The relation between the air mass factor α and the observed zenith angle φ in degrees, as calculated with the commercial program SPITZB[7] from BRUKER, is illustrated in Figure 3.1. The dependence is fitted for

[6]Exceptions exist for species with mainly stratospheric distribution under very high zenith angles. This is known as the *Umkehr* effect (e.g. *Rao* and *Weber*, 1992)

[7]This is a customized version of the SUN_MOON program from the sun-tracker arrangement. The software is sold together with the hardware only.

the interval [55°,87°] with high quality to the numerical function

$$\begin{aligned} \alpha(\varphi) &= a_0 + \frac{a_1}{a_2 * \varphi - 90} \quad \text{with} \\ a_0 &= +0.145 \pm 0.002 \\ a_1 &= -55.31 \pm 0.03 \\ a_2 &= +1.00235 \pm 0.00002. \end{aligned} \tag{42}$$

The range of zenith angle values is restricted by the observation site. At 79° N the sun never rises higher than 35° above the horizon and the other limit is given by surrounding mountains. The suggested function (eq. 42) reproduces the exact values within the line strength shown in Figure 3.1

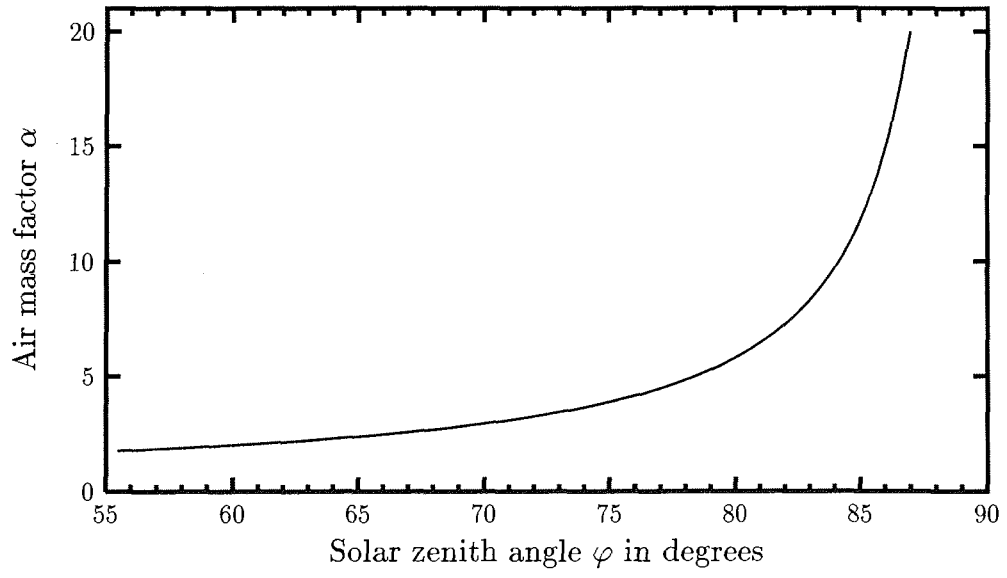

Fig. 3.1: *The air mass factor α of a perfectly mixed trace gas is shown as a function of the observed zenith angle φ of the sun. The absorption of an ideally mixed species is proportional to the air mass factor. It is obvious, that small uncertainties in the determination of the recording geometry have the strongest effect on derived total column amounts at very high zenith angles with the sun low above the horizon. The range of the zenith angle is determined by the observation site. At 79° N the sun is never higher than 35° above the horizon.*

and is superior to the common $1/cos(x)$ approximation, in particular at high zenith angles.

The precision stated by BRUKER for the calculation of the solar zenith angles φ by means of their program SPITZB is better than 0.01^o. That means for a low observation angle of $\varphi = 85^o$ an uncertainty in the air mass factor of less than 0.2 %. However, this accuracy is only valid for the model atmosphere assumed in the algorithm. The total error is expected to be significantly larger. The refraction indices of the atmosphere are not constant, but a function of the variable pressure profile. An alternative is to determine the observed zenith angle iteratively from the astronomical zenith angle in a model atmosphere that takes the actual pT profile into account. Such a ray tracing program is included in the SFIT package, but the operation is time consuming and the difference in results is very small. Thus, the BRUKER program is preferred for convenience. Unfortunately, there are no independent measurements available to check the quality of both algorithms, e.g. by determination of the zenith angle with a sextant. The uncertainty introduced by the calculation of the zenith angle is systematic, but the arising error has the characteristics of a seamingly stochastic cause due to the natural variability of atmospheric parameters. This error is unlikely to be reducible in future, in particular for spectra that have already been recorded.

The creation of the model atmosphere, by means of the program FASTCOD from the SFIT package by *C. Rinsland* (appendix B), which is based on the algorithm of *Clough* et al. (1986), introduces further uncertainties. The uncertainties in the optical path discussed above effect the air mass factors calculated for each model layer. The use of model layers itself with weighted averages of pressure, temperature, and VMRs is another rough approximation to nature. Small changes in the layering scheme used have already a measurable effect on the total column amounts retrieved, as is shown in an example in chapter 4.4. The number of model layers used has also an effect on the retrieved total column amounts that decreases with the total number of layers used. The magnitude of all these uncertainties for the SFIT model atmosphere with 29 layers is estimated from the example discussed in chapter 4.4 to be in the order of 1 to 3 % in terms of total column amounts retrieved.

Another aspect is the time needed for recording a spectrum. During instrumental operation, the earth keeps on rotating around its axis. Thus, the air mass factor is not constant throughout the time needed to record a spectrum. The relative change in air mass with recording time is strongest for large zenith angles, as can be seen from Figure 3.1. As a rule of thumb, recording times of 10 minutes should not be exceeded for zenith angles exceeding 80^o. If a higher S/N is required, the individual spectra can be coadded for the analysis in the way described by *Notholt* (1994a).

It is obvious from Figure 3.1 that small errors in the calculation of the optical path for zenith angles not exceeding 80^o have only a small effect on the air mass factor determined. However, the uncertainties grow fast for zenith angles exceeding roughly 80^o. This is a difficulty in the analysis of spring data (see details in chapter 4.6). At the end of the polar night in early March, the returning sun rises for many days less than 10^o above the horizon, while strong dynamical changes (break up of the polar vortex) and chemical changes (return of photolysis reactions) occur in the atmosphere.

3.2 The use of radio– and ozone–sonde data

Let us assume for the discussion in this section that the instrument is perfectly aligned, that all instrumental parameters are known, that the spectroscopic data base given and the program used for creating the model atmosphere are ideal, and that the observations are performed at zenith angles where the uncertainties in calculated air masses are negligible. The accuracy of the retrieval is then limited by the quality of the pT profile and the VMR profiles used. These profiles all effect the line shape, but they are known in practice only approximately. At many observation sites there is only a climatology available, i.e. an average of meteorological parameters over many years for a certain region on a yearly, seasonal or monthly basis. Temperature profiles taken from climatologies often differ from the true temperature profile for a particular spectrum by several Kelvin, at least in some altitudes. A case study on the effects of errors in the pT profile are calculated in chapters 4.6 and 5.3 and results are given in Figure 4.19 (page 117) and in Table 5.6 (page 150), respectively.

In the latter example featuring ozone, a pT profile with a bias of 2 K in temperature and 1.5 % in pressure leads to an increase in line shape errors by 15 % and an error in the retrieved total column amounts of 4 % on the average, exceeding 8 % in single cases.

An approach to reduce the uncertainties introduced by the pT profile is to derive the pT profile from the spectra themselves. The VMR profiles of N_2, O_2, and CO_2 are almost constant and known with high accuracy. By allowing only small changes to the logarithmic drop in pressure, the temperature profile can be varied until the line shape of a set of selected lines is matched optimally. However, this is a difficult and time consuming task in ground based spectra. The line shape varies nonlinearly with temperature and the sensitivity decreases towards high altitudes and towards very low altitudes (see also the discussion in chapter 4.4). The situation improves for satellite based instruments. The absorption strength of a line as a function of the tangent layer probed can be used in addition to the integral lineshape observed (e.g. *Rinsland* et al., 1992).

An alternative to improve the accuracy of the pT profiles used in the analysis of ground–based FTIR spectra is the use of *in situ* measurements performed by regular radio sondes launched directly at the observation site. At the *Koldewey station*, the sondes are carried by a Helium filled rubber balloon and are launched daily at noon with additional flights available during campaigns. The radio sonde used is a commercial *RS 80* from VAISALA, Finland. It measures pressure, temperature, wind speed, and relative humidity from ground to the explosion altitude of the balloon. The altitude of the sonde can be calculated from the geopotential height, which deviates only by typically 5 to 60 m from the geometric altitude (*Beyerle*, 1994). The maximum altitude is typically between 28 and 34 km, occasionally altitudes up to 36.5 km are reached. The measured data is radio transmitted to the ground station every 10 seconds, yielding a height resolution of typically 40 to 50 m. An example of a wintertime and a summertime pT profile recorded by radio sondes is shown in Figure 3.2.

The accuracy of the pressure and temperature sensors of the radio sonde is very high. The uncertainty stated by VAISALA is 0.4 K for the absolute temperature and 0.5 hPa for the pressure at ground. Before the

discussion on the quality of the pT profile is continued, it is convenient to introduce all other quantities available from balloon borne sondes, since the discussion of the uncertainties is basically the same for all these measurements.

The data on the relative humidity can be used to calculate the tropospheric water vapor VMR. The uncertainties for the relative humidity data are about 5 to 10 % in the troposphere and become unreliable above the tropopause. However, the tropospheric distribution of water vapor makes up more than 95 % of the absorption signal and its distribution shows no significant gradient in the stratosphere. For the calculation of the VMR of $H_2{}^{16}O$ from the pressure p, the temperature T, and the rel-

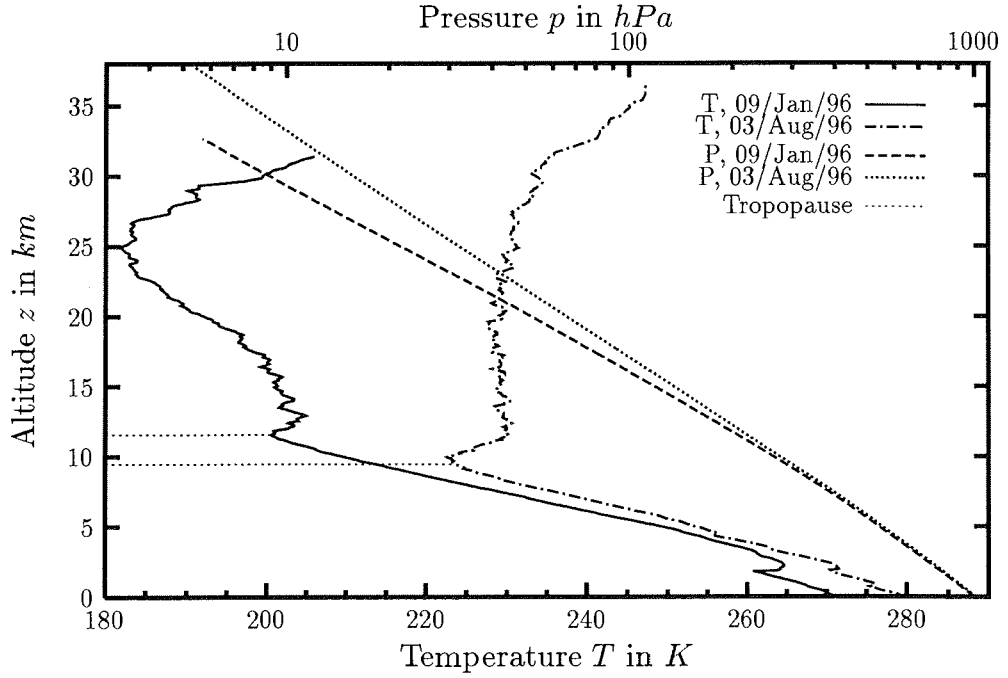

Fig. 3.2: *The pressure and temperature profile recorded by two radio sondes launched at the observation site of Ny–Ålesund. The tropopause is found at 11.1 km in the wintertime example shown and 2 km lower in the summer example. Profiles are displayed from ground to the explosion altitude of the carrying balloon.*

ative humidity $relF$ of the sonde, equation (43) is used. The coefficients for the saturation vapor pressure are taken from (*Smithsonian Institution*, 1966):

$$\begin{aligned} \mathrm{VMR}_{\mathrm{H_2O}} &= \frac{\text{partial pressure } H_2O}{\text{total pressure } p} = \frac{relF}{p} \cdot \text{saturation vapor pressure} \\ \mathrm{VMR}_{\mathrm{H_2O}} &= \frac{relF}{p \cdot hPa^{-1}} \cdot 6.1078 \cdot exp\left\{\frac{17.0809 \cdot (T - 273.15\,K)}{T - 38.975\,K}\right\}. \end{aligned} \quad (43)$$

The quality of the water vapor VMR profile derived from the relative humidity data of the radio sonde by means of equation (43) is demonstrated in Figure 3.3. The lower figure shows the recorded and the simulated spectrum and the figure in the center the corresponding residuals for a H_2O VMR profile calculated according to equation (43). For comparison, the upper figure shows the residuals obtained with all settings being identical except for the VMR profile, which is a climatological average VMR profile termed *'subarctic summer'* taken from the program FASTCOD2 (*Clough* et al., 1986).

It is obvious that the VMR profile calculated from the radio sonde is superior to any climatology, because the latter cannot account for the high variability of water vapor in the troposphere. The use of water vapor profiles calculated from the radio sonde humidity data by equation (43) improves the quality of the modelled spectra significantly. The gain is much more than simply an improvement of accuracy for the retrieval of water. Absorption lines of H_2O and HDO are distributed throughout the infrared spectral region. They are typically strong and due to their abundant distribution in the lower troposphere the lines are very broad. There is almost no spectral interval used in the retrieval that has no interferences from water vapor (see appendix C). Thus, the correct simulation of the water vapor line shape is an important improvement to the retrieval of almost all species studied.

The next valuable information derivable from sonde data is the VMR profile of ozone. The electrochemical concentration cell (ECC) type 4A is the balloon borne sensor used and yields the partial pressure of ozone. An ECC sonde is launched on a regular schedule once a week, but during campaigns up to two ECC sondes per day are available. The ozone

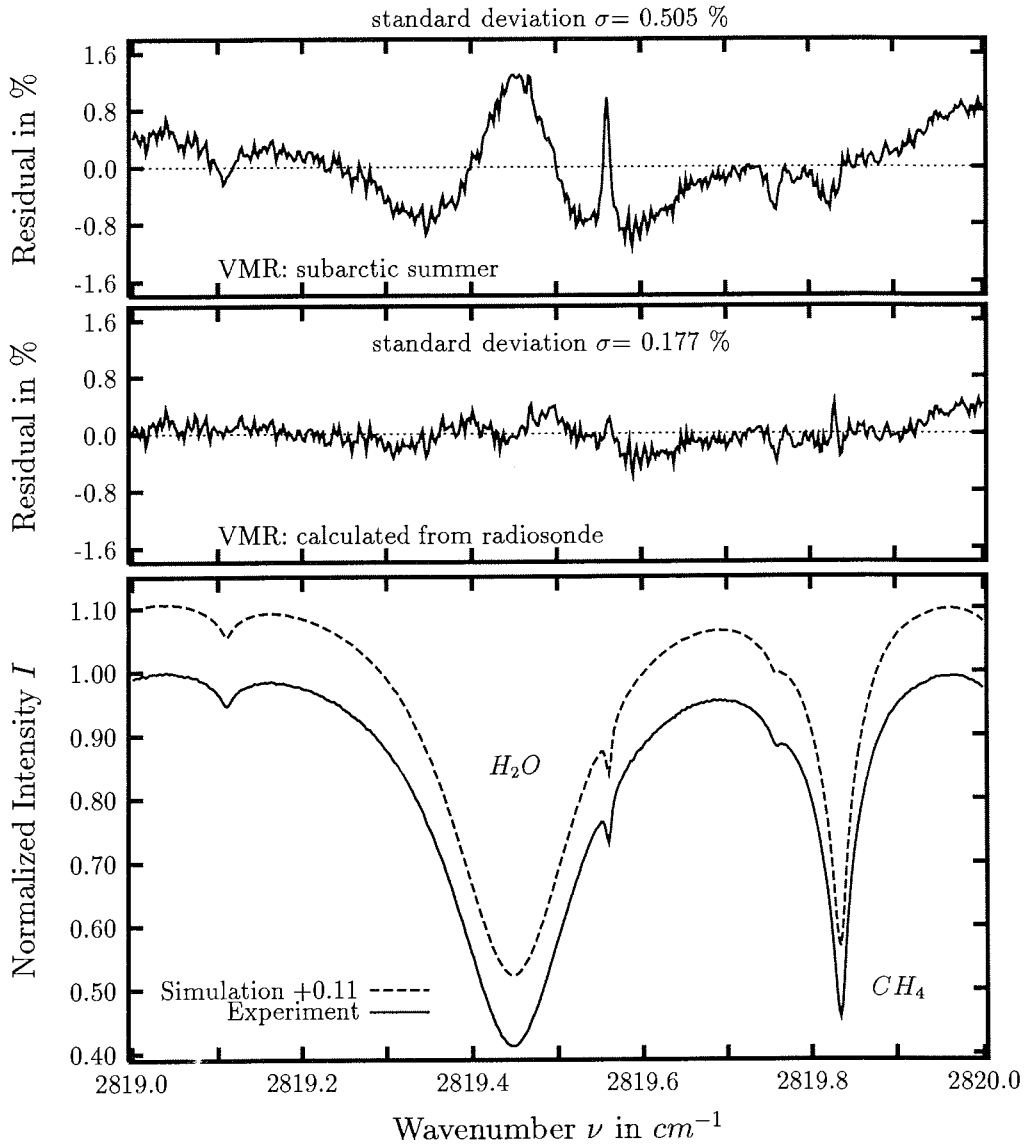

Fig. 3.3: *The quality of the water vapor VMR profile derived from the relative humidity data of the radio sonde by means of equation (43) is demonstrated. The lower figure shows the recorded and the simulated spectrum and the figure in the center the corresponding residuals for a H_2O VMR profile calculated according to equation (43). For comparison, the upper figure shows the residuals obtained with a climatological H_2O VMR profile.*

sonde is always launched in a tandem arrangement with the radio sonde described above on a Helium filled rubber balloon. Average maximum altitudes achieved are the same as for the radio sondes.

The ECC ozone sonde is at least one of the most important instruments that document the long–term change in atmospheric ozone. It gives the longest altitude resolved record of the ozone concentration for the polar atmosphere with the first sondes launched in Antarctica some 40 years ago. For a comprehensive review *Gernandt* et al. (1995 and 1996) are recommended. Compared to satellite instruments, ECC sondes have the advantages of being usable during the polar night, having a higher vertical resolution and with data sampling starting from ground, the results are available in real–time, and the total costs are moderate. The accuracy of ECC and radio sondes has been studied in detail by *Komhyr* (1986) and *Vaisala* (1991). There is also a total column amount available from ozone sondes by integrating the VMR profile, which is completed above the explosion height with a theoretical profile. The total accuracy for this total column amount is about 4 % (*P. von der Gathen*, AWI Potsdam, oral communication).

The improvement to the analysis of IR spectra by using *in situ* ozone VMR profiles is manifold, as in the case of water vapor. Ozone lines have a lesser importance as far as interference with other species is concerned, because the lines are much narrower. But ozone is also a very frequent absorber in recorded spectra and with the known ozone profile the check of the pT profile can be improved significantly. The species N_2 and CO_2 with their constant VMR profile can be used to check the pT profile by analysing the line shape, since the line shape of these species depends on the pT profile only, as mentioned earlier. However, these molecules are less sensitive to pT changes in the stratosphere than ozone, which is mainly distributed in the stratosphere between 18 and 22 km. Thus, ozone improves the quality check for the assumed pT profile.

The other aspect of the *in situ* ozone profiles is the reduction of uncertainties in the ozone retrieval itself. For the reporting of total column amounts of ozone, this does not appear to be highly important. The ozone amount is already known by the ECC sonde data itself and by several other instruments at Ny–Ålesund. But, the significant reduction

in the relative uncertainties of the retrieved total ozone by using *in situ* VMR profiles, is the decisive requirement for the successful investigation of natural isotopic ratios that are discussed in detail in chapter 5.

Summed up, the use of *in situ* sonde data in the analysis of ground based FTIR spectra are a significant improvement to the accuracy achievable in the retrieval of total column amounts. However, it has to be pointed out that this is true only if the air mass sampled by a sonde is the same as the one sampled by the FTIR at recording time. Generally, this is not the case. If the meteorological conditions are stable, one may assume that the sondes sample an air mass that is representative for a couple of hours in the vicinity of the observation site. However, there is no guarantee. A necessary, but not necessarily sufficient check, is the matching of line shapes for N_2, CO_2, and O_3. Helpful are also meteorological maps, like the PV maps discussed in section 4.3, to see whether there are any large scale disturbances. Throughout most of the year, the ECC and radio sonde data proofed to be representative or useful for the analysis of FTIR spectra over the past three years. But difficulties typically arise with very low observation angles – the mean air mass sampled by the FTIR is then typically several hundred kilometers away from the observation site. In particular, spring data are concerned, when the sun stays below 10^o above the horizon or when the optical path crosses the polar vortex edge (see chapter 4.6).

The data from radio and ozone sondes is stored in the NASA–Ames[8] format in ASCII. Both data sets are sent to the European storage center at NILU (*Norsk Institutt for Luftforskning*) in Oslo, Norway, as well as to the WMO (radio sondes) and to the *World Data Ozone Center* in Toronto, Canada, and the NDSC headquarters (ozone sondes) in Hampton, USA. Computer programs have been created for the interactive conversion of sonde data into SFIT compatible files (ECC2REF, AED2PT, AED2VMRW). These programs provide default profiles above the sonde peak height and the user can correct discontinuities at the explosion altitude and sensor failures on a graphics display with manipulation tools that are selectable from a mouse driven menu (see appendix B).

[8]Named after the NASA research center at Ames, USA

3.3 Corrections specific to lunar spectra

The first successful absorption spectra recorded with the moon as a light source that covered large spectral regions of the infrared were accomplished by *J. Notholt* at Ny–Ålesund in the polar winter 1992/93. The general properties and some of the peculiarities of lunar spectra are published in (*Notholt*, 1993a and 1994) and (*Notholt* et al., 1993b). This new measurement technique allows for the first time the recording of absorption spectra during the full moon phases in polar night. Between the end of September and the beginning of March, the sun is not visible at the observation site given. Thus, a large gap has been closed for the observation of seasonal cycles. Moreover, fundamentally new experiments have become possible, like the investigation of atmospheric chemical reactions in the complete absence of photolysis. Another example on this item is given in chapter 5, with the decline in the isotopic enhancement of heavy ozone.

In this section some of the peculiarities of lunar spectra important to the correct retrieval of total column amounts are discussed. Some aspects are illustrated additionally by comparison of lunar and solar spectra recorded within 12 hours. This is the first direct comparison of solar and lunar spectra reported and fills an important gap in the knowledge on lunar absorption spectra. However, the discussion is not always straightforward due to the complicated meteorological conditions during the recording time and the restrictions on the recording geometry. The observation of both the sun and the moon is only possible on a few days in spring and autumn. Additionally, the instrument has to be modified and realigned within a few hours. On the 15^{th} and 16^{th} of March 1995, solar spectra were recorded and lunar spectra during the night in between. On the other nights of that full moon phase, the weather unfortunately remained cloudy. The zenith angles for all the solar spectra are greater than 81^{o} and greater than 76^{o} for the lunar spectra due to the season. However, the detailed discussion of this spring data is postponed to section 4.6.

In spectral regions where the atmosphere is totally opaque and no direct solar or lunar light reaches the surface, the spectral intensity in the recorded spectrum practically never drops to zero, as it should. This

effect is termed the zero level offset of the spectrum. The main contributions to this zero level offset are caused by a variety of sources of spectral emission, discussed in detail by *Schreiber* (1994), and by nonlinearities of the detector. The contribution arising from nonlinearities of the detector are simple to understand. The recorded interferogram has a strong maximum at ZPD and drops sharply with increasing OPD. Thus, saturation of the detector and overmodulation of the subsequent electronics is most likely for the direct center of the interferogram only. Distortions restricted to the center of the interferogram, meaning a small interval in spatial coordinates, effect the FT of the interferogram, i.e. the spectrum, in the form of very broad spectral features.

The spectral flux density of the sun is by orders of magnitude larger than the lunar one, as is described in section 2.1 and is illustrated in Figure 2.1. Thus, the emission originating from the atmosphere and the instrument has a much lesser effect on solar than on lunar spectra. If a mean temperature of e.g. 250 K is assumed for the troposphere, the difference can be estimated from the ratios of a blackbody of 250 K and the blackbodies corresponding to the sun or the moon, respectively, at a given wavenumber. From Figure 2.1 (page 32) the magnitude of the zerolevel offset due to atmospheric emission can be estimated to be less than 0.1 % in solar and about 10 % in lunar spectra at 1000 cm^{-1}. Typical values for the wavenumber dependent zero level offset determined in the solar and lunar spectra are listed in Table 3.1. The zero level offsets given for solar spectra do not exceed 3 %, while values of up to 18.5 % are encountered in the lunar examples. For the lunar spectra, a zerolevel offset of about 10 % is found at 1000 cm^{-1}, as is estimated from the blackbody curves. Thus, in lunar spectra emission dominates the zerolevel offset. In solar spectra, the zerolevel offset of 1 to 3 % is at least by a factor of 10 higher than is estimated from the blackbodies. Thus, the zerolevel offset in solar spectra is assigned to nonlinearities in the detector system. Although the aperture used in solar spectra is smaller than for lunar spectra, the flux entering the detector is higher by at least two orders of magnitude.

The decrease in the zero level offset with wavenumber in lunar absorption spectra is given by the drop of the 255 K blackbody curve represent-

ing the emission sources, which drops faster than the 370 K blackbody curve corresponding to the full moon (compare Figures 2.1 and 3.4). However, a correction of the zero level offset is imperative for lunar spectra.

In search of an adequate correction for lunar absorption spectra, pure emission spectra are studied first. In Figure 3.4, a lunar absorption spectrum is compared to 3 different emission spectra recorded immediately after the absorption spectrum. All spectra shown are recorded without any optical band filters. The first emission spectrum is a spectrum of the night–sky recorded under the same zenith angle as the absorption spectrum, but under opposite azimuthal angle. The remaining two spectra are recorded with a pair of self–made blackbodies consisting each of a black painted copper tube closed at the far end with a heavy copper

Table 3.1: *The table shows typical values for the zero level offset in lunar spectra compared to solar spectra for a variety of important spectral intervals that are relevant in the retrieval of the species listed in the second column. All values are given in percent relative to the maximum spectral intensity encountered in a spectral interval of 10 cm^{-1} centered about the investigated absorption line. For the example illustrated in Figure 3.6, the zerolevel offset is calculated by the ratio of the blackbody portion of the emission spectrum (dashed line at 0.31) and the 100 % transmission level at 1.74 arbitrary intensity units, yielding 17.8 %.*

wavenumber in cm^{-1}	relevant species	zero level offset in % lunar spectra 95031506	lunar spectra 95031508	lunar spectra 95031528	solar spectra 95031504	solar spectra 95032004
780.2	$ClONO_2$	17.4	17.8	18.5	3.1	3.0
829.1	CHF_2Cl	16.1	16.5	16.9	2.9	2.9
868.5	HNO_3	14.8	14.5	15.0	2.4	2.4
989.1	$^{16}O^{18}O^{16}O$	8.2	8.4	8.6	1.3	1.2
1002.6	$^{16}O^{18}O^{16}O$	9.3	9.5	9.8	0.0	0.0
1090.3	$^{16}O^{16}O^{18}O$	6.0	6.2	6.4	1.2	1.2
1146.5	$^{16}O_3$	5.8	5.9	6.1	1.1	1.0
1234.2	COF_2	3.9	4.0	4.1	1.1	1.0

plate. One blackbody is put up close to the solar tracker on top of the roof at ambient temperatures of 255 K. The other one is put up directly at the entrance of the instrument and is operated at 77 Kelvin after cooling with liquid nitrogen under dry air conditions. The total emission of a blackbody follows the *Boltzmann* law and is proportional to T^4. Thus, the emission of the blackbody at 77 K is by more than 2 orders of magnitude smaller than the atmospheric emission at 255 K and the maximum is shifted to 160 cm^{-1}. Thus, the spectrum recorded represents the emission arising from optical components of the instrument itself. The spectrum with the instrument facing the blackbody on top of the roof (255 K blackbody) represents the sum of the instrumental emissions of the previous spectrum and the emission of a totally opaque atmosphere at 255 K. Finally, the night sky emission spectrum additionally shows discrete emission lines in spectral regions where the atmosphere is not totally opaque.

The night sky emission spectrum mirrors to some extend the absorption spectrum. In the spectral interval from 1000 to 1100 cm^{-1} a strong ozone absorption band decreases the intensity in the absorption spectrum, while it increases the emission spectrum intensity. It is vice versa in the spectral range from 750 to 1000 cm^{-1}, where the atmosphere is rather transparent. In the spectral regions below 740 and above 1250 cm^{-1}, the atmosphere is practically totally opaque and the absorption spectrum drops to the night sky emission spectrum, which is identical to the 255 K blackbody spectrum in these spectral regions. In spectral regions of total opaqueness, the emission spectrum of the atmosphere is comparable to a blackbody spectrum of the temperature corresponding to the mean temperature of the lower troposphere, where temperatures and number densities are highest. In the spectral region in between, the atmosphere is only slightly opaque, leading to the difference between the night sky emission spectrum and the 255 K blackbody spectrum shown.

In contrast to solar spectra (not shown), the spectral window above 1900 cm^{-1} cannot be used in absorption spectra with the MCT detector, because the spectral intensity of the moon (Figure 2.1) is too low. The increase seen in Figure 3.4 near 2000 cm^{-1} is too weak for the retrieval of absorption lines. As a consequence the species NO, OCS, N_2 and

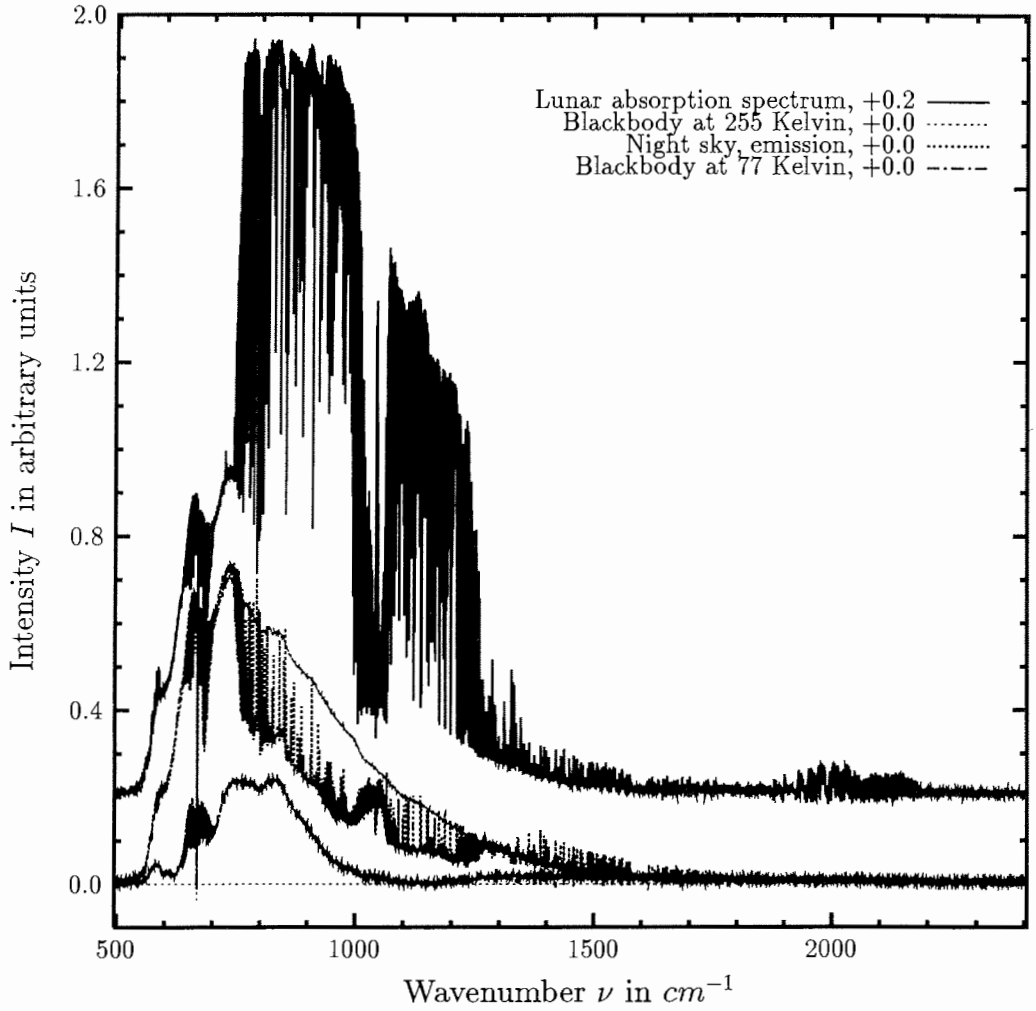

Fig. 3.4: *The comparison of a lunar absorption spectrum to different emission spectra is illustrated. The absorption and the night sky emission spectrum are recorded subsequently, with an identical zenith angle but opposite azimuthal angles. The emission spectrum recorded with a blackbody of 77 K represents the emission of the optical components of the instrument itself, while the remaining one represents a totally opaque atmosphere. All spectra are recorded without any optical filters and the absorption spectrum is shifted for clarity.*

CO are not detectable in lunar spectra with the spectral microwindows commonly used (see appendix C). In spite of the low albedo of the moon does the direct reflectance of solar light become significant towards higher wavenumbers. The visibility of the moon to the human eye is based on this direct reflectance and not on the blackbody radiation. At about 2400 cm^{-1} the spectral flux due to direct reflection becomes as important as the blackbody radiation of the full moon (*Notholt*, 1994a, figure 1). In the spectral region above 2600 to about 4100 cm^{-1} the specialized lunar InSb detector yields high quality absorption spectra again. In that spectral region, an emission correction is not necessary, as can already be estimated from Figure 3.4, because the colder blackbody representing the emitting environment drops faster than the lunar blackbody even without taking the reflection into account.

Taking a look at Figure 3.4, one might suggest to subtract the night sky emission spectrum from the lunar absorption spectrum as a first approximation towards a correction of the lunar absorption spectrum. This is done in Figure 3.5. The original lunar absorption spectrum is compared to itself after subtraction of the night sky spectrum and also to a solar spectrum recorded 12 h later. In the crude resolution given, the overall shape of the resulting lunar difference spectrum is encouraging. The night sky emission spectrum is the key to the correction of lunar absorption spectra.

Emission spectra have typically a significantly lower S/N than absorption spectra, a lower spectral intensity and a lower resolution. As shown in detail by *Brault* (1987), emission spectra with these properties are subject to a significant phase error. This leads in particular to a distortion of the observed lineshape, with lines becoming asymmetric to their corresponding line centers. In mathematical terms the FT of the distorted interferogram yields a complex instead of a real spectrum (see chapter 1). Thus, emission spectra have to be phase corrected before analysis or before subtracting them from any lunar absorption spectrum.

The phase correction can be performed in three ways to extract the real spectrum from the complex spectrum recorded. Originally described by *Mertz* (1967), one method is to calculate the phase angle φ by the ratio of the real part $Re(\nu)$ and the imaginary part $Im(\nu)$ of the complex

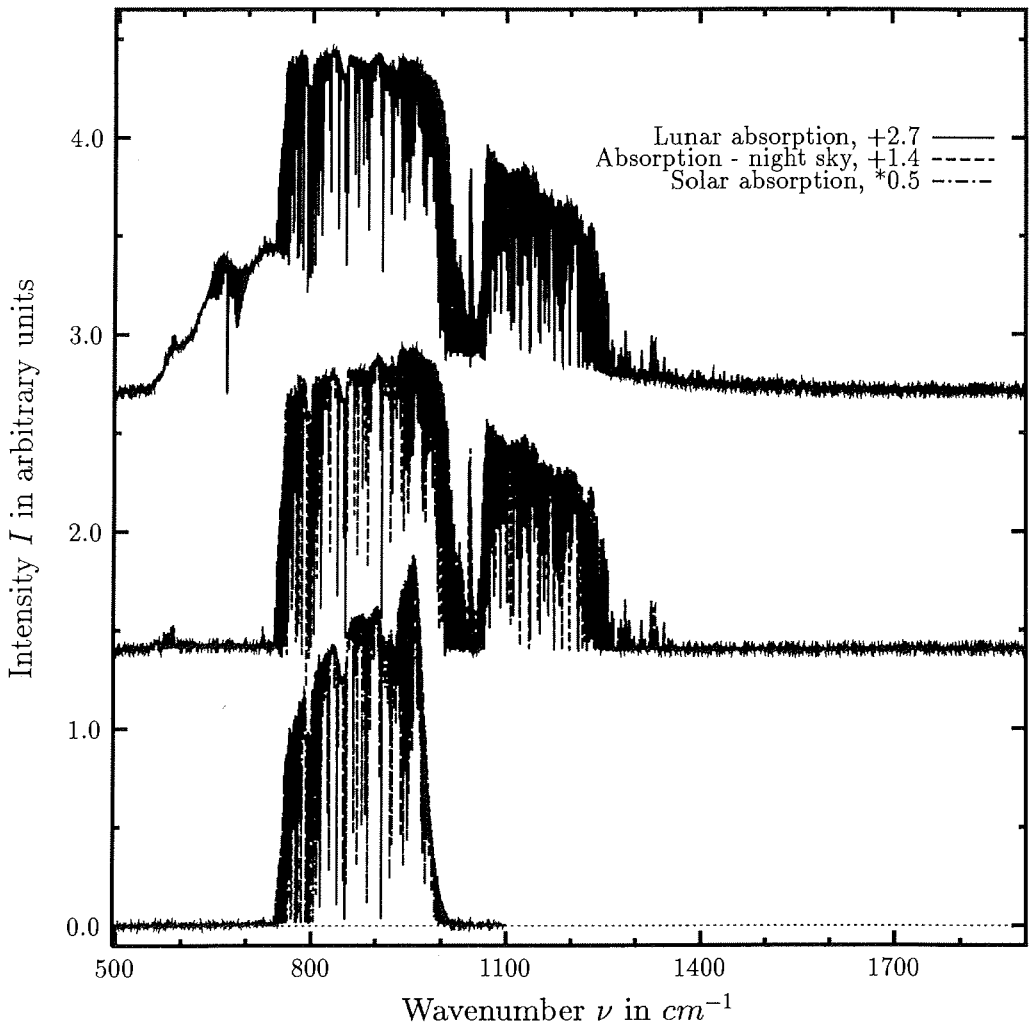

Fig. 3.5: *The lunar absorption spectrum from the previous Figure 3.4 is shown once as recorded and once after subtraction of the night sky emission spectrum. For comparison, a solar spectrum recorded 12 h later is included in the figure. The lunar spectra are shifted for clarity and the solar spectrum is scaled to a comparable intensity. The fall off at the right hand side of the solar spectrum is due to an inevitable optical filter. A filter is not necessary for the weak lunar spectra.*

spectrum $C(\nu)$ given. The angle calculated according to equation (44) is then used to compute a pure amplitude spectrum $S(\nu)$:

$$\varphi(\nu) = \arctan\left(Im(\nu)/Re(\nu)\right) \quad (44)$$

$$S(\nu) = Re\left\{C(\nu) \cdot e^{-i\varphi(\nu)}\right\} \quad (45)$$

Alternatively, the multiplicative phase correction can be applied by multiplying the complex spectrum with its complex conjugated counterpart. However, this method is inferior to the Mertz method for spectra that are not free of noise (*Gronholz* and *Harris*, 1985). Both mathematical corrections require a double sided interferogram. The third method of phase correction uses a totally different approach and is applicable to single sided interferograms. If an absorption spectrum is recorded with identical instrumental settings just prior to the emission spectrum from a bright IR source (hot blackbody, sun), the phase spectrum is known for this with high quality. Under the assumption that the instrumental properties, like the ZPD and the electronics, do not change significantly while recording the emission spectrum subsequently, the phase spectrum from the absorption spectrum is used for the phase correction of the emission spectrum.

In Figure 3.6 the small spectral interval from 774 to 786 cm^{-1} is shown in detail with the lunar absorption and the night sky emission spectrum from figure 3.4. The lowest curve gives the night sky emission spectrum after the Mertz phase correction is applied. The blackbody portion of this emission spectrum is indicated by the dotted line. The latter corresponds to 0.31 intensity units or 18 % of the maximum in the absorption spectrum for the spectral interval shown. To illustrate the line shape distortion caused by the large phase error common in emission spectra, both the phase corrected (top solid line) and the not phase corrected original emission spectrum (broken line in the center) are projected on the absorption spectrum (dotted line) by mirroring and stretching. The asymmetry in the line shape in the not phase corrected spectrum is obvious. The differences in the general lineshape between absorption and emission spectra are due to the lower spectral resolution of the emission spectra and the location of signal formation being limited to the lower troposphere for the highly temperature dependent emission process. For the same reason stratospheric gases like ozone are practically missing in

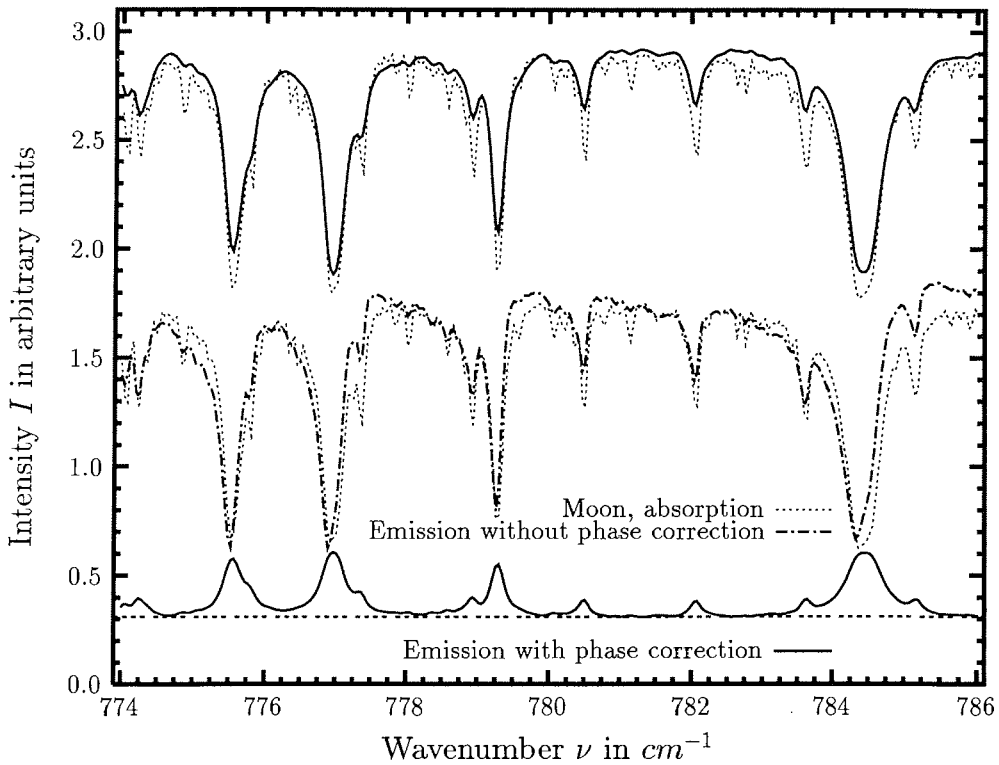

Fig. 3.6: *A more detailed comparison of the lunar absorption and the night sky emission spectrum is shown. The lowest curve (solid line) gives the phase corrected night sky spectrum, with the blackbody portion indicated by the dashed line. To illustrate the line shape distortion caused by the large phase error common in emission spectra, both the phase corrected (top solid line) and the not phase corrected emission spectrum (broken line in the center) have been projected on the absorption spectrum (dotted line) by mirroring and stretching. Differences in the general lineshape between absorption and emission spectra are due to the lower spectral resolution of the emission spectra and to differences in the location of signal formation. Most of the emission arises from the warmer lower troposphere. Thus, stratospheric gases like ozone are practically missing in the emission spectra. For the identification of lines see Figure 3.7 and appendix C, pages 195–201.*

the emission spectra. For identification of individual lines see Figure 3.7 and appendix C, pages 195–201.

3.4 Comparison of solar and lunar results

It is illustrated in Figures 3.4 to 3.6 that the 100 % transmission level of lunar absorption spectra is shifted upward by approximately the amount of the blackbody portion of the corresponding night sky emission spectrum. Thus, the relative absorption strength of an absorption line appears weaker than it really is, if the zero–level shift is ignored. To illustrate this in an example: assuming a 100 % transmission level of 1.0 arbitrary intensity units and an absorption line that absorbs 60 % of this intensity in its line center will look like a line that absorbs only 50 %, if the blackbody–like emission of the atmosphere and of the instrument shifts the whole spectrum up by 20 %. In this case, termed case 0 in Table 3.2, the retrieved total column amounts underestimate the true values significantly.

The following discussion focusses on the case study performed in the 780 cm^{-1} spectral interval. This is the most suitable interval to retrieve $ClONO_2$, which is an important reservoir gas in the fast ozone destruction cycles. At this low wavenumber, both the blackbody portion of the night sky emission spectrum and the atmospheric emission by individual trace gases are significant (Figure 3.6 and 3.7). The spectra discussed are again the solar and lunar spectra recorded within 24 hours in March 1995. Due to the high dynamical and chemical variability in this period, identical total column amounts can only be expected for those species that show very little dynamic variation and that are not subject to a significant chemical processing on the time scales considered.

In the given case, this applies to CO_2 only, because the remaining species (see appendix C) that show a significant absorption in the selected spectral interval, like O_3 and $ClONO_2$, are subject to substantial dynamical and chemical changes. A detailed discussion of the spring data is given in section 4.6.

In case 1 of the case study, the blackbody portion of the night sky

spectrum is determined first (Table 3.1), to set the zero level offset in the analysis software to a realistic value to get the the 100 % transmission level right. This has the advantage over the next alternative described that no additional noise is added to the absorption spectrum. For those species occurring exclusively in the cold stratosphere and consequently have no significant emission, the retrieved total columns are expected to be correct within the statistical errors. However, for an abundant tropospheric species, the emission fills up the absorption lines to a certain degree (Figure 3.7) and the retrieved total column again underestimates the correct amount. Nevertheless, the deviation is considerably lower

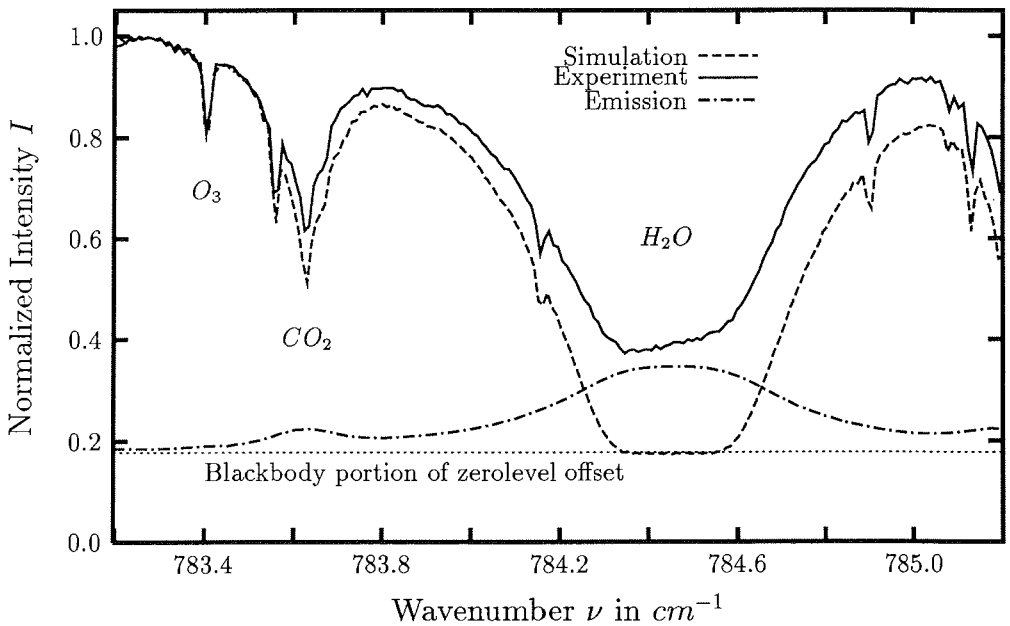

Fig. 3.7: *This figure illustrates some of the difficulties in the retrieval of total columns from lunar absorption spectra. In the simulation the 100 % transmission level and the zerolevel offset corresponding to the blackbody portion of the night sky emission spectrum are set to adequate values (case 2, Table 3.2) and the resulting absorption is calculated for these initial values with zero iteration steps and adequate a priori VMR profiles. In the saturated H_2O line at 784.5 cm^{-1} the zerolevel offset and the strong effect of emission by water vapor itself are obvious.*

than in the totally uncorrected case (Table 3.2).

The next correction approach tested is the subtraction of the phase corrected night sky emission spectrum from the lunar absorption spectrum.

Table 3.2: *This table presents the results from a case study of different retrieval methods applied to lunar absorption spectra. The total column amounts Σ and the total standard deviations of the residuals σ retrieved are listed for $ClONO_2$ and CO_2 and the amounts of CO_2 are compared to the results from the solar spectra. Case 0) no correction is applied to the lunar spectra. Case 1) The blackbody portion of the emission spectrum is taken into account in the retrieval program. Case 2) The emission spectrum is subtracted from the absorption spectrum before the analysis is started. Case 3) The results from Case 1 are mathematically corrected for emission effects as derived from weighted blackbody ratios.*

lunar absorption spectra					
correction method	spectrum	σ in %	$\Sigma ClNO_3$ in $10^{15}cm^{-2}$	ΣCO_2 in $10^{21}cm^{-2}$	rel. deviation from solar in %
case 0	506	0.68	3.27 ±0.31	4.257 ±0.083	-41.57
no	508	0.68	3.54 ±0.36	4.293 ±0.084	-41.07
correction	528	0.81	3.46 ±0.32	4.207 ±0.085	-42.26
case 1	506	0.31	3.66 ±0.16	5.304 ±0.047	-27.29
zerolevel,	508	0.33	4.00 ±0.20	5.363 ±0.051	-26.48
no emission	528	0.38	3.94 ±0.17	5.355 ±0.052	-26.59
case 2	506	0.56	3.61 ±0.22	6.622 ±0.078	-9.23
emission	508	0.57	3.96 ±0.25	6.756 ±0.081	-7.39
spectrum	528	0.61	3.94 ±0.21	6.668 ±0.074	-8.59
case 3	506	0.31	3.95 ±0.17	7.148 ±0.064	-2.02
calculated	508	0.33	4.32 ±0.21	7.228 ±0.069	-0.92
emission	528	0.38	4.25 ±0.19	7.217 ±0.070	-1.07

solar absorption spectra				
correction method	spectrum	σ in %	$\Sigma ClNO_3$ in $10^{15}cm^{-2}$	ΣCO_2 in $10^{21}cm^{-2}$
no	504	0.55	3.27 ±0.10	7.273 ±0.050
correction	608	0.50	3.31 ±0.14	7.317 ±0.052

By this approach, both, the 100 % transmission level and the relative absorption strength of any emission distorted absorption line are corrected. One disadvantage to this method is the increase in noise introduced by the emission spectrum. Another difficulty is the systematic change in the line shape if absorption and emission spectra are recorded at different resolutions, as it is the case for the example spectra discussed. For the absorption spectra, a resolution as high as possible is strived for, to resolve lines free of interference for the analysis. However, to record an emission spectrum at the resolution of 0.02 cm^{-1} with an S/N comparable to a typical 20 *min* absorption spectrum, the whole night is needed. This is simply not feasible, in particular because of the changes in the meteorological situation. Thus, the results listed in Table 3.2 (case 2) are still subject to a considerable systematic bias due to the distortions in the line shape and additionally the retrieval is subject to a higher statistical uncertainty due to the increase in noise introduced by the subtracted emission spectrum.

The third correction method discussed includes a calculated correction for the emission and is also used in a recent publication with a colleague (*Notholt* et al., 1996a). First, the data is processed as in the case 1, i.e. the blackbody portion of the night sky emission spectrum is determined in the spectrum and given to the analysis program to get the 100 % transmission level right. Next, a mean blackbody is calculated from individual blackbodies for each layer of the model atmosphere for each trace gas and each wavenumber of interest. Each individual blackbody of a selected trace gas is then weighted by the concentration profile and after summation the mean blackbody is obtained. The ratio of this mean blackbody to the blackbody of 370 K that represents the full moon describes in first approximation the strength of any atmospheric emission line at any specific wavenumber relative to the 100 % transmission level achievable with the moon as a light source. A number of these relative emission strengths are listed in Table 3.4 for some important spectral line positions and a graphical display of the overall dependence on wavenumber is shown in Figure 3.8. An absolute calibration of the calculated blackbodies is not necessary, because the ratio of emission to absorption is effected by the temperature profile but not by the absolute strength of any transition considered.

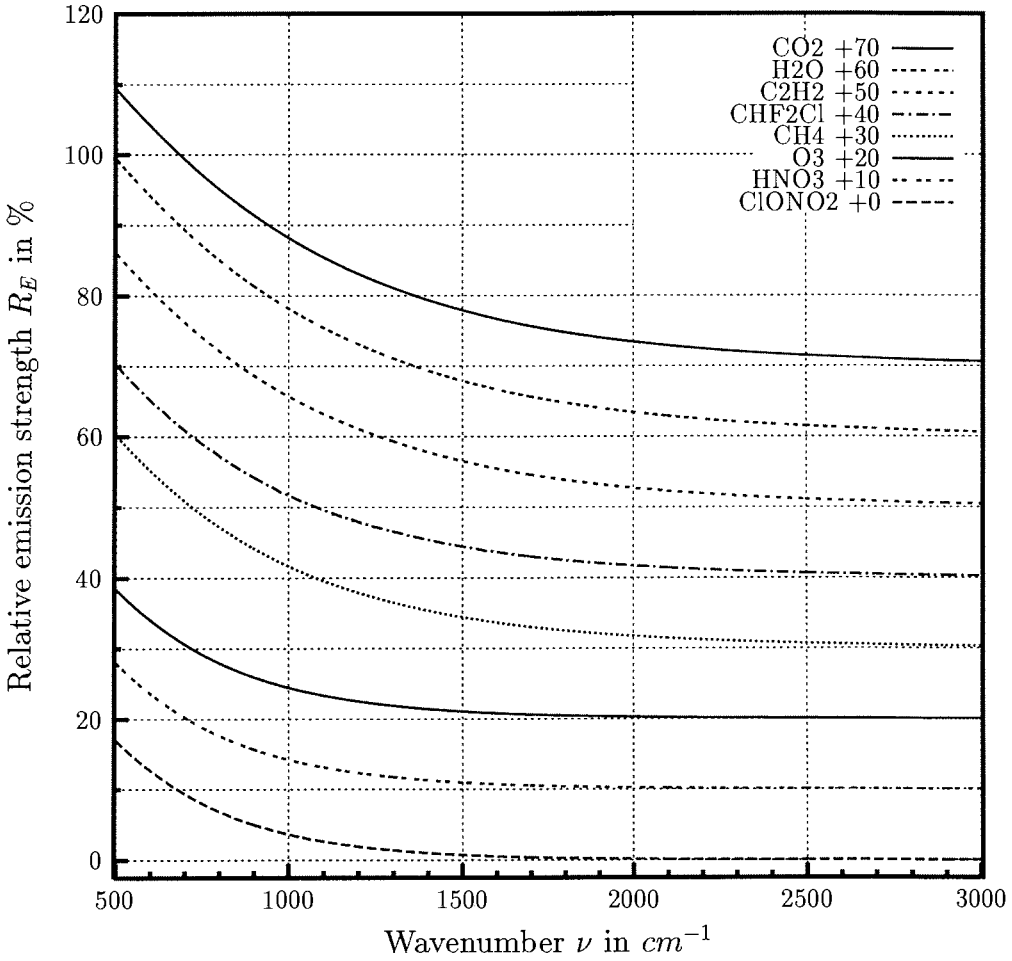

Fig. 3.8: *The emission from selected atmospheric trace gases is compared to the intensity of the lunar spectral flux density as a function of the wavenumber. The emission strength R_E relative to the lunar flux is calculated from weighted blackbodies for each species according to its vertical distribution in terms of number density and the temperatures in different altitudes. The curves shown are based on the radio sonde pT profile from the 15/Mar/95 and the VMR profiles corrected for dynamical effects as described in section 4.6. Please note that the individual curves are shifted for clarity as indicated in the key and that the importance of emission decreases from top to bottom.*

The relative emission strength decreases strictly monotonous with wavenumber (Figure 3.8), because the spectral flux density of the cooler atmospheric blackbody drops faster than the flux of the warmer moon. It is higher for abundant tropospheric species compared to stratospheric species due to the lower temperature in the stratosphere. CO_2, which is an abundant tropospheric species, has a relative emission strength of 26 % at 780 cm^{-1}, while the stratospheric species $ClONO_2$ has a much lower value of 7 % (Table 3.3). Above 2500 cm^{-1} all emission effects become negligible, as can be seen in Figure 3.8.

If the total column amount retrieved for CO_2 in Case 1 is corrected for the calculated emission strength of 25.8 %, the total column amount listed for Case 3 is obtained, which matches almost perfectly the value retrieved in the solar spectra. The remaining difference is smaller than

Table 3.3: *The strength R_E of the atmospheric emission for several species relative to the intensity of the full moon is listed for some important spectral microwindows. The ratios are calculated from blackbody consideration as described in the text. The spectral dependence is illustrated in Figure 3.8 for several trace gases.*

species	wavenumber in cm^{-1}	R_E in %	species	wavenumber in cm^{-1}	R_E in %
C_2H_2	776	23.07	O_3	780	8.42
$ClONO_2$	780	7.32		980	4.74
CO_2	781	25.80		1044	3.94
	2626	0.49		1091	3.44
H_2O	784	25.79		1146	2.93
	868	20.32		2776	0.04
	2819	0.67	N_2O	1202	7.91
CHF_2Cl	829	16.30		2806	0.39
HNO_3	869	6.23	CH_4	1202	7.87
OCS	868	1.59		2836	0.36
	2046	15.25	COF_2	1231	2.06
CCl_2F_2	922	13.72	HDO	2660	0.92
	1161	8.62	C_2H_6	2977	0.34

the systematic uncertainties due to the very low zenith angle of the solar spectra (82^o and 84^o). The differences in $ClONO_2$ are ascribed to dynamical and chemical effects discussed in section 4.6.

In the final retrieval of $ClONO_2$, a smaller spectral interval than in Table 3.2 is used in the analysis, i.e. the interval from 779.9 – 780.45 cm^{-1} instead of 779.3 – 781.3 cm^{-1}. (The data listed in Table 3.2 gives only the results from the wide interval, while the final results from the small interval are included in Table 4.3.) CO_2 has strong absorption lines at 780.08 and 780.50 cm^{-1}, where in particular the latter is highly temperature sensitive. Additionally, there is a weaker CO_2 line at 780.23 cm^{-1}, which is less temperature sensitive but interferes directly with $ClONO_2$ (see appendix C, page 197). Thus, it is vital to treat CO_2 correctly in the retrieval of $ClONO_2$. To reduce the total uncertainties in the retrieval of $ClONO_2$ a two–step wide/narrow analysis is performed as discussed in detail by *Reisinger* et al. (1995). The amount of CO_2 and H_2O is first determined in the wide spectral interval (using method 1). Before the second step, i.e. the analysis in the narrow interval is performed, the *a priori* profiles of CO_2 and other interfering gases like H_2O and C_2H_2 are scaled to the total column amounts retrieved in the wide spectral interval and are kept constant during the analysis in the narrow interval. This reduced total number of adjustable parameters improves the stability of the retrieval in the small microwindow. The uncertainty in the $ClONO_2$ retrieval due to temperature uncertainties is reduced as well. Although the scaling of the CO_2 *a priori* VMR profile to a total column of about $5.35 \cdot 10^{21}$ cm^{-2} is by $\approx$ 27 % too small compared to the real concentration (Table 3.2), this treats the CO_2 line interfering directly with $ClONO_2$ correct, because both lines are effected by emission in the same way. A detailed discussion on the advantages of using a two–step wide/narrow spectral interval in the retrieval of $ClONO_2$ is given in *Reisinger* et al. (1995) and *Rinsland* et al. (1996).

Another approach to overcome the principal difficulties of analysing lunar absorption spectra is to model both processes involved completely, i.e. absorption and emission. Common retrieval programs like FASTCOD2 (*Clough* et al., 1986) and SFIT include only a simple build-in correction for emission effects restricted to solar absorption spectra. At present

it is not possible to choose the temperature of the light source used at recording time. The new algorithm MALT (multiple atmospheric layer transmission) from *D. Griffith*, University of Wollongong, Australia, is basically capable to simulate both, emission and absorption processes, in a model atmosphere. The simulation of emission effects in absorption spectra is more detailed as in the other algorithms mentioned and allows to set all relevant parameters adequate to lunar observations. The details of the program MALT and some applications are described in *Griffith* (1996). However, in the hitherto version of MALT, the different simulations can only be done one at a time and the algorithm has to be modified. In a first approach, the model atmosphere is put up as for the absorption retrieval mode, but with additional emission layers inserted in between these model layers in the troposphere. A light ray that enters the model atmosphere yields a normal stratospheric absorption line from the highest model layer down to the tropopause. In its further simulation down to the observation altitude the light ray passes each model layer twice, once to determine the absorption occurring in that layer and once to calculate the emission that adds to the spectrum. The first preliminary results are encouraging and a common publication with *D. Griffith* is under preparation.

3.5 Approaches to the volume mixing ratio profile retrieval

This section starts the discussion on the retrieval of information on the vertical distribution of atmospheric gases from ground–based spectra. An important requirement to perform this task successfully is a good knowledge of the pT profile and the availability of high resolution spectra with a good S/N recorded on a well aligned instrument. If one or several of these requirements are not met, the total uncertainties increase significantly.

In chapter 2, the line shape of atmospheric absorbers and its dependence on pressure, temperature, and VMR profile are described. If the pT profile and the spectroscopic parameters are known perfectly, the line shape is determined by the vertical distribution of the absorber only. A non realistic VMR profile causes systematic features in the residuals from recorded and simulated spectra. An example of a non optimal VMR pro-

file assumed in the *a priori* profiles of the retrieval algorithm is shown in Figure 4.2, page 87. There are different methods known to retrieve VMR profiles to reduce the line shape uncertainties. For once, the line shape can be inverted directly. There are reports on the successful application of matrix inversion algorithms to sub–millimeter *Wehr* (1993) and to solar IR–spectra *Pougatchev* et al. (1995). However, the difficulty of this task can be estimated from Figure 2.3: The contributions to the total line from different altitudes are not linearly independent. This leads one back to the discussion given at the end of section 2.1 on the complete deconvolution of spectra. Additionally, lunar spectra are very noisy and the resolution is lower than the typical halfwidth of stratospheric trace gases and uncertainties in the pT profile can substantially mislead the inversion in any spectrum (compare section 4.6).

A different approach is the analysis of a diurnal set of spectra. The absorption strength of any line depends on the air mass between the observer and the sun. This variation of absorption strength with the zenith angle of the sun holds information on the VMR profile of the species studied. However, strong restrictions apply to this method for the high latitude of the observation site. The diurnal variation of the solar zenith angle is considerably smaller than at mid–latitudes and never gets below 55^o. In spring, at the end of the polar night, the sun does not rise more than 10^o above the horizon and in summer it is permanently above 10^o. The variability of the air mass is thus quite small within 24 hours, as can be seen from Figure 3.1. Moreover, the method is applicable only to those species that show no significant diurnal variation due to chemical processing driven by photolysis.

However, the reverse processing is sometimes useful to check for systematic uncertainties. If the retrieved total columns of a slow chemical reactant show a significant correlation with the air mass factor, then the assumed *a priori* VMR profile is not adequate to the real vertical distribution. This is useful in particular for molecules that have no strong isolated absorption lines, like many CFCs, because the line shape of the individual lines can not be checked in the residuals of absorption bands.

The third method discussed in detail in the following chapter simulates the dynamical processes common in the polar atmosphere and performs

a gradient search for the minimum in the standard deviation of the residuals between recorded and modelled spectrum. It makes use of the forward model of SFIT. Thus, the mathematical and programming effort is small and the outcome of the optimization is consistent with the normal retrieval algorithm for total column amounts. Additional advantages of this method are the overall good stability against running into unrealistic VMR profiles in particular in noisy or low resolution spectra, compared to direct inversion procedures described above. This is achieved by combining the information from up to 20 spectral microwindows featuring different species and different spectra recorded at different zenith angles. Moreover, the optimization can still be run on a normal PC and the optimization can be stopped before the absolute optimum is reached, yielding a profile typically close to the absolute optimum, if time gets a limiting factor.

However, before the discussion on the details of the algorithm is given, the dynamical features of the arctic atmosphere are described in the next section. These are vital for the understanding of the optimization algorithm.

4 The polar atmosphere and the variability of VMR profiles

4.1 Potential temperature and potential vorticity

At the beginning of this chapter, the potential temperature Θ and the potential vorticity Q are introduced, because these are inevitable for the discussion of atmospheric dynamics, in particular in the polar regions.

The **potential temperature** Θ is defined as the temperature that a considered air parcel will have, if it were compressed dry–adiabatically, i.e. without exchange of heat energy with its surrounding, from its given pressure p and temperature T to normal pressure p_0 of 1013 hPa (e.g. *Roedel*, 1994):

$$\Theta = T \cdot \left(\frac{p_0}{p}\right)^{\frac{c_p - c_v}{c_v}} . \tag{46}$$

T denotes the absolute temperature in *Kelvin*. The potential temperature is a measure for the sum of thermal and potential energy and is conserved if the air parcel moves up or down due to adiabatic warming or cooling. In many cases it is convenient to use the potential temperature instead of the geometrical altitude z as a variable of height (*Beyerle*, 1994). As Θ is a function of z which increases strictly monotonously in any static atmosphere, it can be used for an unambiguos coordinate transformation. This is favorable when dealing with trajectories for example. Any air parcel followed can be plotted in one isentropic height layer. A highly illustrative experiment in this sense is given in *Gathen* et al. (1995) that allows to differentiate between the amount of ozone loss due to chemical processing and that due to dynamical effects by making excessive use of isentropic trajectory calculations.

The **potential vorticity** Q is a conservative quantity for adiabatic transport processes. It combines the laws of the conservation of mass and of the conservation of vorticity ζ. The vorticity gives the strength of an eddy, vortex, or any other horizontal movement of an air mass that has an angular momentum. Let $\vec{v}$ be the horizontal speed vector, then

the vorticity ζ is given by

$$\zeta = \mathrm{rot}_\Theta \vec{v}. \tag{47}$$

It is positive, i.e. points up, for cyclonic movements, and it is negative for anticyclonic movements (note that the potential temperature Θ is used as vertical coordinate). Strictly speaking, ζ is the relative vorticity, since it does not include the effect of the Coriolis force. The absolute vorticity $\eta = \zeta + f$ is the sum of the relative vorticity and the Coriolis parameter f and it is the basis for expressing the potential vorticity Q. In the hydrostatic approximation, Q is defined by:

$$Q = -g \cdot \eta \cdot \frac{\partial \Theta}{\partial p}, \tag{48}$$

with g denoting the terrestrial gravitational acceleration at the surface ($\approx 9.8\,m/s$). The SI units for the potential vorticity are $Km^2s^{-1}kg^{-1}$. For convenience, **p**otential **v**orticity **u**nits (PVU) are favoured in the subsequent text, with $1PVU = 1 \cdot 10^{-6} Km^2s^{-1}kg^{-1}$. As mentioned before, Q does not change for adiabatic transport. Thus, the potential vorticity is comparable to the VMR of an inert atmospheric species that has no sources or sinks. For more details see *Roedel* (1994) and *Beyerle* (1994).

4.2 The vertical structure of the atmosphere

The atmosphere below the stratopause at approximately 50 km, that is termed the *lower* atmosphere in this thesis, is quite well mixed and molecules frequently collide with one another. All atmospheric species that are detectable in the infrared have more than 95 % of all their molecules below the stratopause, indeed, for most of them it is even more than 99 %. Since the FTIR–spectrometer measures total columns, one does not need to know too many details about the mesosphere and higher atmosphere. However, up to altitudes of roughly 80 km, the vertical distribution of gases is still dominated by dynamical effects and the gravitational effect of molecular weight is still negligible. Hence this well mixed altitude range from ground to about 80 km is also known as the homosphere.

The vertical structure of the lower atmosphere is characterized by an exponential decrease in pressure with geometric altitude. For any atmospheric species with a constant VMR profile, this means also exponential decrease in total number density, since the number density is proportional to pressure. The effects on the absorption signal detectable by an FTS is illustrated in Figure 2.3, page 39. The second variable that determines the atmospheric condition is temperature. The temperature decreases with altitude up to approximately 9–12 km at high latitudes and up to 17 km in the tropics. The troposphere is by definition the altitude range from ground up to where the negative temperature gradient ends, the latter altitude being termed the tropopause (see also Figure 3.2, page 53). This definition may not be strictly true near ground, where inversion layers may occur with thicknesses of up to 3 km in polar regions. Above the tropopause, the temperature usually slightly increases and then shows little variation throughout the middle stratosphere, until it reaches a maximum at about 50 km and then decreases again. This temperature maximum is termed the stratopause and gives the upper border of the stratosphere. However, in polar winter the middle stratosphere may exhibit a strong temperature minimum well below the tropopause minimum that is not known at lower latitudes and is one of the key conditions for rapid ozone depletion (see below).

The temperature profile in the homosphere is physically determined by the radiation budget and in the troposphere additionally by dry– and wet–adiabatic expansion and compression in ascending and descending air masses, respectively. The emission of infrared radiation primarily by tropospheric water vapor has the net effect of cooling at its *'top–side'*. This temperature gradient in the troposphere drives strong convection flows leading to highly efficient vertical mixing. As a consequence, only few short lived species show significant gradients in their tropospheric VMR profiles.

In the stratosphere it is almost vice versa. Near the tropopause, IR emission dominates giving low temperatures, while in the middle and upper stratosphere absorption of UV and visible radiation is higher and increases the temperature. The major species for radiation driven stratospheric heating is ozone, the outstanding UV–absorber in our atmosphere.

The arising positive temperature gradient in the stratosphere effectively blocks convectional vertical mixing. Trace gases with only (or dominantly) tropospheric sources, like e.g. the CFCs, N_2O or CH_4, show a negative gradient in their stratospheric VMR profile. The slope depends on the efficiency of the removal processes that are, at least indirect, all driven by photolysis. A positive gradient in VMR profiles is typical for the products of these removal processes, like HF or HCl that have their sources basically in CFC destruction. One can now also understand, why the temperature increase throughout the stratosphere is less pronounced in polar regions and in particular give the reason for the occurrence of a stratospheric temperature minimum in the polar night. In the absence of the sun, stratospheric heating due to absorption of solar radiation cannot occur in polar night and it is generally less pronounced than at lower latitudes, because the zenith angles of the sun are commonly larger. This leads to lower energy depositions at polar sites, because the solar radiation enters the atmosphere at lower latitudes.

4.3 The polar vortex and its dynamics

In polar summer, the vertical structure of the polar atmosphere is comparable to subarctic and mid–latitude conditions. No strong separation of the air masses are observed. After the end of polar day and with the beginning of polar night, the balance between warming due to UV–absorption and cooling due to emission in the infrared is progressively shifted towards lower stratospheric temperatures. This major stratospheric cooling causes a downward movement of air masses, known as subsidence, until a new equilibrium state is met, according to increasing compression that counteracts the cooling. As a consequence of this subsidence, a meridional pressure gradient is inforced and air masses that follow this gradient are deflected eastward due to the Coriolis force. This deflection is observable as a zone of strong westerly winds in the middle and upper stratosphere with wind speeds of more than 100 m/s. This circumpolar wind field is of major importance for the maintenance and further evolution of the vortex, because it blocks effectively the transport of warm air masses from lower latitudes into the polar regions. This latitudinal zone of strong westerly winds gives the outlines of the so called

polar vortex. (For details see *Schoeberl* and *Hartmann* 1991, *Schoeberl* et al. 1992.)

Strong circumpolar wind fields yield high values in potential vorticity (PV), hence air masses inside the polar vortex have high PV values compared to air masses outside the vortex. Typical viewgraphs of the polar vortex show the PV distribution in a polar projection for distinct height layers defined by potential temperature. An example of a rather undisturbed polar vortex is shown in Figure 4.1 for the 475 K layer for the 10^{th} of March 1995. The picture was downloaded from ZARDOZ, the server of the European data center for EASOE and SESAME and has originally been calculated by the Danish Meteorological Institute (DMI) from data of the European Center of Medium–range Weather Forecast (ECMWF). These helpful plots are available for seven different temperature levels on a daily basis. The edge of the polar vortex can be identified from the PV plots as the area of strongest PV gradient. In the example of Figure 4.1 this is the case along the 36 to 42 PVU isolines.

The most striking differences between arctic and antarctic polar vortices are caused by the differences in orography. In the southern hemisphere, the lack of a significant continental orography along the preferred tropospheric wind fields gives little rise to planetary wave activity. Consequently, the antarctic vortex is almost undisturbed and more or less concentric to the south pole. Temperatures can reach very low values inside the antarctic vortex and structures are maintained well into spring. In contrast to the southern hemisphere, the distribution of land masses and mountain ranges in the northern hemisphere give rise to consider-

Fig. 4.1: *Next page: Example of a PV–plot showing a rather undisturbed arctic vortex. The polar projection is shown with a circular latitudinal grid with a spacing of 10° and with the lower vertical axis denoting the Greenwich meridian. The potential vorticity is given in PVU for the 475 K isentropic layer, which corresponds to an altitude of about 20 km inside the vortex and 18 km outside the vortex. The vortex edge is defined by the strongest PV gradient and it is found in this example approximately along the 42 PVU isoline, with Ny–Ålesund inside the vortex but close to its edge.*

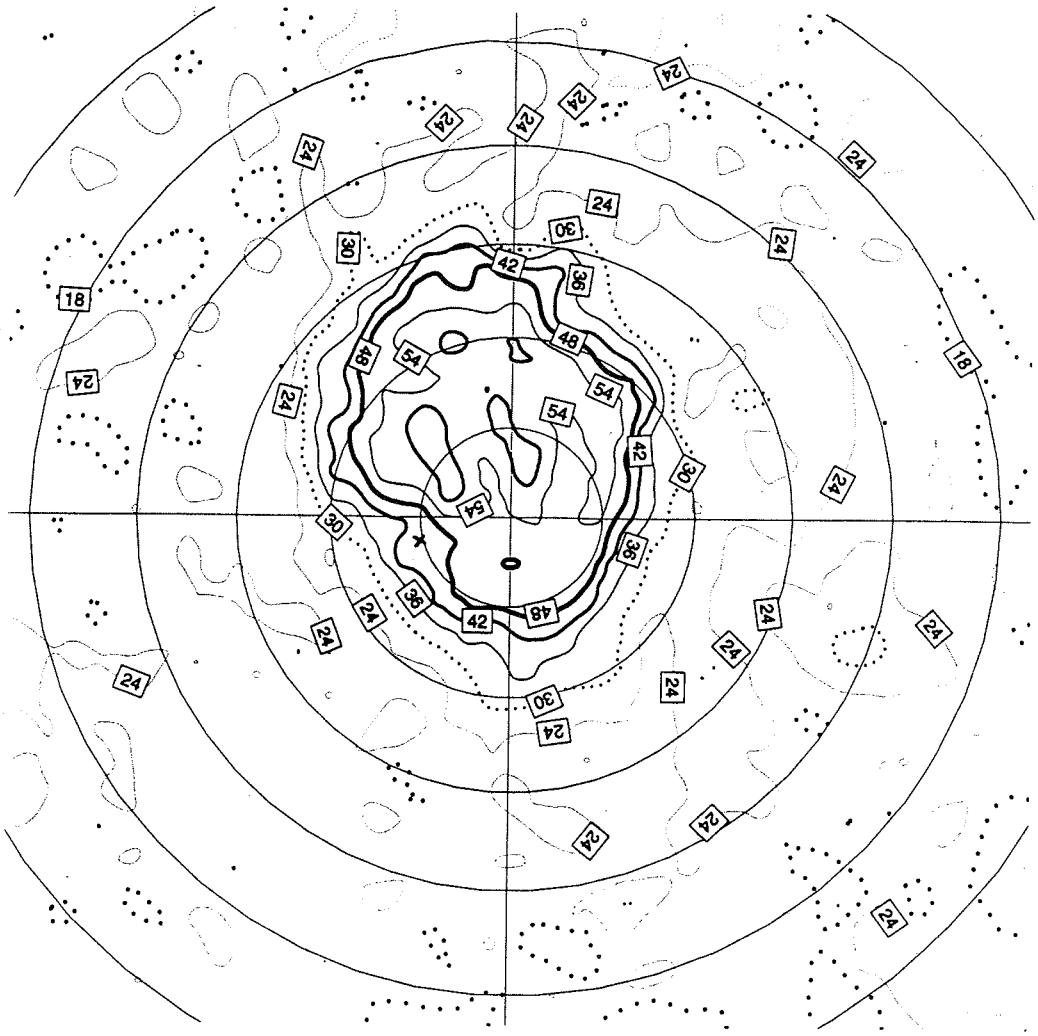
ECMWF
POT. VORT.
ANALYSIS
10 Mar 1995
Day number 69
Level = 475 K
10⁻⁶Km²/kgs
Data produced by DMI
Plotted by isentbw

able planetary wave activity that deform the circular shape of the vortex to an ellipse, banana, dumb–bell, or similar objects and force the polar vortex out of its pole centric position (e.g. Figure 4.11, page 105). The arctic vortex as a whole keeps *'wobbling'* about the pole and is much less stable than the antarctic one, due to energy loss into planetary wave activity. Consequently, the arctic vortex is in general less cold than its antarctic counterpart and breaks up earlier after the return of the sun in polar spring. This is important in the discussion of ozone depletion caused by heterogeneous chemical processing bound to the surface of polar stratospheric clouds (PSCs). PSCs can only exist below a critical threshold temperature, which is maintained throughout long periods in Antarctica but occurs comparatively sporadic in the arctic stratosphere. These facts are the major reasons for the interhemispheric differences in polar ozone depletion (e.g. *Gernandt* et al, 1995 and 1996, *Schoeberl* et al., 1991, *Pawson* et al., 1995).

There are many implications arising from the highly variable dynamics of the northern vortex. It is much more difficult to distinguish between chemical and dynamical changes in trace gases in the arctic atmosphere than in the antarctic one. The most elegant way to overcome this difficulty is to follow a certain air parcel in an aircraft or floating balloon. An example is the previously mentioned work by *Gathen* et al. (1995). However, this is not feasible (or at least not payable at present status) for large instruments like multi–wavelength LIDAR or high resolution FTS. The discussion is continued in more detail in section 4.6.

4.4 Optimizing VMR profiles: results from synthetic spectra

In spring 1996, the NDSC performed a so called *"retrieval intercomparison"* among its members. The intercomparison was designed and organized by *Aaron Goldman* from the University of Denver, Colorado, USA. Two sets of synthetic spectra over a spectral interval of 10 wavenumbers had been calculated with concentrations and VMR profiles not known to the participants. These spectra were distributed together with a pT profile and the two zenith angles used in the calculation of the spectra. On the VMR profiles used for the calculation of the synthetic spectra it

was said that they were *sensuous*, but are likely to have been modified. One might discuss the meaning of *sensuous*, but after the intercomparison was done, the profiles of HCl, the principal species, and NO_2 turned out to have been highly unrealistic (in principle the profiles of HCl and NO_2 were exchanged).

The task of the participants was to retrieve total columns of HCl, CH_4, and NO_2 and, where possible, also information on the VMR profiles used. The height layering scheme used in the analysis was up to the participants, as well as the initial VMR profiles used. Some of the results discussed here have been presented at the at the 6^{th} NDSC Meeting held at Garmisch Partenkirchen, Germany, in April, 1996, and are included in (*Goldman*, 1996).

The participitation was a challenging task for the software developed. The spectra distributed look quite different from known arctic spectra with significantly less distortion due to water vapor and the calculation of the spectra was performed without adding noise. First of all, contribution plots for the whole spectral range are created from 2920 to 2930 cm^{-1} to pick out as many useful intervals for the analysis as possible. From these plots the following spectral microwindows are chosen: 2922.5 - 2923.3 cm^{-1} retrieval of CH_4 and HDO, 2924.9 - 2926.65 cm^{-1} H_2O, 2922.3 - 2923.85 and 2924.7 - 2925.12 cm^{-1} NO_2, and 2925.69 - 2926.20 HCl. The quality of the spectral microwindows in terms of achievable accuracy with respect to interferences was high for CH_4, H_2O, and HDO, moderate for HCl and low for NO_2. The latter is always difficult to retrieve, because it is a weak absorber.

In a first attempt, the given intervals are analysed with three different sets of initial VMR profiles and two different height layering schemes each, giving six datasets. The ARCTIC VMR profile set described in appendix B yielded the least convincing results and is not included in Table 4.1. The other two sets of VMR profiles used are the REFMOD95 from *Curtis Rinsland* and the REFTOON from *Geoffrey Toon* (see appendix B). However, the systematic line–shape errors observed in the residuals of the species CH_4, HCl and NO_2 are high in all analysed spectral intervals. The scheme used for the 29 model layers of SFIT are abbreviated in Table 4.1 as HRS for high resolved lower stratosphere and HRT for high

resolved troposphere with lower boundaries at
0.5, 2, 4, 6, 8, 10, 11, 12, 13, 14, 15, 16, 17, 18, 20, 22, 24, 26, 28, 30, 32, 35, 40, 45, 50, 60, 70, and 80 *km* for HRS and
0.5, 1, 2, 3, 4, 5, 6, 7, 8, 9, 10, 12, 14, 16, 18, 20, 22, 24, 26, 28, 30, 32, 35, 40, 45, 50, 60, 70, and 80 *km* for HRT.
The HRT scheme is commonly used in all the Ny–Ålesund data, except for the lowest layer starting at 20 *m*.

From this first attempt to analyse the data, which corresponds to all

Table 4.1: *Results from the participitation in the retrieval intercomparison of the NDSC in spring 1996. The first column gives the species retrieved and the zenith angle of the spectrum. The second column shows the magnitude for the total column Σ given in that line, and the 1σ uncertainty in the same units. The given uncertainties do not include any systematic errors due to inadequate VMR–profiles. The VMR–profiles and the height layering schemes for the model atmosphere used are indicated above as described in the text.*

species z_angle	VMR–profile ⇒ quantity ⇓	REFTOON HSR	REFTOON HTR	REFMOD95 HSR	REFMOD95 HTR	Optimized HTR	True HTR
CH_4	Σ in $10^{19}cm^{-2}$	3.451	3.442	3.289	3.282	3.320	3.334
70°	1σ uncertainty	0.027	0.026	0.020	0.020	0.003	0.002
CH_4	Σ in $10^{19}cm^{-2}$	3.578	3.574	3.378	3.378	3.327	3.339
82°	1σ uncertainty	0.024	0.024	0.011	0.011	0.004	0.002
HDO	Σ in $10^{22}cm^{-2}$	3.693	3.695	3.766	3.765	3.837	3.824
70°	1σ uncertainty	0.110	0.110	0.089	0.088	0.015	0.007
HDO	Σ in $10^{22}cm^{-2}$	3.762	3.760	3.823	3.825	3.841	3.827
82°	1σ uncertainty	0.065	0.066	0.033	0.033	0.013	0.006
H_2O	Σ in $10^{22}cm^{-2}$	3.611	3.573	3.851	3.821	3.824	3.896
70°	1σ uncertainty	0.007	0.009	0.007	0.007	0.005	0.007
H_2O	Σ in $10^{22}cm^{-2}$	3.525	3.464	3.866	3.833	3.841	3.947
82°	1σ uncertainty	0.023	0.022	0.010	0.010	0.006	0.006
HCl	Σ in $10^{15}cm^{-2}$	3.115	3.123	3.192	3.201	2.424	2.508
70°	1σ uncertainty	0.062	0.063	0.016	0.016	0.004	0.003
HCl	Σ in $10^{15}cm^{-2}$	2.945	2.961	3.174	3.190	2.443	2.516
82°	1σ uncertainty	0.063	0.064	0.019	0.019	0.005	0.004
NO_2	Σ in $10^{15}cm^{-2}$	4.766	4.732	8.707	8.684	8.257	17.56
70°	1σ uncertainty	0.722	0.672	0.967	0.948	0.353	0.56
NO_2	Σ in $10^{15}cm^{-2}$	4.866	4.835	8.841	8.817	8.332	17.47
82°	1σ uncertainty	0.679	0.654	0.876	1.028	0.491	0.50

except the last two columns of Table 4.1, two systematic effects are seen. First, except for HCl, the total column derived is always higher in the spectrum with the higher zenith angle. Even without the exception of HCl, this is also true, when using the true profiles that were used to calculate the spectra and that have been made available after the intercomparison was done (last column of Table 4.1, see also below). Second, rougher layering results in higher total columns. To see this, one has to realize that the bulk of HCl with the VMR profiles used is found in the lower stratosphere, while for all other gases this is the troposphere. To HCl, the HTR scheme is the rougher spaced, while for the other ones it is HSR. The effect in total columns is about 1 to 4 % for the first bias mentioned and may only in parts be ascribed to a bad VMR profile, because it is also found when the true profiles are used. The second effect has an impact of about 0.5 to 1 % on total columns. Both are systematic uncertainties, which have to be ascribed to the retrieval algorithm.

Though this first result is interesting, the quality of individual fits is not satisfying. The systematic line shape errors in the residuals using either REFMOD95 or REFTOON VMR profiles are striking, as can be seen from Figure 4.2. With the known pT profile and with the known spectroscopic data, the vertical distribution is the only parameter left to change the lineshape. Therefore, the *a priori* VMR profiles have to be improved. The VMR profile optimization is achieved in several steps by making use of the programs PROFIL.EXE and OPTIVMR.EXE, which were developed just prior to the intercomparison. The discussion on retrieving information on the vertical distribution of trace gases, which was postponed for these programs at the end of chapter 3, is now continued.

As mentioned earlier, stratospheric cooling causes polar air masses to subside in wintertimes. *Toon* et al. (1992a) suggested that this subsidence can be described mathematically for $z \geq z_{TP}$ in the simple approximation:

$$VMR_{subsided}(z) = VMR_{standard}(z - DOSA \cdot \{z - z_{TP}\}) \ , \qquad (49)$$

where z denotes altitude, z_{TP} stands for the tropopause altitude and $DOSA$ for Degree of Subsidence/Ascent, which is a dimensionless parameter. Negative $DOSA$ values describe stratospheric subsidence, while small positive values describe summer situations, where the stratosphere might warm up more than assumed in the standard profile, which is

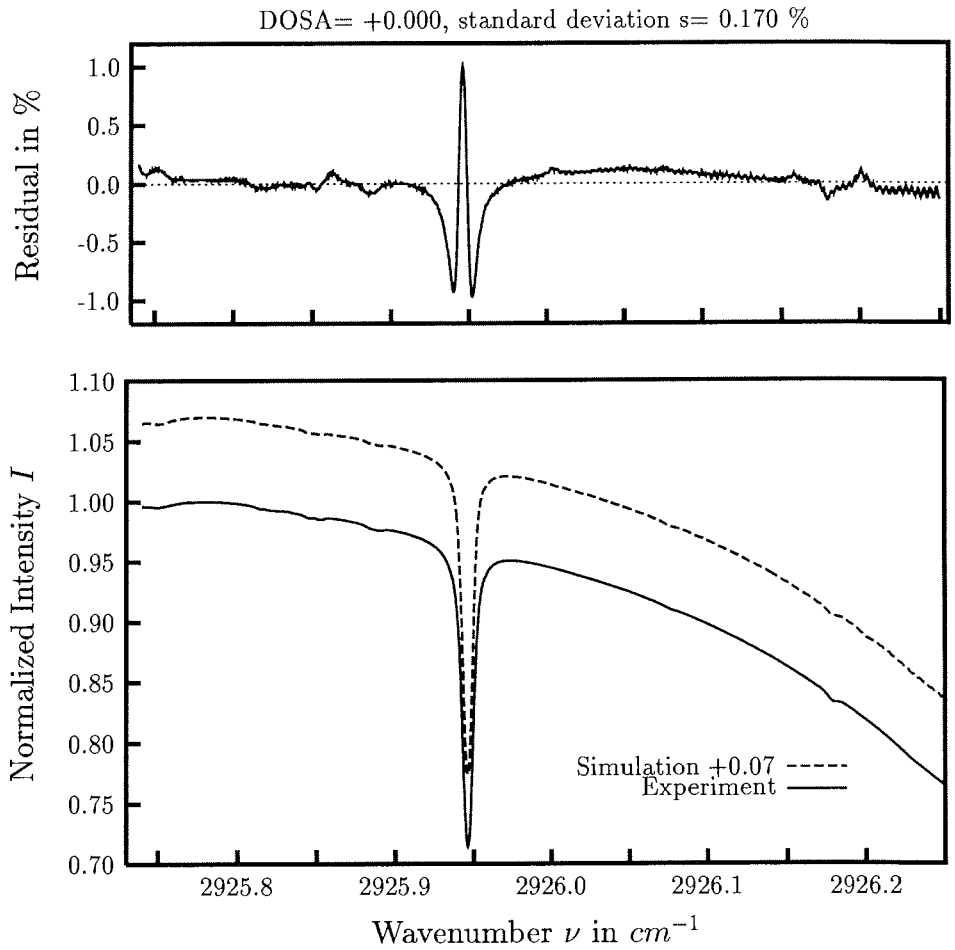

Fig. 4.2: *The residuals indicate an non–optimal a priori VMR profile for HCl. The shown fit to the absorption line of HCl at 2925.9 cm^{-1} is performed with the initial VMR profile taken from the REFMOD95 data set and the synthetic spectrum calculated for a zenith angle of 70°.*

termed an ascent of stratospheric air masses in this thesis. The linear increase of the subsidence with altitude above the tropopause (equation 49) is an assumption that is supported both by aircraft observations (*Toon* et al., 1992a) and by space flights of the ATMOS instrument (*Abrams* et al., 1996).

Besides the occurrence of subsidence in the stratosphere, the tropopause itself undergoes vertical movements. This vertical displacement of the tropopause is often described by a very simple vertical shift of the whole VMR profile. However, in this thesis a more realistic operation is suggested, which uses a linear stretching similar to the DOSA operation. A tropopause elevation is described by stretching the tropospheric profiles from ground to the new tropopause altitude and by crunching the stratospheric profiles towards the stratopause and vice versa if the tropopause moves to lower altitudes. The mathematical description is given by the following equation:

$$\mathrm{VMR(z)} = \begin{cases} \mathrm{VMR}_{std}(z) & : \; z \geq \mathrm{z_{SP}} \\ \mathrm{VMR}_{std}\left(z_{SP} - \frac{\{z_{SP}-z_{TP}\}\cdot\{z_{SP}-z\}}{z_{SP}-\{z_{TP}+\Delta trop\}}\right) & : \; z_{SP} > z > \mathrm{z_{TP}} + \Delta\mathrm{trop} \\ VMR_{std}\left(\frac{z_{TP}}{z_{TP}+\Delta trop}\cdot z\right) & : \; z \leq z_{TP} + \Delta trop \end{cases} \qquad (50)$$

where z_{SP} means stratopause altitude, z_{TP} the reference tropopause altitude, and $\Delta trop$ the vertical displacement of the tropopause relative to the altitude of the tropopause in the standard VMR profile. z_{SP} and z_{TP} can be assumed as fixed with values of 50 km and 10 km, respectively, for the VMR data sets REFMOD95 and REFTOON for the given observation site. Hence we have two equations with one parameter each, i.e. $DOSA$ and $\Delta trop$ that can be adapted to match the standard VMR profiles to typical dynamic distortions. $\Delta trop$ can be recognized from the radio sonde data and be set to an appropriate value without time consuming iteration procedures. This leaves only one parameter that has to be optimized.

To perform any operations on the VMR profiles, the program PROFIL is developed. It makes use of the air mass, pT profile and VMR files created for SFIT and allows to shift, to stretch, to scale and directly manipulate any VMR profile with the mouse on a graphical display. A general description is given in appendix B. For optimizing VMR profiles,

one has to run SFIT again after each manipulation with PROFIL to see the effects. With some practice, line shape errors can be significantly reduced after few iterations. However, the whole procedure is not fully automated and requires skilled attendance. Although time is often the limiting factor in daily analysis, it is highly valuable in case studies.

Alternatively, an automatic VMR profile optimization can be performed with OPTIVMR, which can apply $DOSA$ stretching, shifting of the whole profile, and tropopause displacement operations to the VMR of any specific, all, or a preselected group of species. It can handle up to 20 different microwindows in one run with arbitrary spectra, zenith angles and principal species each. The quantity traced by OPTIVMR is the total standard deviation of the residuals in each microwindow. The search for the global minimum in total residuals, which is assumed to give the most adequate approximation to the true VMR profile, is traced either actively or a given interval of parameter values is scanned.

OPTIVMR is run on all microwindows available for CH_4, HCl and NO_2 for a large interval of $DOSA$ values. The initial profiles used are REFMOD95 with HTR layering, because these did best in the first analysis. The quality of results from the NO_2 microwindows is quite low due to the very low absorption strength of NO_2 and it is not straightforward to derive vertical information with the methods described, because the residuals in the NO_2 microwindows are more or less dominated by other absorption features. For CH_4 the line shape errors diminish almost perfectly, while for HCl the residuals are still left with minor systematic features. From the shape of the residuals, the discrepancy is expected to be caused by the tropospheric part of the HCl VMR not accessible with the $DOSA$ stretching. Thus, the HCl profile is further improved by means of the PROFIL program, starting on a $DOSA$ stretched profile corresponding to the minimum found in the CH_4 profile. The difficulty is that changes in the tropospheric VMR have only a small effect on the line shape.

After the line shapes are matching almost perfectly, the changes determined with PROFIL are transferred to the initial REFMOD95 VMR profile of HCl and the run of OPTIVMR is repeated for HCl. This time, the minimum is found again for the same $DOSA$ of -0.287 as for CH_4

with line shapes almost perfectly fitting the spectrum. The evolution of the residuals as a function of the $DOSA$ is illustrated in the isometrical plot in Figure 4.3. The next Figure 4.4 demonstrates that the minimum in total standard deviation as a function of $DOSA$ is well defined. It is evident that the minima coincide both for different zenith angles and all species investigated.

The improvement to the fit can be estimated by comparing Figures 4.2 and 4.5. The latter one with almost perfect residuals is achieved by using the optimized VMR profiles instead of REFMOD95. The remaining weak distortions are due to uncertainties in the NO_2 profile which is not optimized. A comparison of the initial, the optimized, and the true VMR

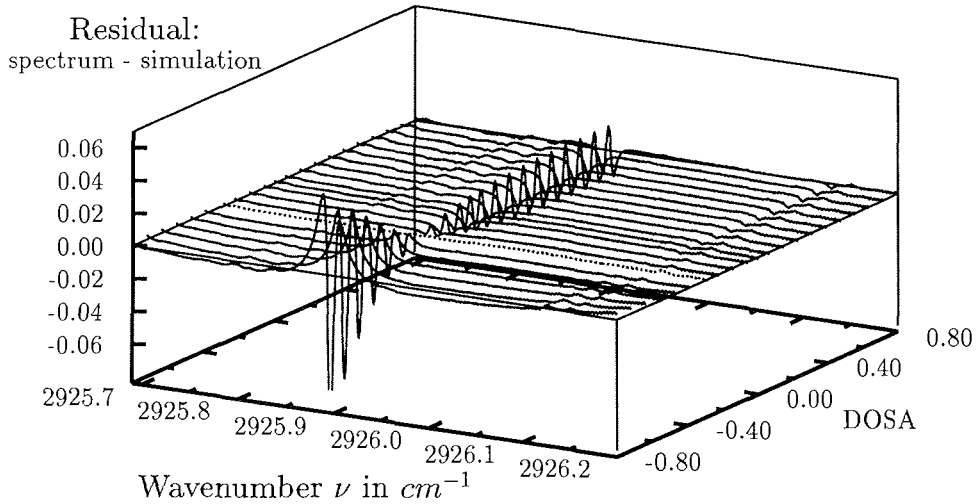

Fig. 4.3: *The evolution of the total residuals in the HCl microwindow for the 70° zenith angle spectrum are shown as a function of the DOSA applied with the program OPTIVMR. The strong systematic features along the center are caused by the HCl line (compare Figure 4.2 and 4.5). The resulting VMR profile that gave the best fit is indicated by the dotted line.*

profiles is displayed in Figure 4.6 for HCl and in Figure 4.7 for CH_4. The methane profile is met almost perfectly below 25 km. Above 20 km the remaining number of molecules becomes so low that changes in the profile have practically no effect on the line shape. For HCl the *true* VMR profile is quite well represented in the altitude range from 15 to 30 km.

Any method used to derive profile information out of a single ground–based observation in a narrow spectral interval is not able to give reliable information above approximately 40 km, because the kernels beyond that altitude are weak. However, the use of *a priori* information on the maximum variability in VMR at high altitudes derived from balloon and satellite experiments decreases the uncertainty in real spectra significantly.

Of much higher importance to the correct retrieval of total column

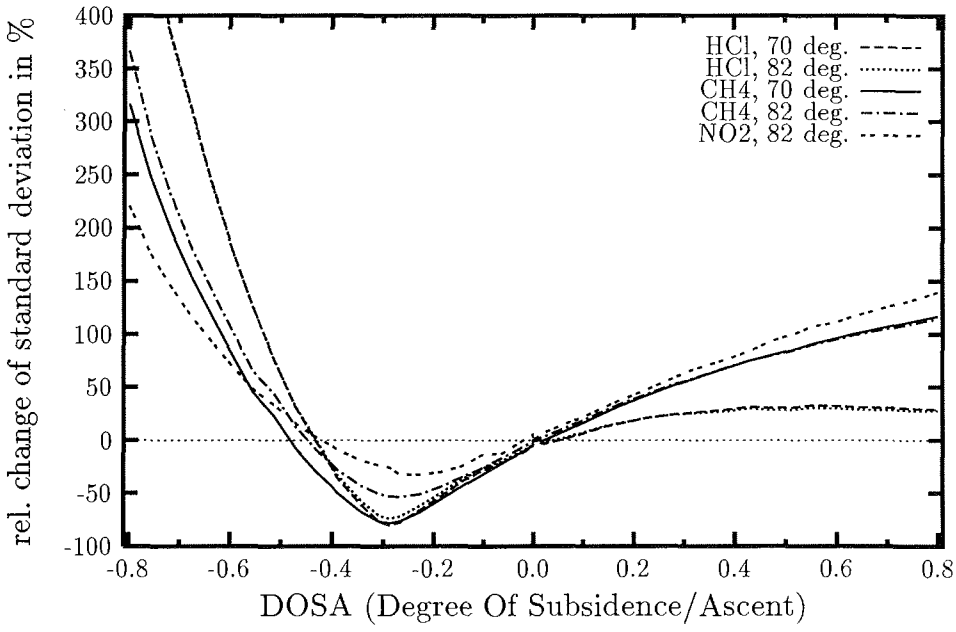

Fig. 4.4: *This figure corresponds to the previous figure and gives the evolution of the total standard deviation as a function of the DOSA for different species and zenith angles. There is a well defined absolute minimum at a DOSA value of -0.287.*

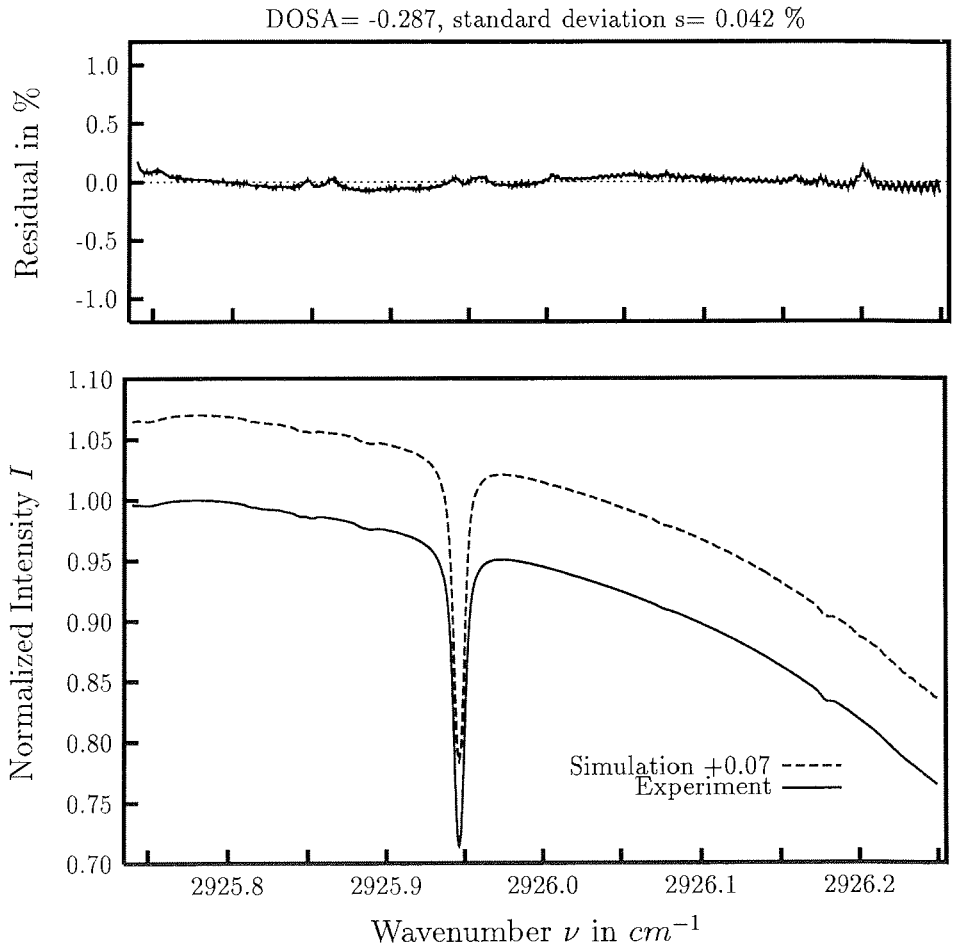

Fig. 4.5: *This is a fit to the same data as in Figure 4.2, but this time with the optimized VMR profiles. The residuals of the HCl absorption line are significantly improved.*

amounts is the correct representation of tropospheric conditions, because the tropospheric contribution is never negligible. The correct retrieval of the tropospheric profile is more difficult than the lower stratospheric part. The relative changes to line shape are small and occur mainly in the far line wings. A particular difficulty in the given HCl spectral interval is the fact that the HCl line is found on a strong slope, i.e. in the line wings of a saturated CH_4 line, and moreover that an additional absorption occurs on that slope caused by H_2O (compare appendix C, page 291). Thus, small changes in the line wings of HCl are not seen in the residuals, if the amounts of methane and water vapor are fitted, too. Even if H_2O and CH_4 are set to their *correct* total columns, as determined in other spectral microwindows, the remaining uncertainties in the retrieval and spectroscopic uncertainties are still sufficient to substantially mislead the HCL tropospheric VMR profile retrieval, as is seen in Figure 4.6.

The situation improves, if large spectral intervals ($\geq 10\ cm^{-1}$) are used

Table 4.2: *Some results from the retrieval intercomparison of the NDSC: Listed are the total columns retrieved and their corresponding relative deviation from the true values for the three species under investigation. The second data line shows the results from Clare Paton Walsh, NPL, who used the same optimizing algorithm. The next line gives the average total columns and average errors (which is not the error of the average column) for all participants. The last line gives the results from a re–analysis with the true profiles that were available after the intercomparison.*

species retrieved ⇒ profiles used ⇓	Σ of CH_4 in $10^{19}cm^{-2}$	Σ of HCl in $10^{15}cm^{-2}$	Σ of NO_2 in $10^{15}cm^{-2}$
author using optimized REFMOD	3.324 (+0.41)	2.434 (-3.04)	8.206 (-53.0)
C. P. Walsh using optimized REFMOD	3.350 (+0.36)	2.521 (+0.42)	8.076 (-53.7)
average participant, diverse profiles	3.3568 (2.95)	2.607 (4.45)	10.67 (40.8)
synthetic spectra	3.3378	2.5104	17.460
author using true profiles	3.3365 (-0.04)	2.5120 (+0.06)	17.572 (+0.64)

to catch the far wings of the absorption lines. An additional bonus to this approach is the gain in information. If several undisturbed CH_4 lines are included in the interval, it is more likely to get the correct slope at the given HCl line. Additionally, purely tropospheric spectra can be recorded in daily life by putting up an artificial IR source on a nearby mountain or building. This yields the correct value near the surface as a starting point for the tropospheric profile.

Figure 4.8 shows the total column amounts of HCl for the two zenith

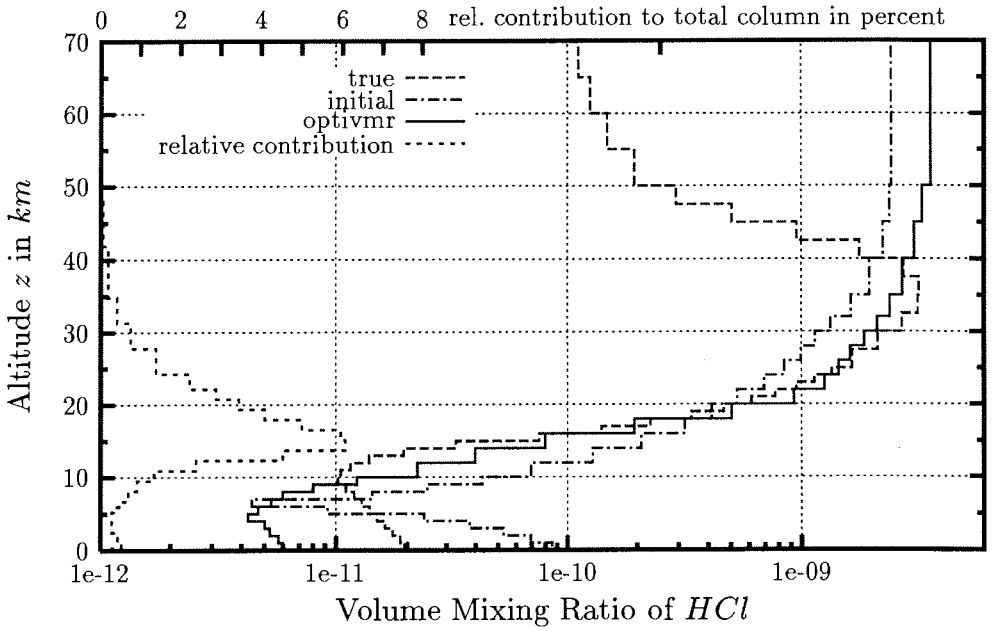

Fig. 4.6: *The VMR profiles of HCl are plotted in half–log scale versus altitude for the cases of the initial REFMOD95 profile (broken line), the optimized profile (solid line) and the true profile (dashed line), which was unknown during retrieval. In the altitude range from 15 to 30 km, the true profile is quite well represented by the optimized profile. The curve on the left corresponds to the upper tic marks (linear scale) and is proportional to the total number density of the optimized profile. The sharp steps in the graphs are given by the number of model layers, which are 29 for the initial and optimized profiles and 50 for the true profile.*

angles given as a function of the $DOSA$ for the modified REFMOD file and also for the true profile. The whole analysis is repeated with the true VMR profiles after the intercomparison to check the consistency. As to be expected, the best fit to lineshapes is achievable with a $DOSA$ of zero applied to the true profiles. The dependence of the total column from the $DOSA$ applied is illustrated in Figure 4.8 and demonstrates two important facts. The errorbars indicate the 1σ uncertainty level estimated from the S/N and the total standard deviation of the residuals. This errorbar fairly underestimates the total uncertainty. The second point is the dependence of the retrieved total column amount from the zenith angle of the spectrum analysed. If the VMR profile is perfectly correct, the derived total column is independent from the zenith angle,

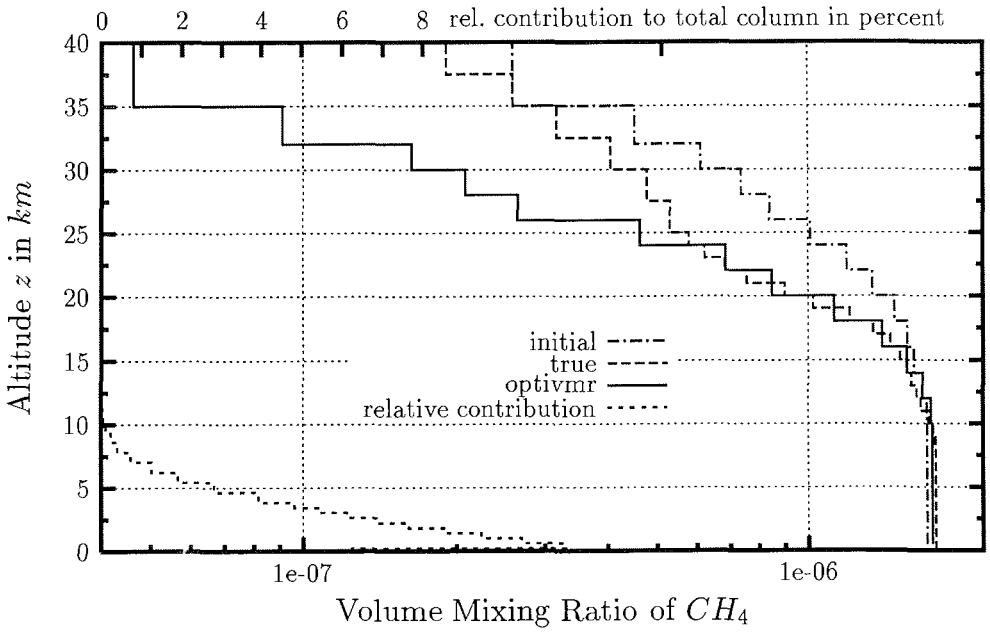

Fig. 4.7: *The CH_4 VMR–profiles are displayed in the same way as in the previous figure of HCl. From ground up to 25 km, the true profile is almost perfectly represented by the optimized profile. The deviations above 25 km have only negligible effects on the total column due to the very low number density compared to lower altitudes.*

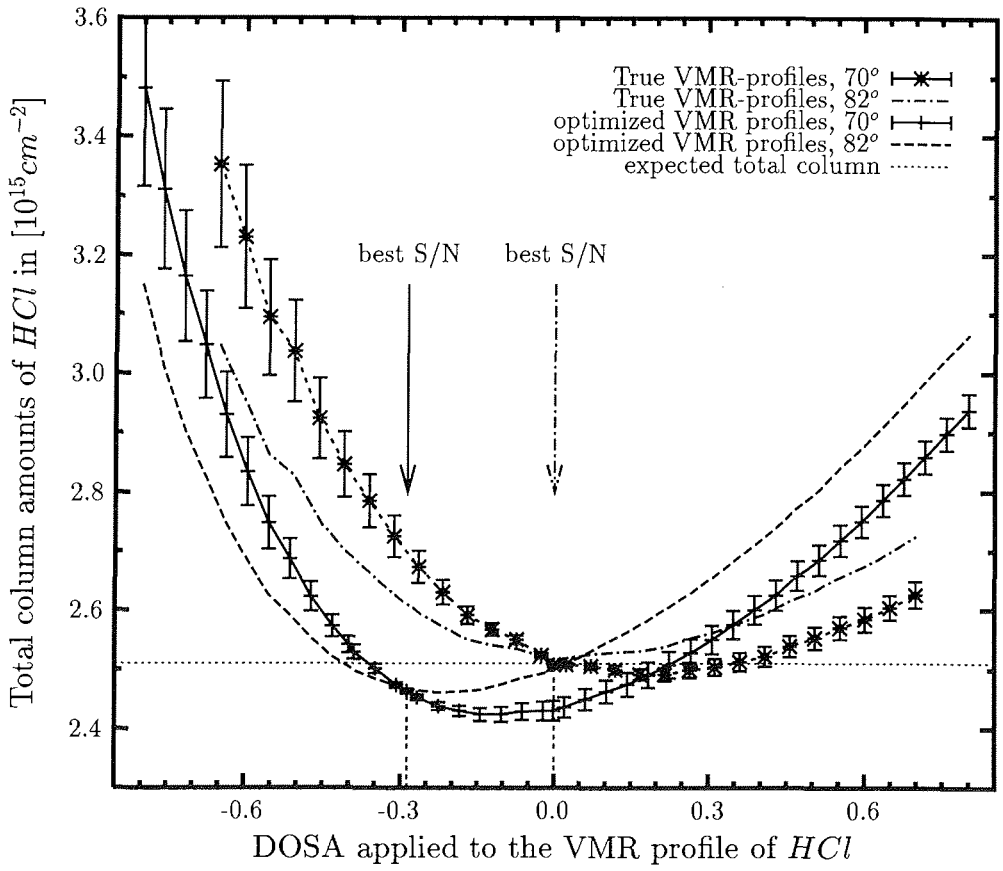

Fig. 4.8: *The dependence of the total column from the degree of subsidence/ascent is demonstrated for the case of HCl for the 2 zenith angles given by using either the optimized VMR profiles or the true profiles. The error bars represent the 1σ uncertainty due to the S/N only and fairly underestimate the total uncertainty. The DOSA values that correspond to the minimum standard deviation or best fit (Fig. 4.4) are indicated by arrows. Note that the curves for different zenith angles intercept at these points: The retrieved total columns are independent from the observational geometry, if the assumed VMR profiles are correct.*

otherwise it is not. Hence, the curves shown do not intercept by chance at the $DOSA$ value which gives the best fit. In spectra with low resolution, like lunar spectra and in spectra where the uncertainty in the pT profile is large, the line shape as the only criterium is typically insufficient. Thus, the retrieved total column as a function of the DOSA can be used as an additional criterium to find the correct VMR profile.

The total columns retrieved with the optimum profiles are listed in Table 4.2. Additionally, the total columns used by *A. Goldman* to calculate the spectra are given as well as the relative deviations of the retrieved total columns from the former. The agreement within 0.4 % in CH_4 and 3 % in HCl documents the high capabilities of the methods used. The small deviation in HCl is mostly due to profile uncertainties in the troposphere, amounts above 10 km altitude agree by better than 0.5 %. For comparison, the average deviations for all participants are given, indicating that the results presented are better than the average. Additionally, the results from *Clare Paton Walsh* from the team of *William Bell* and *Peter Woods* at NPL, GB, are added. They used a copy of the PROFIL program to optimize their profiles, as *William Bell* mentioned in his presentation at the NDSC meeting. This illustrates that the program can be used efficiently by others, too, yielding very similar results. Thus, the case study discussed in this section demonstrates, that even with this simple approach to improve the *a priori* profile one can get results that are competitive with mathematically very sophisticated line shape inversion and kernel averaging programs.

Most participants that used SFIT 1.09 underestimated NO_2 by about 50 %. As mentioned, it is not attempted to optimize the NO_2 profile and the strong deviation is mainly due to the unrealistic profile used for the synthetic spectra. The error is significantly smaller in real spectra. For a copy of the whole report, the reader may address to *A. Goldman* from the University of Denver (goldman@acd.ucar.edu).

4.5 Quantification of trace gas compositions in the arctic summer

After the study of synthetic spectra, results from real spectra recorded in the high Arctic are presented in the remaining sections. In this section, spectra recorded in early summer are discussed in detail. The atlas of spectral microwindows (appendix C) represents data from this section mainly and the reader may check the quality of individual spectral intervals in the appendix.

The meteorological conditions in early summer are generally the most stable occurring throughout the year on Spitsbergen, yielding the most favorable conditions for recording spectra. In summer and late summer air humidity increases significantly with long periods of cloudy weather. In the period studied, the mobile FTIR spectrometer from the British National Physics Laboratory (NPL), operated by *William Bell* and *Clare Paton Walsh*, was also present to perform the instrumental intercomparison for the NDSC. The results of both instruments are highly consistent.

The set of VMR profiles used for all data is the REFTOON set from *Geoffrey Toon* described in appendix B. The period studied from 28 May, 1995 to 1 June, 1995 is characterised by fair stable weather. The tropopause is found at 8.3 *km* on the 28 May and at 9.2 *km* on the other days as observed by the regular radio sondes. First, the low tropopause altitude is accounted for by lowering all VMR profiles according to equation (41). Then OPTIVMR is run on a set of selected microwindows to check for subsidence. The results from this study are shown in Figure 4.9 for the 30 May, 1995. The average DOSA retrieved is zero for the 30 May and the 1 June and it is +0.08 for the 28 May, 1995, probably due to the quite low tropopause on that particular day. However, as the warmer summer atmosphere is not subject to subsidence, a value close to zero is to be expected.

The important criteria for the selection of suitable microwindows for the determination of vertical profile information are:

- Single absorption lines are needed (no bands),
- with an absorption strength between 10 to 70 %,

- which are free of interference from other species (never strictly fullfilled).
- The species shall be chemically inert for being a tracer of dynamical features only.
- The species has to have a significant gradient in its VMR profile.
- Several lines of one species with different lower ground state energies and with different line broadening coefficients are needed.
- Different species with different gradients, i.e. sign and slope, are required,
- which have their bulk concentrations in different altitudes.
- Spectra recorded at highly different zenith angles are necessary.

This ideal set of spectral features is hardly ever available. The best achievable compromise for our data and computing capacities is the set shown in Figure 4.9. CH_4 and N_2O are computed for different wavenumbers with different temperature dependences in their line broadening coefficients and both species show very little variability due to chemical processing. HF and HCl are selected for its opposite sign in VMR gradient. For the investigation of disturbed meteorological conditions discussed in the next section, more time and effort is spent.

The total column amounts of 30 different species are retrieved and are listed in Table 4.3. This includes a number of important greenhouse gases and reactants and reservoir species relevant to stratospheric ozone chemistry and demonstrates the importance of ground–based FTIR observations for the discussion of chemical and climatological questions, in particular in the high arctic where satellite data is incomplete and the synoptic net is wide. The spectral microwindows used in the retrieval are listed in Table C.1, appendix C, page 190 and are illustrated in the atlas of appendix C. The 1σ uncertainties given account for the statistical uncertainties arising from noise in the spectra and for zenith angle uncertainties. Systematic errors due to uncertainties in the pT profile and the *a priori* VMR profiles are not included, but are estimated to be significantly smaller than the 1σ uncertainties given. The meteorological

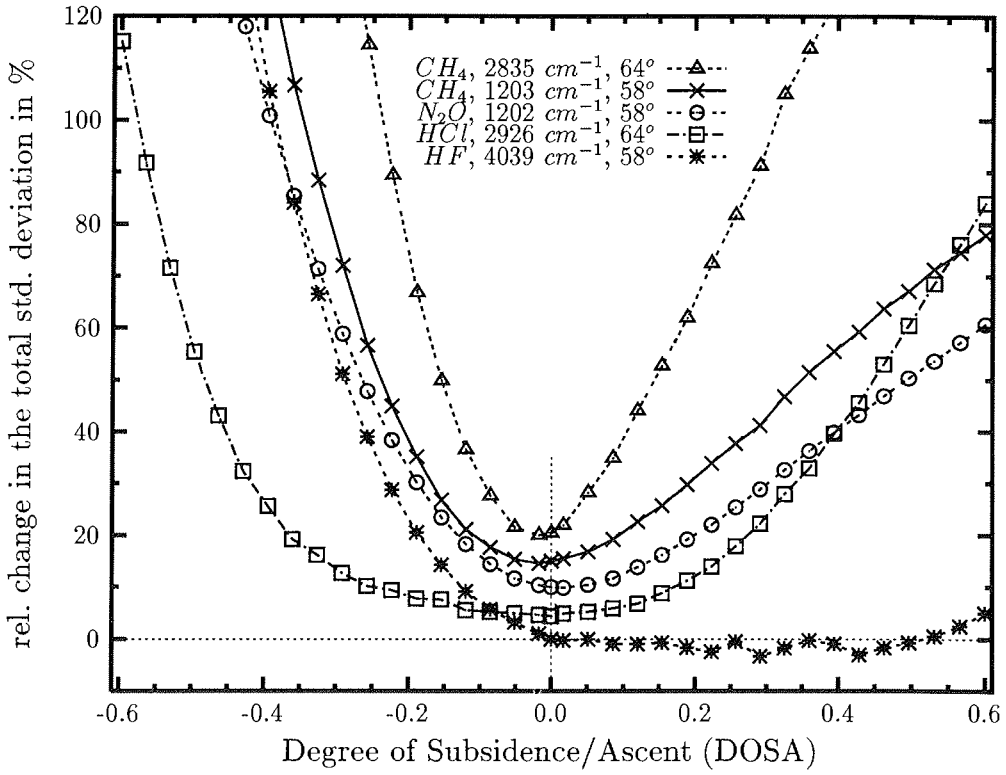

Fig. 4.9: *The total standard deviation of the residuals as a measure of the line shape error is shown as a function of the DOSA. It is comparable to Figure 4.4, but this time real spectra are analysed, which are recorded on the 30/May/1995. The key specifies the species retrieved, the spectral position of the line used and the zenith angle of the sun. The curves of HCl and HF show little sensitivity at small and at positive DOSA values, respectively, in this example and demonstrate that the sensitivity of each species depends on the altitude range effected by the DOSA operation. All other curves show a global minimum at a DOSA value close to zero, which is typical for the undisturbed summer atmosphere. The curves are shifted upward by 5 % each for clarity.*

Table 4.3: *This table gives the average total column amounts and 1σ uncertainties retrieved from the spectra recorded between the 28^{th} of May and 1^{st} of June 1995. Listed are the different species versus the day of recording. The data of water vapor and its isotopes is split up into different sets of spectra as indicated by $^{*)}$ and $^{+)}$ markings (see text in chapter 5).*

species	scale in cm^{-2}	May 28	May 30	June 01
C_2H_2	10^{15}	1.59 ±0.34	1.82 ±0.24	1.42 ±0.32
C_2H_4	10^{14}	3.5 ±0.5	3.5 ±0.3	3.8 ±0.4
C_2H_6	10^{16}	2.02 ±0.04	2.44 ±0.05	2.28 ±0.04
CCl_2F_2	10^{15}	8.97 ±0.19	8.75 ±0.15	8.76 ±0.13
CH_4	10^{19}	3.68 ±0.09	3.71 ±0.05	3.72 ±0.05
$^{13}CH_4$	10^{19}	3.64 ±0.02	3.64 ±0.02	3.65 ±0.01
CH_3D	10^{19}	4.66 ±0.33	4.72 ±0.17	4.67 ±0.17
CHF_2Cl	10^{15}	2.46 ±0.15	2.63 ±0.12	2.38 ±0.08
$ClONO_2$	10^{15}	1.20 ±0.11	0.70 ±0.07	0.64 ±0.09
CO	10^{18}	2.10 ±0.20	2.02 ±0.20	
CO_2	10^{21}	7.66 ±0.06	7.54 ±0.05	7.69 ±0.05
COF_2	10^{14}	4.4 ±0.6	4.1 ±0.5	4.2 ±0.4
H_2O	10^{21}	14.7 ±0.1	24.6 ±0.5	28.9 ±0.7
$H_2{}^{17}O$	10^{21}	15.1 ±0.4	29.1 ±2.2	
$H_2{}^{18}O$ $^{*)}$	10^{21}	14.0 ±0.8	20.9 ±0.5	24.5 ±0.7
$H_2{}^{18}O$ $^{**)}$	10^{21}	15.5 ±0.6	26.4 ±0.8	27.9 ±1.1
HDO $^{+)}$	10^{21}	11.0 ±0.1	16.7 ±0.1	18.8 ±0.1
HDO $^{++)}$	10^{21}	9.73 ±0.1	16.8 ±0.1	17.6 ±0.1
$H^{35}Cl$	10^{15}	6.13 ±0.05	5.76 ±0.06	6.13 ±0.05
$H^{37}Cl$	10^{15}	6.26 ±0.13	5.94 ±0.13	6.23 ±0.11
HCN	10^{15}	5.8 ±1.1		5.7±0.5$^{*)}$
HF	10^{15}	1.67 ±0.03	1.63 ±0.03	1.70 ±0.04
HNO_3	10^{16}	1.86 ±0.08	1.71 ±0.05	1.85 ±0.05
HO_2NO_2	10^{14}	3.9 ±0.8	5.9 ±0.6	4.2 ±1.3
N_2	10^{25}	1.76 ±0.05	1.74 ±0.04	1.75 ±0.08
N_2O	10^{18}	6.37 ±0.06	6.39 ±0.05	6.35 ±0.04
NH_3	10^{13}	<8.0	<8.0	<8.0
NO	10^{15}	5.23 ±0.12	5.43 ±0.15	
NO_2	10^{15}	3.80 ±0.20	3.83 ±0.23	4.12 ±0.20
O_3	10^{18}	9.69 ±0.04	9.24 ±0.04	9.00 ±0.05
OCS	10^{15}	9.43 ±0.24	9.64 ±0.24	
SF_6	10^{13}	9.0 ±1.7	10.1 ±1.4	8.7 ±1.5

$^{*)}$ This amount is observed on the 28/June/1995.

conditions are very stable in the given case and the pT profile from the radio sonde is assumed to be representative for the air masses sampled at recording time. This is backed up by the fact, that the line shapes of N_2 and CO_2 are perfectly met in the simulation (compare appendix C, pages 271 and 265–269).

The absolute accuracy of the total column amounts listed is limited by the accuracy of the spectroscopic data base used. For the data presented in this section and in the following section 4.6 the latest version of the HITRAN**96** data base is used, which became available in June 1996 and contains about 1 million spectroscopic lines. However, the latest version still lacks several important species like all the CFCs, C_2H_4, HO_2NO_2 and others. Additionally, even strong lines with more than 10 % total absorption are occasionally missing (see e.g. appendix C, page 269 or 273). The same applies to uncertainties in the lower ground state energy and in the pressure and temperature coefficients that determine the line shape. The lower ground state energy of $H^{37}Cl$ listed in Table C1 (page 190) for example is unasigned and set to zero, which is of course totally unrealistic.

In some cases, where the line positions of strong lines are obviously inconsistent with all recorded spectra, the line position has been adjusted within the uncertainties given in the data base to meet the observed line positions. To overcome the difficulties of the missing species mentioned, all these are taken from the latest version (revision level 17, *C. Rinsland*, priv. comm. 1996) of the ATMOS AFGL files (*Brown* et al., 1987). The software created to handle the different data formats and to perform the file merging is given in appendix B. Summed up, there is still significant potential for improvement in the accuracy of the spectroscopic data base. At present status the overall error arising from these uncertainties is difficult to calculate and depends to some degree also on the meteorological and geometrical conditions at recording time. The pragmatic way is to use as many lines as possible in the analysis in the hope that spectroscopic uncertainties are scattered statistically about the exact values. Unfortunately, many species have only one or a very limited number of useful spectral windows for their observation.

4.6 Investigation of the atmosphere under disturbed conditions

The meteorological conditions:

The period discussed in this section covers 11 days in early spring 1995, from the 10^{th} of March 1995 to the 21^{st} of March 1995. The sun returned to Ny–Ålesund on the 8^{th} of March and ended polar night. Photolysis returned to the stratosphere some 2–3 weeks earlier, but at least the lower troposphere is still subject to the Arctic Haze phenomenon. Many pollutants that have accumulated in the dark period are now subject to extensive chemical processing. Over the whole period covered, the observation site is well inside the polar vortex (see Figures 4.10 and 4.11), though it came close to the edge of the vortex towards the end of the period. The dynamical variability is high throughout March 1995 as is also illustrated by the strong deformation of the polar vortex shown in the PV–plot from the 17^{th} of March 1995 (Figure 4.11). The 475 K layer shown corresponds to approximately 20 km geometric altitude inside the vortex, which is well in the stratospheric ozone layer.

On all days with observations, no polar stratospheric clouds (PSCs) are observed by the AWI LIDAR operated in the same building (*Jens Biele*, AWI Potsdam, priv. comm. 1996). However, the potential for PSCs inside the polar vortex is given, as can be estimated from stratospheric temperature maps. In the period 10^{th} of March to 21^{st} of March 1995 the stratospheric temperature is low enough to form PSCs over a total area of about $2 \cdot 10^6\ km^2$ in the northern hemisphere (*Peter von der Gathen*, AWI Potsdam, priv. comm. 1996). Thus, it is likely that heterogeneous chemistry occured on the surface of PSCs somewhere inside the polar vortex and that filaments of processed air masses coexisted with filaments that show little chemical impact. The common occurrence of filament structures of more and less chemically processed air is backed up by the ozone MATCH experiments in the EASOE winter 1991/92 (*Gathen* et al., 1995 and *Rex* et al., 1996) and in subsequent winters (*Rex* et al., in preparation, 1996) as well as by model studies (e.g. *Schoeberl* and *Newman*, 1995).

The history of the pT profiles is illustrated in Figures 4.12 and 4.13 by

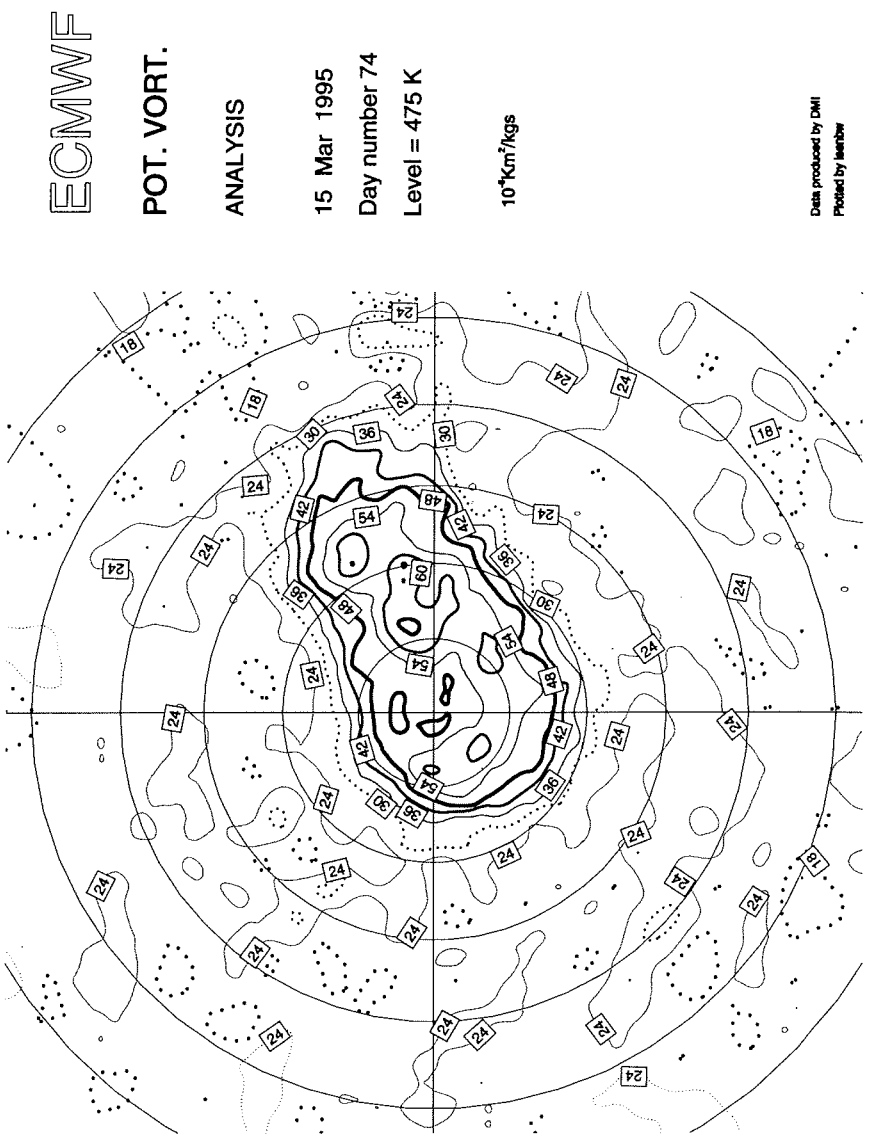

Fig. 4.10: *This is a PV–plot of the northern hemisphere for the 475 K layer for the 15^{th} of March 1995. The observation site located at Ny–Ålesund ($79^{o}N$, $12^{o}E$) is well inside the polar vortex throughout the period studied. The plots are calculated by the DMI and are based on data from the ECMWF. The polar grid is spaced at 10^{o} latitude.*

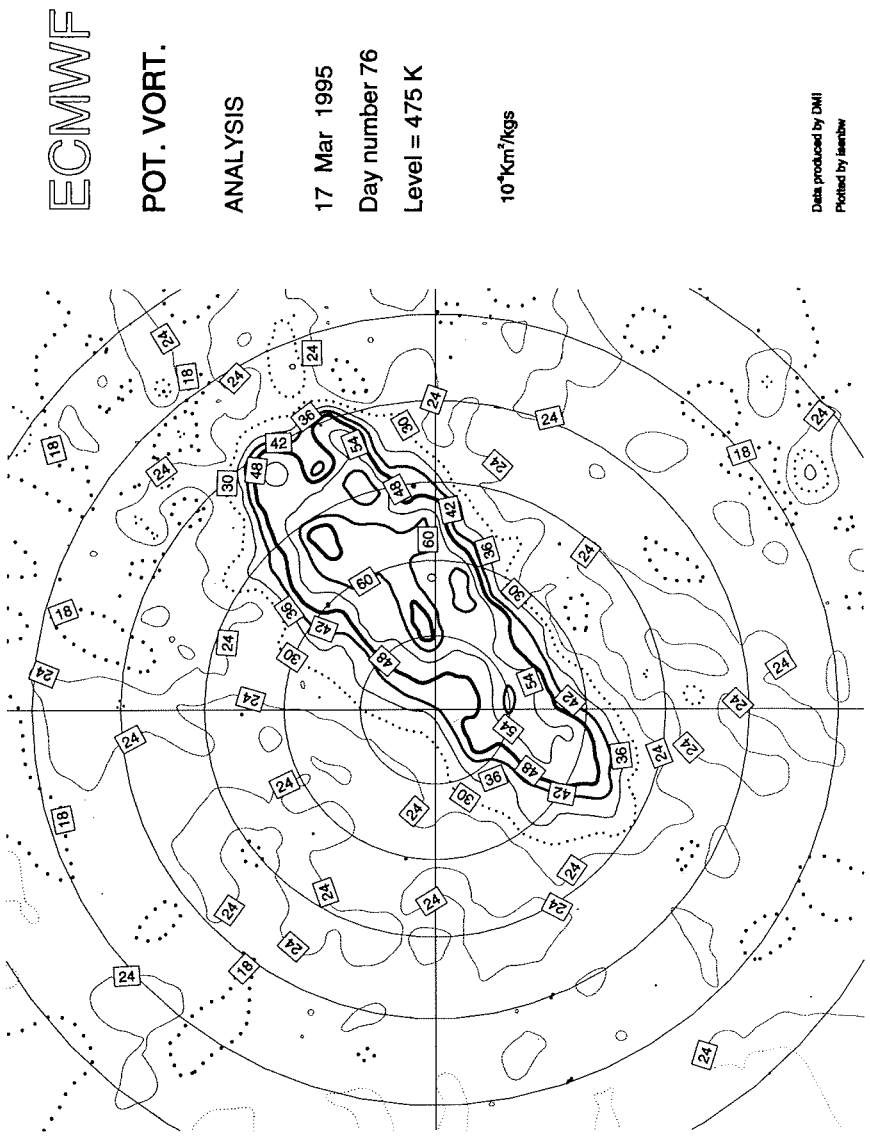

Fig. 4.11: *Like in the previous figure, the potential vorticity distribution is shown for the 475 K layer but for the 17^{th} of March 1995. The observation site is well inside the polar vortex. Note the strong deformation of the arctic vortex, which is common in the northern hemisphere but unknown to the antarctic vortex.*

data from local radio sondes. From Figure 4.12 it can be seen that there is a dramatic change in temperature from the 12^{th} to the 13^{th} March with a strong warming between 8 and 13 km altitude. No significant tropopause can be seen in the latter profile, which slowly recorvers over the following days. Thus, large scale vertical mixing of tropospheric and stratospheric air is possible and might indicate a tropopause folding. In the period

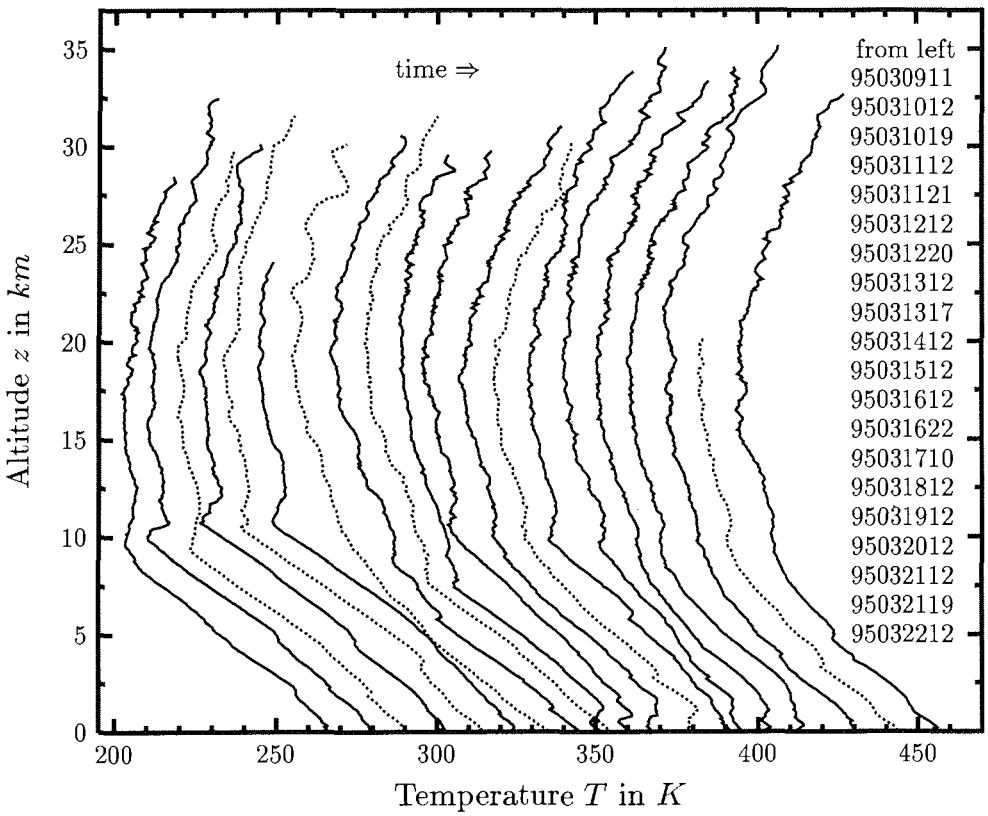

Fig. 4.12: *Evolution of the temperature profile in March 1995 as observed by radio sondes. Regular sondes at noon are represented by solid lines, additional flights by dotted lines. Each profile is shifted right by 10 Kelvin for clarity. The right hand key gives the day and hour of launch in the format YYMMDDHH. Note the sudden strong warming after the 12^{th} of March 1995.*

19^{th} of March to 22^{nd} of March 1995 the tropopause is also quite weak expressed, but changes are slower than in the first example. This possible large scale vertical mixing adds to the uncertainties in the VMR profiles used in the retrieval of the FTIR data. Significant changes can also be seen in the history of the pressure profiles. In Figure 4.12 the relative changes in pressure are plotted, because the absolute change is difficult to see in the normal presentation of the pressure profile. The profile of the 9^{th} of March is fitted to a mathematical function and the relative changes are shown in percent with respect to this reference profile. A significant drop of pressure exceeding 5 % in the troposphere and middle stratosphere is seen after the 12^{th} of March 1995. It reaches its minimum in the troposphere on the 13^{th} and in the stratosphere on the 14^{th} Mar, 1995.

Summed up, the dynamical as well as the chemical situation is highly complex in the period studied. Tropospheric pollutants that have accumulated over the dark period undergo significant chemical processing with the return of photolysis and show a pronounced diurnal variation. Processing of stratospheric air by PSC bound heterogeneous chemistry is likely, but air masses are not effected homogeneously. Instead, the formation of filaments of processed and non–processed air masses is likely. On some days a strong vertical mixing is possible, where the topopause is practically not existent, while on other days the separation of tropospheric and stratospheric air masses is at a normally high level. The total correspondence of retrieved total columns in the comparison of solar and lunar spectra cannot be expected for chemically active or dynamically variable species, like Chloronitrate ($ClONO_2$) or Ozone.

Nevertheless, particular care is taken for the 15^{th} and 16^{th} of March. Solar spectra are recorded on both days and lunar spectra in the perfectly clear full–moon night in between. However, some restrictions apply to the direct comparison of the solar and lunar spectra. Only few spectra could be recorded due to cloudy intervals during the days and due to the time consuming instrumental modifications necessary for the different operation modes, which require a realignment of the optical path. Additionally, the zenith angle of the sun is very low ($\approx 85^{o}$) while lunar zenith angles are smaller than 80^{o}. Note also that there is a strong in-

version layer present in the period 14/Mar – 16/Mar/95 (Figure 4.12), which is also seen, though to a much weaker extent, on the 19^{th} and 20^{th} of March, but which is not seen on other days.

In a simple geometric approximation, the distance over ground of the air mass probed can be estimated. Based on the sine theorem in triangles

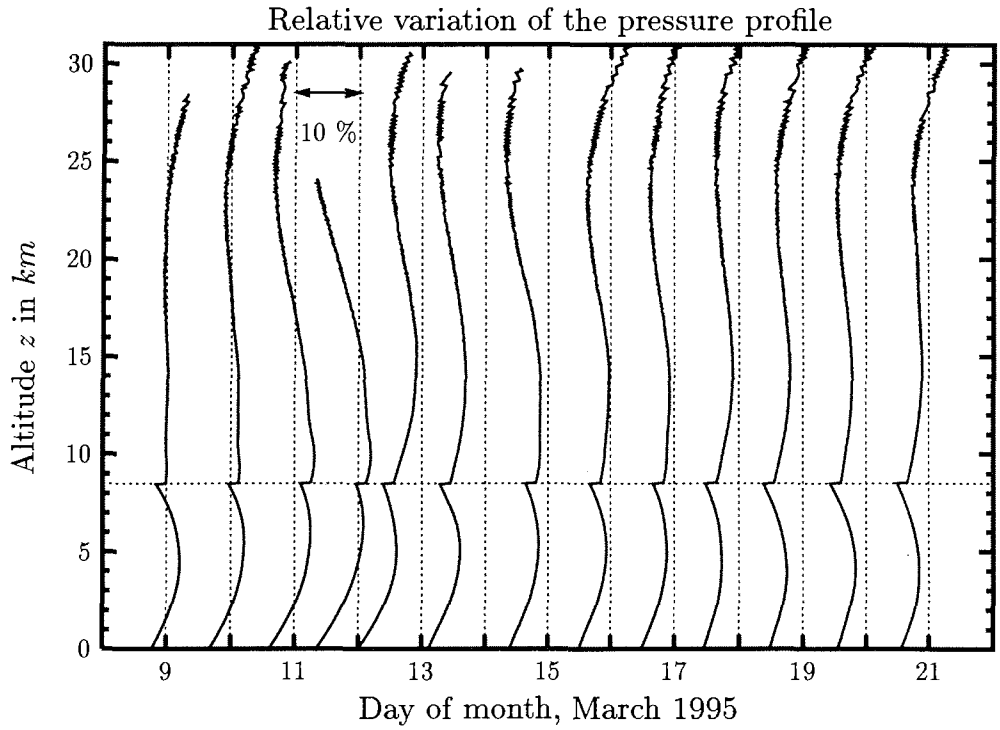

Fig. 4.13: *The evolution of the pressure profile is given as observed by daily radio sondes at noon in March, 1995. The pressure profile of the first day shown, the 9^{th} of March, is fitted to a tropospheric and a stratospheric mathemetical function. Displayed is the relative variation of pressure from this fitted function in percent. Vertical gridlines represent no deviation and are spaced at 10 % deviation from the mathematical function. On the 13 Mar and 14 Mar, 1995, a significant drop in the pressure profile is observed, which is initiated in the troposphere and slowly recovers over the next 48 hours.*

one obtains for the distance over ground s as a function of the zenith angle φ_z (in degrees) and the altitude z:

$$s(\varphi_z, z) \approx \frac{\pi \cdot 6378\,km}{180} \cdot \left\{ \varphi_z - arcsin\left(\frac{6378\,km}{z + 6378\,km} \cdot sin(\varphi_z) \right) \right\} \quad (51)$$

For an ozone sample mainly distributed about 20 km altitude and which is observed under a zenith angle of 85°, the air mass sampled by the FTIR spectrometer is about 200 km away from the observation site. Thus, one cannot expect that air masses probed by radio and ozone sondes at the observation site are representative for the air masses seen by the FTS at high zenith angles or several hours after the launch.

Data retrieval

The first step in the data analysis is the determination of the subsidence. On those days with a well defined tropopause in the radio sonde profile, the derived altitude is used for the tropopause in the VMR–profiles according to the operation of equation 50, page 88. On the remaining days a tropopause at 10 km is assumed. Then OPTIVMR is run on a selected set of microwindows for each day to determine the optimum degree of subsidence. HCl cannot be used in spring for this task, since it is subject to significant chemical processing. The only suitable species left with a positive gradient in VMR is HF. Unfortunately, only three spectra are available that cover the spectral region beyond 4000 cm^{-1}. Among the species with negative gradients in VMR, N_2O and CH_4 suit best the requirements given in the previous section. Two lines of each species are included in the study that have different spectroscopic characteristics as listed in Table C.1 on page 190. The selected lines are at 1202.0 and 2806.3 cm^{-1} for N_2O, at 1202.4 and 2835.7 cm^{-1} for CH_4 and at 4039.0 cm^{-1} for HF.

The results of the retrieval are presented in Figure 4.14 for the CH_4 line at 2835.7 cm^{-1} and in Figure 4.15 for the microwindow at 1202 cm^{-1} that features N_2O and CH_4. For each retrieval, a well defined minimum in the total residuals as a function of the DOSA is found. All these optimum DOSA values indicate a strong subsidence that correspond to negative DOSA values between -0.50 and -0.66. A DOSA value of -0.5 means, that an air mass that is located at 20 km altitude before the

stratospheric cooling starts in late fall is now found at approximately 16 km altitude.

Contrary to the results from early summer presented in the previous section, the optimum DOSA values from different microwindows do not agree. An overview on this fact is given in Figure 4.16 that shows all the

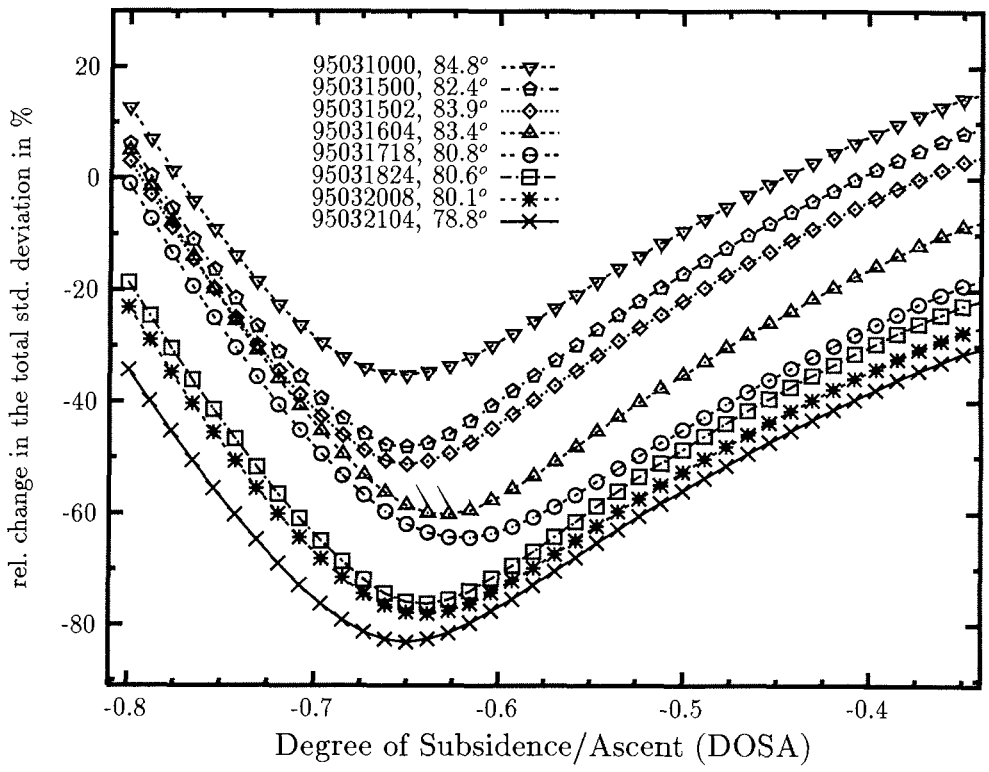

Fig. 4.14: *The relative change in the total standard deviation of the residuals as a measure of the overall line shape errors is shown as a function of the degree of subsidence/ascent. The spectral line analysed is a methane line at 2835.6 cm^{-1} (see appendix C, page 285). The zenith angles and the name of the spectrum that indicates the date (YYMMD-Dxx) are given in the key. The minimum of the curves shown indicate the best estimate for the atmospheric subsidence. All curves intercept at (0,0), but are shifted for clarity in the figure.*

optimum DOSA values retrieved and figures are listed in Table 4.4. It has to be pointed out, that the data shown for the 1202 cm^{-1} retrieval interval is not the average of the N_2O and the CH_4 line in that interval, but that the optimum DOSA given for that interval is representative for each of the two species individually. From this fact one can exclude the assumption that the different gradients in the initial VMR profile are the reason for the observed offsets between the retrievals from the lines of

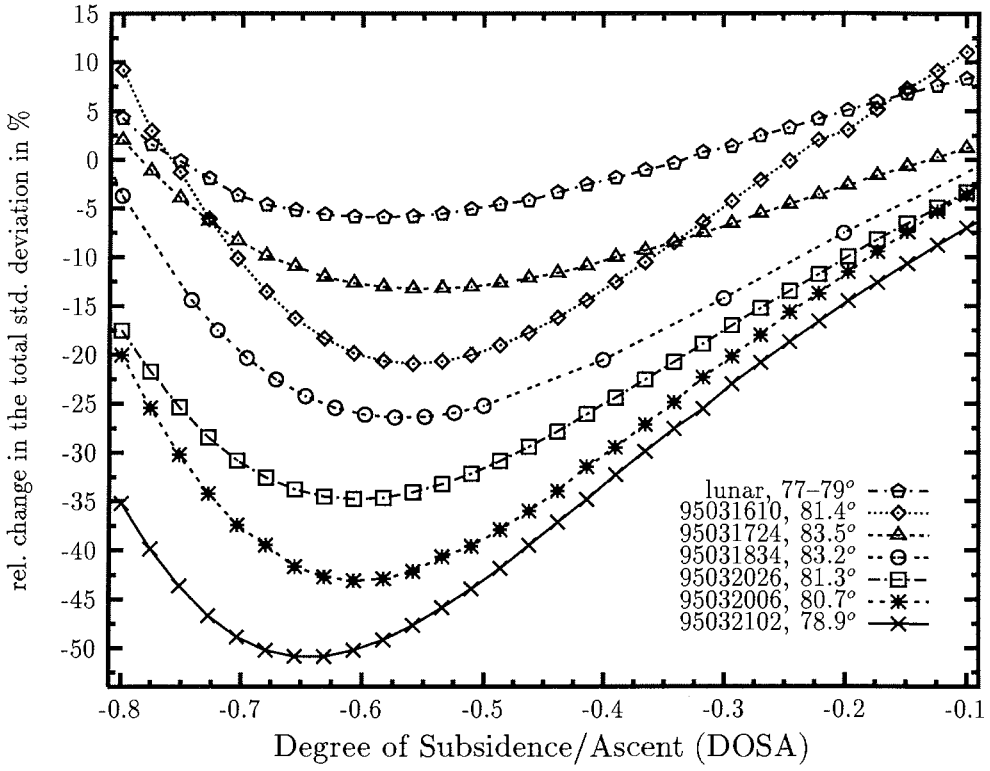

Fig. 4.15: *Like in the previous figure, the change in total standard deviation of the residuals as a measure of the overall line shape errors is shown as a function of the DOSA. This time the microwindow at 1202 cm^{-1} is analysed, that holds one line of CH_4 and N_2O each. The minima are representative for each of the two species individually, but do not agree with Figure 4.14. For discussion see text and the comparison in the next figure.*

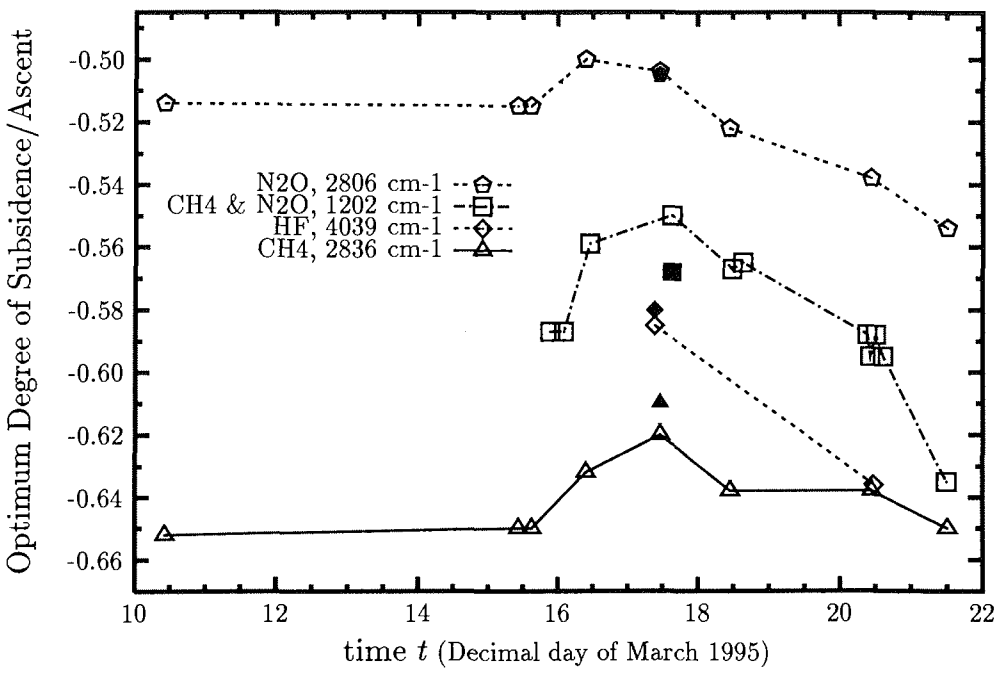

Fig. 4.16: *This figure gives an overview on all optimum DOSA values retrieved in March 1995. There are systematic offsets between the different microwindows, which is not observed in the early summer data discussed in the previous section. Differences are ascribed to uncertainties in the pT profile. The filled symbols are the results from a re–analysis of spectra from the 17^{th} of March 1995 with a modified pT profile, which causes a shift of the optimum DOSA in most lines. Tic marks correspond to 0:00 h.*

N_2O and CH_4 at higher wavenumbers – this would imply that the DOSA operation itself (equation 49, page 86) is inadequate.

The explanation suggested instead are the uncertainties in the pT profile that are responsible for the bias between the different microwindows studied. The first hint on errors in the pT profile is derived from the systematic features in the residuals of CO_2, as illustrated in Figure 4.17. Due to the practically gradient free VMR profile, these systematic signatures can only be ascribed to an inadequate pT profile.

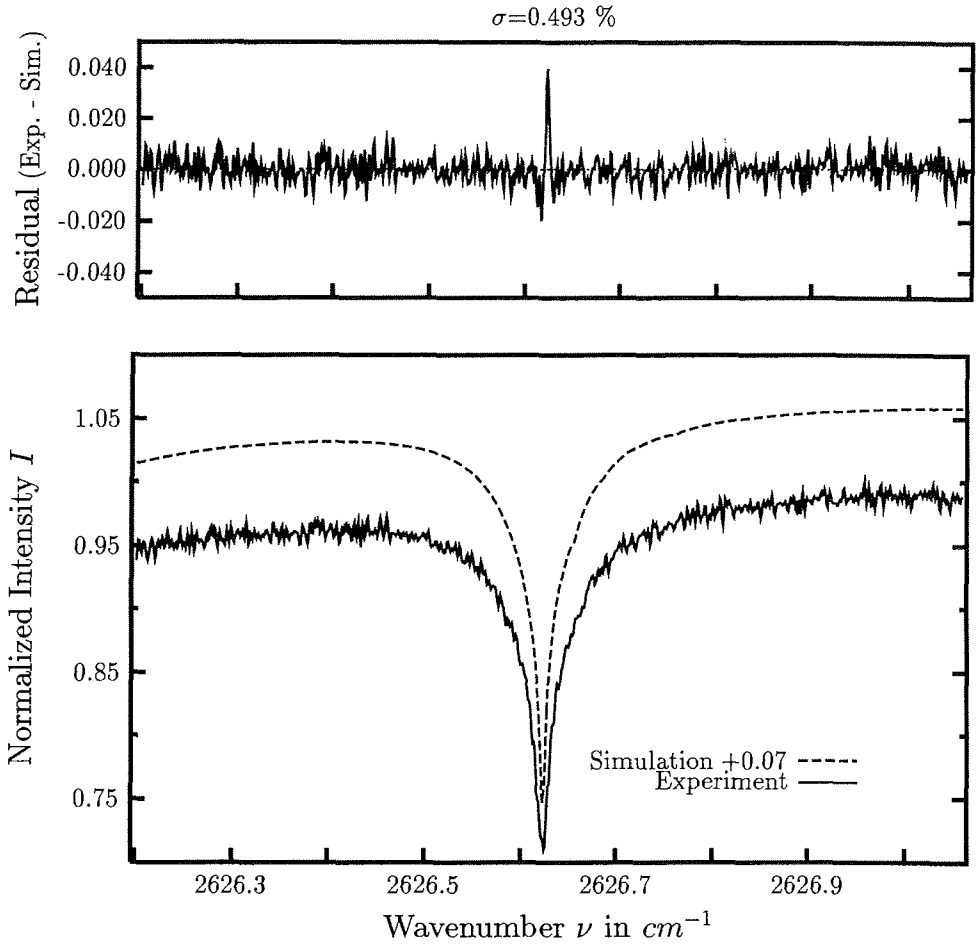

Fig. 4.17: *This figure shows a fit to a recorded absorption line of CO_2. There are significant systematic signatures in the residuals that indicate an inadequate pT profile in the simulation. Errors in the VMR profile can be excluded, because CO_2 is well mixed throughout the homosphere. The spectrum is recorded on the 17^{th} of March 1995 at noon at a zenith angle of 80.1° with an OPD of 257 cm and boxcar apodization.*

To learn more about the effects of pT uncertainties on the retrieved optimum DOSA, a case study is performed for the spectra recorded on the 17^{th} of March 1995. A modified pT profile is set up, where the temperature is increased by 2 K from ground to 10 km, by 3 K from 10 to 20 km and by 4 K above 20 km altitude. The pressure is corrected for the increase in temperature according to the thermodynamic equation on ideal gases, i.e. for the recorded pressure a thermodynamic temperature is calculated, then the 2–4 K are added to this thermodynamic temperature and the reverse calculation then gives the pressure used for the modified pT profile.

The results from the DOSA retrieval with this modified pT profile are also included in Figure 4.16 and are represented by filled symbols. As can be seen, the retrieved optimum DOSA values are closer to one another. Although individual optimum DOSA values change significantly in the case study, the average optimum DOSA does not. The uncertainties in

Table 4.4: *In the table the optimum DOSA values retrieved are listed for each day. Given are both the individual values for each species and line position and the mean DOSA value for all individual optima, termed the global optimum DOSA. The data is plotted in Figure 4.16. Missing entries in the table are due to an incomplete series of spectral regions recorded.*

	individual optimum DOSA value					mean
species	N_2O	N_2O	CH_4	CH_4	HF	DOSA
line position	2806.3	1202.0	1202.4	2835.7	4039.0	value
10/Mar/95	-0.514			-0.652		-0.583
15/Mar/95	-0.515			-0.650		-0.583
lunar		-0.587	-0.587			-0.587
16/Mar/95	-0.500	-0.559	-0.559	-0.632		-0.563
17/Mar/95	-0.504	-0.550	-0.550	-0.620	-0.585	-0.562
18/Mar/95	-0.522	-0.566	-0.566	-0.638		-0.573
20/Mar/95	-0.538	-0.592	-0.592	-0.638	-0.636	-0.599
21/Mar/95	-0.554	-0.635	-0.635	-0.650		-0.619
pT study	-0.505	-0.568	-0.568	-0.610	-0.580	-0.566

the pT profile can explain the observed biases at least to a large extent. Other sources of uncertainty are the spectroscopic line parameters that may have a stronger effect in the colder spring time air masses than in the warmer summer data presented before.

To get more information on the correct value for the subsidence, the retrieved total column amounts are analysed as a function of the DOSA. In the discussion of the synthetic spectra in section 4.4 it is shown that the retrieved total column amounts give additional insight into the matter. Unfortunately, the variation in the zenith angle is very small due to the season. But the statement given in section 4.4 can be extended. The total columns retrieved in different microwindows should also yield the same results – supposed there is no known bias under well known conditions that are caused by uncertainties in the spectroscopic data base. The different lines of N_2O and CH_4 have quite different ground state energies (see Table C.1, page 190). Consequently, they will react different to uncertainties in the pT profile.

In Figure 4.18 the retrieved total column amounts of CH_4 are presented for both lines studied and for all spectra analysed in the DOSA retrieval. It is interesting to notice that the retrieved curves show opposite signs in their gradients and thus give well defined interception points. The interception points are scattered between -0.50 and -0.65 and agree almost perfectly with the mean DOSA value from the search for the minimum residuals for the given day (Table 4.4). In N_2O the case is very similar, except for the gradients of the retrieved curves, which have the same sign, but the difference is significant and again well defined interception points are observed. The curves are not shown in a separate figure, but an example for the 17^{th} of March 1995 is included in Figure 4.19. Like in the previous case of methane, the interception points are scattered about DOSA values between 0.50 and -0.65 and are close to the mean DOSA listed in Table 4.4.

Before concluding on these facts, the results from the case study with the modified pT profile are included in the discussion. In Figure 4.19 the retrieved total column amounts as a function of the DOSA value are compared for the simulations using either the regular radio sonde pT profile or the modified pT profile described before. It is evident that the

curves representing the total column amounts for the regular pT profile intercept almost perfectly at the mean DOSA value retrieved for that day from the minimum residual search (Table 4.4, Figure 4.16). This is not the case for the data from the modified pT profile. Both, for N_2O and CH_4 does the interception point not match the mean DOSA retrieved in the minimum residual search (compare Table 4.4) and the interception points are different for CH_4 and N_2O.

The average degree of subsidence/ascent determined in this work of

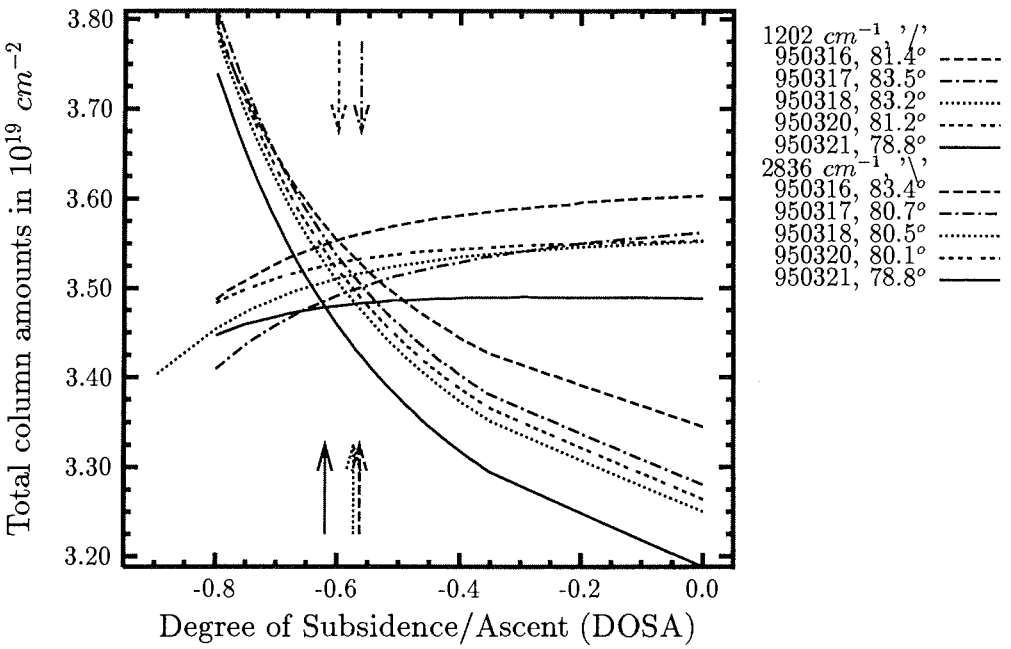

Fig. 4.18: *The total column amounts obtained for CH_4 in the DOSA retrieval as a function of the DOSA value is shown for the two spectral lines analysed. Curves that correspond to the spectral line at 1202.4 cm^{-1} show a positive gradient while those from the spectral line at 2835.6 cm^{-1} show a negative slope. In the absence of uncertainties, the points of interception yield the correct DOSA for that day. The interception points observed are close to the mean DOSA values given in Table 4.4. The latter ones are indicated by arrows in the figure.*

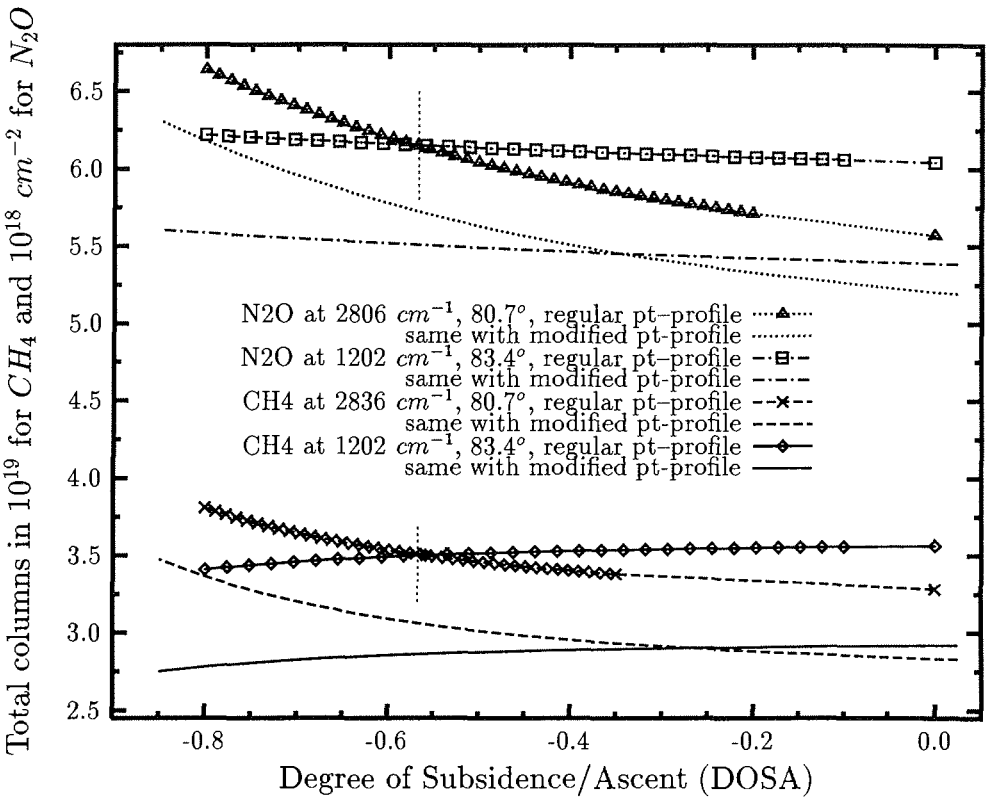

Fig. 4.19: *In this figure the total column amounts retrieved as a function of the DOSA value are compared for two different pT profiles used in the analysis. The curves with symbols are calculated with the regular pT profiles from the radio sondes from spectra recorded under a zenith angle as given in the key, while the curves without symbols represent results for the same data by using a modified pT profile in the retrieval. The vertical lines mark the mean DOSA from Table 4.4. With the regular pT profiles, the total column amounts agree for the different N_2O and for the different CH_4 lines at the the derived mean DOSA value, while this is not the case when using the modified pT profile.*

about -0.583 are also in reasonable agreement with aircraft measurements by *Toon* et al., (1992a) and thermal emission measurements from an aircraft during the AASE campaign reported by *Traub* et al. (1995) that were performed in the Arctic in the period January to March 1992. The atmospheric cooling occurs over a period of approximately 5 months until the final warming typically starts in the second half of March. If one ascribes a constant subsidence rate for the whole winter period to the DOSA value retrieved in March, a subsidence rate of 1.25 km per month is obtained for an air parcel originally found at 25 km altitude. In the seasonal cycles shown in *Notholt* et al. (1996a) it is seen that the assumption of a constant rate of subsidence is adequate. A subsidence rate of 1.25 km per month equals 0.48 mm/s, which is in good agreement with the subsidence rate of 0.5 mm/s reported by *Traub* et al. (1995).

From all this data it is concluded, that the mean DOSA value determined in the search for the minimum in line shape residuals and from the mean interception points in the total column curves gives the most consistent description of the subsidence occurring in the spring time atmosphere. After application of the global optimum DOSA to the *a priori* VMR–profiles, the retrieved total columns from different species, different lines of the same species and from spectra recorded under different zenith angles agree best. It is assumed that this gives the best approximation derivable from the given FTIR data to the unknown real VMR–profiles. It is evident from the total column curves shown (Figures 4.8 and 4.18), that omitting any correction for the subsidence leads to significant systematic errors in the total columns retrieved that are minimized by the approach of the global optimum DOSA.

Final results

The daily mean DOSA values given in Table 4.4 are applied to each set of VMR profiles before the final retrieval of all the trace gases studied. Excluded from the operation are only the VMR profiles of ozone, which are taken from the available *in situ* data, and water vapor, which shows only a small gradient in the stratosphere and where data up to 12 km altitude is available from *in situ* data as well.

The total columns retrieved for 29 of the 32 species studied are listed

in table 4.5. Data on the heavy isotopomers of ozone are included in chapter 5.

A discussion of the seasonal variation of the species measured and of the relevance to atmospheric chemistry is given in *Notholt* et al. (1996a and 1996b). However, a brief comment is given below on some of the figures presented here. In the publications mentioned, the retrieval is not performed with SFIT, but with the GGG algorithm from *Geoffrey Toon.* All data of the past 4 years has been re-analysed to get a homogeneous set of total column amounts for the average seasonal cycles, which is simply much faster to do on a set of workstations than on individual PCs as required for SFIT.

Minor differences between figures presented here and in the publications *Notholt* et al. (1996a and 1996b) are ascribed to the different retrieval algorithms. If one compares the summer data, then significant differences are seen only in CCl_2F_2, $ClONO_2$, and HCN. In the retrieval of CCl_2F_2 and HCN additional microwindows are used in this work compared to the earlier publications. $ClONO_2$ yields a very weak absorption signal in summer and small differences in the retrieval have strong effects on the total column amounts retrieved. The two step wide/narrow retrieval approach described in chapter 3 (page 73) is a very careful treatment of the task. Following *Reisinger* et al. (1995) and *Rinsland* et al. (1996), this technique is superior to the one step retrieval performed with the GGG algorithm. The differences in March are larger, as can be expected from the significantly higher dynamical and chemical variability. However, an underlying bias is seen in the data that is ascribed to the DOSA of about -0.58 used in this work compared to the average value of -0.41 used in the earlier publications. The retrieval in the earlier work is based on the minimum search in total residuals of HF and N_2O only.

Many tropospheric pollutants can accumulate over the dark winter period in the absence of photolysis and free hydroxil radicals (OH). Anthropogenic pollutants like C_2H_6, C_2H_2, and CO are transported from midlatitudes into the Arctic and can reach central European concentrations on Spitsbergen in late winter. In lack of significant local sources, concentrations drop in summer when decomposition is faster than the efficiency of transport. These are typical examples for a species with a

Table 4.5: *This table gives the average total column amounts retrieved from the spectra recorded in March and for comparison the average values from Table 4.3 for the period May/June 1995 are also included. Typical 1σ uncertainties are given for the 21^{st} of March. Listed are the different species versus the day of recording. All spectra are solar absorption spectra except for the column entitled 'night' that holds lunar spectra.*

species	scale cm^{-2}	Mar 10	Mar 15	night 15/16	Mar 16	Mar 17	Mar 18	Mar 20	Mar 21	May/ June
C_2H_2	$E15$	12.7	9.66	8.56	11.0	9.87	9.10	10.5 ±0.27	8.95	1.61
C_2H_4	$E14$		5.7	4.0	5.6	2.2	1.7	4.3 ±1.4		3.60
C_2H_6	$E16$	4.47	3.85		4.11	3.71	3.67	4.14 ±0.08	3.42	2.25
CCl_2F_2	$E15$		7.83	7.81	7.78	7.43	7.57	7.55 ±0.16	7.71	8.83
CH_4	$E19$	3.54	3.51	3.45	3.54	3.50	3.53	3.53 ±0.09	3.50	3.70
$^{13}CH_4$	$E19$			3.53	3.64	3.53	3.46	3.57 ±0.03	3.46	3.64
CH_3D	$E19$			4.43	4.30	4.11	4.16	4.15 ±0.29	4.16	4.68
CHF_2Cl	$E15$		2.38	2.34	2.39	2.46	2.67	2.46 ±0.08		2.49
$ClONO_2$	$E15$		3.99	4.51	4.04	3.56	4.59	5.13 ±0.32		0.85
CO	$E18$				2.83	2.77	2.68	±0.2		2.05
CO_2	$E21$	7.56	7.56		7.63	7.42	7.54	7.61 ±0.11	7.43	7.63
COF_2	$E14$			5.3	5.6	5.5	6.1	5.5 ±1.1	6.4	4.22
H_2O	$E21$	16.3	14.7		10.5	7.04	5.25	5.86 ±0.07	8.95	22.73
$H_2{}^{17}O$	$E21$	11.4	13.3		7.97	5.57	4.07	4.88 ±0.42	7.32	25.31
$H_2{}^{18}O$ *)	$E21$			8.23	9.59	4.15	4.91	5.17 ±0.30	8.46	19.78
$H_2{}^{18}O$ **)	$E21$	16.5	14.8		10.1	7.35	5.37	5.88 ±0.08	9.01	23.26
HDO +)	$E21$			5.87	7.12	2.66	3.73	3.54 ±0.04	6.53	15.51
HDO ++)	$E21$	11.4	9.50		6.30	4.43	3.42	3.27 ±0.04	6.04	14.71
$H^{35}Cl$	$E15$	3.39	3.28		3.44	3.33	3.50	3.35 ±0.08	3.61	5.97
$H^{37}Cl$	$E15$	3.72	3.48		3.63	3.44	3.78	3.47 ±0.11	3.89	6.11
HCN	$E15$						3.73	3.69 ±0.13		5.78
HF	$E15$					2.34	2.40	2.46 ±0.04		1.67
HNO_3	$E16$		2.09	2.25	2.25	2.20	2.24	2.31 ±0.05		1.80
HO_2NO_2	$E14$		<2.0		4.1	4.0	4.3	5.0 ±0.5		4.66
N_2O	$E18$	6.13	6.18	6.01	6.17	6.10	6.09	6.22 ±0.05	6.03	6.37
NH_3	$E13$		15.0	8.5	16.4	<8.0	<8.0	11.0 ±2.4		<8.0
NO	$E15$				4.38			3.22 ±0.23		5.33
NO_2	$E15$	1.67	1.02		1.01	1.14	1.36	1.24 ±0.19	1.75	3.92
O_3	$E18$	8.20	7.27	6.56	7.46	7.87	8.14	7.63 ±0.13	7.69	9.31
OCS	$E15$				9.15	9.13	8.98	9.07 ±0.29		9.53
SF_6	$E13$		12.8	11.4	8.6	8.6	8.9	5.9 ±2.94		9.29

pronounced seasonal cycle. Compared to mid or tropic latitudes, the differences between minimum and maximum concentrations in the seasonal cycle are normally largest in the polar regions (*Notholt* et al., 1996a). This difference in tropospheric pollutants is also seen in Table 4.5 by comparing early spring and summer data.

Very little variation is seen in trace gases with major tropospheric sources and with a very long life time, like the CFCs. The changes in HF, which has also a long life time in the atmosphere but with its sources in the stratosphere, are caused by dynamical effects such as subsidence. The variability of NO in March reflects mainly diurnal cycles, concentrations are significantly higher in the morning hours. This variability ceases with the beginning of polar day and is thus not observed in the data from May and June. Remarkable is the huge amplitude in water vapor variability. Individual column amounts from 10^{21} to 10^{23} cm^{-2} are observed.

Significant changes are also seen in ozone. On the 20^{th} of March 1995 the so far record low ozone for Spitsbergen was observed by an ECC–sonde with 301 Dobson units. A depletion in total column by 25 % is seen in the ECC ozone sonde data with a 50 % reduction in parts of the lower stratosphere compared to spring data observed only three years earlier, as is illustrated in Figure 4.20. Low values are also seen by the FTIR spectrometer that are by about 25 % lower than in the summer spectra. The concentration of $ClONO_2$ peaks after the end of polar night. The removal of active chlorine into ClO and further reaction with NO_2 yields high amounts of $ClONO_2$, which then slowly returns to normal concentrations as chlorine is transferred back into the reservoir species HCl.

The species HO_2NO_2, NH_3 and SF_6 are very difficult to retrieve in the spectra, because they all interfere heavily with water vapor (see appendix C). Without an excellent knowledge of the water vapor VMR profile there is no point in retrieving their amounts, which is checked for each spectrum in HDO and H_2O lines free of interference. Particular care is taken in the retrieval of HO_2NO_2. These are the first total column amounts of HO_2NO_2 reported for the Arctic.

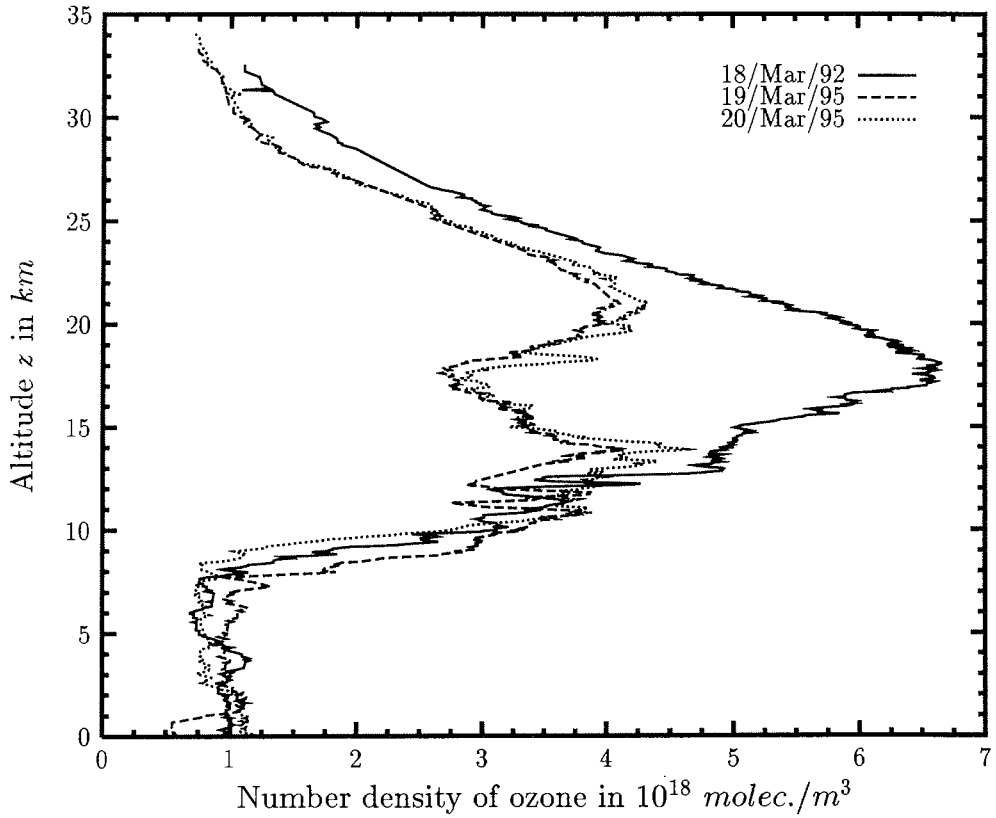

Fig. 4.20: *This figure compares the ozone molecule number density profiles observed by ECC ozone sondes in March 1995 to a profile recorded three years earlier in the same location. In the lower stratosphere a substantial depletion in ozone is seen in the 1995 data. The profiles yield total column amounts of 403 Dobson units* ($10.8 \cdot 10^{18}\, cm^{-2}$) *on the 18th of March 1992 and only 301 DU* ($8.09 \cdot 10^{18}\, cm^{-2}$) *on the 20th March, 1995.*

5 Information derivable from natural isotopic ratios

5.1 Isotopic fractionation and natural isotopic ratios

All types of atoms that only differ by the number of neutrons in their nucleus are called the *isotopes* of a certain element, which is determined by the number of protons in the nucleus. There are different isotopes known for all common elements in nature. Except for the primordial elements and their decay products and except for the production of radioactive atoms by cosmic radiation, all natural isotopes on earth are stable and not radioactive. The main concern of this chapter is the description of natural isotopic ratios in stable atmospheric molecules. However, it should be mentioned that radioactive components are also highly interesting and can serve as excellent tracers, but an FTIR spectrometer is simply not the best choice to investigate this matter. All elements have a most abundant isotopic species, which is termed the bulk species in this chapter, that typically makes up a fraction of more than 99 %. The other minor isotopes are often termed according to their mass, like heavy oxygen for oxygen isotopes with masses exceeding 16 atomic units. Analogously, molecules are termed heavy or light isotopomers, if they contain a rare isotope instead of the most abundant one. The chemical properties of the isotopes of one element are identical and only small deviations in reaction rates are known that are caused by the difference in atomic mass.

The isotopic compositions of elements are variable, because their isotopes are fractionated in the course of certain chemical and physical processes occurring in nature. The most important elements that show significant fractionation and which are common in biogeochemical cycles are Hydrogen (H), Carbon (C), Nitrogen (N), Oxygen (O), and Sulfur (S). Looking for the causes of isotopic fractionation, one finds theorems like *"The fractionation is due to slight variations in the physical and chemical properties of isotopes and is proportional to differences in their masses"*, which is quoted from the textbook of *Faur* (1986). However, it is shown that this theorem is incomplete and has to be rewritten. The strict ascribing of fractionation effects exclusively to mass differences has been a paradigma for theoretical physicists and the debate concerning heavy

ozone enrichment, lasting over the past 15 years, is only about to be resolved in these days. However, many relevant fractionation processes can be well treated on the basis of mass differences, as is outlined briefly in the first two sections of this chapter. To readers not familiar with isotopic fractionation processes relevant to the atmosphere, the excellent review article by *Kaye* (1987) and the more detailed textbook edited by the same author (1992) are recommended.

On the molecular scale the isotopic substitution effects the vibrational potential function $V_{vib}(r)$. For the example of a diatomic molecule, this can be illustrated by changes to the Morse oscillator (e.g. *Finkelnburg*, 1976)

$$V_{vib}(r) = D_0 \cdot (1 - exp\{-\alpha \cdot (r - r_0)\})^2, \tag{52}$$

where r is the distance between the two atoms, r_0 the distance at the potential minimum, α describes the steepness of the potential well, and D_0 the maximum depth of the potential.

There are a limited number of bound states to the Morse potential. The vibrational energies E_{vib} of these bound states are calculated to be (*Finkelnburg*, 1976)

$$E_{vib} = h \cdot c \cdot \omega_0 \cdot \left(n + \frac{1}{2}\right) - \frac{h^2 \cdot c^2}{4 \cdot D_0} \cdot \omega_0^2 \cdot \left(n + \frac{1}{2}\right)^2. \tag{53}$$

The Planck constant is denoted by h, the speed of light by c, the eigenfrequency by ω_0, and n is an integer. If one compares the eigenfrequencies ω_0 of an unsubstituted to a substituted molecule with the respective reduced masses of μ and μ^*, then the relative change in the eigenfrequencies is inversely proportional to the square root of the ratio of the reduced masses

$$\frac{\omega_0^*}{\omega_0} = \sqrt{\frac{\mu}{\mu^*}}. \tag{54}$$

This means that the anharmonic term in equation 53 changes more upon isotopic substitution than the harmonic one does. One consequence is that the heavier of two isotopomers typically supports more bound states (*Kaye*, 1987). Another important aspect is seen when looking at the zero point energy, which is given by equation 53 for $n = 0$. In the harmonic approximation, i.e. by neglecting the smaller right hand term in equation

53 for $n = 0$, the zero point energy is seen to be inversely proportional to the square root of the reduced mass μ (compare equation 54). That means that a higher mass leads to a lower zero point energy.

The differences in the vibrational frequencies among different isotopomers are the key to distinguish between them in spectroscopic measurements. The presence of a heavy isotope in a molecule shifts the eigenfrequencies of that molecule towards lower wavenumbers compared to the normal molecule. Even heavy isotopomers of same mass, but with the heavy isotope found at different positions within the molecule, can be distinguished directly, like e.g. $^{16}O^{18}O^{16}O$ and $^{18}O^{16}O^{16}O$ that are both heavy ozone of mass 50.

The general expectance that isotopes are more or less uniformly distributed over all molecules and phases implies that it is energetically not favourable for a rare isotope to occur primarily in any particular phase or molecule. But the zero point energy is strictly mass dependent, as has just been shown. Thus, one may expect for thermodynamical equilibrium, that a distribution over phases and molecules is observed that maximizes the incorporation of a heavy isotope into the lowest energy state available. At low temperatures the zero point energy constitutes the major part of the total energy available to a molecule and thus this aspect is relevant to stratospheric observations (*Kaye*, 1987). In other words, one can say that bonds formed by the heavier isotopomer are stronger and therefore less easily broken. This makes the heavier isotopomer slightly less reactive and influences the equilibrium constants of the chemical composition and decomposition reactions.

The rotational energy levels of a diatomic molecule can be described in the approximation of the harmonic oscillator to illustrate the effects of isotopic substitution (*Kaye*, 1987). The rotational potential function $V_{rot}(r)$ is then given by

$$V_{rot}(r) = \frac{1}{2} \cdot k \cdot (r - r_0)^2, \tag{55}$$

where k denotes the force constant of the chemical bond. In first approximation the rotational energy levels are given by (*Kaye*, 1987)

$$E_{rot} = B_n \cdot j(j+1) - D_n \cdot \{j(j+1)\}^2 \quad \text{with} \tag{56}$$

$$B_n = \frac{h}{8 \cdot \pi^2 \cdot c \cdot \mu \cdot r_0^2} - \alpha_0(n + \frac{1}{2})$$
$$D_n = D_0 + \beta_0(n + \frac{1}{2}).$$

The constants α_0, β_0, and D_0 depend on the form of the potential energy curves, but generally the first term in B_n, which is inversely proportional to the reduced mass μ, is dominant (*Kaye*, 1987). So again a dependence on mass for the energy levels is found.

The mathematical description of polyatomic molecules is more complicated and increases with the number of normal modes, which are not all effected in the same way. However, the mass dependence is maintained, but the scale of the effect becomes unevenly distributed over different bands. It has to be pointed out here that practically all known isotopic fractionation processes based on differences in molecular mass have effects only in the permil scale. The important exception to this rule is hydrogen, which is discussed below. Except for water, the symmetry selective fractionation process discussed in the succeeding section is about two orders of magnitude stronger than all the mass dependent fractionation processes occurring in the atmosphere.

The isotopic effects in the rotational and in particular in the vibrational energy levels play also an important role in phase transitions, which make evaporation, condensation, melting, freezing, and sublimation to common natural fractionation processes. The largest effects in phase transitions are due to the vapor pressure isotope effect (*Kaye*, 1987) as discussed in detail in *Jancso* and *van Hook* (1974). The calculations are complex and show a substantial variation in magnitude and sign of the isotopic fractionation. The general strong dependence of the vapor pressure effect on the vibrational frequencies lead to a much larger vapor pressure isotopic effect in light atoms than in heavy atoms (*Kaye*, 1987). In particular is the effect much larger in the D/H than in the $^{18}O/^{16}O$ fractionation in atmospheric water. As a general rule does the heavier of two isotopomers have the lower vapor pressure, but exceptions are known (*Kaye*, 1987). The efficiency of fractionation is described by the fractionation factor α, which can be a complicated function of temperature and pressure for any element or molecule. A detailed mathematical description for most

species relevant to the atmosphere is given in *Richet* et al. (1977).

The direct effect of gravitation on the VMR profile of different molecules is not significant in the homosphere, in particular below the stratopause. Heavier molecules become progressively less abundant compared to molecules of lower mass with altitude in low pressure regimes, where the average distance travelled by a molecule between two collisions exceeds the *cm* scale. However, the total number of molecules above the stratopause is negligible in the signal formation of absorption lines observable from ground. Thus, the differences directly introduced by gravitation into the VMR profiles of different isotopomers with different molecular mass is of no concern in the data presented in this work.

5.2 Measuring isotopic ratios in FTIR spectra

The information derivable from isotopic ratios measured in the atmosphere is manifold and depends on the isotopes and biogeochemical cycles involved. The isotopic ratios are discussed for four molecule families measured. Main emphasis is put on ozone, which is discussed in detail in the next section and essential parts are published in *Meier* and *Notholt* (1996a), while a brief discussion is given below for water vapor, methane, (*Meier* and *Notholt*, 1995) and hydrogen chloride.

The observed isotopic abundances are reported in the so called δ–notation, usually in permil or sometimes in percent enrichment, relative to some standard agreed upon. For the example of an observed deuterium abundance, the δD value is defined by:

$$\delta D = \left\{ \frac{(D/H)_{obs}}{(D/H)_{ref}} - 1 \right\} * 1000\,. \tag{57}$$

The reference abundances used in this work are listed in Table 5.1. They agree with *de Bièvre* et al. (1984) and with the ratios assumed in the HITRAN96 spectroscopic data base.

5.2.1 Water vapor

In water vapor heavy isotopes are common both in hydrogen and in oxygen. The four most abundant species are $H_2\ ^{16}O$, $H_2\ ^{18}O$, $H_2\ ^{17}O$, and $HD\ ^{16}O$. Their abundances are normally compared to the reference composition of standard mean ocean water (SMOW) as listed in Table 5.1. Isotopic fractionation occurs both in physical phase transitions and in chemical formation and decomposition reactions. The physical phase transitions are of minor importance to most atmospheric molecules, since they hardly ever leave the gas phase. The most important exception to this rule is water, which frequently undergoes evaporation, condensation, melting, freezing and sublimation processes, in particular in the troposphere. In the stratosphere the influence from methane decomposition becomes important while the phase transitions diminish (*Kaye*, 1987, *Rinsland* et al., 1984). However, the signal seen by the ground–based FTIR spectrometer represents tropospheric conditions only and the following discussion focusses on tropospheric conditions. An isotopic fractionation by phase transitions might also be significant in HNO_3 in polar regions in the course of PSC formation, but no studies are known so far.

The isotopic signals in tropospheric water are the product of the pressure and temperature history of the air mass probed (*Dansgaard* 1953 and 1964, *Kaye* 1987). This is a consequence of the temperature dependence of the isotopic fractionation factor. Changes in temperature and pressure cause a net flux of water vapor from the gas phase into other phases and the isotopic composition will change towards the new equilibrium composition assigned to the new conditions. Changes in temperature can be significant for the air masses probed and equilibrium states cannot be assumed. Thus, the isotopic composition is expected to be the product of the temperature history and not simply of the temperature at sample time.

The VMR profile of water vapor used in the retrieval of FTIR spectra is calculated from the relative humidity data of the radio sonde, as discussed in chapter 3. The sensor cannot differentiate between different isotopomers, but it will essentially represent the VMR profile of $H_2\ ^{16}O$, which

is by far the most abundant species (Table 5.1). The heavy isotopomers, in particular HDO, are strongly depleted in the troposphere compared to SMOW (see below). This depletion is known to show a steep temperature sensitive gradient in the troposphere, leading to increasing depletion with altitude (*Eriksson*, 1965). One consequence is that a systematic error is introduced into the analysis of FTIR spectra, if the same relative vertical distribution is assumed in all water vapor species. A wrong VMR profile in the retrieval of total column amounts yields a systematic error that varies with the zenith angle (e.g. *Rao* and *Weber*, 1992). This systematic error can be observed in retrieved data, when plotting the total columns of HDO versus the zenith angle (not illustrated).

In a heuristic approach to reduce this systematic bias, the VMR profiles of the heavy water isotopomers are corrected under the assumption of an average depletion profile, which is illustrated in Figure 5.1. The δ–profiles shown are estimated from profiles measured originally by *Ehhalt* in Nebraska, as reprinted in *Kaye* (1987). With the introduction of this simple correction, no significant systematic variation of retrieved HDO columns with the zenith angle are observed anymore and the differences in the scaling factors applied to the VMR profile of HDO compared to

Table 5.1: *These are the reference isotopic abundances used in the presentation of measured isotopic abundances in the δ–notation. Figures are taken from the HITRAN96 compilation (L. S. Rothman, private communication 1996) and agree with de Bièvre et al. (1984).*

species	reference isotopic abundance	species	reference isotopic abundance
$H_2{}^{16}O$	0.997317	$^{16}O^{16}O^{16}O$	0.992901
$H_2{}^{18}O$	0.00199983	$^{16}O^{16}O^{18}O$	0.00398194
$H_2{}^{17}O$	0.000372	$^{16}O^{18}O^{16}O$	0.00199097
$HD{}^{16}O$	0.00031069	$^{16}O^{16}O^{17}O$	0.000740
$^{12}CH_4$	0.98827	$^{16}O^{17}O^{16}O$	0.000370
$^{13}CH_4$	0.01110	$H{}^{35}Cl$	0.757587
$^{12}CH_3D$	0.00061575	$H{}^{37}Cl$	0.242257

H_2O in the retrieval is much smaller than the total δD depletion observed throughout the year. Thus, this correction appears legitime.

The isotopic composition is measured both in lunar and solar FTIR spectra in the microwindows listed in Table C.1, page 190. The total columns retrieved are listed in Tables 4.3 (page 101) and 4.5 (page 120) for the spring and summer data discussed before, respectively. The species $H_2\ ^{16}O$, $H_2\ ^{18}O$, and $HD\ ^{16}O$ are analysed on a routine basis, while data for $H_2\ ^{17}O$ is presented for the first time. Both $H_2\ ^{17}O$ lines studied interfere with other water vapor species that have significantly stronger absorptions in the microwindows studied and care has to be taken in the analysis.

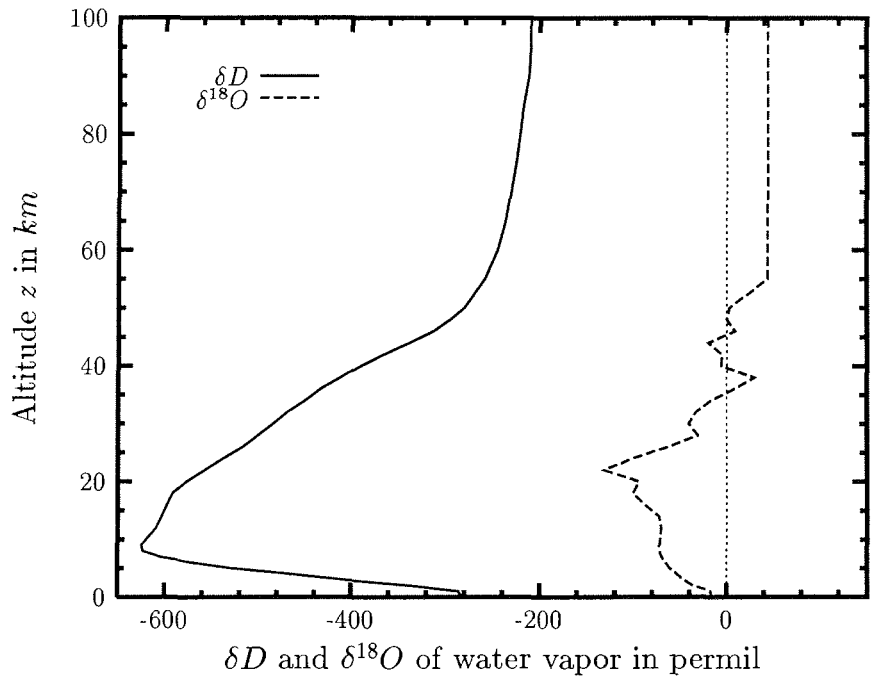

Fig. 5.1: *The δ–profile for Deuterium and ^{18}O enrichment in water vapor is shown, which is used to calculate the VMR profiles of heavy water vapor from the humidity data of the radio sondes. The δ–values are given relative to the reference abundances listed in Table 5.1.*

The different sets of $H_2\ ^{18}O$ and HDO data, as indicated by footnotes in Tables 4.3 and 4.5, are retrieved in different spectral regions, i.e. different spectra. Since the variation in water vapor is typically large, isotopic ratios are exclusively calculated for data from within the same spectrum. Above 2500 cm^{-1} the spectra contain suitable absorption lines of all species studied, while below 1400 cm^{-1} no adequate line of $H_2\ ^{16}O$ is known so far. The different spectra happened to see largely different air masses and reporting average values for the rare isotopomers only in the tables would substantially mislead the reader when estimating the isotopic ratios from this data. (The HDO and $H_2\ ^{18}O$ total columns marked with one asterisk are from the lower wavenumber spectra.)

In Figure 5.2 the seasonal cycle for the isotopic abundance of HDO in water vapor is illustrated. The data is retrieved from spectra of three

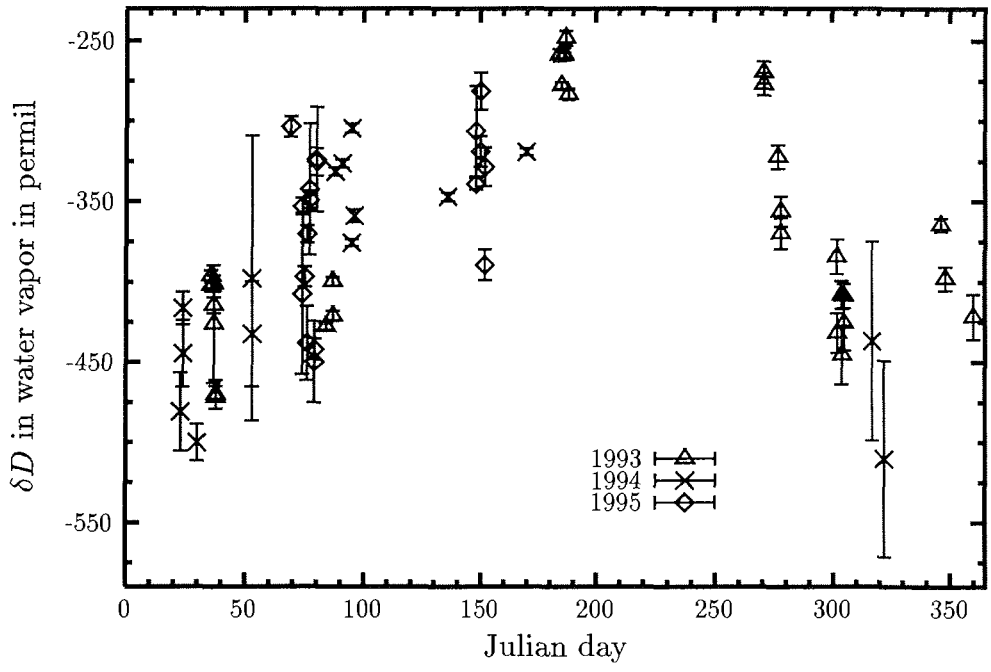

Fig. 5.2: *This figure illustrates the seasonal cycle of δHDO in water vapor over arctic Spitsbergen. Deuterium is considerably underrepresented in particular in cold periods.*

different years, but no significant interannual variation is seen. However, the seasonal signal is significant and substantially more pronounced than at mid–latitudes. Due to the atlantic gulf stream, warm and humid tropospheric air can penetrate into the high arctic in summer, while in winter very cold polar air masses can be observed, which leads to the

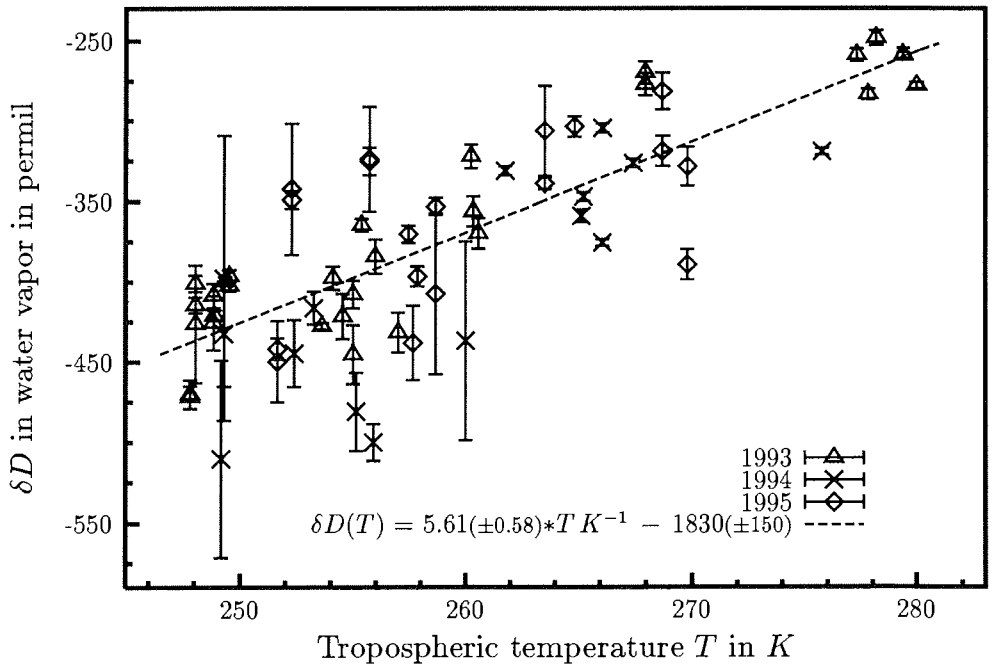

Fig. 5.3: *This graph shows the correlation of the δD values in water vapor with the mean temperature of the lower troposphere (0 - 4 km altitude) deduced from daily radio sondes. Although the complete pT history of the air masses probed is not known, it is demonstrated that the data from the past 3 years is highly correlated with the actual temperature of the air mass probed. In a linear approximation the dependence on temperature is fitted to a function as given in the key. The linear correlation coefficient is $r = 0.77$. Due to temporal variability, the temperature data are uncertain by typically 2 to 3 K, which adds a horizontal error bar, but which is omitted in the figure to maintain an acceptable readability.*

high seasonal amplitude. The weather in Ny–Ålesund is known to change completely and frequently within a few hours, which is often accompanied by a reversal in wind direction. This is reflected by the considerable variation in Figure 5.2. For a more detailed discussion a correlation with basic meteorological data like wind fields is planned for the future.

To illustrate the temperature dependence of isotopic fractionation, which is particularly pronounced in atmospheric water, the same data is plotted over tropospheric temperature in Figure 5.3. The tropospheric temperature is taken from the daily radio sonde launched at noon and represents the average temperature from ground to 4 km altitude. A clear correlation of the isotopic abundance of Deuterium is seen with temperature. HDO is more depleted in cold air masses, as can be expected from the lower vapor pressure of the heavier species. The considerable variation seen is assigned to two facts. First, the radio sonde typically probes a different air mass than the FTS, which adds a horizontal error bar of typically 2 or 3 K. Second, the isotopic composition of the air mass sampled is the product of the temperature history and not simply of the actual temperature. The transport and change in pressure and temperature are faster than the time needed to reach thermodynamic equilibrium on the isotopic scale.

The isotopic ratio of Deuterium and Hydrogen in water vapor can be measured with high precision in FTIR spectra and the analysis is without significant complications. The broad and strong absorptions can also be well determined in lunar spectra during full moon phases. The error bars shown can still be significantly reduced by using more spectral features (in the data of 1993 and 1994 only one absorption line is analysed so far). Even if the absolute calibration of the spectroscopic data base in isotopic terms still shows some systematic uncertainties, the relative change in the isotopic signal observed can serve as an excellent tracer to characterize the history and origin of tropospheric air masses. Polar air masses are significantly more depleted in Deuterium than air masses from the comparatively warm atlantic ocean. Another application in future is the correlation with isotopic data from precipitation analysis. A better understanding of isotopic signals in precipitation will improve the quality of the temperature reconstruction in palaeoclimatology e.g. from ice core

drilling projects. Understanding the past improves also the chances to predict the future of the global climate.

5.2.2 Carbon and deuterium in methane

Carbon

The abundance of ^{14}C is too low for a quantification, but the abundances of ^{13}C and ^{12}C can be well detected with the FTS. The isotopic abundances of ^{13}C in atmospheric methane are known to be depleted by about -47 *permil* (e.g. *Lowe* et al., 1994) with respect to abundances in typical geologic samples. From Carbon it is well known that living organisms preferably take up the bulk species ^{12}C and have a lower ratio of $^{13}C/^{12}C$ in their bodies than ambient non–biogenic material. For example, in the metabolism of methane producing bacteria (methanogens), the enzymatic reactions select for lighter isotopes. Thus biologically produced CH_4 tends to have less ^{13}C, i.e. a lower $\delta^{13}C$. The biomass from which CH_4 is produced by methanogens is already depleted in ^{13}C compared to geological CO_2 ($\delta^{13}C \approx$ 10 to 35 *permil*) and the produced CH_4 is therefore depleted in ^{13}C by 45 to 80 *permil* in total (*Boone* in Khalil, 1993). Biomass burning and Coal mining release methane that is less depleted in heavy carbon with mean values of -22 and -37 for $\delta^{13}C$, respectively. These are increasing the atmospheric mean value of $\approx$ -47 *permil* (*Stevens* in *Khalil* 1993).

The isotopic compositions of the different types of emission are well known from small scale case studies. However, from these spot measurements the importance of specific groups of sources can not be calculated for global scales, but the measurement of isotopic ratios in different regions of the earth can add important information to that question (*Khalil* 1993, *Khalil* and *Rasmussen* 1990, *Lassey* et al. 1993, *Lowe* et al. 1994, *Lacroix* 1993).

Most recently new interest has arisen to the reaction of methane with free Chlorine radicals in the lower stratosphere in the course of ozone destruction chemistry (*Brenninkmeijer* et al., 1996, and references therein). The reaction of $Cl + CH_4$ is found to show a large fractionation (*Sauer-*

essig et al., 1995). However, *'large'* in the context of chemical equilibrium constants means that changes in the $\delta^{13}C$ values of stratospheric methane in the order of one *permil* are observed (*Brenninkmeijer* et al., 1996).

This leads one directly to the principle difficulties of measuring significant changes in the isotopic abundances of methane isotopomers by means of FTIR spectroscopy. Atmospheric methane is known to show a $\delta^{13}C$ of typically -47 *permil* (*Lowe* et al., 1994). The maximum variation observed by *Lowe* et al. (1994) does not exceed 1 *permil* over a period of more than 4 years. At present, no chance is seen to achieve an accuracy of one *permil* or better in the determination of isotopic ratios derived from FTIR solar absorption spectra. The uncertainties introduced by the spectroscopic data base on the absolute absorption strength of individual lines and their dependence on temperature are already too large on their own to achieve the accuracy needed. Additionally, the pT profile used in the analysis introduces further uncertainties, to recall only some of the uncertainties discussed in section 3.1.

However, individual sources of methane are known to vary considerably stronger with $\delta^{13}C$ values between -80 *permil* for mud gases and tundra emissions over -37 *permil* as mean value for coal mining up to -12 *permil* in biomass burning (*Stevens* in *Khalil*, 1992). Thus, large amplitudes due to local effects are possible and the isotopic abundances retrieved are listed in Table 5.2.

Unfortunately, the uncertainties are still too high at present to deduce any reliable information. But it is pointed out that both $\delta^{13}C$ and δD show clear seasonal differences that hint on a significant change in the sources of the methane probed. Note also that the seasonal trends have opposite sign. However, it is also evident that the absolute values given are highly unrealistic. Systematic uncertainties, in particular in the spectroscopic parameters, are assumed to be the major cause, and it cannot be excluded that small uncertainties in the temperature parameters can produce seasonal amplitudes of several 10 *permil* or more. The identification of a higher number of suitable spectral intervals for the retrieval is expected to improve the situation.

If the trend seen in ^{13}C is at least in principle correct and an offset of

about 50 *permil* is assumed, then the differences in the isotopic abundances can be well understood. The production of methane more depleted in ^{13}C is assigned to decomposition by methanogens in the wet tundra, which is only possible in the short summer period. The observation building is located in low lying tundra and local emissions can be significant. In winter and spring, these sources are missing and a background signal is seen. Ny–Ålesund is a former coal mining town (appendix A) and coal mining is still performed in several places on Spitsbergen. Thus, the occasional occurrence of air masses enriched in emissions from coal mining that are significantly less depleted in ^{13}C is possible.

Deuterium

The absolute values of δD as given in Table 5.2 appear even more unrealistic than the $\delta^{13}C$ values listed. But the difference between spring and summer data is significant for the average values and for some individual days (e.g. 17/Mar/95 compared to 30/May/95). Deuterium in methane is more enriched in the summer spectra than in the spring data.

Table 5.2: *The retrieved isotopic abundances of heavy methane are listed. The differences among individual days are not significant in most cases for the statistical uncertainties given. However, clear trends can be seen that are to be investigated in future studies. The data in the first line is derived from lunar spectra.*

date	$\delta^{13}C$ in CH_4 in *permil*	δD in CH_4 in *permil*
15/Mar/95	21.73 ±81.89	282.82 ±198.32
16/Mar/95	14.83 ±33.30	199.72 ±80.86
17/Mar/95	6.56 ±29.02	170.18 ±66.12
18/Mar/95		141.09 ±86.27
20/Mar/95	-0.84 ±34.06	162.79 ±75.70
21/Mar/95	-7.73 ±25.49	192.21 ±59.73
28/May/95	-2.19 ±36.27	278.11 ±90.49
30/May/95	-5.47 ±19.28	291.30 ±46.87
01/Jun/95	-14.33 ±17.95	262.23 ±45.06

Kaye (1987) reports δD values for methane ranging from -478 to -42 permil, with natural gases typically between -275 and -130 permil. The large offset to data reported here is ascribed to isotopic uncertainties in the HITRAN data base used. However, positive δD values cannot be excluded in principle, as is shown by *Coleman* et al. (1981). He found that methane oxidizing bacteria substantially enhance the δD value in the methane produced. This gives the same possible explanation for the seasonal difference in δD as outlined for $\delta^{13}C$. Local signals from methane producing bacteria in the tundra yield a decrease in $\delta^{13}C$ and an increase in δD.

5.2.3 Chlorine in HCl

Chlorine has got two common isotopes and several isotopes with small abundances. About three quarters are ^{35}Cl and almost one quarter is ^{37}Cl (Table 5.1). The observation of the isotopic ratios in HCl and other chlorine containing species gives additional insight into the kinetics of chlorine chemistry relevant to stratospheric ozone. There are isotopically pure absorption lines known for HCl (appendix C) that are suitable for the study of isotopic ratios. The isotopic ratios retrieved are listed in Table 5.3

Unfortunately, the accuracy of the spectroscopic data is not very high, in particular in the microwindow used for $H^{37}Cl$. Thus, the systematic uncertainties of the isotopic ratios retrieved is large and the seasonal difference observed is not significant taking these into account. Nevertheless, it is shown that FTIR observations yield isotopic information on chlorine and it is expected that improvements in the spectroscopic data will reduce the systematic uncertainties significantly. Isotopic information on chlorine gives additional insight into chlorine chemistry, in particular on the large isotopic effect observed in the reaction of chlorine with methane in the stratosphere (*Saueressig* et al., 1995, *Brenninkmeijer* et al., 1996).

The accuracy of isotopic FTIR data can be improved significantly, if either collected air masses are measured in a multi–path gas cell under constant conditions of pressure and temperature, because this excludes the uncertainties introduced by the temperature dependences of the line

Table 5.3: *The retrieved isotopic abundances of chlorine in HCl are listed. The differences among individual days are not significant for the statistical uncertainties given. However, a seasonal difference is seen between spring and summer data, which is to be investigated in more detail in future studies.*

date	$\delta^{37}Cl$ in HCl in *permil*
10/Mar/95	96.1 ± 110.5
15/Mar/95	60.6 ± 61.3
16/Mar/95	56.4 ± 93.6
17/Mar/95	35.2 ± 80.8
18/Mar/95	80.3 ± 77.4
20/Mar/95	43.8 ± 100.2
21/Mar/95	78.2 ± 75.6
mean March	64.3 ± 22.1
28/May/95	22.0 ± 19.1
30/May/95	31.6 ± 36.0
01/Jun/95	15.7 ± 15.1
mean May/June	19.8 ± 12.1

parameters, or by putting up an artificial IR–source at some hundred meters distance to record local spectra, whereas uncertainties in the optical path and in the pressure and temperature dependences of line parameters are also reduced substantially.

5.3 The particular case of heavy ozone

Since the first isotopic *in situ* measurements of O_3 had been reported by *Mauersberger* (1981) with enrichments of up to 40 % in $^{50}O_3$, there has been a long and sometimes controversial discussion about this strong isotopic enhancement in heavy ozone (e.g. *Blake et al.* 1984, *Rinsland et al.* 1985, *Kaye* 1986, *Mauersberger* 1987, *Goldman et al.* 1989, *Morton et al.* 1990). While observational data confirmed the high excess of $^{50}O_3$, the theoretical understanding of the mechanisms involved is still far from

satisfying. A slight depletion of stratospheric heavy ozone was predicted by *Kaye* (1986). However, more recent studies expect a slight enhancement based on laboratory investigations (*Thiemens* and *Jackson* 1990, *Morton et al.* 1990, *Kaye* 1992, *Mauersberger* 1993) and have shown excellent agreement with tropospheric conditions (*Krankowski et al.*, 1995). The FTIR data presented in this section add further evidence to a symmetry selective enrichment in atmospheric ozone and differences during polar day and polar night add completely new aspects to the discussion. Essential parts are published in *Meier* and *Notholt* (1996a).

5.3.1 Data retrieval

Total column amounts of atmospheric species are retrieved from FTIR–spectra, recorded with a ground–based BRUKER 120M commercial spectrometer at Ny–Ålesund, Spitsbergen. Solar spectra are recorded up to the maximum resolution of 0.0035 cm^{-1}, while lunar spectra are obtained at a resolution of 0.02 cm^{-1} to maintain an acceptable signal to noise ratio (S/N). A clear advantage of this optical instrument over a mass spectrometer based technique is the ability to distinguish between $^{16}O^{16}O^{18}O$ and $^{16}O^{18}O^{16}O$, which are of same mass and make up more than 99 % of $^{50}O_3$.

The absorption features used are listed in Table 5.4 and a plotted example is given in Figure 5.4. While most of the $^{16}O^{18}O^{16}O$ lines given were already suggested by *Rinsland et al.*, (1985), who reported the first isotopic ratios of heavy ozone derived by ground–based FTIR–observation, only the absorption features near 1044 cm^{-1} had been proposed for $^{16}O^{16}O^{18}O$. To improve statistics the unresolved ν_1 band Q branch near 1090 cm^{-1} is included, which holds about 200 absorption lines of $^{16}O^{16}O^{18}O$ and also the absorption lines near 1025 and 1002 cm^{-1}, which suffer from a slight interference of $^{16}O^{16}O^{18}O$ with $^{16}O^{18}O^{16}O$, but allow measurement of the sum of both heavy lines and at least one of the heavy species independently.

The data analysis is performed with SFIT V1.09d. The difficulties arising from the ignoration of the pressure shift are negligible in all spectral microwindows used, because no significant absorption lines of methane occur in any of the spectral regions analysed for the heavy ozone study.

Table 5.4: *This table lists the absorption features used for the retrieval of the total column amounts of the ozone isotopomers. Given are the line position, the intensity at 296 K, and the lower state energy* E''_{LSt}.

$^{16}O^{18}O^{16}O$			$^{16}O^{16}O^{18}O$		
line position in cm^{-1}	intensity in 10^{22} $cm/molec.$	energy E''_{LSt} in cm^{-1}	line position in cm^{-1}	intensity in 10^{22} $cm/molec.$	energy E''_{LSt} in cm^{-1}
976.388	0.19	518.74	1002.606	0.40	328.42
976.711	0.11	595.54	1025.745	0.11	172.48
977.925	0.31	421.41	1043.440	0.60	230.37
979.480	0.38	374.92	1044.013	0.46	288.06
980.732	0.36	369.64	1044.217	0.52	266.41
989.118	0.51	221.97	1090.372*	0.02	57.35
993.791	0.46	172.17			

$^{16}O_3$			$^{16}O_3$		
line position in cm^{-1}	intensity in 10^{22} $cm/molec.$	energy E''_{LSt} in cm^{-1}	line position in cm^{-1}	intensity in 10^{22} $cm/molec.$	energy E''_{LSt} in cm^{-1}
976.552	0.85	1500.56	988.945	1.64	1373.45
976.653	0.75	1524.90	989.250	4.89	1170.40
977.660	3.10	1356.99	993.712	17.30	948.24
977.857	1.94	1447.80	1090.766	1.61	113.09
979.302	1.11	1518.95	1146.472	3.95	372.41
980.113	2.91	1363.31	1146.669	4.28	301.67
980.646	1.17	1600.52			

*) That $^{16}O^{16}O^{18}O$ line is only given as an example for the unresolved ν_1 band Q branch.

However, a case study is performed on a set of microwindows and no differences are obtained in the results. Thus, in the retrieval of ozone presented in this section it does not matter, whether the previous version 1.09d or the latest version 1.09e of SFIT is used.

The spectroscopic data base used is the previously described ATMOS AFGL (*Brown* et al., 1987) spectroscopic data base, revision level 17 (*C. Rinsland* 1995, priv. comm.), which widely agrees with the HITRAN92 data base (*Rothman et al.*, 1992). The pT profiles from ground to about 30 km altitude are taken from daily radio sondes launched at the observation site, while ozone VMR profiles are taken from ECC-sondes launched

at the same location within ±12 h for half of the spectra and within ±2 day for all spectra analysed. Tropospheric water VMRs are calculated from the relative humidity data of the radio sondes, as already described in previous sections.

To minimize systematic errors, isotopic abundances are calculated only from different absorption lines within the *same* spectrum recorded. Furthermore, only those spectra are analysed, for which it is likely that air

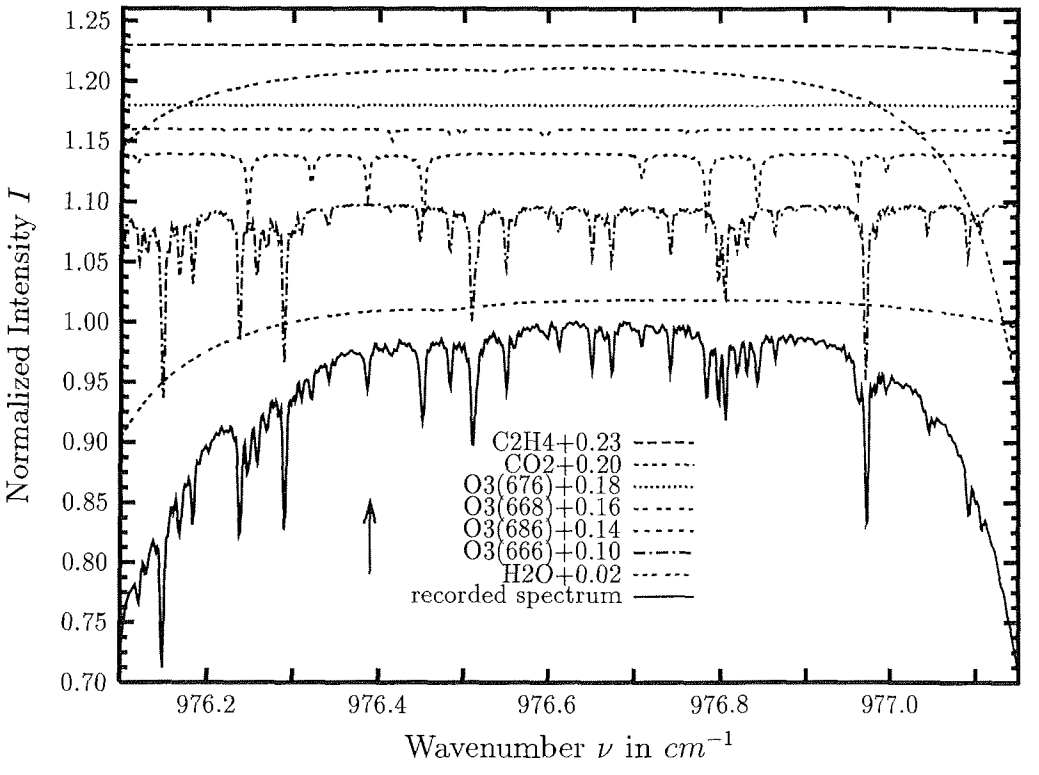

Fig. 5.4: *Example of results from a search for suitable primary lines producing the heavy ozone absorption features analysed. The recorded intensity of the spectrum is shown in the lowest curve over wavenumber. The contributions of all absorbing species in this selected interval are plotted individually and are shifted for clarity. At 976.39 cm^{-1} a well isolated line of $^{16}O^{18}O^{16}O$ can be identified (see arrow).*

masses probed by the sondes are representative for light paths at the spectroscopic recording time.

The ECC-sonde VMR-profile essentially represents the $^{16}O_3$, because it cannot differentiate between isotopes, but approximately 99.3 % of the probed O_3 is of mass 48 (see Table 5.1). This VMR–profile for $^{16}O_3$ should not be used for heavy ozone without corrections, because it is known from mid–latitude *in situ* experiments that $^{50}O_3$ enhancement can show a strong variation with altitude (*Mauersberger*, 1981 and 1987). Thus, a correction for the heavy ozone VMR is needed to minimize known systematic uncertainties, like in the discussion of water vapor profiles for heavy water isotopomers in the previous section.

The inversion of line shape or the variation of total column with zenith angle in high arctic spectra is unfortunately too weak to derive heavy

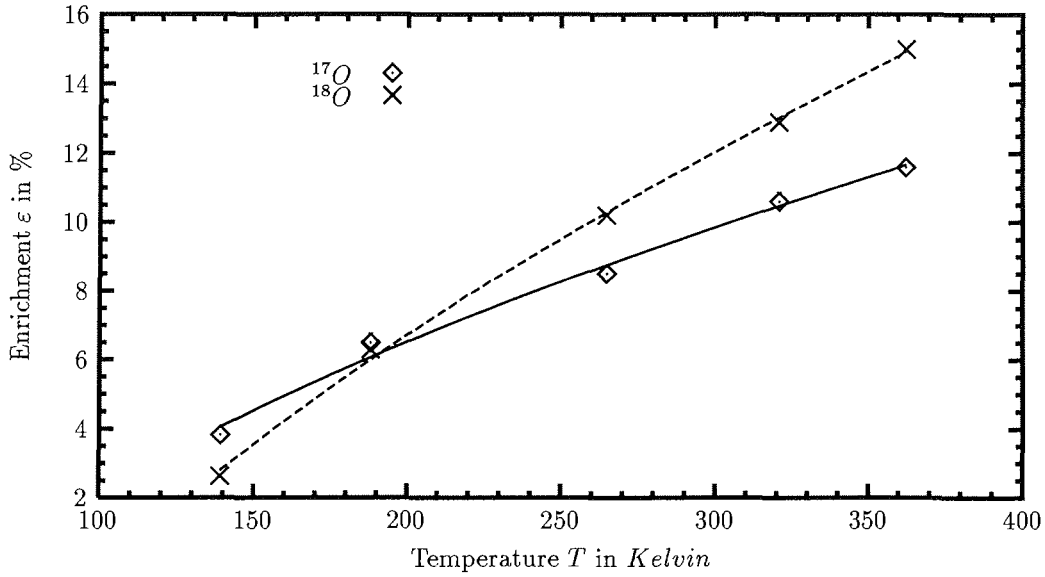

Fig. 5.5: *This figure illustrates the temperature dependence of heavy ozone enrichment at a pressure of 66.7 hPa as determined in laboratory studies. The data is quoted from Morton et al. (1990) and is fitted to mathematical functions as indicated by the curves.*

ozone VMR-profiles from the FTIR-spectra themselves with the high accuracy needed. Therefore, the calculation of a correction to the known $^{16}O_3$ profiles is suggested as outlined below, to derive the heavy ozone VMR–profiles.

It is known from recent laboratory experiments that the enhancement in heavy ozone shows a characteristic dependence from pressure and temperature (*Morton* et al. 1990, *Thiemens* and *Jackson* 1990, *Mauersberger* et al. 1993, *Mauerberger* priv. comm. 1995). All available data from these laboratory studies are fitted to an empiric function for heavy ozone enhancement depending on pressure and temperature. The fitted data are shown in Figures 5.5 and 5.6 and the coefficients for the fitted functions are listed in Table 5.5.

The laboratory data shown in Figures 5.5 and 5.6 give averages for the mass 50 and mass 49 heavy isotopes. In first approximation, the heavy isotope takes any of the 3 possible positions within the ozone molecule by equal chance, so that roughly one third of the heavy isotopes is expected to form symmetric ozone, i.e. $^{16}O^{18}O^{16}O$ and $^{16}O^{17}O^{16}O$, and the other two third are found in the asymmetric forms, i.e. $^{16}O^{16}O^{18}O$ and $^{16}O^{16}O^{17}O$. With this assumption, which is also made by the research groups that measured the spectroscopic data of heavy ozone for the spectroscopic data base HITRAN92 (*Flaud et al.* 1986, *Camy-Peyret et al.* 1986), the enrichment ε for ozone of mass 50 is calculated from pressure p and temperature T for each layer by the equation (60).

$$f(T) = a_0 \cdot \sqrt{a_1 \cdot T}, \quad \text{for } T \in [130\,K, 270\,K] \tag{58}$$

$$g(p) = b_{const}, \quad \text{for } p < 20\,hPa\,(^{49}O_3) \text{ and } p < 40\,hPa\,(^{50}O_3)$$

$$g(p) = b_0 + b_1 \cdot ln\left(\frac{p}{hPa}\right) + b_2 \cdot ln^2\left(\frac{p}{hPa}\right) + b_3 \cdot ln^3\left(\frac{p}{hPa}\right) + b_4 \cdot ln^4\left(\frac{p}{hPa}\right)$$

$$\text{for } p \in [20\,hPa, 90000\,hPa] \tag{59}$$

$$\varepsilon(\mathrm{T,p}) = f(T) + g(p) - g(66.661\,hPa)\ ^{9} \tag{60}$$

The results are in percent enrichment relative to the natural isotopic ratios in molecular oxygen and the coefficients are listed in Table 5.5.

[9] if no enhancement in the symmetric isotopomers is assumed, as is discussed later in this chapter, than this equation derived for mass 50 and mass 49 mixtures of heavy ozone has to be multiplied with a factor of 3/2 for the asymmetric isotopomers and with zero for the symmetric species. This is done in case 3 of the case study discussed below (Table 5.7).

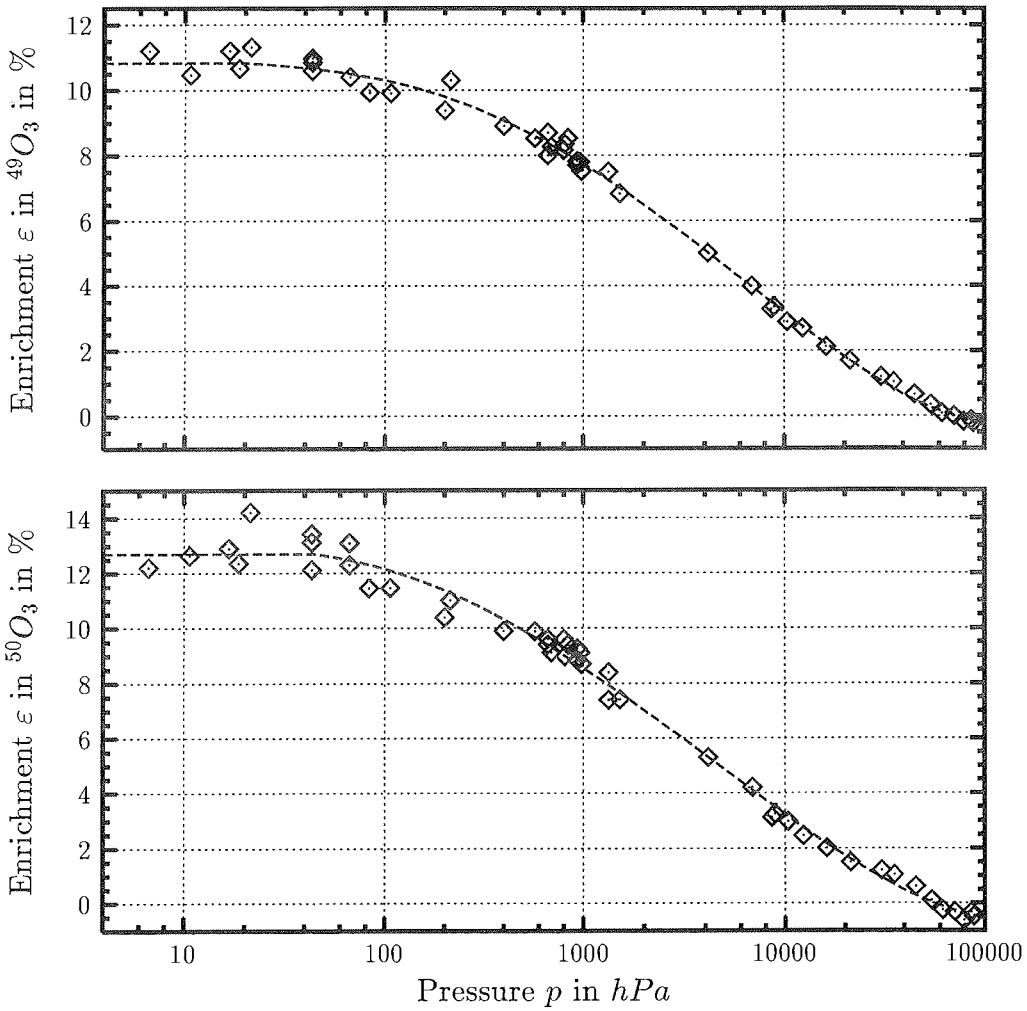

Fig. 5.6: *The pressure dependence of heavy ozone enrichment at a temperature of 321 K is shown as determined in laboratory studies by mass spectrometric means for $^{49}O_3$ (top) and $^{50}O_3$ (bottom). The data is quoted from Morton et al. (1990), Thiemens and Jackson (1990), and Mauersberger et al. (1993) and is fitted to mathematical functions as indicated by the curves.*

Table 5.5: *The coefficients retrieved for equation (58) at a pressure of 66.661 hPa and for equation (59) at a temperature of 321 K are listed. The quantity '%' in the first column denotes percent enrichment relative to the natural isotopic ratio of $^{18}O/^{16}O$ in mean atmospheric molecular oxygen (Table 5.1).*

species ⇒	$^{49}O_3$		$^{50}O_3$	
coefficient ⇓	value	uncertainty	value	uncertainty
a_0 in %	− 8.29	±0.67	−16.90	±0.45
a_1 in K^{-1}	+ 1.096	±0.088	+ 2.791	±0.094
$b_{const} in \%$	+10.83	±0.2	+12.70	±0.2
b_0 in %	+13.2	±1.1	+10.9	±2.0
b_1 in %	− 2.2	±1.1	+ 0.99	±1.5
b_2 in %	+ 0.76	±0.21	+ 0.01	±0.37
b_3 in %	− 0.115	±0.022	− 0.050	±0.038
b_4 in %	+ 0.00491	±0.00080	+ 0.00295	±0.00142

Figure 5.7 illustrates the enrichment expected in the atmosphere as a function of altitude as calculated from equation 60. Enrichments are calculated from the pT profile of two radio sondes launched on the 3^{rd} of July 1993 and on the 30^{th} of January 1994. Above the explosion altitude of ≈30 *km* the sonde pT profile is smoothly fitted into an arctic climatology. A significant variation with altitude is observed, which reaches a maximum between 40 and 45 *km* altitude and agrees qualitatively well with *in situ* data reported by *Mauersberger* (1981). However, the absolute enrichment calculated is about a factor of 2 smaller in the stratosphere than the *in situ* data, but yields realistic tropospheric values when compared with *Krankowski* et al. (1995). Note also that lower temperatures in winter yield significantly lower enrichments, in particular in the lower stratosphere between 18 and 20 *km* altitude in the center of the ozone layer.

It has to be pointed out that the expression $\varepsilon(T,p)$ is based on the measurements of the temperature dependence at one pressure only and for the pressure dependence at one temperature only. Thus, equation

60 is not valid for tuples of pT beyond the pT–ridges studied, if the overall dependence is significantly non–linear. The laboratory data does not cover all stratospheric conditions and a further extension is strongly encouraged, but at present no better data is available. Thus, the given expression is estimated to be the best approximation possible at present time.

Summed up, the ozone VMR profiles measured *in situ* by ECC ozone sondes are used directly for $^{16}O_3$, while for all heavy species of ozone a small correction is applied to this VMR profile based on the pT–profile and equation 60. The derived expected enrichments are assumed to be equal for symmetric and asymmetric heavy ozone in the calculation of

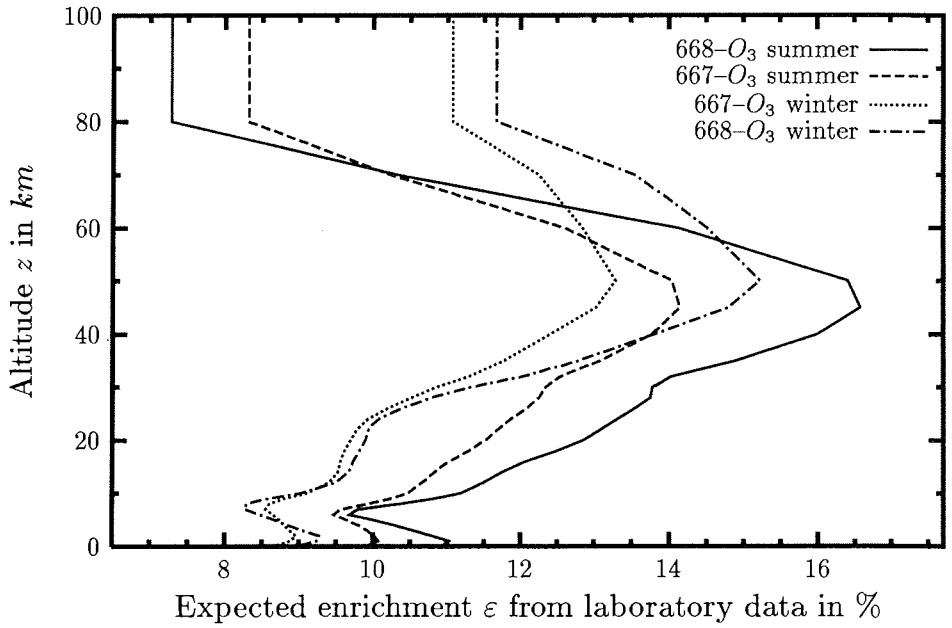

Fig. 5.7: *The calculated expected enrichment for $^{16}O^{16}O^{18}O$ and $^{16}O^{16}O^{17}O$ is shown as a function of altitude for a summer and a winter pT profile according to the laboratory studies that have been fitted to a function in pressure and temperature (equation 60). The pT profiles below 30 km are taken from radio sondes launched at Ny–Ålesund on the 3^{rd} of July 1993 and 30^{th} of January 1994.*

the VMR correction, which is consistent with the spectroscopic data base used. The effects of omitting this correction in heavy ozone VMR profiles or using different correction approaches are investigated in a case study below.

5.3.2 Discussion of the retrieved isotopic abundances

The observed isotopic abundances are reported in percent enrichment ε for ratios of total column amounts relative to the natural isotopic ratio $^{18}O/^{16}O$ in atmospheric oxygen in the usual form:

$$^{16-16-18}\varepsilon = \left\{ \frac{\left(^{16}O^{16}O^{18}O/^{16}O_3\right)_{obs}}{\left(^{16}O^{16}O^{18}O/^{16}O_3\right)_{ref}} - 1 \right\} * 100 \qquad (61)$$

The reference values are listed in Table 5.1 and comply with *de Bièvre et al.* (1984).

The results for isotopic ratios determined from solar and lunar absorption spectra are displayed in Figure 5.8 and the daily means are listed in Table 5.6. The error bars shown account for a 1 σ uncertainty level due to S/N, zenith angle determination, channeling, emission and imperfect congruence of light- and sonde paths.

Polar day: (samples 1,2 and 20–37) From Figure 5.8 one can clearly see that the two most abundant heavy ozone isotopes are significantly enhanced. The asymmetric $^{16}O^{16}O^{18}O$ is significantly more enhanced than the symmetric $^{16}O^{18}O^{16}O$ and averages are 15.4±0.9 % for $^{16}O^{16}O^{18}O$ and 11.2±1.4 % for $^{16}O^{18}O^{16}O$. The variation of the isotopic signal within the same air mass is small and within the error bars indicated, confirming the good reproducibility of the analysis. The enrichments observed in the ground based spectra given are also in excellent agreement with most recent FTIR data recorded with the ATMOS instrument from space (*Irion* et al., 1996). *F. Irion* and coworkers report average enrichments of 15(±5) % for asymmetric and 10(±7) % for symmetric heavy ozone and no significant change with latitude or season is observed in sunlit air masses.

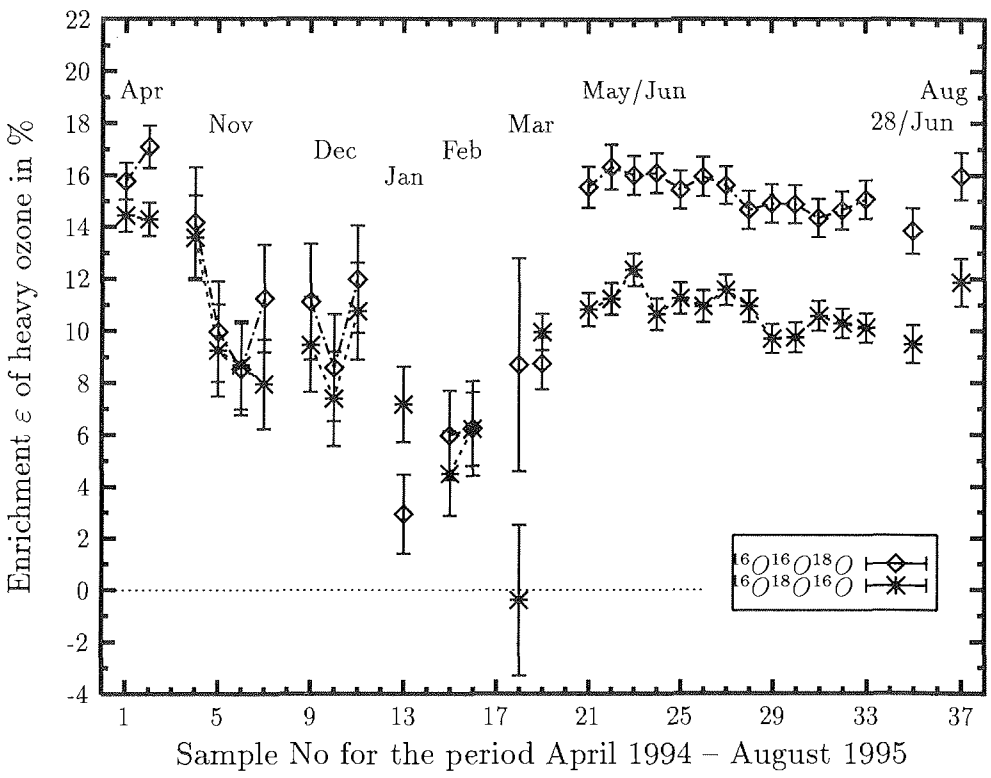

Fig. 5.8: *The isotopic enrichments of $^{16}O^{16}O^{18}O$ and $^{16}O^{18}O^{16}O$ relative to natural isotopic ratios in atmospheric oxygen are shown as observed in solar and lunar absorption spectra recorded with a ground–based FTIR–spectrometer. Error bars shown account for a 1 σ uncertainty level in statistical and known systematic uncertainties.*

Polar night: (samples 4–16) The lunar spectra recorded during polar night conditions show considerably stronger variability and underly larger uncertainties due to lower S/N. Lunar spectra show a lower enrichment of 9.0±3.3 % for $^{16}O^{16}O^{18}O$ and 8.5±2.5 % for $^{16}O^{18}O^{16}O$. An interesting aspect is the progressing decline of enrichment. The polar vortex builds up in November and enclosed air masses cool down over the winter period. At first glance, these results could comply with the idea that lower stratospheric temperatures give lower enrichments in heavy ozone, as one would expect from the laboratory experiments (compare Figures 5.5 and

Table 5.6: *The daily means for total column amounts Σ of $^{16}O_3$ and the retrieved enrichments ε in heavy ozone in percent relative to the natural isotopic ratios in atmospheric oxygen are listed. Data listed for the 18^{th} March 1995 hold the mean value from all solar spectra for the period 15^{th} to 21^{st} Mar 1995. The uncertainties σ_{st} in percent enrichment account for statistical uncertainties only.*

Date of observation	type	$\Sigma\ ^{16}O_3$ in $10^{18}\ cm^{-2}$	$^{16}O^{18}O^{16}O$		$^{16}O^{16}O^{18}O$	
			ε in %	σ_{st}	ε in %	σ_{st}
01/Apr/94	solar	9.87	14.43	0.63	15.77	0.72
06/Apr/94	solar	10.59	14.29	0.65	17.09	0.81
13/Nov/94	lunar	7.64	13.58	1.64	14.17	2.13
16/Nov/94	lunar	8.57	9.25	1.77	9.97	1.93
18/Nov/94	lunar	8.51	8.67	1.70	8.52	1.77
19/Nov/94	lunar	7.69	7.95	1.73	11.25	2.06
13/Dec/94	lunar	8.13	8.42	1.82	9.85	2.14
18/Dec/94	lunar	8.01	10.75	1.86	11.98	2.06
18/Jan/95	lunar	8.29	7.16	1.45	2.93	1.53
13/Feb/95	lunar	8.89	4.50	1.63	5.97	1.72
14/Feb/95	lunar	8.49	6.22	1.41	6.24	1.82
15/Mar/95	lunar	7.38	8.7	2.4	-0.39	1.72
18/Mar/95	solar	7.76	8.74	0.92	9.95	0.73
28/May/95	solar	9.75	11.47	0.62	15.94	0.80
30/May/95	solar	9.20	11.07	0.60	15.54	0.75
01/Jun/95	solar	9.27	10.13	0.56	14.76	0.74
28/Jun/95	solar	9.08	9.48	0.74	13.84	0.88
03/Aug/95	solar	8.34	11.86	0.91	15.96	0.91

5.7). But the situation is not that straightforward, because no ozone is formed in polar night and little information is available on when the observed ozone is formed and under what atmospheric conditions.

See also that differences in enrichment between the symmetric and the asymmetric species appear to be lower than in sunlit times. Intramolecular flip mechanisms within $^{16}O^{16}O^{18}O$ and $^{16}O^{18}O^{16}O$ could possibly account for the latter effect and intermolecular exchange reactions with molecular oxygen could as well contribute to both effects. This item is further investigated in a forthcoming paper.

Transitional period: (samples 18–19) Sample 18 gives the average over 3 lunar spectra and sample 20 shows the average from 9 spectra for asymmetric and from 13 spectra for symmetric heavy ozone. The mean values for all spectra are 8.7±1.0 % enrichment for asymmetric and 8.0±0.9 % enrichment for symmetric heavy ozone. This is a higher enrichment than in the previous full moon phase in polar night, but it is still a significantly lower enrichment than observed in polar day. Both species show a diurnal variation if the enrichments from individual spectra are plotted (not shown), but with a phase delay of several hours to one another. This phase delay is responsible for the strong differences in the lunar sample, because the diurnal minimum of enrichment in symmetric heavy ozone coincides with the lunar recording time. This is not the case for asymmetric heavy ozone. This period is to be studied in much more detail in the near future.

Besides the uncertainties discussed above, there are additional errors specific to isotopic ratios. To learn more about these, four case studies are performed that are listed in Table 5.7. The study is carried out with

Table 5.7: *This table displays the results from the case study concerning effects from possible systematic errors (see text). The increase in statistical errors and the deviations in retrieved total columns Σ are given in percent relative to the reference run and the resulting absolute change in heavy ozone enrichment ε. The upper lines give the changes in the average values, while the lower lines (values in brackets) denote the maximum change encountered in the 14 spectra analysed.*

manipulation	statistic error	Σ $^{16}O_3$	Σ $^{16}O^{18}O^{16}O$	Σ $^{16}O^{16}O^{18}O$	enrichment ε in heavy O_3 $^{16}O^{18}O^{16}O$	$^{16}O^{16}O^{18}O$
pressure & temperature	+14.8 (+30.3)	−4.08 (−8.36)	−1.10 (−5.75)	−3.53 (−7.88)	+3.43 (+4.54)	+0.94 (+3.29)
no isotopic correction	+1.0 (+4.8)	0.01 (−0.26)	+0.50 (+0.90)	−1.73 (−5.35)	+0.56 (+1.08)	−2.01 (−3.18)
asymmetric correction	−1.1 (−0.4)	+0.01 (+0.03)	+0.47 (+0.93)	−0.26 (−0.32)	+0.63 (+2.02)	−0.32 (−0.38)
enhanced stratospheric	+0.4 (+6.5)	−0.02 (−0.27)	+0.63 (+0.96)	−3.60 (−6.24)	+0.72 (+1.17)	−3.82 (−6.44)

the 14 solar spectra recorded in May and June 1995. In the first run, the temperature is increased by 2 K and the pressure by 2.5 % and the isotopic corrections are calculated according to these manipulated pT data. In the 2^{nd} case study, the original pT information is taken, but identical relative VMR-profiles are used for all O_3 species, which means that the isotopic correction is omitted. Case 3 is identical to the 2^{nd} one except for asymmetric heavy ozone. All enhancement of heavy ozone is assumed exclusively in the asymmetric isotopomer by multiplying the isotopic correction term for $^{16}O^{16}O^{18}O$ with 3/2. Finally, the isotopic correction of the previous run is doubled for the stratosphere but the tropospheric part is kept as before, which is comparable to reported *in situ* measurements (*Mauersberger*, 1981).

Incorrect data for pressure and temperature, as in the first run, considerably increases the statistical error due to increased line–shape errors. An error of this magnitude becomes obvious in the analysis and concerned spectra can be rejected from isotopic analysis. In the last 3 case studies, only the isotopic correction applied to heavy ozone is studied and since no isotopic correction is applied to symmetric ozone in all cases 2 to 4, the retrieved enrichments are of comparable order for symmetric heavy ozone. Systematic uncertainties of 0.6 % in $^{16}O^{18}O^{16}O$ enrichment do not add much to the error bars indicated. For asymmetric ozone, total enrichments are lower by 2.0 %, if the isotopic correction is omitted (case 2) and lower by 3.8 % for the strongest correction (case 4). In case 3, where all heavy ozone is assumed to be present in the asymmetric isotopomers and in amounts that comply with the laboratory data, effects are small and line–shape errors are even slightly smaller than in the reference case.

To figure out which correction is the most adequate, the data is checked for a systematic variation in total columns and enrichments with the observation angle for the cases 2–4 and the reference case. No significant trends are detected in any case, probably due to the small variation in air masses for the given spectra and the comparatively small change in the VMR–profile caused by the different calculated corrections.

In Figure 5.8 the mean isotopic enhancements in heavy ozone derived from the solar FTIR spectra presented are compared to recent laboratory studies on the dependence of enrichment from the symmetry of the con-

cerned isotopic species. The laboratory data is quoted from *Mauersberger* et al. (1993), which are determined with a mass spectrometer facility. To overcome the disadvantage of mass instead of symmetry selectivity of the detector system, a cleverly thought–out set of isotopically enriched reference gases is used. It is obvious in the figure, that the average enrichment for mass 50 ozone agrees excellent for FTIR and laboratory data. Further, in the laboratory data a clear symmetry selectivity of

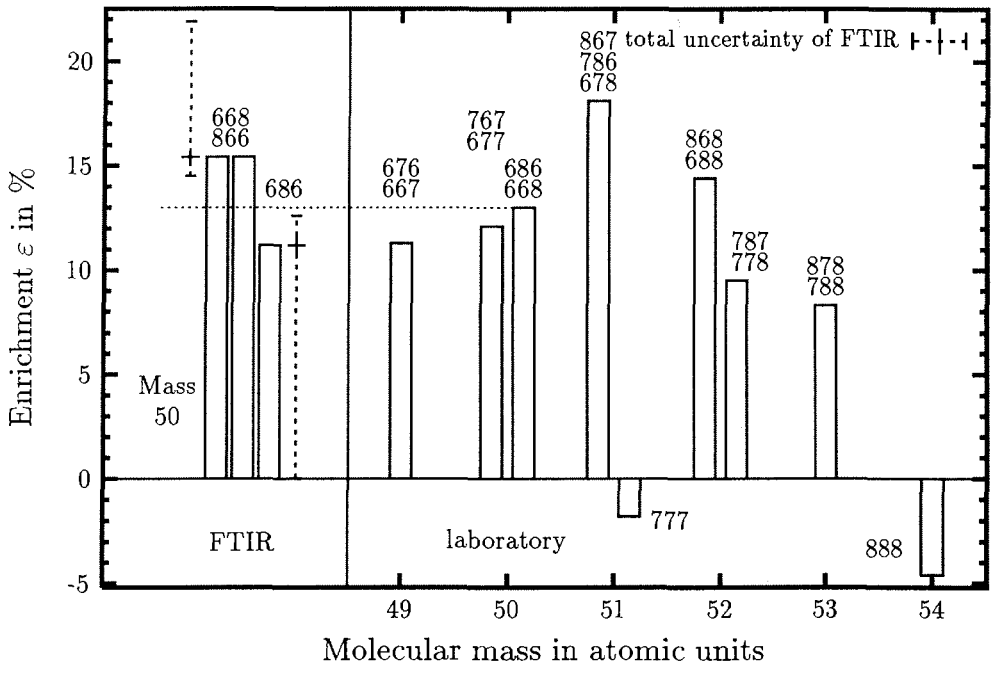

Fig. 5.9: *Comparison of isotopic enrichments derived from atmospheric FTIR measurements with recent laboratory studies. The FTIR data are the averages from solar spectra for the two most abundant heavy ozone species. The laboratory data is replotted from data published by* Mauersberger *et al. (1993). The absolute uncertainties for the latter data are 1 % enrichment (except for $^{17}O^{17}O^{17}O$ with 2 %). The uncertainties for FTIR data are 0.9 % enrichment for $^{16}O^{16}O^{18}O$ and 1.4 % for $^{16}O^{18}O^{16}O$ without the uncertainties of the spectroscopic database and as large as indicated in the figure with spectroscopic uncertainties.*

the enhancement is seen. Totally symmetric species like $^{17}O^{17}O^{17}O$ and $^{18}O^{18}O^{18}O$ are depleted as is expected from classical mass dependent fractionation processes, as outlined in section 5.1 and as calculated for the particular case of ozone by *Kaye* (1986). But with increasing asymmetry the heavy isotopomers show a significant enhancement with a maximum of 21 % for the most asymmetric group of $^{16}O^{17}O^{18}O$, $^{16}O^{18}O^{17}O$, and $^{18}O^{16}O^{17}O$. The FTIR data presented indicate that the enhancements in the two most abundant heavy ozone species $^{16}O^{16}O^{18}O$ and $^{16}O^{18}O^{16}O$ also split up with a significantly stronger enhancement in the asymmetric heavy species.

However, the most important source of systematic error in the FTIR data appears to be the spectroscopic data base HITRAN. There is a large uncertainty in the accuracy of the isotopic composition in the reference gas used, which had been created by silent electric discharge from molecular oxygen of known isotopic composition. In contrast to O_2, the isotopic composition of ozone cannot be directly measured by mass–spectrometric methods, due to the presence of different isotopomers of same mass. Thus, absolute line intensities for $^{16}O^{18}O^{16}O$ were calculated theoretically under the assumption of a dipole moment derivative equivalent to that of $^{16}O_3$. The corresponding intensities of $^{16}O^{16}O^{18}O$ have then been determined by comparison with the symmetric species assuming a 2:1 abundance ratio between asymmetric and symmetric heavy ozone (*Flaud et al.* 1986, *Camy-Peyret et al.* 1986), which might not be realistic when compared with the results from *Mauersberger et al.* (1993) discussed in the previous paragraph. To estimate an upper limit for the resulting systematic uncertainty, one could assume zero enhancement in symmetric ozone in the sample gas. This would alter the derived average enhancements in solar spectra from 11 % to 0 % for $^{16}O^{18}O^{16}O$ and from 15.5 % to 21 % for $^{16}O^{16}O^{18}O$.

5.3.3 Conclusions on the symmetry selective heavy ozone enrichment

The data presented in this section on isotopic abundances in heavy ozone are the first ground based observations with an optical instrument that showed a significant fractionation in ozone. Compared to the pionier-

ing work by *Rinsland* et al. (1985), the improvements in the accuracy achieved are ascribed to the excellent knowledge of the pT– and ozone VMR–profiles and the use of a higher number of spectral intervals in the retrieval. The optical detection of the enhancement is a completely independent detection method compared to *in situ* balloon borne mass spectrometers or grab sampling methods with a following mass spectrometric analysis (e.g. *Schueler* et al., 1990). The overall good agreement of the results from the different experiments make the observed enhancements undeniable to any theoretical physicist.

It is shown that even ground–based lunar absorption spectra, that are of poorer quality than the solar spectra presented, allow the study of the enhancement effects in heavy ozone. This allows for the first time to report data on the isotopic abundances in ozone in dark air masses and offers a unique test for the understanding of the fractionation processes. In the absence of photolysis, no ozone is formed and the polar vortex effectively blocks the transport of air masses from lower latitudes allowing a considerable aging of the isotopic signal enclosed. These unique conditions in nature are only available at the very high latitudes.

From Figures 5.8 it is evident that both symmetric and asymmetric $^{50}O_3$ are significantly enhanced and that the asymmetric species at least in sunlit air masses is significantly more enhanced than the symmetric one. Thus, theoretical models that cannot account for the observed symmetry selectivity are inadequate or incomplete.

If all enhancements in heavy ozone are to be present in the asymmetric species only, as suggested by *Mauersberger* et al. (1993) (see Figure 5.9), then inconsistencies with results reported here are tentatively ascribed to isotopic uncertainties in the HITRAN data base. This is also backed up by the case studies performed, where an enhancement in asymmetric O_3 only (case 3) gave the best fit to line shapes in recorded data.

A possible explanation for the observed enrichment is discussed by *Anderson* et al. in *Kaye* (1992). The enrichment cannot be understood in terms of conventional relaxation theory, thus it is suggested that the low lying $^3B_2$ and $^3A_2$ metastable states are involved in the formation process. Combined with an appropriate, but as yet unknown symmetry

selective relaxation process, such states could provide the explanation for the observed symmetry selective enrichments. It is mentioned in the beginning of this chapter, that heavy isotopomers support more bound states compared to the normal isotopomer and it is known from quantum mechanics that the number of allowed and forbidden transitions in a molecule depend on the symmetry. Thus, in other words, if the postulated metastable ozone is one step in the ozone formation process, then quantum mechanical selection rules can explain the enhanced likeliness for heavy isotopomers to enter a bound state from the metastable state. This idea agrees with the experimental data presented that show a pronounced enrichment in asymmetric heavy ozone.

A thorough understanding of the ozone production mechanism is vital in the discussion of the global ozone depletion. Each ozone molecule in sunlit air masses of the lower stratosphere is destroyed and recycled every 15 to 30 minutes on the average, depending on latitude and season (*R. Lehmann*, AWI Potsdam, priv. comm. 1996). Thus, even small changes in the production characteristics have a significant influence on the equilibrium concentration of ozone in the atmosphere. As the isotopic enrichments in heavy ozone are theoretically not fully understood at present, one has to admit that the ozone production mechanism is not fully understood. The consequences are manifold.

6 Summary and prospects

In this thesis it is shown that ground based FTIR spectroscopy is a powerful technique in the study of the lower atmosphere of our planet. It is demonstrated that the abundances of some 30 different species can be quantified in terms of total column amounts. Moreover does the determination of isotopic ratios and the derivation of dynamic information open a wide field of principally new applications to ground based infrared spectrometers.

The given observation site in the high Arctic is of particular importance to global networks for several reasons. Satellite data is incomplete at high latitudes due to their orbits that often do not cover the polar regions and due to their instrumentations, which often require solar occultation not available in polar night. The synoptic net of ground based observations is wide compared to mid–latitudes. The instrument yields atmospheric spectra throughout the year, including polar night. The infrared spectrometer quantifies several atmospheric species with key functions in stratospheric ozone depletion that are not detectable by any other ground based instrument operated in the Arctic at present. This includes $ClONO_2$ and HCl. The detection of anthropogenic pollutants mainly distributed in the troposphere is not disturbed by local pollution in this remote area. Last, but not least, is the amplitude in seasonal cycles largest at high latitudes and if a climatic change is to occur, then the signals are expected to be highest at high latitudes.

Main emphasis in this work is put on improvements in the data retrieval. To illustrate the different sources of uncertainties, the signal formation in the instrument is discussed in the first chapter, while the second and third chapter are devoted to the analysis of recorded spectra. In principle, the recorded spectrum is compared to a simulated spectrum. The quality of the analysis is limited by uncertainties in the simulated spectrum in most cases. It is not the aim of this work to improve the central fitting algorithm that calculates the absorption spectrum and compares it to the recorded spectrum. Instead, the information available to this central retrieval element is improved. Thus, the discussion given for the example of the retrieval program SFIT is not limited to the SFIT algorithm, but

is also valid for any other retrieval software. However, some difficulties are highlighted that are specific to SFIT, like for example the discussion of the pressure shift in section 2.3, and serve as an example for individual difficulties that are specific to any particular algorithm.

One important step ahead is to provide all data available from other instruments, in particular from *in–situ* sondes, to the algorithm that puts up the model atmosphere. The use of pT profiles from radio sondes is a common technique, but ECC ozone sondes are not regularly available at many sites and the use of the relative humidity data is suggested and performed on a regular scale for the first time. New in the discussion on the relevance of using *in situ* ozone profiles is the aspect to reduce the profile uncertainties for the determination of isotopic ratios in ozone (see below). It is the first comprehensive discussion on the relevance of all three data sets, i.e. pT profile, ozone VMR profile, and water vapor profile information, to the quality of FTIR measurements with case studies to all of them. The reduction in the uncertainties of isotopic ratios determined in ozone by one order of magnitude compared to previous publications is ascribed to the use of these *in–situ* data.

Lunar absorption spectra add further difficulties to the retrieval of total column amounts, as discussed in sections 3.3 and 3.4. Emission from the atmosphere and optical parts of the instrument are no longer a minor correction, but make up a substantial portion of up to 20 % of the recorded signal. In a case study with solar and lunar spectra that are recorded within 24 hours, several correction approaches are discussed in a direct comparison of solar and lunar retrieval results. It is demonstrated that lunar spectra not corrected or only partially corrected for emission yield highly unrealistic results that for example underestimate CO_2 by more than 40 %. This underlines the importance of an emission correction. The correction of lunar spectra based on blackbody calculations yields total column amounts of CO_2 that agree within 2 % with the solar data, which is well within the statistical and zenith angle uncertainties. The good agreement can also be seen in other species than discussed in chapter 3 for trace gases with small chemical and dynamical variabiltity as listed in Table 4.3.

The polar atmosphere is subject to a variety of dynamical changes, like

the substantial subsidence of stratospheric air masses in winter, which is unknown to lower latitudes. Chapter 4 describes the large meteorological patterns, in particular the polar vortex, and its seasonal variation. Taking these large scale changes into account is an important improvement to the model atmosphere used in the FTIR data retrieval. In section 4.3 the degree of subsidence/ascent (DOSA) operation is introduced that describes the subsidence of stratospheric air inside the polar vortex and an additional operation to account for changes in the tropopause altitude is suggested. The capability of the algorithms designed is demonstrated first on synthetic spectra from the participation in an international retrieval intercomparison. From ground to 25 km altitude the VMR profile of CH_4 is reproduced excellently with total columns agreeing within 0.4 %. The profile optimization is then applied to summer spectra (section 4.5) that offer the most favorable recording conditions and finally to early spring data (section 4.6) that are the most complex and difficult spectra to analyse. Omitting a correction for the subsidence is shown to underestimate the total column amount of e.g. methane by 7 % for the example given in Figure 4.18.

In early spring, at the end of polar night, photolysis returns to the atmosphere and large chemical processing starts. The stratosphere is still cold enough for the formation of polar stratospheric clouds (PSCs) in some locations inside the polar vortex and allow for a significant ozone depletion in air masses floating through, due to heterogenous chemistry occurring on the surface of the PSCs. Additionally, the dynamical variability is strong, both horizontally with filaments of more or less chemically processed air masses passing by and vertically with the dilution up to the complete break up of the tropopause on individual days. The observation geometry is restricted by the low elevation of the sun. Thus, air masses probed by the FTS are some 200 km away and the profile information from the *in situ* sondes underly large uncertainties, as is illustrated by significant line shape errors in species with known VMR profile.

In spite of all these difficulties, well defined optimum values for the degree of subsidence are derived that agree both in the picture of overall line shape quality and total column amounts retrieved and underline the consistency of the DOSA approach. Thus, it is obvious that for the given

situation the detailed DOSA retrieval is superior to any direct line shape inversion algorithm for the retrieval of vertical information, because the latter is expected to be substantially mislead by the uncertainties in the pT profile and the lunar spectra included in the DOSA approach are to noisy. It is also shown that the rate of subsidence of 0.5 mm/s derived from the FTIR spectra agree well with studies from aircrafts published by other authors.

The fifth and last chapter is devoted to the study of natural isotopic ratios in selected trace gases. In the first sections the fractionation processes caused by mass differences are described. The strongest effect is expected for heavy water as a consequence of frequent phase transitions. This is illustrated by the seasonal cycle of the deuterium abundance in water vapor and its correlation with the temperature of the air mass probed. The isotopic ratios of heavy carbon and deuterium in methane are more difficult to retrieve and the relative uncertainties are large. This is due to the much weaker fractionation occurring in methane compared to water. However, seasonal signals are observed and can be interpreted by local emission from methanogens in the wet tundra in summer. The situation in $H^{37}Cl$ is subject to large spectroscopic uncertainties from interfering species, which allow only a very preliminary discussion of the results retrieved.

The last section of the main part discusses in detail the strong enhancement of heavy ozone. Great care is taken in the analysis and a series of case studies is performed to estimate the effects from possible systematic uncertainties. The results from sunlit air masses are in good agreement with several *in situ* experiments from other groups using balloon borne mass spectrometer or grab samplers with subsequent mass spectrometric analysis, as well as with a very recent spectroscopic study from space. The advantage of the spectroscopic detection is that even isotopes of same mass are distinguished by differences in their symmetry, which plays a key role in the theoretical understanding of the enhancement. However, the observed enrichments are in sharp contrast to publications based on theoretical studies that expect a depletion in heavy ozone.

It is shown that the two most abundant species of heavy ozone, i.e. $^{16}O^{18}O^{16}O$ and $^{16}O^{16}O^{18}O$, are significantly enriched with average values

as high as 11 % and 15.5 %, respectively, in sunlit airmasses. The asymmetric species is significantly more enriched than the symmetric one in sunlit air masses, while it is not in polar night. The isotopic ratios derived from lunar spectra are the first isotopic data reported so far on ozone for air masses that stayed in darkness for a longer period. The isotopic fractionation is expected to occur in the formation process and a decline in the enrichment is expected for air masses where continuous production is cut off due to the absence of sunlight. This decline is observed in the FTIR data presented and confirms the idea that the enrichment occurs at least mainly if not exclusively in the production process.

Thus, the data on the isotopic abundances in ozone as observed in FTIR data strongly support new ozone formation models that postulate the existence of a metastable molecule in the formation process. From this metastable molecule a selection for heavy, in particular asymmetric heavy isotopomers is possible, when returning to a stable bound state. Heavy isotopomers support more bound states and have simply more allowed transitions, which can explain the enrichment observed. Small uncertainties in the production rate of ozone due to a wrong ozone formation model can play an important role in the discussion on the observed decline in global stratospheric ozone, because each ozone molecule in sunlit air masses is destroyed and reformed in the middle and upper stratosphere every 15 to 30 minutes on the average.

In the near future it is planned to further improve and to simplify the analysis of lunar absorption spectra. The general idea is to include the effects of emission directly in the retrieval algorithm. SFIT includes a simple correction adequate for solar spectra, but it does not allow to set the temperature of the IR source to lunar temperatures. Cooperation is started with *David Griffith* to adapt the MALT algorithm and the first results are encouraging. Most recently *T. von Clarman*, Fz Karlsruhe, mentioned that the RAT algorithm is now also capable for this task and a cooperation is also planned with him.

On the three species reported for the first time in arctic spectra, i.e. C_2H_4, NH_3 and in particular HO_2NO_2 a seasonal cycle is to be retrieved. A publication is planned with colleagues that also include aspects on the chemical relevance of these molecules.

To improve the accuracy in the retrieval of VMR profiles, in particular in the troposphere, it is planned to put up an artificial IR source near surface to determine the concentration of individual molecules at ground level. This concentration is then used as the starting point in the tropospheric VMR retrieval.

All other future activities will focus on the search of more suitable spectral microwindows for the retrieval of atmospheric species with particular emphasis on intervals suitable for the retrieval of isotopic ratios. In particular. it is expected to quantify $^{16}O^{16}O^{17}O$ to show the mass independence of the enrichment. Isotopic data on methane and water vapor is expected to become more reliable with the use of more spectral intervals, some of which are already known. It will be attempted to extend the isotopic studies to CO_2 and CO.

Finally it is planned to reanalyse all spectra recorded in the past five years to derive a seasonal cycle of the isotopic enrichment in heavy ozone. For the lunar data a trajectory analysis is planned to check for a correlation of declining enhancement with the age of the air mass in darkness. The diurnal signal seen in early March will be further investigated and be compared to the trajectory results. This might allow to calculate the poorly known recombination rate of ozone.

Acknowledgements

I gratefully acknowledge the help of many friends and colleagues that contributed to complete this thesis. I thank all colleagues from the research department Potsdam, in particular Hartwig Gernandt as the head of the atmospheric branch, Justus Notholt for guidance and discussion, Eduard Claudius and Uwe Eggert for maintaining an excellent computational infrastructure and for assistance in software questions, Edo Becker for discussion and for the recording of FTIR spectra, Ralph Lehmann for chemical modelling, for help in mathematical questions, and the *'tea and cookies'* discussion panel, Markus Rex for discussion on atmospheric dynamics, Peter von der Gathen for valuable information on ozone sondes and lidar observations, Jens Biele for information on lidar observations, Günter Schwarz for discussion on isotopic fractionation, Klaus Dethloff for discussion of theoretical aspects, Thomas Seiler, Andreas Herber, Sigrid Debatin, and Jürgen Gräser for assistance concerning radio sonde data, and Ingeborg Sass and Marit Stein for their friendly assistance in accessing literature.

The help from the Koldewey station staff, in particular from Hauke Schütt, Ingo Beninga, Ute Schwartz, Thomas Seiler, and Rainer Lilischkis that recorded many of the spectra on Spitsbergen is gratefully acknowledged. I also like to thank Prof. Ernst Augstein from AWI Bremerhaven for supporting my employment and for encouraging research in Potsdam in many ways. Thanks also to the highly cooperative editor in charge Dr. Franz Rieman for getting this report printed.

I like to thank Curtis Rinsland for providing SFIT and for many helpful discussions, Konrad Mauersberger for the discussion on isotopic signals in ozone, Geoffrey Toon for discussion on dynamic parameters, William Bell, Johan Mellqvist, Hans Fast and all their co-workers for discussion and helpful comments on the SFIT TOOLS, James Hannigan for porting SFIT to OS/2, the designers of the non–profit softwares LATEX and GNUPLOT with which the complete layout of the thesis is created, Laurence Rothman for providing the HITRAN data base and all those numerous colleagues that did the spectroscopic measurements for the HITRAN data base.

I like to thank Dr. habil. Hermann Lühr for raising my interest on atmospheric physics. I gratefully acknowledge the support from the Braunschweig home team including in particular Annette Paul for carefully reading and suggesting many improvements to the thesis, Stefan Röttger for many helpful information on software questions, Olaf T. Wachsmuth for answering any question on computer hardware, and Inge Meyerhoff, Anja Honig, and Stefan Kraft for their individual support. I also like to thank my former fellow students Robert Braun and Birgit Irmscher for discussion and support as a friend. Many thanks also to my family and friends for showing understanding when the thesis took most my time.

Finally, I like to thank both Prof. Dr. Peter Weidelt for acceptance on short notice of being one of the referees to this thesis and Prof. Dr. Uwe Keyser for supervising the thesis, for the time they spent on helpful discussions and for many suggestions that helped to improve the thesis.

References

Abrams, M. C., G. L. Manney, M. R. Gunson, M. M. Abbas, A. Y. Chang, A. Goldman, F. W. Irion, H. A. Michelsen, M. J. Newchurch, C. P. Rinsland, R. J. Salawitch, G. P. Stiller, and R. Zander, *"ATMOS/ATLAS-3 observations of long-lived tracers and descent in the Antarctic vortex in November 1994"*, Geophys. Res. Let., in press, 1996.

Adrian, G. P., T. v. Clarmann, H. Fischer, and H. Oelhaf *"Trace gas measurements with the ground-based MIPAS experiment during the arctic winters 1990 to 1992"*, in *IRS'92: Current problems in atmospheric radiation*, edited by S. Keevallik and O. Kärner, Deepak Publishing, Hampton, Virginia, 359–362, 1993.

Anderson, S. M. and K. Mauersberger, *"Ozone absorption spectroscopy in search of low-lying electronic states"*, J. Geophys. Res., **100**, 3033–3048, 1995.

Anderson, S. M., K. Mauersberger, J. Morton, and B. Schueler, *"Heavy ozone anomaly"*, in *"Isotope effects in gas-phase chemistry"*, edited by *J. A. Kaye*, ACS symposium series 502, Washington DC, USA, 1992.

Anderson, S. M., J. Morton, and K. Mauersberger, *"Laboratory measurements of ozone isotopomers by tunable diode laser absorption spectroscopy"*, Chem. Phys. Let., **156**, 175–180, 1989.

Bell, R. J., *"Introductory Fourier Transform Spectroscopy"*, Academic Press, New York, 382 pp., 1972.

Beer, R., *"Remote sensing by Fourier Transform Spectrometry"*, Wiley, New York, USA, 153 pp., 1992.

Bergmann, L., and C. Schaefer, *"Lehrbuch der Experimentalphysik - Band III, Optik"*, 8^{th} edition, edited by H. Grobrecht, 1119 pp., W. de Gruyter Verlag, Berlin, 1987.

Beyerle, G., *"Multiwavelength LIDAR measurements of stratospheric volcanic aerosols and polar stratospheric clouds on Spitsbergen (79°N, 12°E)"*, ScD thesis, reports on polar research, Vol. 138, Alfred-Wegener-Institute, ISSN 0176-5027, Bremerhaven. 1994.

Bièvre, P. de, M. Gallet, N. E. Holden, and I. L. Barnes, *"Isotopic abundances and atomic weights of the elements"*, J. Phys. Chem. Ref. Data **13**, 809–891, 1984.

Bjørdal, A., (editor) *"Research in Svalbard - 1996"*, yearly report, Norsk Polarinstitutt, Oslo, 1996.

Blake A. J., S. T. Gibson, and D. G. McCoy, *"Photodissociation of $^{16}O^{18}O$ in the Atmosphere"*, J. Geophys. Res., **89**, 7277–7284, 1984.

Blom, C. E., H. Fischer, N. Glatthor, T. Gulde, and M. Höpfner, *"Airborne measurements during the European Arctic Stratospheric Experiment: coloumn amounts of HNO_3 and O_3 derived from FTIR emission sounding"*, Geophys. Res. Let., **21**, 1351–1354, 1994.

Born, M. and E. Wolf, *"Principles of optics"*, 6^{th} edition, 808 pp., Pergamon Press, Oxford, 1989.

Brasseur, G. P. and S. Solomon, *"Aeronomy of the middle atmosphere"*, 2^{nd} edition, 452 pp., Reidel publ. (Kluwer group), Dordrecht, The Netherlands, 1995.

Brasseur, G. P., A. K. Smith, and C. F. Granier, *"The stratosphere: An introduction"*, in *"The role of the stratosphere in global change"*, edited by M. L. Chanin, NATO ASI series, Series 1: Global Environment Change, Vol. 8, Springer Verlag Berlin, 1–27, 1992.

Brault, J. W., *"High precision Fourier Transform Spectrometry: The critical role of phase corrections"*, Mikrochimica Acta, **III**, 215–227, 1987.

Breitsprecher, R., P. Terrel, V. Calderwood–Schnorr, W. V. A. Morris, *"Pons–Collins: Globalwörterbuch Deutsch–Englisch (I) / Englisch–Deutsch (II)"*, pp. 1380 (I) & 1390 (II), 1^{st} ed., Collins London (1983), reprinted by Collins–Klett, Stuttgart, 1986.

Brenninkmeijer, C. A. M., R. Müller, P. J. Crutzen, D. C. Lowe, M. R. Manning, R. J. Sparks, and P. F. J. van Velthoven, *"A large ^{13}CO deficit in the lower antarctic stratosphere due to 'ozone hole' chemistry: part I, observations"*, Geophys. Res. Let., **23**, 2125–2128, 1996.

Brigham, E. O., *"FFT – Schnelle Fourier–Transformation"*, Oldenburg Verlag, 301 pp., München, 1992.

Brown, L. R., C. B. Farmer, C. P. Rinsland, and R. A. Toth, *"Molecular line parameters for the atmospheric trace molecule spectroscopy experiment"*, Appl. Opt., **26**, 5154–5179, 1987.

Camy-Peyret C., J.-M. Flaud, A.Perrin, V. M. Devi, C. Rinsland, and M. A. H. Smith, *"The hybrid–type Volumes ν_1 and ν_3 of $^{16}O^{16}O^{18}O$: Line positions and intensities"*, J. Mol. Spectrosc., **118**, 345–354, 1986.

Chamberlain, J., G. W. Chantry, and N. W. B. Stone, *"The principles of interferometric spectroscopy"*, Wiley Press, Chichester, 347 pp., 1979.

Champeney, D. C., *"Fourier transforms and their physical applications"*, Academic Press, London, 256 pp, 1973.

Chipperfield, M. P., D. Cariolle, P. Simon, R. Ramaroson, and D. J. Lary, *"A three–dimensional modeling study of trace species in the Arctic lower stratosphere during winter 1989–1990"*, J. Geophys. Res., **98**, 7199–7218, 1993.

Ciais, P. and J. Jouzel, *"Deuterium and oxygen 18 in precipitation: Isotopic model, including mixed cloud processes"*, J. Geophys. Res., **99**, 16793–16803, 1994.

Clarmann, T. von, *"RAT: A computational tool for retrieval of atmospheric trace gas profiles from infrared spectra"*, Kernforschungsanstalt[10] Karlsruhe, Germany, KfK–report 5423, 1994.

Clarmann, T. von, H. Fischer, F. Friedl–Vallon, A. Linden, H. Oelhaf, C. Piesch, and M. Seefeldner, *"Retrieval of stratospheric O_3, HNO_3, and $ClONO_2$ profiles from 1992 MIPAS–B limb emission spectra: method, results, and error analysis"*, J. Geophys. Res., **98**, 20495–20506, 1993.

Clarmann, T. von, *"Die Bestimmung von Mischungsverhältnissen stratosphärischer Spurengase aus Emissionsspektren im infraroten Spektralbereich"*, Sc.D. thesis, Kernforschungsanstalt Karlsruhe, Germany, KfK–report 4698, 1990.

Clarmann, T. von, *"Untersuchungen zur Strahldichteberechnung mit Linie–für–Linie–Computerprogrammen"*, Diplomarbeit in meteorology (≈*Master's thesis*), Universität München, Meteorologisches Institut, Munich, Germany, 1986.

Clough, S. A. et al., *"FASCOD3: Spectral simulation"*, in *Proc. of IRS88 on current problems in atmosph. rad.,* edited by J. Lenoble et al., Hampton, Va., 1989.

Clough, S. A., F. X. Kneizys, E. P. Shettle, and G. P. Anderson, *"Atmospheric radiance and transmittance: FASCOD2"*, paper presented at the 6^{th} Conference on Atmospheric Radiation, Am. Meteorol. Soc., Williamsburg, Va., USA, 1986 (software is available from ONTAR Corp., 129 University Road, Brookline, Mass.).

Clough, S. A., F. X. Kneizys, L. S. Rothman, and W. O. Gallery, *"Atmospheric spectral transmittance and radiance: FASCOD1B"*, SPIE, **277**, 152–166, 1981.

Cohen, E. R. and B. N. Taylor, *"The 1986 adjustment of the fundamental physical constants"*, CODATA bulletin **63**, Pergamon Press, 1986.

Coleman, D. D., J. B. Risati, and M. Schoell, *"Fractionation of carbon and hydrogen isotopes by methane–oxidizing bacteria"*, Geochim. Cosmochim. Acta, **45**, 1033–1037, 1981.

Crutzen, P. J. and F. Arnold, *"Nitric acid cloud formation in the cold antarctic stratosphere: a major cause for the springtime ozone hole"*, Nature, **324**, 651–655, 1986.

Cubasch, U., *"Das Klima der nächsten 100 Jahre"*, Phys. Bl., **48**, 83–88, 1992.

Dansgaard, W., *"Stable isotopes in precipitation"*, Tellus, **16**, 436–468, 1964.

Dansgaard, W., *"The abundance of ^{18}O in atmospheric water and water vapor"*, Tellus, **5**, 461–470, 1953.

[10]Recently, the research center has been renamed to *Forschungszentrum Karlsruhe* (FzK).

Engel, A. and U. Schmidt, *"Vertical profile measurements of Carbonylsulfide in the stratosphere"*, Geophys. Res. Let., **20**, 2219–2222, 1994.

Eriksson, E., *"Deuterium and oxygen-18 in precipitation and other natural waters: some theoretical considerations"*, Tellus, **17**, 498–512, 1965.

Faure, G., *"Principles of isotope geology"*, 589 pp., Wiley, New York, 1986.

Finkelnburg, W., *"Einführung in die Atomphysik"*, 525 pp., Springer, Berlin, 1976.

Flaud, J.-M., C. Camy-Peyret, V. M. Devi, C. Rinsland, and M. A. H. Smith, *"The ν_1 and ν_3 Volumes of $^{16}O^{18}O^{16}O$: Line positions and intensities"*, J. Mol. Spectrosc., **118**, 334–344, 1986.

Friedle, A. *"Fehleranalyse der Interferogrammaufnahme des Fouriespektrometers MIPAS-LM"*, Diplomarbeit in Physik (≈*Master's thesis*), Institut für Meteorologie und Klimaforschung, Universität Karlsruhe, Germany, 1993.

Gathen, P. von der, M. Rex, N. R. P. Harris, D. Lucic, B. M. Knudsen, G. O. Braathen, H. De Backer, R. Fabian, H. Fast, M. Gil, E. Kyrö, I. S. Mikkelsen, M. Rummukainen, J. Stähelin, and C. Varotsos, *"Observational evidence for chemical ozone depletion over the Arctic in winter 1991–92"*, Nature, **375**, 131–134, 1995.

Geller, M., *"A high-resolution atlas of the infrared spectrum of the sun and the earth atmosphere from space – Volume III: Key to identification of solar features"*, JPL CalTech, NASA ref. publication 1224, Washington D.C., 1992.

Gernandt, H., A. Herber, P. von der Gathen, M. Rex, A. Rinke, S. Wessel, and S. Kaneto, *Variability of ozone and aerosols in the polar atmosphere"*, Proc. NIPR Symp. Polar Meteorol. & Glaciol., Nat. Inst. of Polar Res., Tokyo, in press, 1996.

Gernandt, H., P. von der Gathen, K. Dethloff, and S. Kaneto, *"Long-term change of stratospheric ozone in the Antarctic and differences to the Arctic"*, Int. Conf. on Ozone in the Lower Stratosphere, Halkidiki, Greece, 15–20 May, 1995.

Gernandt, H. (editor), *"Polare Atmosphärenforschung in Potsdam"*, report on the activities of the atmospheric research branch established at Potsdam in 1992, Alfred–Wegener–Institut, Potsdam, 1994.

Gernandt, H., P. Glöde, U. Feister, G. Peters, and B. Thees, *"Vertical distributions of ozone in the lower stratosphere over Antarctica and their relations to the spring depletion"*, Planet. Space Sci., **37**, 915–933, 1989.

Goldman, A., *"Report on the retrieval intercomparison of the NDSC – spring 1996"*, internal report of the NDSC presented at the 6^{th} NDSC Meeting in Garmisch–Partenkirchen, April 1996.

Goldman, A., F. J. Murcray, D. G. Murcray, J. J. Kosters, C. P. Rinsland, J.-M. Flaud, C. Camy-Peyret, and A. Barbe, *"Isotopic abundances of stratospheric ozone from ballone-borne high-resolution infrared solar spectra"*, J. Geophys. Res., **94**, 8467–8473, 1989.

Griffith, D. W. T., *"Synthetic calibration and quantitative analysis of gas-phase FT-IR spectra"*, Appl. Spectr., **50**, 59–70, 1996.

Gronholz, J. and W. Herres, *"Understanding FT-IR Data Processing"*, combined reprint of Huethig Publishers (obtainable from BRUKER, Karlsruhe), Instr. and Computers, **1**, 1984 and **3**, 1985.

Holm, K., *"Interessante Daten über Longyearbyen und Umgebung"* (also available in english), pp. 58, Halvdan Falch Bokbinderi, Bodø (Norway), ISSN 82–992142–3–8, 1991.

Höpfner, M., *"Das flugzeuggetragene Fernerkundungsexperiment MIPAS-FT: Auswertung und Interpretation der arktischen Meßkampagnen 1991/92 und 1992/93"*, ScD. thesis, Kernforschungsanstalt Karlsruhe, Germany, KfK–report 5438, 1994.

Houghton, J. T. (editor), *"The Global Climate"*, Cambridge University Press, 1984.

Humlicek, J., *"Optimized Computation of the Voigt and complex probabaility functions"*, J. Quant. Spectrosc. Radiat. Transfer, **27**, 437–444, 1982.

Irion, F. W., M. R. Gunson, C. P. Rinsland, Y. L. Yung, M. C. Abrams, A. Y. Chang, and A. Goldman, *"Heavy ozone enrichment from ATMOS infrared solar spectra"*, Geophys. Res. Let., **23**, 2377–2380, 1996.

Jancso, G. and W. A. van Hook *"Condensed phase isotope effects - especially vapor pressure isotope effects"*, Chem. Rev. **74**, 689–750, 1974.

Kaye, J. A., (editor), *"Isotope effects in gas-phase chemistry"*, 438 pp., ACS series 502, Washington DC, 1992.

Kaye, J. A., *"Mechanisms and observations of isotope fractionation of molecular species in planetary atmospheres"*, Rev. Geophys., **25**, 1609–1658, 1987.

Kaye, J. A., *"Theoretical analysis of isotope effects on ozone formation in oxygen photochemistry"*, J. Geophys. Res., **91**, 7865–7874, 1986.

Keyser, U., *"Absolutmessung der β-Summenspektren aller Spaltprodukte nach thermischer Spaltung von ^{235}U und ^{239}Pu an einem externen Neutronenleiter"*, Habilitationsschrift, Technische Universität Carolo–Wilhelmina zu Braunschweig, 1986.

Khalil, M. A. K., *"Atmospheric methane: sources, sinks, and role in global change"*, NATO ASI series 1, Vol. 13, pp. 561, Springer, Berlin, 1993.

Khalil, M. A. K. and R. A. Rasmussen, *"Constraints on the global sources of methane and an analysis of recent budgets"*, Tellus, **42B**, 226–236, 1990.

Kohlrausch, F., *"Praktische Physik"*, Vol. 1, 23rd edition, 724 pp., Teubner Verlag, Stuttgart, 1985.

Komhyr, W. D., *"Ozone measuremnets to 40 km altitude with 4A Electrochemical Concentration Cell (ECC) ozonesondes used with 1680 MHz radiosondes"*, NOAA technical memorandum ERL ARL–149, operations handbook, 1986.

Kopka, H., *"LATEX – Eine Einführung"*, pp. 445, 4th ed., Addison–Wesley, Bonn, 1992.

Krankowski, D., F. Bartecki, G. G. Klees, K. Mauersberger, and K. Schellenbach, *"Measurement of heavy isotope enrichment in tropospheric ozone"*, Geophys. Res. Let., **22**, 1713–1716, 1995.

Lacroix, A. V., *"Unaccounted–for sources of fossil and isotopically–enriched methane and their contribution to the emission inventory: A review and synthesis"*, Chemosphere, **26**, 5007–557, 1993.

Lassey, K. R., D. C. Lowe, C. A. M. Brenninkmeijer, and A. J. Gomez, *"Atmospheric methane and its carbon isotopes in the southern hemisphere: Their time serie and an instructive model"*, Chemosphere, **26**, 95–109, 1993.

Lassey, K. R., D. C. Lowe, and M. R. Manning, *"A source inventory of atmospheric methane in New Zealand and its global perspective"*, J. Geophys. Res., **97**, 3751–3765, 1992.

Lide, D. R., (editor), *"CRC handbook of chemistry and physics"*, 72nd ed., CRC press, Boca Raton USA, 1991.

Lowe, D. C., C. A. Brenninkmeijer, G. W. Brailsford, K. R. Lassey, A. J. Gomez, and E. G. Nisbet, *"Concentration and ^{13}C records of atmospheric methane in New Zealand and Antarctica: evidence for changes in methane sources"*, J. Geophys. Res., **99**, 16913–16925, 1994.

Mauersberger, K., J. Morton, B. Schueler, J. Stehr, and S. M. Anderson *"Multi-isotope study of ozone: implications for the heavy ozone anomaly"*, Geophys. Res. Let., **20**, 1031–1034, 1993.

Mauersberger, K., *"Ozone isotope measurement in the stratosphere"*, Geophys. Res. Let., **14**, 80–83, 1987.

Mauersberger, K., *"Measurement of Heavy Ozone in the Atmosphere"*, Geophys. Res. Let., **8**, 935–937, 1981.

Mehlum, F., *"Birds and mammals of Svalbard"*, pp. 140, Polarhåndbok No. 5, Norsk Polarinstitutt, Oslo, 1990.

Meier, A. and B. Wuntke, *"Life strategies of* Phalaropus fulicarius *and aspects of human impact on this high arctic wader"*, in preparation for Animal Behaviour, 1997.

Meier, A. and J. Notholt, *"Determination of the isotopic abundances of heavy ozone as observed in arctic ground-based FTIR-spectra"*, Geophys. Res. Let., **23**, 551–554, 1996a.

Meier, A. and J. Notholt, *"Observation of a significant symmetry selectivity in the enrichment of isotopically heavy ozone in arctic air masses"*, 18^{th} int. polar science meeting in Potsdam in March 1996, Terra Nostra, Alfred-Wegener-Stiftung, 47–48, 1996b.

Meier, A. and J. Notholt, *"Seasonal cycles of isotopic abundances of $^{18}O/^{16}O$, $^{13}C/^{12}C$, and D/H in ozone, methane and water vapor, derived from ground-based arctic FTIR measurements"*, contribution presented at the 20^{th} General Assembly of the European Geophysical Society in Hamburg in March 1995, Annal. Geophysicae, suppl. III, Vol. **13**, p. 718, 1995.

Meier, A., J. Notholt, and S. Peil *"Column densities of stratospheric trace gases in the undisturbed arctic summer atmosphere"*, contribution presented at the 19^{th} General Assembly of the European Geophysical Society in Grenoble in April 1994, Annal. Geophysicae, suppl. III, Vol. **12**, p. 658, 1994.

Mertz, L., Infrared Physics, **7**, p. 17, 1967.

Morton, J., J. Barnes, B. Schueler, and K. Mauersberger, *"Laboratory studies of ozone"*, J. Geophys. Res., **95**, 901–907, 1990.

Norton, R. H. and C. P. Rinsland, *"ATMOS data processing and science analysis methods"*, Appl. Opt., **30**, 389–400, 1991.

Notholt, J., G. Toon, F. Stordal, S. Solberg, N. Schmidbauer, A. Meier, E. Becker, and B. Sen, *"Seasonal variations of atmospheric trace gases in the high arctic at 79° N"*, submitted to J. Geophys. Res., 1996a.

Notholt, J., A. Meier, and E. Becker *"Seasonal cycles of stratospheric HCl, $ClONO_2$, HNO_3, and NO_2 in the Arctic during winter 1994/95 compared to previous winters"*, 18^{th} int. polar science meeting in Potsdam in March 1996, Terra Nostra, Alfred-Wegener-Stiftung, p. 53, 1996b.

Notholt, J., P. v. d. Gathen, and S. Peil, *"Heterogenous conversion of HCl and $CLONO_2$ during the arctic winter 1992/1993 initiating ozone depletion"*, J. Geophys. Res., **100**, 11269–11274, 1995a.

Notholt, J., A. Meier, and S. Peil, *"Total column densities of tropospheric and stratospheric trace gases in the undisturbed Arctic summer atmosphere"*, J. Atmosph. Chem., **20**, 311–332, 1995b.

Notholt, J., I. Beninga, and O. Schrems, *"Shipborne FT-IR measurements of atmospheric trace gases on a south (33°S) to north (53°N) atlantic traverse"*, Appl. Spectrosc., **49**, 1525–1527, 1995c.

Notholt, J., *"The Moon as a light source for FTIR measurements of stratospheric trace gases during the polar night: Application for HNO_3 in the Arctic"*, J. Geophys. Res., **99**, 3607–3614, 1994a.

Notholt, J., *"FTIR measurements of HF, N_2O, and CFCs during the Arctic polar night with the moon as light source, subsidence during winter 1992/93"*, Geophys. Res. Let., **21**, 2385–2388, 1994b.

Notholt, J., *"The moon as light source for FTIR measurements of stratospheric trace gases during the polar night: application for HNO_3 in the Arctic"*, J. Geophys. Res., **99**, 3607–3614, 1993.

Notholt, J., R. Neuber, O. Schrems, and T. v. Clarmann, *"Stratospheric trace gas concentrations in the Arctic polar night derived by FTIR-spectroscopy with the moon as light source"*, Geophys. Res. Let., **20**, 2059–2062, 1993.

Oelhaf, H., T. von Clarmann, H. Fischer, F. Friedl-Vallon, C. Fritzsche, A. Linden, C. Piesch, M. Seefeldner, and W. Völker, *"Stratospheric $ClONO_2$ and HNO_3 profiles inside the Arctic vortex from MIPAS-B limb emission spectra obtained during EASOE"*, Geophys. Res. Let., **21**, 1263–1266, 1994.

Paul, A., *"Untersuchungen zur Adsorption und zum Transport von radioaktiven Ionen auf Carnauba-Wachs-Aerosolen"*, ScD. thesis, Technische Universität Carolo-Wilhelmina zu Braunschweig, 1995.

Pawson, S., B. Naujokat, and K. Labitzke, *"On the polar stratospheric cloud formation potential of the northern stratosphere"*, J. Geophys. Res., **100**, 23215–23225, 1995.

Perkins, W. D., *"Fourier Transform-Infrared Spectroscopy"*, J. Chem. Education, **63**, pp. A5–A9, 1986.

Peterson, D. B. and J. M. Margitan (editors), *"Upper atmospheric research satellite correlative measurements program (UARS-CMP) balloon data atlas"*, NASA, Washington DC, 1995.

Pierluissi, J. H., P. C. Vanderwood, and R. B. Gomez, *"Fast calculational algorithm for the Voigt profile"*, J. Qunat. Spectrosc. Radiat. Transfer, **18**, 555-558, 1977.

Pougatchev, N. S., B. J. Connor, and C. P. Rinsland *"Infrared measurements of the ozone vertical distribution above Kitt Peak"*, J. Geophys. Res., **100**, 16689–16697, 1995.

Press, W. H., S. A. Teukolsky, W. T. Vetterlind, and B. P. Flannery, *"Numerical recipes in C: the art of scientific computing"*, 2^{nd} ed., pp. 994, Cambridge University Press, 1992.

Rao, K. N. and A. Weber (editors), *"Spectroscopy of the earth's atmosphere and interstellar medium"*, Academic Press, San Diego CA, 1992.

Reisinger, A. R., N. B. Jones, W. A. Matthews, and C. P. Rinsland, *"Southern hemisphere midlatitude ground-based measurements of $ClONO_2$: Method of analysis, seasonal cycle, and long-term trend"*, J. Geophys. Res., **100**, 23183–23193, 1995.

Rex, M., P. von der Gathen, N. R. P. Harris, et al., *"In-situ measurements of stratospheric ozone depletion rates in the arctic winter 1991/92: A lagrangian approach"*, submitted to J. Geophys. Res., 1996.

Richet, P., Y. Bottinga, and M. Javoy *"A review of hydrogen, carbon, nitrogen, oxygen, sulphur, and chlorine stable isotope fractionation among gaseous molecules"*, Ann. Rev. Earth Planet. Sci., **5**, 65–110, 1977.

Rinsland, C. P., R. Zander, P. Demoulin, and E. Mahieu, *"$ClONO_2$ total vertical column abundances above the Jungfraujoch station, 1986–1994: Long-term trend and winter-spring enhancements"*, J. Geophys. Res., **101**, 3891–3899, 1996.

Rinsland, C. P., M. R. Gunson, R. Zander, and M. Lopez-Puertas, *"Middle and upper atmosphere pressure-temperature profiles and the abundances of CO_2 and CO in the upper atmosphere from ATMOS/Spacelab 3 observations"*, J. Geophys. Res., **97**, 20479–20495, 1992.

Rinsland, C. P., J. S. Levine, A. Goldman, N. D. Sze, M. K. W. Ko, and D. W. Johnson, *"Infrared measurements of HF and HCl total column abundances above Kitt Peak, 1977–1990: seasonal cycles, long-term increases, and comparison with model calculations"*, J. Geophys. Res., **96**, 15523–15540, 1991a.

Rinsland, C. P., M. R. Gunson, J. C. Foster, R. A. Toth, C. B. Farmer, and R. Zander, *"Stratospheric Profiles of Heavy Water Vapor Isotopes and CH_3D from Analysis of the ATMOS Spacelab 3 Infrared Solar Spectra"*, J. Geophys. Res., **96**, 1057–1068, 1991b.

Rinsland, C. P., L. R. Brown, and C. B. Farmer, *"Infrared spectroscopic detection of sulfur hexafluoride (SF_6) in the lower stratosphere and upper troposphere"*, J. Geophys. Res.,**95**, 5577–5585, 1990.

Rinsland, C. P., A. Goldman, F. J. Murcray, F. H. Murcray, R. D. Blatherwick, and D. G. Murcray, *"Infrared measurements of atmospheric gases above Mauna Loa. Hawaii, in February 1987"*, **93**, 12607–12626, 1988.

Rinsland, C. P., V. Malathy Devi, J.-M. Flaud, C. Camy-Peyret, M. A. H. Smith, and G. M. Stokes *"Identification of ^{18}O-Isotopic Lines of Ozone in Infrared Ground-Based Solar Absorption Spectra"*, J. Geophys. Res., **90**, 10719–10725, 1985.

Rinsland, C. P., A. Goldman, V. Malathy Devi, B. Fridovich, D. G. D. Snyder, G. D. Jones, F. J. Murcray, M. A. H. Smith, R. K. Seals jr., M. T. Coffey, and W. G. Mankin, *"Simultaneous stratospheric measurements of H_2O, HDO, and CH_4 from balloon-borne and aircraft infrared solar absorption spectra and tunable diode laser laboratory spectra of HDO"*, J. Geophys. Res., **89**, 7259–7266, 1984.

Roedel, W., *"Physik unser Umwelt – Die Atmosphäre"*, Springer Verlag, Berlin, 2. Auflage, pp. 467, 1994.

Rothman, L. et al., *"The HITRAN molecular database: Edition of 1991 and 1992"*, J. Quant. Spectrosc. Radiat. Transfer, **48**, 469–507, 1992.

Saueressig, G., P. Bergamaschi, J. N. Crowly, H. Fischer, and G. W. Harris, *"Carbon isotope effect in the reaction of CH_4 with Cl atoms"*, Geophys. Res. Let., **22**, 1225–1228, 1995.

Schoeberl, M. R. and P. A. Newman, *"A multiple-level trajectory analysis of vortex filaments"*, J. Geophys. Res., **100**, 25801–25815, 1995.

Schoeberl, M. R., L. R. Lait, P. A. Newman, and J. E. Rosenfield, *"The structure of the polar vortex"*, J. Geophys. Res., **97**, 7859–7882, 1992.

Schoeberl, M. R. and D. L. Hartmann, *"The dynamics of the stratospheric polar vortex and its relation to springtime ozone depletions"*, Science, **251**, 46–52, 1991.

Schönwiese, C.–D. und B. Diekmann, *"Der Treibhauseffekt"*, ISSN 3499-185121, paperback ed., Rowohlt Reinbeck, 1991.

Schreiber, J., *"Untersuchung und Reduktion der Eigenstrahlung des Fourierspektrometers BOMEM-DA2"*, Diplomarbeit in physics (*Master's thesis*), Universität Karlsruhe, Germany, Institut für Meteorologie und Klimaforschung, 1994.

Schueler, B., B. Morton, and K. Mauersberger, *"Measurement of isotopic abundances in collected stratospheric ozone samples"*, Geophys. Res. Let., **17**, 1295–1298, 1990.

Smithsonian Institution, *"Smithsonian meteorological table"*, 6^{th} revised ed., Washington DC, 1966.

Solomon, S., "Progress towards a quantitative understanding of Antarctic ozone depletion", Nature, **347**, 347–354, 1990.

Stößel, W., *"Fourieroptik"*, Springer Verlag Berlin, 268 pp., 1993.

Thiemens, M. H. and T. Jackson, *"Pressure dependency for heavy isotope enhancement in ozone formation"*, Geophys. Res. Let., **17**, 717–719, 1990.

Thiemens, M. H. und T. Jackson, *"New experimental evidence for production of isotopically heavy O_3"*, Geophys. Res. Let., **15**, 639-642, 1988.

Toon G. C., C. B. Farmer, P. W. Schaper, et al., *"Evidence for Subsidence in the 1989 Arctic Winter Stratosphere from Airborne Infrared Composition Measurements"*, J. Geophys. Res., **97**, 7963–7970, 1992a.

Toon G. C., C. B. Farmer, P. W. Schaper, L. L. Lowes, and R. H. Norton, *"Composition measurements of the 1989 arctic winter stratosphere by airborne infrared solar absorption spectroscopy"*, J. Geophys. Res., **97**, 7939–7961, 1992b.

Traub, W. A., K. W. Jucks, G. G. Johnson, and K. V. Chance, *"Subsidence of the arctic stratosphere determined from thermal emission of hydrogen fluoride"*, J. Geophys. Res., **100**, 11261–11267, 1995.

Vaisala (manufacturer), *"Vaisala Ozonsonde OES"*, user's manual, edition OES-T0533-13, Helsinki, Finland, April 1991.

Wehr, T., *"Bestimmung atmosphärischer Spurengehalte aus Spektren eines flugzeuggestützten Submillimeter–Radiometers"*, Diplomarbeit in physics (≈*Master's thesis*), Institut für Fernerkundung, Universität Bremen, Germany, 1993.

Weiner, E. S. C. and J. M. Hawkins, *"The Oxford guide to the english language"*, Guild Publishing by arrangement with Oxford University Press, pp. 577, 1989.

Wetzel, G., T. von Clarmann, H. Oelhaf, and H. Fischer, *"Vertical profiles of N_2O_5 along with CH_4, N_2O, and H_2O in the late Arctic winter retrieved from MIPAS–B infrared limb emission measurements"*, J. Geophys. Res., **100**, 23173–23181, 1995.

Wuntke, B., A. Meier, M. Pribbernow, and J. Ulbricht *"On the breeding ecology of the Grey–necked Phalarope in small populations"*, in preparation for Ecologica, 1997.

Wuntke, B. and A. Meier, *"Life strategies of waders in the high Arctic"*, Terra Nostra, 18^{th} int. polar science meeting, Alfred–Wegener–Stiftung, p. 83, 1996.

Zeilik, M., S. A. Gregory, and E. v. P. Smith, *"Introductory astronomy and astrophysics"*, 568 pp., Saunders College publ., Fort Worth, USA, 1992.

Appendix

A Maps and general data from arctic Svalbard

The archipelago of Svalbard has a size of 62700 km^2 and consists of the islands Spitsbergen, Nordaustlandet, Kong Karls Land, Barenstsøya, Edgeøya, Hopen, Prins Karls Forland, Bjørnøya and some minor islands. It is assumed that the vikings were the first to discover Spitsbergen before 1200 A.C. In their language *'Svalbard'* meant *'cold coast'* – a striking name. It was rediscovered in 1596 by the Dutch William Barents, who named the archipelago *Spitzbergen*, meaning acute angled or steep mountains, which is also quite descriptive. Since the Svalbard treaty has been signed in 1925, it is now under Norwegian administration. It is ruled by the *Sysselmannen* (governor) who is appointed by the Norwegian King. The capital is Longyearbyen with slightly more than 1000 inhabitants, the northernmost regular airport and even a university of its own.

The climate is high arctic and with only 200 mm water equivalent pre-

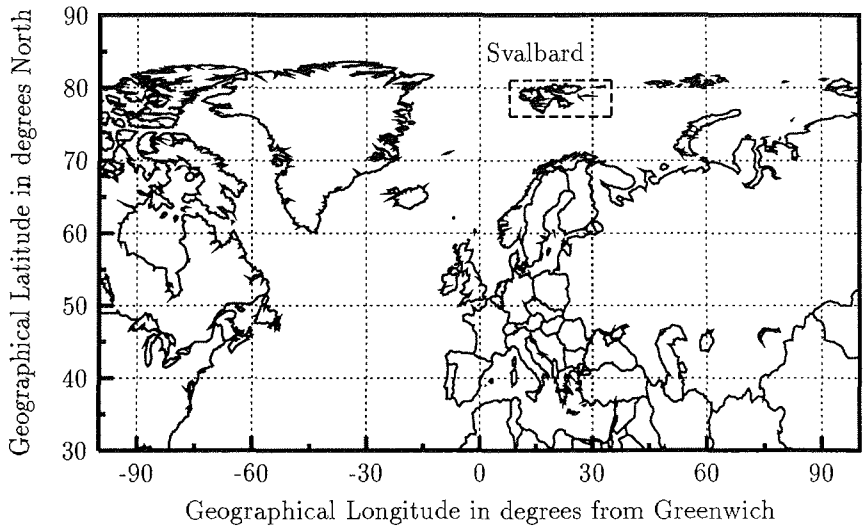

Fig. A.1: *This figure shows a sketch of the northern hemisphere. The location of the Svalbard archipelago is marked by framing. See detailed map in the next figure.*

cipitation per year a semi desert. However, due to the mild influence of the northatlantic gulf stream, it is less cold than areas at same latitude in Siberia. The coldest temperature ever recorded at Longyearbyen until 1990 was -46.3 C and the highest +21.3 C. Average temperatures are -13.9 C in March and +6.5 C in July and -4.8 C for the decades 1931 to 1961. Wind speeds are generally high.

More than 50 % of the area is declared as natural reserve and is the home to 164 indigenic vascular plant species of which 36 are endemic to arctic islands. Only 9 synanthropic species are known and all plant life is

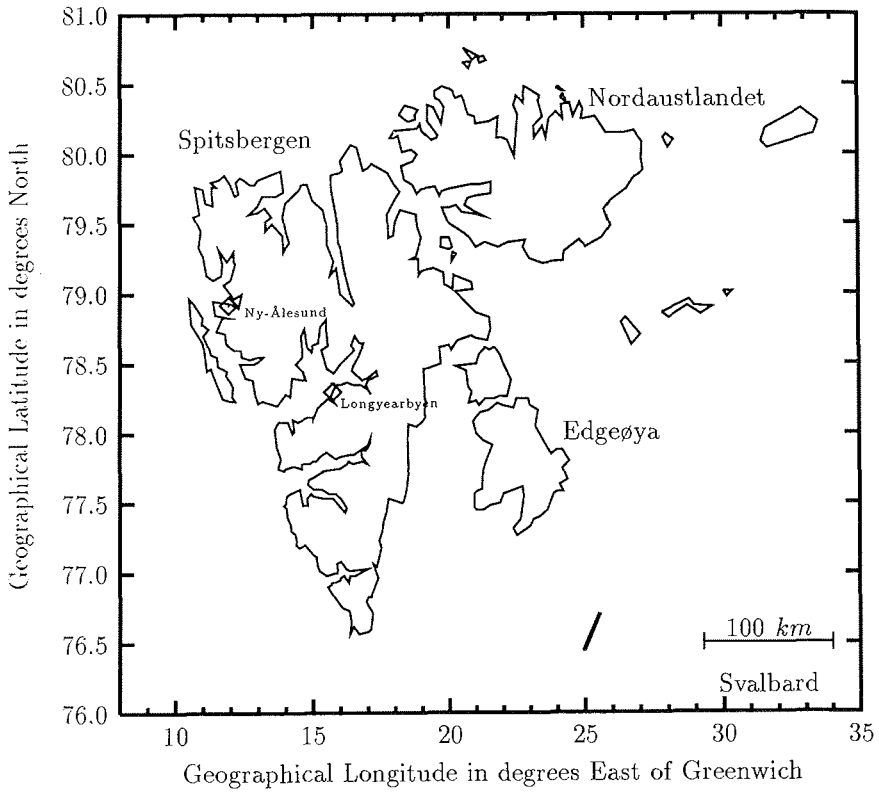

Fig. A.2: *The map shows the archipelago of Svalbard in the European high Arctic. The FTIR-spectrometer is located at Ny–Ålesund (78.92°N, 11.94°E) on the main island Spitsbergen. (Longitudinal degrees are normalized to 79° North.)*

restricted to the lowlands below 200 *m*. The botanist knows dwarf forms of trees like the arctic willow *Salix polaris* – however, these *'trees'* grow no taller than 5 *cm*. At 79°N, the polar night lasts for 120 days and for 129 julian days the sun will stay above the horizon. Only few terrestrial vertebrates will regularly winter on the islands. Indeed it is only one bird species, the Svalbard ptarmigan *Lagopus mutus hyperboreus* and three mammal species, the Svalbard reindeer *Rangifer tarandus platyrhynchus*, the Arctic fox *Alopex lagopus*, and the Polar bear *Ursus maritimus*. However, marine life is rich throughout the year and during summer there are 164 different bird species known of which 30 species breed regularly on the archipelago. In one of these species, the Grey–necked phalarope (*Phalaropus fulicarius*), the author takes particular interest (*Wuntke* and *Meier*, 1996, and *Wuntke* et al. in *Bjørdal* 1996). Results from most recent studies concerning the breeding ecology of this high arctic bird species and human impact studies are under preparation (*Meier* and *Wuntke*, 1997 and *Wuntke* et al., 1997).

Ny–Ålesund is located at the Kongsfjord (*kings bay*) and had been founded as a coal mining town. Coal had been exploited from 1918 to 1963 by the *Kings Bay Kull Compani*. It was the starting point to many famous North Pole expeditions including the zeppelin flights by Amundsen and Nobile. After a bad mining accident in 1962, the mining was closed down in 1963 and the first research station has been established by the Norwegian Polar Institute. The Kings Bay Kull Compani has been restructured and it has become the logistic backbone of the research town by supplying power, water, food, transportation, lodging, maintenance of buildings, waste management etc. The research facilities have been extended ever since, including satellite technology and a clean air research station on top of the Zeppelinfjellet with its own cable car. Ny–Ålesund has the world's northernmost post office and inhabitants are up to 200 in summer and about 20 in wintertime. There is one regular flight per week to Longyearbyen in winter and 3–4 per week in summer. Occasionally supply ships and in summer an increasing number of short–visit tourist ships come to the Ny–Ålesund pier.

Since 1990 the Alfred–Wegener–Institute is renting the *Blue House* where the all–year research station *Carl Koldewey* has been established.

In summer 1994 a new building has been added, the NDSC building, that hosts most of the atmospheric instruments like the FTIR spectrometer, sun photometer, and multiwavelength LIDAR (all operated by AWI), the microwave radiometer and a DOAS instrument optimized for stratospheric investigations (operated by the university of Bremen, Germany) and one optimized for tropospheric studies (operated by NILU, Norway), and additional rooms for guest experiments and campaigns. Before the FTIR–spectrometer was moved to the new building in November 1994, it was operated in a container originally designed to transport frozen meat. The *Koldewey* station is operated with a permanent staff of 2 scientists or engineers. (Data on history, climate, and wildlife is taken from *Holm*, 1991 and *Mehlum*, 1990. For more details on research activities see *Gernandt*, 1994 and *Bjørdal*, 1996.)

B The retrieval software

B.1 The basic SFIT algorithm from NASA

The central element in the retrieval software is the forward model that creates the model atmosphere and performs the least squares fitting between the recorded and the synthetic spectrum. The program used is SFIT (Spectral least–squares FITting program) created by *Curtis Rinsland* from NASA Langley Research Center at Hampton, VA, USA. All results presented in this manuscript are calculated with the version 1.09d, if nothing else is specified. In the sections 4.4 and 4.6 all data is reanalysed for the reasons discussed in section 2.3 with the pre-release of the latest version 1.09e that became available on the 31/May/1996.

The documentation shipped with SFIT is sparse and other sources of information are quite scattered. The documentation shipped with the diskettes gives no details on the algorithms used and focusses on the operation of the program. There are no hints on publications or other sources of information given in the documentation. However, some of the underlying physics are found in chapters 2 and 3 of the text book edited by *Rao* and *Weber* (1992), where *Rinsland* is one of the authors. More details can be found in *Rinsland* (1990 and 1991a) and *Norton* and *Rinsland* (1991). The description of SFIT itself is so brief that it is quoted from the documentation almost without abridgement:

"SFIT is a menu–driven, nonlinear least–squares spectral fitting program designed for the retrieval of total vertical column amounts from infrared solar absorption spectra recorded with a Fourier transform spectrometer. Up to 5 gases may be retrieved simultaneously from fittings of intervals up to about 4 cm^{-1} wide (for a monochromatic point spacing of 0.0005 cm^{-1}). Solar CO lines and a wide variety of instrumental parameters may be modeled and either constrained to preassigned values or fitted. The program runs on 386 or 486 PCs with a minimum of 4 MB of memory. [..] Up to 200 spectra may be fitted sequentially with a single run of SFIT 1.09d. Additional programs are provided for obtaining hard copies, generating SFIT–compatible binary files, running atmospheric ray tracing calculations, and generating line–by–line simulations."

The wide variety of instrumental parameters that SFIT can model include the maximum OPD, the FOV, a variety of common apodization functions, offsets in the wavenumber calibration, the zerolevel offset, the 100 % transmission level, the slope of the 100 % transmission level, a simple phase error, and channel spectra. It can be added that SFIT runs very stable and even slightly faster in a DOS fullscreen session of IBM's operating system OS/2 2.x and 3.0. The program is also available as a true 32 bit executable for OS/2. The source code has successfully been ported to OS/2 by *James Hannigan* from NCAR at Boulder and is significantly faster than the original DOS version. However, the results are identical for all variants mentioned.

Before the retrieval of total columns is started with the SFIT program, the observed zenith angle of the IR source used, i.e. the sun or the moon, is determined. This is performed with the commercial program SPITZB[11] from BRUKER, which calculates the astronomical and the observed angle of the sun and the moon, the corresponding air mass factor, and the illuminated area of the moon in percent from the given time, date and location. The meaning of the air mass factor and the uncertainties of the zenith angle determination are discussed in chapter 3. With the calculated observed zenith angle, the creation of the model atmosphere is started. Additionally, a pressure and temperature profile and a set of *a priori* VMR profiles are needed. From this input data, 3 files are created with the FASTCOD[12] program, which represent the model atmosphere for the subsequent use with SFIT. The files created are 1) the MAS file that contains the air mass in units of $cm \cdot atm$ for each of the 29 model layers for the observed zenith angle given and for a zenith angle of zero degrees; 2) the PTP file that contains the pressure–temperature profile with weighted average temperatures and pressures for each model layer and the underlying height scheme used; 3) the MIX file that contain the pressure weighted average VMR values for each model layer and each of the 56 species supported by SFIT.

A set of *a priori* VMR profiles is shipped with the SFIT package which

[11]This is a customized version of the SUN_MOON program from the sun-tracker arrangement. The software is sold together with the hardware only.

[12]This program is from the RAYTRACE folder of the SFIT package and is a derivative of the software with identical name from *Clough* et al., 1986.

is known as the REFMOD95 file. The profiles included are derived from a series of ATMOS space missions for most of the species (e.g. *Norton* and *Rinsland* 1991, *Rinsland* et al. 1991b). However, some profiles are also taken from the US standard atmosphere, from balloon experiments, or include model predictions for altitudes not sampled (e.g. *Smith*, 1982). For a number of molecules, the VMR profiles from the REFMOD95 set are unrealistic for high latitudes. Tropospheric pollutants like CO or $C2H2$ have no sources in the polar regions and the tropopause is typically lower. Before September 1995, a modified set of VMR profiles was used. Wherever arctic or subarctic data were available (e.g. *Oelhaf* et al. 1994, *Clarmann* et al. 1993, *Engel* et al,. 1994), these data were inserted into the REFMOD95 data set as well as two profiles taken from FASTCOD2 (*Clough* et al., 1986) for N_2O and NO_2 for *'subarctic'* conditions. The difficulty with this customized ARCTIC dataset is that the ratios of certain trace gases are not representing a realistic chemical equilibrium in all altitudes. The self consistency of this VMR profile set is not good enough to perform the profile optimization given in chapter 4.

Since September 1995 an improved VMR profile set has become available from *Geoffrey Toon* (private communication, 1995), which is termed the REFTOON VMR set in this work. The profiles are derived from mid–latitude balloon experiments described in (*Peterson* and *Margitan*, 1995). The mid–latitudinal profiles are transformed to high latitudes by the subsidence operation (see chapter 4) as suggested by *Toon* (1989) and as described in (*Notholt* et al., 1996a). This data set combines two advantages. The given set of VMR profiles is highly consistent and the latitudinal changes in the profiles are accounted for in a manner that preserves the ratios of any two profiles. This is an important aspect. Changes in the observed total column from one day to another can be ascribed to chemical, to dynamical or to both processes. Dynamical changes do not change the ratio of chemically inert gases at a given altitude, which therefore can be used as tracers for dynamical effects and can serve as a basis for estimating the chemical impact on an active species (*Notholt*, 1994b).

B.2 New extensions: the SFIT TOOLS

This section gives only a brief description on the general performance of some of the programs from the SFIT–TOOLS developed by the author. In a separate volume the printed source code is available from the author. The latest version of the SFIT–TOOLS package can be downloaded via INTERNET from the anonymous ftp–server:

'ftp.irf.se/pub/NDSC/sfit-tools' (IP 192.71.13.4)

and includes a detailed manual on all programs. However, this site might change in the future, but the actual INTERNET location can be obtained by writing an email to my new address (Arndt.Meier@irf.se) or to any NDSC member. The whole package consists of some 20 programs with a total size of more than 2 Mbytes. All programs are written in *C'* and are executable under DOS and under the virtuell DOS of OS/2. An edition in true OS/2 code is under preparation.

B.2.1 PROFIL

To perform any operations on the VMR profiles, the program PROFIL is developed. It makes use of the air mass, pT profile and VMR file created for SFIT and presents any species selected by the user from a menu on a graphics screen. The vertical profile of VMR and total number density are displayed and the exact total column corresponding to this *a priori* profile is given. The user can select among the numerous manipulation tools, like a simple vertical shift of the whole profile, the tropopause displacement, a stratospheric stretching with the DOSA parameter, the multiplication of a selected altitude range, the normalization of the profile to a given total column amount, direct manipulation by grabbing the profile with the mouse, undo, a complete sub-menue with similar tools to deal with isotopic corrections (see chapter 5), etc. Although the program is very simple to use, the user has to be aware of the consequences implied by his manipulations.

For optimizing VMR profiles, one has to run SFIT again after each manipulation to see the effects. It is recommended to make use of the backup file, so that changes applied with PROFIL are reproducible. With

some practice, line shape errors can be significantly reduced after few iterations. However, the whole procedure is *'man and machine'* and hence time often is the limiting factor in daily analysis. It is highly valuable in case studies, but an automated program is needed for regular performance.

B.2.2 OPTIVMR

An automation of VMR optimization is given with the program OPTIVMR and some additional small programs to run the batch job, namely OPTINI to create an initial stearing file, ISITOKAY to select and evaluate individual microwindows, and WHOSNEXT that handles the copying of most files involved in the batch. OPTIVMR can apply $DOSA$ stretching, shifting of the whole profile, and tropopause displacement operations to the VMR of any specific, all, or a preselected group of species. It can handle up to 20 different microwindows in one run with arbitrary spectra, zenith angles and principal species each. The quantity traced by OPTIVMR is the total standard deviation of the residuals in each microwindow. Within each microwindow, the user may set a weighting box to pronounce the center of a specific line within that microwindow and each microwindow can be assigned an individual weight among the set of all microwindows for the search of the global minimum. The search for the global minimum in total residuals, which is assumed to give the most adequate approximation to the true VMR profile, can be set either to *'actively'*, i.e. following the gradient in total standard deviation, or to *'passively'*, i.e. scanning a selected interval of $DOSA$ or shift values with a selected stepsize. However, combinations of options of the same group, say shifting and $DOSA$ stretching, still have to be performed in subsequent runs of the batch. All relevant information is collected in individual log–files, so that the history of residuals and total columns retrieved is available for graphical presentation after the batch is completed. On a normal 486 PC a typical run with 15 microwindows and 40 iteration steps can be done over night. The total standard deviation for each microwindow as a function of the $DOSA$ or shift amount, as plotted in Figure 4.5, is shown on a graphics screen at the end of the batch.

B.2.3 PBPVIEW

This program displays the results from a retrieval with SFIT on a graphics screen. The recorded spectrum, the simulation and the residuals are shown in different color over wavenumber. In a status bar the total standard deviation, the zenith angle, and the positions of two cursors are given that can be moved through the spectrum by mouse and key-pad independently. PBPVIEW from the SFIT–TOOLS is also shipped with the SFIT–package from *Curtis Rinsland* and has become the standard display program for SFIT.

B.2.4 CONTRIB

Contrib is a batch that calculates a contribution plot (appendix C) with SFIT for any spectral interval specified. It comprises the executables CFGLFIND, CREATDUM, KILLDUMM, HLPCONTR, and CON2GNU. With the help of CFGLFIND the spectroscopic data is split up into subsets that hold data on exactly one species. SFIT is then run on each of these spectroscopic subsets with zero iteration steps. CON2GNU then prepares one comprehensive file from all the individual SFIT runs, i.e. a files with ASCII columns is created with one column for each species in the order of maximum absorption. Details on the retrieval are included in the header and an optional plotting file is created for the Freeware plotting program GNUPLOT.

B.2.5 ECC2REF, AED2PT, and AED2VMRW

This group of programs converts *in situ* sonde data given in the NASA-Ames format into the formats required for the model atmosphere of SFIT. All programs have a graphical display with mouse support and allow to fit standard profiles smoothly to the sonde data at the peak altitude. AED2PT converts radio sonde data into a pT profile, AED2VMRW yields the isotope corrected water vapor VMR profiles from the relative humidity data, and ECC2REF reads ECC ozone sonde data and converts them into isotope corrected ozone VMR profiles.

B.2.6 HIT2CFGL, CFGLHEAV, and MERGECFG

These programs are required to convert spectroscopic data from the HITRAN96 data base into subsets of CFGL–files in the SFIT 1.09e format. HIT2CFGL reads the HITRAN96 spectral file and creates subsets of 20 cm^{-1} width each. In this process the molecule indices are renamed according to the SFIT conventions and the data format is adapted. CFGLHEAV allows to rename molecule indices, in particular to toggle the status of isotopomers between being a dependent or an independent species. Finally, MERGECFG allows to replace the spectroscopic data of an individual species by data from the earlier SFIT 1.09d spectral files (BFGL–files). This allows in particular to insert missing species like the CFCs into the spectroscopic data from the HITRAN96 edition.

C Atlas of important spectral microwindows

This appendix contains a list of important spectral microwindows most of which are used to determine the total column amounts given in this work. In Table C.1 the microwindows of the atlas are listed by the principal species in alphanumerical order and include some details on the spectroscopic properties. A detailed isotopic ascription is only given for the rare isotopomers.

For each entry in the table the reader finds a detailed description in the atlas with two figures each. The first figure, termed the contribution plot, gives an example of a recorded spectrum over typically twice the size of the microwindow used in the analysis. This figure shows the contribution to the total signal for each species individually and the simulations are shifted for clarity by the amount specified in the key. For the creation of the single species simulations a subset of the data base is used, which contains exclusively spectroscopic data of the species under study. The calculated absorptions represent the total columns according to the *a priori* VMR profiles used and are uncertain by several percent. Wherever possible, the *a priori* VMR–profile is set to an adequate value known from previous analysis. However, for weak absorbers that are not quantifiable reliably in our spectra, like SO_2, H_2CO, SO_2, ClO, etc, the uncertainty is much larger.

The second figure for each microwindow gives an example of a simulated spectrum fitted to the recorded spectrum. The lower part shows the experimental or recorded spectrum (solid line) and the simulated spectrum (dashed line, shifted for clarity), while the upper part of the figure shows the residual (recorded minus simulated spectrum). Below the second figure there is a short table that describes the spectrum and the settings used in the analysis. All species that have absorption lines in the spectral interval shown in the contribution plot example are listed in the order of descending absorption strength. They are grouped in 3 categories: 1) major species with $\geq$ 1 %, 2) minor species with $\geq$ 0.1 %, and 3) weak species with $<$ 0.1 % absorption strength in the example.

Tab. C.1: *This table contains a list of important spectral microwindows used in atmospheric FTIR spectroscopy. The species of major interest for each spectral interval is listed in alphanumerical order. If no single lines but bands are present, the line position is marked with an asterisk '*)' and the line given represents the strongest line occurring in that band. Detailed figures and additional information for each entry is found on the page given in the last column. ν_0 is the central line position, index is the AFGL/SFIT species encoding, I the intensity in $cm^{-1}/(molec.\ cm^{-2})$ at 296 K, E''_{LST} is the lower state energy, γ_{air} denotes the air broadening coefficient (HWHM) and α_T is the coefficient for the temperature dependence of γ_{air}. Spectroscopic data are taken from the HITRAN96 data base except for C_2H_4, HO_2NO_2, and CFC's, which are from the SFIT package.*

species	index	ν_0 in in cm^{-1}	I in $cm/molec.$	γ_{air} in cm^{-1}/atm	E''_{LST} in cm^{-1}	α_T of γ_{air}	page
C_2H_2	401	776.171	7.69E-21	0.0702	1177.75	0.75	195
C_2H_2	401	3250.662	2.02E-19	0.0803	214.10	0.75	303
C_2H_2	401	3304.965	2.46E-19	0.0818	105.89	0.75	307
C_2H_4	391	947.031	4.72E-19	0.0750	65.84	0.50	213
C_2H_6	381	2976.795*)	1.94E-20	0.1000	121.47	0.50	293
CCl_2F_2	321	921.112*)	2.85E-20	0.0550	275.43	0.75	211
	321	921.725*)	5.83E-20	0.0550	9.85	0.75	
	321	923.117*)	6.98E-20	0.0550	9.66	0.75	
CCl_2F_2	321	1160.947*)	9.19E-20	0.0300	80.00	0.50	239
	321	1161.065	8.88E-20	0.0300	50.00	0.50	
CH_3D	63	1199.995	6.97E-24	0.0600	251.26	0.75	241
CH_3D	63	1204.305	6.22E-25	0.0600	89.90	0.75	245
	63	1204.305	5.92E-24	0.0600	164.24	0.75	
	63	1204.328	9,61E-24	0.0600	328.22	0.75	
CH_4	61	1202.421	1.06E-21	0.0499	1096.13	0.75	243
CH_4	61	2835.676	1.88E-22	0.0661	62.88	0.75	285
CH_4	61	2903.876	6.19E-22	0.0614	219.91	0.75	287
$^{13}CH_4$	62	1234.226	1.79E-22	0.0528	575.25	0.75	251
CHF_2Cl	421	829.044	2.27E-20	0.0300	230.00	0.50	205
ClO	181	833.297	2.23E-21	0.0930	47.71	0.75	206
	181	833.297	2.23E-21	0.0930	47.71	0.75	
ClO	181	834.625	2.07E-21	0.0930	37.18	0.75	207
	181	834.625	2.07E-21	0.0930	37.18	0.75	

species	index	ν_0 in in cm^{-1}	I in $cm/molec.$	γ_{air} in cm^{-1}/atm	E''_{LST} in cm^{-1}	α_T of γ_{air}	page
$ClONO_2$	271	780.220*)	2.01E-22	0.1400	36.99	0.50	197
CO	51	2111.543	3.72E-19	0.0599	138.39	0.69	261
CO	51	2158.300	3.34E-19	0.0667	23.07	0.69	263
CO_2	23	2626.630	4.31E-25	0.0734	100.14	0.73	271
COF_2	361	1231.020*)	2.22E-20	0.0845	164.71	0.94	249
COF_2	361	1233.455*)	6.22E-21	0.0534	689.96	0.75	251
	361	1234.408*)	3.10E-20	0.0845	94.00	0.94	
COF_2	361	1951.948*)	3.70E-20	0.0845	70.63	0.94	255
H_2O	11	2819.449	6.38E-24	0.0839	782.41	0.64	281
H_2O	11	3162.084	2.75E-24	0.0338	1690.67	0.64	297
	11	3162.131	1.08E-24	0.0465	2142.60	0.64	
	11	3163.827	1.78E-23	0.0959	136.16	0.64	
H_2O	11	3249.199	2.04E-24	0.0720	2275.37	0.64	301
	11	3249.472	1.58E-23	0.0733	982.91	0.64	
$H_2{}^{18}O$	12	1205.080	8.76E-25	0.0967	1279.80	0.68	247
$H_2{}^{18}O$	12	3165.101	2.79E-24	0.0997	23.76	0.64	297
$H_2{}^{18}O$	12	3205.412	2.01E-24	0.0879	172.88	0.64	299
$H_2{}^{17}O$	13	3249.938	1.96E-25	0.0853	224.31	0.64	301
$H_2{}^{17}O$	13	3305.877	2.48E-25	0.0916	79.23	0.64	307
$H^{35}Cl$	151	2775.761	2.88E-19	0.0541	312.73	0.46	277
$H^{35}Cl$	151	2821.569	4.16E-19	0.0724	125.21	0.71	283
$H^{35}Cl$	151	2925.897	4.19E-19	0.0793	20.88	0.76	291
$H^{37}Cl$	152	2904.111	7.55E-20	0.0894	0.00	0.74	287
HCN	281	3287.248	3.23E-19	0.1116	106.42	0.50	305
HCN	281	3305.544	1.30E-19	0.1431	8.87	0.50	307
HDO	491	1206.020	3.98E-24	0.0605	709.17	0.64	247
	491	1206.036	3.98E-24	0.0595	709.17	0.64	
	491	1206.366	2.25E-24	0.0786	683.61	0.64	
HDO	491	2657.330	5.38E-24	0.0952	221.84	0.64	273
HDO	491	2660.512	5.47E-24	0.0930	217.04	0.64	275
HF	141	4038.963	2.37E-18	0.0895	41.11	0.51	309
HNO_3	121	868.524*)	1.15E-20	0.1100	130.31	0.75	209
HO_2NO_2	361	802.579*)	7.53E-22	0.0845	503.16	0.94	203
	251	802.812*)	6.25E-22	0.1000	104.56	0.75	
	251	803.031*)	1.26E-22	0.1000	363.66	0.75	
N_2	411	2403.565	3.31E-28	0.0487	143.22	0.50	265
N_2	411	2411.127	1.55E-28	0.0481	179.02	0.50	267
N_2	411	2418.652	2.83E-28	0.0476	218.78	0.50	269
N_2O	41	1202.026	1.21E-21	0.0700	620.59	0.79	243
N_2O	41	2806.313	7.54E-22	0.0814	37.71	0.76	279

species	index	ν_0 in in cm^{-1}	I in $cm/molec.$	γ_{air} in cm^{-1}/atm	E''_{LST} in cm^{-1}	α_T of γ_{air}	page
NH_3	111	967.3462	5.45E-19	0.0998	85.86	0.75	215
NO	81	1900.071	2.03E-20	0.05	80.22	0.71	253
	81	1900.071	2.32E-20	0.05	80.22	0.71	
	81	1900.070	1.77E-20	0.05	80.22	0.71	
NO	81	1900.082	2.32E-20	0.05	80.30	0.71	253
	81	1900.082	1.77E-20	0.05	80.30	0.71	
	81	1900.082	2.03E-20	0.05	80.30	0.71	
NO_2	101	2914.643	5.85E-21	0.0630	46.40	0.50	289
	101	2914.645	5.34E-21	0.0630	46.41	0.50	
	101	2914.652	5.58E-21	0.0630	54.65	0.50	
O_3	31	781.181	3.97E-22	0.0688	357.50	0.76	
O_3	31	782.653	2.54E-22	0.0708	446.56	0.76	201
	31	782.772	2.83E-22	0.0707	376.83	0.76	
O_3	31	1146.669	4.28E-22	0.0726	301.67	0.76	237
O_3	31	2775.826	6.46E-23	0.0803	50.64	0.76	277
O_3	31	3039.987	1.31E-22	0.0714	158.75	0.76	295
	31	3040.111	2.00E-22	0.0764	30.20	0.76	
$^{16}O^{18}O^{16}O$	31	975.250	1.69E-23	0.0715	545.59	0.76	217
$^{16}O^{18}O^{16}O$	33	976.388	1.86E-23	0.0714	518.74	0.76	219
	33	976.711	1.12E-23	0.0704	595.54	0.76	
$^{16}O^{18}O^{16}O$	33	977.925	3.10E-23	0.0704	421.41	0.76	221
$^{16}O^{18}O^{16}O$	33	979.480	3.80E-23	0.0691	374.92	0.76	223
$^{16}O^{18}O^{16}O$	33	980.732	3.60E-23	0.0748	369.64	0.76	225
$^{16}O^{18}O^{16}O$	33	989.118	5.14E-23	0.0716	221.97	0.76	227
$^{16}O^{18}O^{16}O$	33	993.767	2.74E-23	0.0714	228.19	0.76	229
	33	993.791	4.56E-23	0.0706	172.17	0.76	
$^{16}O^{18}O^{16}O$	33	1002.610	1.04E-23	0.0714	63.48	0.76	231
	33	1002.621	2.06E-23	0.0697	410.21	0.76	
$^{16}O^{16}O^{18}O$	32	1002.606	4.04E-23	0.0725	328.42	0.76	231
	32	1002.612	4.94E-23	0.0748	330.18	0.76	
$^{16}O^{16}O^{18}O$	32	1043.440	6.96E-23	0.0725	230.37	0.76	233
	32	1044.013	4.60E-23	0.0723	288.06	0.76	
	32	1044.217	5.16E-23	0.0728	266.41	0.76	
$^{16}O^{16}O^{18}O$	32	1090.372*)	2.11E-24	0.0704	57.35	0.76	235
OCS	191	2045.084	6.79E-19	0.0872	300.54	0.50	257
	191	2045.579	7.13E-19	0.0876	285.13	0.50	
OCS	191	2055.861	9.17E-19	0.0964	48.68	0.50	259
SF_6	501	947.930*)	1.45E-20	0.0500	79.24	0.65	213
	501	947.959*)	1.47E-20	0.0500	96.18	0.65	

A two step wide–narrow retrieval is used, if the table below the figure indicates two intervals. I) denotes the wide interval where all major species with broad absorption features are fitted. The *a priori* VMR profiles are then rescaled according to the results in interval I) and are kept constant in the second stage of the retrieval, which is then restricted to the narrow interval II) and to a subset of species. A typical example for this is the retrieval of $ClONO2$ (page 197) as discussed on page 73.

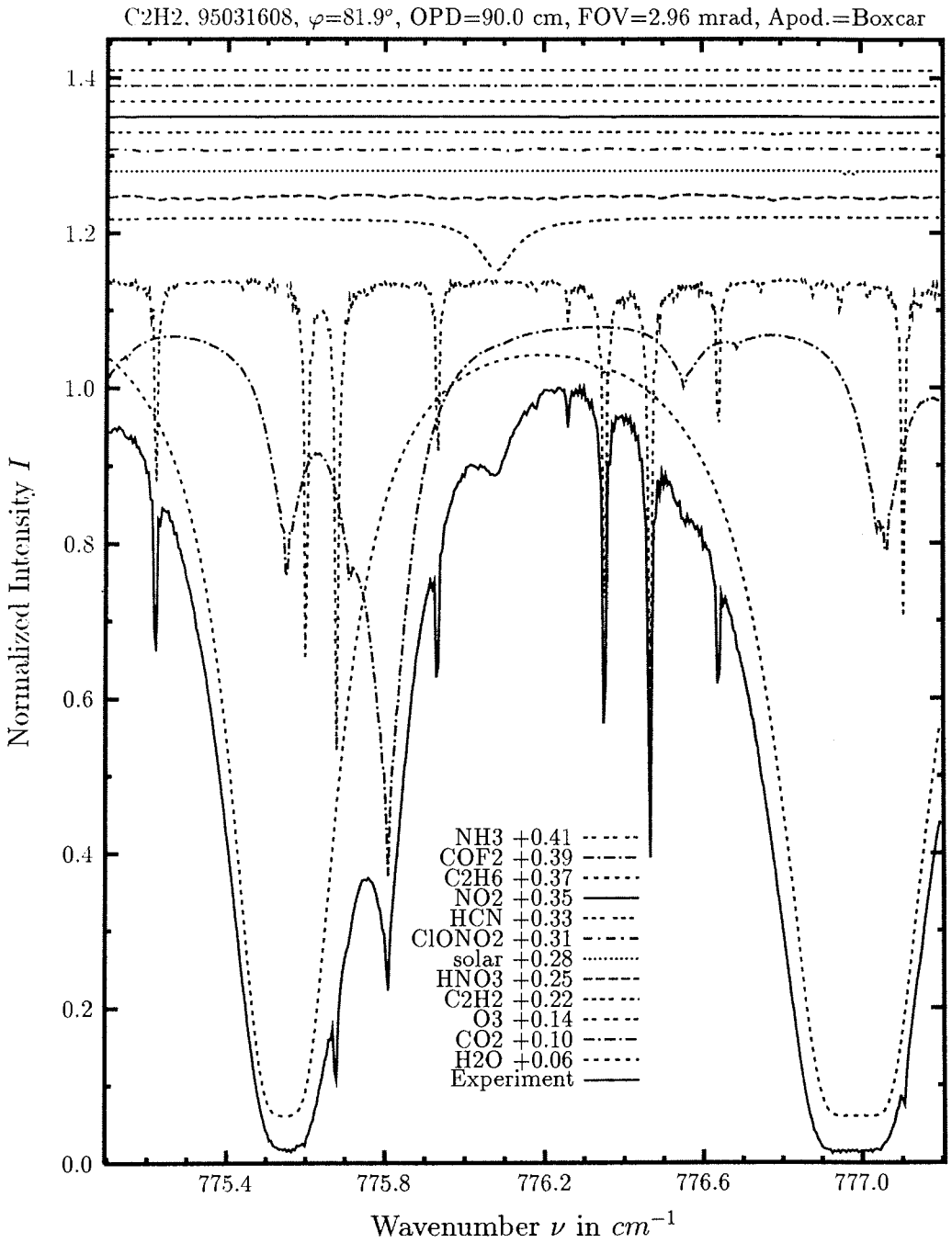
C2H2, 95031608, φ=81.9°, OPD=90.0 cm, FOV=2.96 mrad, Apod.=Boxcar
Normalized Intensity I
Wavenumber ν in cm⁻¹
0.0
0.2
0.4
0.6
0.8
1.0
1.2
1.4
775.4
775.8
776.2
776.6
777.0
NH3 +0.41
COF2 +0.39
C2H6 +0.37
NO2 +0.35
HCN +0.33
ClONO2 +0.31
solar +0.28
HNO3 +0.25
C2H2 +0.22
O3 +0.14
CO2 +0.10
H2O +0.06
Experiment

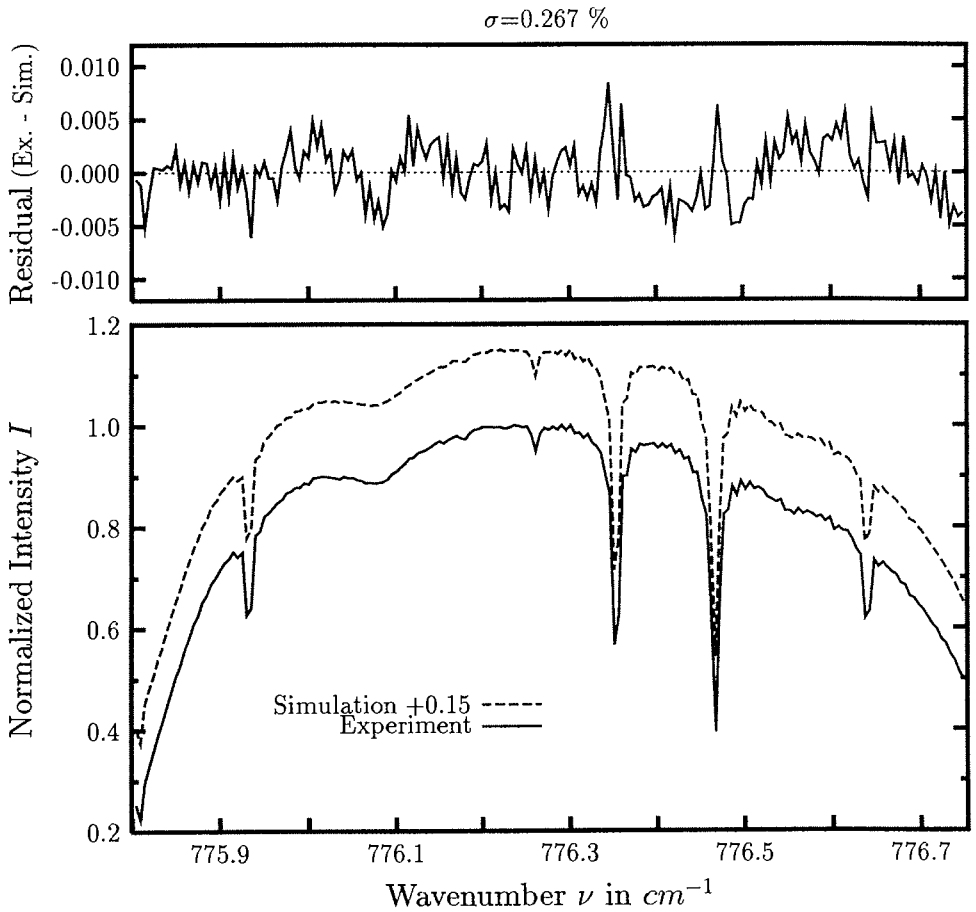

investigated species	: **C_2H_2**
line position ν_0	: 776.081 cm^{-1}
major species	: H_2O. CO_2, O_3, C_2H_2
minor species	: HNO_3, solar, $ClONO_2$, HCN, NO_2
weak species	: C_2H_6, COF_2, NH_3, ClO
name of the spectrum	: 95031608
zenith angle, apodization	: 81.9°, boxcar
max. OPD, field of view	: 90.0 cm, 2.96 $mrad$
spectral interval fitted	: 775.80 - 776.75 cm^{-1}
retrieved total column	: $1.23 \cdot 10^{16}\, cm^{-2}$

comments: C_2H_2 is significantly less abundant in polar summer than compared to the spring data shown.

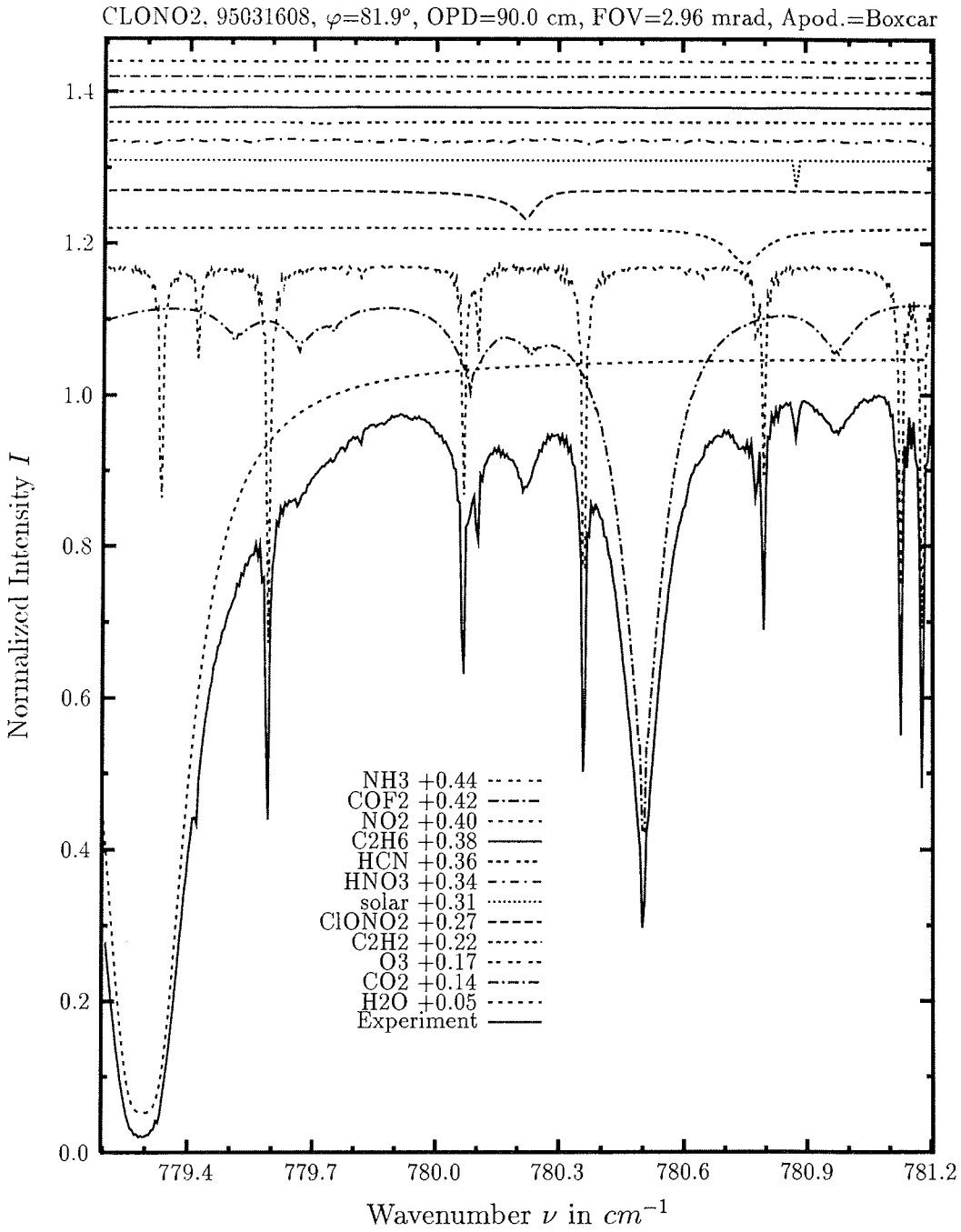
CLONO2, 95031608, φ=81.9°, OPD=90.0 cm, FOV=2.96 mrad, Apod.=Boxcar
Normalized Intensity I
Wavenumber ν in cm⁻¹
0.0
0.2
0.4
0.6
0.8
1.0
1.2
1.4
779.4
779.7
780.0
780.3
780.6
780.9
781.2
NH3 +0.44
COF2 +0.42
NO2 +0.40
C2H6 +0.38
HCN +0.36
HNO3 +0.34
solar +0.31
ClONO2 +0.27
C2H2 +0.22
O3 +0.17
CO2 +0.14
H2O +0.05
Experiment

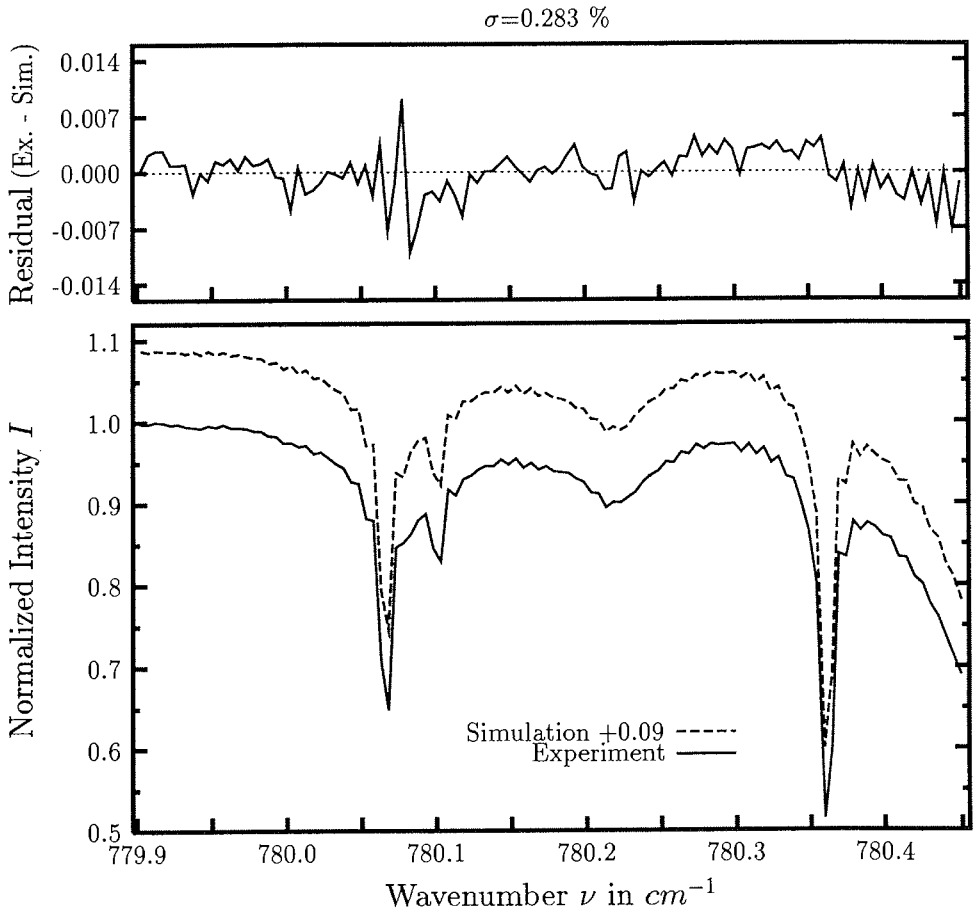

investigated species	: **$ClONO_2$**
line position ν_0	: 780.220*) cm^{-1}
major species	: H_2O, CO_2, O_3, C_2H_2, $ClONO_2$, solar
minor species	: HNO_3, HCN, C_2H_6, NO_2
weak species	: COF_2, NH_3
name of the spectrum	: 95031608
zenith angle, apodization	: 81.9°, boxcar
max. OPD, field of view	: 90.0 cm, 2.96 $mrad$
spectral interval fitted	: I) 779.55 - 781.10 cm^{-1}, II) 779.90 - 780.45 cm^{-1}
retrieved total column	: $3.70 \cdot 10^{15}$ cm^{-2}

comments: The VMR profile of CO_2 is scaled to the amount determined in the interval I) and then kept constant in the narrow retrieval interval II).

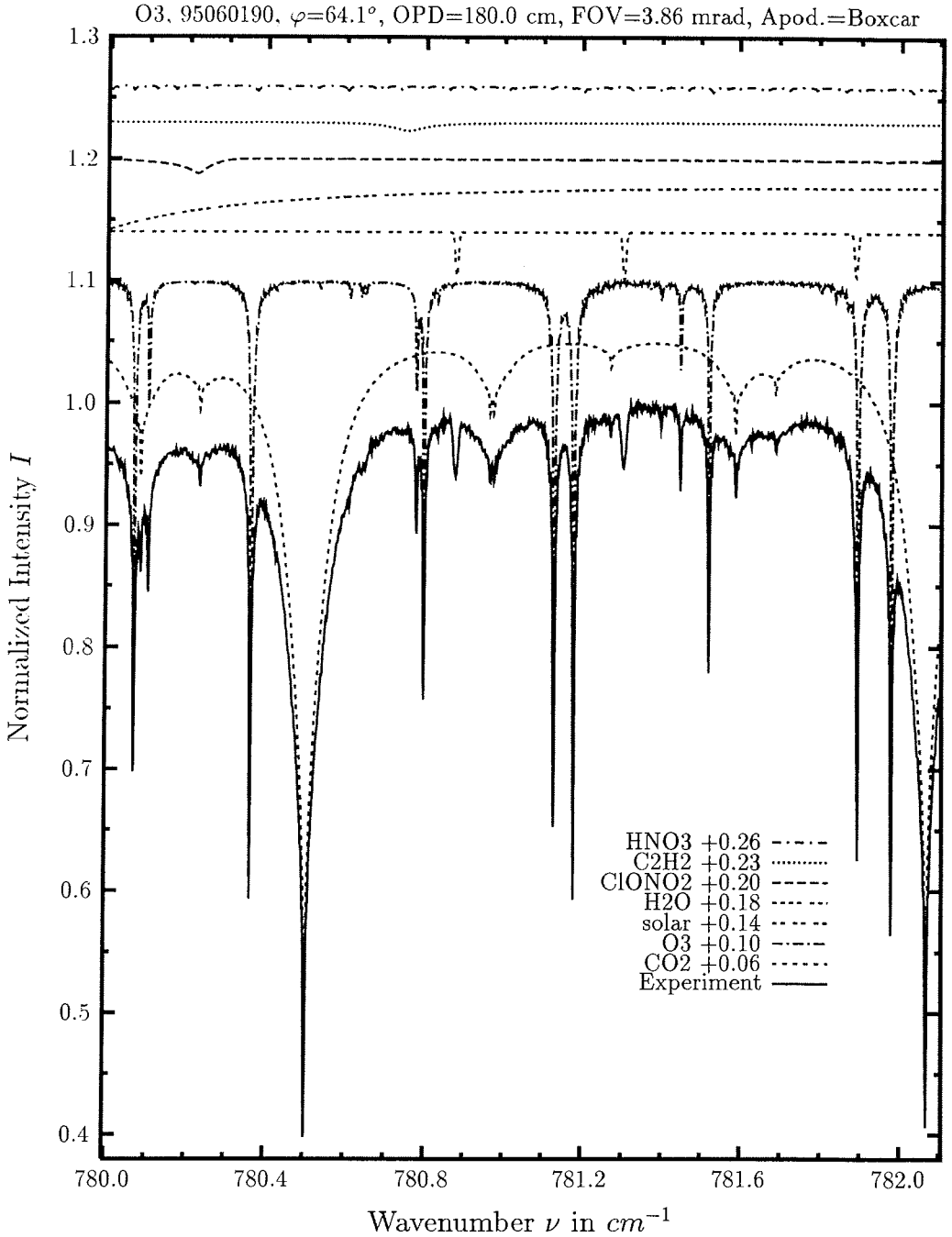
O3, 95060190, φ=64.1°, OPD=180.0 cm, FOV=3.86 mrad, Apod.=Boxcar
Normalized Intensity I
Wavenumber ν in cm⁻¹
1.3
1.2
1.1
1.0
0.9
0.8
0.7
0.6
0.5
0.4
780.0
780.4
780.8
781.2
781.6
782.0
HNO3 +0.26
C2H2 +0.23
ClONO2 +0.20
H2O +0.18
solar +0.14
O3 +0.10
CO2 +0.06
Experiment

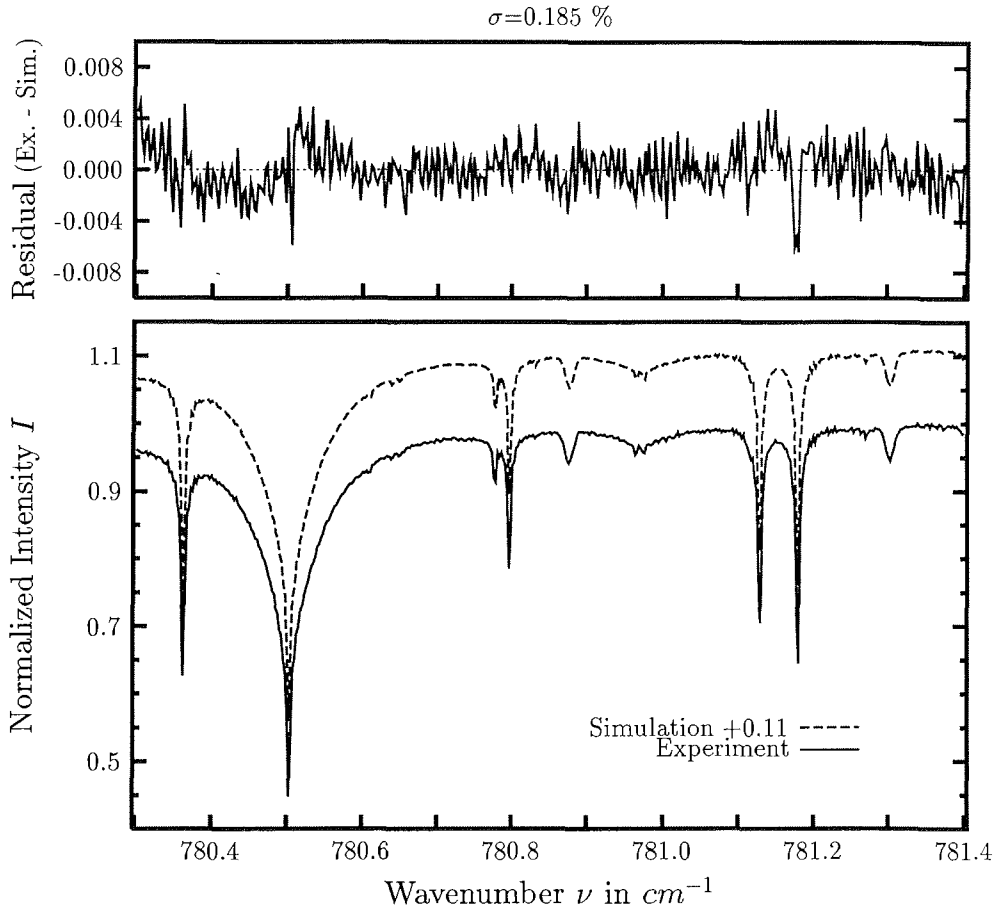

investigated species	: **O_3**
line position ν_0	: 781.130, 781.181 cm^{-1}
major species	: CO_2, O_3, solar, H_2O, $ClONO_2$
minor species	: C_2H_2, HNO_3
weak species	:
name of the spectrum	: 95052870
zenith angle, apodization	: 58.6°, boxcar
max. OPD, field of view	: 180.0 cm, 3.86 $mrad$
spectral interval fitted	: 780.30 – 781.40 cm^{-1}
retrieved total column	: $1.00 \cdot 10^{19}\, cm^{-2}$

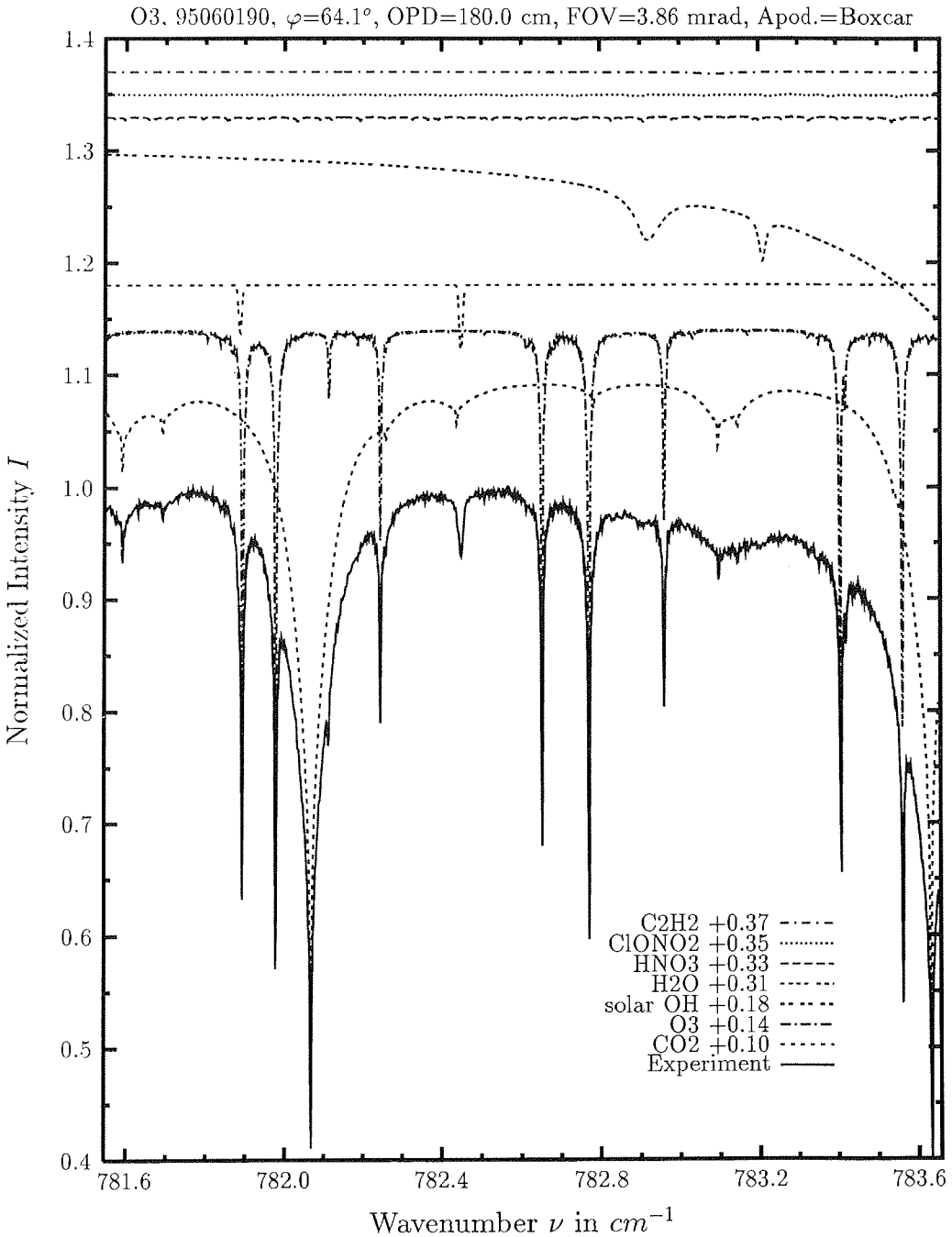
O3, 95060190, φ=64.1°, OPD=180.0 cm, FOV=3.86 mrad, Apod.=Boxcar
Normalized Intensity I
Wavenumber ν in cm⁻¹
1.4
1.3
1.2
1.1
1.0
0.9
0.8
0.7
0.6
0.5
0.4
781.6
782.0
782.4
782.8
783.2
783.6
C2H2 +0.37
ClONO2 +0.35
HNO3 +0.33
H2O +0.31
solar OH +0.18
O3 +0.14
CO2 +0.10
Experiment

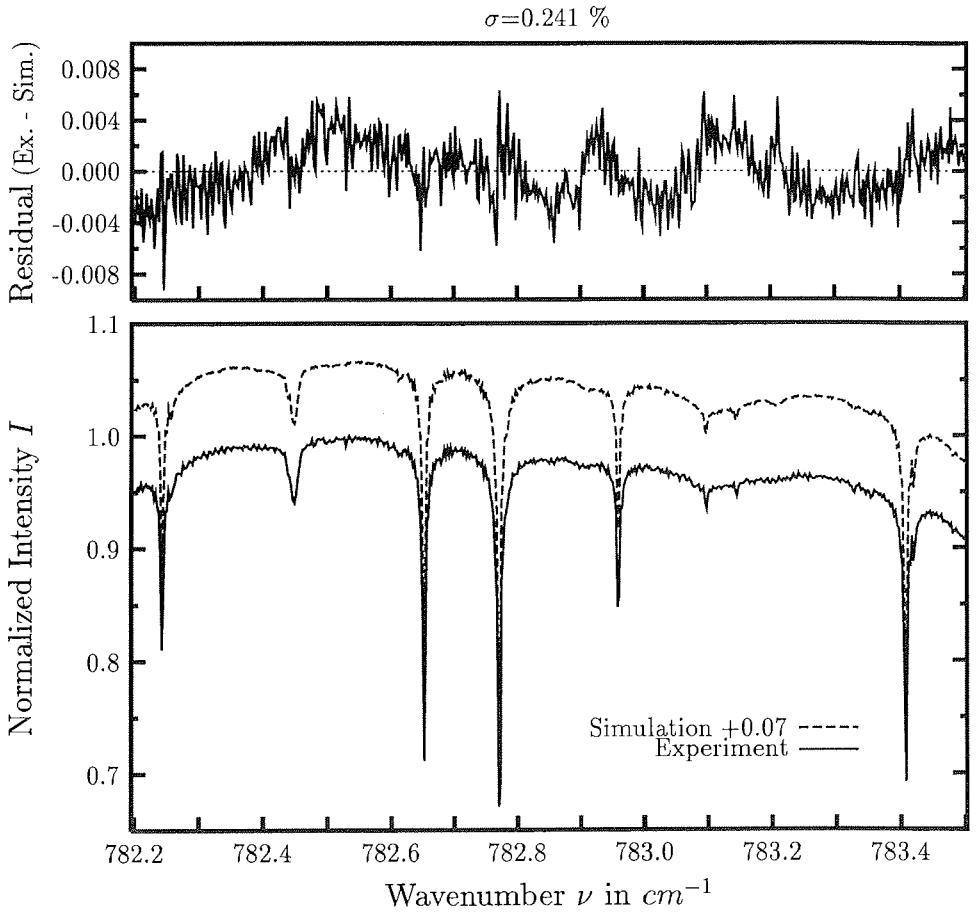

investigated species	: **O_3**
line position ν_0	: 782.653, 782.772 cm^{-1}
major species	: CO_2, O_3, H_2O, solar
minor species	: HNO_3, $ClONO_2$, C_2H_2
weak species	: NH_3
name of the spectrum	: 95052870
zenith angle, apodization	: 58.6°, boxcar
max. OPD, field of view	: 180.0 cm, 3.86 $mrad$
spectral interval fitted	: 782.20 – 783.50 cm^{-1}
retrieved total column	: $9.99 \cdot 10^{18}$ cm^{-2}

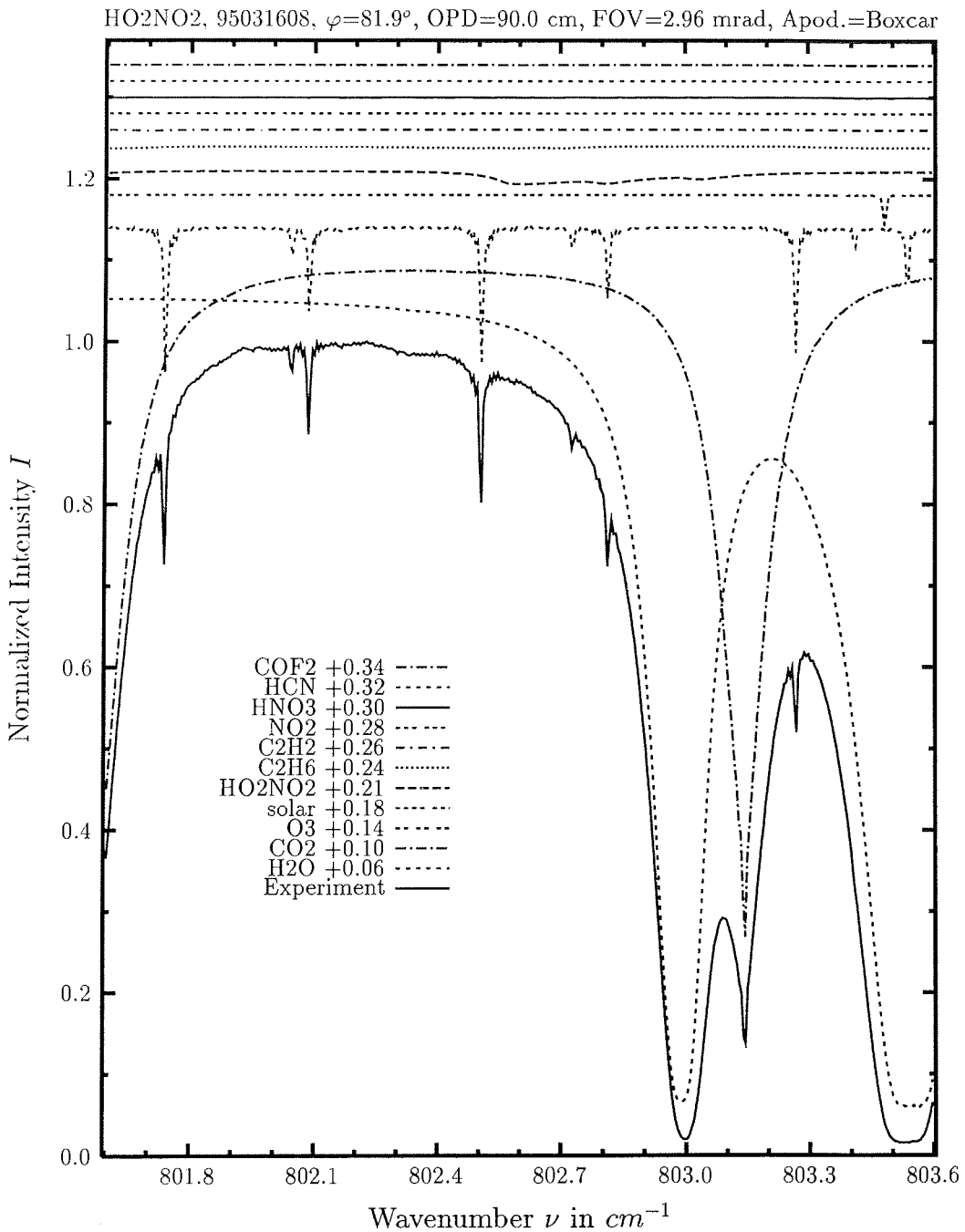
HO2NO2, 95031608, φ=81.9°, OPD=90.0 cm, FOV=2.96 mrad, Apod.=Boxcar
Normalized Intensity I
Wavenumber ν in cm⁻¹
0.0
0.2
0.4
0.6
0.8
1.0
1.2
801.8
802.1
802.4
802.7
803.0
803.3
803.6
COF2 +0.34
HCN +0.32
HNO3 +0.30
NO2 +0.28
C2H2 +0.26
C2H6 +0.24
HO2NO2 +0.21
solar +0.18
O3 +0.14
CO2 +0.10
H2O +0.06
Experiment

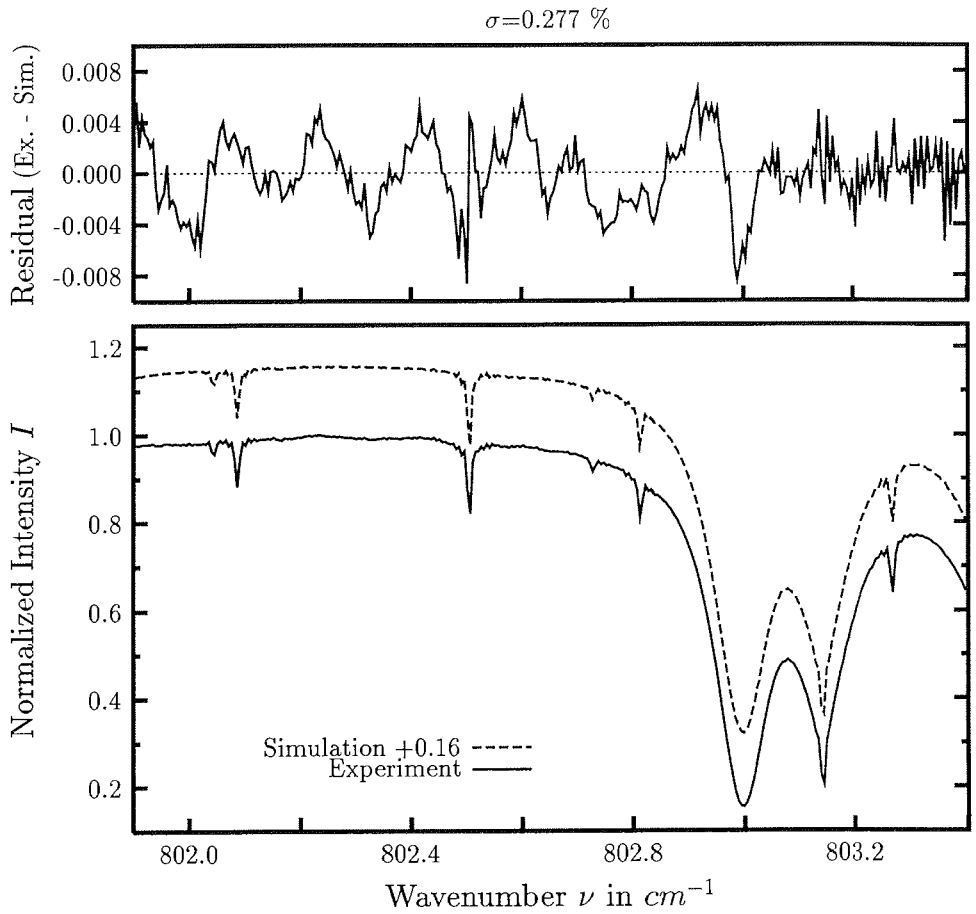

investigated species	: **HO_2NO_2**
line position ν_0	: 802.579*), 802.812*), 803.031*) cm^{-1}
major species	: H_2O, CO_2, O_3, solar, HO_2NO_2
minor species	: C_2H_6, C_2H_2
weak species	: NO_2, HNO_3, HCN, COF_2, NH_3, ClO
name of the spectrum	: 95032004
zenith angle, apodization	: 81.4°, boxcar
max. OPD, field of view	: 90.0 cm, 2.96 $mrad$
spectral interval fitted	: 801.90 – 803.40 cm^{-1}
retrieved total column	: $4.69 \cdot 10^{14}\ cm^{-2}$

comments: The line shape of the water vapor line must be well simulated.

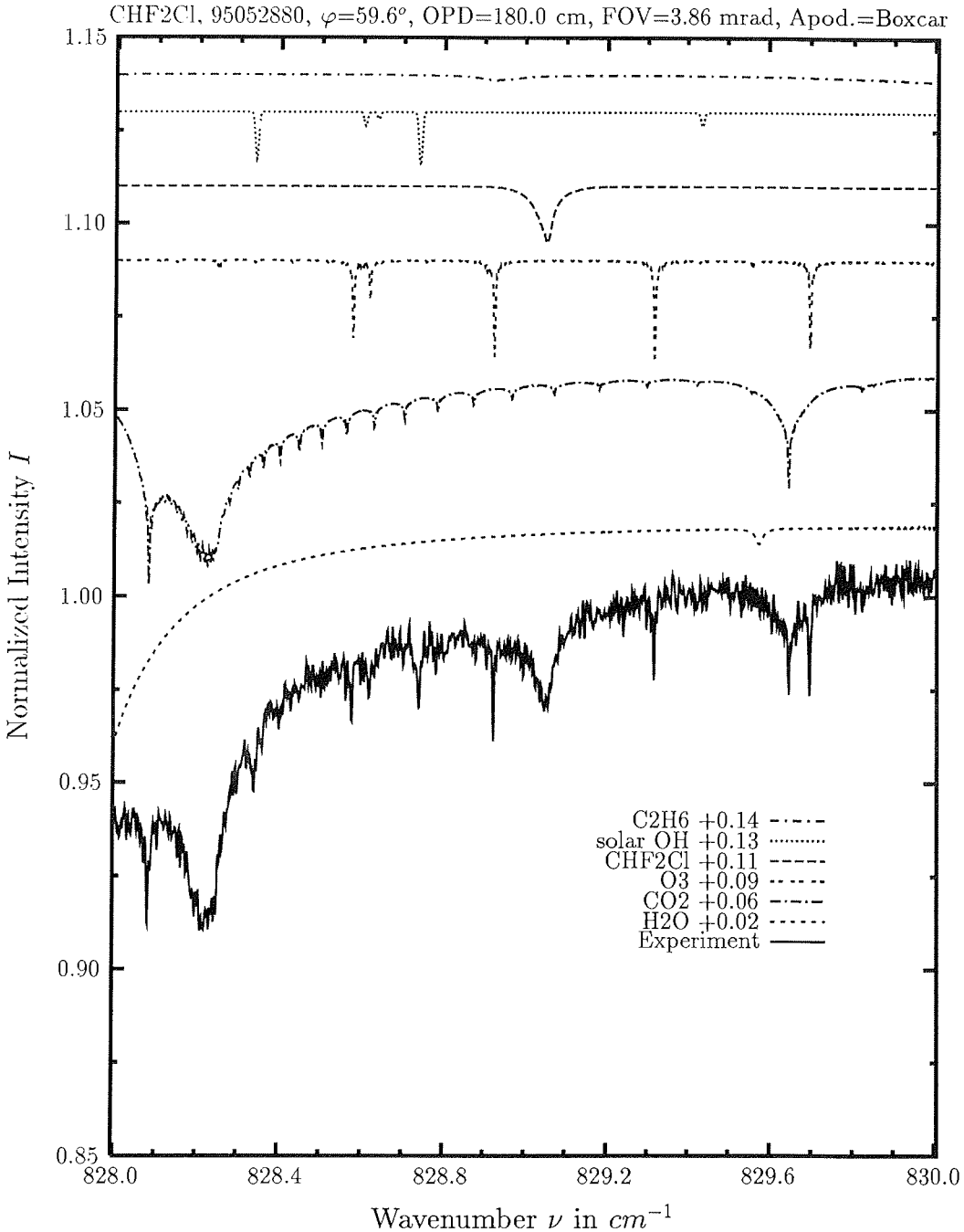
CHF2Cl, 95052880, φ=59.6°, OPD=180.0 cm, FOV=3.86 mrad, Apod.=Boxcar
Normalized Intensity I
Wavenumber ν in cm⁻¹
1.15
1.10
1.05
1.00
0.95
0.90
0.85
828.0
828.4
828.8
829.2
829.6
830.0
C2H6 +0.14
solar OH +0.13
CHF2Cl +0.11
O3 +0.09
CO2 +0.06
H2O +0.02
Experiment

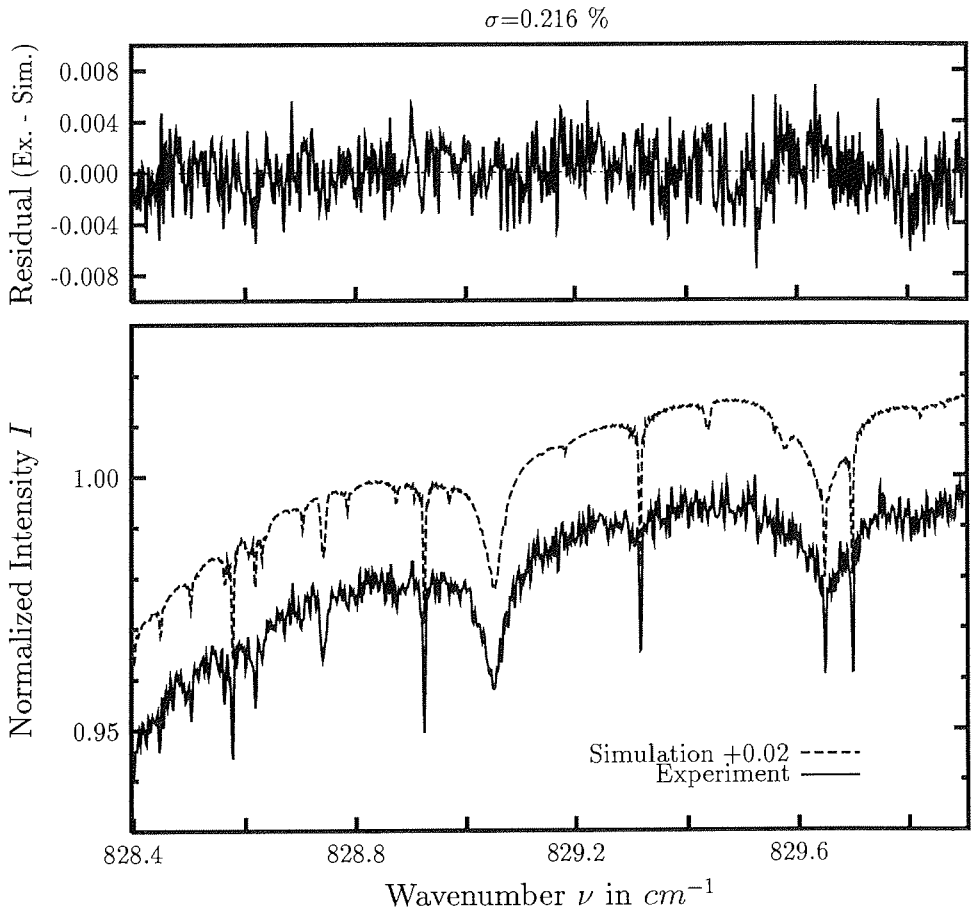

investigated species	: **CHF_2Cl**
line position ν_0	: 829.044 cm^{-1}
major species	: H_2O, CO_2, O_3, CHF_2Cl, solar
minor species	: C_2H_6
weak species	:
name of the spectrum	: 95060190
zenith angle, apodization	: 64.2°, boxcar
max. OPD, field of view	: 180.0 cm, 3.86 $mrad$
spectral interval fitted	: 828.40 – 829.90 cm^{-1}
retrieved total column	: $2.31 \cdot 10^{15}\, cm^{-2}$

comments: The line parameters of CO_2 at 828.2 cm^{-1} are inconsistent with recorded spectra.

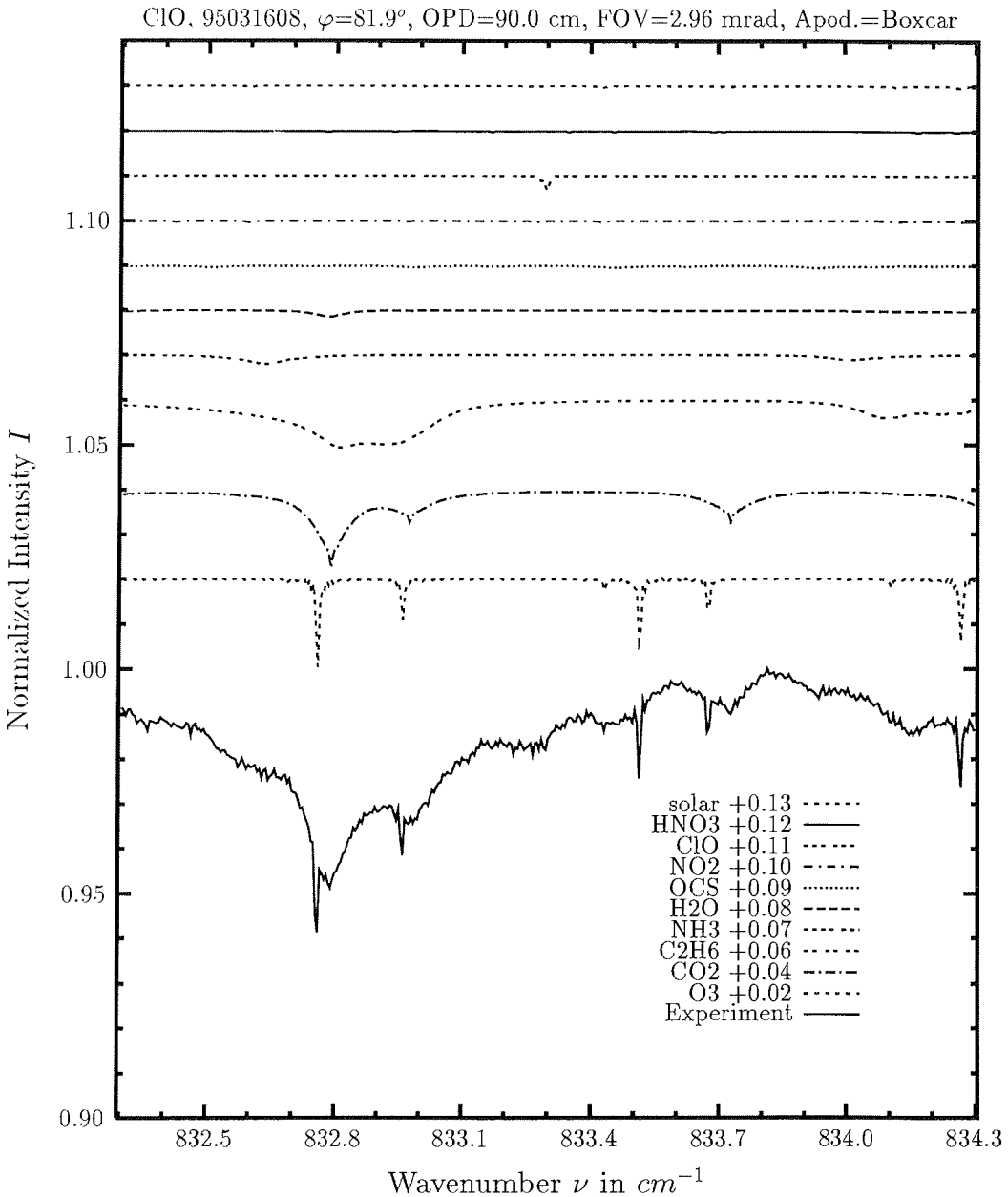

comments: *ClO* is at or below the detection limit. The absorption of *ClO* shown is calculated with 10 times the normal concentration.

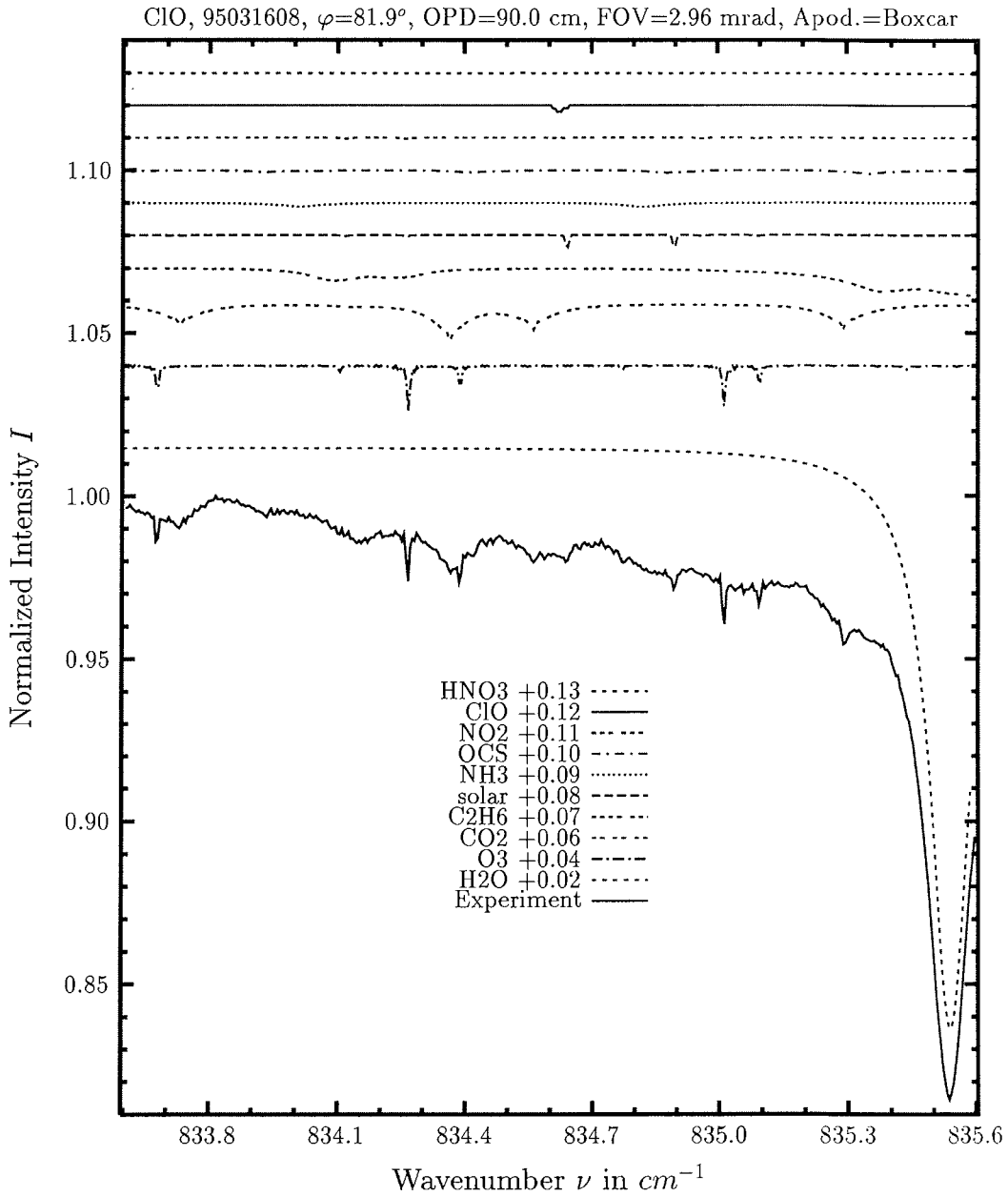

comments: *ClO* is at or below the detection limit. The absorption of *ClO* shown is calculated with 10 times the normal concentration.

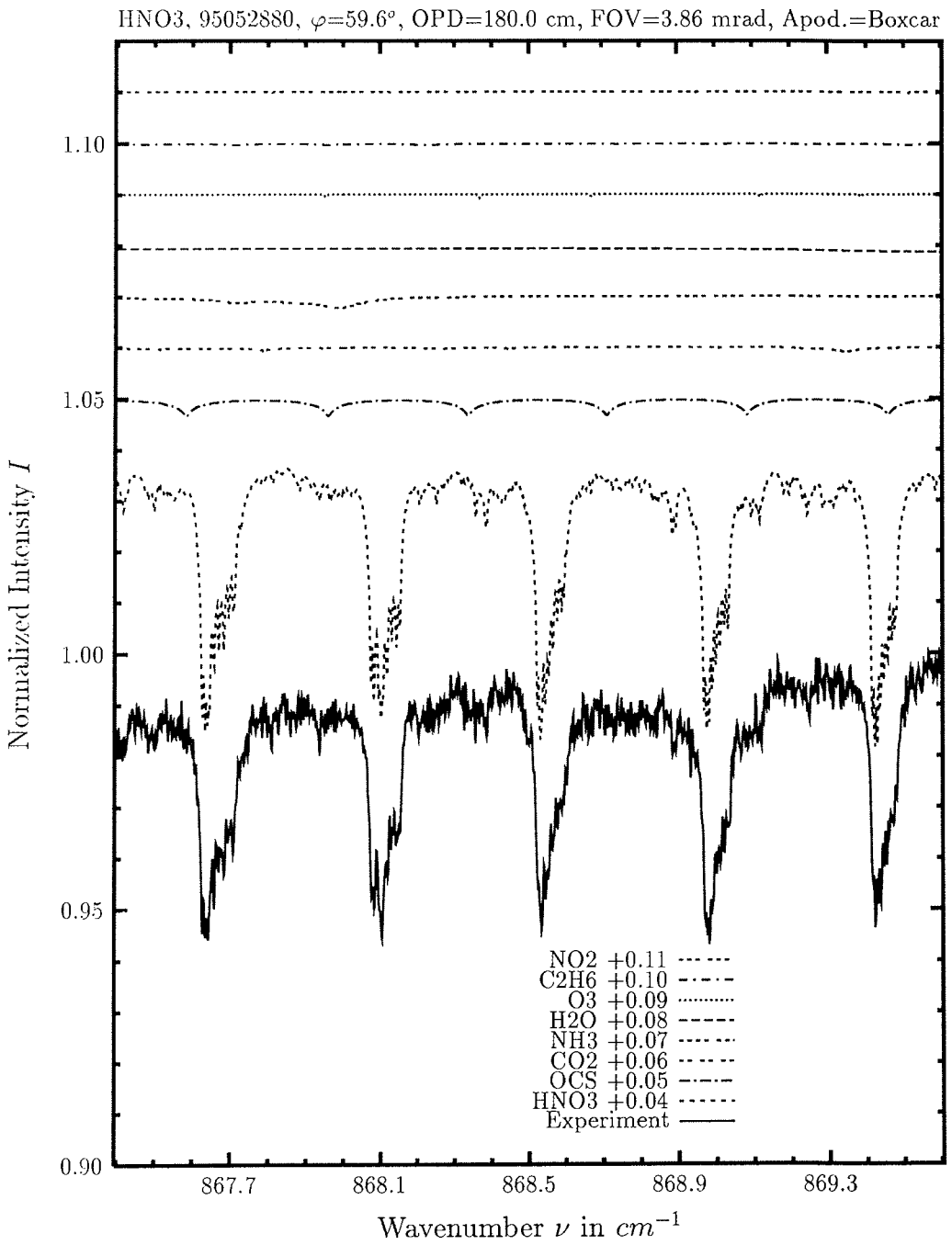
HNO3, 95052880, φ=59.6°, OPD=180.0 cm, FOV=3.86 mrad, Apod.=Boxcar
1.10
1.05
1.00
0.95
0.90
Normalized Intensity I
867.7
868.1
868.5
868.9
869.3
Wavenumber ν in cm⁻¹
NO2 +0.11
C2H6 +0.10
O3 +0.09
H2O +0.08
NH3 +0.07
CO2 +0.06
OCS +0.05
HNO3 +0.04
Experiment

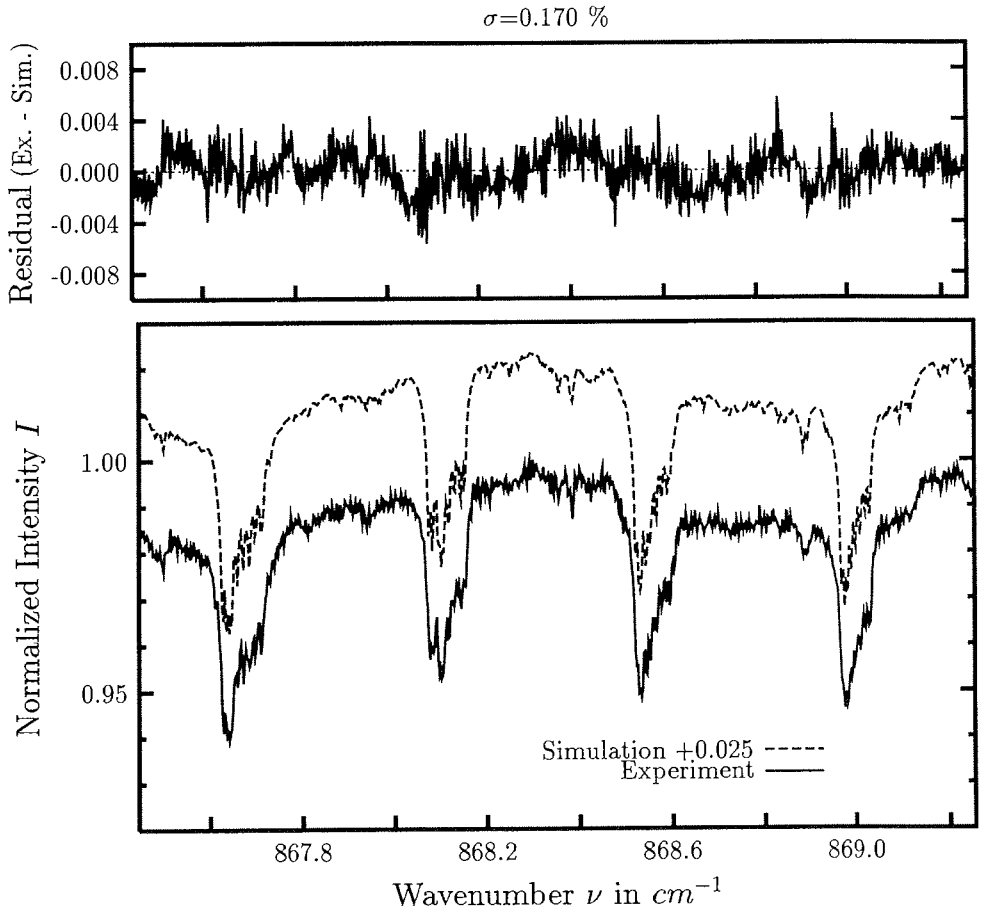

investigated species	: **HNO_3**
line position ν_0	: 868.524*) cm^{-1}
major species	: HNO_3, OCS
minor species	: CO_2, NH_3, H_2O, O_3
weak species	: C_2H_6, NO_2, ClO, C_2H_2
name of the spectrum	: 95052870
zenith angle, apodization	: 58.6°, boxcar
max. OPD, field of view	: 180.0 cm, 3.86 $mrad$
spectral interval fitted	: 867.45 - 869.25 cm^{-1}
retrieved total column	: $1.86 \cdot 10^{16}$ cm^{-2}

comments: There is some channeling in the fitted spectrum shown, which is taken into account in the simulation.

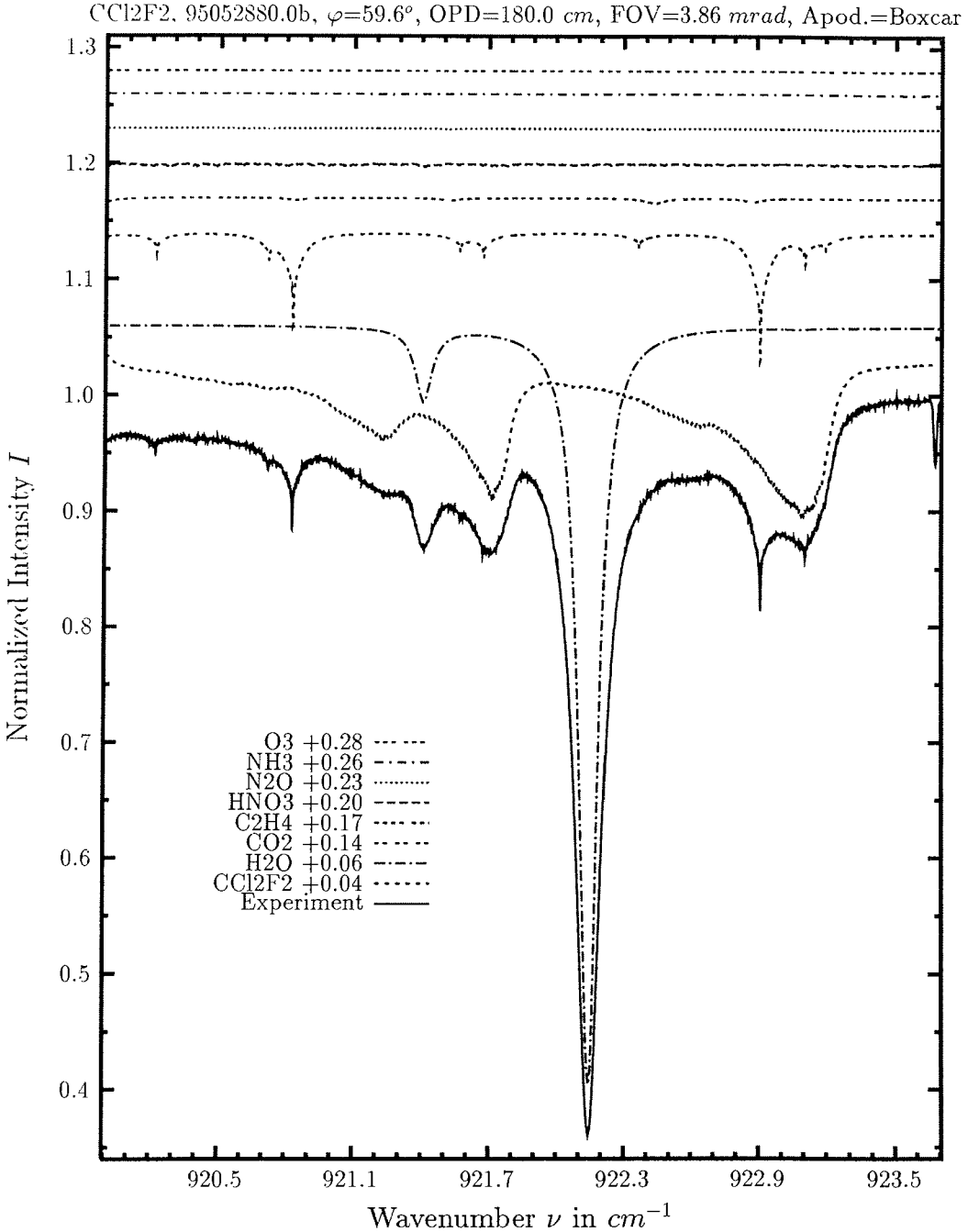
CCl2F2, 95052S80.0b, φ=59.6°, OPD=180.0 cm, FOV=3.86 mrad, Apod.=Boxcar
Normalized Intensity I
Wavenumber ν in cm⁻¹
1.3
1.2
1.1
1.0
0.9
0.8
0.7
0.6
0.5
0.4
920.5
921.1
921.7
922.3
922.9
923.5
O3 +0.28
NH3 +0.26
N2O +0.23
HNO3 +0.20
C2H4 +0.17
CO2 +0.14
H2O +0.06
CCl2F2 +0.04
Experiment

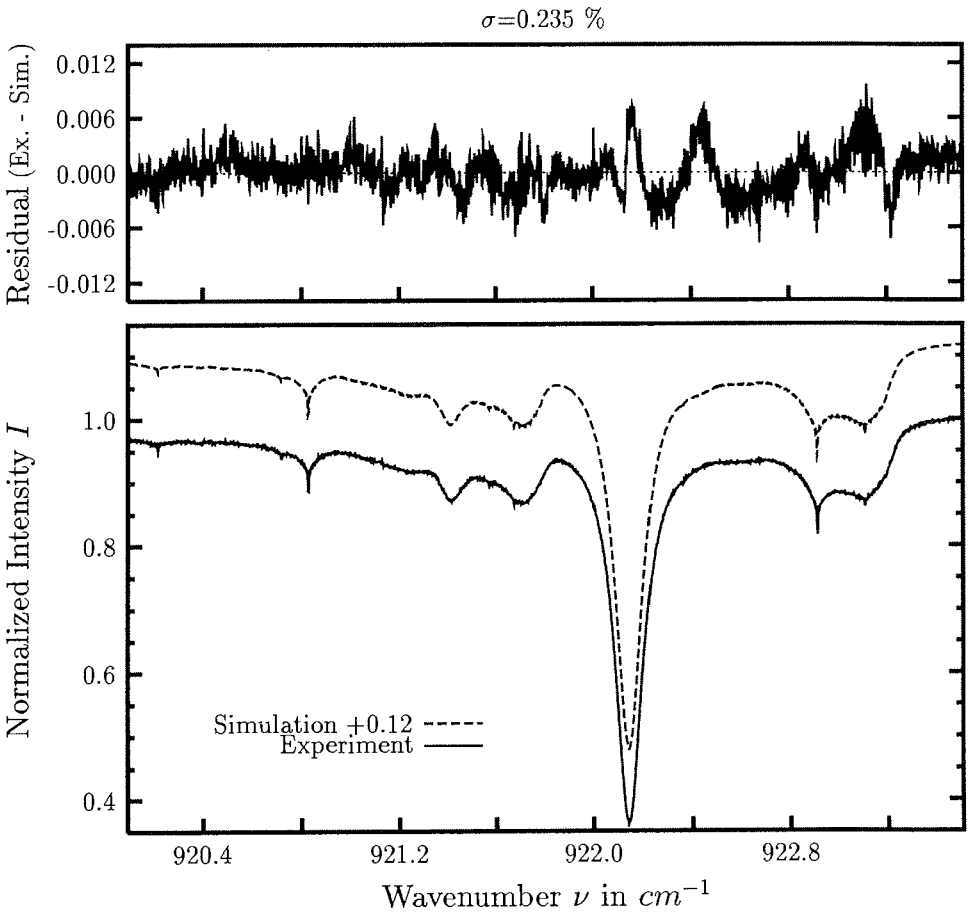

investigated species	: $\mathbf{CCl_2F_2}$
line position ν_0	: 921.112*), 921.725*), 923.117*) cm^{-1}
major species	: H_2O, CCl_2F_2, CO_2
minor species	: HNO_3, C_2H_4
weak species	: N_2O, NH_3, O_3
name of the spectrum	: 95052880
zenith angle, apodization	: 59.6°, boxcar
max. OPD, field of view	: 180.0 cm, 3.86 $mrad$
spectral interval fitted	: 920.10 - 923.50 cm^{-1}
retrieved total column	: $8.34 \cdot 10^{15}$ cm^{-2}

comments: The quality achievable in fitting CCl_2F_2 is higher in this spectral interval than at 1161 cm^{-1}, supposed the water vapor line is well simulated.

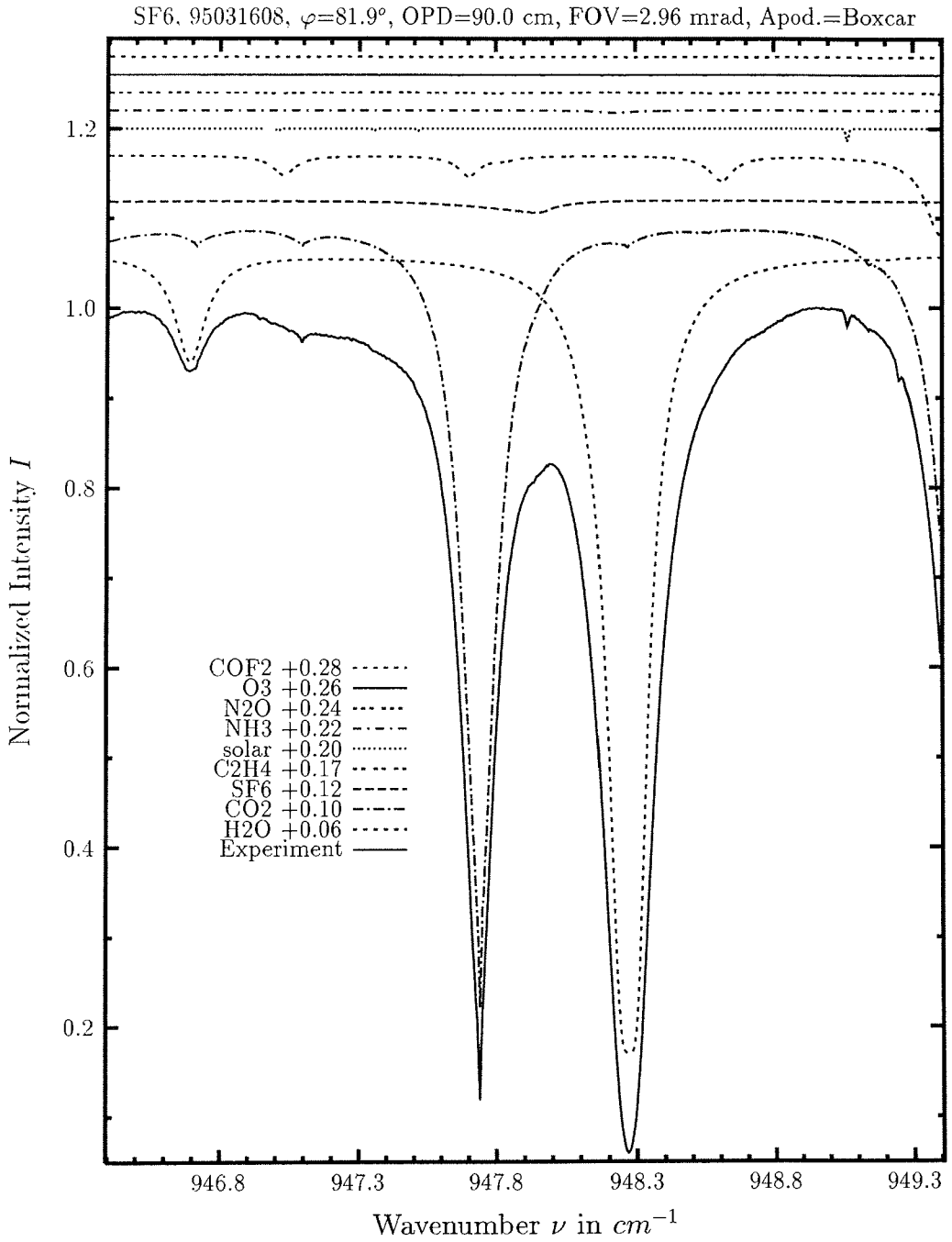
SF6, 95031608, φ=81.9°, OPD=90.0 cm, FOV=2.96 mrad, Apod.=Boxcar
Normalized Intensity I
1.2
1.0
0.8
0.6
0.4
0.2
COF2 +0.28
O3 +0.26
N2O +0.24
NH3 +0.22
solar +0.20
C2H4 +0.17
SF6 +0.12
CO2 +0.10
H2O +0.06
Experiment
946.8
947.3
947.8
948.3
948.8
949.3
Wavenumber ν in cm⁻¹

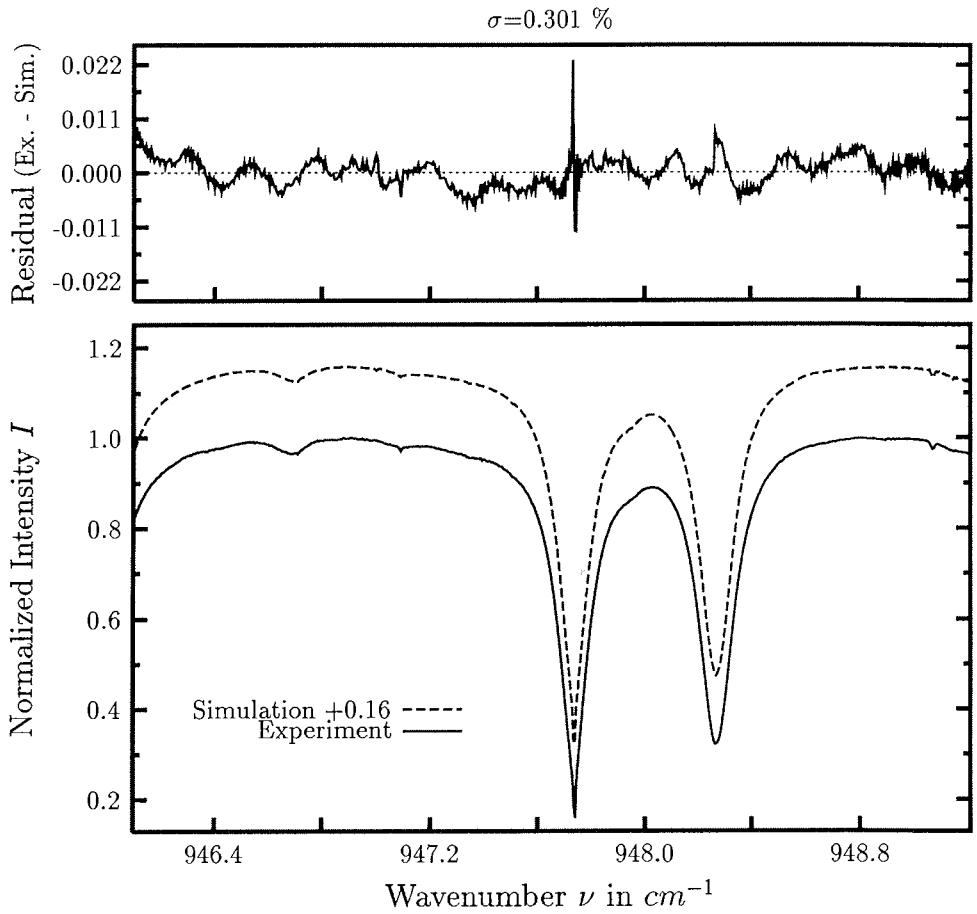

investigated species	: **SF_6, C_2H_4**
line position ν_0	: 947.930*), 947.959*) cm^{-1}
major species	: H_2O, CO_2, C_2H_4, solar, SF_6
minor species	: NH_3, N_2O, O_3
weak species	: COF_2, CH_4, HNO_3, NO_2
name of the spectrum	: 95031820
zenith angle, apodization	: 81.5°, boxcar
max. OPD, field of view	: 90.0 cm, 2.96 $mrad$
spectral interval fitted	: 946.00 - 949.20 cm^{-1}
retrieved total column	: $8.8 \cdot 10^{13}\, cm^{-2}$

comments: The line shape of the water vapor line must be well simulated.

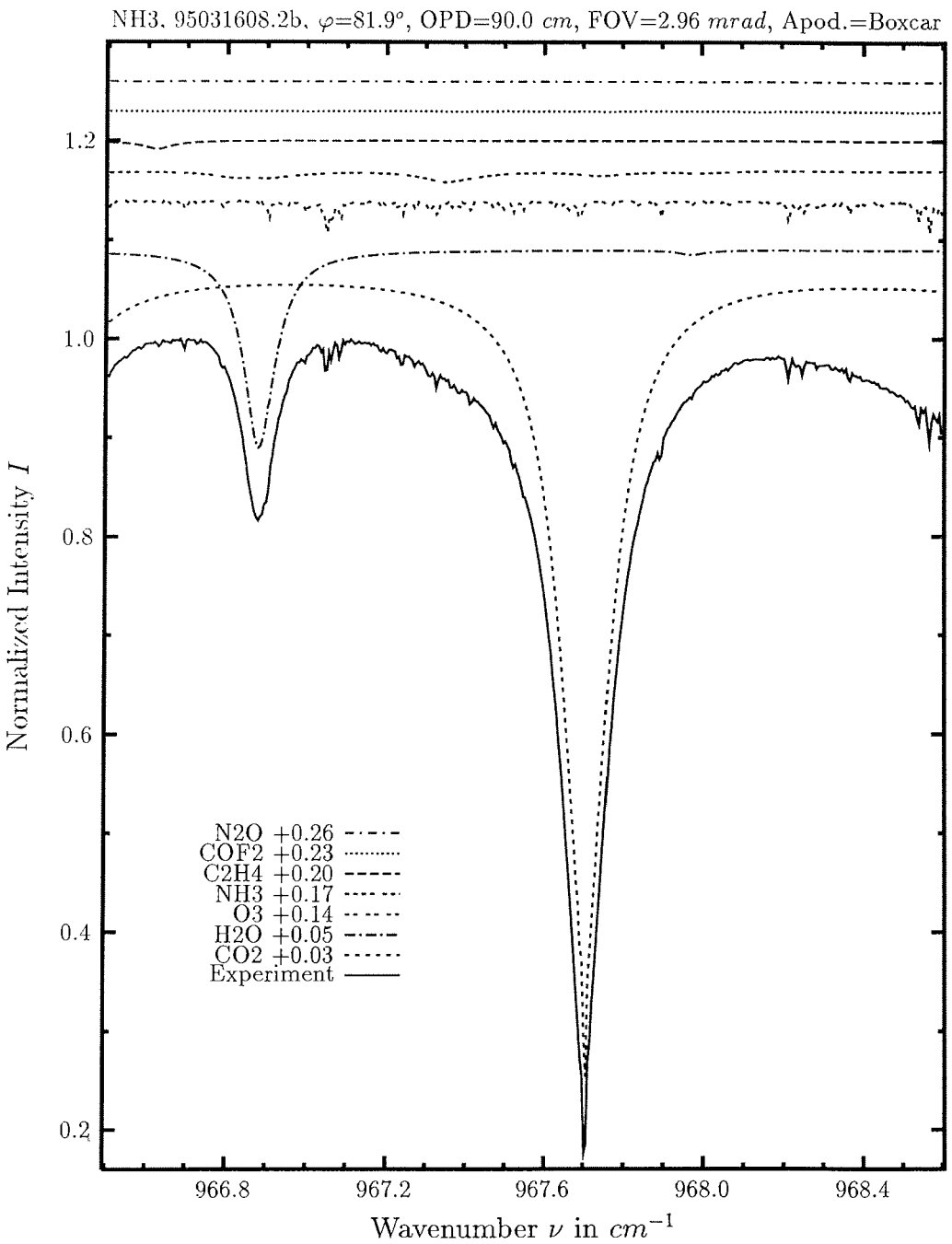
NH3, 95031608.2b, φ=81.9°, OPD=90.0 cm, FOV=2.96 mrad, Apod.=Boxcar
Normalized Intensity I
1.2
1.0
0.8
0.6
0.4
0.2
966.8
967.2
967.6
968.0
968.4
Wavenumber ν in cm⁻¹
N2O +0.26
COF2 +0.23
C2H4 +0.20
NH3 +0.17
O3 +0.14
H2O +0.05
CO2 +0.03
Experiment

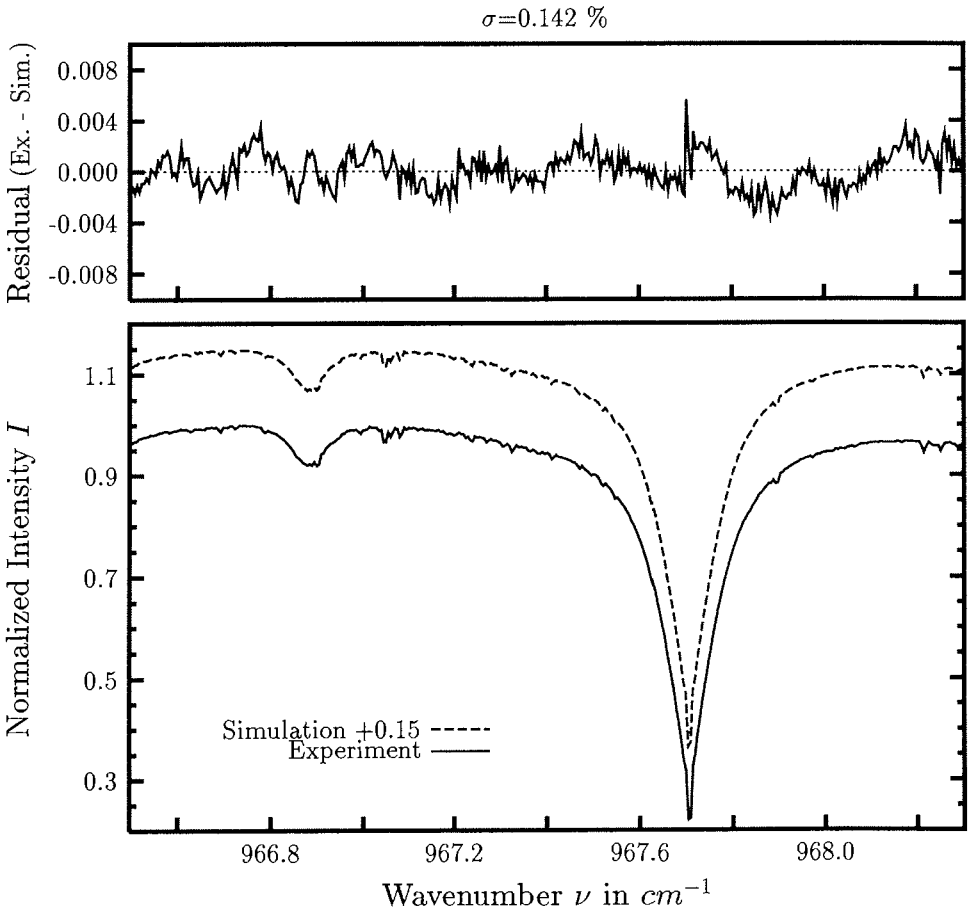

investigated species	: **NH_3**
line position ν_0	: 967.346
major species	: CO_2, H_2O, O_3, NH_3
minor species	: C_2H_4, COF_2, N_2O, CH_4
weak species	: NO_2
name of the spectrum	: 95032004
zenith angle, apodization	: 81.3°, boxcar
max. OPD, field of view	: 90.0 cm, 2.96 $mrad$
spectral interval fitted	: 966.50 - 968.30 cm^{-1}
retrieved total column	: $1.10 \cdot 10^{14}\, cm^{-2}$

comments: NH_3 is a weak absorber in the Arctic and care is to be taken in the simulation of the strong interferences by CO_2 and H_2O. The H_2O line appears to suffer from large spectroscopic uncertainties yielding unsensuous total column amounts.

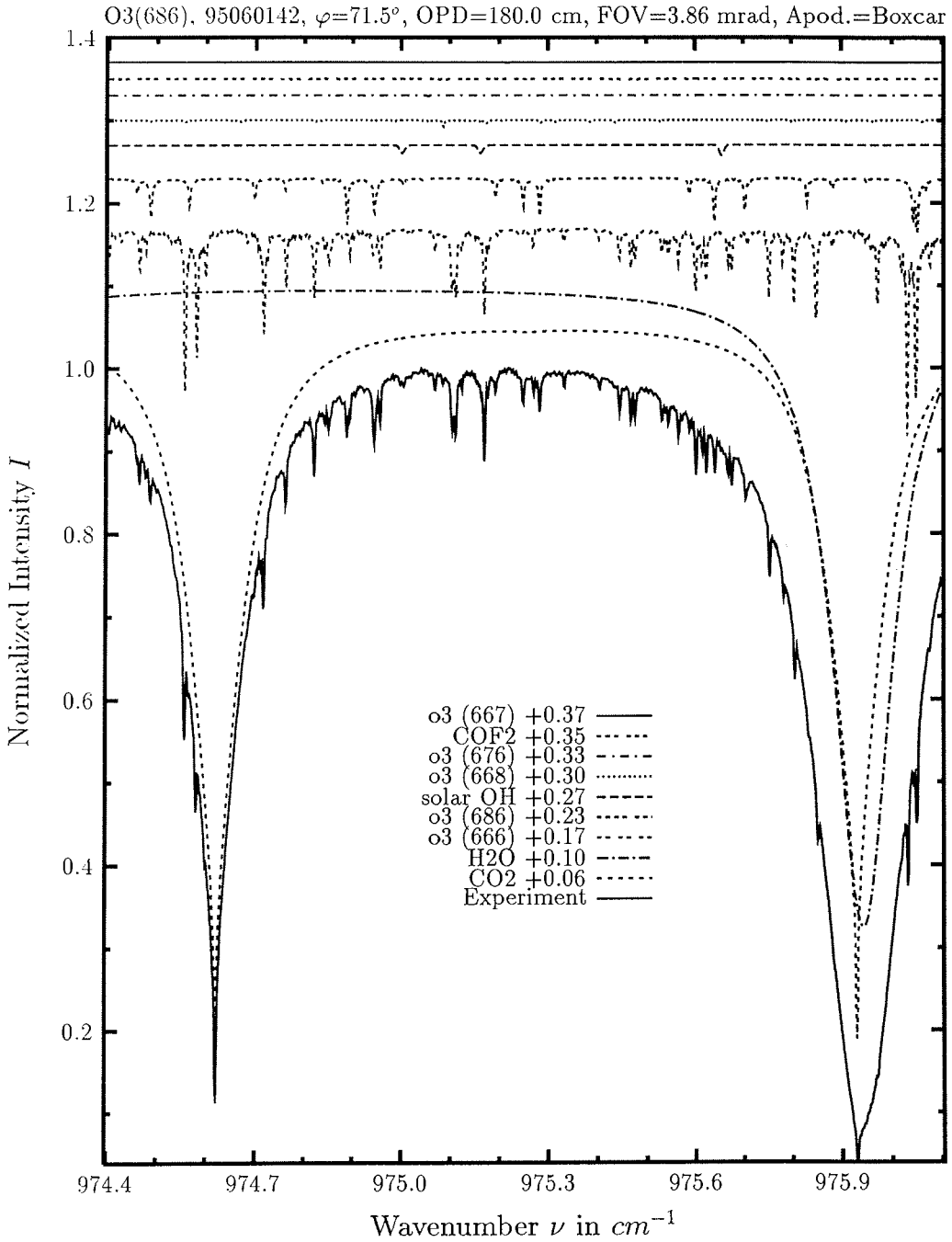
O3(686), 95060142, φ=71.5°, OPD=180.0 cm, FOV=3.86 mrad, Apod.=Boxcar
Normalized Intensity I
Wavenumber ν in cm⁻¹
1.4
1.2
1.0
0.8
0.6
0.4
0.2
974.4
974.7
975.0
975.3
975.6
975.9
o3 (667) +0.37
COF2 +0.35
o3 (676) +0.33
o3 (668) +0.30
solar OH +0.27
o3 (686) +0.23
o3 (666) +0.17
H2O +0.10
CO2 +0.06
Experiment

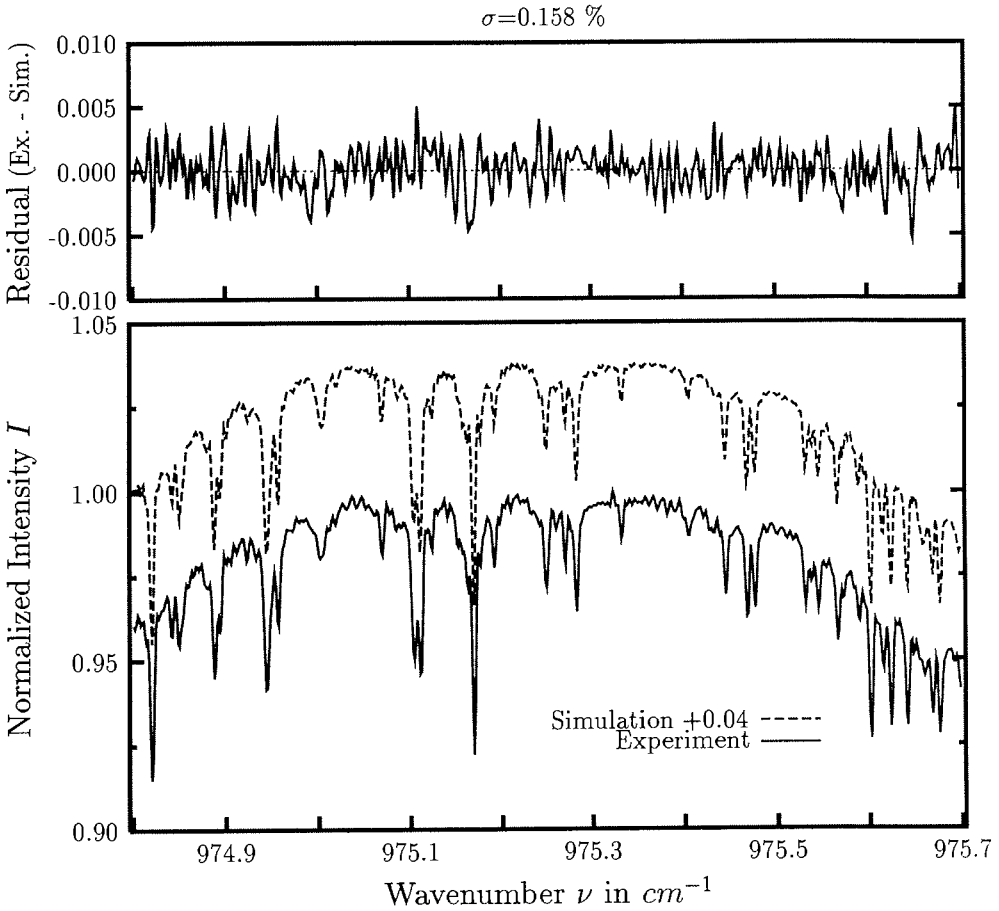

investigated species	: $^{16}O^{18}O^{16}O$
line position ν_0	: 975.250 cm^{-1}
major species	: CO_2, H_2O, O_3, $^{16}O^{18}O^{16}O$, solar
minor species	: $^{16}O^{16}O^{18}O$, $^{16}O^{17}O^{16}O$, COF_2
weak species	: $^{16}O^{16}O^{17}O$
name of the spectrum	: 95052880
zenith angle, apodization	: 59.6°, boxcar
max. OPD, field of view	: 180.0 cm, 3.86 $mrad$
spectral interval fitted	: 974.80 - 975.70 cm^{-1}
retrieved total column	: $1.17 \cdot 10^{19}\, cm^{-2}$

comments: High resolution is vital for all isotopic studies in ozone.

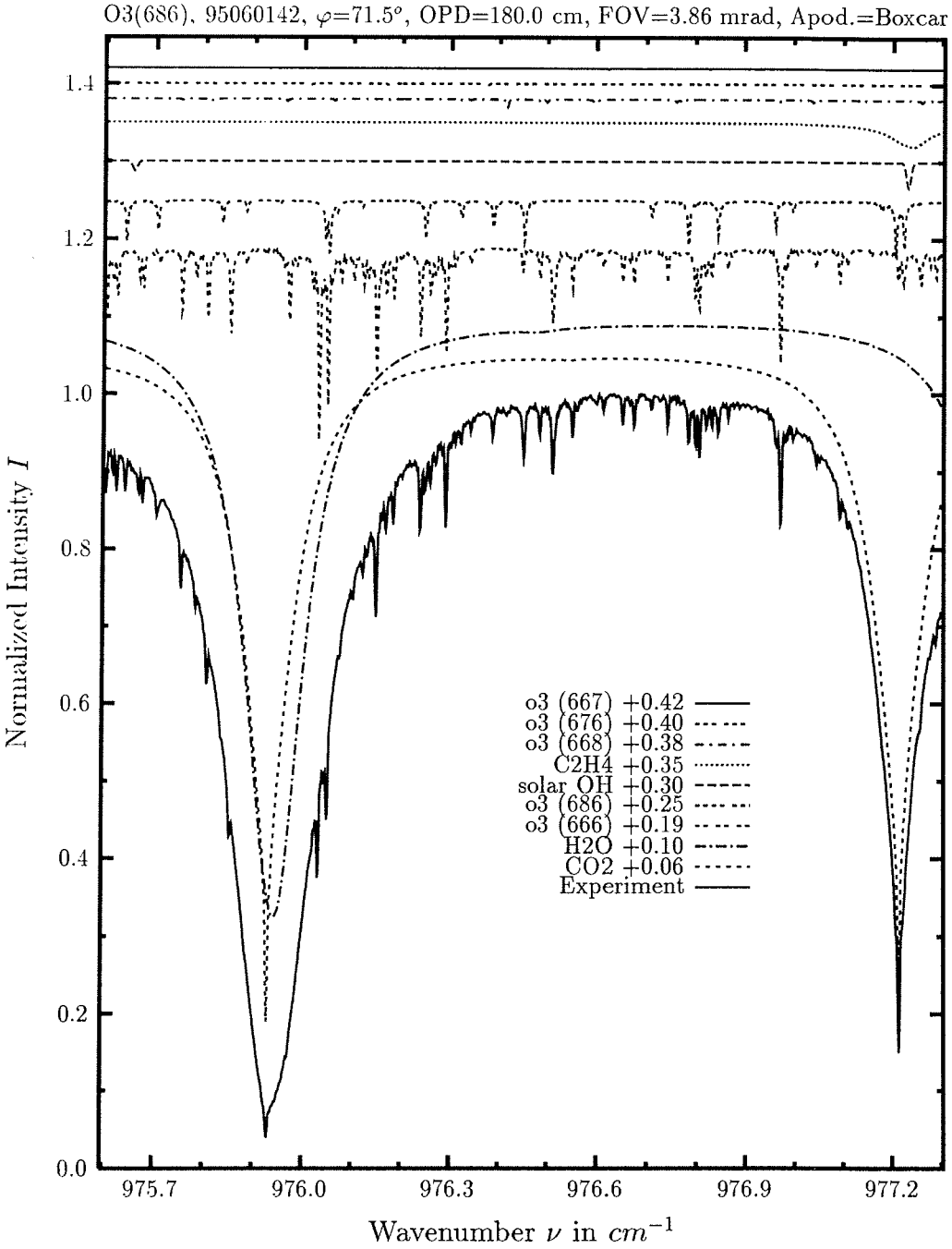
O3(686), 95060142, φ=71.5°, OPD=180.0 cm, FOV=3.86 mrad, Apod.=Boxcar
Normalized Intensity I
Wavenumber ν in cm⁻¹
1.4
1.2
1.0
0.8
0.6
0.4
0.2
0.0
975.7
976.0
976.3
976.6
976.9
977.2
o3 (667) +0.42
o3 (676) +0.40
o3 (668) +0.38
C2H4 +0.35
solar OH +0.30
o3 (686) +0.25
o3 (666) +0.19
H2O +0.10
CO2 +0.06
Experiment

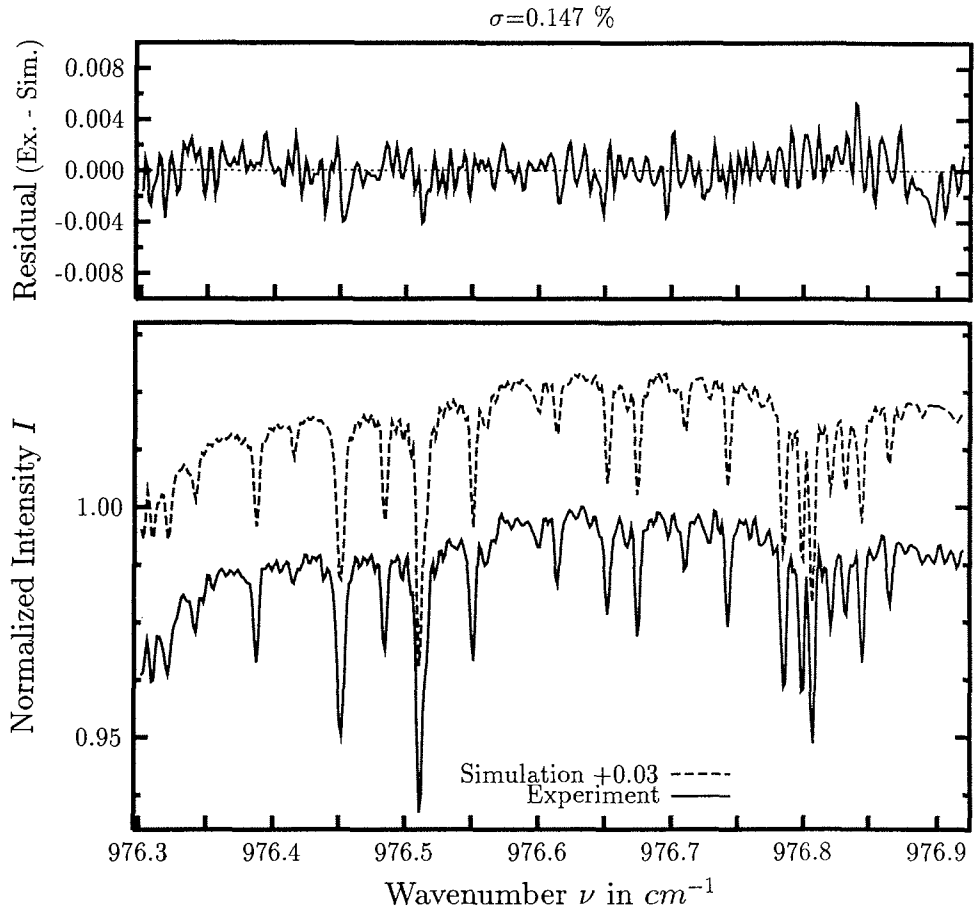

investigated species	: **$^{16}O^{18}O^{16}O$**
line position ν_0	: 976.388, 976.711 cm^{-1}
major species	: CO_2, H_2O, O_3, $^{16}O^{18}O^{16}O$, solar, C_2H_4
minor species	: $^{16}O^{16}O^{18}O$, $^{16}O^{17}O^{16}O$
weak species	: $^{16}O^{16}O^{17}O$
name of the spectrum	: 95053024
zenith angle, apodization	: 57.3°, boxcar
max. OPD, field of view	: 180.0 cm, 3.86 $mrad$
spectral interval fitted	: 976.30 – 976.92 cm^{-1}
retrieved total column	: $9.87 \cdot 10^{18}\ cm^{-2}$

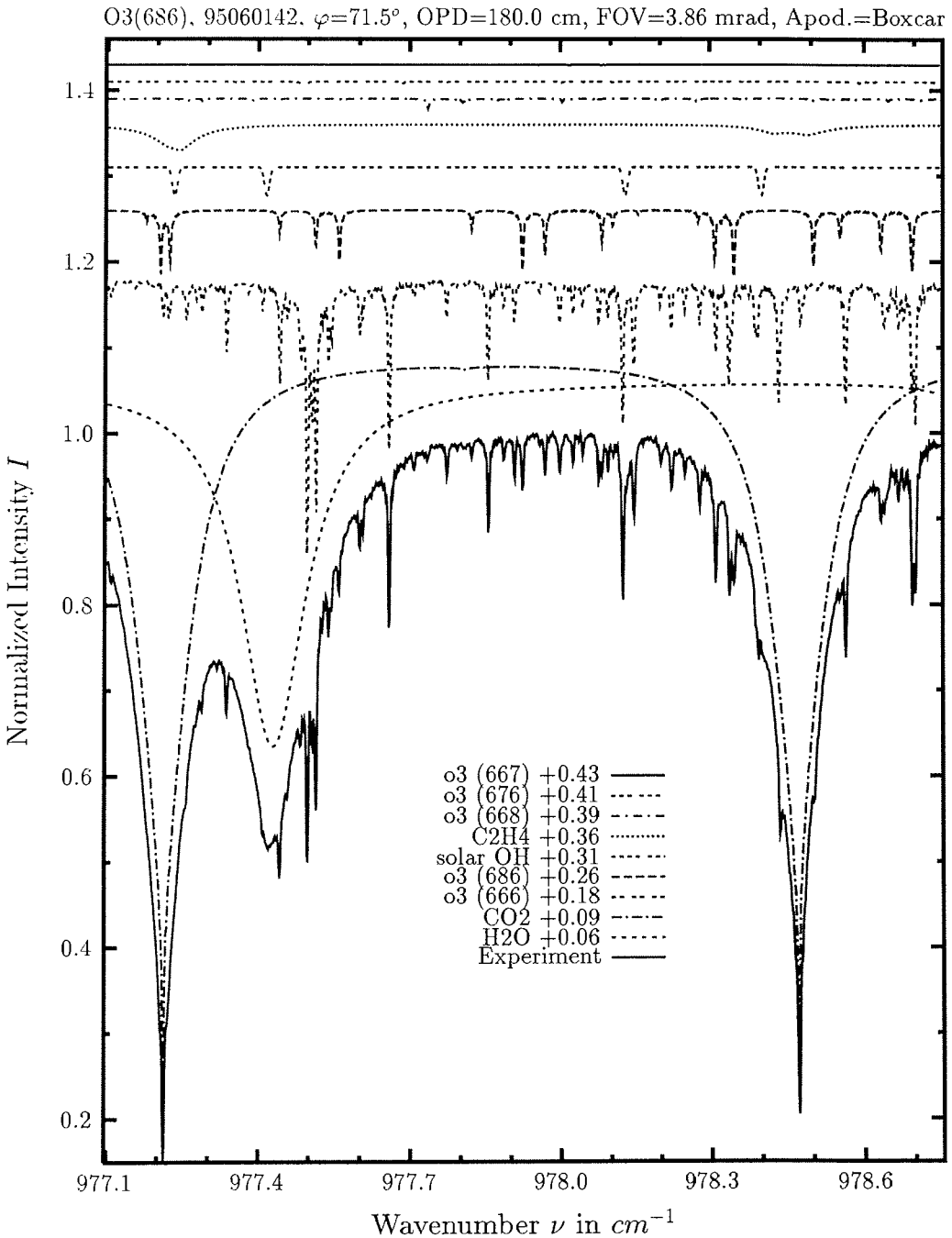
O3(686), 95060142, φ=71.5°, OPD=180.0 cm, FOV=3.86 mrad, Apod.=Boxcar
Normalized Intensity I
1.4
1.2
1.0
0.8
0.6
0.4
0.2
977.1
977.4
977.7
978.0
978.3
978.6
Wavenumber ν in cm⁻¹
o3 (667) +0.43
o3 (676) +0.41
o3 (668) +0.39
C2H4 +0.36
solar OH +0.31
o3 (686) +0.26
o3 (666) +0.18
CO2 +0.09
H2O +0.06
Experiment

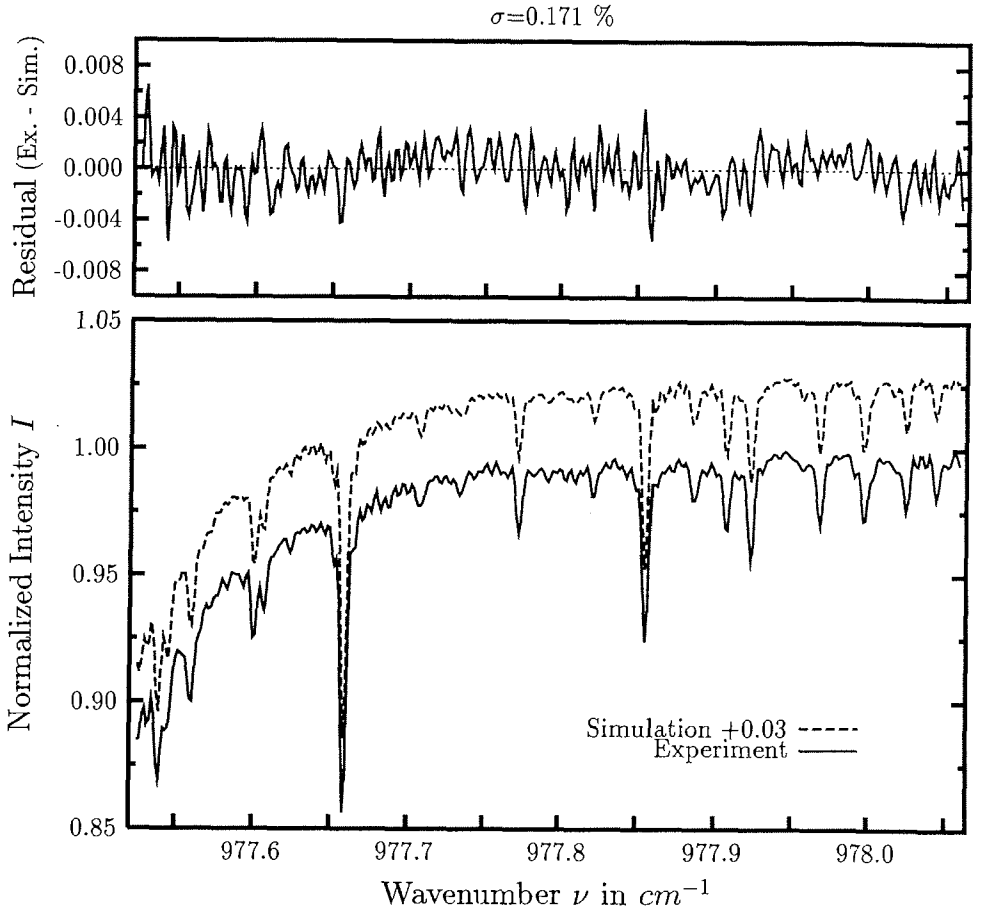

investigated species	: $\mathbf{^{16}O^{18}O^{16}O}$
line position ν_0	: 977.925 cm^{-1}
major species	: CO_2, H_2O, O_3, $^{16}O^{18}O^{16}O$, solar
	: C_2H_4, $^{16}O^{16}O^{18}O$
minor species	: $^{16}O^{17}O^{16}O$
weak species	: $^{16}O^{16}O^{17}O$
name of the spectrum	: 95053024
zenith angle, apodization	: 57.3°, boxcar
max. OPD, field of view	: 180.0 cm, 3.86 $mrad$
spectral interval fitted	: 977.52 - 978.06 cm^{-1}
retrieved total column	: $1.00 \cdot 10^{19}\, cm^{-2}$

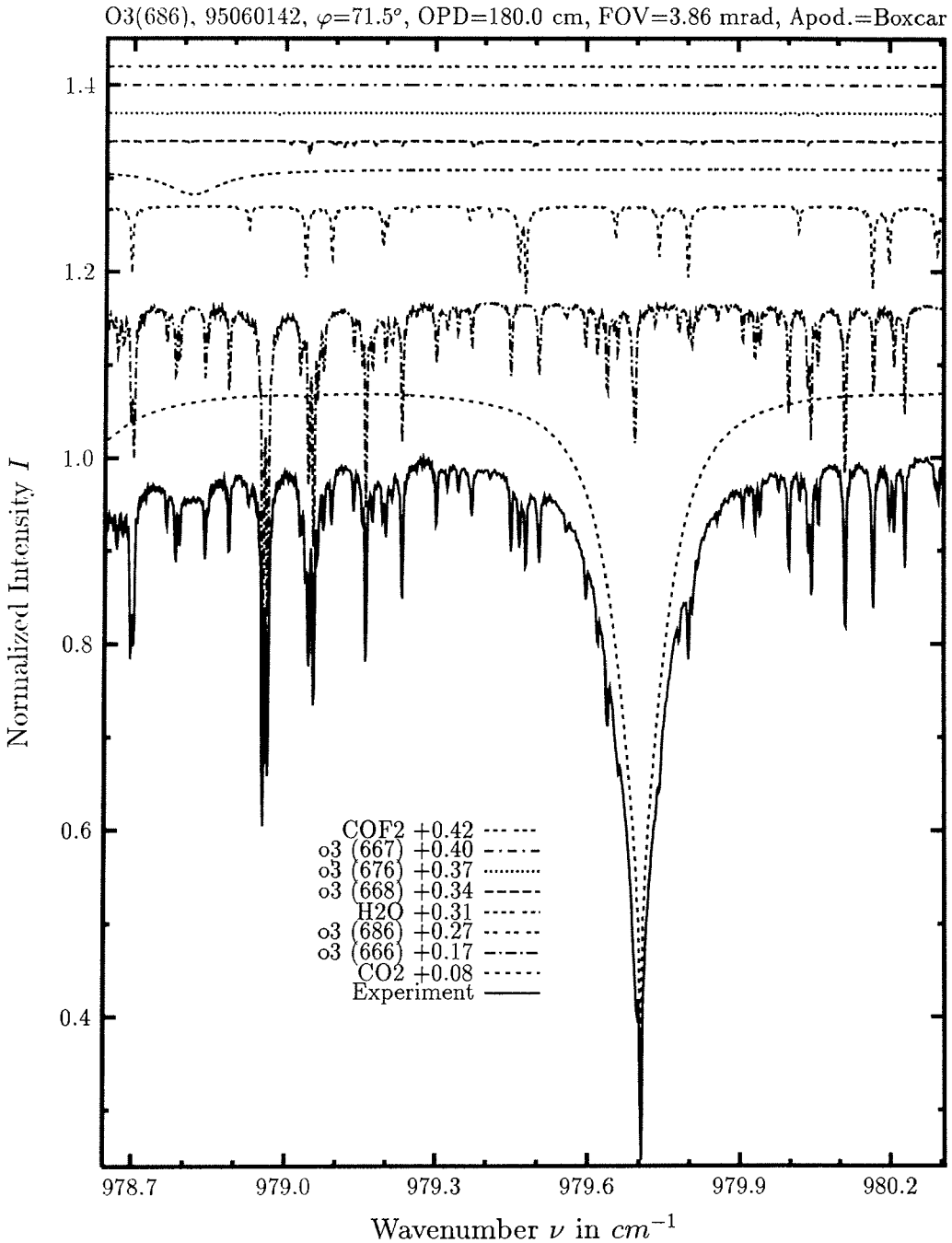
O3(686), 95060142, φ=71.5°, OPD=180.0 cm, FOV=3.86 mrad, Apod.=Boxcar
Normalized Intensity I
1.4
1.2
1.0
0.8
0.6
0.4
COF2 +0.42
o3 (667) +0.40
o3 (676) +0.37
o3 (668) +0.34
H2O +0.31
o3 (686) +0.27
o3 (666) +0.17
CO2 +0.08
Experiment
978.7
979.0
979.3
979.6
979.9
980.2
Wavenumber ν in cm⁻¹

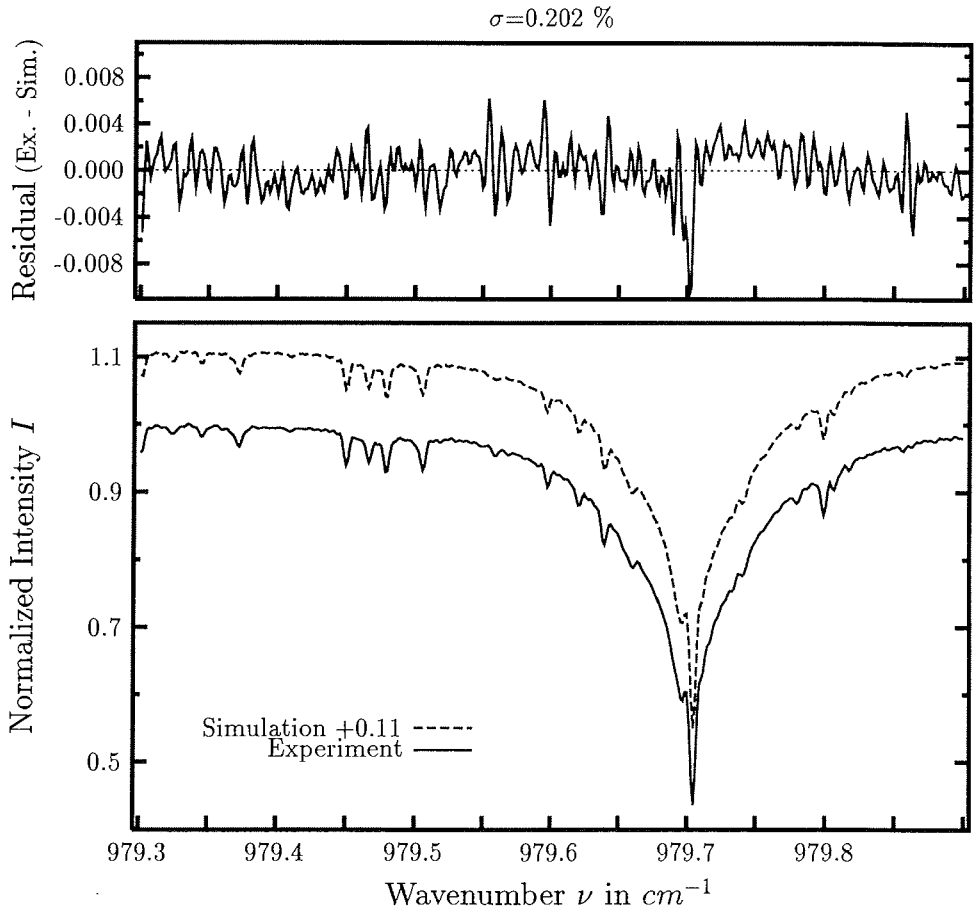

investigated species	: $^{16}O^{18}O^{16}O$
line position ν_0	: 979.480 cm^{-1}
major species	: CO_2, O_3, $^{16}O^{18}O^{16}O$, H_2O, $^{16}O^{16}O^{18}O$
minor species	: $^{16}O^{17}O^{16}O$, $^{16}O^{16}O^{17}O$
weak species	: COF_2
name of the spectrum	: 95053028
zenith angle, apodization	: 57.7°, boxcar
max. OPD, field of view	: 180.0 cm, 3.86 $mrad$
spectral interval fitted	: 979.30 – 979.90 cm^{-1}
retrieved total column	: $1.03 \cdot 10^{19}$ cm^{-2}

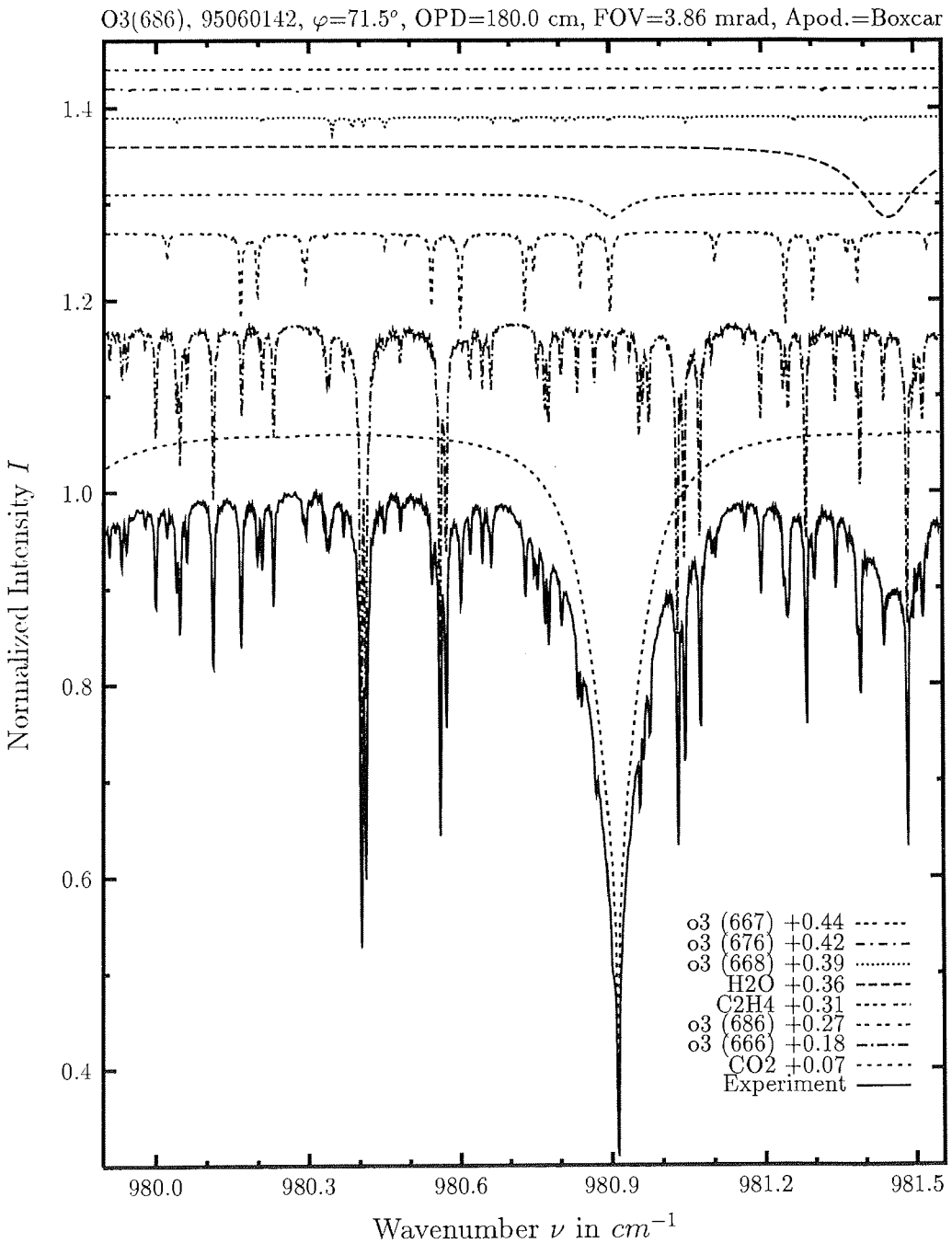
O3(686), 95060142, φ=71.5°, OPD=180.0 cm, FOV=3.86 mrad, Apod.=Boxcar
Normalized Intensity I
1.4
1.2
1.0
0.8
0.6
0.4
980.0
980.3
980.6
980.9
981.2
981.5
Wavenumber ν in cm⁻¹
o3 (667) +0.44
o3 (676) +0.42
o3 (668) +0.39
H2O +0.36
C2H4 +0.31
o3 (686) +0.27
o3 (666) +0.18
CO2 +0.07
Experiment

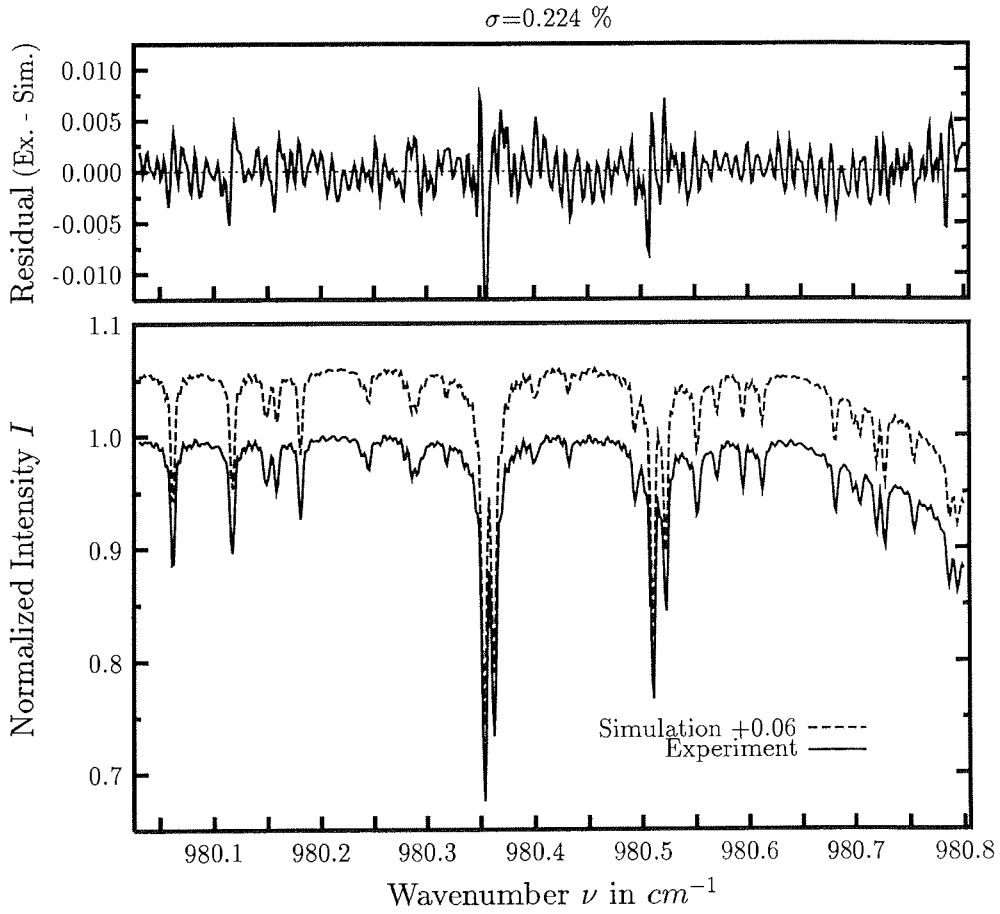

investigated species	: $\mathbf{^{16}O^{18}O^{16}O}$
line position ν_0	: 980.732 cm^{-1}
major species	: CO_2, O_3, $^{16}O^{18}O^{16}O$, H_2O, C_2H_4, $^{16}O^{16}O^{18}O$
minor species	: $^{16}O^{17}O^{16}O$, $^{16}O^{16}O^{17}O$
weak species	:
name of the spectrum	: 95053028
zenith angle, apodization	: 57.7°, boxcar
max. OPD, field of view	: 180.0 cm, 3.86 $mrad$
spectral interval fitted	: 980.08 - 980.85 cm^{-1}
retrieved total column	: $1.03 \cdot 10^{19}\, cm^{-2}$

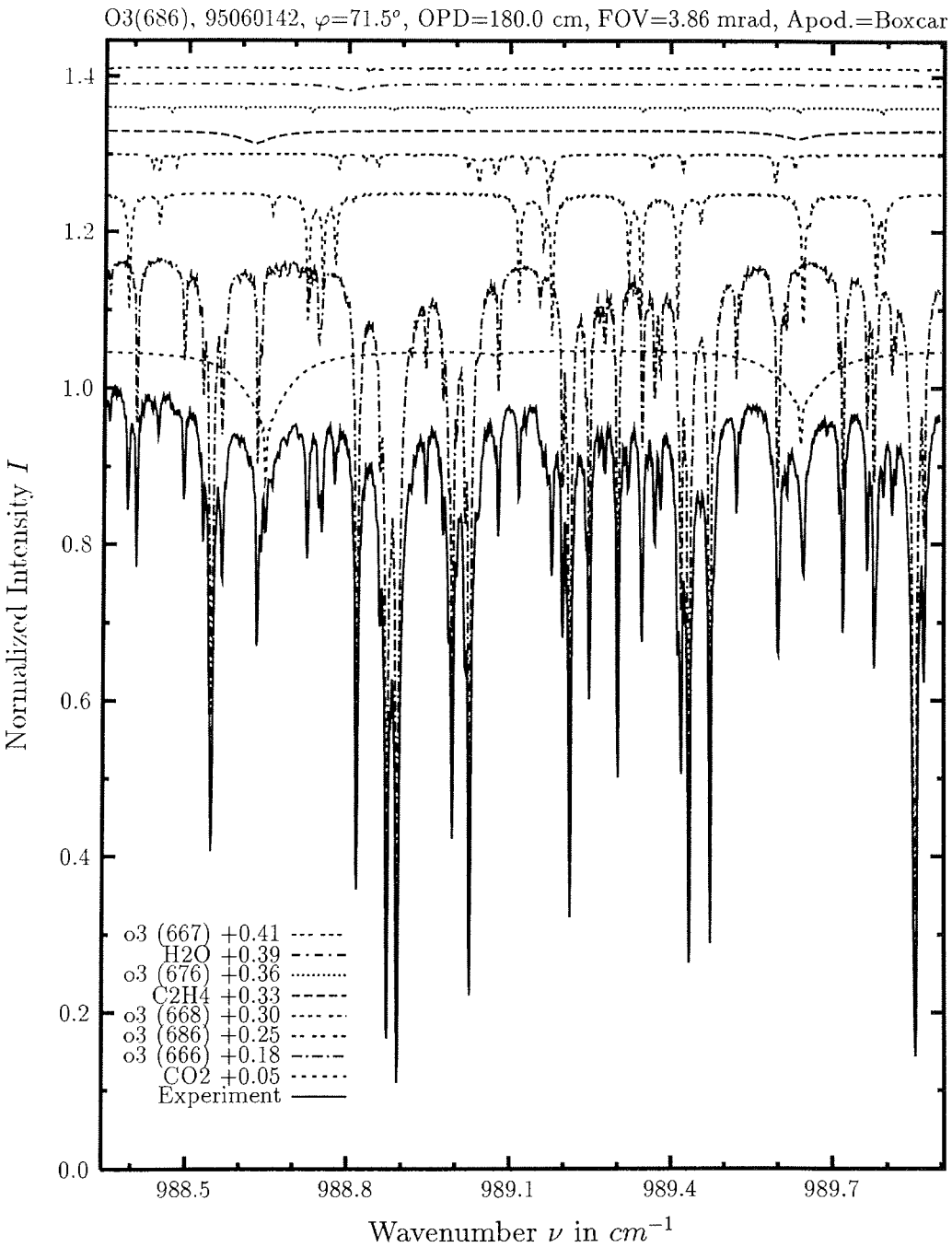
O3(686), 95060142, φ=71.5°, OPD=180.0 cm, FOV=3.86 mrad, Apod.=Boxcar
Normalized Intensity I
Wavenumber ν in cm⁻¹
1.4
1.2
1.0
0.8
0.6
0.4
0.2
0.0
988.5
988.8
989.1
989.4
989.7
o3 (667) +0.41
H2O +0.39
o3 (676) +0.36
C2H4 +0.33
o3 (668) +0.30
o3 (686) +0.25
o3 (666) +0.18
CO2 +0.05
Experiment

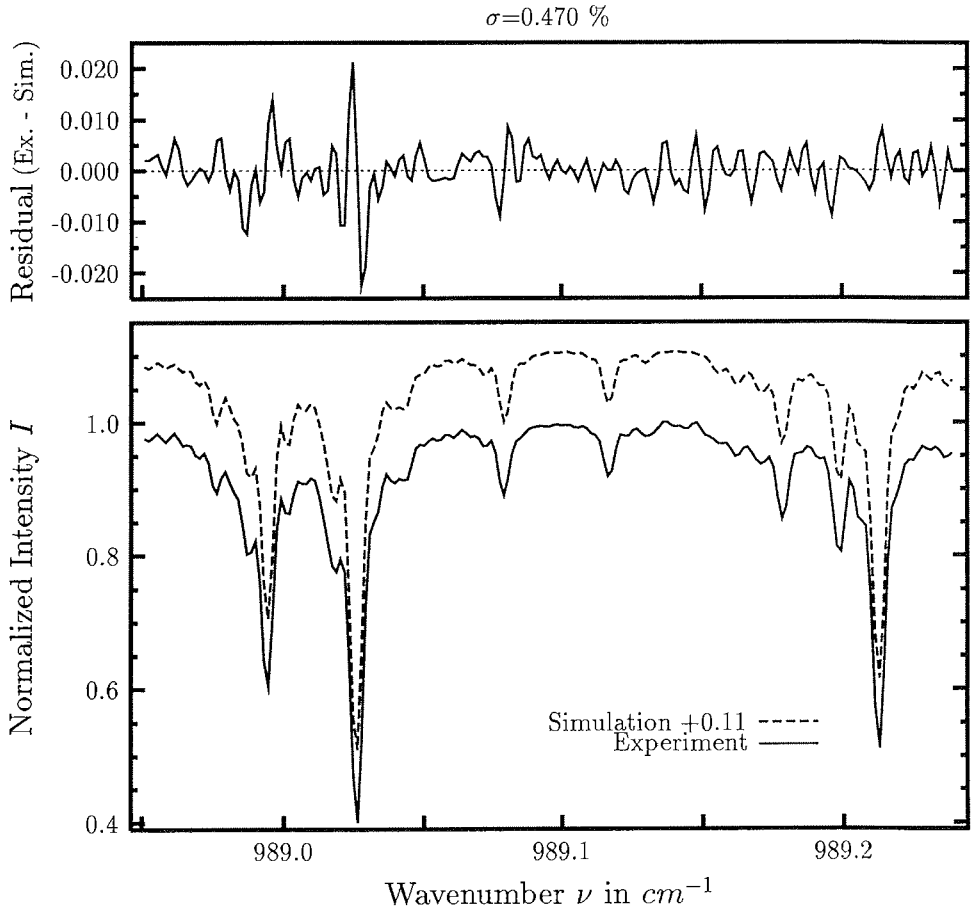

investigated species	:	$^{16}O^{18}O^{16}O$
line position ν_0	:	989.118 cm^{-1}
major species	:	O_3, $^{16}O^{18}O^{16}O$, CO_2, $^{16}O^{16}O^{18}O$, C_2H_4
minor species	:	$^{16}O^{17}O^{16}O$, H_2O, $^{16}O^{16}O^{17}O$
weak species	:	
name of the spectrum	:	95053024
zenith angle, apodization	:	57.3°, boxcar
max. OPD, field of view	:	180.0 cm, 3.86 $mrad$
spectral interval fitted	:	I) 988.95 - 989.24 cm^{-1}, II) 989.05 - 989.24 cm^{-1}
retrieved total column	:	$9.93 \cdot 10^{18}$ cm^{-2}

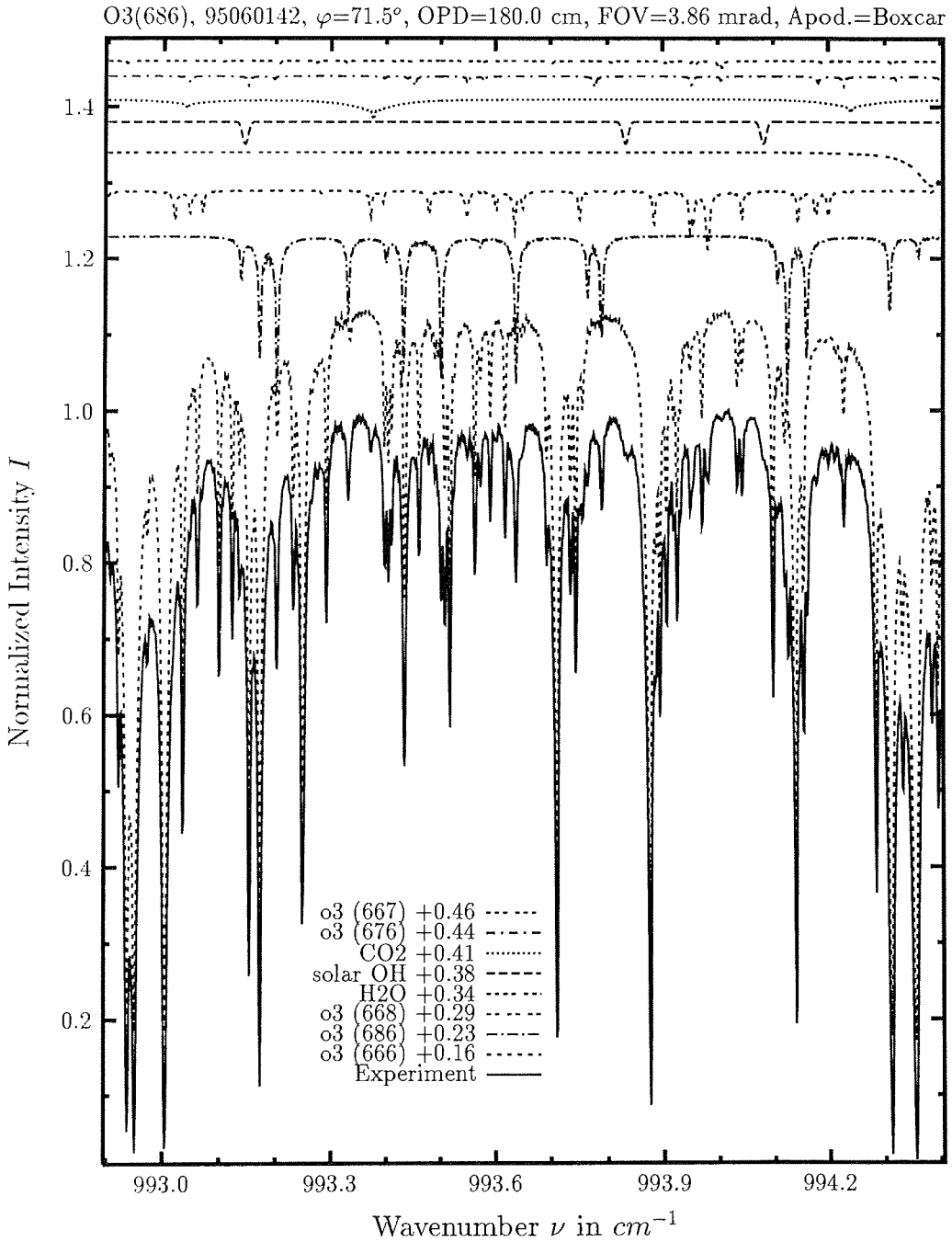
O3(686), 95060142, φ=71.5°, OPD=180.0 cm, FOV=3.86 mrad, Apod.=Boxcar
Normalized Intensity I
1.4
1.2
1.0
0.8
0.6
0.4
0.2
993.0
993.3
993.6
993.9
994.2
Wavenumber ν in cm⁻¹
o3 (667) +0.46
o3 (676) +0.44
CO2 +0.41
solar OH +0.38
H2O +0.34
o3 (668) +0.29
o3 (686) +0.23
o3 (666) +0.16
Experiment

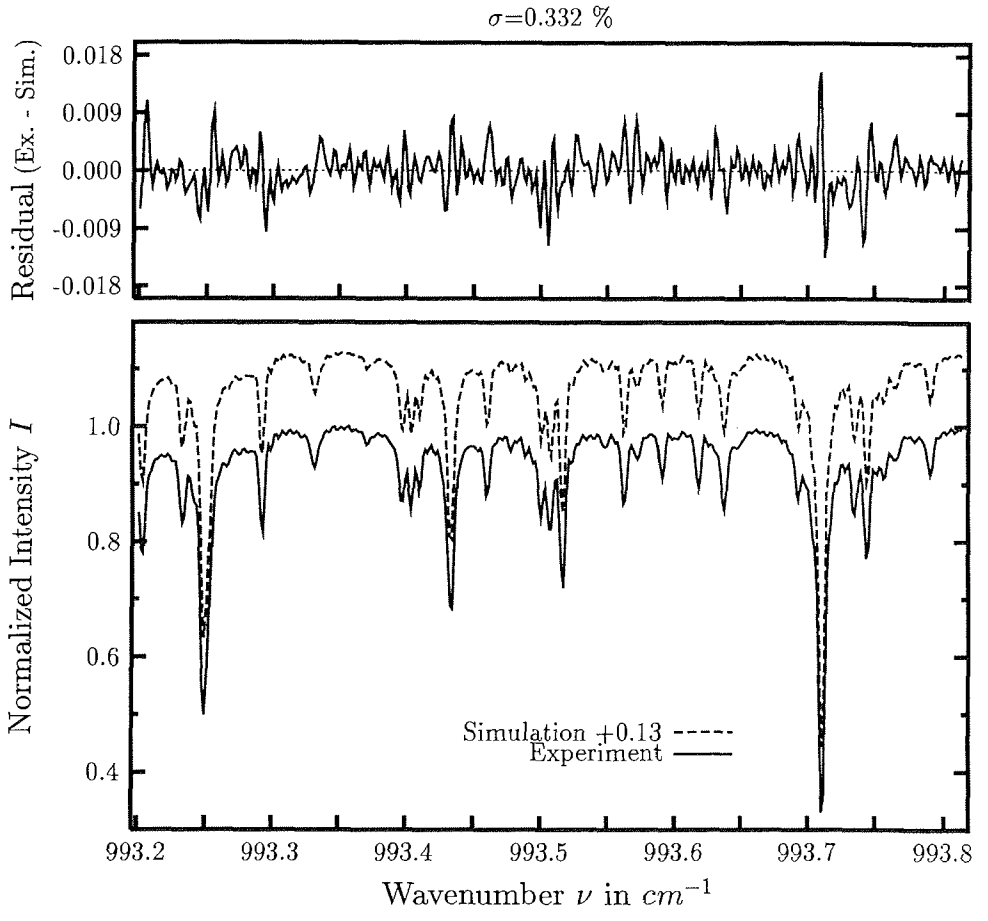

investigated species	: $\mathbf{^{16}O^{18}O^{16}O}$
line position ν_0	: 993.767, 993.791 cm^{-1}
major species	: O_3, $^{16}O^{18}O^{16}O$, $^{16}O^{16}O^{18}O$, H_2O,
	: solar, CO_2, $^{16}O^{17}O^{16}O$
minor species	: $^{16}O^{16}O^{17}O$
weak species	:
name of the spectrum	: 95053034
zenith angle, apodization	: 57.9°, boxcar
max. OPD, field of view	: 180.0 cm, 3.86 $mrad$
spectral interval fitted	: 993.20 – 993.813 cm^{-1}
retrieved total column	: $1.02 \cdot 10^{19}\ cm^{-2}$

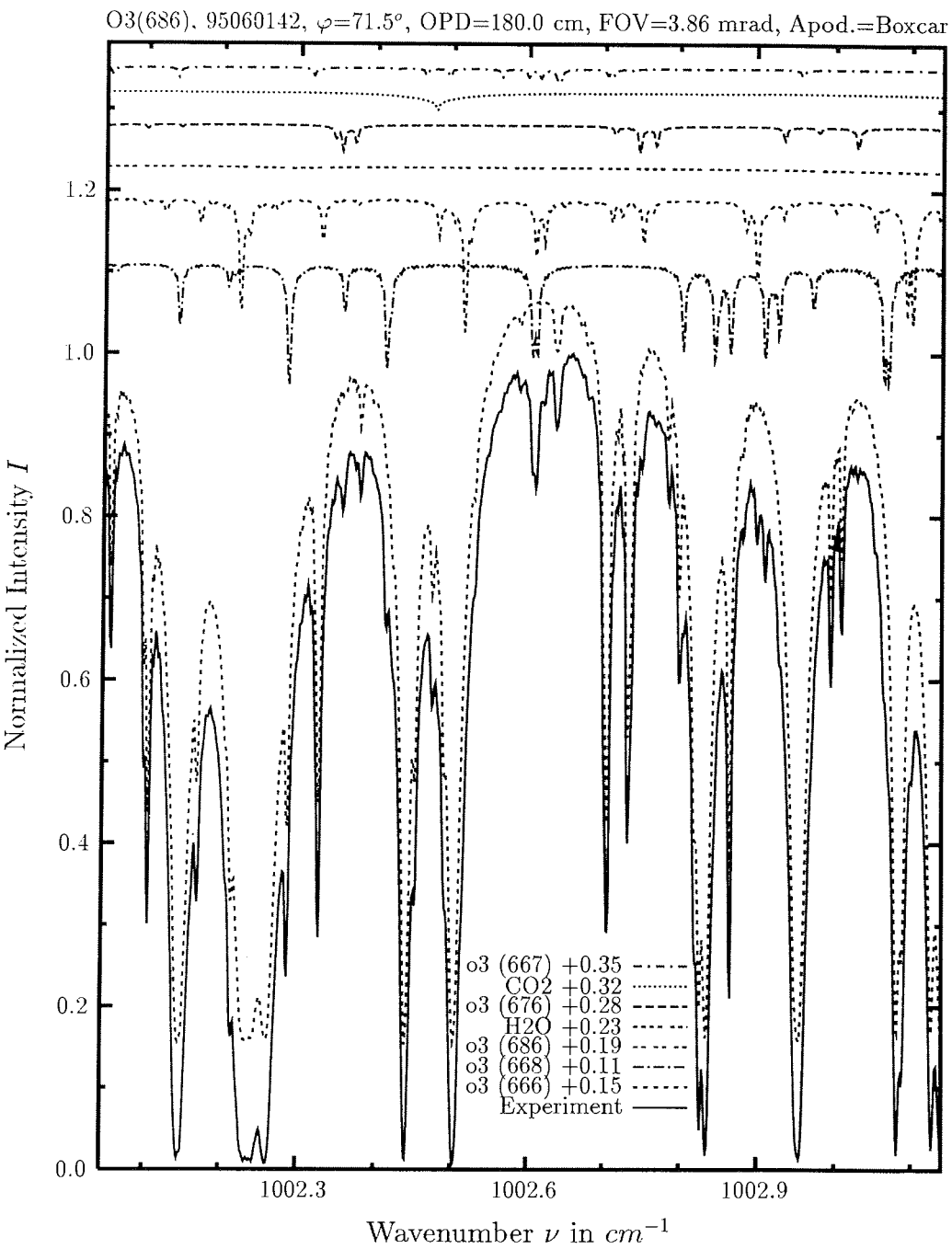
O3(686), 95060142, φ=71.5°, OPD=180.0 cm, FOV=3.86 mrad, Apod.=Boxcar
Normalized Intensity I
Wavenumber ν in cm⁻¹
0.0
0.2
0.4
0.6
0.8
1.0
1.2
1002.3
1002.6
1002.9
o3 (667) +0.35
CO2 +0.32
o3 (676) +0.28
H2O +0.23
o3 (686) +0.19
o3 (668) +0.11
o3 (666) +0.15
Experiment

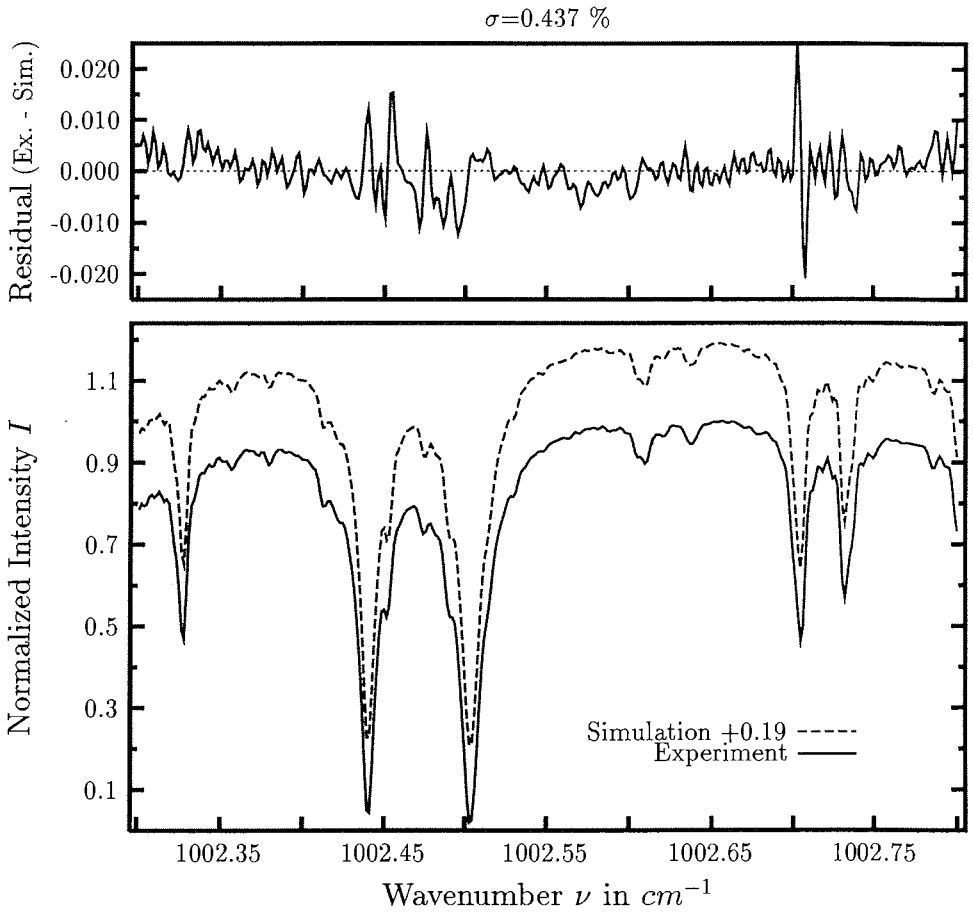

investigated species	:	$^{16}O^{16}O^{18}O$, $^{16}O^{18}O^{16}O$
line position ν_0	:	1002.606, 1002.621 cm^{-1}
major species	:	O_3, $^{16}O^{16}O^{18}O$, $^{16}O^{18}O^{16}O$, H_2O,
	:	$^{16}O^{17}O^{16}O$, CO_2, $^{16}O^{16}O^{17}O$
minor species	:	
weak species	:	
name of the spectrum	:	95053028
zenith angle, apodization	:	57.7°, boxcar
max. OPD, field of view	:	180.0 cm, 3.86 $mrad$
spectral interval fitted	:	I) 1002.30 – 1002.80 cm^{-1}, II) 1002.55 – 1002.80 cm^{-1}
retrieved total column	:	$1.06 \cdot 10^{19}\, cm^{-2}$, $1.04 \cdot 10^{19}\, cm^{-2}$

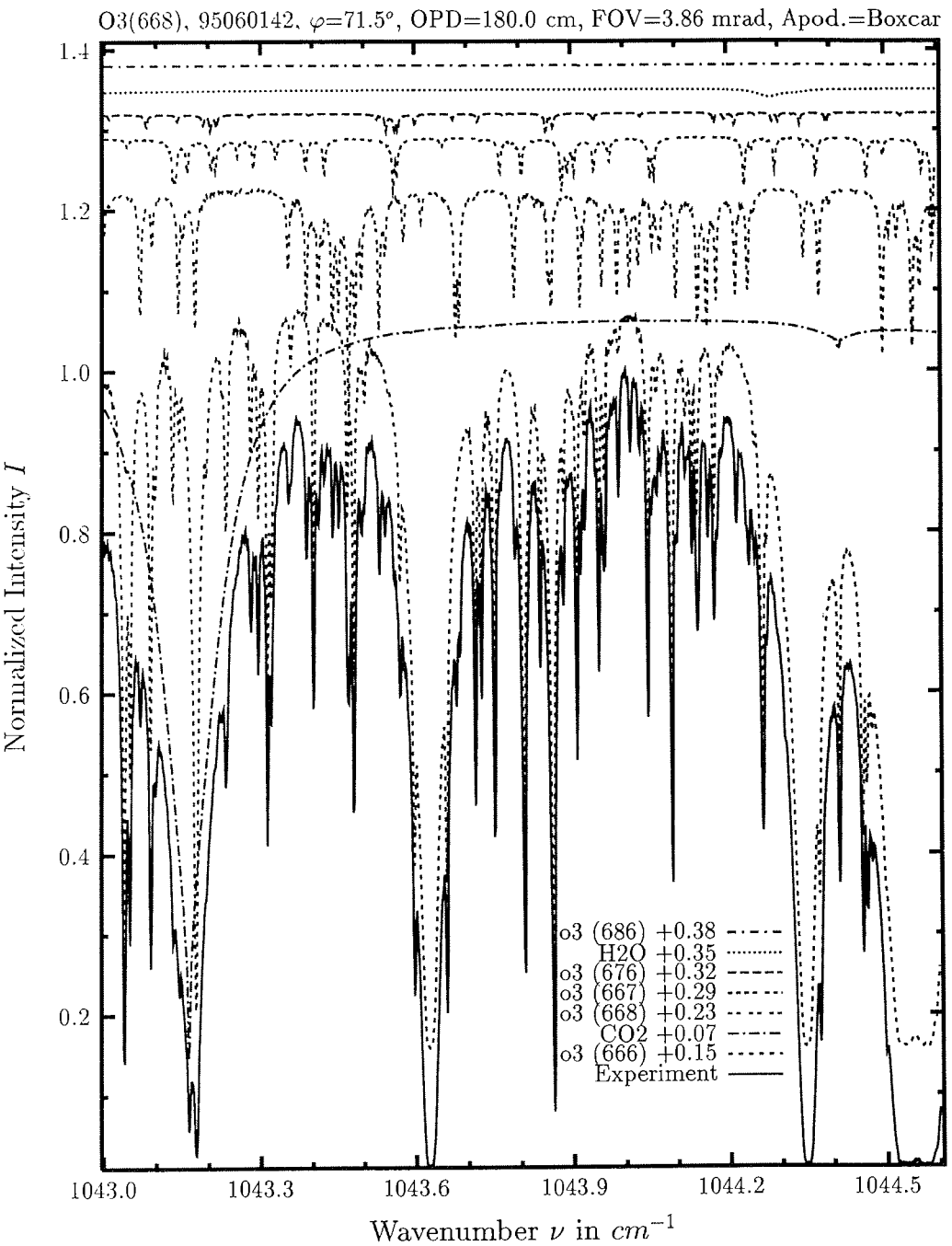
O3(668), 95060142, φ=71.5°, OPD=180.0 cm, FOV=3.86 mrad, Apod.=Boxcar
Normalized Intensity I
Wavenumber ν in cm⁻¹
1.4
1.2
1.0
0.8
0.6
0.4
0.2
1043.0
1043.3
1043.6
1043.9
1044.2
1044.5
o3 (686) +0.38
H2O +0.35
o3 (676) +0.32
o3 (667) +0.29
o3 (668) +0.23
CO2 +0.07
o3 (666) +0.15
Experiment

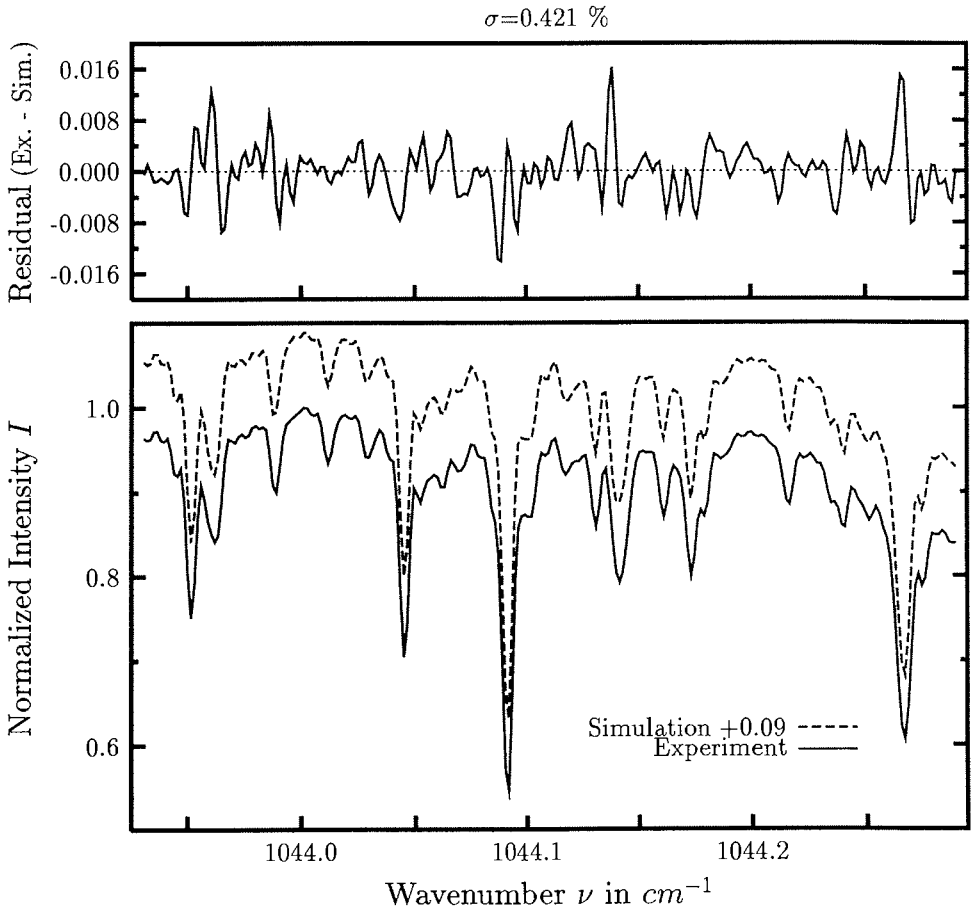

investigated species	:	$^{16}O^{16}O^{18}O$
line position ν_0	:	1043.440, 1044.013, 1044.217 cm^{-1}
major species	:	O_3, CO_2, $^{16}O^{16}O^{18}O$, $^{16}O^{16}O^{17}O$, $^{16}O^{17}O^{16}O$, H_2O
minor species	:	$^{16}O^{18}O^{16}O$
weak species	:	
name of the spectrum	:	95053024
zenith angle, apodization	:	57.3°, boxcar
max. OPD, field of view	:	180.0 cm, 3.86 $mrad$
spectral interval fitted	:	I) 1043.93 - 1044.29 cm^{-1}, II) 1043.26 - 1043.57 cm^{-1}
retrieved total column	:	$1.01 \cdot 10^{19}\ cm^{-2}$

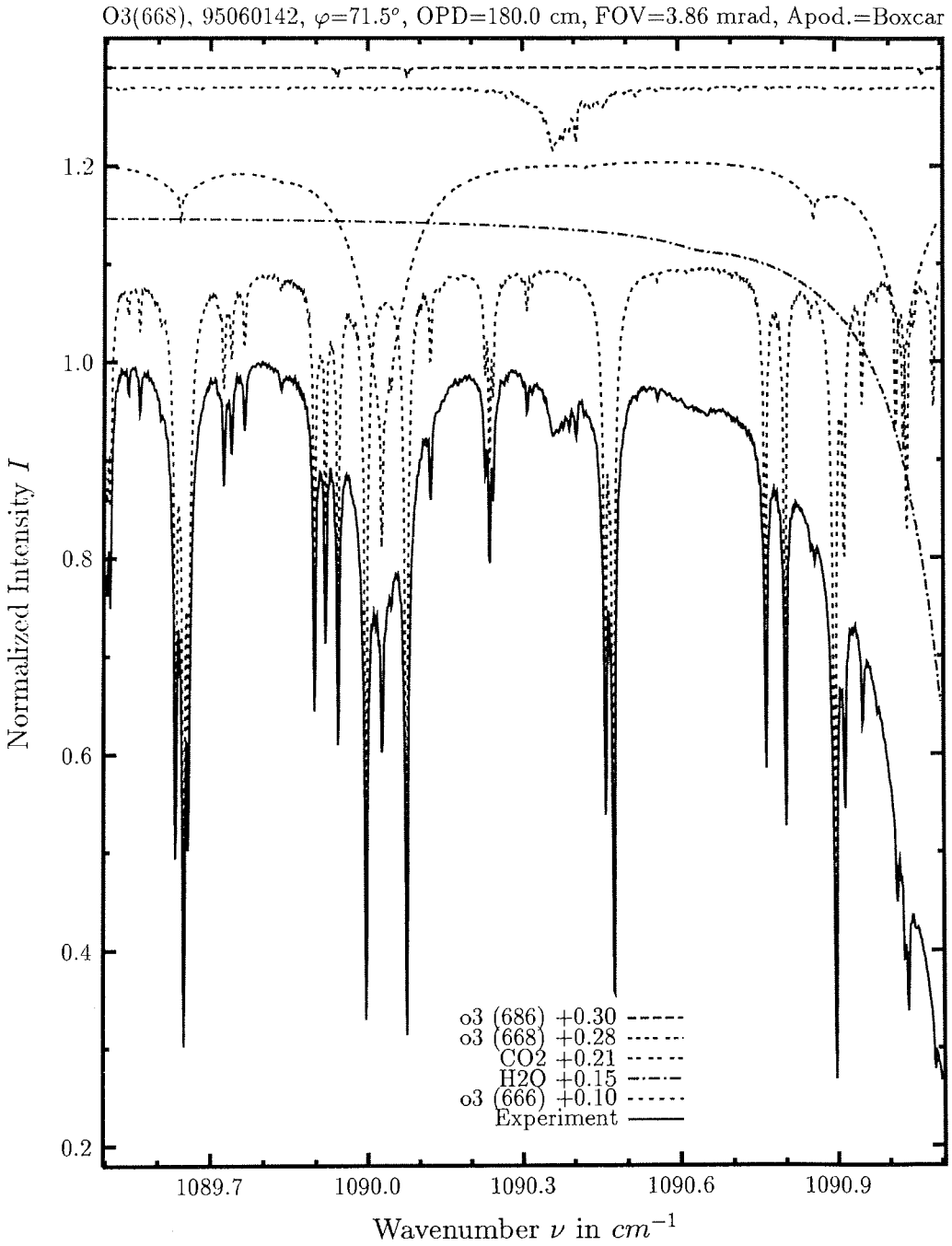
O3(668), 95060142, φ=71.5°, OPD=180.0 cm, FOV=3.86 mrad, Apod.=Boxcar
Normalized Intensity I
1.2
1.0
0.8
0.6
0.4
0.2
1089.7
1090.0
1090.3
1090.6
1090.9
Wavenumber ν in cm⁻¹
o3 (686) +0.30
o3 (668) +0.28
CO2 +0.21
H2O +0.15
o3 (666) +0.10
Experiment

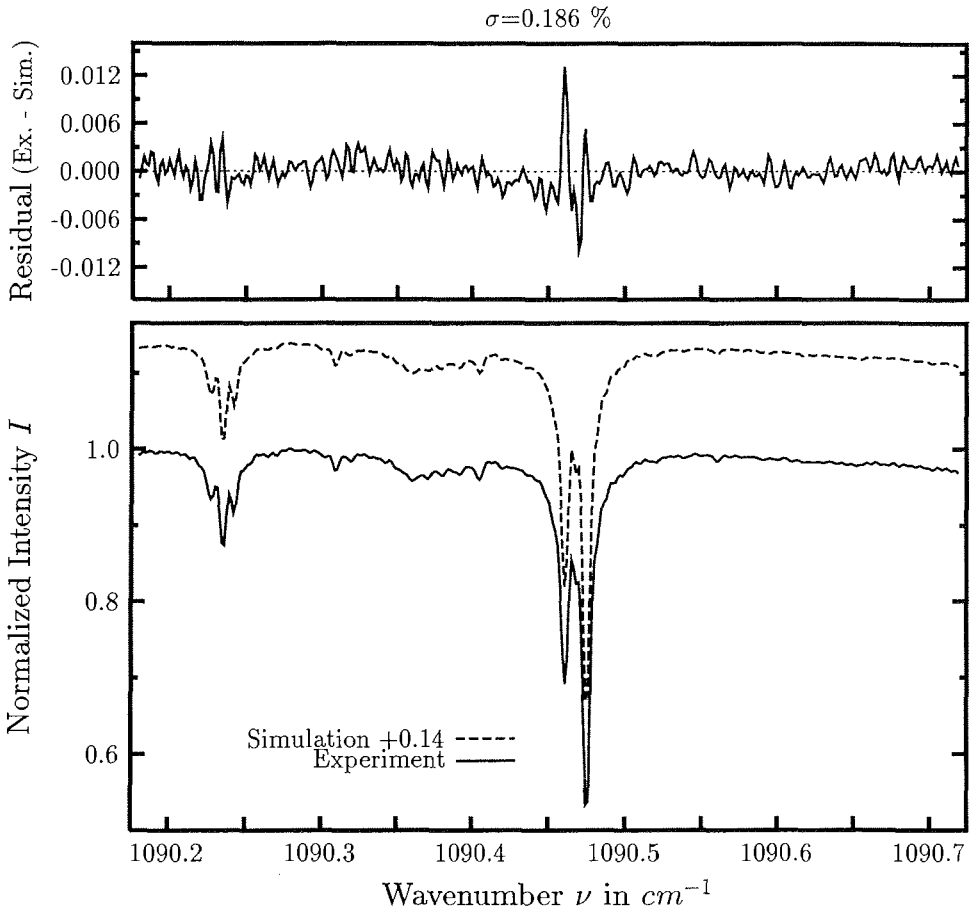

investigated species	: $^{16}O^{16}O^{18}O$
line position ν_0	: 1090.372*) cm^{-1}
major species	: O_3, H_2O, CO_2, $^{16}O^{16}O^{18}O$
minor species	: $^{16}O^{18}O^{16}O$
weak species	:
name of the spectrum	: 95053028
zenith angle, apodization	: 57.7°, boxcar
max. OPD, field of view	: 180.0 cm, 3.86 $mrad$
spectral interval fitted	: 1090.18 – 1090.72 cm^{-1}
retrieved total column	: $1.13 \cdot 10^{19}\, cm^{-2}$

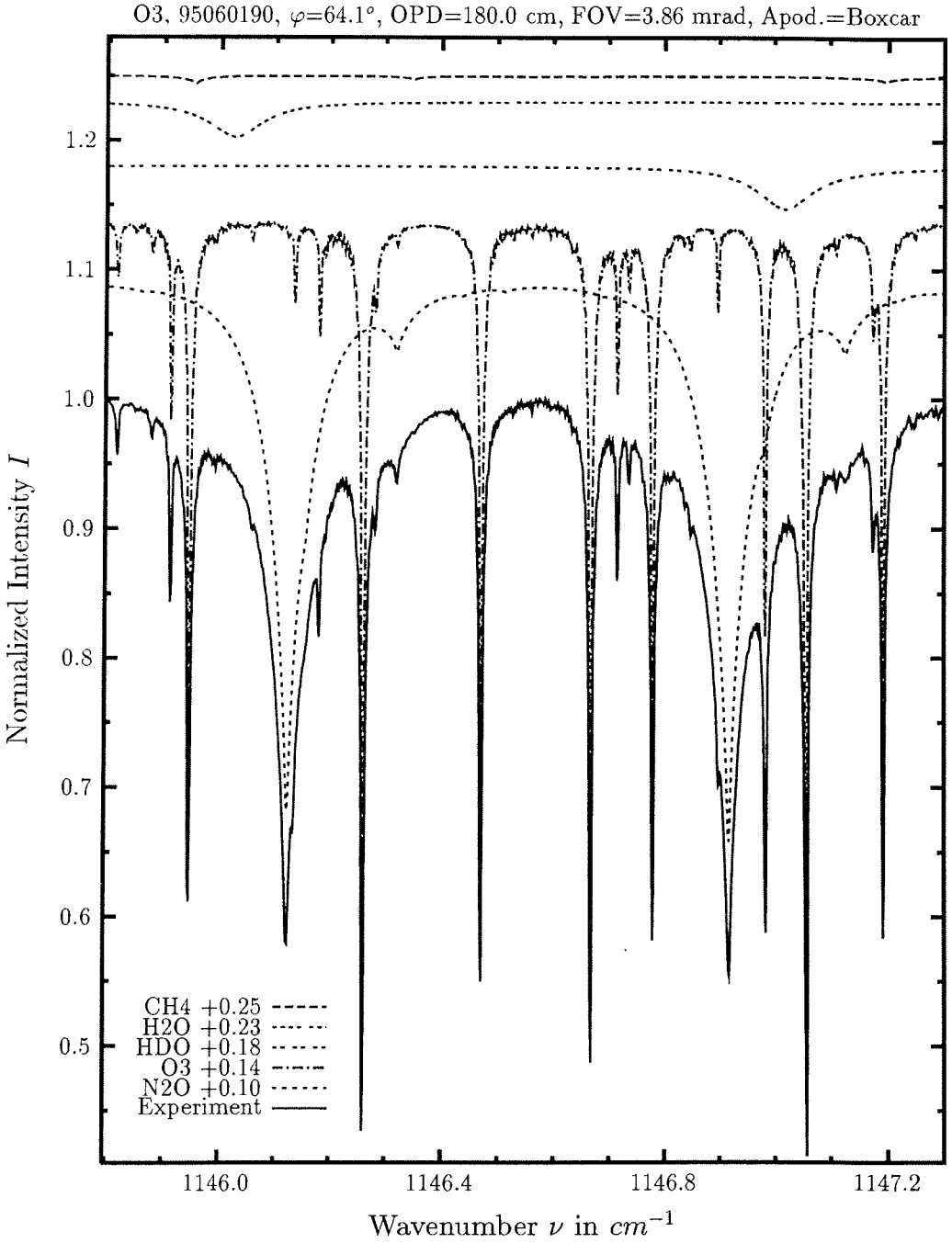
O3, 95060190, φ=64.1°, OPD=180.0 cm, FOV=3.86 mrad, Apod.=Boxcar
Normalized Intensity I
1.2
1.1
1.0
0.9
0.8
0.7
0.6
0.5
CH4 +0.25
H2O +0.23
HDO +0.18
O3 +0.14
N2O +0.10
Experiment
1146.0
1146.4
1146.8
1147.2
Wavenumber ν in cm⁻¹

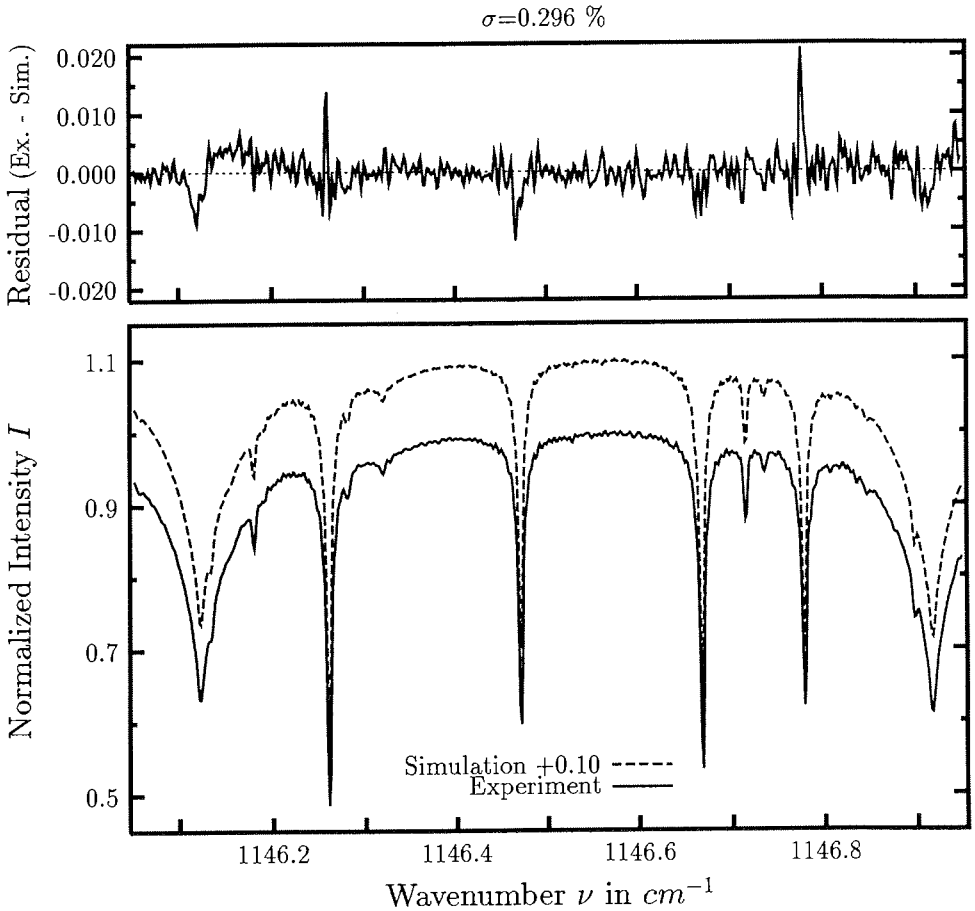

investigated species	:	$^{16}O^{16}O^{16}O$
line position ν_0	:	1146.472, 1146.669 cm^{-1}
major species	:	O_3, N_2O, HDO, H_2O
minor species	:	CH_4
weak species	:	
name of the spectrum	:	95052876
zenith angle, apodization	:	59.0°, boxcar
max. OPD, field of view	:	180.0 cm, 3.86 $mrad$
spectral interval fitted	:	I) 1145.50 - 1147.45 cm^{-1}, II) 1146.05 - 1146.95 cm^{-1}
retrieved total column	:	$9.56 \cdot 10^{18}\ cm^{-2}$

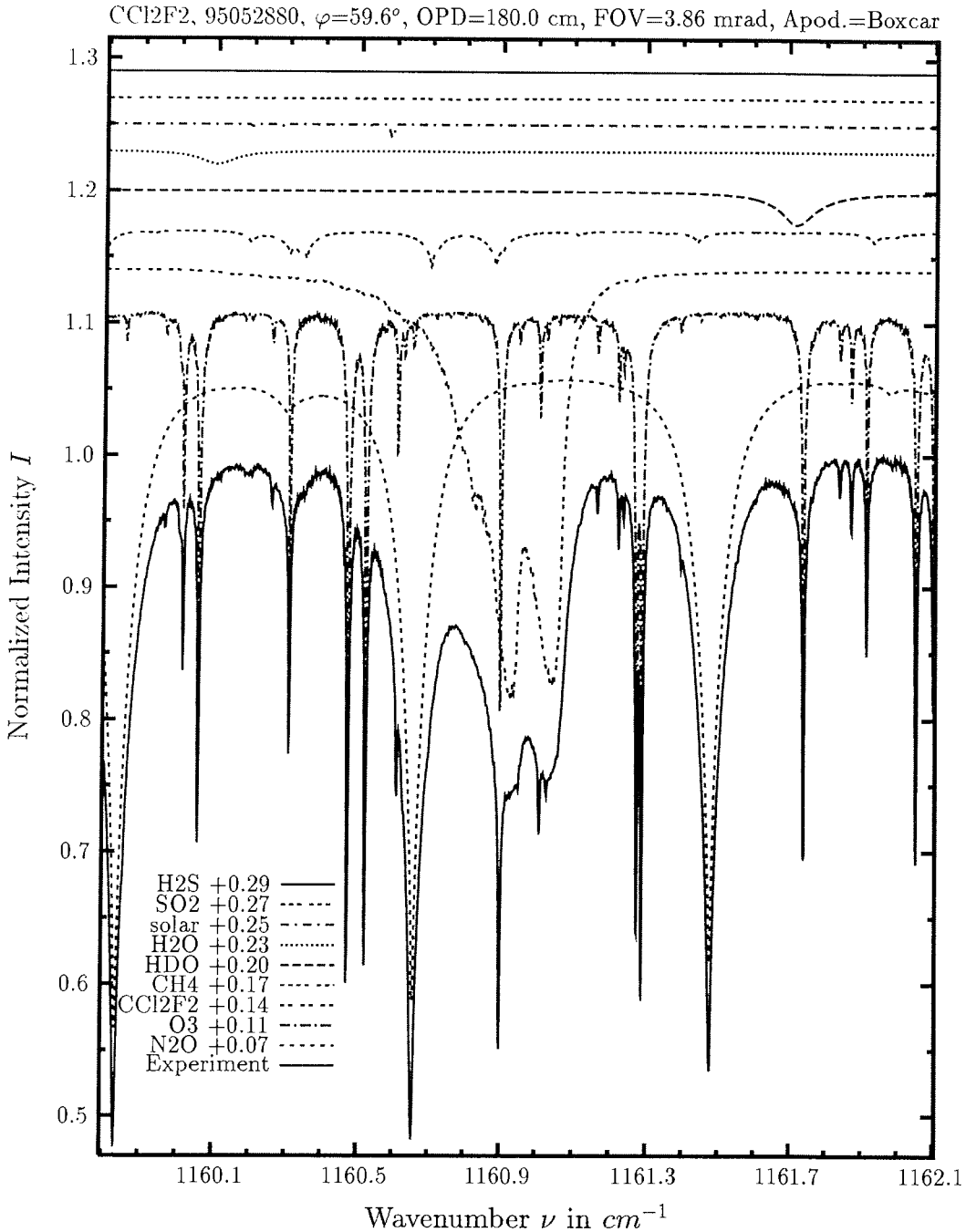
CCl2F2, 95052880, φ=59.6°, OPD=180.0 cm, FOV=3.86 mrad, Apod.=Boxcar
Normalized Intensity I
Wavenumber ν in cm⁻¹
1.3
1.2
1.1
1.0
0.9
0.8
0.7
0.6
0.5
1160.1
1160.5
1160.9
1161.3
1161.7
1162.1
H2S +0.29
SO2 +0.27
solar +0.25
H2O +0.23
HDO +0.20
CH4 +0.17
CCl2F2 +0.14
O3 +0.11
N2O +0.07
Experiment

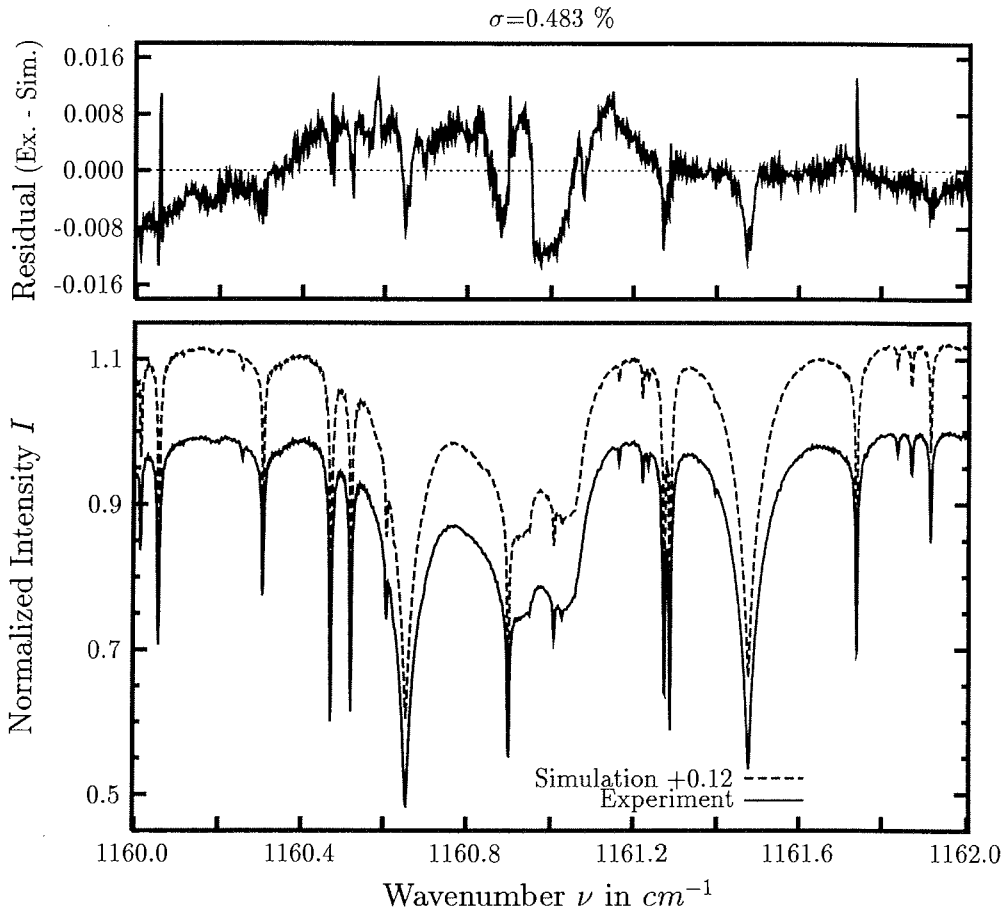

investigated species	: $\mathbf{CCl_2F_2}$
line position ν_0	: 1160.947*), 1161.065*) cm^{-1}
major species	: N_2O, O_3, CCl_2F_2, CH_4, HDO, H_2O
minor species	: solar, SO_2
weak species	: H_2S, HO_2NO_2
name of the spectrum	: 95052880
zenith angle, apodization	: 59.6°, boxcar
max. OPD, field of view	: 180.0 cm, 3.86 $mrad$
spectral interval fitted	: 1160.00 - 1162.00 cm^{-1}
retrieved total column	: $8.96 \cdot 10^{15}$ cm^{-2}

comments: The simulation achievable with the spectroscopic data from the NASA AFGL files does not meet the observed spectrum. CFC's are not included in the HITRAN data base.

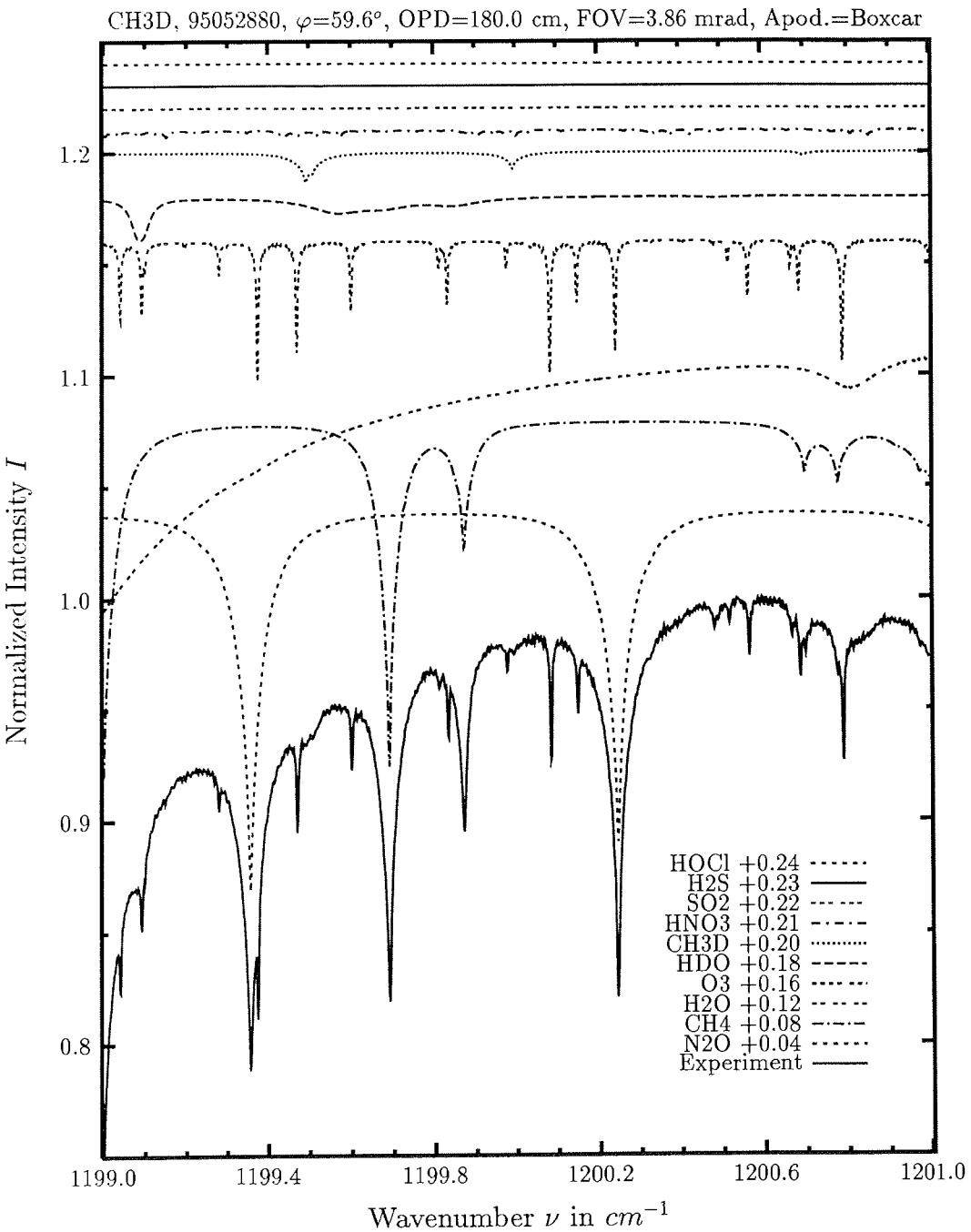
CH3D, 95052880, φ=59.6°, OPD=180.0 cm, FOV=3.86 mrad, Apod.=Boxcar
Normalized Intensity I
1.2
1.1
1.0
0.9
0.8
1199.0
1199.4
1199.8
1200.2
1200.6
1201.0
Wavenumber ν in cm⁻¹
HOCl +0.24
H2S +0.23
SO2 +0.22
HNO3 +0.21
CH3D +0.20
HDO +0.18
O3 +0.16
H2O +0.12
CH4 +0.08
N2O +0.04
Experiment

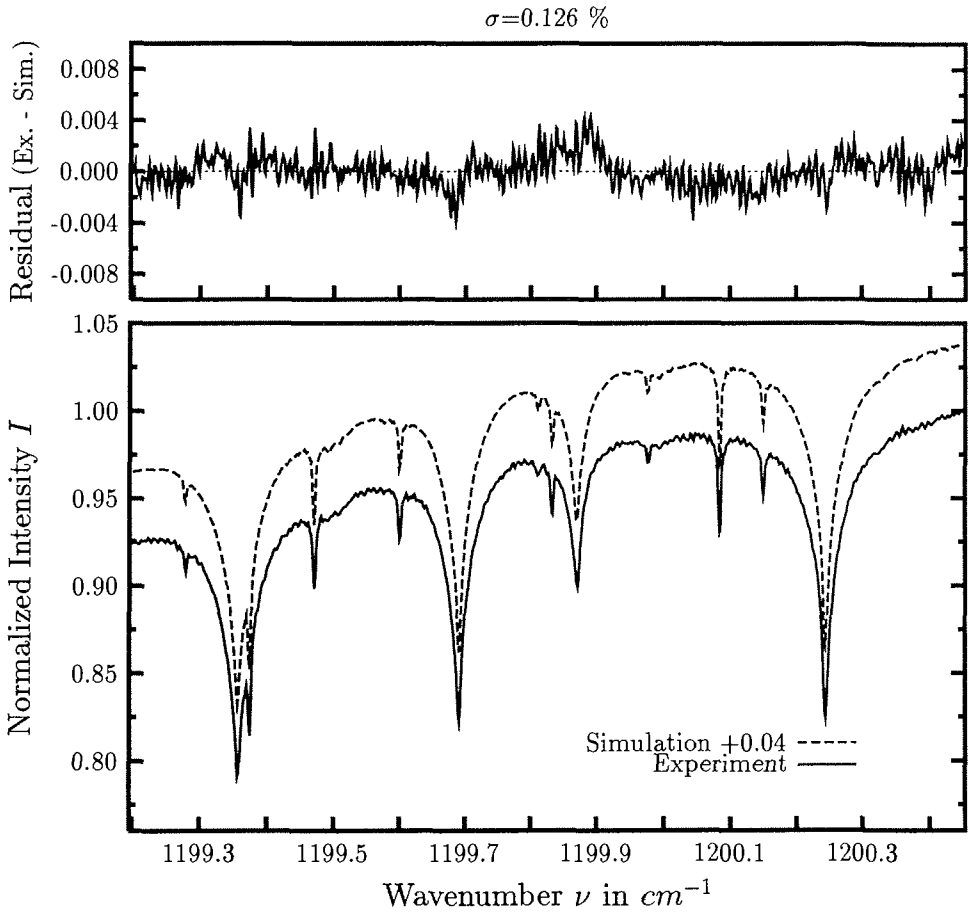

investigated species	: **CH_3D**
line position ν_0	: 1199.995 cm^{-1}
major species	: N_2O, CH_4, H_2O, O_3, HDO, CH_3D
minor species	: HNO_3
weak species	: SO_2, H_2S, $HOCl$, C_2H_2, H_2O,2 NH_3
name of the spectrum	: 95052880
zenith angle, apodization	: 59.6°, boxcar
max. OPD, field of view	: 180.0 cm, 3.86 $mrad$
spectral interval fitted	: 1199.20 - 1200.45 cm^{-1}
retrieved total column	: $4.74 \cdot 10^{19}\, cm^{-2}$

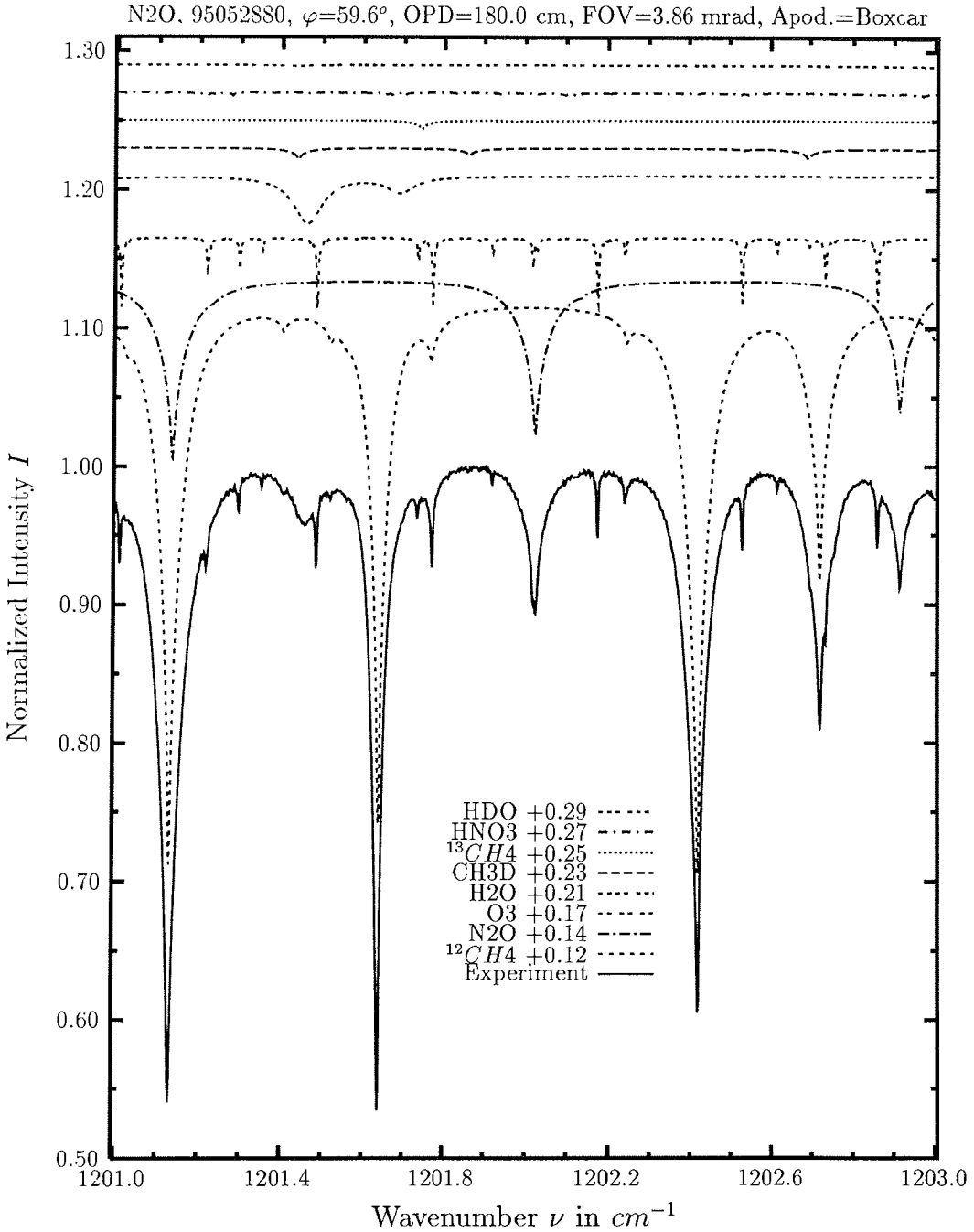
N2O, 95052S80, φ=59.6°, OPD=180.0 cm, FOV=3.86 mrad, Apod.=Boxcar
Normalized Intensity I
Wavenumber ν in cm⁻¹
1.30
1.20
1.10
1.00
0.90
0.80
0.70
0.60
0.50
1201.0
1201.4
1201.8
1202.2
1202.6
1203.0
HDO +0.29
HNO3 +0.27
13CH4 +0.25
CH3D +0.23
H2O +0.21
O3 +0.17
N2O +0.14
12CH4 +0.12
Experiment

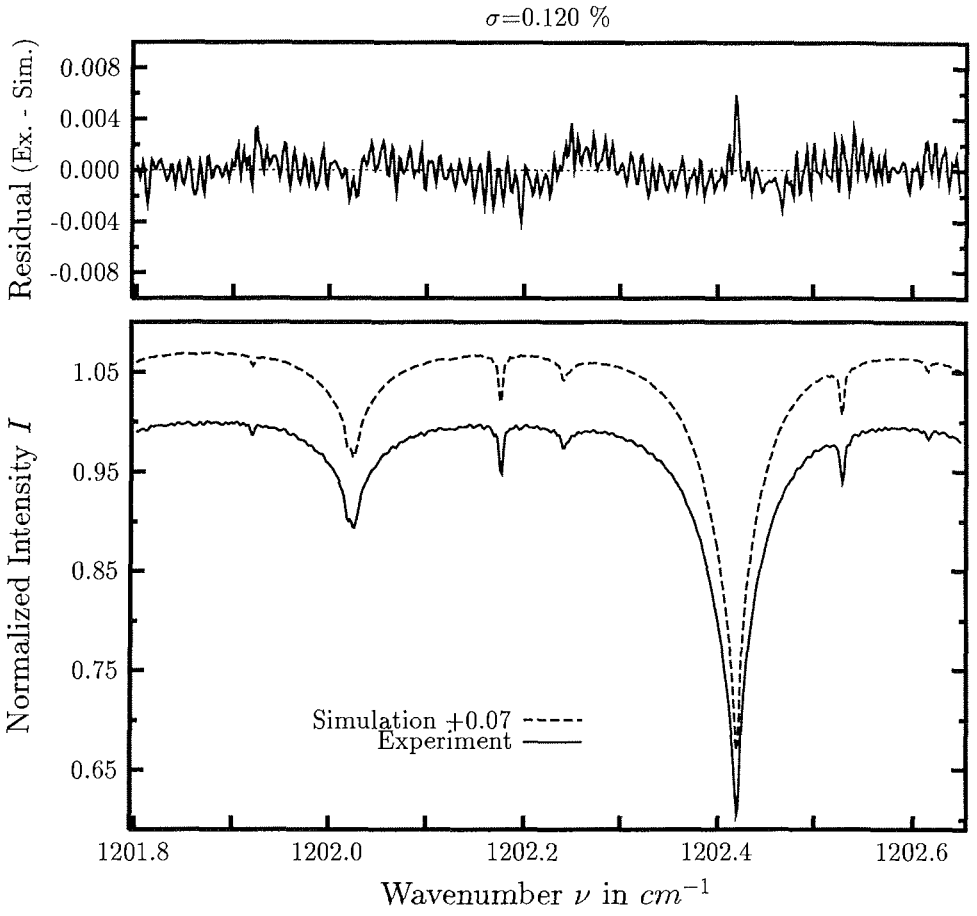

investigated species	: **N_2O, CH_4**
line position ν_0	: 1202.026, 1202.421 cm^{-1}
major species	: $12CH_4$, N_2O, O_3, H_2O
minor species	: CH_3D, $13CH_4$, HNO_3
weak species	: HDO
name of the spectrum	: 95052880
zenith angle, apodization	: 59.6°, boxcar
max. OPD, field of view	: 180.0 cm, 3.86 $mrad$
spectral interval fitted	: 1201.80 – 1202.65 cm^{-1}
retrieved total column	: $6.25 \cdot 10^{18}\, cm^{-2}$, $3.63 \cdot 10^{19}\, cm^{-2}$

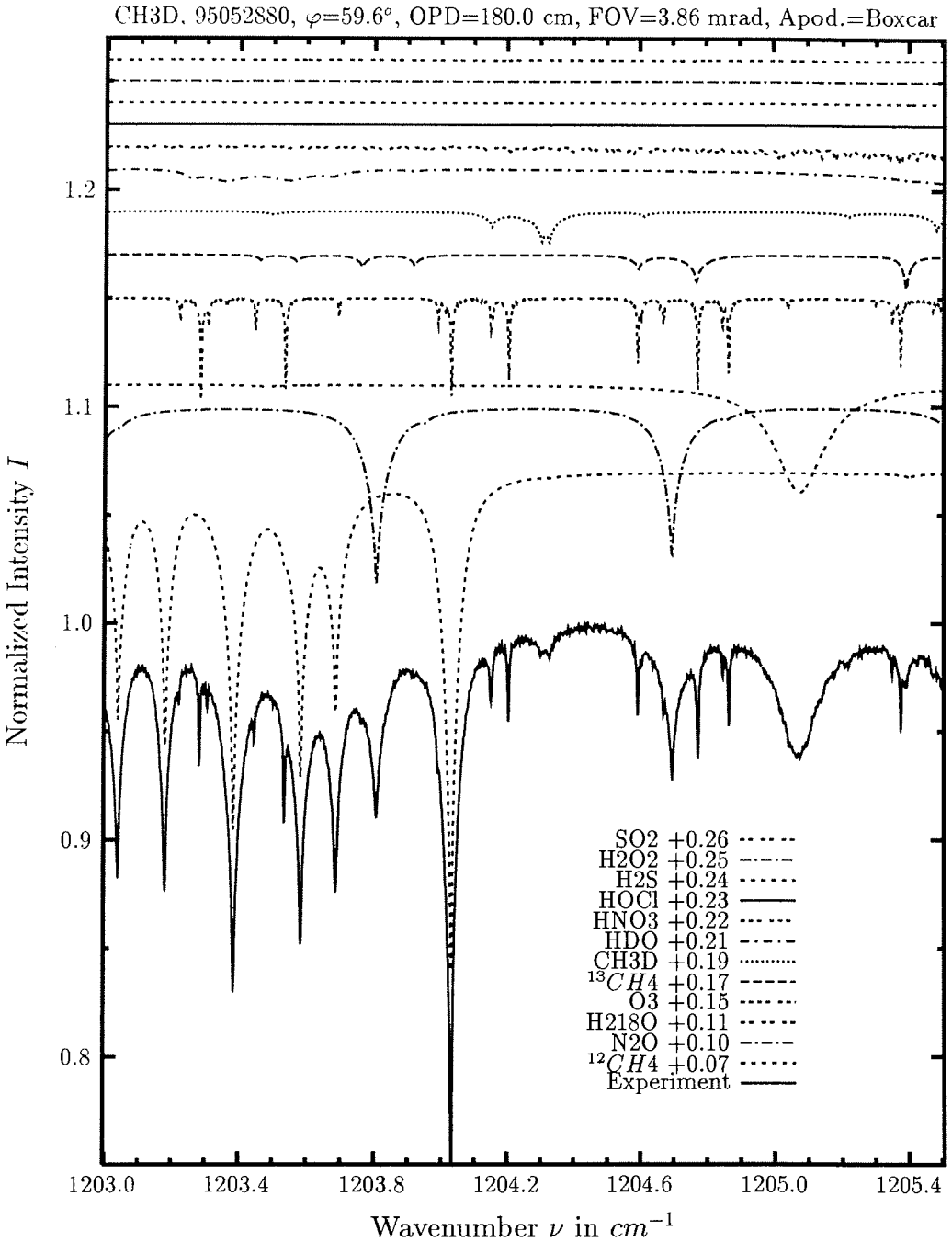
CH3D, 95052880, φ=59.6°, OPD=180.0 cm, FOV=3.86 mrad, Apod.=Boxcar
Normalized Intensity I
1.2
1.1
1.0
0.9
0.8
1203.0
1203.4
1203.8
1204.2
1204.6
1205.0
1205.4
Wavenumber ν in cm⁻¹
SO2 +0.26
H2O2 +0.25
H2S +0.24
HOCl +0.23
HNO3 +0.22
HDO +0.21
CH3D +0.19
13CH4 +0.17
O3 +0.15
H218O +0.11
N2O +0.10
12CH4 +0.07
Experiment

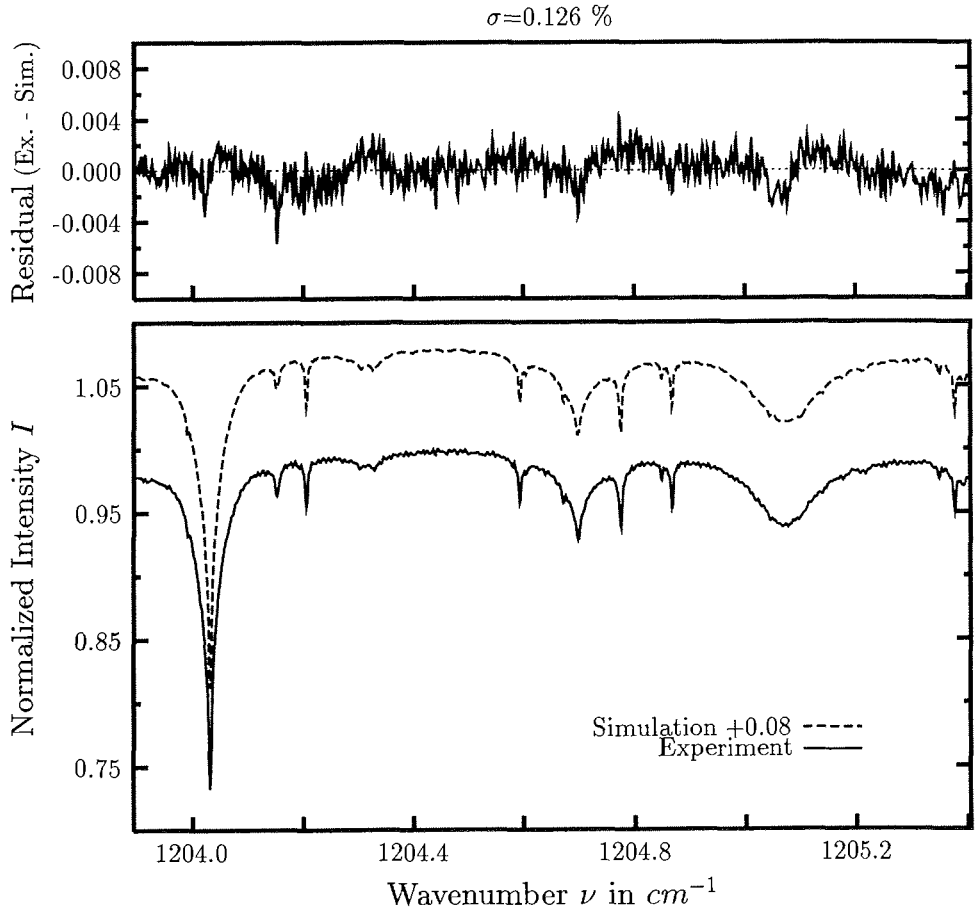

investigated species	: **CH_3D, $H_2^{18}O$**
line position ν_0	: 1204.305 & 1204.328 cm^{-1}, 1205.080 cm^{-1}
major species	: $^{12}CH_4$, N_2O, $H_2{}^{18}O$, O_3, $^{13}CH_4$, CH_3D
minor species	: HNO_3, HDO, $H_2{}^{16}O$
weak species	: $HOCl$, H_2S, H_2O_2, SO_2, NH_3
name of the spectrum	: 95052880
zenith angle, apodization	: 59.6°, boxcar
max. OPD, field of view	: 180.0 cm, 3.86 $mrad$
spectral interval fitted	: 1203.90 – 1205.40 cm^{-1}
retrieved total column	: $4.69 \cdot 10^{19}\,cm^{-2}$, $1.51 \cdot 10^{22}\,cm^{-2}$

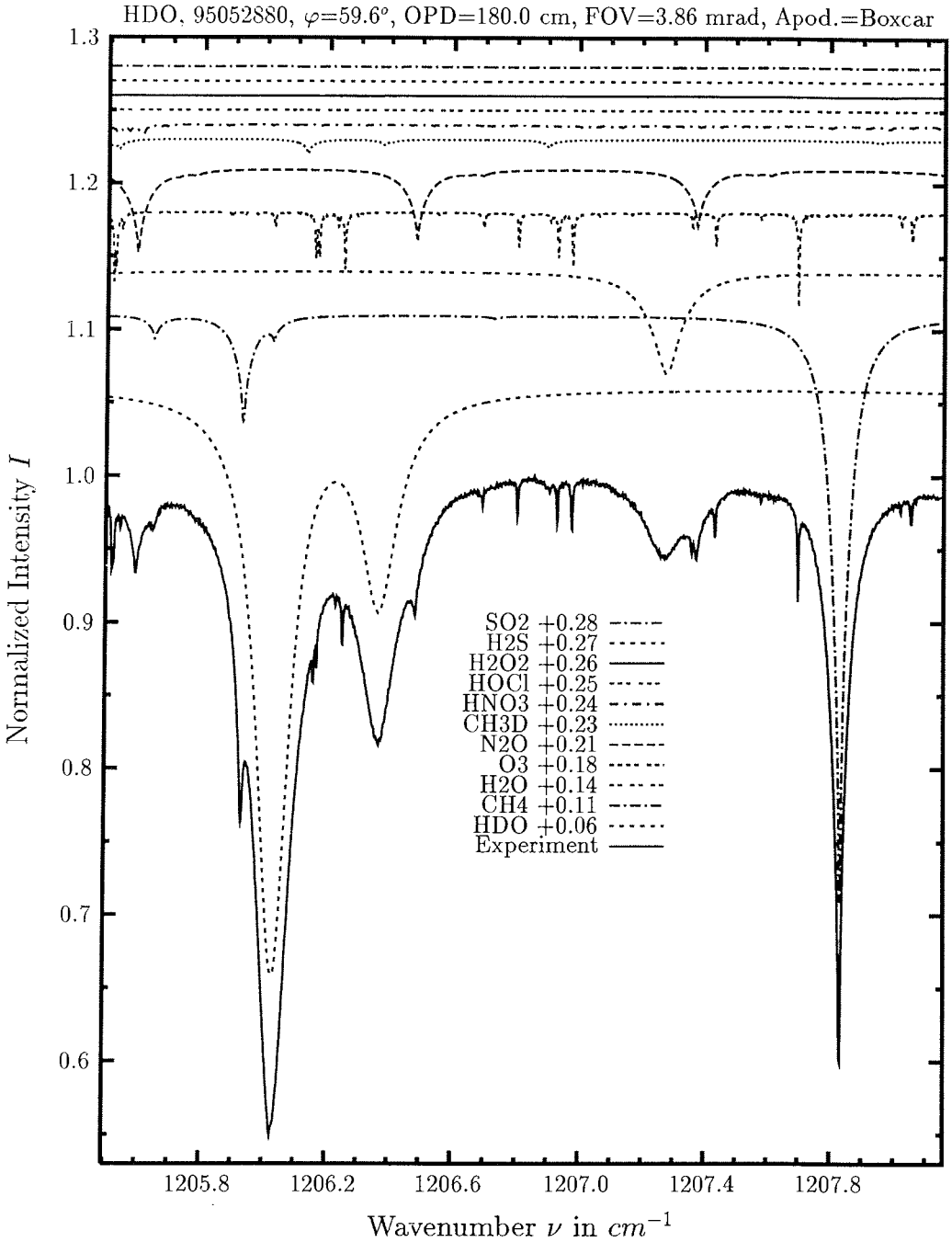
HDO, 95052880, φ=59.6°, OPD=180.0 cm, FOV=3.86 mrad, Apod.=Boxcar
Normalized Intensity I
Wavenumber ν in cm⁻¹
1.3
1.2
1.1
1.0
0.9
0.8
0.7
0.6
1205.8
1206.2
1206.6
1207.0
1207.4
1207.8
SO2 +0.28
H2S +0.27
H2O2 +0.26
HOCl +0.25
HNO3 +0.24
CH3D +0.23
N2O +0.21
O3 +0.18
H2O +0.14
CH4 +0.11
HDO +0.06
Experiment

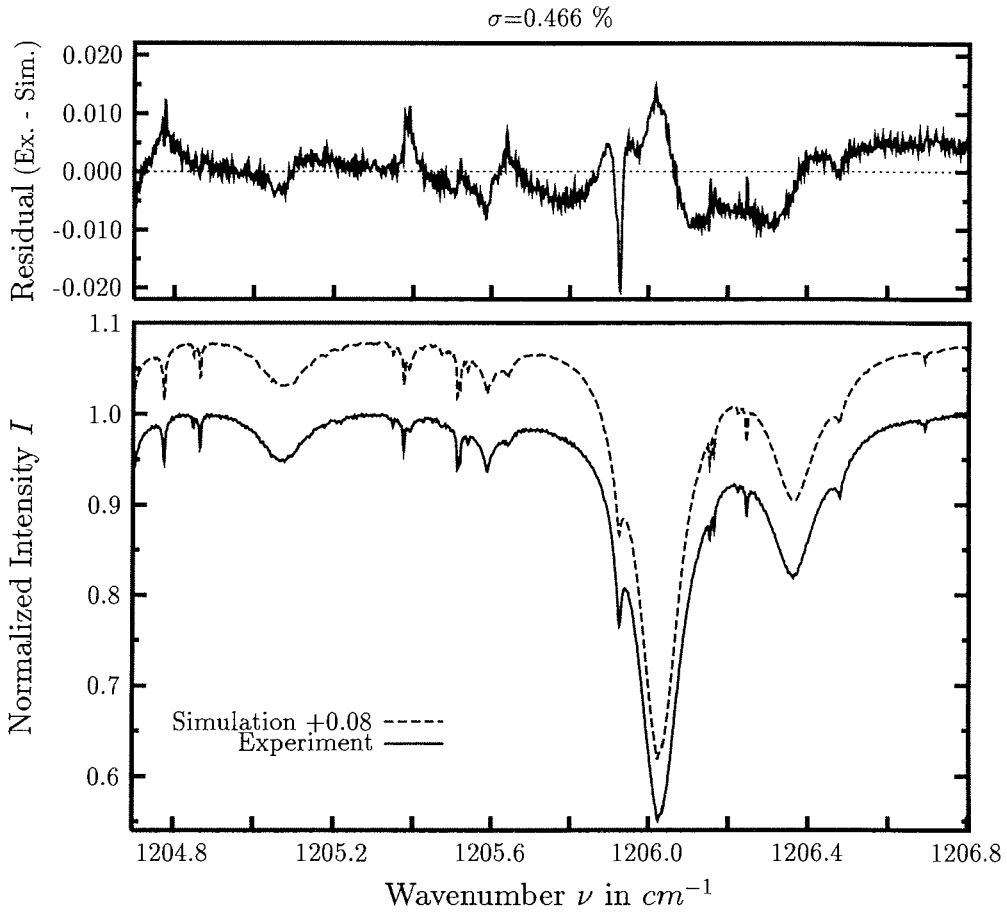

investigated species	: **HDO**
line position ν_0	: 1206.020, 1206.036, 1206.366 cm^{-1}
major species	: CH_4, HDO, H_2O, O_3, N_2O
minor species	: CH_3D, HNO_3
weak species	: $HOCl$, H_2O,2 H_2S, SO_2, C_2H_2, NH_3
name of the spectrum	: 95052880
zenith angle, apodization	: 59.6°, boxcar
max. OPD, field of view	: 180.0 cm, 3.86 $mrad$
spectral interval fitted	: 1204.70 – 1206.80 cm^{-1}
retrieved total column	: $1.12 \cdot 10^{22}\, cm^{-2}$

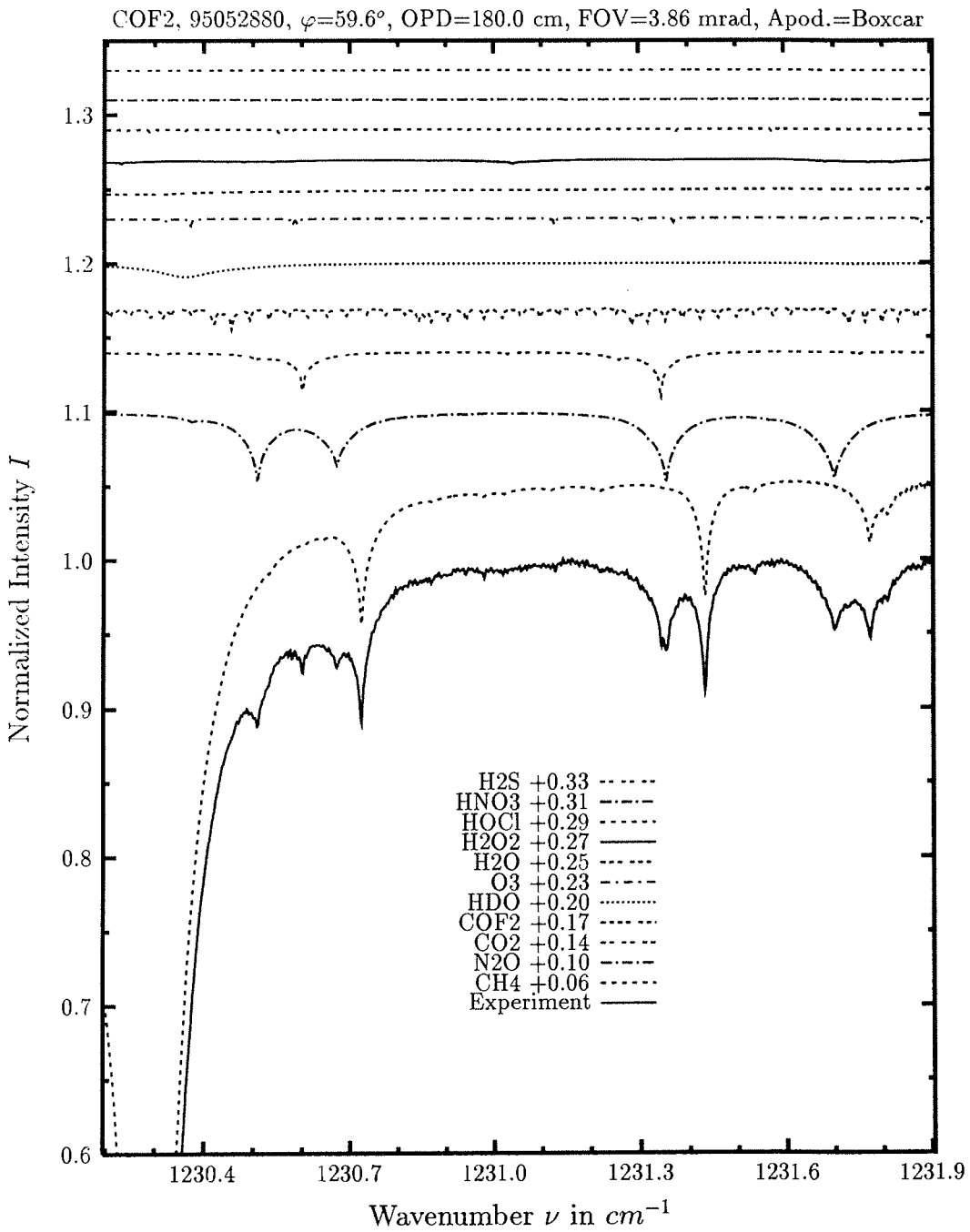
COF2, 95052880, φ=59.6°, OPD=180.0 cm, FOV=3.86 mrad, Apod.=Boxcar
Normalized Intensity I
1.3
1.2
1.1
1.0
0.9
0.8
0.7
0.6
1230.4
1230.7
1231.0
1231.3
1231.6
1231.9
Wavenumber ν in cm⁻¹
H2S +0.33
HNO3 +0.31
HOCl +0.29
H2O2 +0.27
H2O +0.25
O3 +0.23
HDO +0.20
COF2 +0.17
CO2 +0.14
N2O +0.10
CH4 +0.06
Experiment

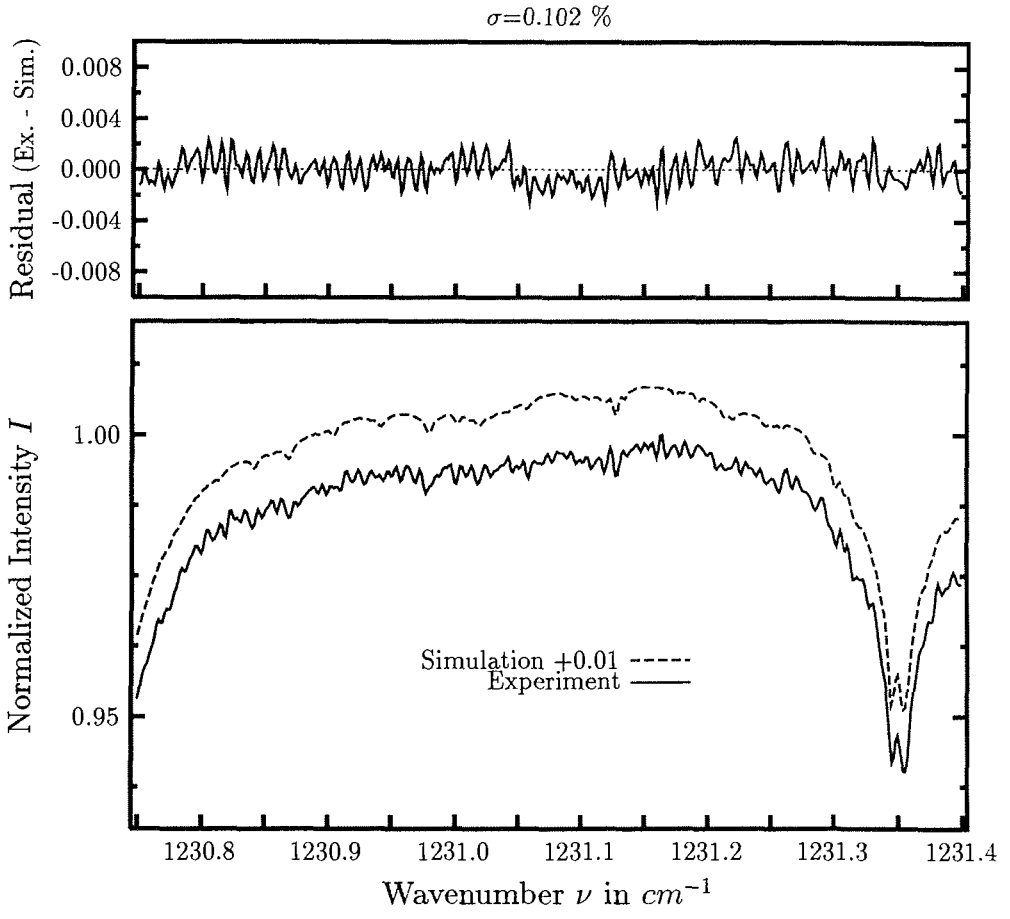

investigated species	: **COF_2**
line position ν_0	: 1231.020*) cm^{-1}
major species	: CH_4, N_2O, CO_2, COF_2, HDO
minor species	: O_3, H_2O, $HOCl$
weak species	: HNO_3, H_2S
name of the spectrum	: 95053034
zenith angle, apodization	: 57.9°, boxcar
max. OPD, field of view	: 180.0 cm, 3.86 $mrad$
spectral interval fitted	: 1230.75 - 1231.40 cm^{-1}
retrieved total column	: $3.96 \cdot 10^{14}$ cm^{-2}

comments: COF_2 is a weak absorber that needs high resolution spectra with a good S/N. The contribution plot is calculated with twice the amount retrieved.

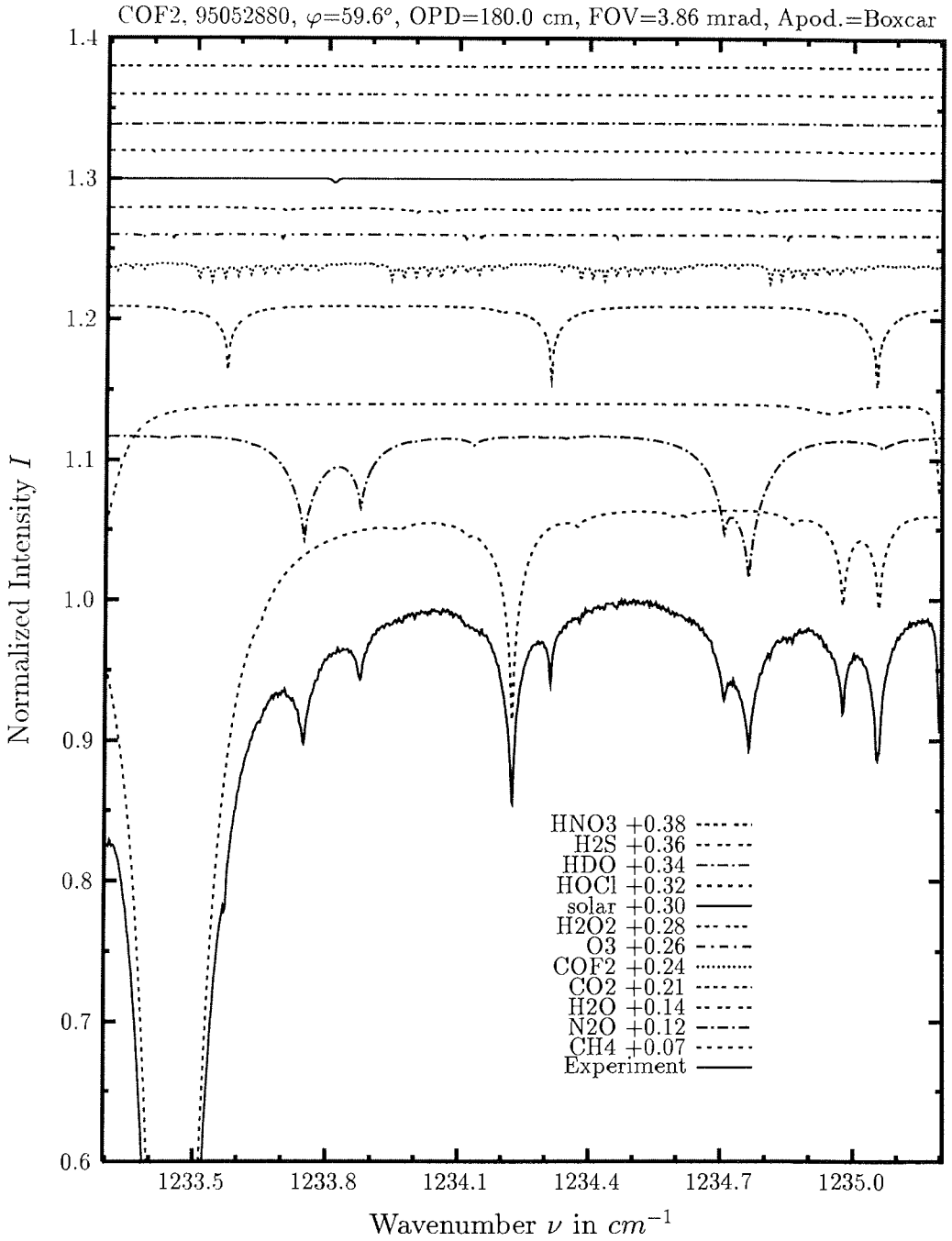
COF2, 95052880, φ=59.6°, OPD=180.0 cm, FOV=3.86 mrad, Apod.=Boxcar
Normalized Intensity I
Wavenumber ν in cm⁻¹
1.4
1.3
1.2
1.1
1.0
0.9
0.8
0.7
0.6
1233.5
1233.8
1234.1
1234.4
1234.7
1235.0
HNO3 +0.38
H2S +0.36
HDO +0.34
HOCl +0.32
solar +0.30
H2O2 +0.28
O3 +0.26
COF2 +0.24
CO2 +0.21
H2O +0.14
N2O +0.12
CH4 +0.07
Experiment

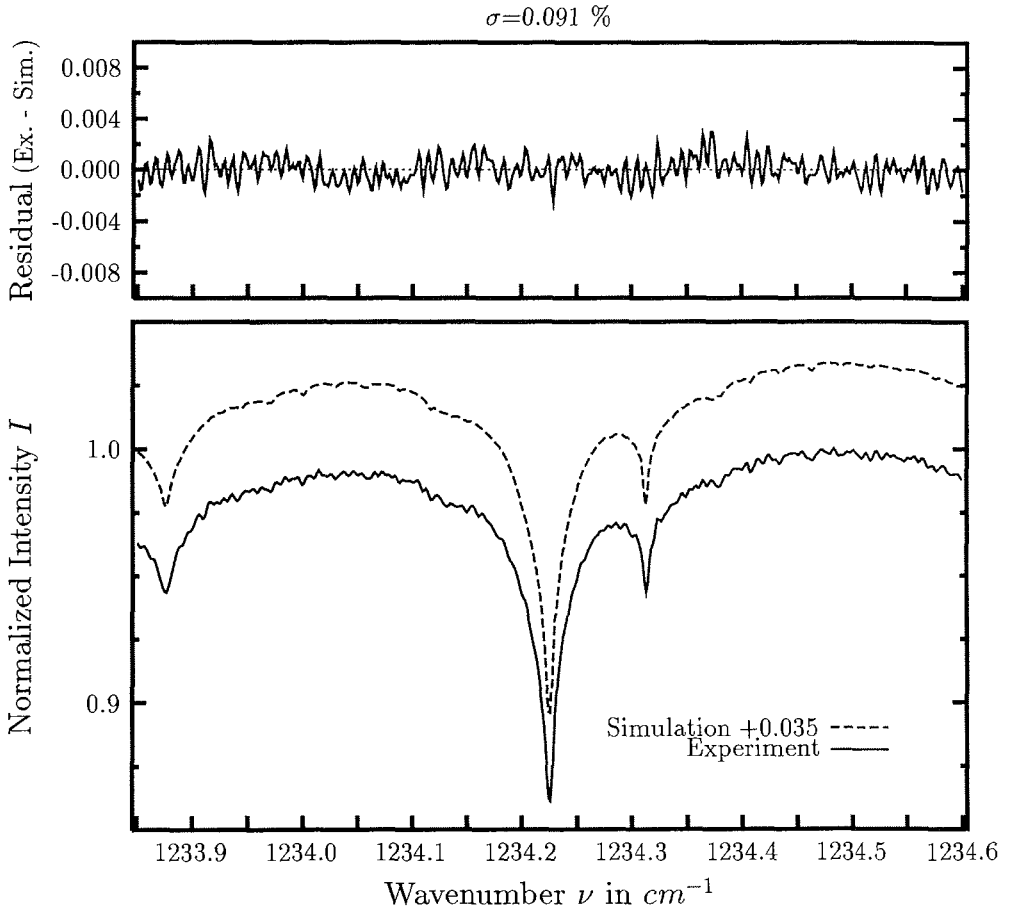

investigated species	: **COF_2, $^{13}CH_4$**
line position ν_0	: 1234.408*) & 1233.455*), 1234.226 cm^{-1}
major species	: CH_4, N_2O, H_2O, CO_2, COF_2
minor species	: O_3, H_2O_2, solar
weak species	: $HOCl$, HDO, H_2S, HNO_3
name of the spectrum	: 95053028
zenith angle, apodization	: 57.7°, boxcar
max. OPD, field of view	: 180.0 cm, 3.86 $mrad$
spectral interval fitted	: 1233.85 – 1234.60 cm^{-1}
retrieved total column	: $3.67 \cdot 10^{14}\ cm^{-2}$

comments: COF_2 is a weak absorber that needs high resolution spectra with a good S/N. The contribution plot is calculated with twice the amount retrieved.

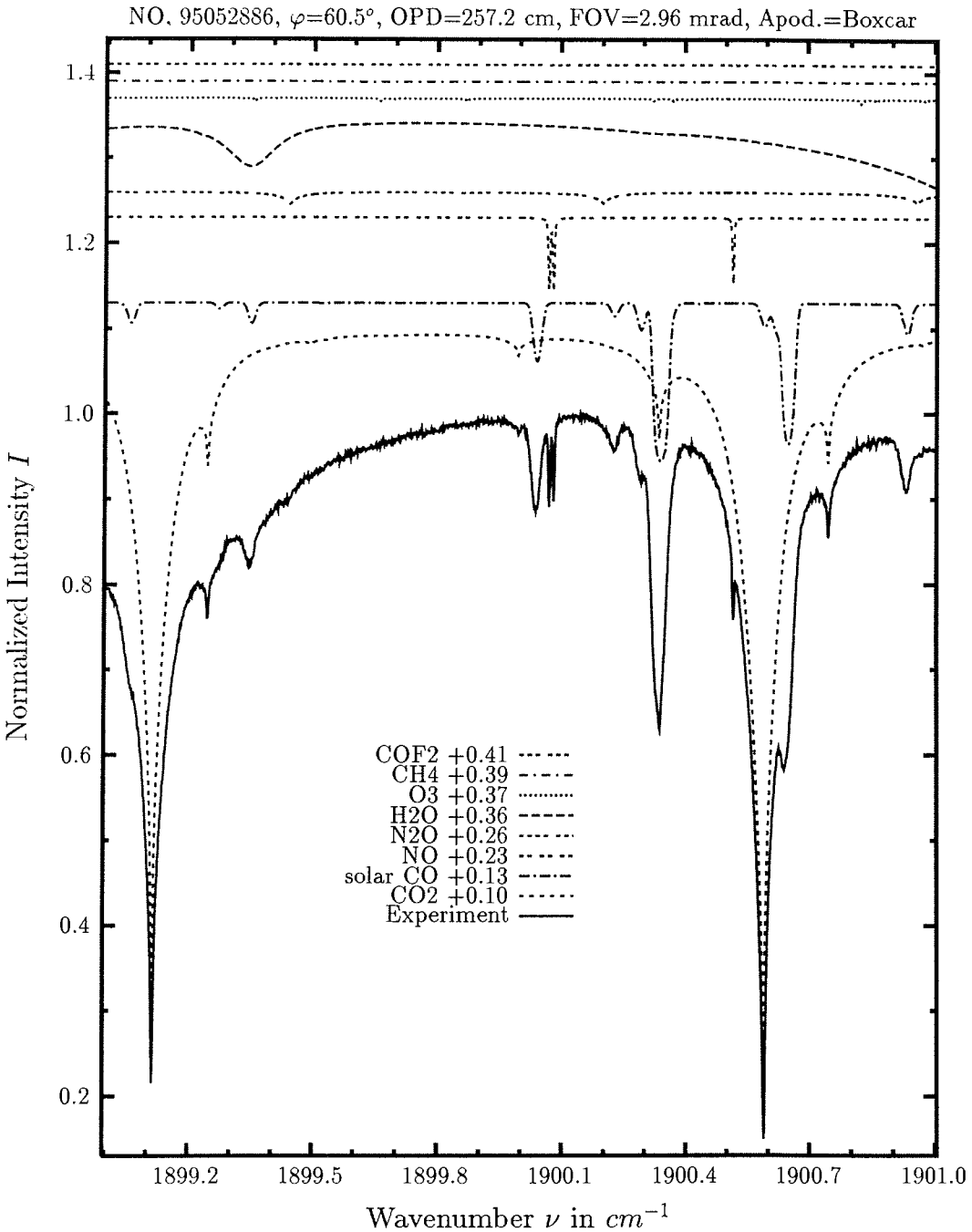
NO, 95052886, φ=60.5°, OPD=257.2 cm, FOV=2.96 mrad, Apod.=Boxcar
Normalized Intensity I
1.4
1.2
1.0
0.8
0.6
0.4
0.2
COF2 +0.41
CH4 +0.39
O3 +0.37
H2O +0.36
N2O +0.26
NO +0.23
solar CO +0.13
CO2 +0.10
Experiment
1899.2
1899.5
1899.8
1900.1
1900.4
1900.7
1901.0
Wavenumber ν in cm⁻¹

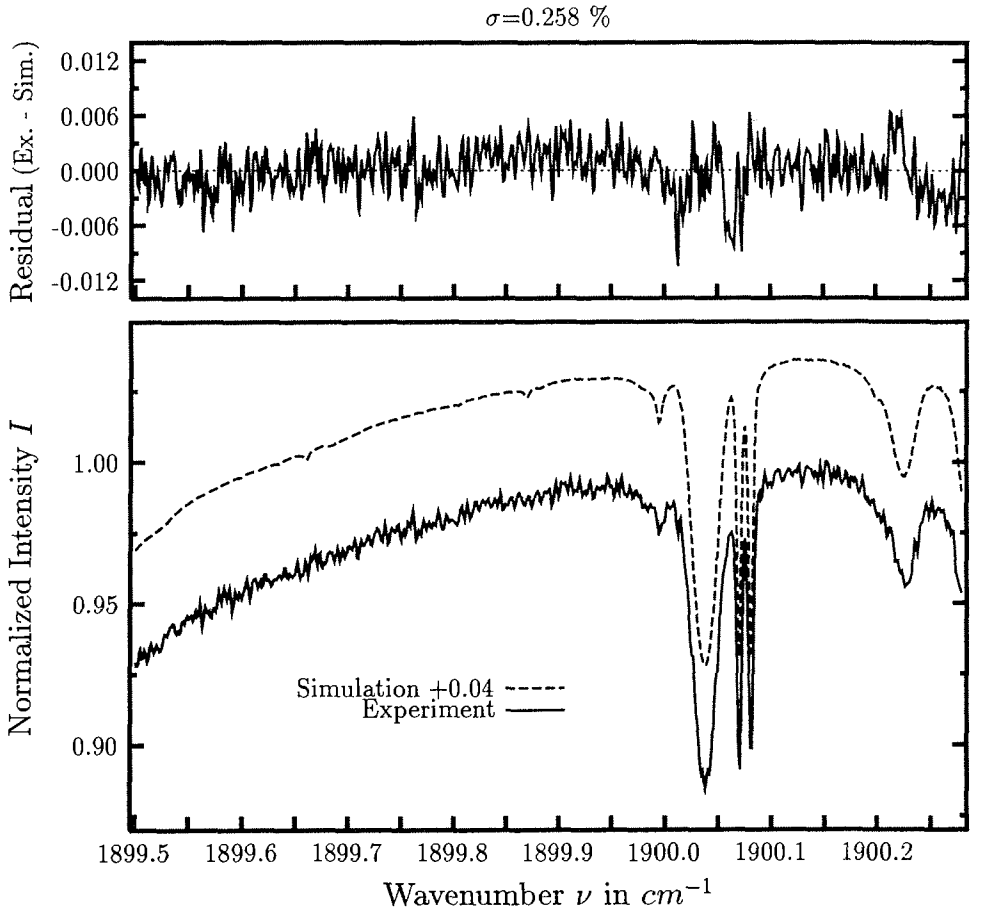

investigated species	: **NO**
line position ν_0	: 1900.071, 1900.082 cm^{-1}
major species	: CO_2, solar, NO, H_2O, N_2O
minor species	: O_3, CH_4
weak species	: COF_2, $COClF$
name of the spectrum	: 95052886
zenith angle, apodization	: 60.5°, boxcar
max. OPD, field of view	: 257.2 cm, 2.96 $mrad$
spectral interval fitted	: I) 1899.40 - 1901.00 cm^{-1}, II) 1899.50 - 1900.28 cm^{-1}
retrieved total column	: $5.23 \cdot 10^{15}$ cm^{-2}

comments: The solar CO line is very close to the narrow absorption of NO and need to be fitted carefully.

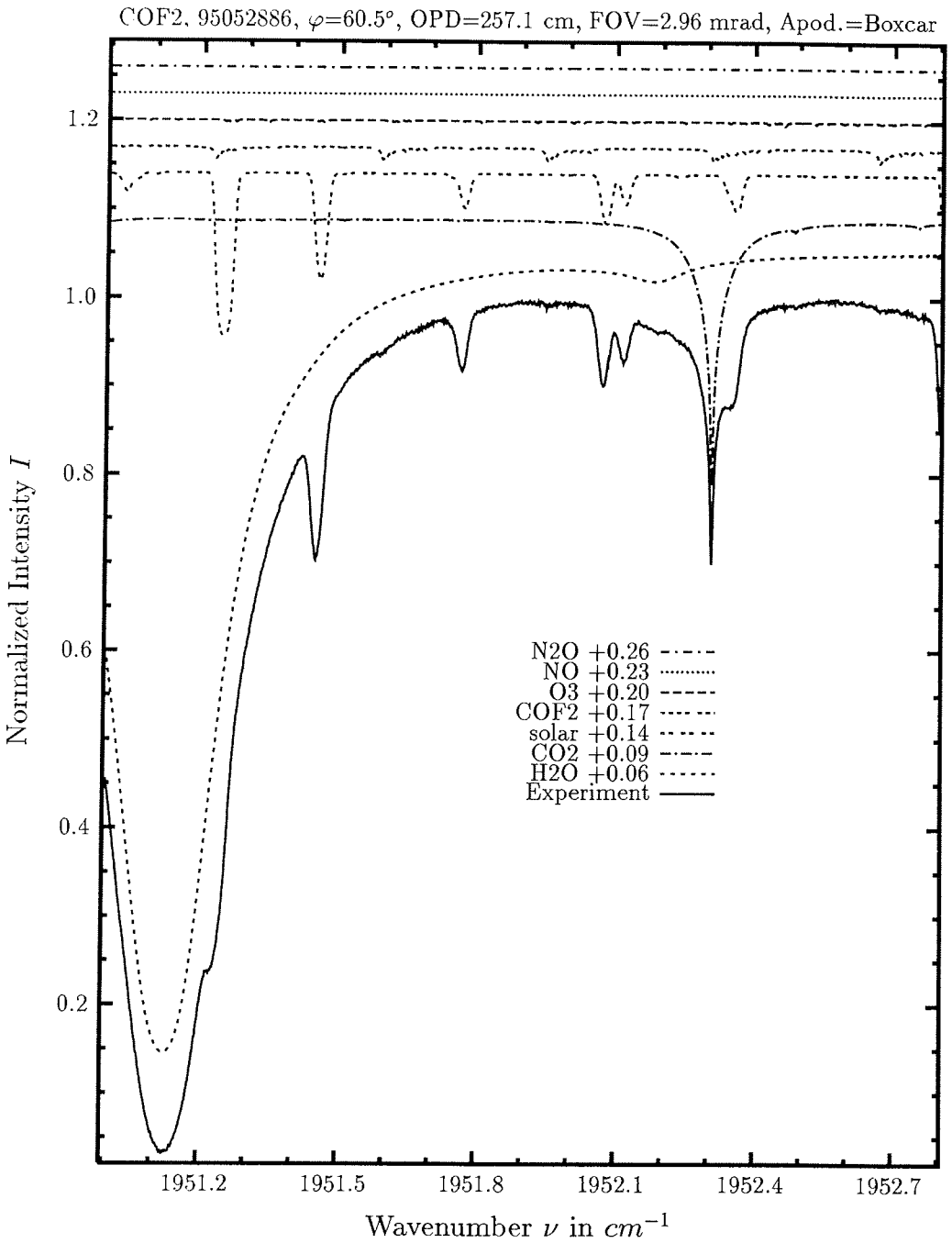
COF2, 95052886, φ=60.5°, OPD=257.1 cm, FOV=2.96 mrad, Apod.=Boxcar
Normalized Intensity I
1.2
1.0
0.8
0.6
0.4
0.2
1951.2
1951.5
1951.8
1952.1
1952.4
1952.7
Wavenumber ν in cm⁻¹
N2O +0.26
NO +0.23
O3 +0.20
COF2 +0.17
solar +0.14
CO2 +0.09
H2O +0.06
Experiment

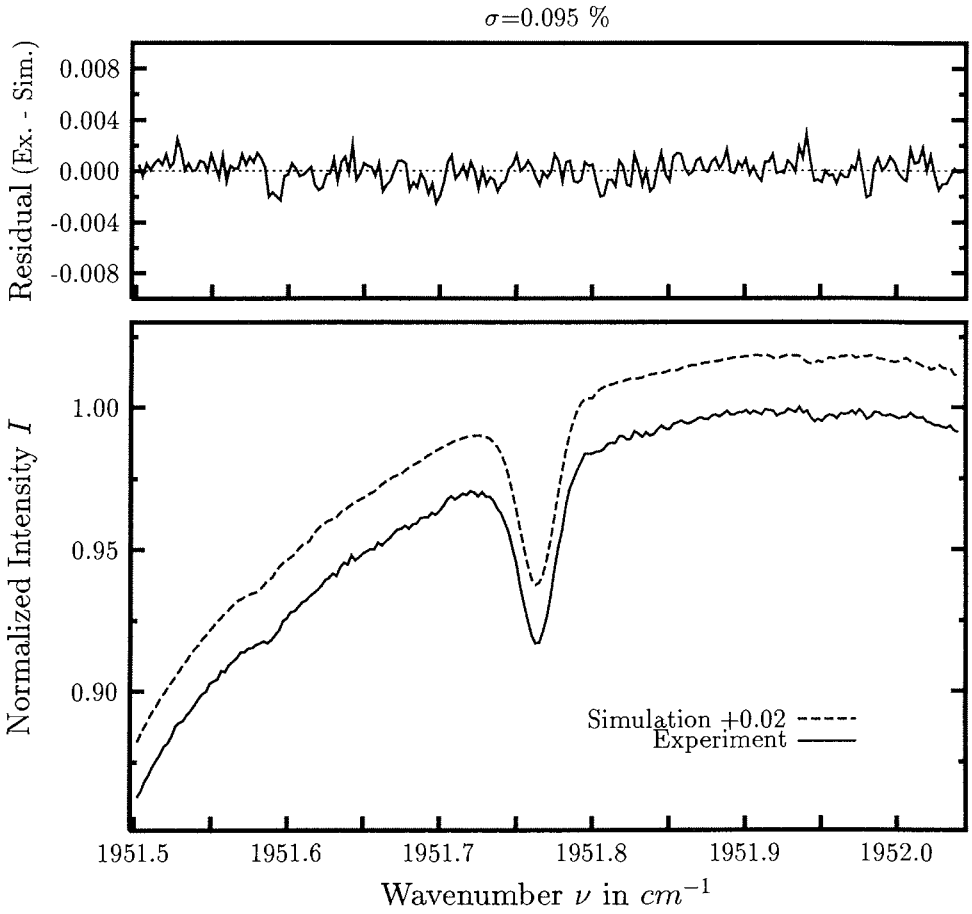

investigated species	: **COF_2**
line position ν_0	: 1951.948*) cm^{-1}
major species	: H_2O, CO_2, solar, COF_2
minor species	: O_3
weak species	: NO, N_2O
name of the spectrum	: 95053054
zenith angle, apodization	: 59.6°, boxcar
max. OPD, field of view	: 257.1 cm, 2.96 $mrad$
spectral interval fitted	: I) 1951.10 - 1952.70 cm^{-1}, II) 1951.50 - 1952.04 cm^{-1}
retrieved total column	: $3.62 \cdot 10^{14}$ cm^{-2}

comments: COF_2 is a weak absorber that needs high resolution spectra with a good S/N. The contribution plot is calculated with twice the amount retrieved.

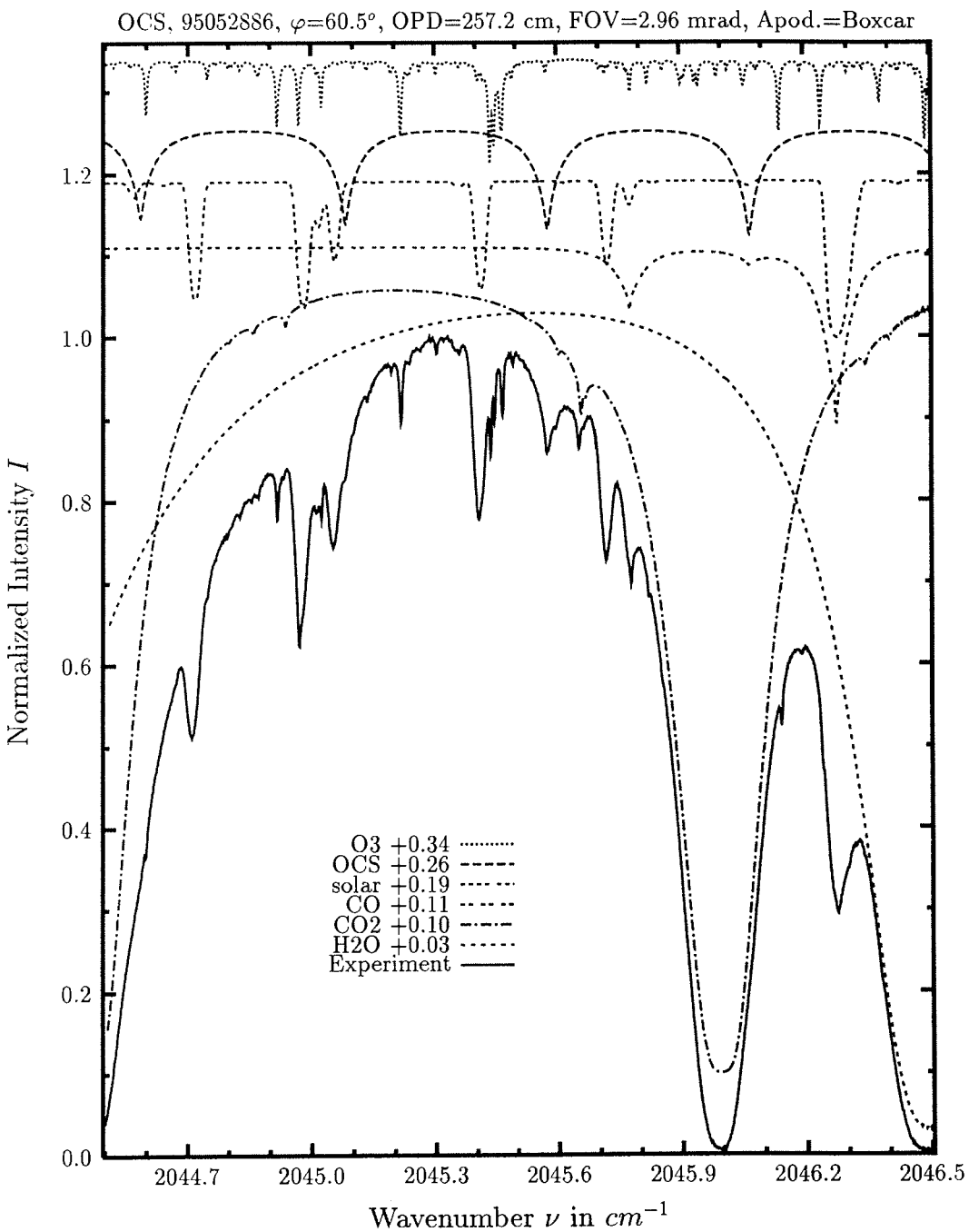
OCS, 95052886, φ=60.5°, OPD=257.2 cm, FOV=2.96 mrad, Apod.=Boxcar
Normalized Intensity I
Wavenumber ν in cm⁻¹
0.0
0.2
0.4
0.6
0.8
1.0
1.2
2044.7
2045.0
2045.3
2045.6
2045.9
2046.2
2046.5
O3 +0.34
OCS +0.26
solar +0.19
CO +0.11
CO2 +0.10
H2O +0.03
Experiment

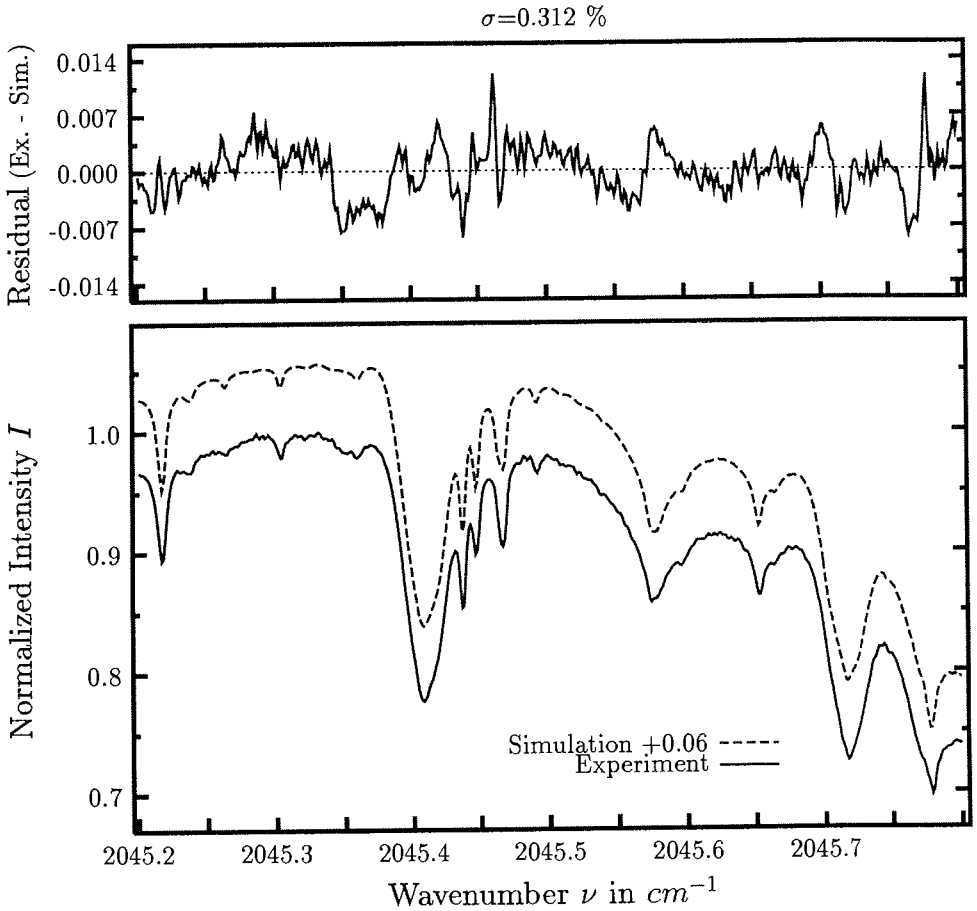

investigated species	: **OCS**
line position ν_0	: 2045.084, 2045.579 cm^{-1}
major species	: H_2O, CO_2, terr. CO, solar CO, OCS
minor species	: O_3
weak species	: CH_4, OH, NO, NH_3
name of the spectrum	: 95052886
zenith angle, apodization	: 60.5°, boxcar
max. OPD, field of view	: 257.1 cm, 2.96 $mrad$
spectral interval fitted	: 2045.20 – 2045.80 cm^{-1}
retrieved total column	: $9.61 \cdot 10^{15}$ cm^{-2}

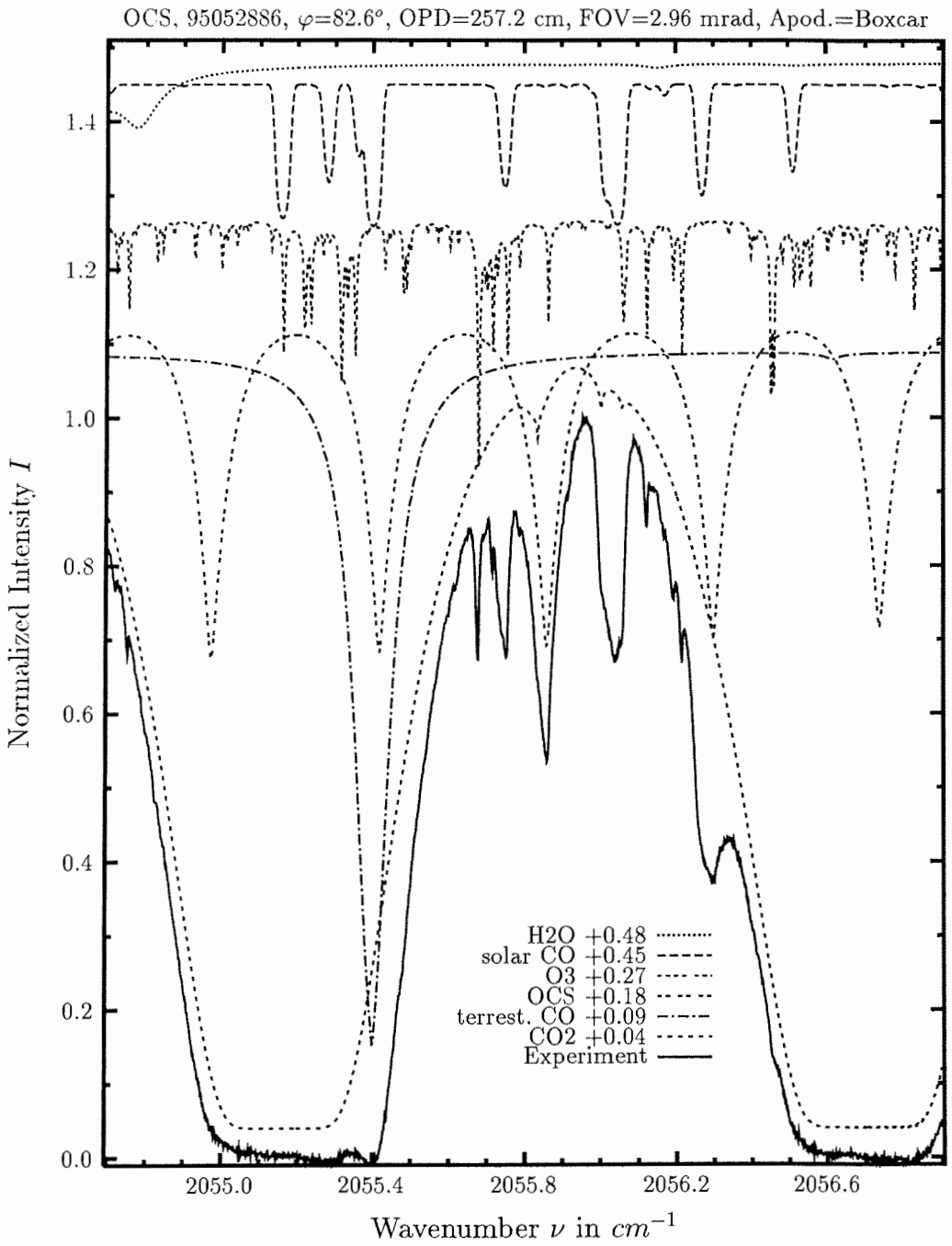
OCS, 95052886, φ=82.6°, OPD=257.2 cm, FOV=2.96 mrad, Apod.=Boxcar
Normalized Intensity I
1.4
1.2
1.0
0.8
0.6
0.4
0.2
0.0
2055.0
2055.4
2055.8
2056.2
2056.6
Wavenumber ν in cm⁻¹
H2O +0.48
solar CO +0.45
O3 +0.27
OCS +0.18
terrest. CO +0.09
CO2 +0.04
Experiment

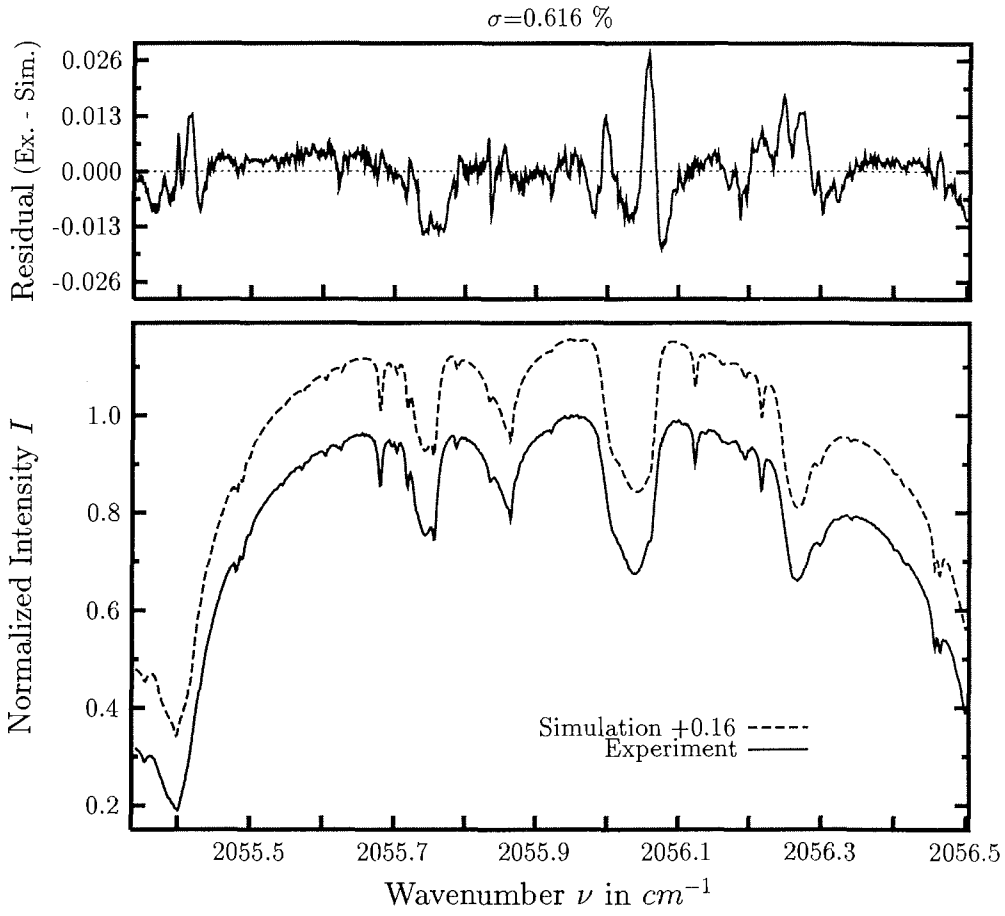

investigated species	: **OCS**
line position ν_0	: 2055.861 cm^{-1}
major species	: CO_2, CO, OCS, O_3, solar, H_2O
minor species	:
weak species	: CH_4, HI, N_2, N_2O, NH_3, NO, OH
name of the spectrum	: 95052886
zenith angle, apodization	: 60.5°, boxcar
max. OPD, field of view	: 257.1 cm, 2.96 $mrad$
spectral interval fitted	: 2055.34 – 2056.50 cm^{-1}
retrieved total column	: $9.19 \cdot 10^{15}\, cm^{-2}$

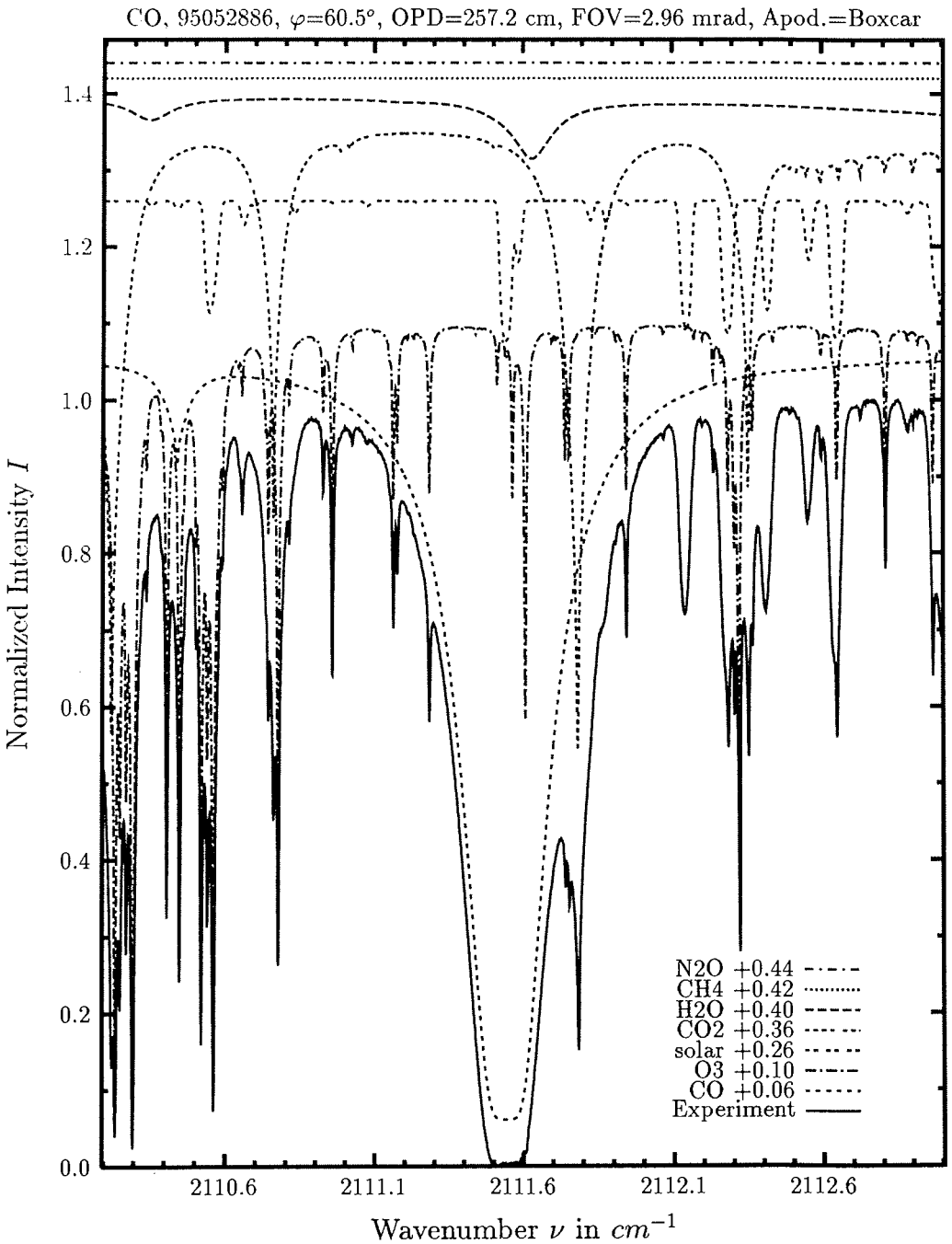
CO, 95052886, φ=60.5°, OPD=257.2 cm, FOV=2.96 mrad, Apod.=Boxcar
Normalized Intensity I
1.4
1.2
1.0
0.8
0.6
0.4
0.2
0.0
2110.6
2111.1
2111.6
2112.1
2112.6
Wavenumber ν in cm⁻¹
N2O +0.44
CH4 +0.42
H2O +0.40
CO2 +0.36
solar +0.26
O3 +0.10
CO +0.06
Experiment

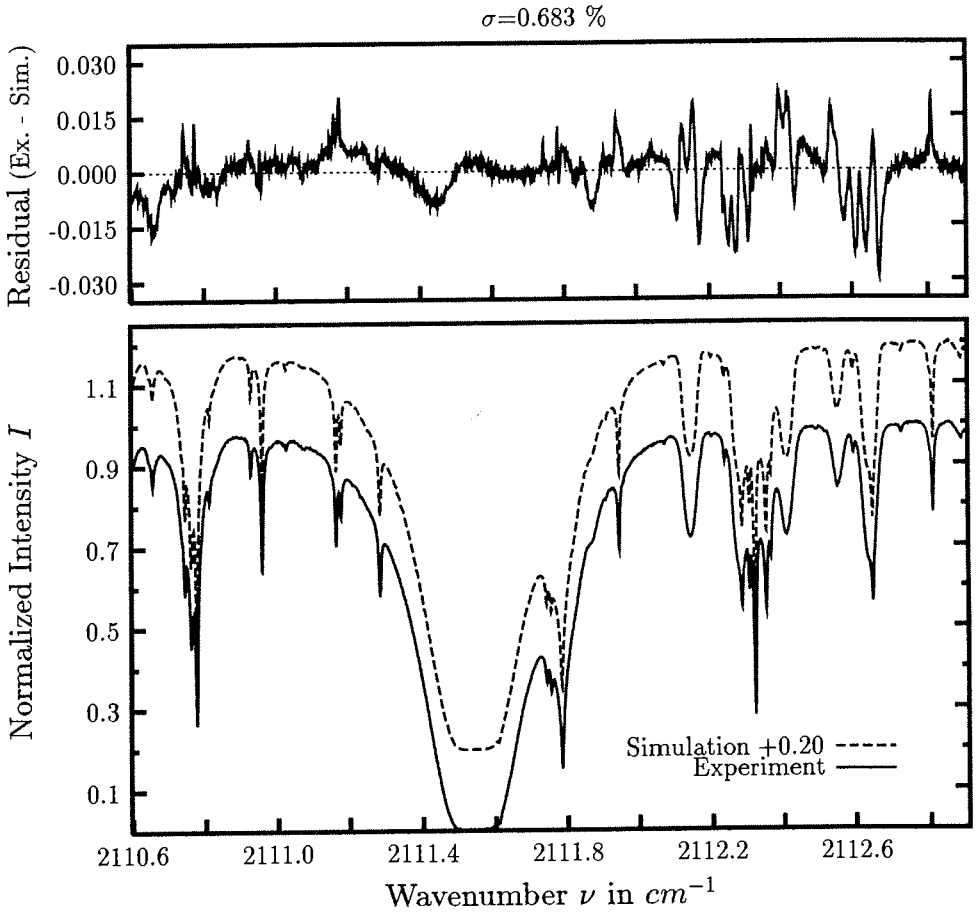

investigated species	: terrestrial **CO**
line position ν_0	: 2111.543 cm^{-1}
major species	: CO, O_3, CO_2, solar CO, H_2O
minor species	: CH_4
weak species	: N_2O, N_2, NH_3
name of the spectrum	: 95052886
zenith angle, apodization	: 60.5°, boxcar
max. OPD, field of view	: 257.2 cm, 2.96 $mrad$
spectral interval fitted	: 2110.60 – 2112.90 cm^{-1}
retrieved total column	: $2.11 \cdot 10^{18}\ cm^{-2}$

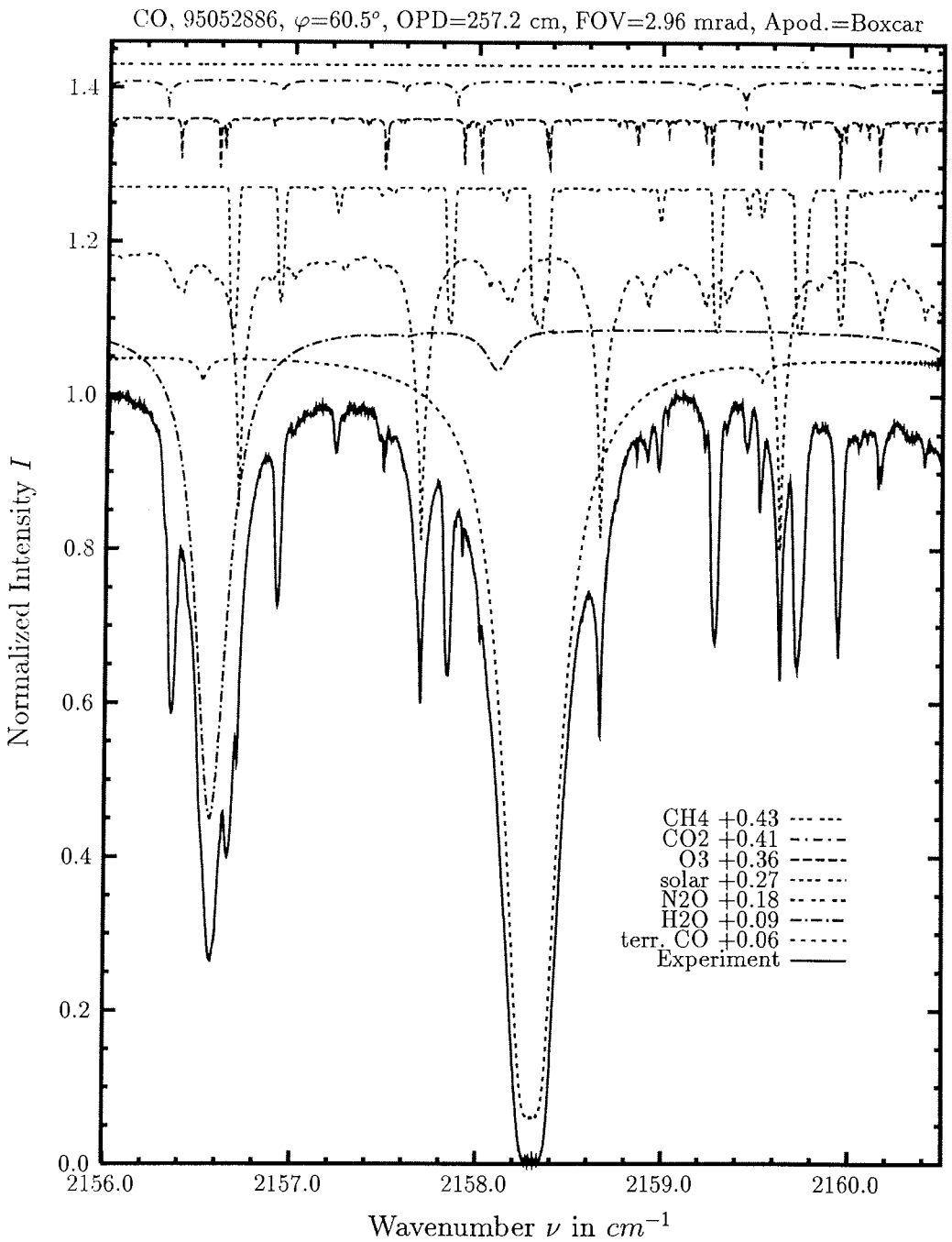
CO, 95052886, φ=60.5°, OPD=257.2 cm, FOV=2.96 mrad, Apod.=Boxcar
Normalized Intensity I
Wavenumber ν in cm⁻¹
0.0
0.2
0.4
0.6
0.8
1.0
1.2
1.4
2156.0
2157.0
2158.0
2159.0
2160.0
CH4 +0.43
CO2 +0.41
O3 +0.36
solar +0.27
N2O +0.18
H2O +0.09
terr. CO +0.06
Experiment

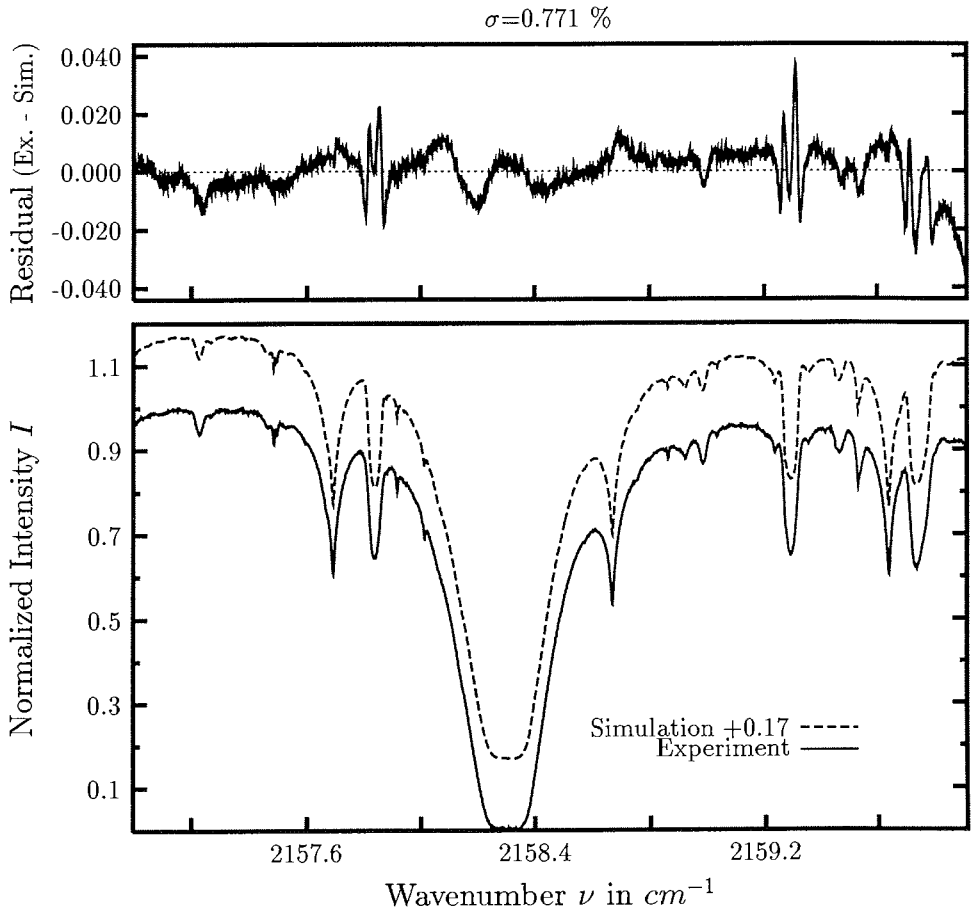

investigated species	: terrestrial **CO**
line position ν_0	: 2158.300 cm^{-1}
major species	: CO, H_2O, N_2O, solar CO, O_3, CO_2
minor species	: CH_4
weak species	: OH, NO, NH_3, H_2O, OH
name of the spectrum	: 95052886
zenith angle, apodization	: 60.5°, boxcar
max. OPD, field of view	: 257.2 cm, 2.96 $mrad$
spectral interval fitted	: 2157.00 – 2159.90 cm^{-1}
retrieved total column	: $2.09 \cdot 10^{18}\, cm^{-2}$

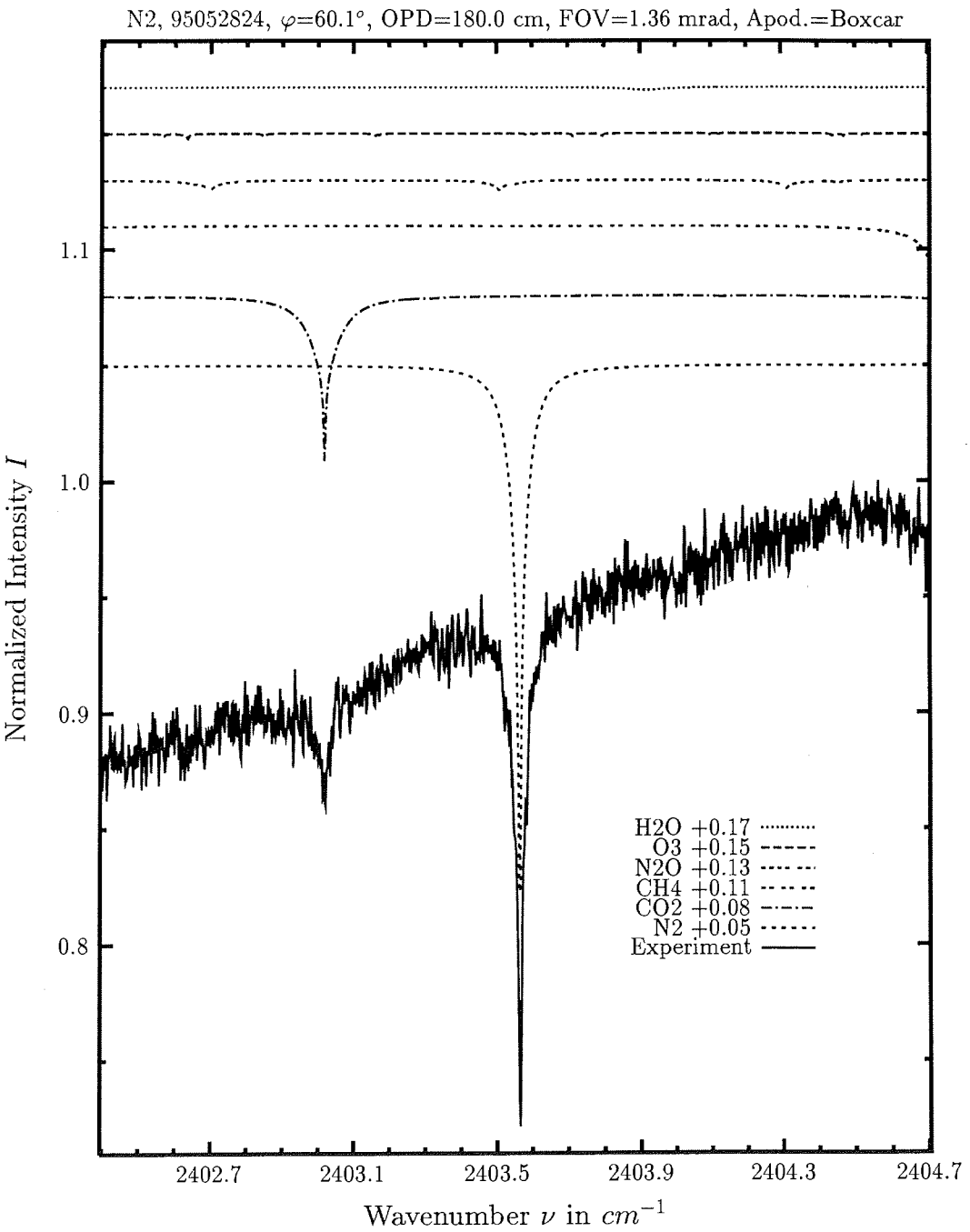
N2, 95052824, φ=60.1°, OPD=180.0 cm, FOV=1.36 mrad, Apod.=Boxcar
Normalized Intensity I
1.1
1.0
0.9
0.8
H2O +0.17
O3 +0.15
N2O +0.13
CH4 +0.11
CO2 +0.08
N2 +0.05
Experiment
2402.7
2403.1
2403.5
2403.9
2404.3
2404.7
Wavenumber ν in cm⁻¹

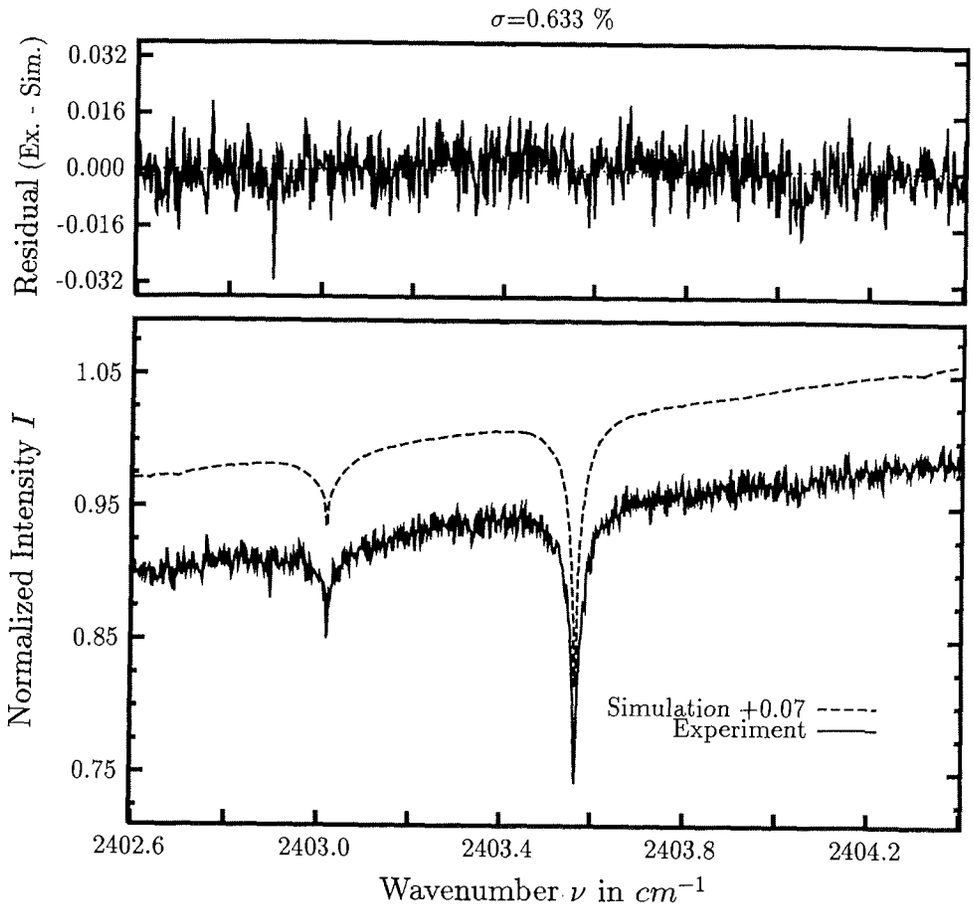

investigated species	: $\mathbf{N_2}$
line position ν_0	: 2403.565 cm^{-1}
major species	: N_2, CO_2, CH_4
minor species	: N_2O, O_3, H_2O
weak species	: H_2O, NH_3, OH, HBr
name of the spectrum	: 95053013
zenith angle, apodization	: 57.2°, boxcar
max. OPD, field of view	: 180.0 cm, 1.36 $mrad$
spectral interval fitted	: 2402.60 - 2404.40 cm^{-1}
retrieved total column	: $1.69 \cdot 10^{25}$ cm^{-2}

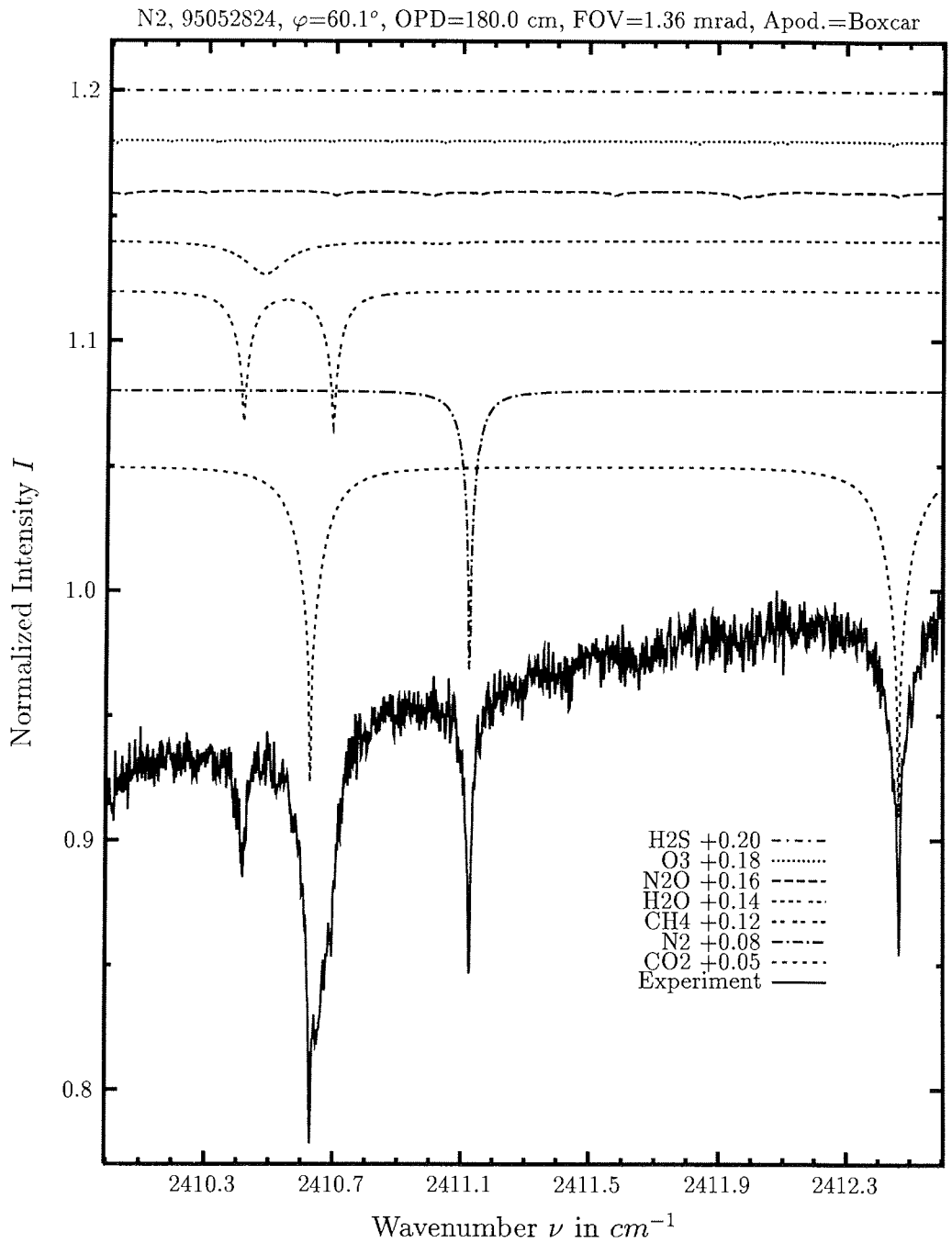
N2, 95052824, φ=60.1°, OPD=180.0 cm, FOV=1.36 mrad, Apod.=Boxcar
Normalized Intensity I
1.2
1.1
1.0
0.9
0.8
2410.3
2410.7
2411.1
2411.5
2411.9
2412.3
Wavenumber ν in cm⁻¹
H2S +0.20
O3 +0.18
N2O +0.16
H2O +0.14
CH4 +0.12
N2 +0.08
CO2 +0.05
Experiment

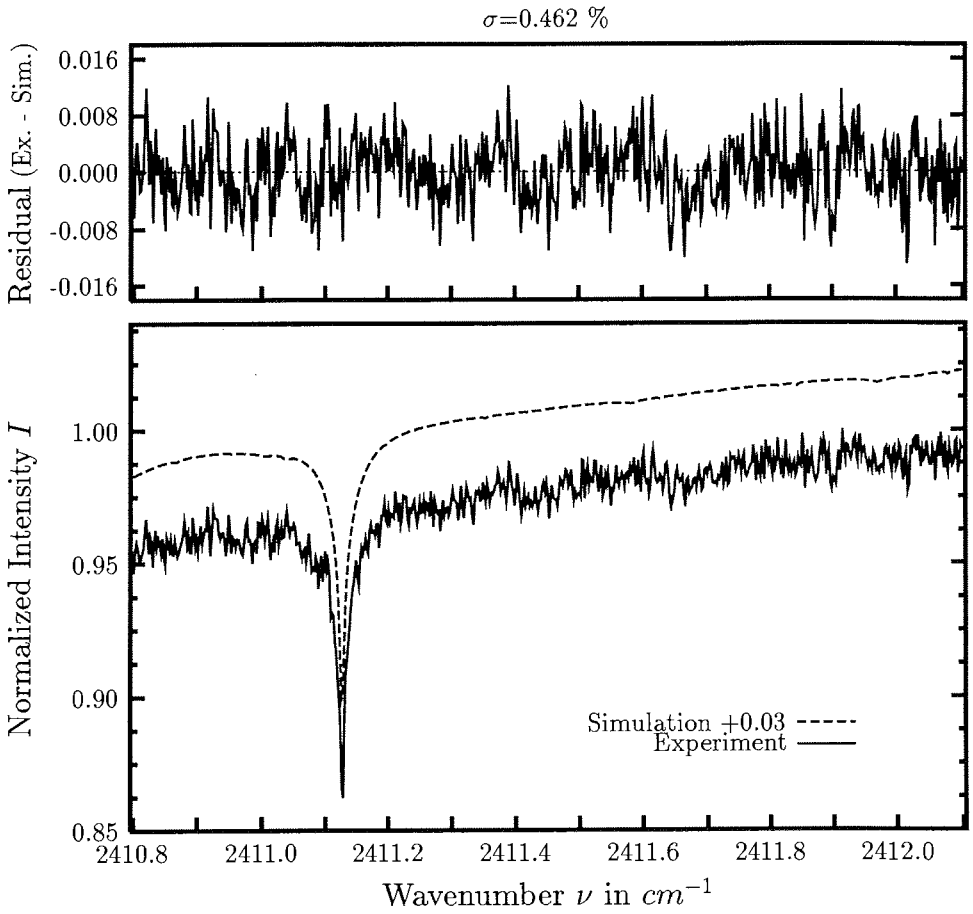

investigated species	: **N_2**
line position ν_0	: 2411.127 cm^{-1}
major species	: CO_2, N_2, CH_4, H_2O
minor species	: N_2O, O_3
weak species	: H_2S
name of the spectrum	: 95053013
zenith angle, apodization	: 57.2°, boxcar
max. OPD, field of view	: 180.0 cm, 1.36 $mrad$
spectral interval fitted	: 2410.80 – 2412.10 cm^{-1}
retrieved total column	: $1.70 \cdot 10^{25}$ cm^{-2}

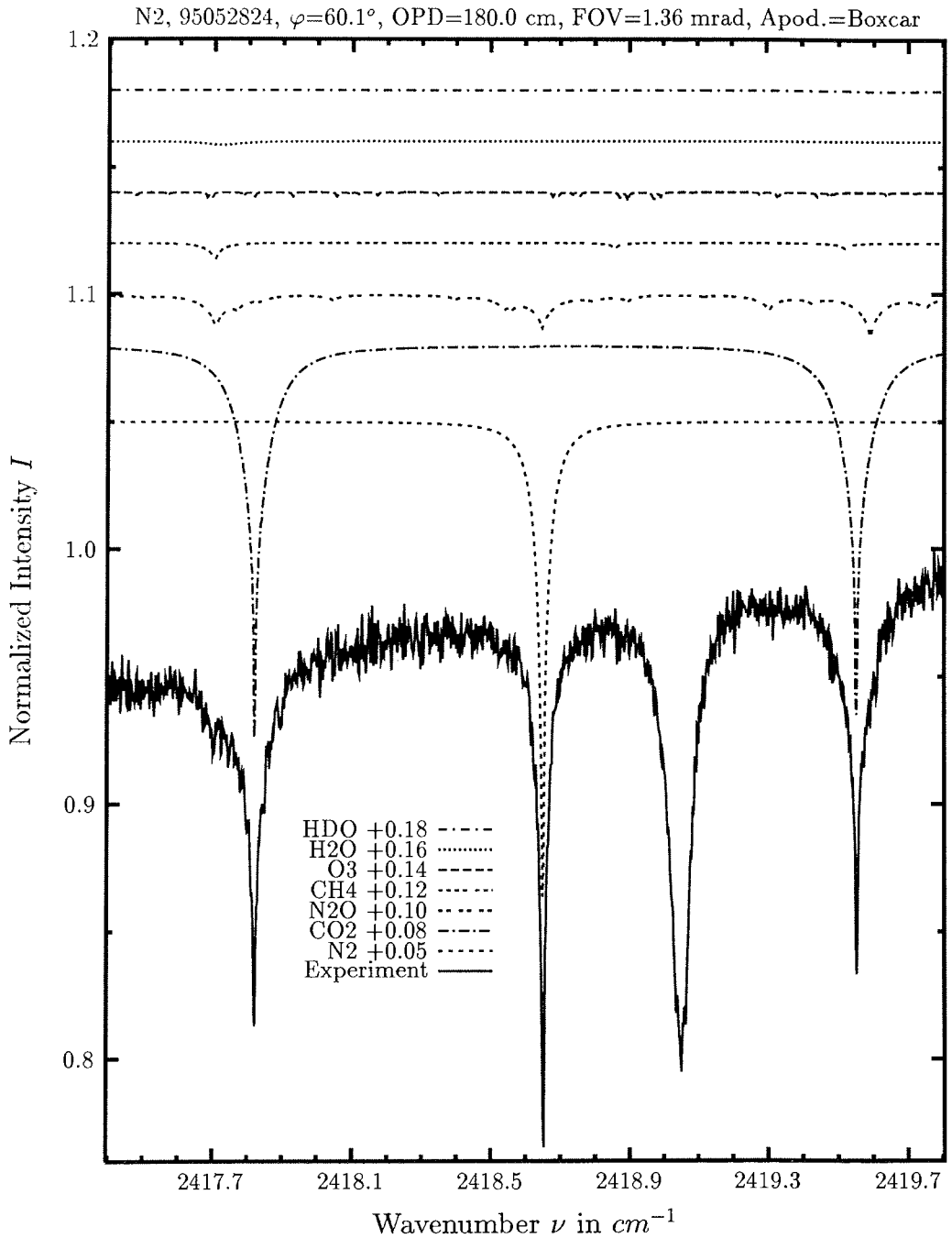
N2, 95052824, φ=60.1°, OPD=180.0 cm, FOV=1.36 mrad, Apod.=Boxcar
1.2
1.1
1.0
0.9
0.8
Normalized Intensity I
HDO +0.18
H2O +0.16
O3 +0.14
CH4 +0.12
N2O +0.10
CO2 +0.08
N2 +0.05
Experiment
2417.7
2418.1
2418.5
2418.9
2419.3
2419.7
Wavenumber ν in cm⁻¹

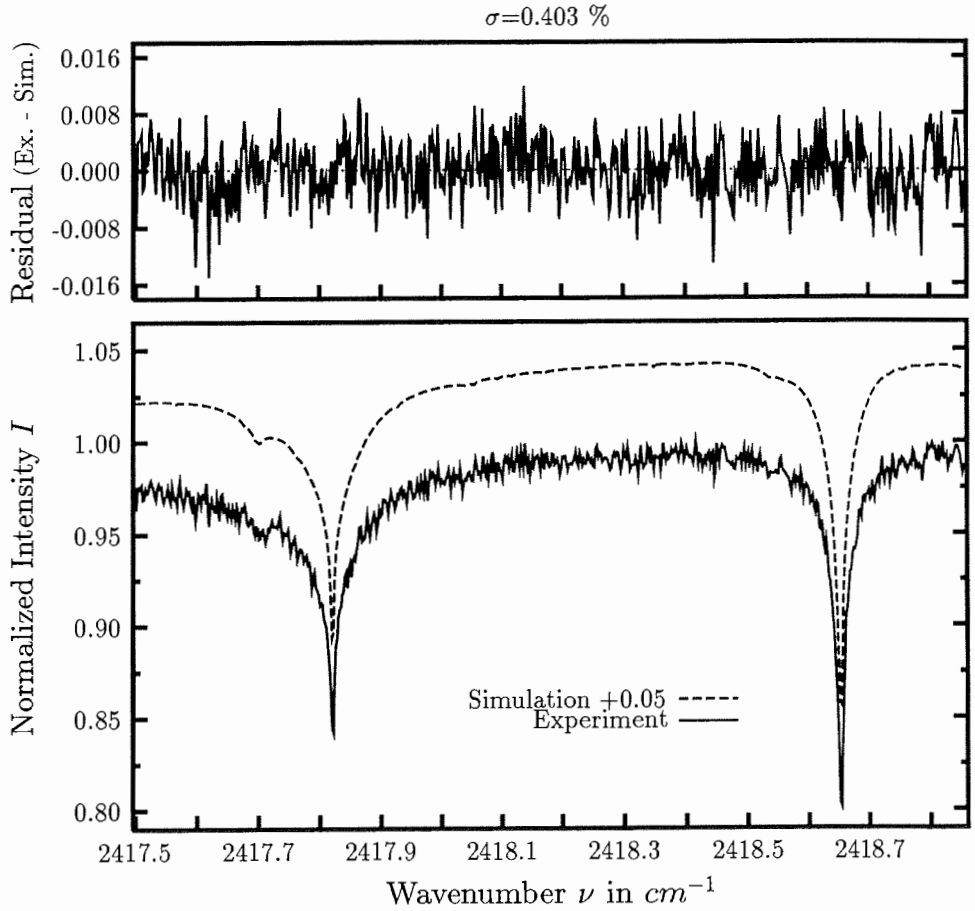

investigated species	: **N_2**
line position ν_0	: 2418.652 cm^{-1}
major species	: N_2, CO_2, N_2O, CH_4
minor species	: O_3, H_2O
weak species	: HDO
name of the spectrum	: 95053013
zenith angle, apodization	: 57.2°, boxcar
max. OPD, field of view	: 180.0 cm, 1.36 $mrad$
spectral interval fitted	: I) 2417.5 - 2419.3, II) 2417.50 - 2418.85 cm^{-1}
retrieved total column	: $1.81 \cdot 10^{25}$ cm^{-2}

comments: Unknown absorption at 2419.04 cm^{-1}, but likely caused by N_2O.

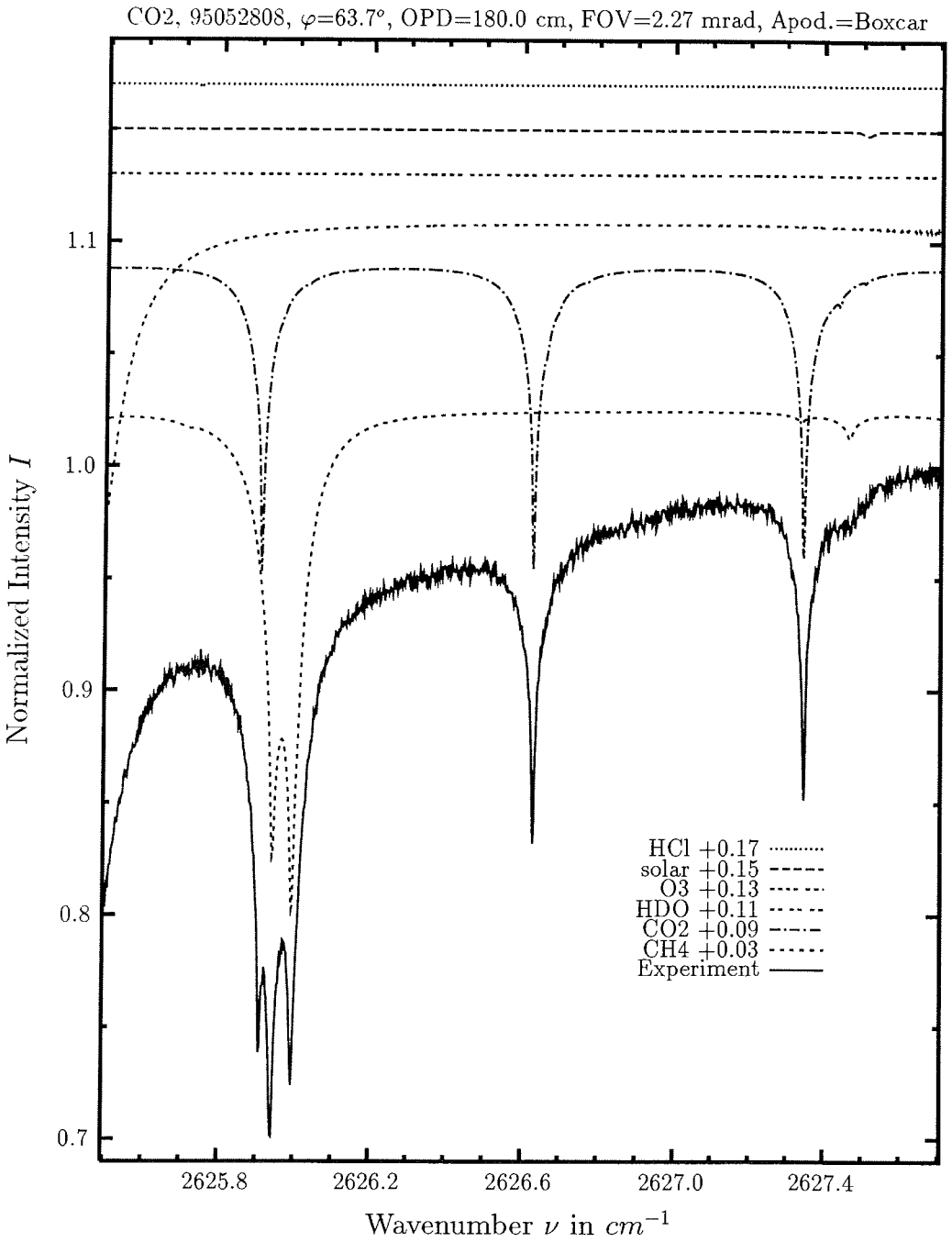
CO2, 95052808, φ=63.7°, OPD=180.0 cm, FOV=2.27 mrad, Apod.=Boxcar
Normalized Intensity I
1.1
1.0
0.9
0.8
0.7
2625.8
2626.2
2626.6
2627.0
2627.4
Wavenumber ν in cm⁻¹
HCl +0.17
solar +0.15
O3 +0.13
HDO +0.11
CO2 +0.09
CH4 +0.03
Experiment

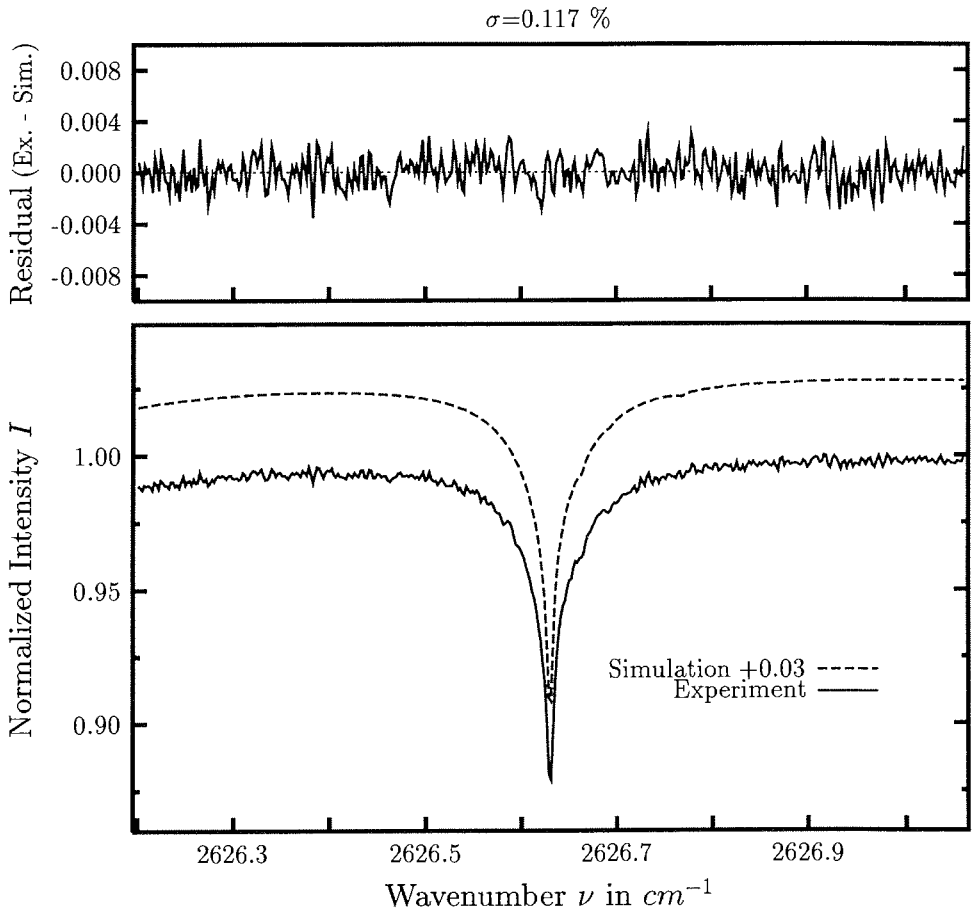

investigated species	: **CO_2**
line position ν_0	: 2626.630 cm^{-1}
major species	: CH_4, CO_2, HDO
minor species	: solar, O_3
weak species	: HCl
name of the spectrum	: 95052824
zenith angle, apodization	: 60.1°, boxcar
max. OPD, field of view	: 180.0 cm, 1.36 $mrad$
spectral interval fitted	: I) 2625.35 - 2627.06 cm^{-1}, II) 2626.20 - 2627.06 cm^{-1}
retrieved total column	: $8.01 \cdot 10^{21}$ cm^{-2}

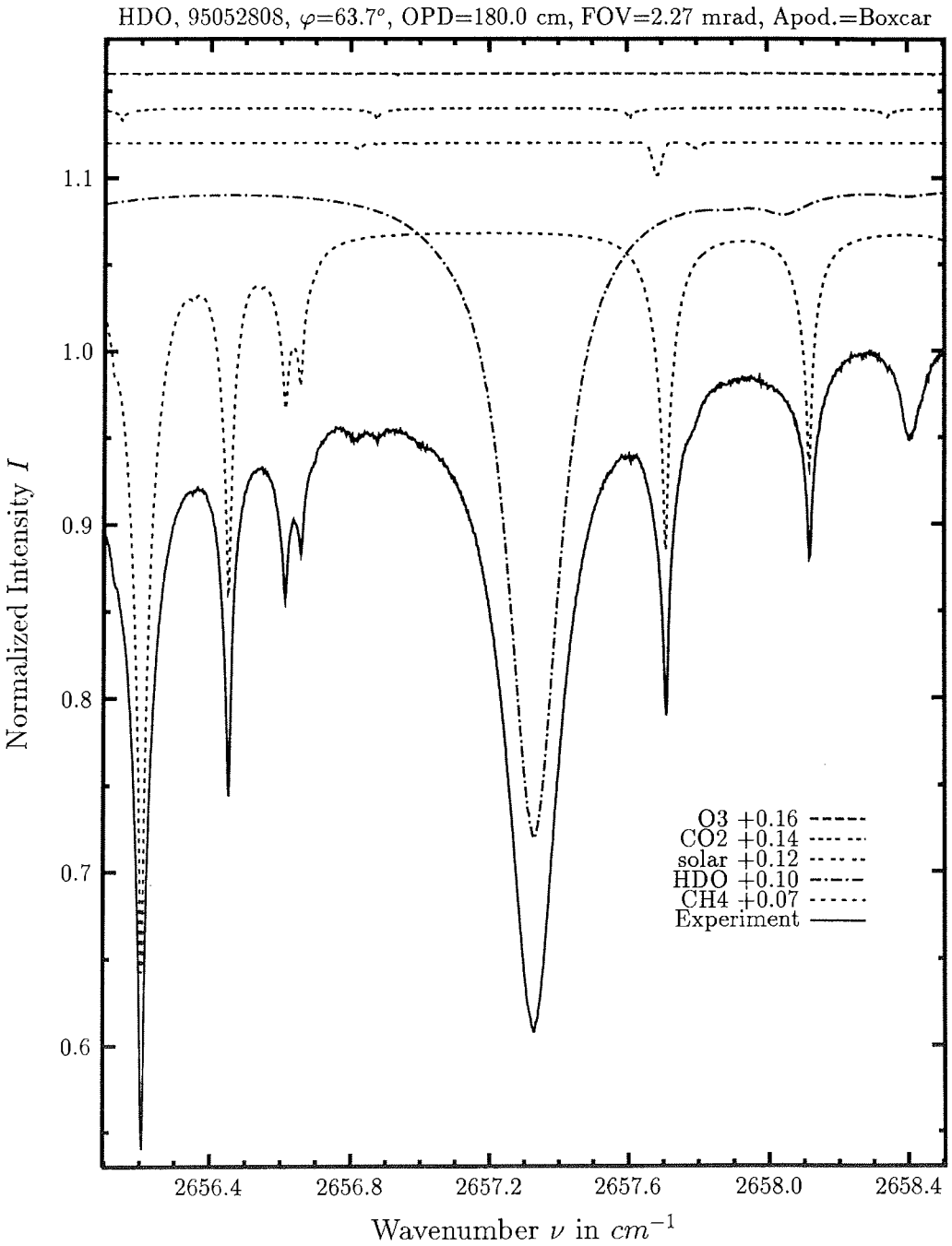
HDO, 95052808, φ=63.7°, OPD=180.0 cm, FOV=2.27 mrad, Apod.=Boxcar
Normalized Intensity I
1.1
1.0
0.9
0.8
0.7
0.6
2656.4
2656.8
2657.2
2657.6
2658.0
2658.4
Wavenumber ν in cm⁻¹
O3 +0.16
CO2 +0.14
solar +0.12
HDO +0.10
CH4 +0.07
Experiment

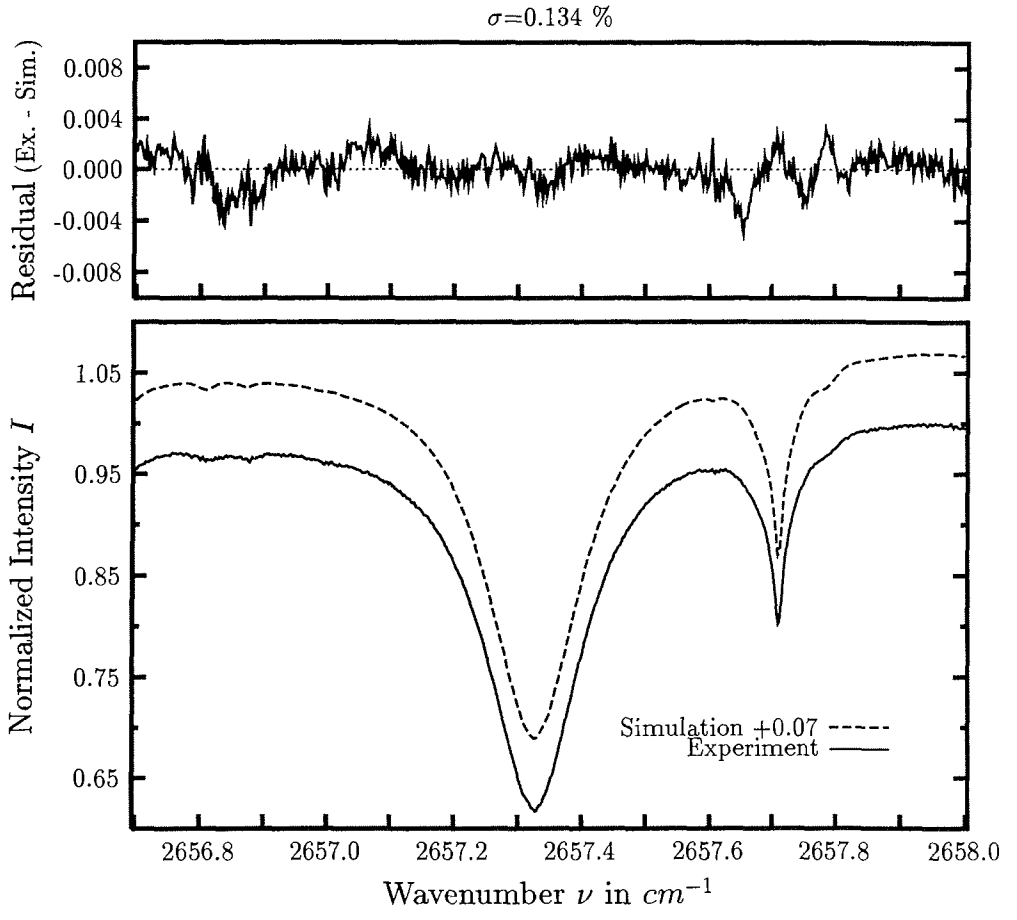

investigated species	: **HDO**
line position ν_0	: 2657.330 cm^{-1}
major species	: HDO, CH_4, solar
minor species	: CO_2
weak species	: O_3
name of the spectrum	: 95052808
zenith angle, apodization	: 63.7°, boxcar
max. OPD, field of view	: 180.0 cm, 1.36 $mrad$
spectral interval fitted	: I) 2656.51 – 2658.50 cm^{-1}, II) 2656.70 – 2658.00 cm^{-1}
retrieved total column	: $9.82 \cdot 10^{21}$ cm^{-2}

comments: Unassigned absorption at 2658.44 cm^{-1}, but likely caused by HDO.

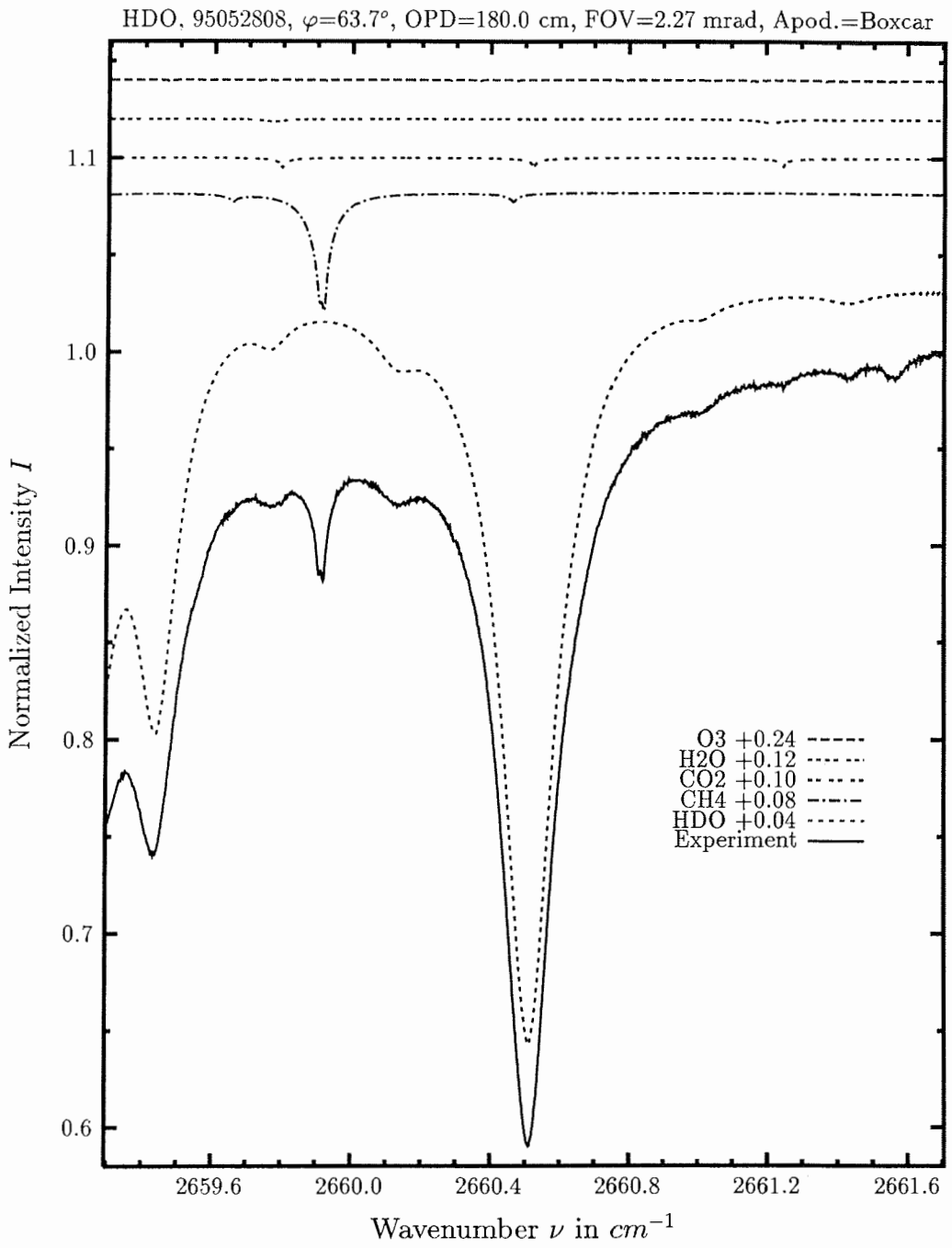
HDO, 95052808, φ=63.7°, OPD=180.0 cm, FOV=2.27 mrad, Apod.=Boxcar
Normalized Intensity I
1.1
1.0
0.9
0.8
0.7
0.6
2659.6
2660.0
2660.4
2660.8
2661.2
2661.6
Wavenumber ν in cm⁻¹
O3 +0.24
H2O +0.12
CO2 +0.10
CH4 +0.08
HDO +0.04
Experiment

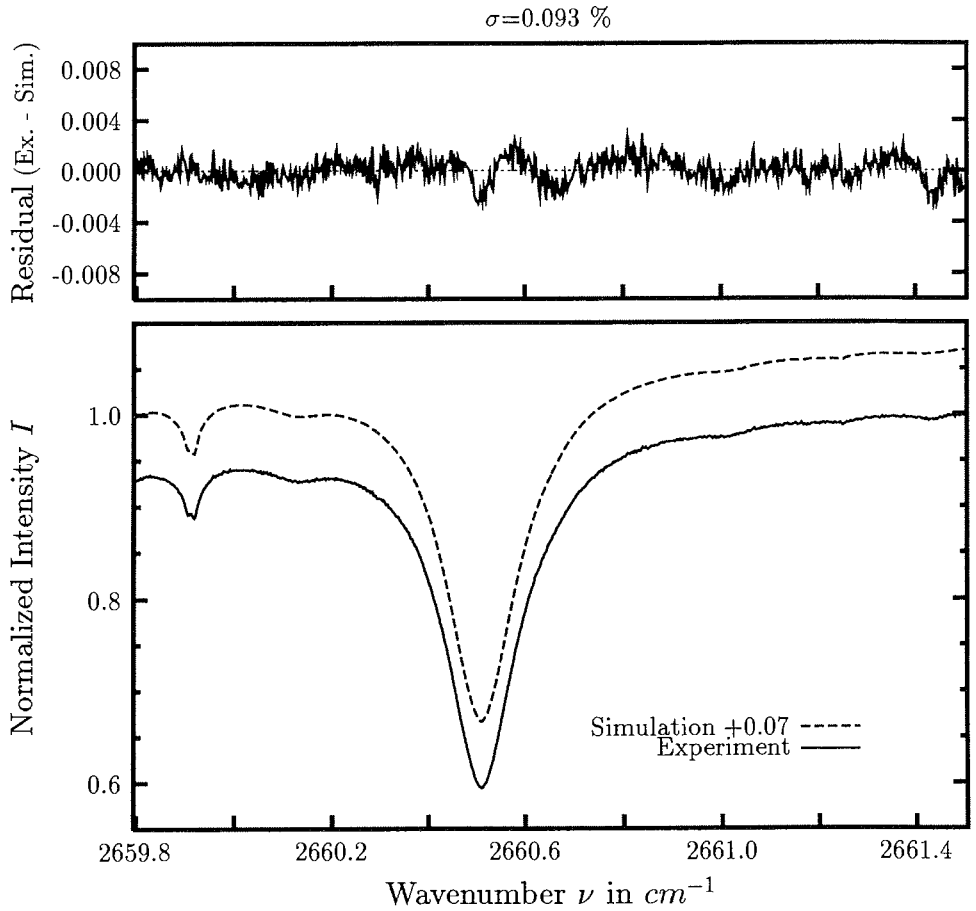

investigated species	: **HDO**
line position ν_0	: 2660.512 cm^{-1}
major species	: HDO, CH_4, CO_2
minor species	: H_2O
weak species	: O_3
name of the spectrum	: 95052808
zenith angle, apodization	: 63.7°, boxcar
max. OPD, field of view	: 180.0 cm, 1.36 $mrad$
spectral interval fitted	: 2659.80 – 2661.50 cm^{-1}
retrieved total column	: $9.70 \cdot 10^{21}$ cm^{-2}

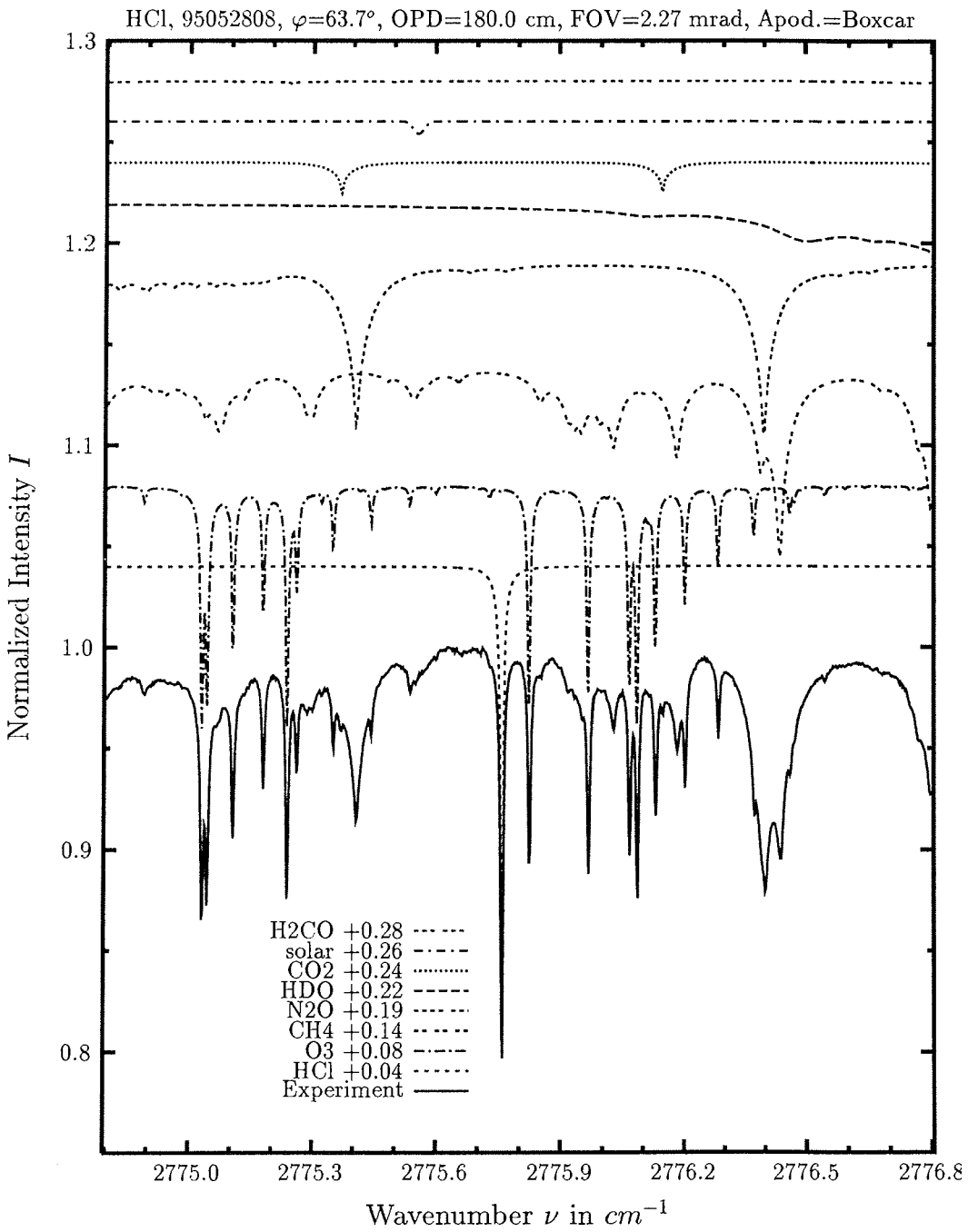
HCl, 95052808, φ=63.7°, OPD=180.0 cm, FOV=2.27 mrad, Apod.=Boxcar
Normalized Intensity I
1.3
1.2
1.1
1.0
0.9
0.8
H2CO +0.28
solar +0.26
CO2 +0.24
HDO +0.22
N2O +0.19
CH4 +0.14
O3 +0.08
HCl +0.04
Experiment
2775.0
2775.3
2775.6
2775.9
2776.2
2776.5
2776.8
Wavenumber ν in cm⁻¹

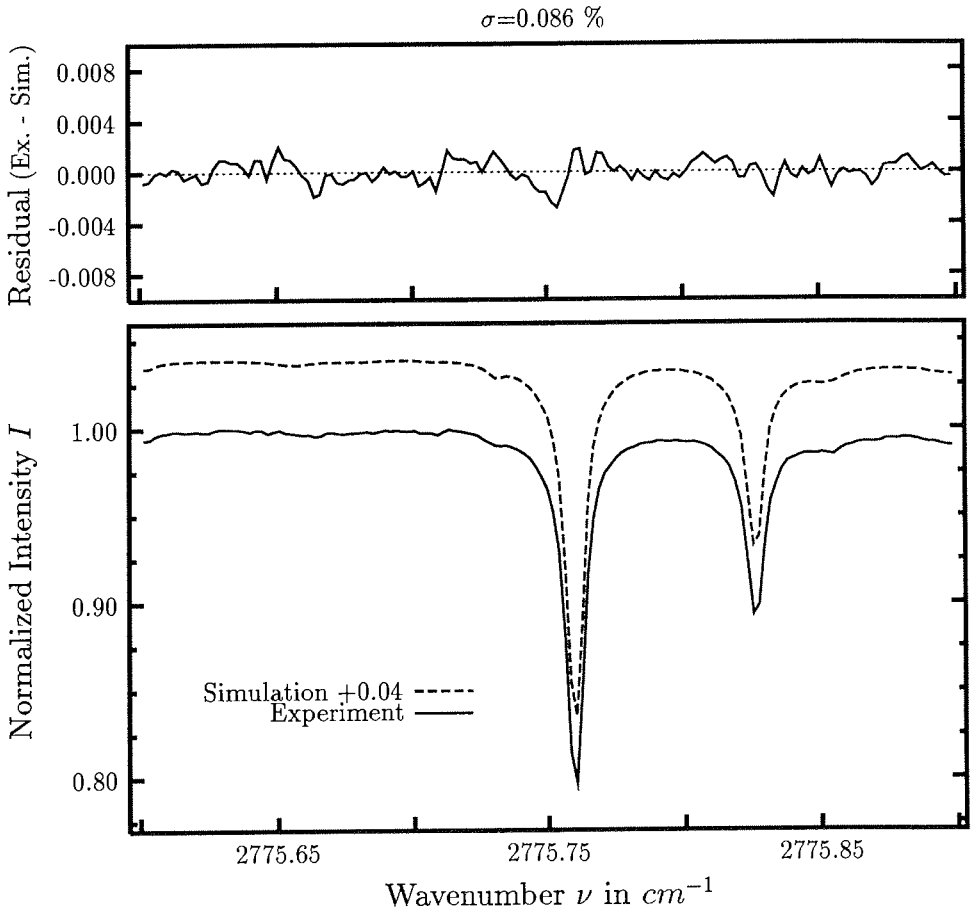

investigated species	: **HCl, O_3**
line position ν_0	: 2775.761, 2775.826 cm^{-1}
major species	: HCl, O_3, CH_4, N_2O, HDO, CO_2, solar
minor species	: solar, H_2CO
weak species	: H_2O, SO_2, NH_3
name of the spectrum	: 95052808
zenith angle, apodization	: 63.7°, boxcar
max. OPD, field of view	: 180.0 cm, 2.27 $mrad$
spectral interval fitted	: 2775.60 – 2775.90 cm^{-1}
retrieved total column	: $9.43 \cdot 10^{18}\ cm^{-2}$, $5.99 \cdot 10^{15}\ cm^{-2}$

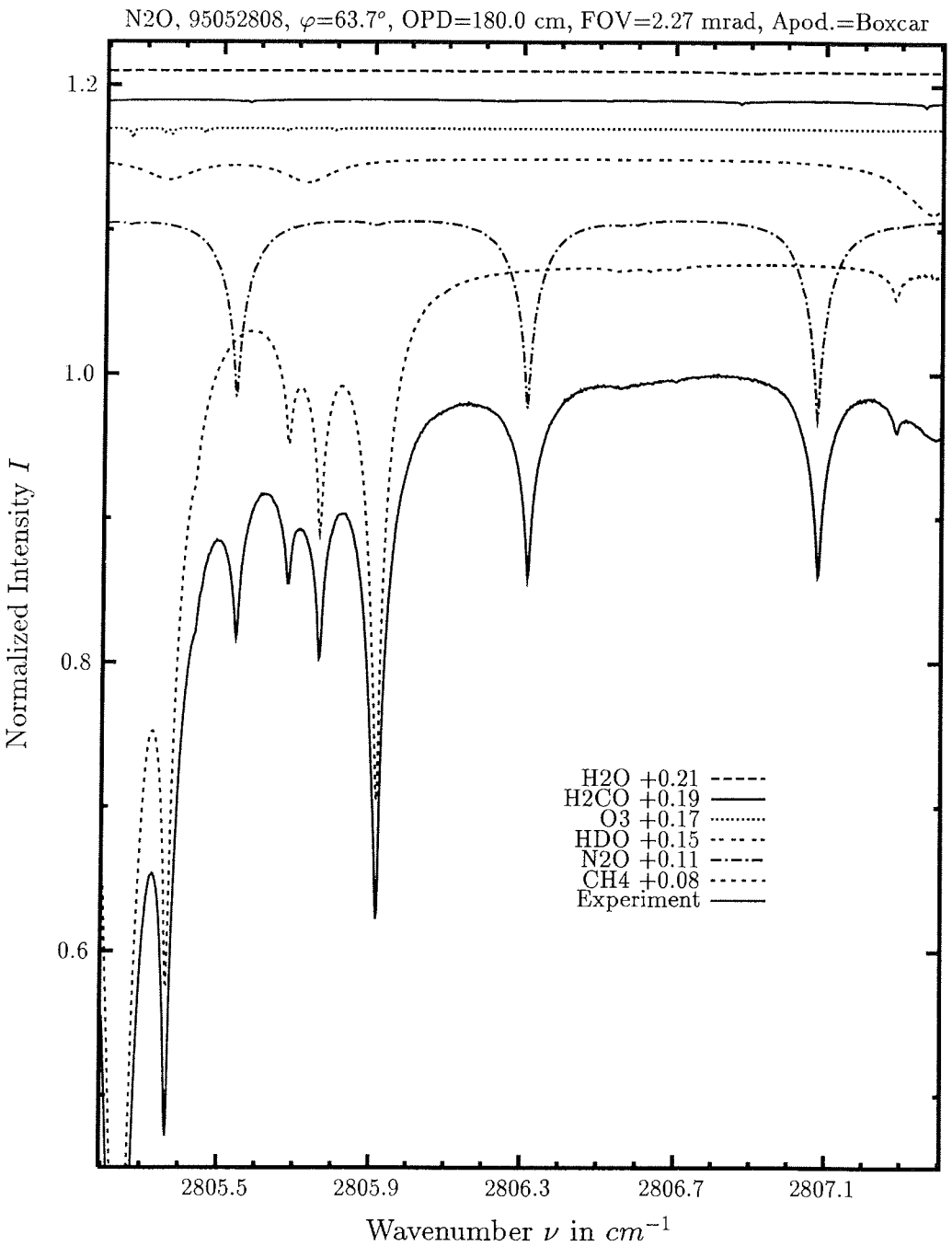
N2O, 95052808, φ=63.7°, OPD=180.0 cm, FOV=2.27 mrad, Apod.=Boxcar
1.2
1.0
0.8
0.6
Normalized Intensity I
H2O +0.21
H2CO +0.19
O3 +0.17
HDO +0.15
N2O +0.11
CH4 +0.08
Experiment
2805.5
2805.9
2806.3
2806.7
2807.1
Wavenumber ν in cm⁻¹

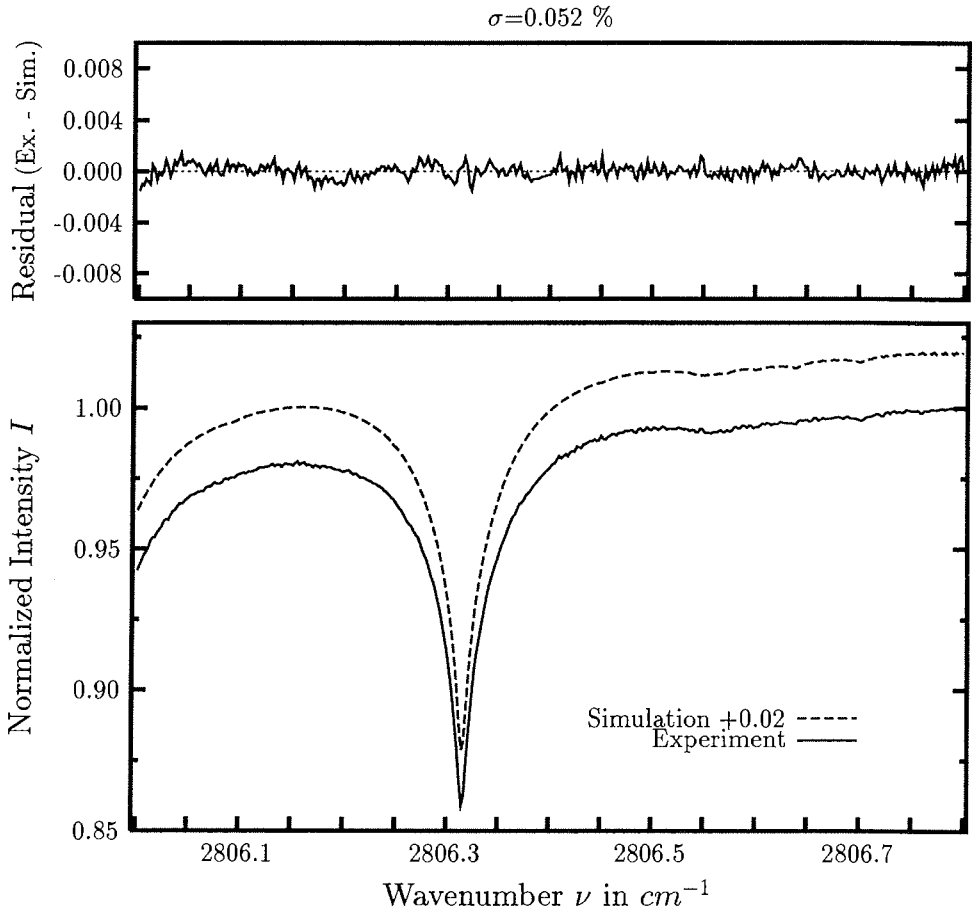

investigated species	: **N_2O**
line position ν_0	: 2806.313 cm^{-1}
major species	: CH_4, N_2O, HDO
minor species	: O_3, H_2CO
weak species	: H_2O
name of the spectrum	: 95052808
zenith angle, apodization	: 63.7°, boxcar
max. OPD, field of view	: 180.0 cm, 2.27 $mrad$
spectral interval fitted	: 2806.00 – 2806.80 cm^{-1}
retrieved total column	: $6.43 \cdot 10^{18}\ cm^{-2}$

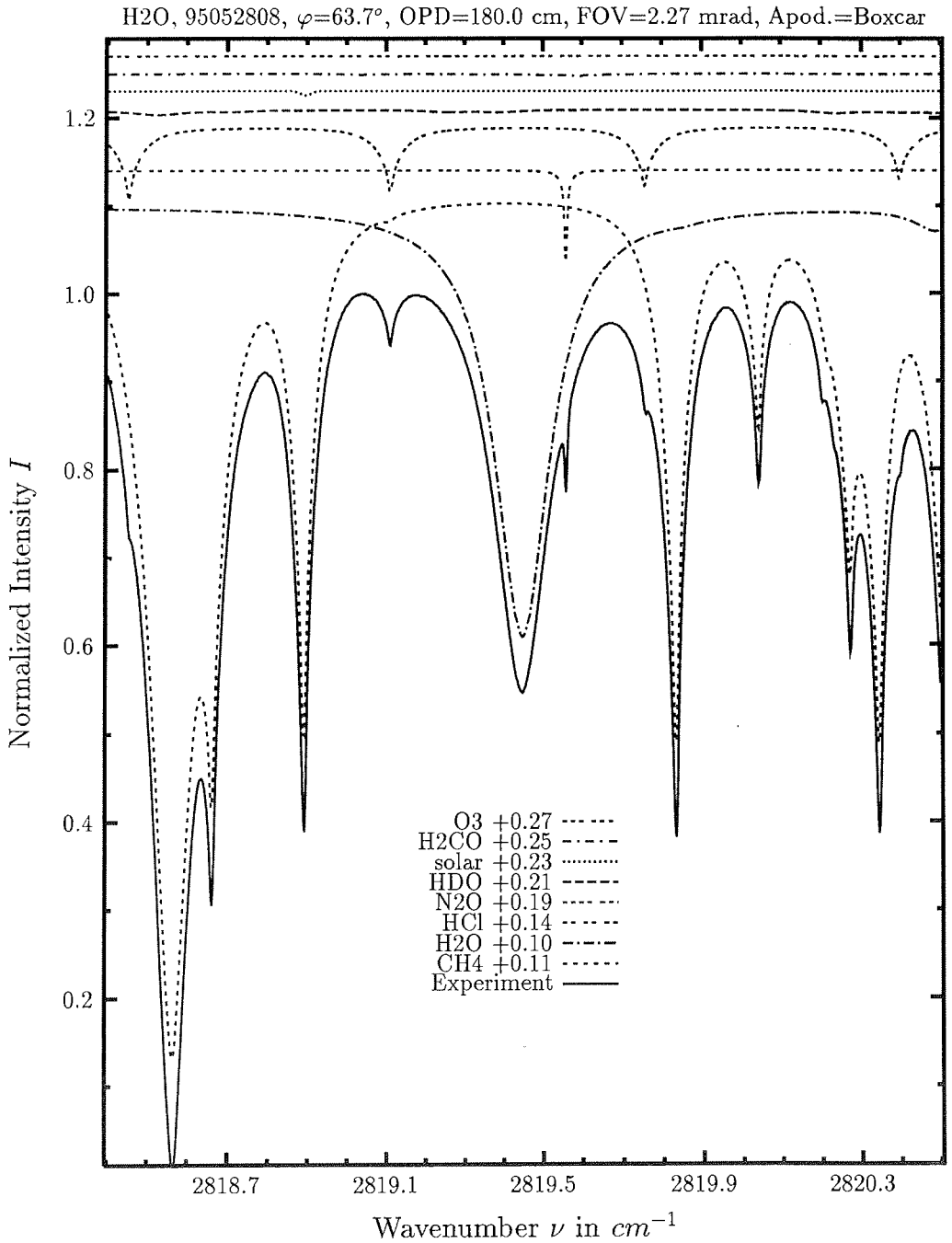
H2O, 95052808, φ=63.7°, OPD=180.0 cm, FOV=2.27 mrad, Apod.=Boxcar
Normalized Intensity I
1.2
1.0
0.8
0.6
0.4
0.2
2818.7
2819.1
2819.5
2819.9
2820.3
Wavenumber ν in cm⁻¹
O3 +0.27
H2CO +0.25
solar +0.23
HDO +0.21
N2O +0.19
HCl +0.14
H2O +0.10
CH4 +0.11
Experiment

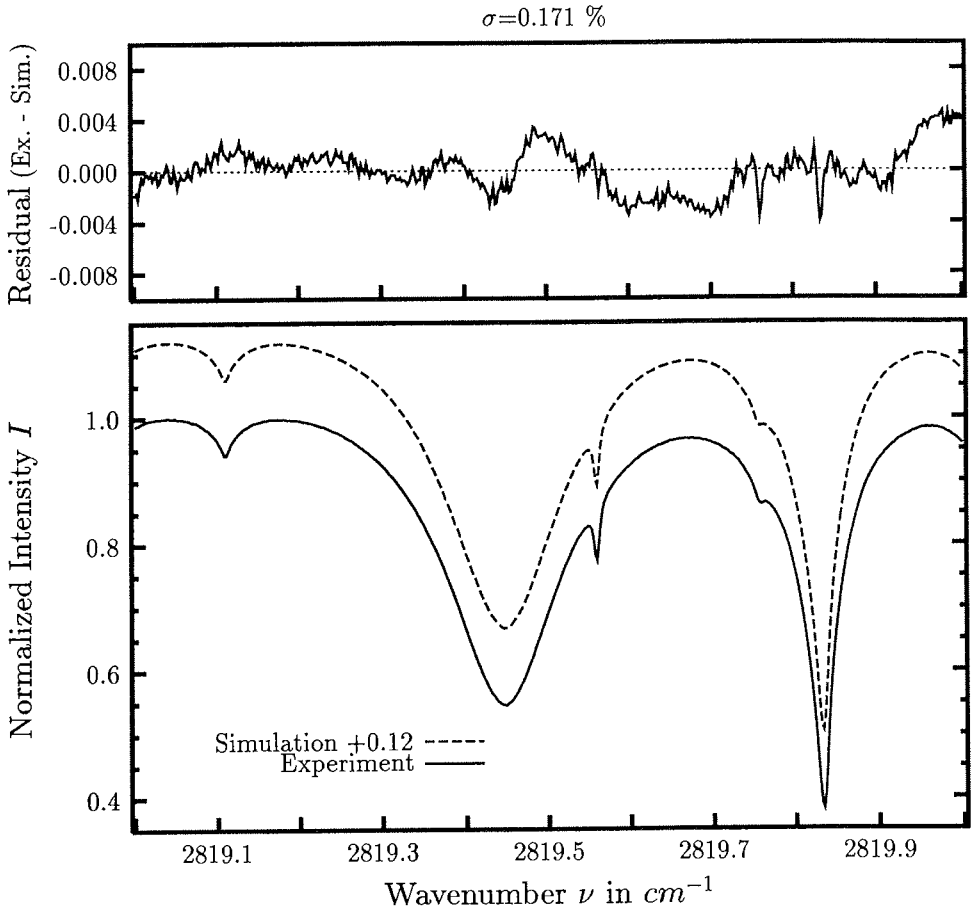

investigated species	: **H_2O**
line position ν_0	: 2819.449 cm^{-1}
major species	: CH_4, H_2O, HCl, N_2O
minor species	: HDO, solar
weak species	: H_2CO, O_3
name of the spectrum	: 95052808
zenith angle, apodization	: 63.7°, boxcar
max. OPD, field of view	: 180.0 cm, 2.27 $mrad$
spectral interval fitted	: 2819.00 – 2820.00 cm^{-1}
retrieved total column	: $1.47 \cdot 10^{22}$ cm^{-2}

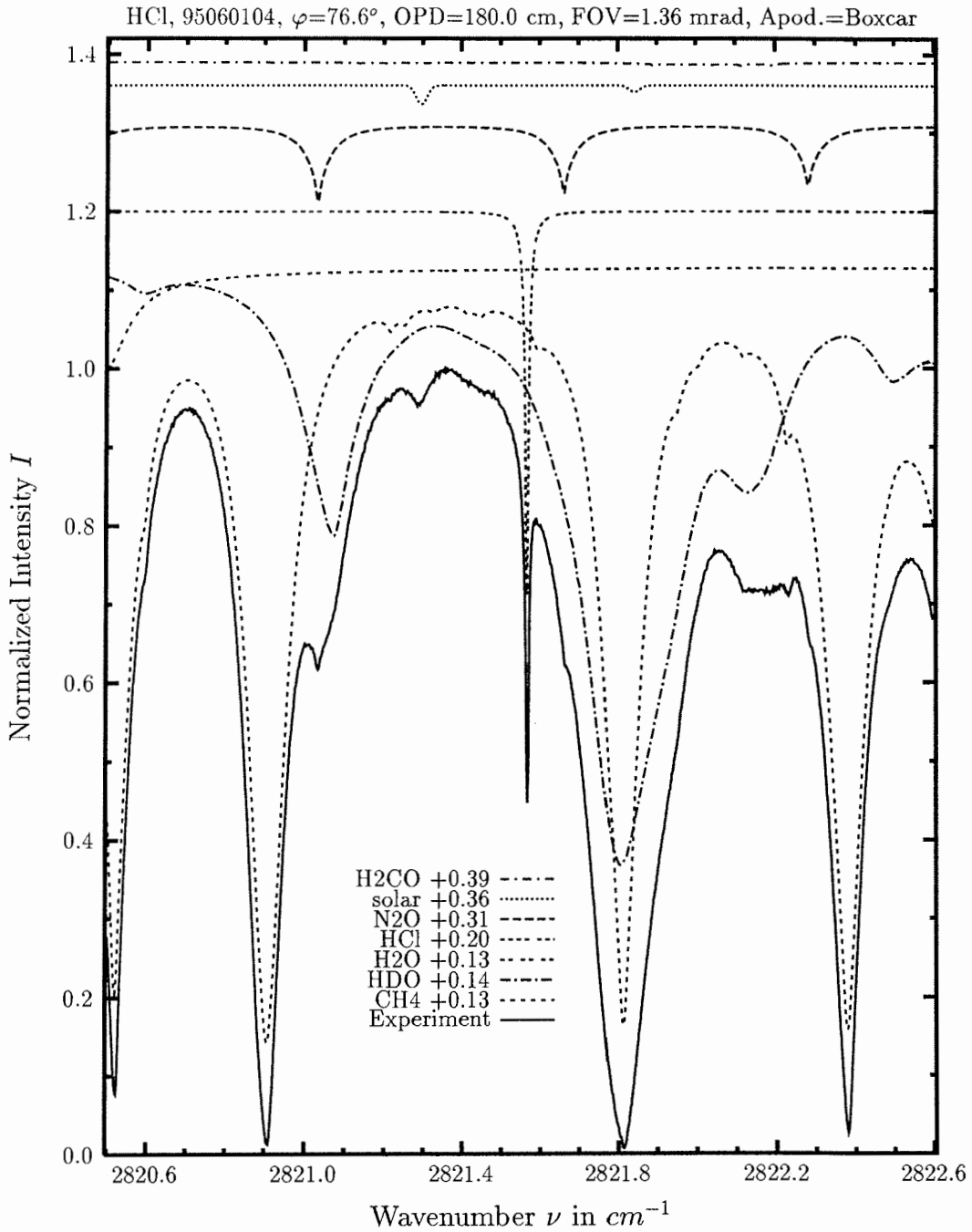
HCl, 95060104, φ=76.6°, OPD=180.0 cm, FOV=1.36 mrad, Apod.=Boxcar
Normalized Intensity I
Wavenumber ν in cm⁻¹
1.4
1.2
1.0
0.8
0.6
0.4
0.2
0.0
2820.6
2821.0
2821.4
2821.8
2822.2
2822.6
H2CO +0.39
solar +0.36
N2O +0.31
HCl +0.20
H2O +0.13
HDO +0.14
CH4 +0.13
Experiment

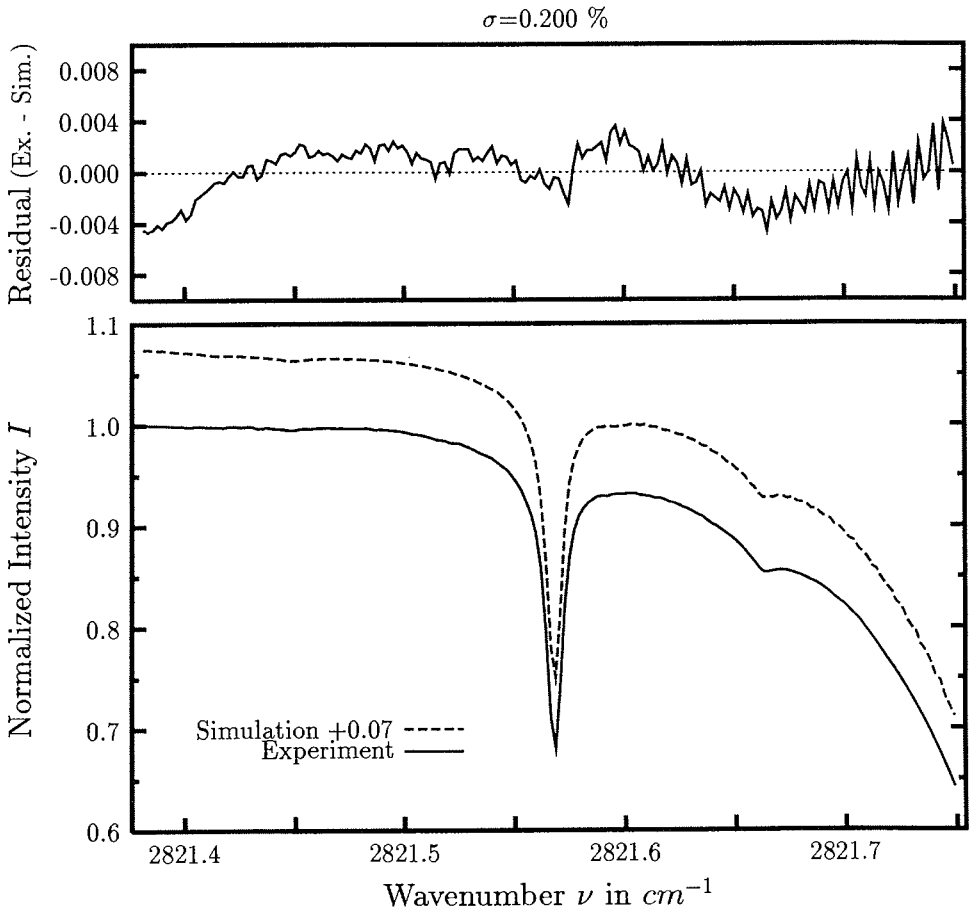

investigated species	: **HCl**
line position ν_0	: 2821.569 cm^{-1}
major species	: CH_4, HDO, HCl, H_2O, N_2O, solar
minor species	: H_2CO
weak species	:
name of the spectrum	: 95052808
zenith angle, apodization	: 63.7°, boxcar
max. OPD, field of view	: 180.0 cm, 2.27 $mrad$
spectral interval fitted	: I) 2820.70 - 2822.20 cm^{-1}, II) 2821.38 - 2821.75 cm^{-1}
retrieved total column	: $6.36 \cdot 10^{15}$ cm^{-2}

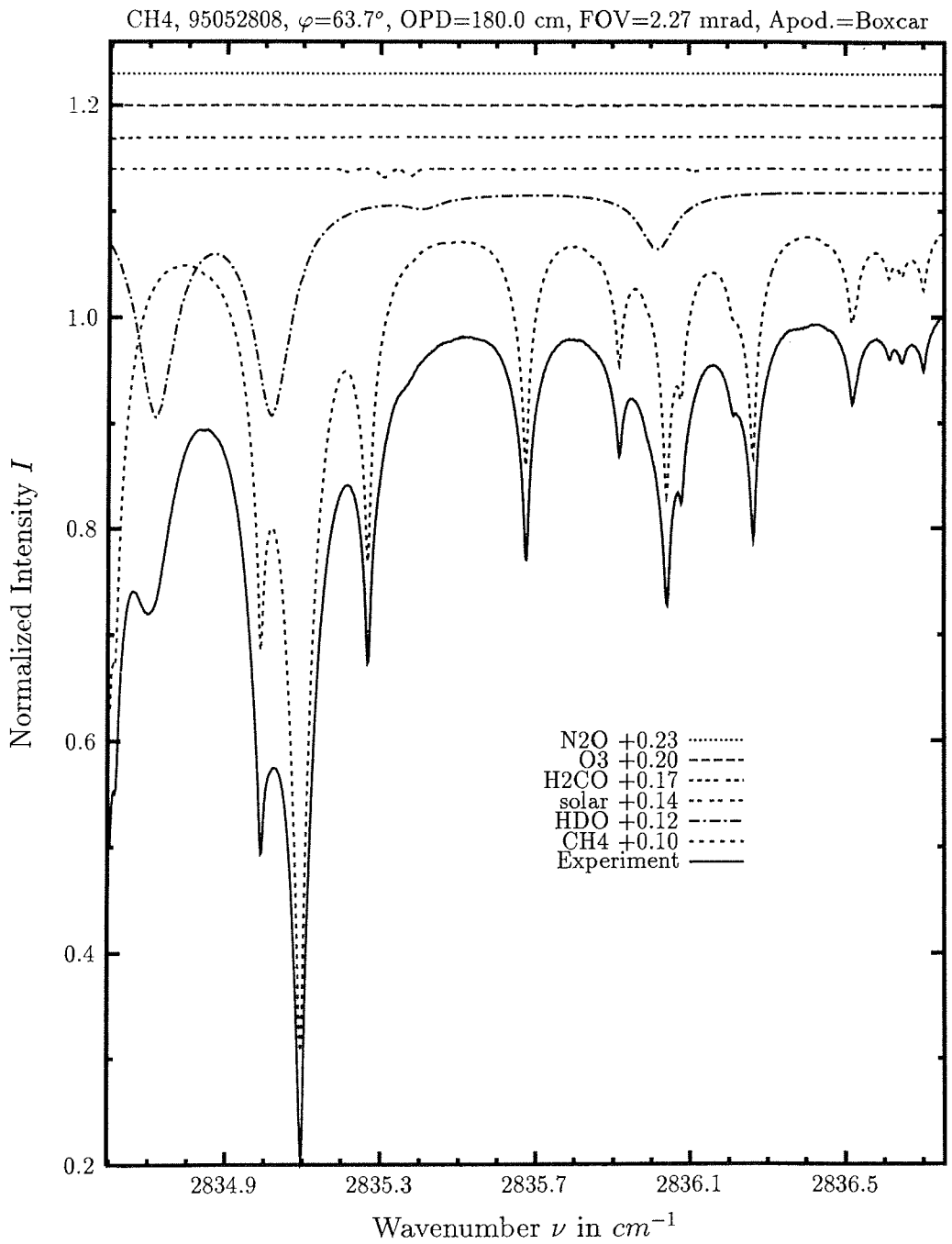
CH4, 95052808, φ=63.7°, OPD=180.0 cm, FOV=2.27 mrad, Apod.=Boxcar
Normalized Intensity I
1.2
1.0
0.8
0.6
0.4
0.2
2834.9
2835.3
2835.7
2836.1
2836.5
Wavenumber ν in cm⁻¹
N2O +0.23
O3 +0.20
H2CO +0.17
solar +0.14
HDO +0.12
CH4 +0.10
Experiment

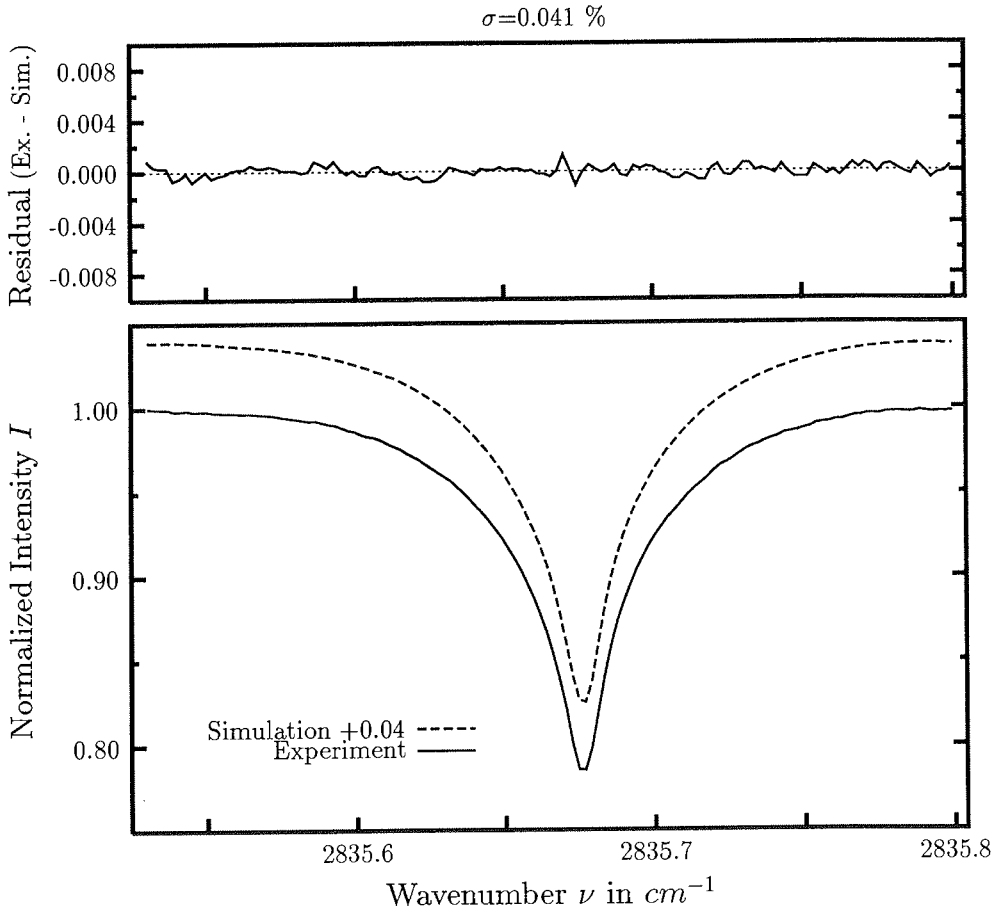

investigated species	: **CH_4**
line position ν_0	: 2835.676 cm^{-1}
major species	: CH_4, HDO
minor species	: solar
weak species	: H_2CO, O_3, N_2O
name of the spectrum	: 95052808
zenith angle, apodization	: 63.7°, boxcar
max. OPD, field of view	: 180.0 cm, 2.27 $mrad$
spectral interval fitted	: 2835.53 – 2835.80 cm^{-1}
retrieved total column	: $3.70 \cdot 10^{19}$ cm^{-2}

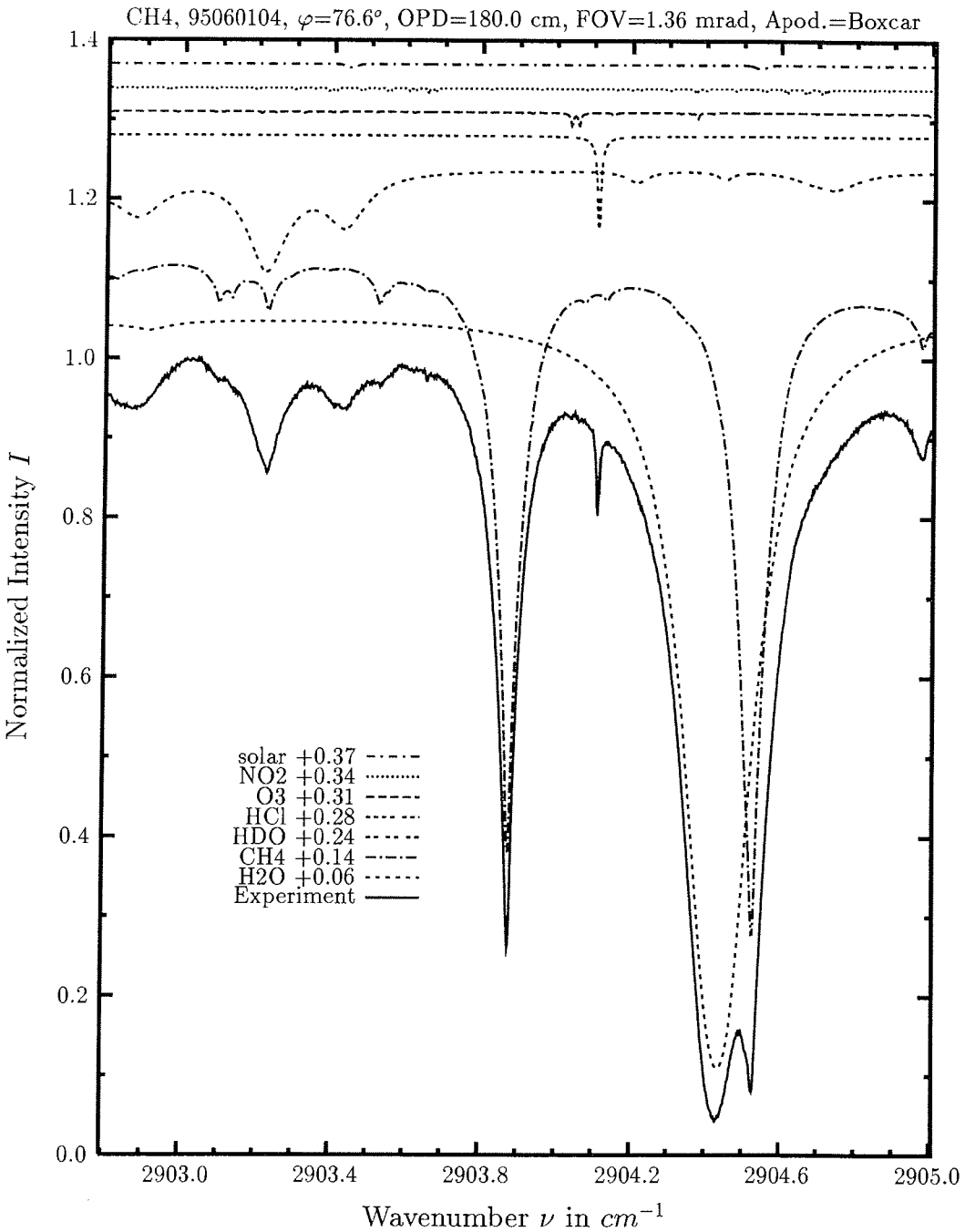
CH4, 95060104, φ=76.6°, OPD=180.0 cm, FOV=1.36 mrad, Apod.=Boxcar
Normalized Intensity I
Wavenumber ν in cm⁻¹
1.4
1.2
1.0
0.8
0.6
0.4
0.2
0.0
2903.0
2903.4
2903.8
2904.2
2904.6
2905.0
solar +0.37
NO2 +0.34
O3 +0.31
HCl +0.28
HDO +0.24
CH4 +0.14
H2O +0.06
Experiment

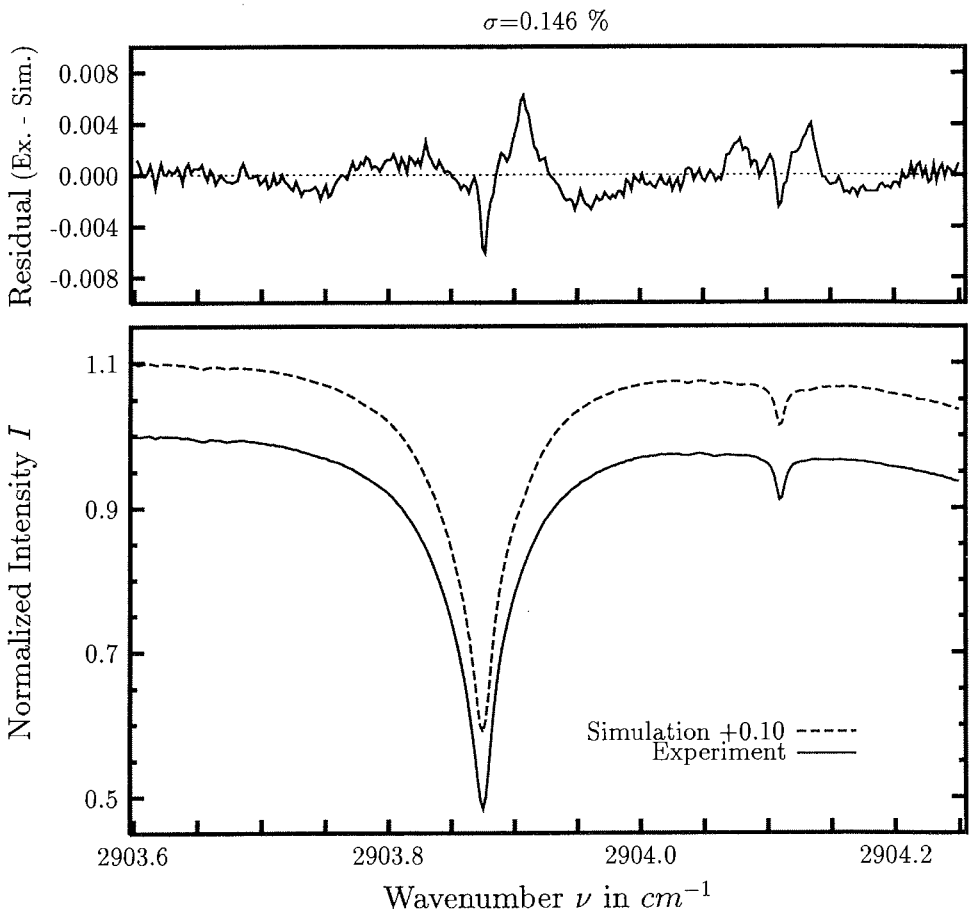

investigated species	: **CH_4, HCl**
line position ν_0	: 2903.876, 2904.111 cm^{-1}
major species	: H_2O, CH_4, HDO, HCl, O_3
minor species	: NO_2, solar
weak species	:
name of the spectrum	: 95052808
zenith angle, apodization	: 63.7°, boxcar
max. OPD, field of view	: 180.0 cm, 2.27 $mrad$
spectral interval fitted	: CH_4: I) 2903.60 - 2904.80 cm^{-1}, II) 2903.60 - 2904.25 cm^{-1}
	: HCl: III) 2903.95 - 2904.30 cm^{-1}
retrieved total column	: $3.55 \cdot 10^{19}\, cm^{-2}$, $6.52 \cdot 10^{15}\, cm^{-2}$

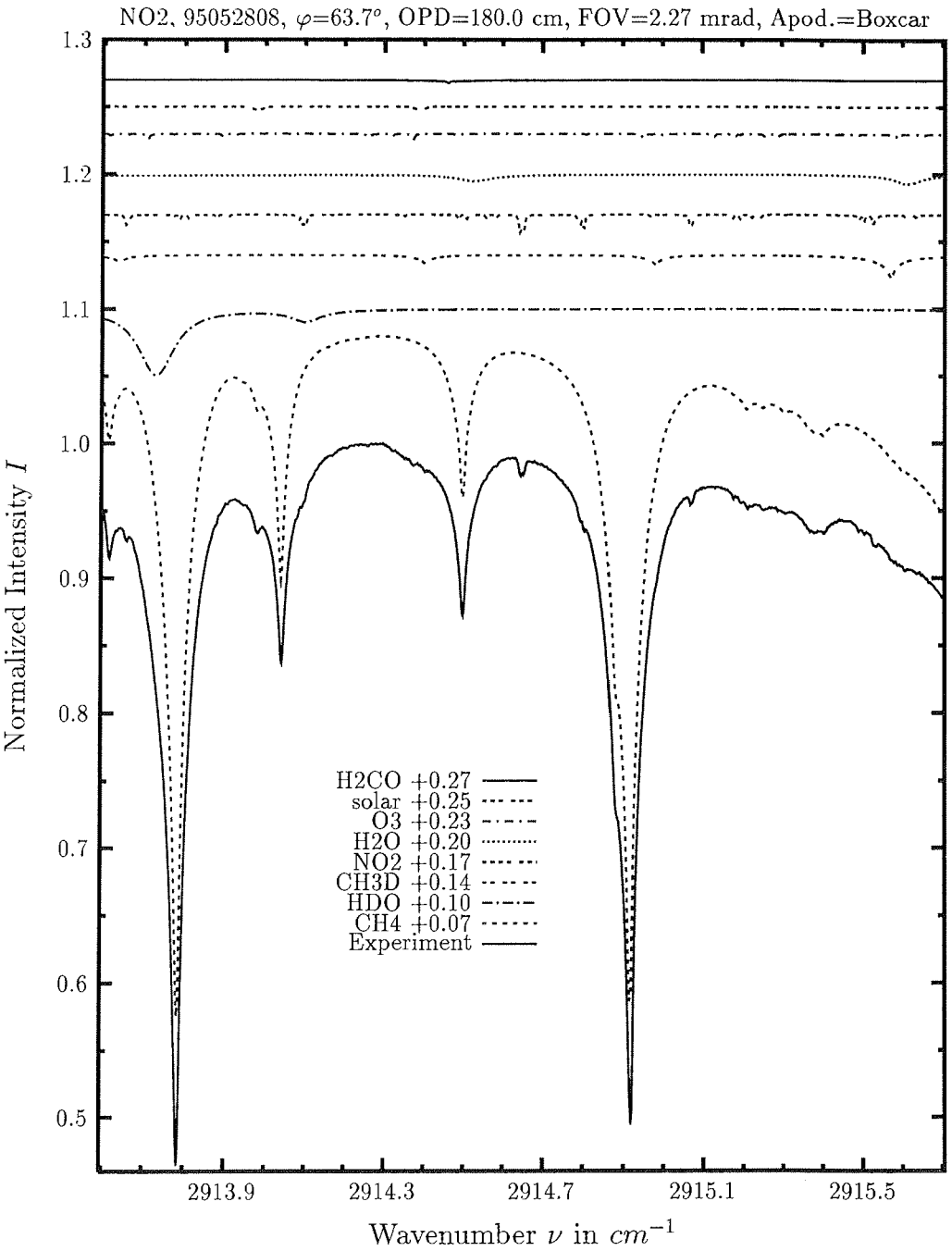
NO2, 95052808, φ=63.7°, OPD=180.0 cm, FOV=2.27 mrad, Apod.=Boxcar
Normalized Intensity I
1.3
1.2
1.1
1.0
0.9
0.8
0.7
0.6
0.5
2913.9
2914.3
2914.7
2915.1
2915.5
Wavenumber ν in cm⁻¹
H2CO +0.27
solar +0.25
O3 +0.23
H2O +0.20
NO2 +0.17
CH3D +0.14
HDO +0.10
CH4 +0.07
Experiment

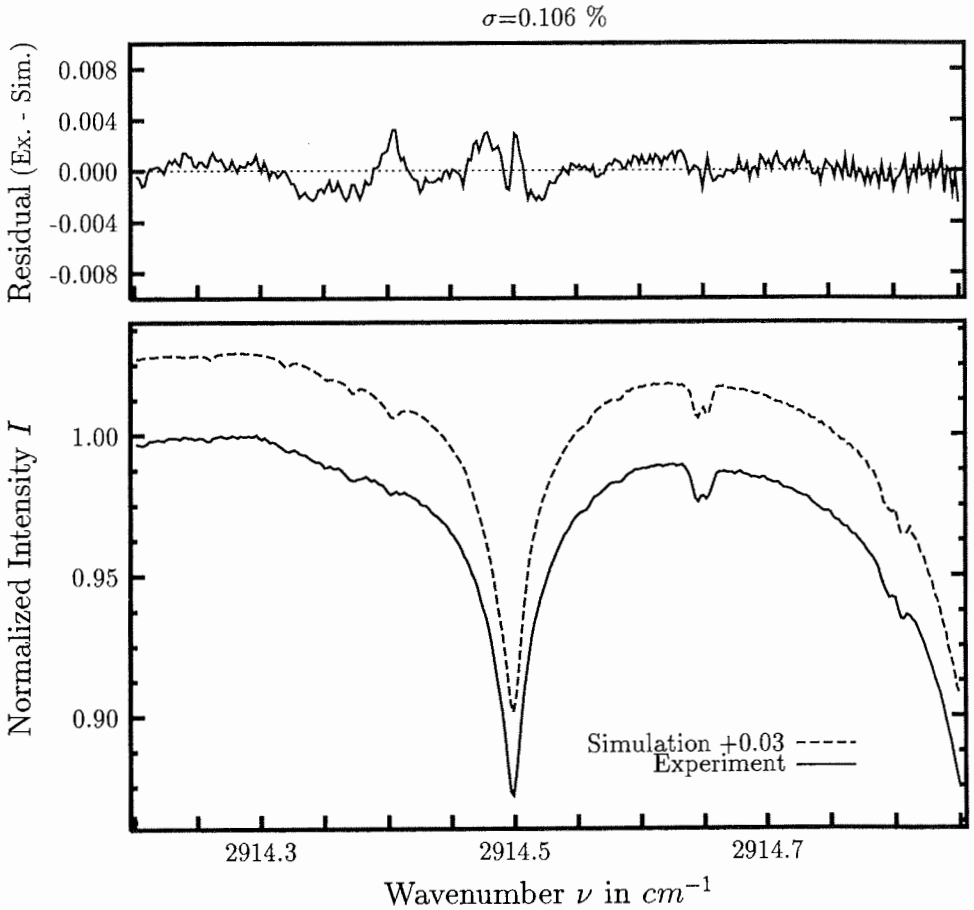

investigated species	: **NO_2**
line position ν_0	: 2914.643, 2914.645, 2914.652 cm^{-1}
major species	: CH_4, HDO, CH_3D, NO_2
minor species	: H_2O, O_3, solar
weak species	: H_2CO
name of the spectrum	: 95052808
zenith angle, apodization	: 63.7°, boxcar
max. OPD, field of view	: 180.0 cm, 2.27 $mrad$
spectral interval fitted	: I) 2914.20 – 2915.20 cm^{-1}, II) 2914.20 – 2914.85 cm^{-1}
retrieved total column	: $3.72 \cdot 10^{15}$ cm^{-2}

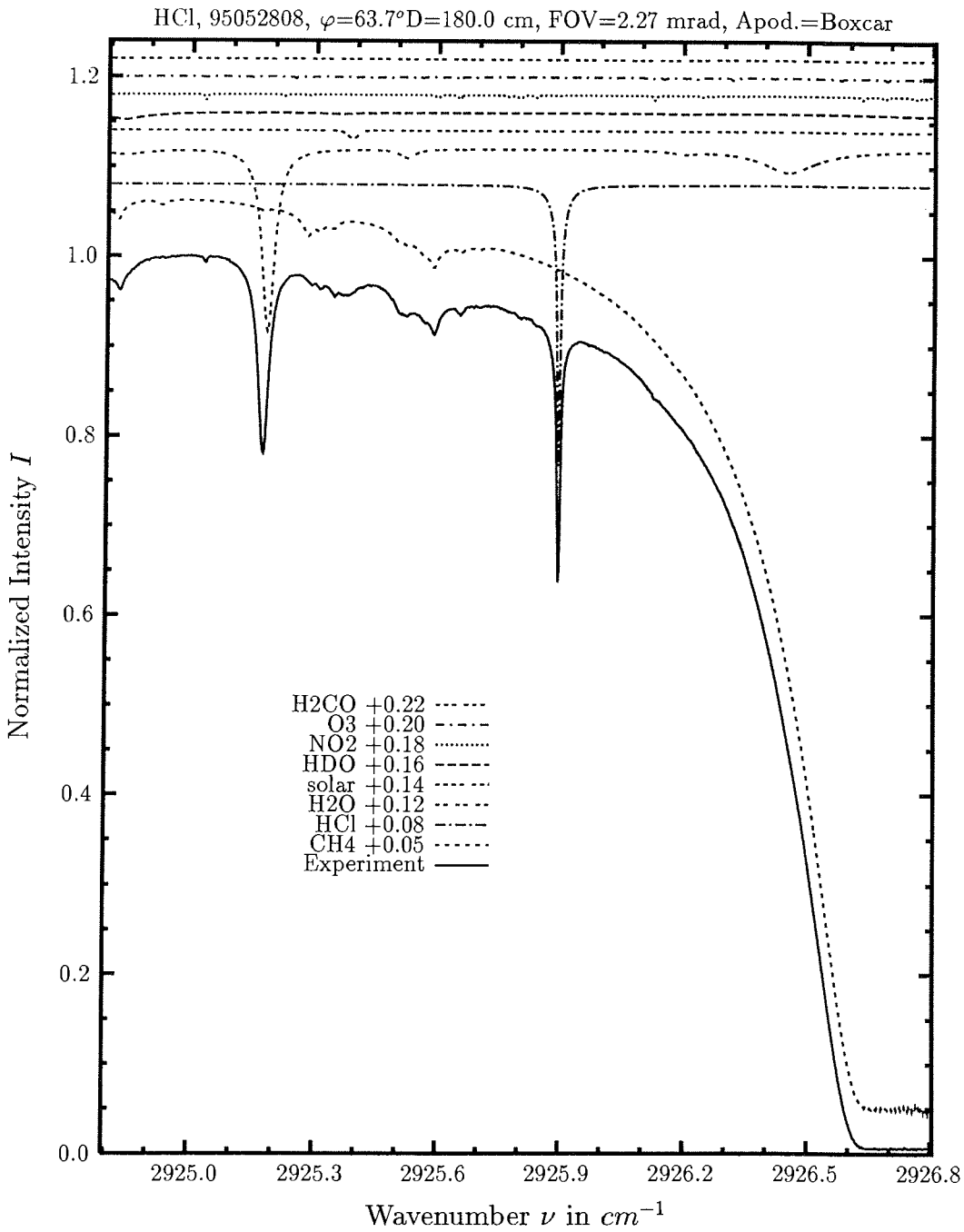
HCl, 95052808, φ=63.7°D=180.0 cm, FOV=2.27 mrad, Apod.=Boxcar
Normalized Intensity I
Wavenumber ν in cm⁻¹
1.2
1.0
0.8
0.6
0.4
0.2
0.0
2925.0
2925.3
2925.6
2925.9
2926.2
2926.5
2926.8
H2CO +0.22
O3 +0.20
NO2 +0.18
HDO +0.16
solar +0.14
H2O +0.12
HCl +0.08
CH4 +0.05
Experiment

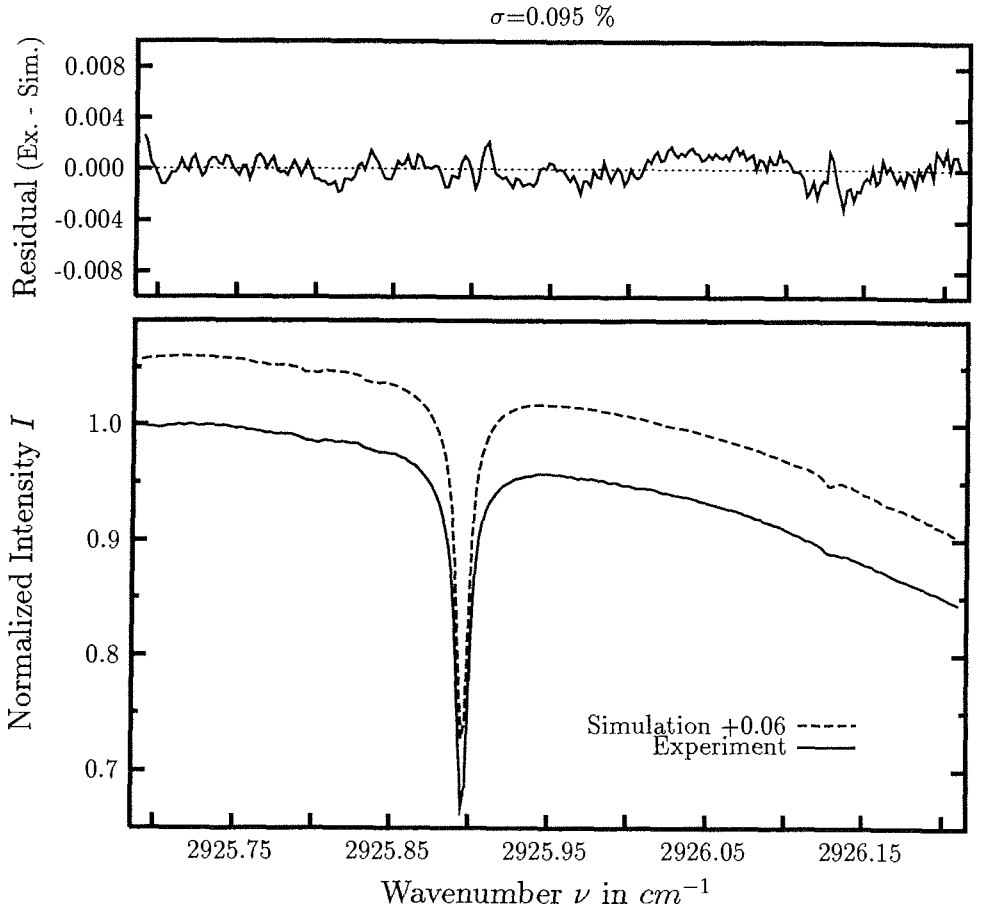

investigated species	: **HCl**
line position ν_0	: 2925.897 cm^{-1}
major species	: CH_4, HCl, H_2O
minor species	: solar, HDO, NO_2, O_3
weak species	: H_2CO, CH_3Cl
name of the spectrum	: 95052808
zenith angle, apodization	: 63.7°, boxcar
max. OPD, field of view	: 180.0 cm, 2.27 $mrad$
spectral interval fitted	: 2925.69 - 2926.21 cm^{-1}
retrieved total column	: $6.14 \cdot 10^{15}$ cm^{-2}

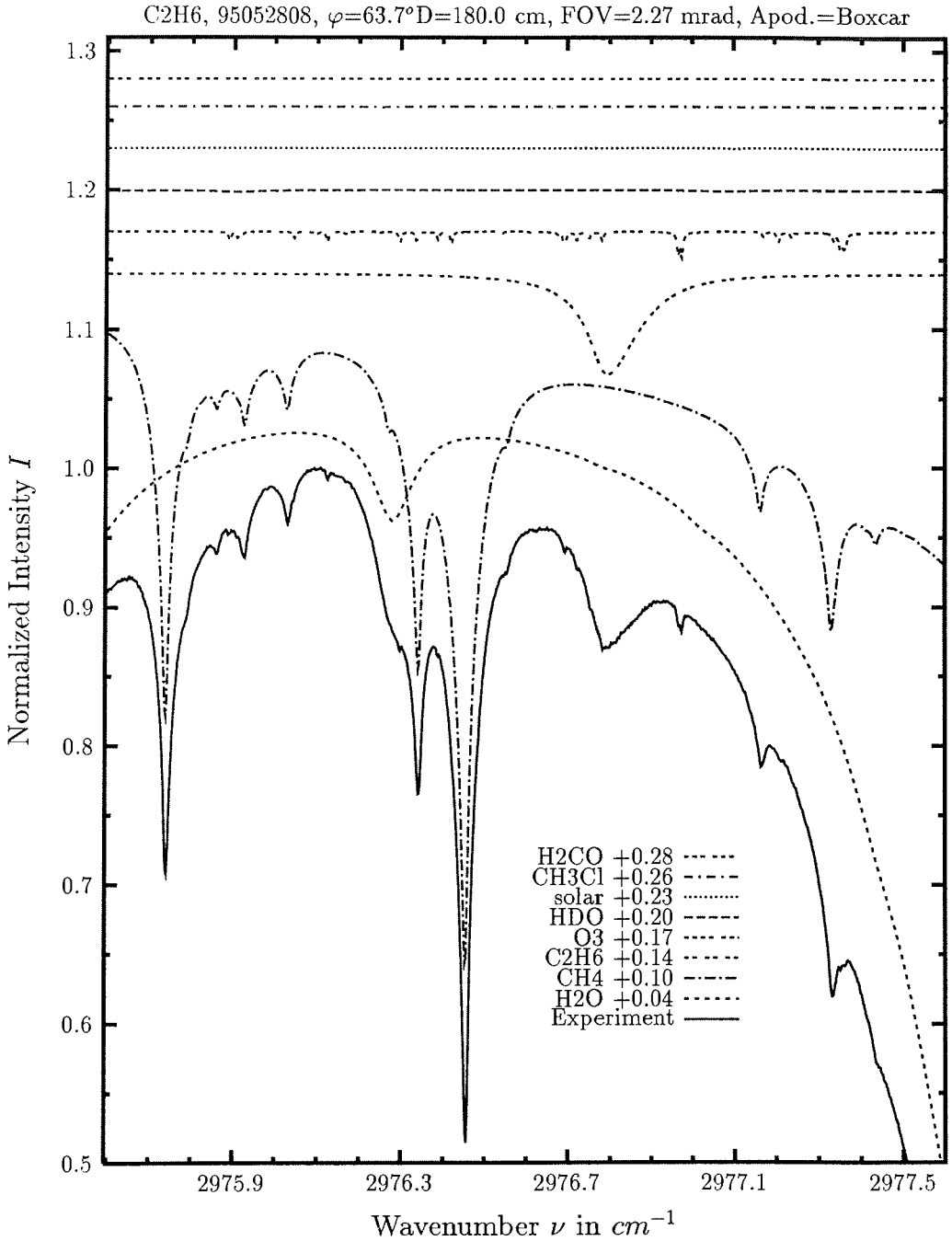
C2H6, 95052808, φ=63.7°D=180.0 cm, FOV=2.27 mrad, Apod.=Boxcar
Normalized Intensity I
Wavenumber ν in cm⁻¹
1.3
1.2
1.1
1.0
0.9
0.8
0.7
0.6
0.5
2975.9
2976.3
2976.7
2977.1
2977.5
H2CO +0.28
CH3Cl +0.26
solar +0.23
HDO +0.20
O3 +0.17
C2H6 +0.14
CH4 +0.10
H2O +0.04
Experiment

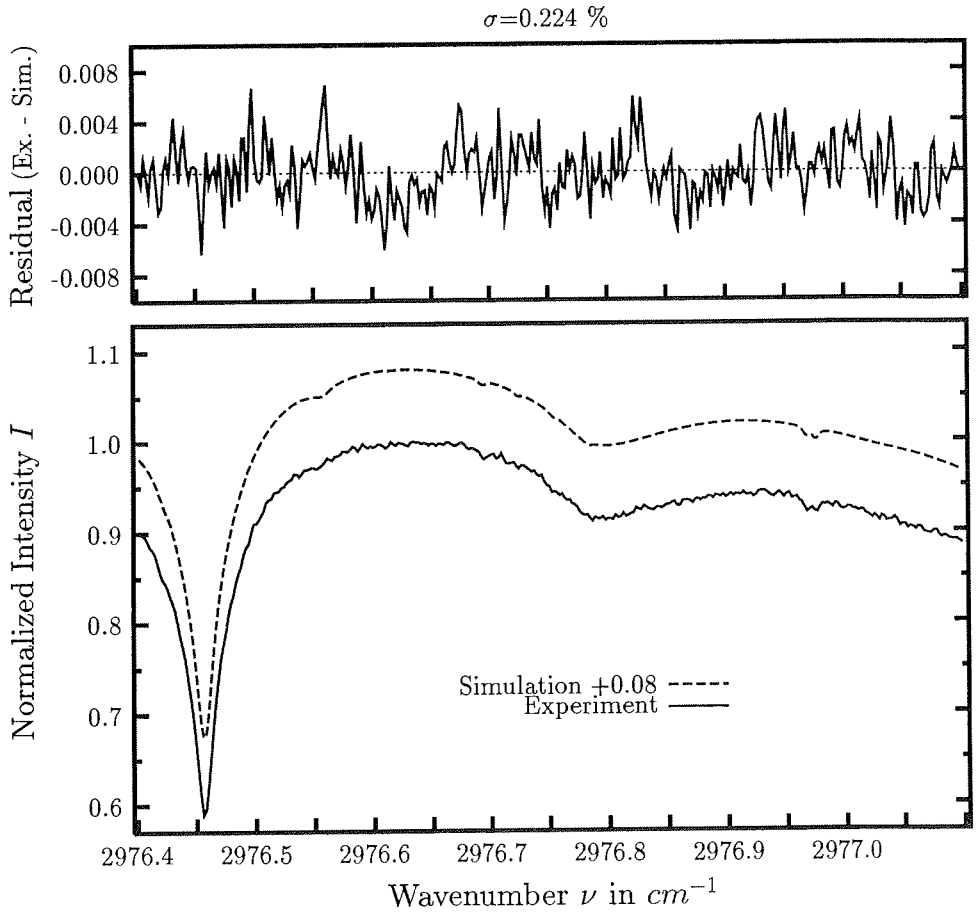

investigated species	: $\mathbf{C_2H_6}$
line position ν_0	: 2976.795*) cm^{-1}
major species	: H_2O, CH_4, C_2H_6, O_3
minor species	: HDO
weak species	: solar, CH_3Cl, H_2CO
name of the spectrum	: 95060162
zenith angle, apodization	: 58.8°, boxcar
max. OPD, field of view	: 180.0 cm, 1.36 $mrad$
spectral interval fitted	: 2976.40 – 2977.10 cm^{-1}
retrieved total column	: $2.11 \cdot 10^{16}$ cm^{-2}

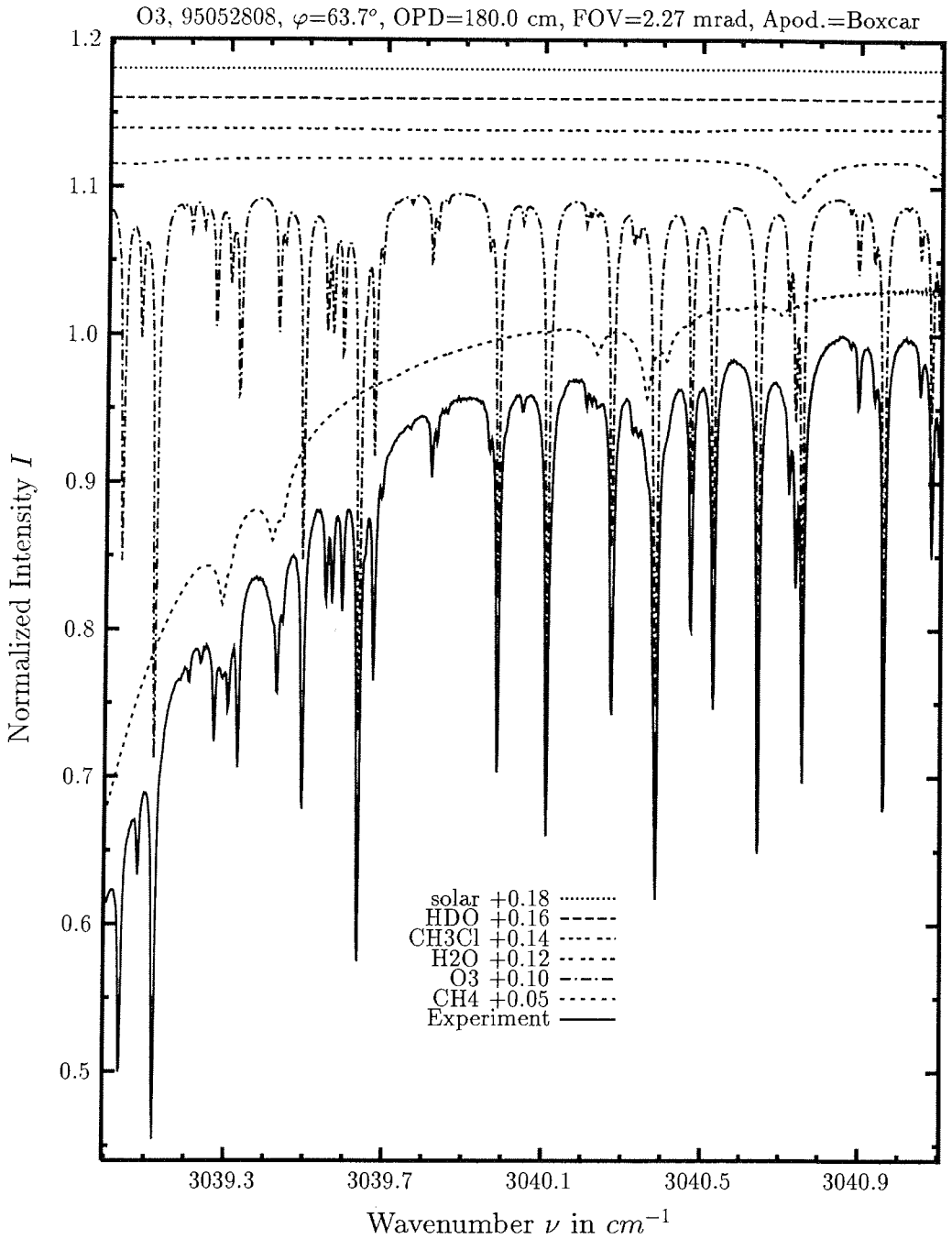
O3, 95052808, φ=63.7°, OPD=180.0 cm, FOV=2.27 mrad, Apod.=Boxcar
Normalized Intensity I
1.2
1.1
1.0
0.9
0.8
0.7
0.6
0.5
3039.3
3039.7
3040.1
3040.5
3040.9
Wavenumber ν in cm⁻¹
solar +0.18
HDO +0.16
CH3Cl +0.14
H2O +0.12
O3 +0.10
CH4 +0.05
Experiment

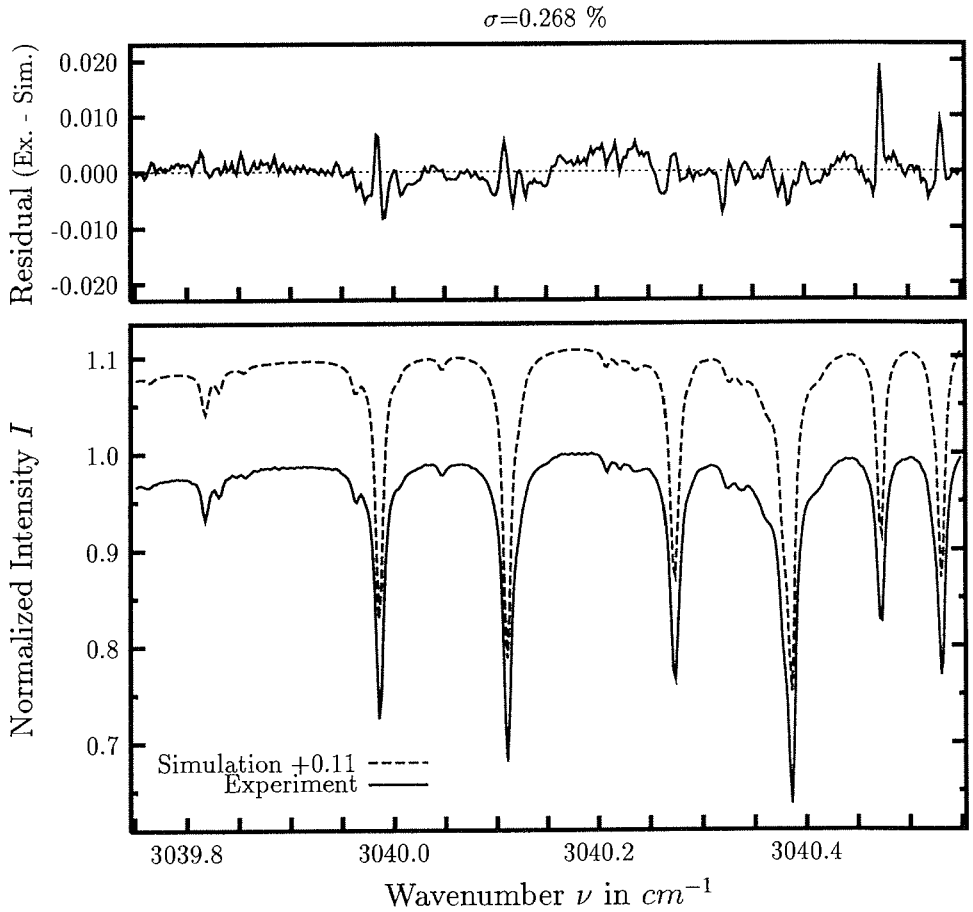

investigated species	: **O_3**
line position ν_0	: 3039.987, 3040.111 cm^{-1}
major species	: O_3, CH_4, H_2O
minor species	: CH_3Cl
weak species	: HDO, solar
name of the spectrum	: 95052808
zenith angle, apodization	: 63.7°, boxcar
max. OPD, field of view	: 180.0 cm, 2.27 $mrad$
spectral interval fitted	: 3039.75 – 3040.55 cm^{-1}
retrieved total column	: $9.45 \cdot 10^{18}\, cm^{-2}$

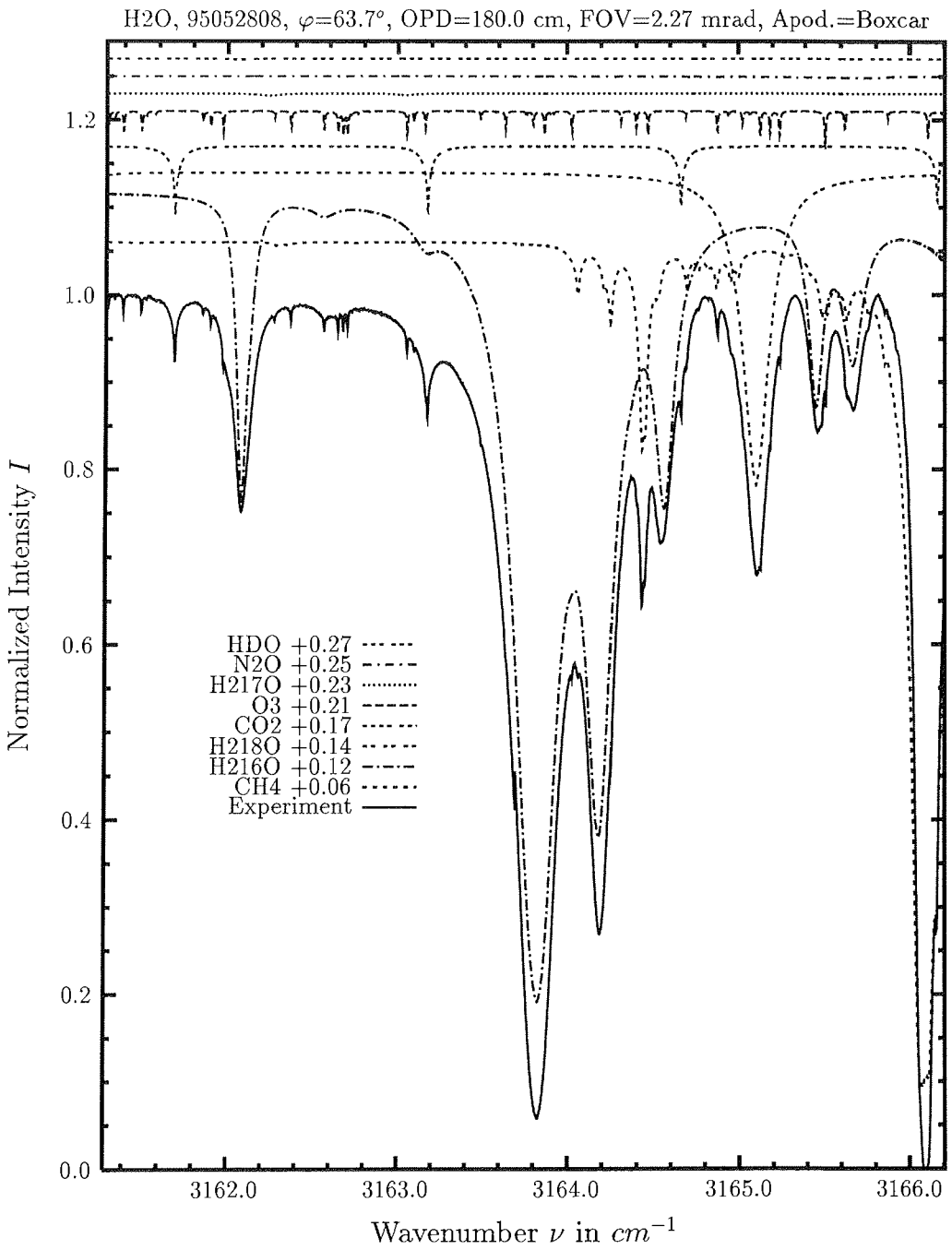
H2O, 95052808, φ=63.7°, OPD=180.0 cm, FOV=2.27 mrad, Apod.=Boxcar
Normalized Intensity I
Wavenumber ν in cm⁻¹
HDO +0.27
N2O +0.25
H217O +0.23
O3 +0.21
CO2 +0.17
H218O +0.14
H216O +0.12
CH4 +0.06
Experiment
0.0
0.2
0.4
0.6
0.8
1.0
1.2
3162.0
3163.0
3164.0
3165.0
3166.0

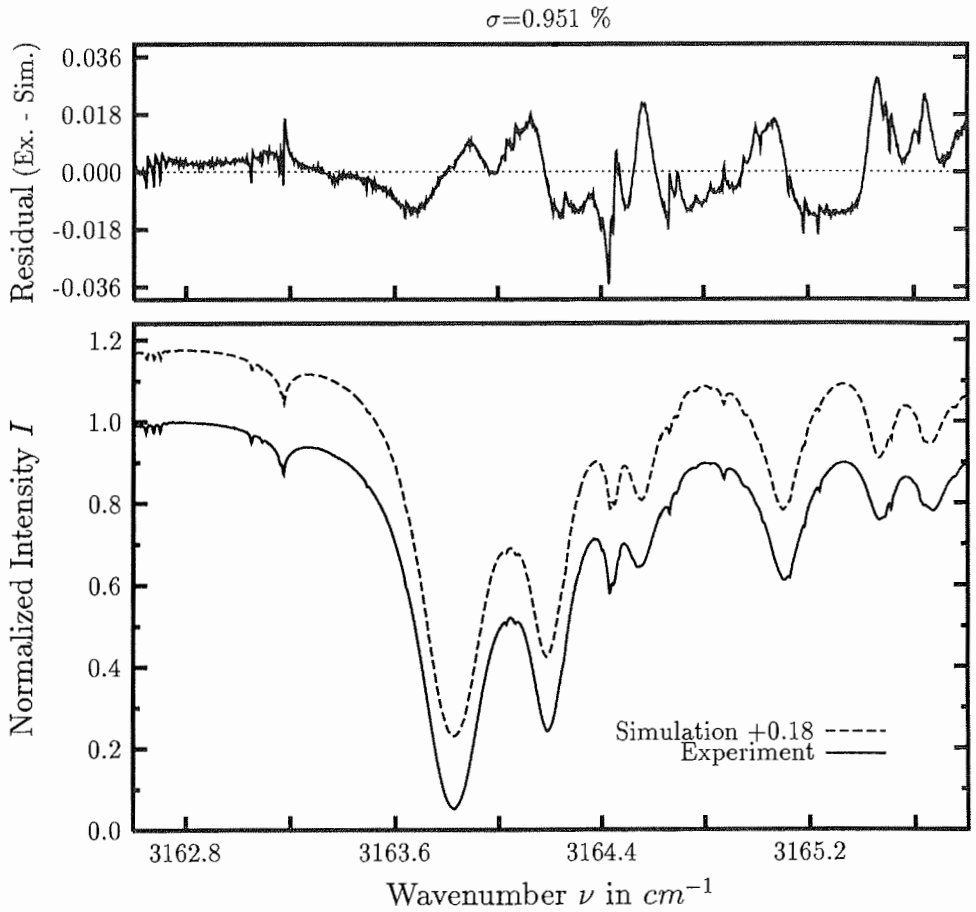

investigated species	: $\mathbf{H_2\,{}^{18}O}$ at 3165.101 cm^{-1} and
	: $\mathbf{H_2\,{}^{16}O}$
line position ν_0	: 3162.084, 3162.131, 3163.827, 3164.185 cm^{-1}
major species	: CH_4, $H_2\,{}^{16}O$, $H_2\,{}^{18}O$, CO_2, O_3
minor species	: $H_2\,{}^{17}O$
weak species	: N_2O, HDO
name of the spectrum	: 95052808
zenith angle, apodization	: 63.7°, boxcar
max. OPD, field of view	: 180.0 cm, 2.27 $mrad$
spectral interval fitted	: 3162.60 – 3165.80 cm^{-1}
retrieved total column	: $1.69 \cdot 10^{22}\,cm^{-2}$

comments: The spectroscopic data of H_2O appears unrealistic. Compare absorption at 3162.08 and 3163.83 cm^{-1}.

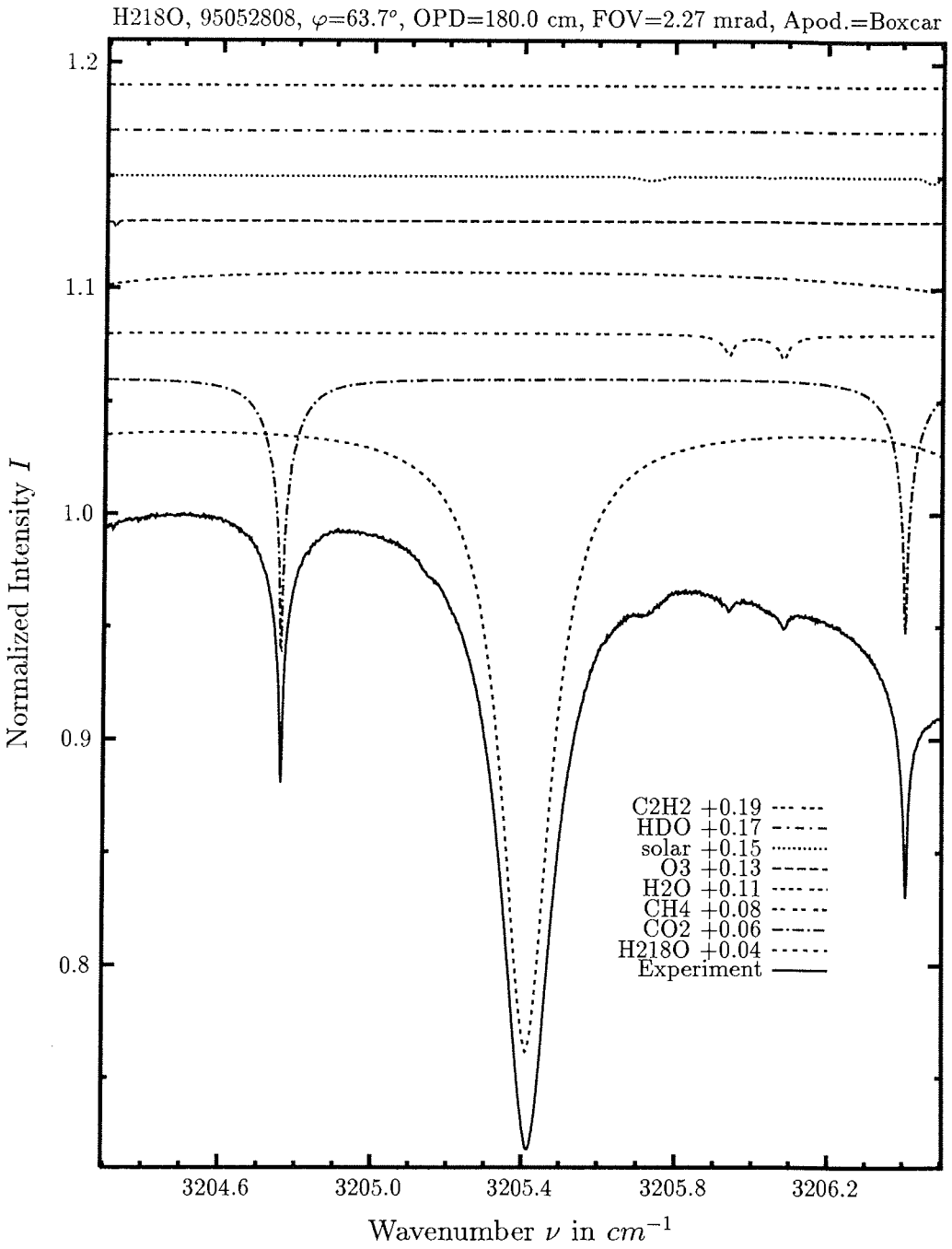
H218O, 95052808, φ=63.7°, OPD=180.0 cm, FOV=2.27 mrad, Apod.=Boxcar
Normalized Intensity I
1.2
1.1
1.0
0.9
0.8
3204.6
3205.0
3205.4
3205.8
3206.2
Wavenumber ν in cm⁻¹
C2H2 +0.19
HDO +0.17
solar +0.15
O3 +0.13
H2O +0.11
CH4 +0.08
CO2 +0.06
H218O +0.04
Experiment

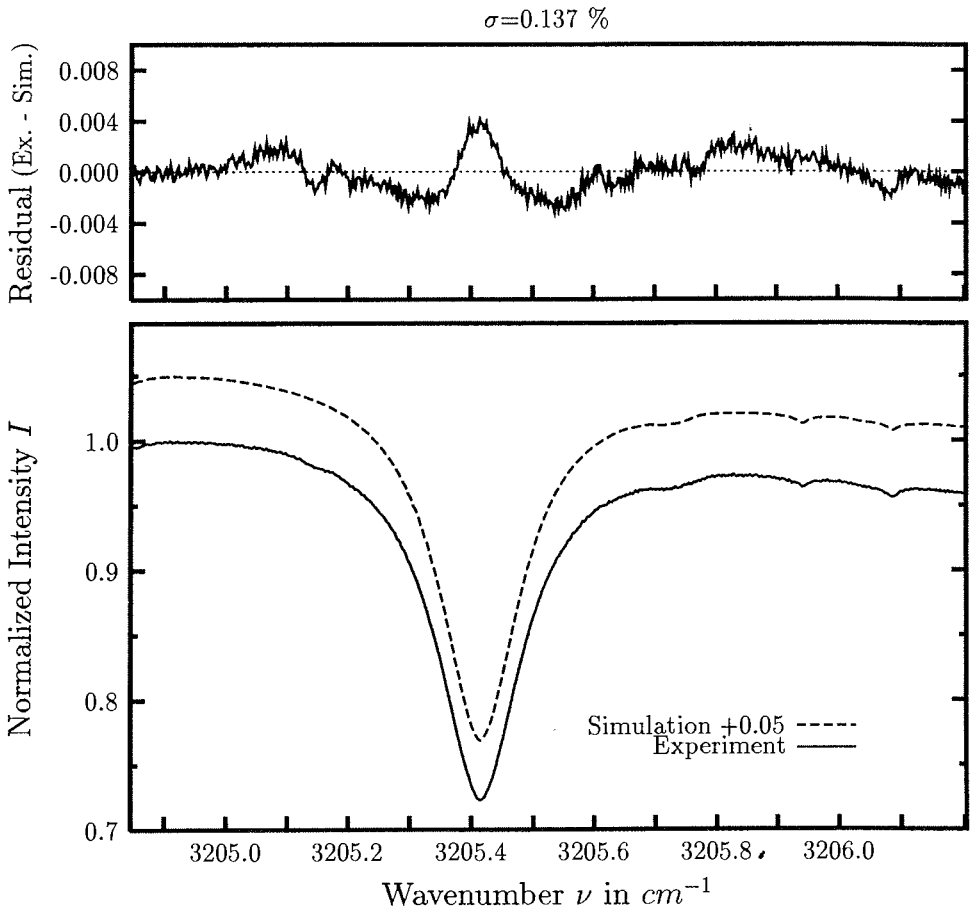

investigated species	: **$H_2\,{}^{18}O$**
line position ν_0	: 3205.412 cm^{-1}
major species	: $H_2\,{}^{18}O$, CO_2, CH_4, H_2O
minor species	: O_3, solar
weak species	: HDO, C_2H_2
name of the spectrum	: 95052808
zenith angle, apodization	: 63.7°, boxcar
max. OPD, field of view	: 180.0 cm, 2.27 $mrad$
spectral interval fitted	: 3204.85 – 3206.20 cm^{-1}
retrieved total column	: $1.55 \cdot 10^{22}\ cm^{-2}$

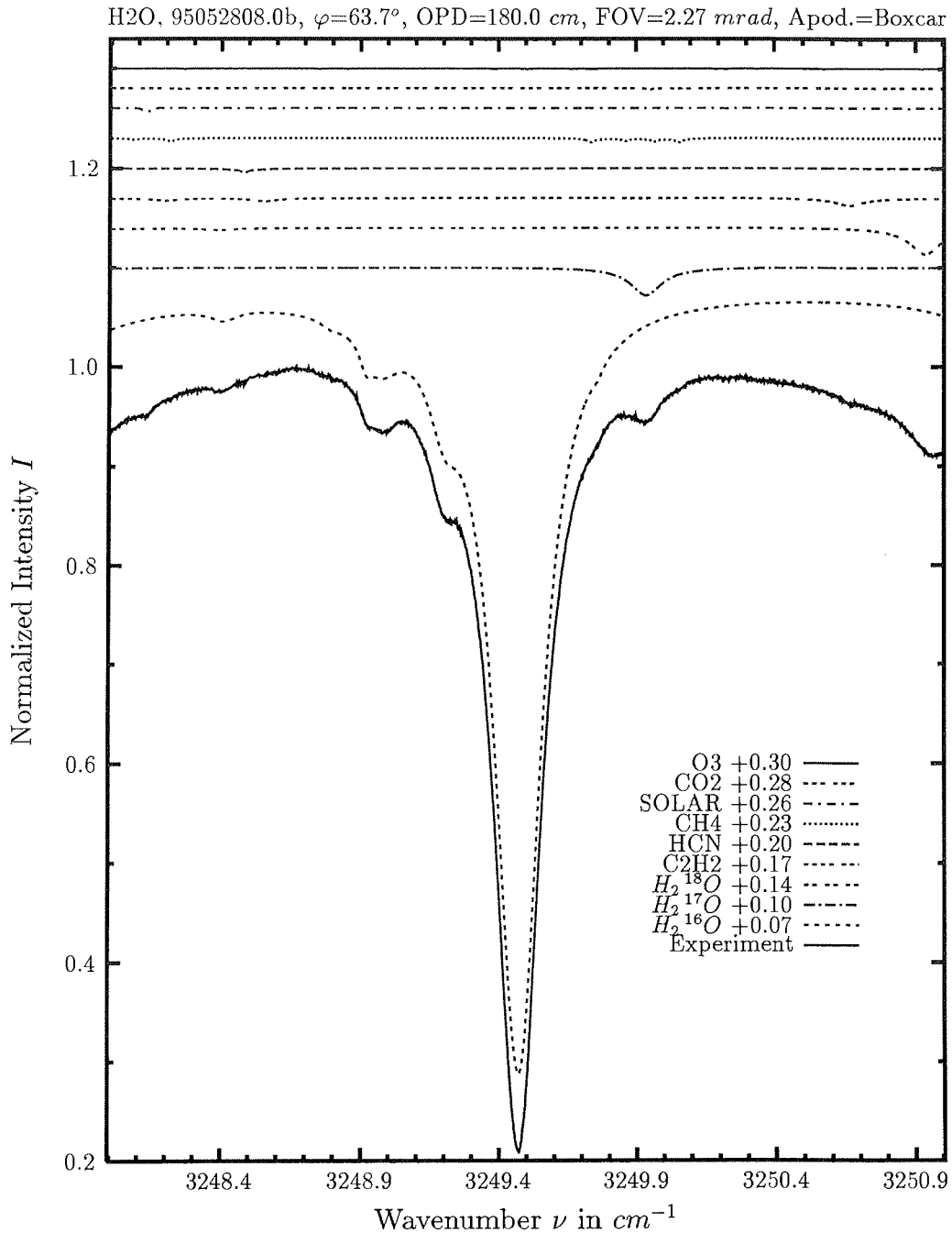
H2O, 95052808.0b, φ=63.7°, OPD=180.0 cm, FOV=2.27 mrad, Apod.=Boxcar
Normalized Intensity I
1.2
1.0
0.8
0.6
0.4
0.2
3248.4
3248.9
3249.4
3249.9
3250.4
3250.9
Wavenumber ν in cm⁻¹
O3 +0.30
CO2 +0.28
SOLAR +0.26
CH4 +0.23
HCN +0.20
C2H2 +0.17
H2 18O +0.14
H2 17O +0.10
H2 16O +0.07
Experiment

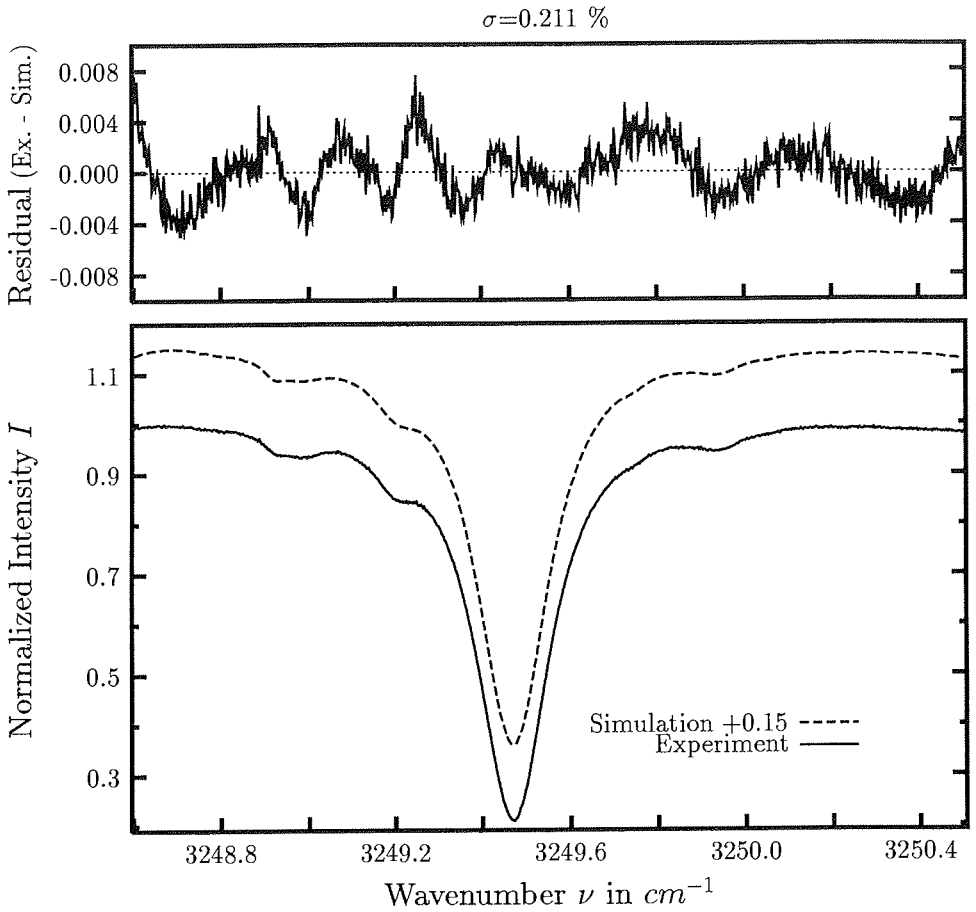

investigated species	: **$H_2{}^{16}O$, $H_2{}^{17}O$**
line positions ν_0	: 3249.472 and 3249.938 cm^{-1}
major species	: $H_2{}^{16}O$, $H_2{}^{17}O$, $H_2{}^{18}O$
minor species	: C_2H_2, HCN, CH_4, solar, CO_2
weak species	: O_3
name of the spectrum	: 95052808
zenith angle, apodization	: 63.7°, boxcar
max. OPD, field of view	: 180.0 cm, 1.36 $mrad$
spectral interval fitted	: 3248.60 – 3250.50 cm^{-1}
retrieved total column	: $1.48 \cdot 10^{22}$ cm^{-2}

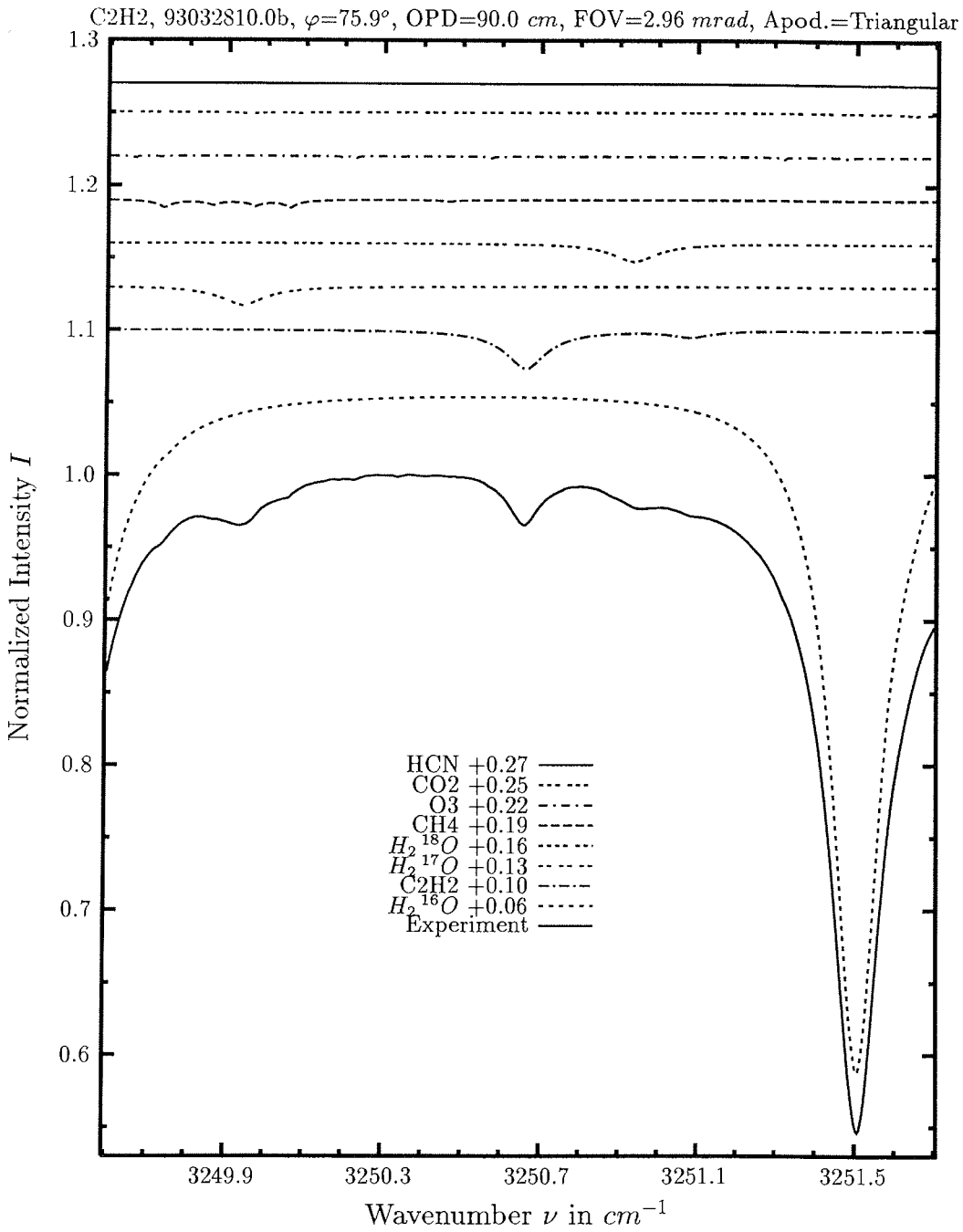
C2H2, 93032810.0b, φ=75.9°, OPD=90.0 cm, FOV=2.96 mrad, Apod.=Triangular
Normalized Intensity I
Wavenumber ν in cm⁻¹
1.3
1.2
1.1
1.0
0.9
0.8
0.7
0.6
3249.9
3250.3
3250.7
3251.1
3251.5
HCN +0.27
CO2 +0.25
O3 +0.22
CH4 +0.19
H2 18O +0.16
H2 17O +0.13
C2H2 +0.10
H2 16O +0.06
Experiment

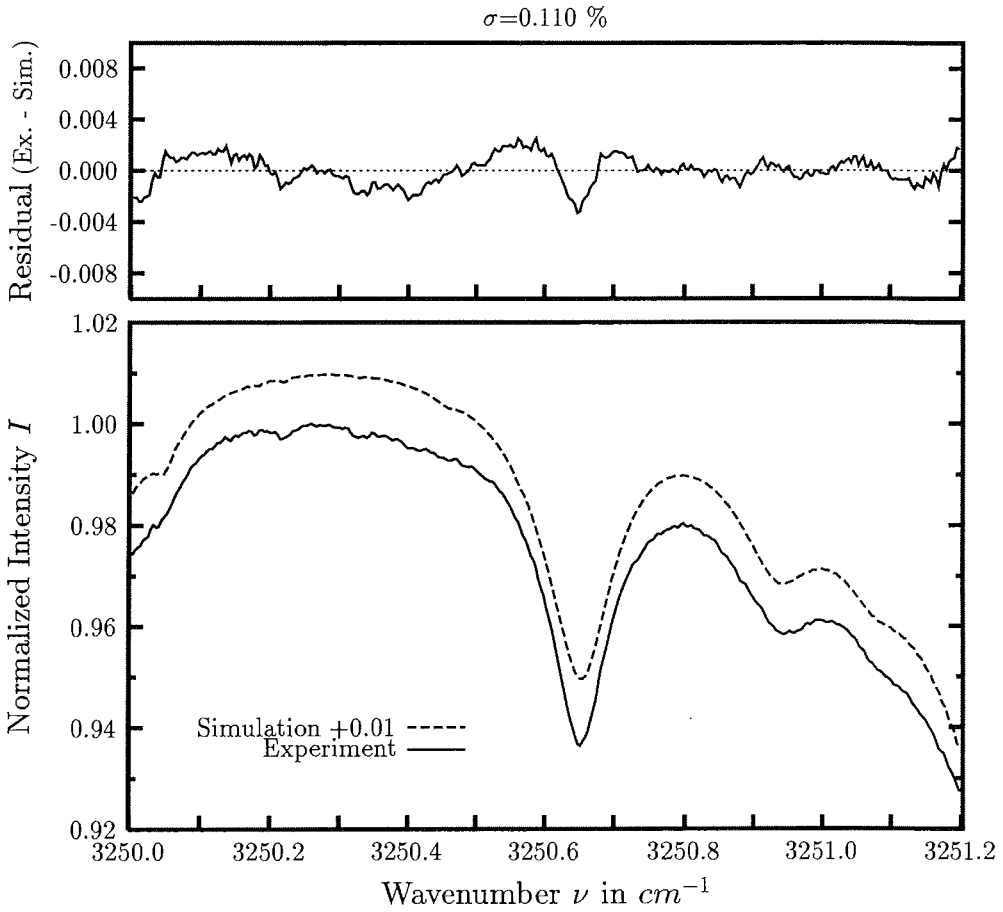

investigated species	: $\mathbf{C_2H_2}$
line position ν_0	: 3250.662 cm^{-1}
major species	: H_2O, C_2H_2
minor species	: CH_4, O_3, CO_2
weak species	: HCN, solar, HDO, NO, OH
name of the spectrum	: 95032010
zenith angle, apodization	: 79.7°, boxcar
max. OPD, field of view	: 90.0 cm, 2.96 $mrad$
spectral interval fitted	: 3250.00 – 3251.20 cm^{-1}
retrieved total column	: $1.04 \cdot 10^{16}$ cm^{-2}

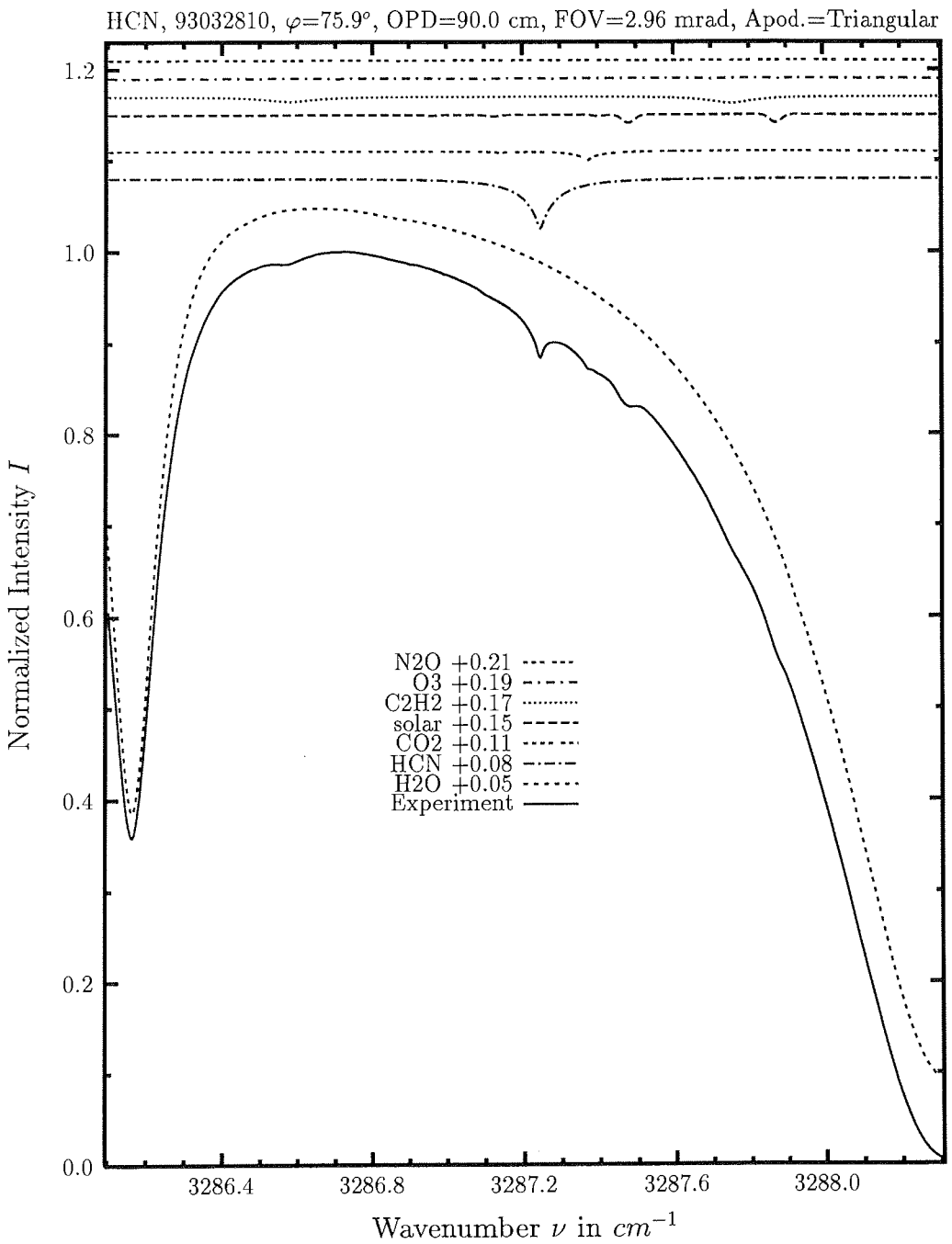
HCN, 93032810, φ=75.9°, OPD=90.0 cm, FOV=2.96 mrad, Apod.=Triangular
Normalized Intensity I
Wavenumber ν in cm⁻¹
1.2
1.0
0.8
0.6
0.4
0.2
0.0
3286.4
3286.8
3287.2
3287.6
3288.0
N2O +0.21
O3 +0.19
C2H2 +0.17
solar +0.15
CO2 +0.11
HCN +0.08
H2O +0.05
Experiment

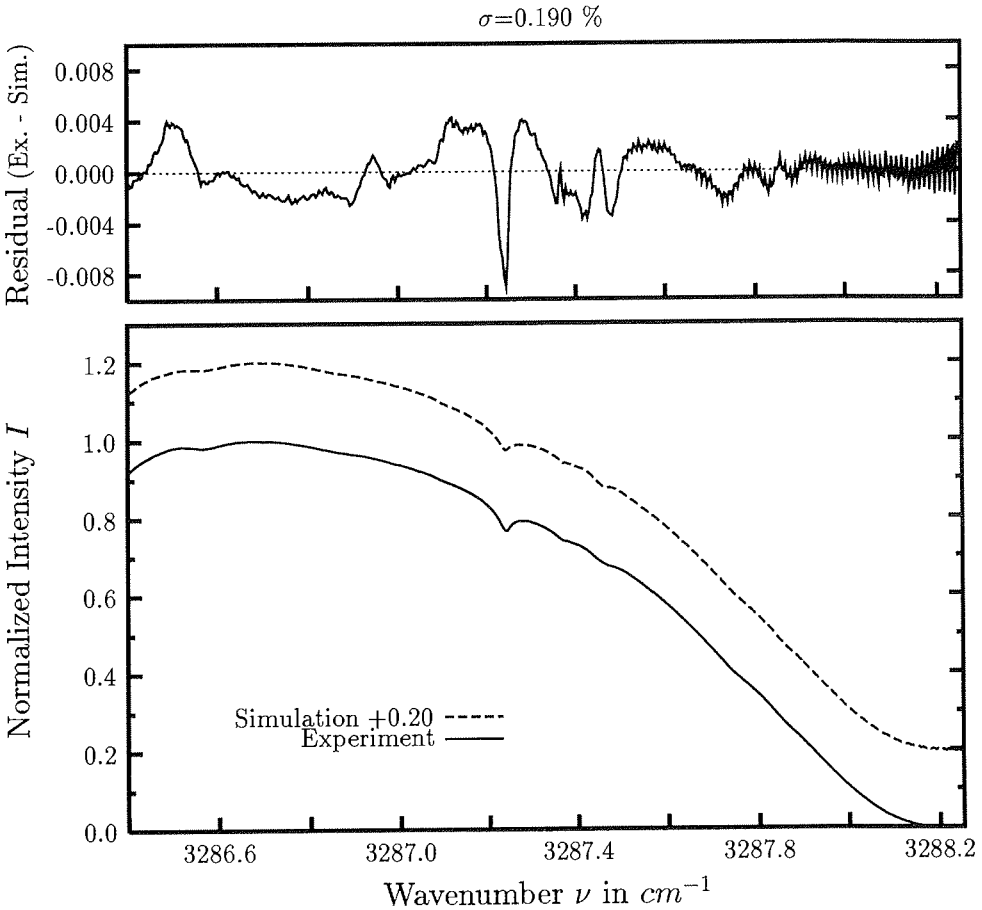

investigated species	: **HCN**
line position ν_0	: 3287.248 cm^{-1}
major species	: H_2O, HCN, CO_2
minor species	: solar, C_2H_2
weak species	: O_3, N_2O, NO, NH_3
name of the spectrum	: 95031814
zenith angle, apodization	: 83.4°, boxcar
max. OPD, field of view	: 90.0 cm, 2.96 $mrad$
spectral interval fitted	: 3286.40 – 3288.25 cm^{-1}
retrieved total column	: $3.76 \cdot 10^{15}$ cm^{-2}

comments: The spectroscopic data of H_2O at 3286.2 and 3288.4 cm^{-1} are inconsistent.

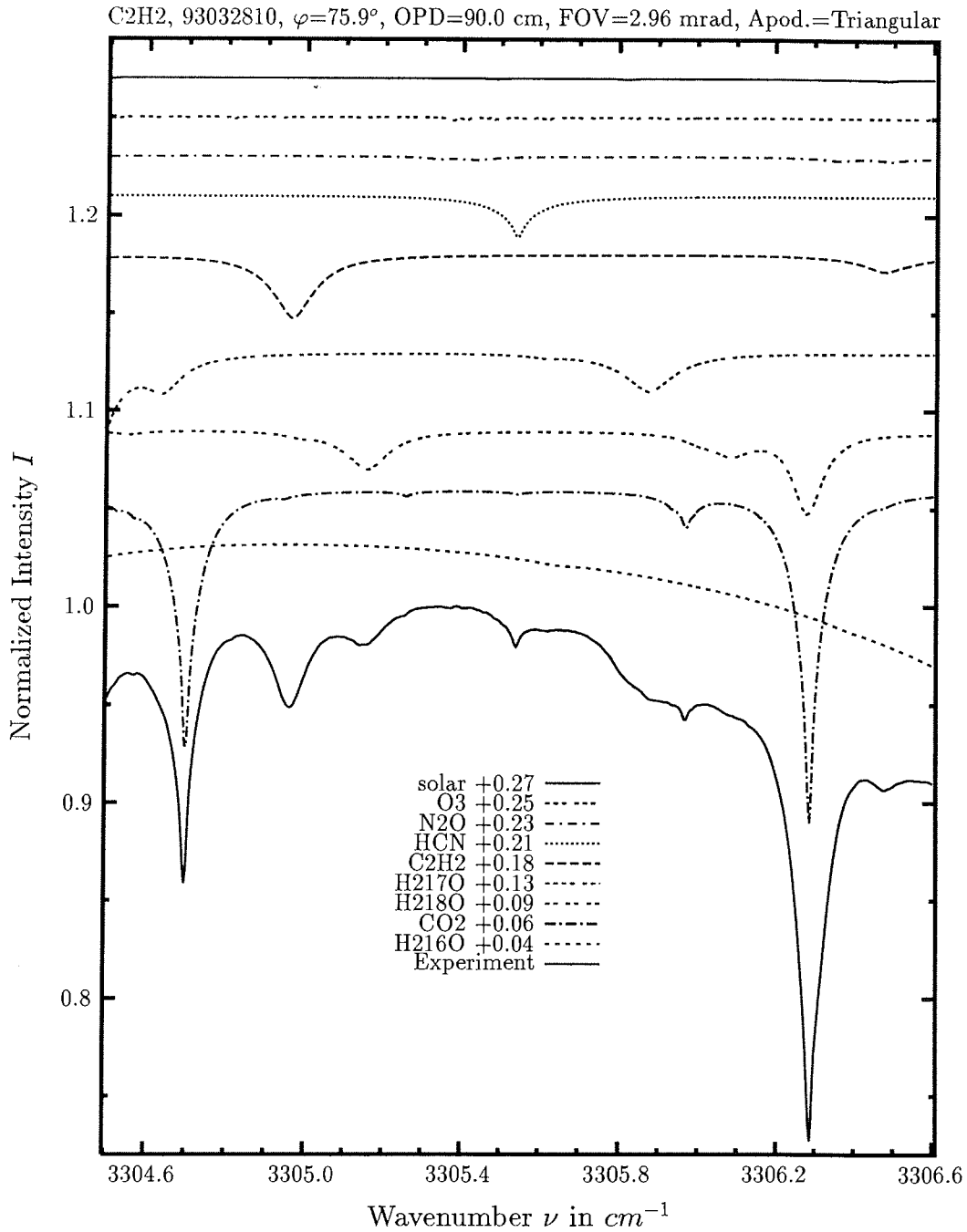
C2H2, 93032810, φ=75.9°, OPD=90.0 cm, FOV=2.96 mrad, Apod.=Triangular
Normalized Intensity I
1.2
1.1
1.0
0.9
0.8
3304.6
3305.0
3305.4
3305.8
3306.2
3306.6
Wavenumber ν in cm⁻¹
solar +0.27
O3 +0.25
N2O +0.23
HCN +0.21
C2H2 +0.18
H217O +0.13
H218O +0.09
CO2 +0.06
H216O +0.04
Experiment

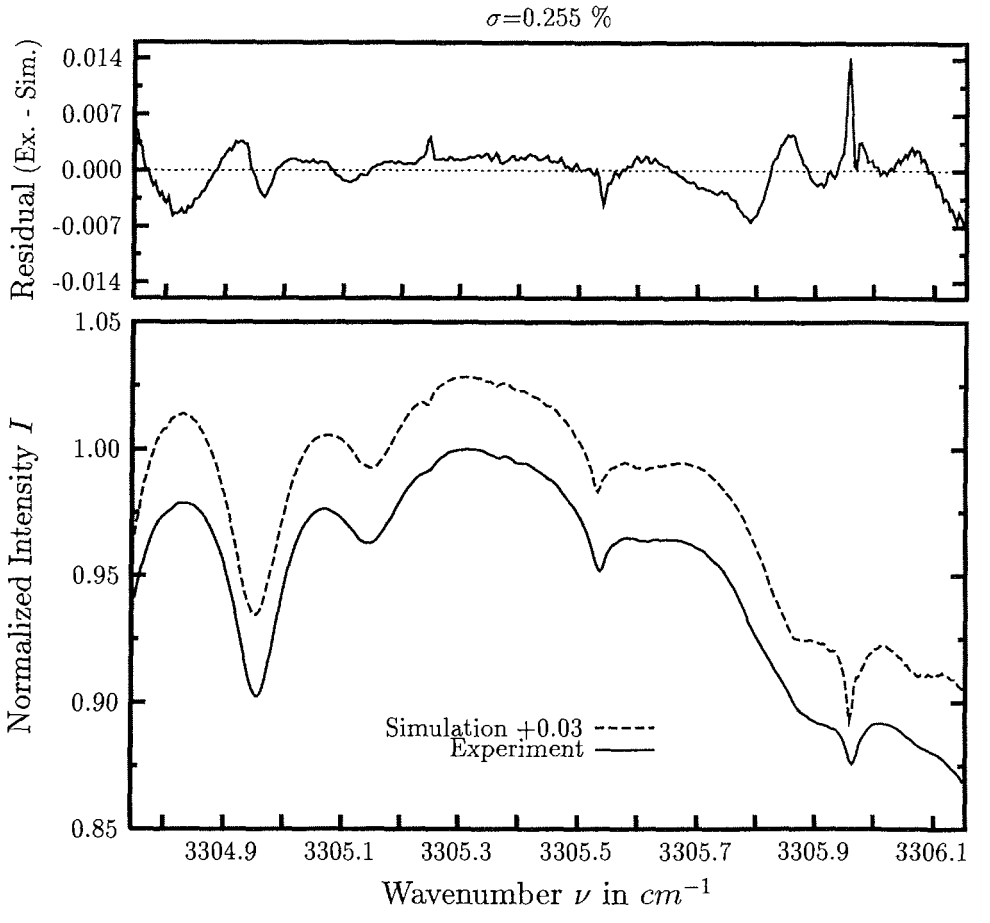

investigated species	: **C_2H_2, HCN, $H_2{}^{17}O$**
line position ν_0	: 3304.965, 3305.544, 3305.877 cm^{-1}
major species	: CO_2, H_2O, $H_2{}^{18}O$, $H_2{}^{17}O$, C_2H_2, HCN
minor species	: N_2O, O_3
weak species	: solar
name of the spectrum	: 95031814
zenith angle, apodization	: 83.4°, boxcar
max. OPD, field of view	: 90.0 cm, 2.96 $mrad$
spectral interval fitted	: 3304.75 – 3306.15 cm^{-1}
retrieved total column	: $3.67 \cdot 10^{15}\ cm^{-2}$, $9.35 \cdot 10^{15}\ cm^{-2}$

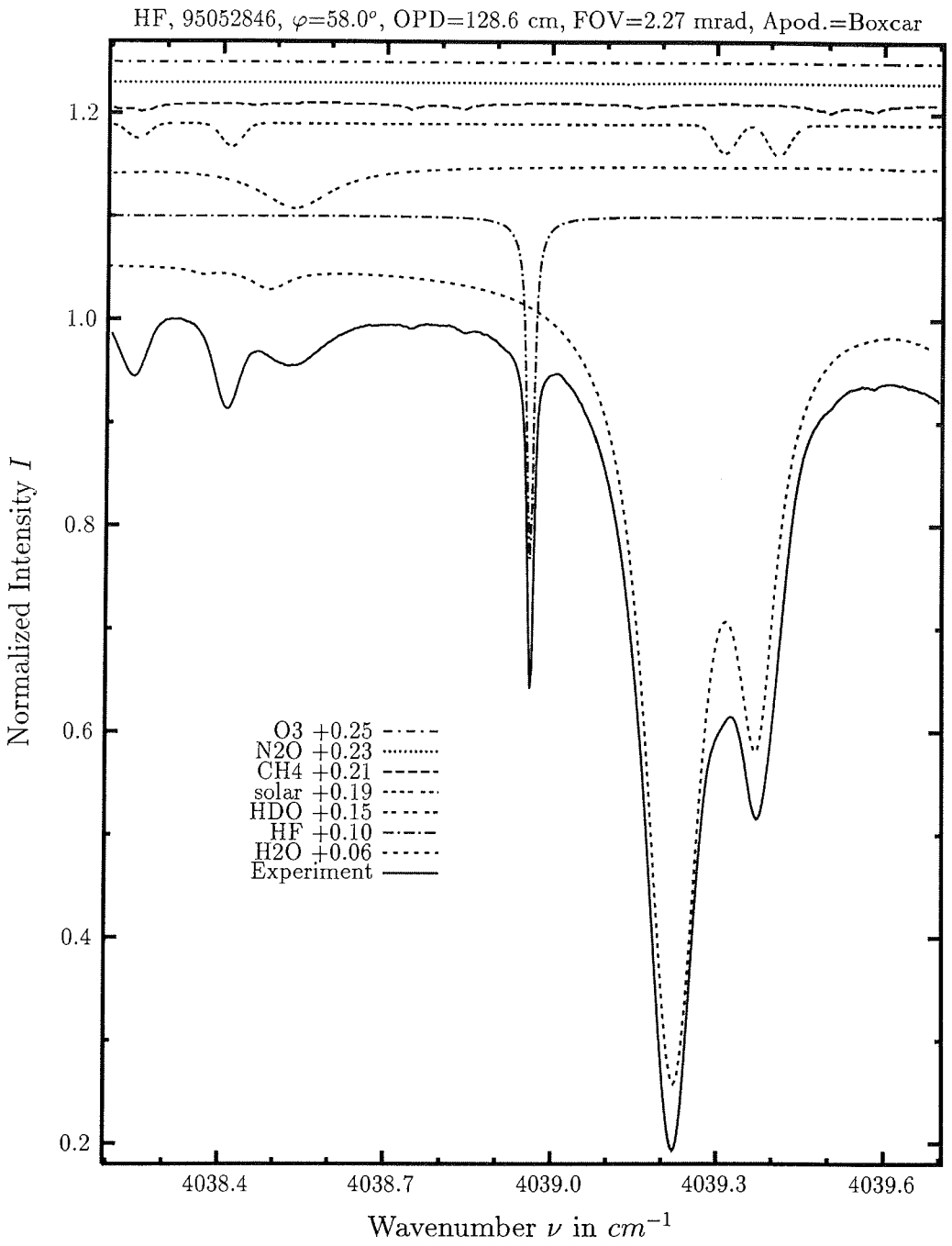
HF, 95052846, φ=58.0°, OPD=128.6 cm, FOV=2.27 mrad, Apod.=Boxcar
Normalized Intensity I
1.2
1.0
0.8
0.6
0.4
0.2
O3 +0.25
N2O +0.23
CH4 +0.21
solar +0.19
HDO +0.15
HF +0.10
H2O +0.06
Experiment
4038.4
4038.7
4039.0
4039.3
4039.6
Wavenumber ν in cm⁻¹

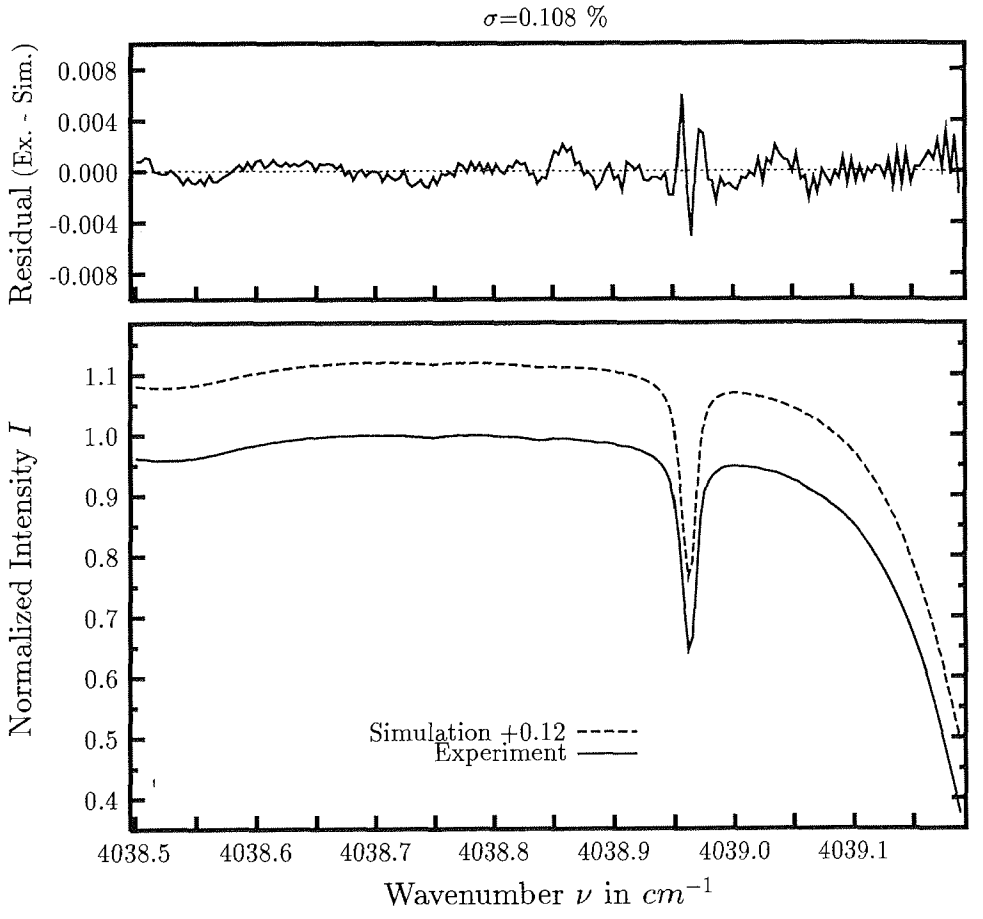

investigated species	: **HF**
line position ν_0	: 4038.963 cm^{-1}
major species	: H_2O, HF, HDO, solar
minor species	: CH_4
weak species	: N_2O, O_3, CO
name of the spectrum	: 95052842
zenith angle, apodization	: 58.2°, boxcar
max. OPD, field of view	: 128.6 cm, 2.27 $mrad$
spectral interval fitted	: I) 4038.00 – 4040.05 cm^{-1}, II) 4038.50 – 4039.19 cm^{-1}
retrieved total column	: $1.67 \cdot 10^{15}$ cm^{-2}

Folgende Hefte der Reihe „Berichte zur Polarforschung" sind bisher erschienen:

* **Sonderheft Nr. 1/1981** – „Die Antarktis und ihr Lebensraum",
Eine Einführung für Besucher – Herausgegeben im Auftrag von SCAR
Heft Nr. 1/1982 – „Die Filchner-Schelfeis-Expedition 1980/81",
zusammengestellt von Heinz Kohnen
* **Heft Nr. 2/1982** – „Deutsche Antarktis-Expedition 1980/81 mit FS 'Meteor'",
First International BIOMASS Experiment (FIBEX) – Liste der Zooplankton- und Mikronektonnetzfänge
zusammengestellt von Norbert Klages
Heft Nr. 3/1982 – „Digitale und analoge Krill-Echolot-Rohdatenerfassung an Bord des Forschungsschiffes 'Meteor'" (im Rahmen von FIBEX 1980/81, Fahrtabschnitt ANT III), von Bodo Morgenstern
Heft Nr. 4/1982 – „Filchner-Schelfeis-Expedition 1980/81",
Liste der Planktonfänge und Lichtstärkemessungen
zusammengestellt von Gerd Hubold und H. Eberhard Drescher
* **Heft Nr. 5/1982** – „Joint Biological Expedition on RRS 'John Biscoe', February 1982",
by G. Hempel and R. B. Heywood
* **Heft Nr. 6/1982** – „Antarktis-Expedition 1981/82 (Unternehmen 'Eiswarte')",
zusammengestellt von Gode Gravenhorst
Heft Nr. 7/1982 – „Marin-Biologisches Begleitprogramm zur Standorterkundung 1979/80 mit MS 'Polarsirkel' (Pre-Site Survey)" – Stationslisten der Mikronekton- und Zooplanktonfänge sowie der Bodenfischerei
zusammengestellt von R. Schneppenheim
Heft Nr. 8/1983 – „The Post-Fibex Data Interpretation Workshop",
by D. L. Cram and J.-C. Freytag with the collaboration of J. W. Schmidt, M. Mall, R. Kresse, T. Schwinghammer
* **Heft Nr. 9/1983** – „Distribution of some groups of zooplankton in the inner Weddell Sea in summer 1979/80",
by I. Hempel, G. Hubold, B. Kaczmaruk, R. Keller, R. Weigmann-Haass
Heft Nr. 10/1983 – „Fluor im antarktischen Ökosystem" – DFG-Symposium November 1982
zusammengestellt von Dieter Adelung
Heft Nr. 11/1983 – „Joint Biological Expedition on RRS 'John Biscoe', February 1982 (II)",
Data of micronecton and zooplankton hauls, by Uwe Piatkowski
Heft Nr. 12/1983 – „Das biologische Programm der ANTARKTIS-I-Expedition 1983 mit FS 'Polarstern'",
Stationslisten der Plankton-, Benthos- und Grundschleppnetzfänge und Liste der Probennahme an Robben und Vögeln, von H. E. Drescher, G. Hubold, U. Piatkowski, J. Plötz und J. Voß
* **Heft Nr. 13/1983** – „Die Antarktis-Expedition von MS 'Polarbjörn' 1982/83" (Sommerkampagne zur Atka-Bucht und zu den Kraul-Bergen), zusammengestellt von Heinz Kohnen
* **Sonderheft Nr. 2/1983** – „Die erste Antarktis-Expedition von FS 'Polarstern' (Kapstadt, 20. Januar 1983 – Rio de Janeiro, 25. März 1983)", Bericht des Fahrtleiters Prof. Dr. Gotthilf Hempel
Sonderheft Nr. 3/1983 – „Sicherheit und Überleben bei Polarexpeditionen",
zusammengestellt von Heinz Kohnen
* **Heft Nr. 14/1983** – „Die erste Antarktis-Expedition (ANTARKTIS I) von FS 'Polarstern' 1982/83",
herausgegeben von Gotthilf Hempel
Sonderheft Nr. 4/1983 – „On the Biology of Krill *Euphausia superba*" – Proceedings of the Seminar and Report of the Krill Ecology Group, Bremerhaven 12.-16. May 1983, edited by S. B. Schnack
Heft Nr. 15/1983 – „German Antarctic Expedition 1980/81 with FRV 'Walther Herwig' and RV 'Meteor'" – First International BIOMASS Experiment (FIBEX) – Data of micronekton and zooplankton hauls
by Uwe Piatkowski and Norbert Klages
Sonderheft Nr. 5/1984 – „The observatories of the Georg von Neumayer Station", by Ernst Augstein
Heft Nr. 16/1984 – „FIBEX cruise zooplankton data",
by U. Piatkowski, I. Hempel and S. Rakusa-Suszczewski
Heft Nr. 17/1984 – „Fahrtbericht (cruise report) der 'Polarstern'-Reise ARKTIS I, 1983",
von E. Augstein, G. Hempel und J. Thiede
Heft Nr. 18/1984 – „Die Expedition ANTARKTIS II mit FS 'Polarstern' 1983/84",
Bericht von den Fahrtabschnitten 1, 2 und 3, herausgegeben von D. Fütterer
Heft Nr. 19/1984 – „Die Expedition ANTARKTIS II mit FS 'Polarstern' 1983/84",
Bericht vom Fahrtabschnitt 4, Punta Arenas-Kapstadt (Ant-II/4), herausgegeben von H. Kohnen
Heft Nr. 20/1984 – „Die Expedition ARKTIS II des FS 'Polarstern' 1984, mit Beiträgen des FS 'Valdivia' und des Forschungsflugzeuges 'Falcon 20' zum Marginal Ice Zone Experiment 1984 (MIZEX)",
von E. Augstein, G. Hempel, J. Schwarz, J. Thiede und W. Weigel
Heft Nr. 21/1985 – „Euphausiid larvae in plankton samples from the vicinity of the Antarctic Peninsula, February 1982", by Sigrid Marschall and Elke Mizdalski